

## Part III

# Detector Components

# Contents

## III Detector Components

<b>3</b>	<b>Magnets, Toroids, and Beam Pipes</b>	<b>3-1</b>
3.1	Overview . . . . .	3-1
3.2	Requirements . . . . .	3-5
3.2.1	Requirements on the Vertex Magnet . . . . .	3-5
3.2.2	Requirements on the Toroid . . . . .	3-6
3.2.3	Beampipe Requirements . . . . .	3-6
3.2.4	Fault Tolerance . . . . .	3-7
3.2.5	Installation and Surveying . . . . .	3-8
3.2.6	Control and Monitoring . . . . .	3-8
3.2.7	Electrical Requirements . . . . .	3-9
3.2.8	ES&H Requirements . . . . .	3-9
3.2.9	Dependencies with Respect to Other Detectors . . . . .	3-9
3.3	Technical Description and Design of the Magnets, Toroids, and Beampipes . . . . .	3-10
3.3.1	Vertex Magnet . . . . .	3-10
3.3.2	Muon Toroids . . . . .	3-19
3.3.3	Beampipes . . . . .	3-31
3.4	Power Supply Summary . . . . .	3-33
3.5	Integration and Testing Plan . . . . .	3-34
3.5.1	Vertex Magnet tests and integration into the BTeV spectrometer . . . . .	3-35
3.5.2	Toroid tests and Integration into the BTeV spectrometer . . . . .	3-36
3.5.3	Tests and Integration of the beampipe sections into the BTeV spectrometer . . . . .	3-39
3.6	Completed and Planned R&D . . . . .	3-40
3.6.1	Vertex Magnet . . . . .	3-40
3.6.2	Muon Toroids . . . . .	3-40
3.6.3	Beampipes . . . . .	3-41
3.7	Vertical Trajectory of Beams in C0 . . . . .	3-41
<b>4</b>	<b>The Pixel Vertex Detector</b>	<b>4-1</b>
4.1	Introduction . . . . .	4-1
4.2	Requirements . . . . .	4-1

4.2.1	Resolution . . . . .	4-2
4.2.2	Efficiency . . . . .	4-2
4.2.3	Radiation Tolerance . . . . .	4-3
4.3	Overview . . . . .	4-3
4.4	Summary of completed R&D . . . . .	4-5
4.4.1	Introduction . . . . .	4-5
4.4.2	Sensor Development . . . . .	4-6
4.4.3	Pixel readout chip . . . . .	4-14
4.4.4	Bump bonding development . . . . .	4-21
4.4.5	Multichip Module . . . . .	4-24
4.4.6	RF shielding issues . . . . .	4-29
4.4.7	Mechanical support, cooling and vacuum system . . . . .	4-30
4.5	Technical Description . . . . .	4-45
4.5.1	Pixel Detector Specifications . . . . .	4-45
4.5.2	Front-end chip . . . . .	4-47
4.5.3	Sensor . . . . .	4-49
4.5.4	Bump Bonding . . . . .	4-51
4.5.5	Modules . . . . .	4-51
4.5.6	Readout and control . . . . .	4-53
4.5.7	Mechanical Support . . . . .	4-54
4.5.8	Vacuum vessel . . . . .	4-61
4.5.9	Cooling . . . . .	4-62
4.5.10	Vacuum system . . . . .	4-64
4.5.11	Feed-through board . . . . .	4-70
4.5.12	Actuators . . . . .	4-71
4.5.13	RF shielding . . . . .	4-72
4.5.14	Power distribution . . . . .	4-73
4.5.15	Control and Monitoring . . . . .	4-74
4.6	Ongoing Prototyping Efforts . . . . .	4-75
4.7	Production - QA and Testing . . . . .	4-77
4.7.1	Overview . . . . .	4-77
4.7.2	Sensor Tests . . . . .	4-78
4.7.3	Pixel Readout chips . . . . .	4-79
4.7.4	Bump Bonding . . . . .	4-79
4.7.5	HDI and interconnect flex cable . . . . .	4-80
4.7.6	Substrate . . . . .	4-80
4.7.7	Substrate support structure . . . . .	4-81
4.7.8	Feed-through board . . . . .	4-81
4.7.9	Database . . . . .	4-81
4.8	Performance . . . . .	4-82
4.8.1	Spatial Resolution . . . . .	4-82
4.8.2	Pattern Recognition Capability . . . . .	4-83

4.8.3	Radiation Hardness . . . . .	4-84
4.8.4	Material Thickness . . . . .	4-85
4.8.5	Readout Speed . . . . .	4-85
4.8.6	Physics Capability . . . . .	4-86
4.9	Cost, schedule and Risk analysis . . . . .	4-86
4.9.1	Cost . . . . .	4-86
4.9.2	Schedule . . . . .	4-86
4.9.3	Production Risk Analysis . . . . .	4-87
4.9.4	Operation Risk Analysis . . . . .	4-90
<b>5</b>	<b>Charged Particle Identification System</b>	<b>5-1</b>
5.1	Introduction . . . . .	5-1
5.2	Requirements . . . . .	5-2
5.2.1	Physics Requirements . . . . .	5-2
5.2.2	Radiation hardness . . . . .	5-3
5.2.3	Geometrical Requirements . . . . .	5-3
5.2.4	Mirror Requirements . . . . .	5-3
5.2.5	Electronics Requirements . . . . .	5-4
5.2.6	Readout Requirements . . . . .	5-5
5.2.7	Electrical and magnetic interference . . . . .	5-6
5.2.8	Mechanical Properties of the front end hybrids . . . . .	5-6
5.2.9	Cooling System . . . . .	5-6
5.2.10	Gas and Liquid Systems . . . . .	5-6
5.2.11	Power Supplies . . . . .	5-7
5.2.12	Monitoring . . . . .	5-7
5.2.13	Electrical Requirements . . . . .	5-8
5.2.14	Electronics Protection . . . . .	5-8
5.2.15	Functional Requirements . . . . .	5-8
5.2.16	Requirements on Rest of BTeV . . . . .	5-8
5.3	Technical Description . . . . .	5-9
5.3.1	Selection of RICH Radiators . . . . .	5-9
5.3.2	Liquid Radiator . . . . .	5-15
5.3.3	Gas Radiator . . . . .	5-15
5.3.4	Mirrors . . . . .	5-18
5.3.5	Photodetector Planes and Tank Structure . . . . .	5-21
5.3.6	Photodetectors for the $C_4F_8O$ radiator . . . . .	5-22
5.3.7	Photodetectors for the $C_5F_{12}$ Liquid Radiator . . . . .	5-30
5.3.8	Power Supplies . . . . .	5-32
5.3.9	Monitoring . . . . .	5-33
5.4	Completed R & D . . . . .	5-34
5.4.1	Development of MAPMT System for the Gas Radiator . . . . .	5-34
5.4.2	Development of HPD System for the Gas Radiator . . . . .	5-45



5.4.3	Mirrors . . . . .	5-51
5.4.4	Liquid Radiator . . . . .	5-58
5.4.5	Radiation Damage Studies . . . . .	5-63
5.5	Planned R&D . . . . .	5-64
5.5.1	Further Beam Test of the Gas Radiator RICH . . . . .	5-64
5.5.2	Beam Test of the Liquid Radiator RICH . . . . .	5-65
5.5.3	R&D on Mirrors . . . . .	5-65
5.5.4	Mirror And MAPMT Plane Alignment . . . . .	5-67
5.6	Production Quality Assurance and Testing . . . . .	5-72
5.6.1	Photon Detectors for Gas System . . . . .	5-72
5.6.2	Single Anode PMT Tests for Liquid System . . . . .	5-76
5.6.3	Readout Electronics . . . . .	5-76
5.6.4	Mirror Tile testing . . . . .	5-78
5.6.5	Liquid and Gas Radiators . . . . .	5-78
5.6.6	Testing of High and Low Voltage Power Supplies . . . . .	5-78
5.6.7	High and Low Voltage Cables . . . . .	5-80
5.6.8	MAPMT and PMT Electronics Cooling Cooling System . . . . .	5-80
5.7	Expected Performance of the RICH . . . . .	5-80
5.7.1	Detector Simulations . . . . .	5-81
5.7.2	Signal Simulations . . . . .	5-93
<b>6</b>	<b>Electromagnetic Calorimeter</b>	<b>6-1</b>
6.1	General Overview . . . . .	6-1
6.2	Basic Requirements . . . . .	6-3
6.3	Lead Tungstate Crystals . . . . .	6-4
6.3.1	Test Bench Measurements . . . . .	6-7
6.3.2	IHEP Test Beam Facility . . . . .	6-11
6.3.3	Resolutions . . . . .	6-11
6.3.4	Light response non-uniformity . . . . .	6-15
6.3.5	Radiation Hardness . . . . .	6-20
6.3.6	Crystal Specification . . . . .	6-32
6.4	Photodetectors and Read-out Electronics . . . . .	6-34
6.4.1	Photomultipliers . . . . .	6-34
6.4.2	PMT gain variations and monitoring . . . . .	6-36
6.4.3	High Voltage Distribution System . . . . .	6-38
6.4.4	Front-End Electronics . . . . .	6-38
6.5	Calibration and Light Monitoring System . . . . .	6-44
6.5.1	Energy Calibration using Electrons . . . . .	6-44
6.5.2	Light Pulser System . . . . .	6-48
6.5.3	Light Monitoring System for BTeV Calorimeter . . . . .	6-53
6.6	Mechanical Structure . . . . .	6-59
6.6.1	Cooling and Humidity Control System . . . . .	6-61

6.7	Detector Assembly, Installation and Integration . . . . .	6-62
6.7.1	Testing Prior to Moving to C0 . . . . .	6-63
6.7.2	Transportation of Elements to C0 . . . . .	6-63
6.8	Detector Performance . . . . .	6-64
6.8.1	ECAL Simulation . . . . .	6-64
6.8.2	Photon and $\pi^0$ 's Reconstruction Procedure . . . . .	6-65
6.8.3	Physics Simulation . . . . .	6-67
6.9	Schedule and Costs . . . . .	6-74
6.9.1	Planning . . . . .	6-74
6.9.2	Costs . . . . .	6-74
6.10	Organization . . . . .	6-74
6.10.1	Participating institutes . . . . .	6-74
6.10.2	Responsibilities . . . . .	6-75
<b>7</b>	<b>Muon Detector</b>	<b>7-1</b>
7.1	Introduction . . . . .	7-1
7.2	Muon System Overview . . . . .	7-1
7.2.1	General design considerations . . . . .	7-1
7.2.2	Baseline muon system . . . . .	7-2
7.3	Requirements for the BTeV Muon System . . . . .	7-4
7.3.1	Physics requirements . . . . .	7-5
7.3.2	Toroid requirements . . . . .	7-5
7.3.3	Proportional tube performance requirements . . . . .	7-5
7.3.4	Detector installation and support requirements . . . . .	7-6
7.3.5	Geometry requirements . . . . .	7-6
7.3.6	Correction dipole requirements . . . . .	7-6
7.3.7	Control and monitoring . . . . .	7-7
7.3.8	Software requirements . . . . .	7-7
7.3.9	ES&H requirements . . . . .	7-8
7.3.10	Electrical requirements . . . . .	7-8
7.3.11	Front-end electronics requirements . . . . .	7-8
7.3.12	Internal Interlocks . . . . .	7-9
7.4	Technical Description . . . . .	7-9
7.4.1	Muon detectors . . . . .	7-10
7.4.2	Front-end electronics . . . . .	7-11
7.4.3	Mounting, support, and infrastructure . . . . .	7-12
7.5	Design trade-offs . . . . .	7-17
7.5.1	Magnetized vs. non-magnetized toroids . . . . .	7-17
7.6	Past Research and Development Work . . . . .	7-19
7.6.1	Summer 1999 beam test . . . . .	7-19
7.6.2	Plank design/construction . . . . .	7-19
7.6.3	Plank and gas tests . . . . .	7-22

7.6.4	Construction database . . . . .	7-22
7.6.5	Wire tension measurement . . . . .	7-22
7.6.6	Detector construction and support . . . . .	7-23
7.6.7	Front-end electronics . . . . .	7-25
7.7	Planned Research and Development Work . . . . .	7-27
7.7.1	MTEST beam test . . . . .	7-27
7.7.2	High dose test . . . . .	7-29
7.7.3	Prototype electronics and plank interface . . . . .	7-30
7.7.4	Mechanical refinements and tests . . . . .	7-31
7.7.5	Octant test stand . . . . .	7-32
7.7.6	Plank construction jig . . . . .	7-34
7.7.7	Prototype gas system . . . . .	7-34
7.7.8	C0 background studies . . . . .	7-34
7.7.9	Simulation and reconstruction work . . . . .	7-35
7.8	Production Plan . . . . .	7-35
7.8.1	Construction overview . . . . .	7-36
7.8.2	Plank fabrication . . . . .	7-39
7.8.3	Fabrication of manifolds, support ribs, and Delrin inserts . . . . .	7-40
7.8.4	Electronics QAP . . . . .	7-42
7.8.5	Octant assembly and QAP . . . . .	7-43
7.9	Installation, Integration and Testing Plans (at C0) . . . . .	7-43
7.9.1	Transportation of muon detector octants to C0 . . . . .	7-43
7.9.2	Installation of muon system elements at C0 . . . . .	7-44
7.9.3	Testing of muon system elements at C0 . . . . .	7-47
7.10	Performance . . . . .	7-48
7.10.1	Occupancies . . . . .	7-48
7.10.2	Dimuon trigger . . . . .	7-50
7.11	Test Results . . . . .	7-50
<b>8</b>	<b>Forward Straw Detector</b>	<b>8-1</b>
8.1	Introduction . . . . .	8-1
8.2	Requirements . . . . .	8-1
8.3	Baseline Design . . . . .	8-2
8.4	Detector Components . . . . .	8-2
8.4.1	Module Description . . . . .	8-2
8.4.2	Module Components . . . . .	8-4
8.4.3	Half-view frame description . . . . .	8-9
8.4.4	Half-view frame components . . . . .	8-10
8.4.5	Special Module for Forward Silicon support . . . . .	8-16
8.4.6	Station 7 . . . . .	8-16
8.4.7	Beam-Line Supports . . . . .	8-18
8.4.8	Material Budget . . . . .	8-20

8.5	Calibration, Monitoring and Control Systems . . . . .	8-21
8.5.1	Straw Gas System . . . . .	8-21
8.5.2	Water Cooling System . . . . .	8-23
8.5.3	Environmental Control and Monitoring . . . . .	8-24
8.6	Performance . . . . .	8-24
8.6.1	Resolution . . . . .	8-24
8.6.2	Occupancy and Tracking efficiency . . . . .	8-24
8.7	Front-End Electronics . . . . .	8-28
8.7.1	Introduction . . . . .	8-28
8.7.2	Anode Pinning Plate (APP) . . . . .	8-28
8.7.3	High Voltage Network Card (HVNC) . . . . .	8-29
8.7.4	High Voltage/Low Voltage Bus (HVLVB) . . . . .	8-30
8.7.5	Preamplifier/Discriminator Card (PDC) . . . . .	8-30
8.7.6	Time to Digital Converter Card (TDCC) . . . . .	8-31
8.7.7	TDC ASIC . . . . .	8-32
8.7.8	I/O Interface . . . . .	8-33
8.7.9	Data Combiner Board (DCB) - Straw Daughter Card . . . . .	8-41
8.7.10	Straw High Voltage System . . . . .	8-42
8.7.11	Straw Low Voltage System . . . . .	8-42
8.8	Installation, Integration and Testing Plans . . . . .	8-43
8.8.1	Summary of Testing Prior to Moving to C0 . . . . .	8-43
8.8.2	Transportation of Straw Detector Equipment to C0 . . . . .	8-43
8.8.3	Installation of Straw Detector at C0 . . . . .	8-43
8.8.4	Testing at C0 . . . . .	8-45
8.9	R&D , Open Design Issues . . . . .	8-45
8.9.1	Prototype Detector . . . . .	8-45
8.9.2	Straw Material . . . . .	8-46
8.9.3	Gas Studies . . . . .	8-47
8.9.4	Aging studies . . . . .	8-58
8.9.5	Capillary Fusing . . . . .	8-62
8.9.6	Magnetic Field Effects . . . . .	8-67
8.9.7	Beam Test Results . . . . .	8-68
8.10	Production, Production Testing, and Quality Assurance Plan . . . . .	8-76
8.10.1	Straw Preparation Site . . . . .	8-76
8.10.2	Anode Preparation Site . . . . .	8-76
8.10.3	Module Assembly Sites, including MOX-Silicon Support . . . . .	8-76
8.10.4	Half-View Assembly Sites . . . . .	8-77
8.10.5	Electronics Sites . . . . .	8-77
8.10.6	Survey Site . . . . .	8-78
8.10.7	Gas and Environmental Monitoring Site . . . . .	8-78
8.10.8	Other Systems . . . . .	8-79
8.10.9	Various tooling and fixtures . . . . .	8-79

8.10.10	Test Beam Studies . . . . .	8-79
<b>9</b>	<b>Forward Silicon Tracker</b>	<b>9-1</b>
9.1	Introduction . . . . .	9-1
9.2	Forward Silicon Tracker general requirements . . . . .	9-2
9.2.1	Resolution and mass . . . . .	9-3
9.2.2	Read Out . . . . .	9-3
9.2.3	Radiation hardness . . . . .	9-4
9.2.4	Dimensions . . . . .	9-4
9.2.5	Electrical & Magnetic Interference . . . . .	9-5
9.3	Sensors . . . . .	9-5
9.4	Electronic read out . . . . .	9-8
9.4.1	Read out chip . . . . .	9-8
9.5	Hybrids and Flex cables . . . . .	9-15
9.6	Mechanical support and cooling system . . . . .	9-17
9.6.1	Requirements . . . . .	9-17
9.6.2	Implementation . . . . .	9-19
9.6.3	Fiber grating positioning monitor . . . . .	9-22
9.6.4	Cooling system . . . . .	9-24
9.7	R & D . . . . .	9-26
9.7.1	Sensors characterization and irradiation tests . . . . .	9-26
9.8	DAQ system for tests and production . . . . .	9-32
9.8.1	Introduction . . . . .	9-32
9.8.2	Description . . . . .	9-32
9.9	Forward Silicon Tracker Production Plan . . . . .	9-36
9.9.1	Introduction . . . . .	9-36
9.9.2	Logical Organization of the Production . . . . .	9-37
9.9.3	Half-Plane Production . . . . .	9-37
9.9.4	External Support Mechanics . . . . .	9-40
9.9.5	Cooling System . . . . .	9-41
9.9.6	External Cables . . . . .	9-41
9.9.7	Low & High Voltage Power Supplies . . . . .	9-41
9.9.8	Junction Cards . . . . .	9-41
9.9.9	Data Combiner Boards . . . . .	9-41
9.10	Installation, Integration and Testing Plans (at C0) for the Forward Silicon Tracker . . . . .	9-42
9.10.1	Introduction . . . . .	9-42
9.10.2	Preliminary installation of the Forward Silicon Tracker services . . . . .	9-42
9.10.3	Summary of Testing Prior to Moving to C0 . . . . .	9-43
9.10.4	Transportation of Level 2 Subproject Elements to C0 . . . . .	9-43
9.10.5	Installation of Level 2 Subproject Elements at C0 . . . . .	9-44
9.10.6	Testing at C0 . . . . .	9-45

<b>10 Front End Electronics</b>	<b>10-1</b>
10.1 Introduction . . . . .	10-1
10.2 Pixel Detector . . . . .	10-2
10.2.1 Overview . . . . .	10-2
10.2.2 Component Quantities and Locations . . . . .	10-3
10.2.3 Data Structure . . . . .	10-3
10.2.4 Occupancy and Data Rate Estimate . . . . .	10-3
10.2.5 Initialization, Control, and Monitoring . . . . .	10-5
10.3 RICH Detector . . . . .	10-5
10.3.1 Overview . . . . .	10-5
10.3.2 Component Quantities . . . . .	10-6
10.3.3 Data structure . . . . .	10-7
10.3.4 Occupancy and Data Rate Studies . . . . .	10-8
10.3.5 Initialization, Control and Monitoring . . . . .	10-8
10.4 Electromagnetic Calorimeter . . . . .	10-9
10.4.1 Overview . . . . .	10-9
10.4.2 Component Quantities and Locations . . . . .	10-10
10.4.3 Data Structure . . . . .	10-10
10.4.4 Occupancy and Data Rate Estimate . . . . .	10-11
10.4.5 Initialization, Control, and Monitoring . . . . .	10-11
10.5 Muon Detector . . . . .	10-12
10.5.1 Overview . . . . .	10-12
10.5.2 Component Quantities and Locations . . . . .	10-12
10.5.3 Data Structure . . . . .	10-12
10.5.4 Occupancy and Data Rate Estimate . . . . .	10-14
10.5.5 Installation, Control and Monitoring . . . . .	10-15
10.6 Forward Straw Detector . . . . .	10-15
10.6.1 Overview . . . . .	10-15
10.6.2 Component Quantities and Locations . . . . .	10-16
10.6.3 Data Structure . . . . .	10-17
10.6.4 Occupancy and Data Rate Estimate . . . . .	10-17
10.6.5 Initialization, Control, and Monitoring . . . . .	10-18
10.7 Forward Silicon Detector . . . . .	10-18
10.7.1 Overview . . . . .	10-18
10.7.2 Component Quantities and Locations . . . . .	10-19
10.7.3 Data Structure . . . . .	10-19
10.7.4 Occupancy and Data Rate Estimate . . . . .	10-19
10.7.5 Initialization, Control, and Monitoring . . . . .	10-20
10.8 Data Rate Summary . . . . .	10-21

# Chapter 3

## Magnets, Toroids, and Beam Pipes

### 3.1 Overview

Three large extended mechanical assemblies dominate the layout of the BTeV spectrometer: the Vertex Magnet (dipole), the muon toroids, and the Tevatron beampipe. Their location in the C0 Collision Hall and their relation to the other detector components is shown in Figs. 3.1 and 3.2. The active detector elements of the spectrometer must be designed to fit within the constraints presented by these three components.

The Vertex Magnet in the BTeV spectrometer provides the magnetic field around the Tevatron collision point that enables the silicon pixel detector to determine both the direction and momentum of particles produced in the proton-antiproton collisions. This is essential for the proposed displaced vertex trigger to work. The forward tracker uses the full field volume from the particle interaction to the end of the magnet, including the field beyond the pixel detector, to produce an even better measurement of the momentum than is possible with just the pixel detector alone.

The Vertex Magnet is based on the existing SM3 magnet (currently part of the decommissioned Fermilab MEast Spectrometer). The magnet operated in MEast from 1982 until 1997, at a central field of about 0.8 Tesla, serving experiments E605, E772, E789, and E866. This magnet is shown in its current form in Fig. 3.3.

The SM3 magnet was assembled by welding together, in place, various blocks of iron recovered from the Nevis Cyclotron. It has a total weight of 500 metric tons. After disassembly and transport to C0, the magnet, modified by the addition of pole-piece shims, will be reassembled in the C0 Assembly Hall and rolled into the C0 Collision Hall.

Studies with magnetostatic modeling programs have led to a design for new pole-piece inserts for SM3. These pole-pieces yield a central field of 1.6 Tesla, and an integrated dipole field of 5.2 T-m. The magnet will be oriented so that charged particles are deflected in the vertical plane. The vertical deflection of the Tevatron beam by the Vertex Magnet is compensated by two conventional dipoles at each end of the Collision Hall.

The two muon toroids at the north end of the Collision Hall provide the bend field that enables the muon chambers to detect and determine the momentum of energetic muons from

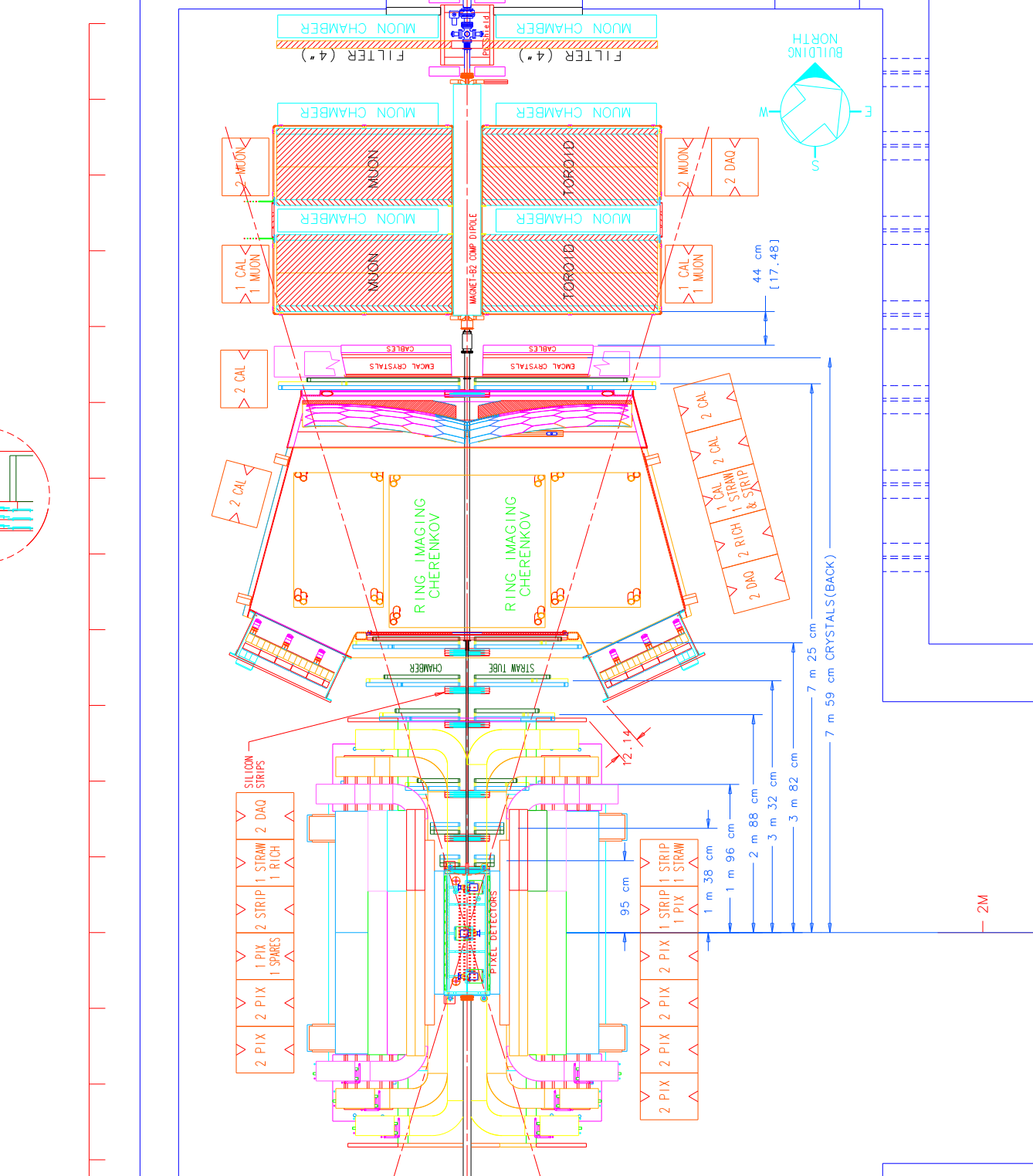


Figure 3.1: Plan view of BTeV Detector showing mechanical details that emphasize the relation of the Vertex Magnet, Beam Pipes and Toroids to the other detector components



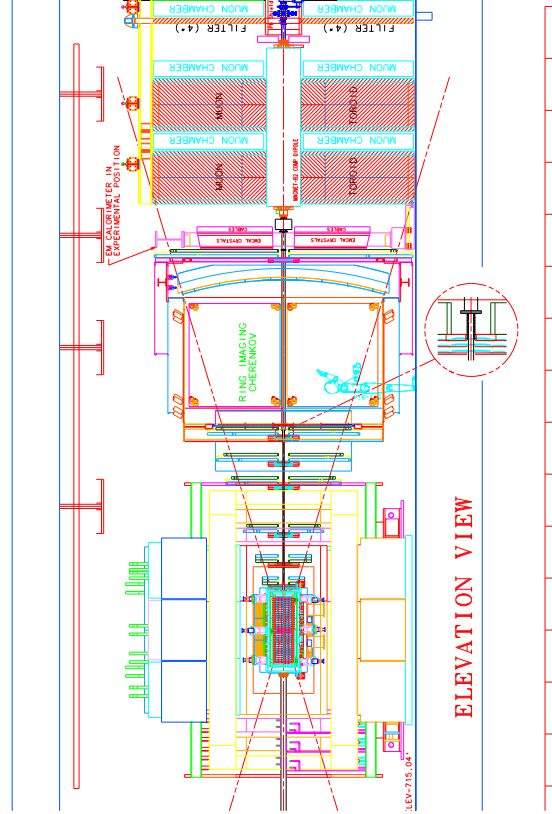


Figure 3.2: Elevation view of BTeV Detector showing mechanical details that emphasize the relation of the Vertex Magnet, Beam Pipes and Toroids to the other detector components

the collision point. The toroids at both the north and south end of the Collision Hall provide support for the compensating dipoles. Both the north and south pair of toroids also provide the absorber material that prevents hadrons, electrons and photons from penetrating and registering in the muon detectors. To provide both a large integrated magnetic field and enough absorption of hadrons, each toroid is constructed of a meter thick soft iron core energized by a pair of coils that span both toroids in the pair. The iron slabs that form the toroids will be recovered from the existing SM12 magnet in the MEast Spectrometer.

The beampipe provides the vacuum for, and encloses, the circulating Tevatron proton and antiproton beams. It must be able to conduct the wall current associated with the circulating beams. It must also be as thin as possible in order to minimize the reinteraction



Figure 3.3: Photograph of the SM3 dipole as it currently exists in the Meson Area at Fermilab

of particles emanating from the collision point. The plan is to construct the beampipe in sections. The 1" diameter beampipe in the region of the forward tracking chambers will be made by modifying the existing CDF RunIIb beryllium beam pipe. The 2" diameter beampipe inside the RICH detector will be made by modifying the existing CDF Run I beryllium beampipe.

Since the Vertex Magnet and muon toroids are very large assemblies, they will be assembled in the C0 assembly building and rolled into the C0 Collision Hall.

## 3.2 Requirements

This section describes the high level requirements for the BTeV Vertex Magnet (VM), Toroid Magnets (TM) and Beampipes (BP). The purpose of the VM is to provide a strong uniform magnetic field in the region of the silicon pixel detector in order to allow the momentum of high-energy particles to be determined at the trigger level and to provide a large integrated magnetic field to provide excellent mass resolution for multibody decays of B hadrons when the pixel detector and forward tracker are used together to determine track momentum. The purpose of the TM is to provide a magnetized iron absorber that will absorb all hadrons emitted from the interaction region and hence will identify muons (since a muon is the only charged particle that can penetrate 2 meters of iron) and, by deflecting the muons magnetically, help confirm their momentum for purposes of triggering the data acquisition system. The purpose of the BP is to provide the high vacuum containment for the accelerator beams through the BTeV apparatus.

The current design of the BTeV detector has one spectrometer arm on the anti-proton side of a large vertex dipole magnet at the interaction point in C0. The Vertex Magnet provides a region of strong uniform magnetic field to house the silicon pixel vertex detector. The last detector station in the spectrometer is a muon detection station that includes large magnetized iron toroids. The Tevatron proton and antiproton beams are transported through the detector in a small diameter beampipe that must be kept as thin and lightweight as possible to minimize reinteraction of the secondary particles from the initial proton-antiproton collision.

### 3.2.1 Requirements on the Vertex Magnet

The silicon pixel vertex detector has a length of 1.23 m and extends to  $\pm 5$  cm transversely. A magnetic field of at least 15 kilogauss insures that the strength of the field does not dominate the fractional error in the determination of the momentum by the pixel detector. The silicon pixel detector is capable of making approximately a 2% measurement of particle momenta. Integrated field strength, along the z-axis, of at least 1.5 GeV/c is needed to achieve the planned momentum resolution, and hence mass resolution, of the BTeV spectrometer. An important constraint on the allowable field variation derives from the need to align the silicon pixels for each separate experimental run while the field is excited to full strength.

**Magnetic field strength:** The VM must develop a magnetic field of at least 15 kilogauss at the center and integrated field strength 5 T-m along the z-axis corresponding to a  $P_t$  kick of 1.5 GeV/c.

**Magnetic field uniformity:** The VM must produce a magnetic field that varies by less than 1% over the full extent of the silicon pixel detector in order to facilitate the determination of the pixel alignment constants. Provision must be made to measure the spatial variation of the VM magnetic field over the aperture of the spectrometer, before installation, to 0.2% accuracy relative to the maximum field value.

**Field non-linearities:** These must conform to Fermilab Tevatron standards [1].

**Lifetime:** The VM must be designed to operate (consistent with its design goals, and the need to ramp the magnet from low to full excitation for every collider store) over the expected lifetime of the experiment.

### 3.2.2 Requirements on the Toroid

Many physics studies in BTeV depend on accurate identification of muons by their ability to penetrate 2 meters of iron. There is also a requirement to implement a stand-alone muon trigger at Level 1, which requires the measurement of muon momenta, independent of the silicon pixels and forward tracking system.

**Magnetic field strength:** The TM must develop a magnetic field of at least 1.4 Tesla at all radii.

**Toroid size:** The TM must cover the full transverse size of the muon chambers.

**Toroid thickness:** The system of two toroids and one absorber in the muon detector must be a total of at least 12 hadronic interaction lengths thick (2.0 meters for iron).

**Field non-linearities:** These must conform to Fermilab Tevatron standards [1].

**Lifetime:** The TM must be designed to operate (consistent with its design goals) over the expected lifetime of the experiment.

### 3.2.3 Beampipe Requirements

The BTeV beampipe includes the large torispherical windows at the ends of the silicon pixel detector vacuum box. The instantaneous luminosity that the BTeV detector can handle will be limited by the background of tertiary particles arising from the reinteraction of secondary particles in the beampipe walls; thus they must be kept as thin as possible. In order to achieve maximum acceptance for B-hadron decay products, the beampipe should allow detectors to be placed at angles as small as 10 milliradians with respect to the collision point. The successful storage of protons and antiprotons in the accelerator, and the minimization of background interactions with residual gas, requires a very high vacuum in the beampipe.

**Beampipe wall thickness:** The BP walls must be thinner than 0.5 mm of Aluminum equivalent in both radiation and interaction length and have a straightness of better than 1 mm per meter. The BP torispherical window must be thinner than 1 mm of Aluminum equivalent.

**Beampipe vacuum:** The BP must reach a vacuum of less than  $10^{-8}$  torr when installed in the Tevatron.

**Beampipe radius:** The BP must have an ID of at least 24 mm and an OD of less than 27 mm for all longitudinal positions within 4 m of the interaction point. For the region between 4 m and the entrance to the compensating dipole at about  $z = 8$  m the ID must be at least 35 mm and the OD less than 55 mm. The flanges connecting the sections of the BP at  $z = 4$  m and at  $z = 7$  m must be as light and as thin as possible in order to minimize both the number of radiation lengths and interaction lengths seen by secondary particles.

**Robustness:** Since the BP will be exposed in some sections during normal usage, it should be protected from impacts by small or light objects that could result in its collapse.

### 3.2.4 Fault Tolerance

The VM, TM, and BP are the largest elements in the BTeV spectrometer and are the core and backbone of the BTeV spectrometer. Repairs to any one of them in the event of failure will be extremely disruptive, requiring the disassembly of many detector elements to facilitate repairs. Engineering and initial testing of these systems must address the need for these elements to function reliably throughout the entire BTeV program, which could be as long as ten years of operation.

**VM testing:** The VM coils must be renovated and tested to a power level 110% of normal excitation for a period of at least 24 hours.

Surface damage to the coils has been repaired in the past. A major internal coil failure in one of the six vertex magnet coils would require extensive burning and reinsulating of the coil. The option would exist to run the BTeV spectrometer with one coil disconnected, yielding a central field of about 1.35 Tesla, until a convenient Tevatron off period allowed such an extensive repair. Note that the largest flexing forces on the coil occur when the magnet power supply trips off (an event which has occurred about 100 times in the last 20 years). During normal Tevatron ramps the derivative of the current is an order of magnitude smaller than during a trip.

**TM testing:** The TM system must be run at a power level 110% of normal excitation for a period of at least 24 hours.

Since the toroid coils are individually insulated, and separated, repairs of a damaged coil would be simple if the damage was accessible. If the damage was inaccessible, the damaged coil could be removed from the circuit and the toroid would then run with a 4 in magnetic field.

**BP testing:** The failure of the BP would be particularly disruptive to both the BTeV detector and the Tevatron accelerator complex. The beampipe design must have a mechanical safety factor of 3. The BP must reach vacuum levels of less than  $10^{-8}$  torr in bench tests.

As described below, a beryllium beam pipe protection system will be implemented. In case of a failure of a beryllium section of the beam pipe, a conventional aluminum beam pipe can be substituted, with a small loss in sensitivity of the BTeV spectrometer, until the beam pipe can be rebuilt or replaced with a spare. We will also fabricate a spare 2" beryllium

beam pipe as part of the original beryllium beam pipe renovation in FY08. In addition we will purchase a spare 1" beryllium beam pipe in FY09.

### 3.2.5 Installation and Surveying

The VM and TM will be the first elements of the BTeV detector installed in the C0 Collision Hall. Their large weight will cause a general depression of the C0 Collision Hall with respect to the Tevatron accelerator. Since most of the BTeV detector systems will be mounted either directly on, or at least with reference to the VM, TM or BP, provision must be made for regular survey of the VM, TM and BP with respect to the Tevatron accelerator coordinates.

**Internal Survey:** A coordinate reference system for the BTeV detectors needs to exist, and be maintainable over the life of the experiment. This coordinate system should be anchored on the walls of the C0 Collision Hall but include the VM as a fundamental element in the primary coordinate system and survey. Provision must be made for easy accessibility to its primary survey reference fiducials throughout the course of the experiment.

**Installation of VM and TM:** It is anticipated that the VM and TM will be transported to the Collision Hall by sharing a common set of Hilman rollers. Thus provision must be made for subsequent small adjustments of their positions after initial installation.

**BP Survey:** The transverse position of the BP with respect to the Tevatron beam must be controlled and understood precisely. Provision must be made to locate and secure the BP position transversely to within 1 mm at all points between the Pixel detector and the RICH detector entrance and to 2 mm beyond this region.

### 3.2.6 Control and Monitoring

The electrical excitation levels of the VM and the TM, as well as the high vacuum status of the BP are of such critical importance to the operation of the Tevatron accelerator that the primary control and monitoring of these components will be under the control of the Fermilab Accelerator Division Main Control Room through the ACNET control system. Nevertheless, BTeV will also want to have an independent measure of these parameters available through the experiment monitoring and control system.

**VM, TM and BP Monitoring:** The excitation and status of the VM, TM, and BP will be controlled and monitored by the ACNET control system using standard Tevatron control systems and protocols. The BTeV experiment will indirectly monitor these systems through an interface to the ACNET control system.

**Alarms:** The BTeV detector control and monitoring system will include alarms and limits on the excitation and status of the VM, TM, and BP systems via the interface to the ACNET control system. It must also include Hall probe field measurements with 0.2% absolute accuracy and vacuum measurements with an accuracy of  $10^{-9}$  torr local to the BTeV experiment.

### 3.2.7 Electrical Requirements

Standard Accelerator Division high current power supplies will power the VM and TM. These supplies will be installed by, and maintained by, the Accelerator Division Power Supply Group following the electrical standards adopted by the Accelerator Division. Members of the BTeV group will not be allowed to service or modify these devices in any way. The power supply must excite the Vertex Magnet to 4200 Amps with a stability of 0.1% per hour.

**Compliance with Accelerator Division Electronics Standards:** The electrical excitation of the VM and TM will comply with the Accelerator Division Electrical Standards.

Vacuum pumps for the BP will be provided by the Accelerator Division and will be under the sole control of Accelerator Division personnel. Note that the vacuum inside the Pixel detector vacuum tank is provided by the BTeV group and is addressed in the Pixel section of the TDR.

**BP vacuum pump standards:** The BP vacuum pumps will be installed by Accelerator Division personnel according to Accelerator Division Electrical Standards.

### 3.2.8 ES&H Requirements

The VM, TM and BP will have stored energy (electrical, magnetic and vacuum) that could constitute safety hazards.

**Electrical safety:** All electrical aspects of the VM, TM and BP will conform to the Fermilab ES&H manual on electrical safety.

**Vacuum Safety:** All aspects of the BP system will conform to the Fermilab ES&H manual on Vacuum Systems.

### 3.2.9 Dependencies with Respect to Other Detectors

The designs of the VM and TM have been developed based on reusing existing components from the E866 experiment at Fermilab. The renovation, modification and testing of these components may uncover some restrictions on the design and operation of the VM and TM.

**Existing Components:** The performance envelope of the VM and TM will be sensitive to any problems that may be uncovered in the status of existing components from Fermilab experiment E866 that are to be reused. In particular, the fringe magnetic fields of the VM and TM may be large enough to effect the operation of some of the spectrometer elements thus necessitating the addition of soft iron shield plates to the TM and VM designs.

The BTeV collaboration has obtained possession of the 2" CDF Run I beryllium beam pipe and the 1" CDF Run IIb beryllium beam pipe. We will modify these beam pipes for use in the BTeV spectrometer.

### 3.2.9.1 Design Implications for other BTeV components

The VM and the TM determine the gross mechanical layout of the BTeV spectrometer and hence directly affect the design of all the detectors. The beam pipe and the Pixel vacuum tank are directly connected and hence the vacuum achieved in either is affected by both.

**Beryllium beampipes:** No spectrometer component can be designed to mount directly on the beampipe since the beryllium beam pipes are very thin and fragile.

**Vertex Magnet fringe field:** All spectrometer components must be designed to withstand the magnetic forces that occur on magnetic materials in the extensive fringe field region of the VM. In addition, all spectrometer components must be able to withstand the transient induced eddy current forces that occur on any electrically conducting material in the VM fringe field region when the VM is ramped to maximum current, or, more importantly, when it trips off.

## 3.3 Technical Description and Design of the Magnets, Toroids, and Beampipes

### 3.3.1 Vertex Magnet

A schematic of the BTeV Vertex Magnet is shown in Fig. 3.4. The magnet is modified from the SM3 magnet by the addition of new pole-piece inserts. The reason for this is to get higher field in the region of the silicon pixel vertex detector. This improves the resolution of the pixel detector's stand-alone momentum measurement. It also increases the integrated field, which improves the combined momentum measurement of the pixel system and the forward tracker.

With the pole-piece modifications shown, electrostatic, finite element analysis calculations predict a central field of 1.6 Tesla, and an integrated dipole field of 5.2 T-m. a number of different calculations have been made with variations of the gap in the pole inserts, and variations on the flux return plate configuration, in order to understand better the central field and the fringe field of this magnet near the RICH and EmCal photomultiplier tubes. The results of the electrostatic calculations have also been incorporated in the simulation codes used to predict the response of the BTeV spectrometer to the B-decay events of interest.

The magnet will be oriented so that charged particles are deflected in the vertical plane. The vertical deflection of the Tevatron beam by the Vertex Magnet is compensated by two conventional dipoles at each end of the spectrometer. This orientation is necessary to fit the BTeV spectrometer into the C0 Collision Hall while achieving the design acceptance. The basic physical characteristics of the Vertex Magnet are given in Table 3.1.

The magnet is centered on the interaction region thus creating the potential for two forward spectrometers but only one spectrometer is proposed at this time.

The steps required to turn SM3 into the BTeV Vertex Magnet and install it into the C0 Collision Hall are the following:



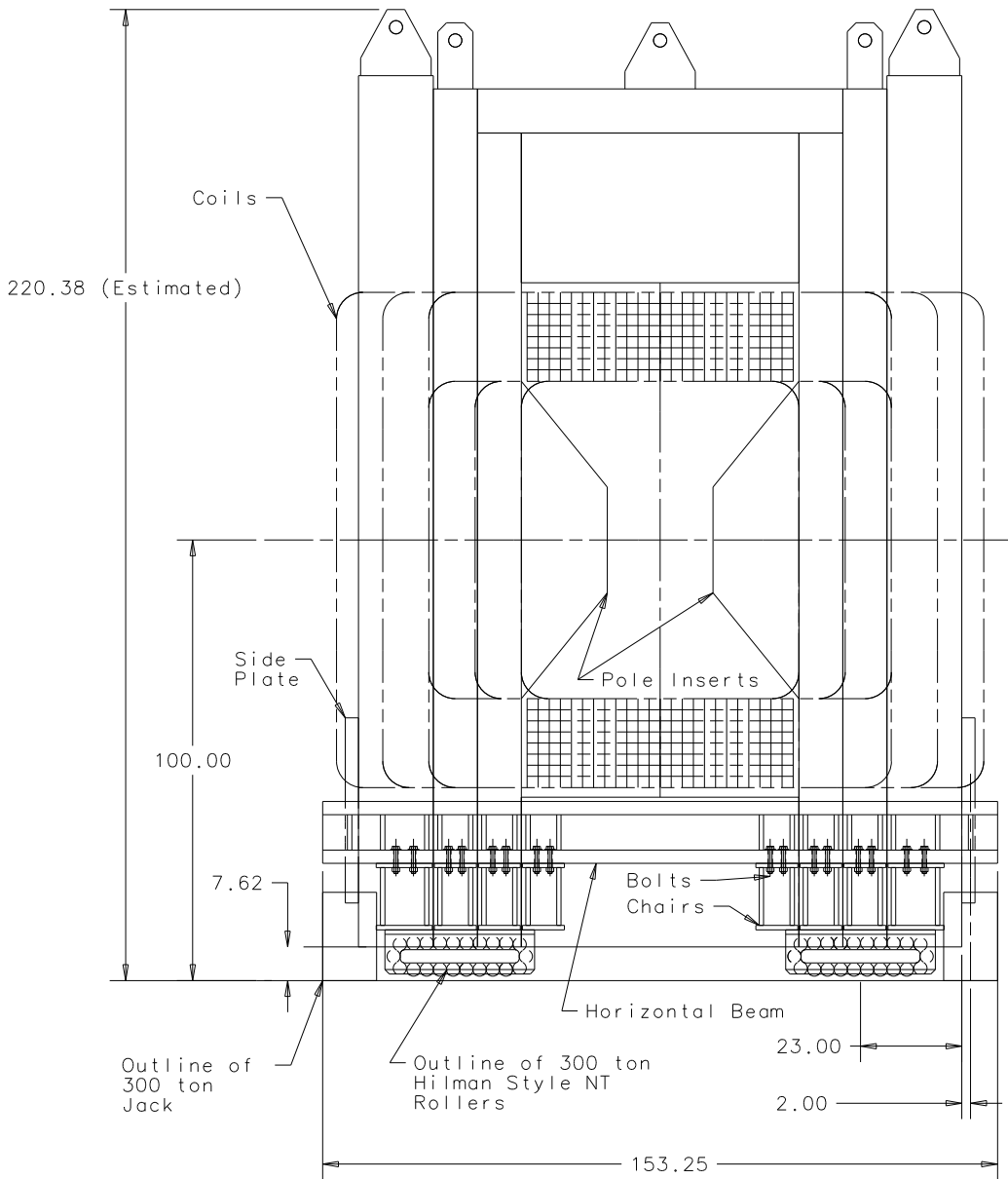


Figure 3.4: Cross section of the BTeV Vertex Magnet (modified SM3 dipole) with rollers and pole piece inserts. All dimensions are in inches.

Table 3.1: BTeV/C0 Vertex Magnet Properties

Property	Value	Comment
$\int B \times dl$	5.2 T-m	2.6 T-m on each side of center of IR
Central Field	1.6 Tesla	
Steel Length	3.2 m	
Overall length	5.3 m	
Magnet Vert. aperture	$\pm 0.3$ rad	
Magnet Horz. aperture	$\pm 0.3$ rad	

1. disassemble the existing SM3 magnet in the Meson Area Detector Building and transport the pieces to the C0 Assembly Hall;
2. procure the pole-piece shims and additional fixturing;
3. reassemble, with the new pole piece shims, the SM3 magnet using the C0 Assembly Hall crane;
4. hook the magnet to temporary utilities and protection systems and map its field; and
5. move the magnet into the Collision Hall and hook up its utilities and protection systems.

In the following, we describe each step of this process.

### 3.3.1.1 SM3 Disassembly sequence and Transportation to C0 Assembly Hall

In this section, the SM3 disassembly sequence is summarized. The steps are shown schematically in figures 3.5, through 3.12. An associated plan shows how each piece of SM3 will be stored in the C0 Assembly Hall to facilitate reassembly with the 30 ton crane. The step by step disassembly and storage plan is available elsewhere.

1. Disconnect water and power
2. Dismount the flux return plates, Fig. 3.5(left)
3. Remove spacer Posts, Fig. 3.5(right).
4. Install Coil Support Brackets, Fig. 3.6(left).

The weight of the coils and support plate are:

Item	Approximate Weight	Number
Inner Coil	5.5 tons	2
Middle Coil	6.0 tons	2
Outer Coil	6.5 tons	2
ASP	2.6 tons	
Total Coils and ASP	38.6 tons	

5. Remove first East yoke block, Fig. 3.6(left).
6. Remove second East yoke block, Fig. 3.6(right).
7. Remove East 10" thick pieces (2 pcs), Fig 3.7(left).
8. Remove upper Yoke blocks (3 pcs), Fig 3.7(right).
9. Remove shims between the Coils and iron blocks.
10. Remove East Inner 10" thick blocks.
11. Remove 85" wide block, Fig. 3.8(left).
12. Remove 42" wide Slab, Fig. 3.8(right).
13. Remove 6 Coils, Figs. 3.9(left) and 3.9(right). The Coils will be stored in Meson Detector Building until needed at C0.
14. Remove Aluminum support plate, Fig. 3.10(left).
15. Dismount remaining West iron blocks and bottom iron blocks in order, see figures Fig. 3.10(left) to Fig. 3.12(left).

The final view of the dismounted magnet is shown in Fig. 3.12(right). The disassembled pieces of the Vertex Magnet will be stored in the Meson Detector Building or on a hardstand (under a tarpaulin) at C0 so they will be ready for reassembly in the C0 Assembly Hall as soon as needed.

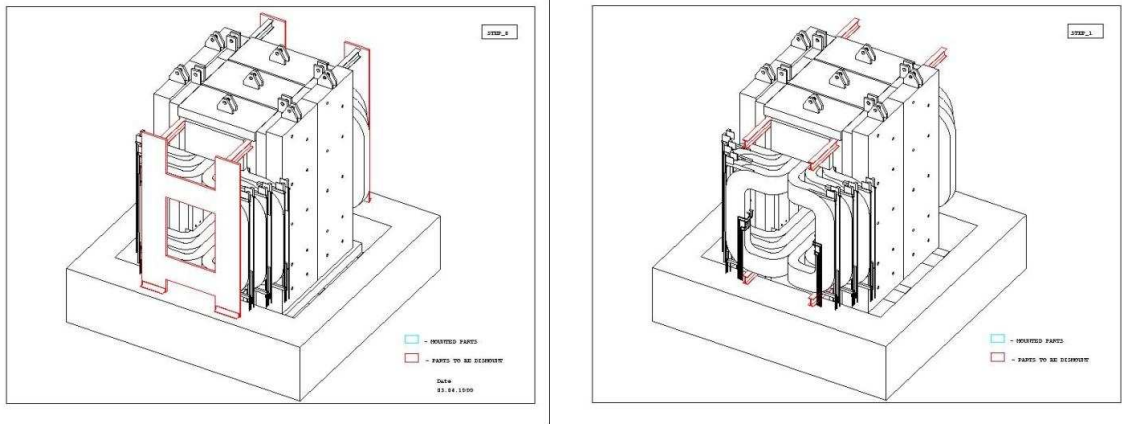


Figure 3.5: SM3 Analysis Magnet disassembly steps 1 (left) and 2 (right)

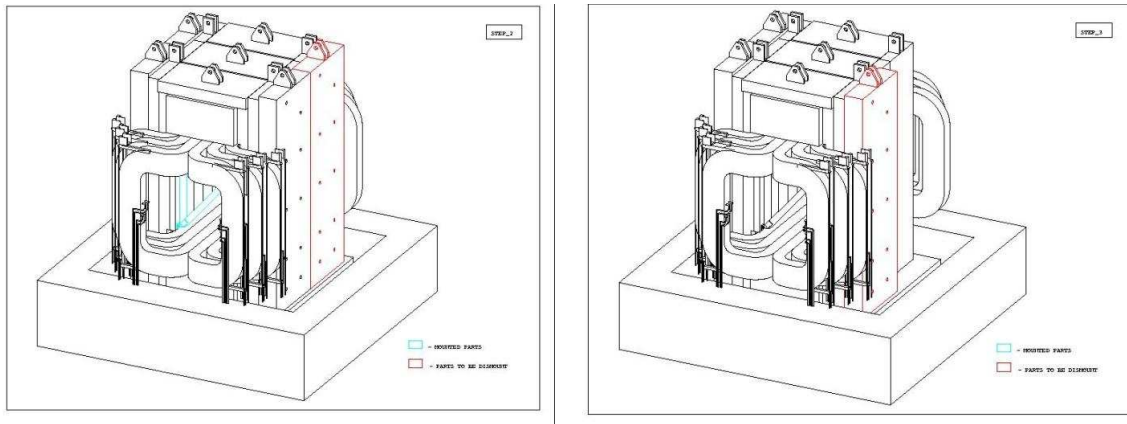


Figure 3.6: SM3 Analysis Magnet disassembly steps 3 (left) and 4 (right)

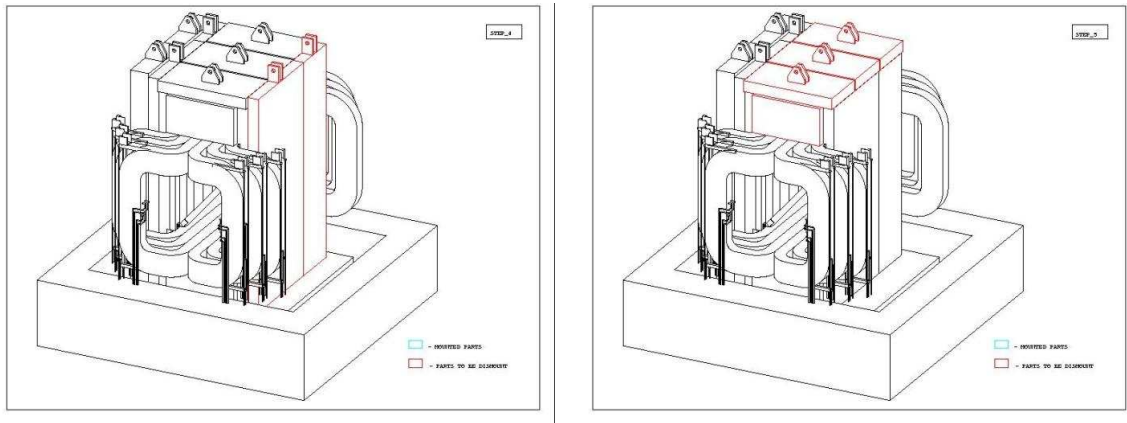


Figure 3.7: SM3 Analysis Magnet disassembly steps 5 (left) and 6 (right)

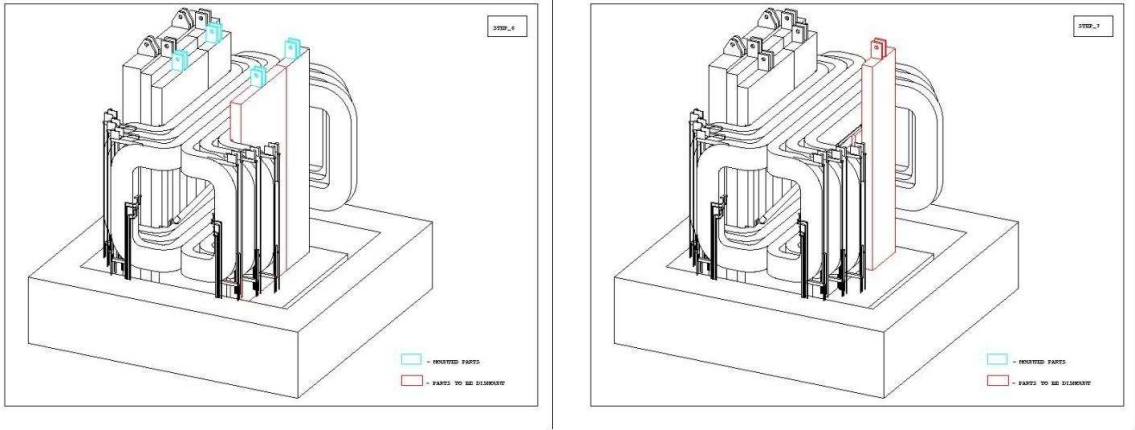


Figure 3.8: SM3 Analysis Magnet disassembly steps 7 (left) and 8 (right)

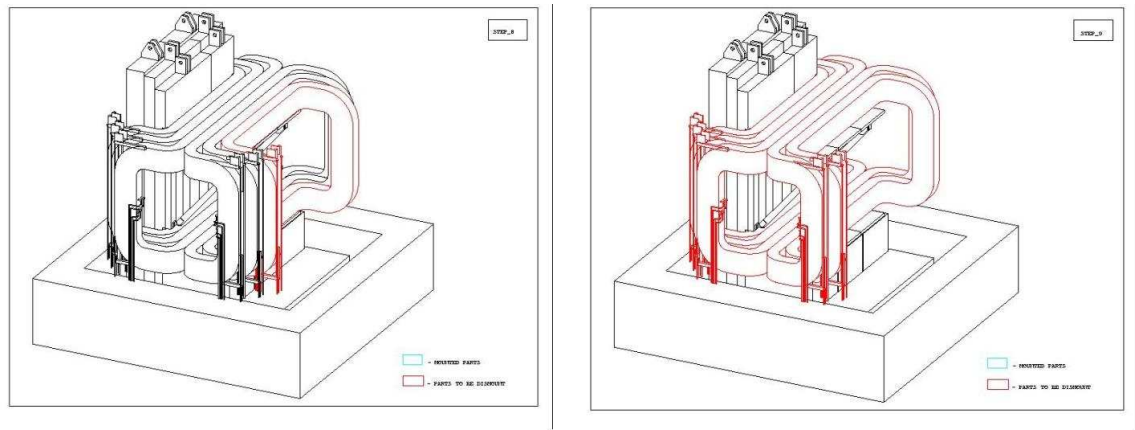


Figure 3.9: SM3 Analysis Magnet disassembly steps 9 (left) and 10 (right)

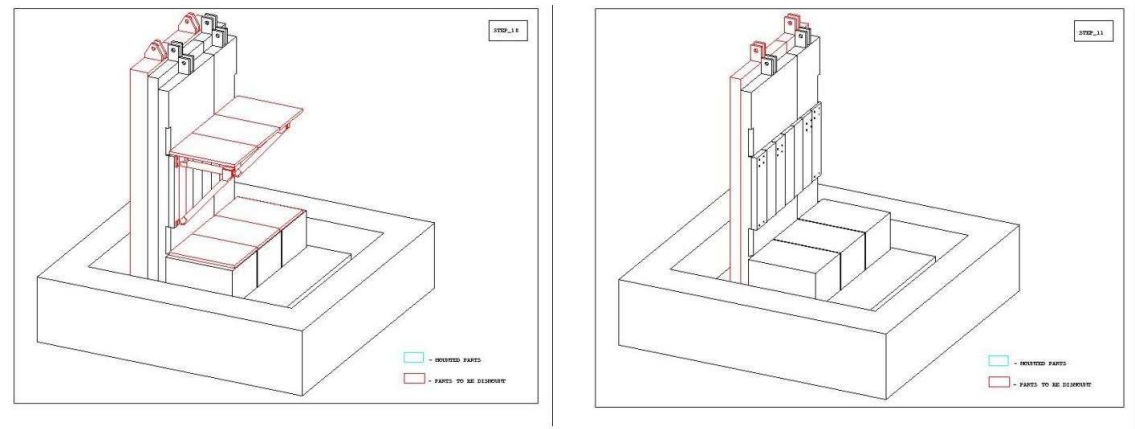


Figure 3.10: SM3 Analysis Magnet disassembly steps 11 (left) and 12 (right)

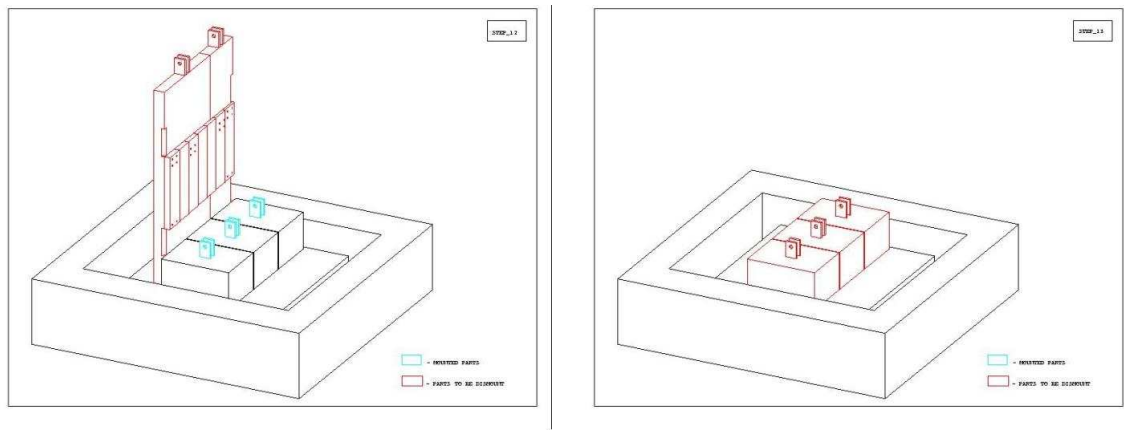


Figure 3.11: SM3 Analysis Magnet disassembly steps 13 (left) and 14 (right)

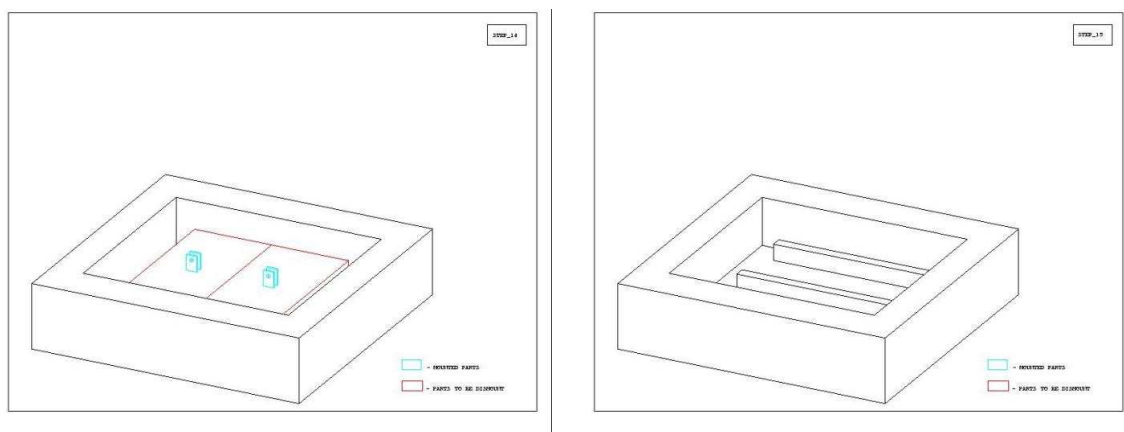


Figure 3.12: SM3 Analysis Magnet disassembly steps 15 (left) and 16 (right)

### 3.3.1.2 Design and Procurement of Shims and Additional Fixturing

The prints for the fixtures fabricated to assemble the SM3 magnet in 1982 have been recovered. New fixtures needed to disassemble SM3 and reassemble it in the C0 Assembly Hall are being designed based on the original fixture design. The shims were designed using the magnetostatic computer code OPERA. They will be fabricated from high quality soft iron.

### 3.3.1.3 Reassembly of Magnet, with the new pole piece shims, using the C0 Assembly Hall Crane

The magnet will be reassembled at C0 under the C0 Assembly Hall 30 ton crane using a procedure that is almost exactly the reverse of the disassembly procedure given in detail above. The only major difference is that during steps 7, 8 and 13 of the procedure shown

above, the new pole-piece shims will be substituted for the existing SM3 pole-piece shims. This also requires a modification of the aluminum support plate brackets used in step 11.

#### **3.3.1.4 Connection of the magnet to temporary utilities and protection systems and mapping of its field**

The magnetic field will be mapped while the Vertex Magnet is in the Assembly Hall. To do this, a short temporary connection from the power supplies in the C0 Assembly Hall to the assembled magnet will be constructed from water-cooled bus. The magnet LCW water will be connected to the LCW header in the Assembly Hall that also supplies LCW to the power supplies. The power supplies and controls will be connected and tested under the control of the Accelerator Division ACNET control system.

The Ziptrack magnet measuring system will be renovated, modified, installed, and used to measure the magnetic field of the assembled magnet over an extensive x,y,z grid of points including the extensive fringe field region of the magnet. The data from the Ziptrack measurements will then be transferred to BTeV permanent data storage. The Ziptrack has been used recently by E907 at Fermilab [2] but will need some modification to measure the tapered pole insert regions of the Vertex Magnet gap.

#### **3.3.1.5 Movement of the magnet into the Collision Hall and hookup to its utilities and protection systems**

The Hilman rollers from the C0 shielding door will be mounted on the magnet support structure and the magnet will be pulled into the C0 Collision Hall, using the existing C0 hydraulic cylinder pulling system, during a long Tevatron maintenance shutdown. The permanent water-cooled bus, LCW water connections, and control and safety systems will then be reconnected. After allowing two weeks for settling, the magnet will be shimmed into its final location on the C0 interaction point.

#### **3.3.1.6 Power, Cooling, Control, Monitoring, and Utility Systems**

The magnet will be connected to a pair of standard Accelerator Division PEI power supplies operated in series. The magnet will operate at 4200 Amps at 125 Volts. One supply will be operated in current mode and the other in voltage mode. The magnet and power supply cooling will be provided from the existing Tevatron tunnel LCW water system. This does not add significantly to the complexity of the existing system since there currently exist at C0 conventional magnets in the Tevatron lattice that will be removed for the BTeV installation. The existing ACNET control system can handle all the control and monitoring functions necessary to run the BTeV magnets without the need for system expansion. The C0 Collision Hall HVAC system has been sized appropriately to remove the heat radiated from the coils of the magnets during full excitation.

### 3.3.1.7 Magnetostatic Analysis of BTeV Dipole Magnet

The ANSYS finite element program was used to calculate the field in the BTeV dipole magnet. The finite element model consists of 590,000 elements and 605,000 nodes, with an element size in the region of the magnet center of 2.5 cm. The iron and coils are shown in Fig. 3.13. The air and iron are modeled with the ANSYS SOLID96 element, using the generalized scalar potential option. Coils are modeled with SOURCE36 current source elements. The vertical sextupole moment of the vertex magnet is less than 4 Units which is smaller than the sextupole moment of a standard Tevatron dipole and much smaller than the strength of the sextupole correctors in the Tevatron.

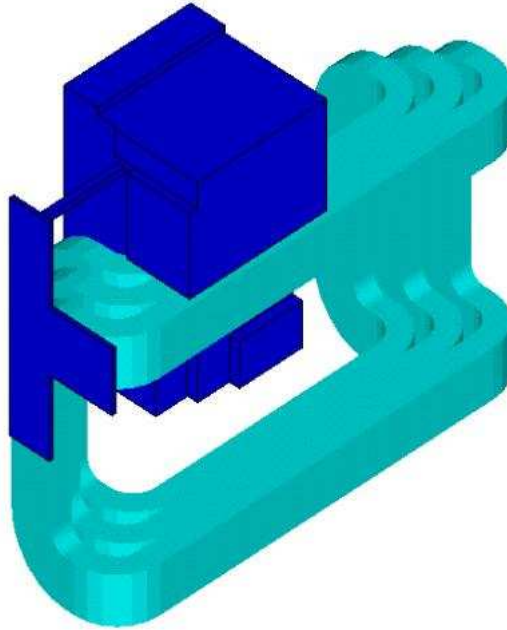


Figure 3.13: Finite Element Analysis Model of BTeV Dipole (air elements and half of coils removed for clarity)

The BH curve is shown in Fig. 3.14. The data are available elsewhere. This curve was measured for iron used in the MINOS detector, and its shape very closely matches that of the BTeV iron (which was originally recovered from the Nevis cyclotron) when the BTeV iron curve is corrected for hysteresis. The pole piece iron will be specified to have magnetic properties at least as good as the MS10360 curve. Thus the MS10360 curve is assumed for simulating the pole piece and the recovered SM3 iron for this analysis.

Results show that, with an operating current of 4200 amps, the magnet central field is 1.59 T, and  $\int B \times dl$ , integrated along the axis, is 5.24 T-m.



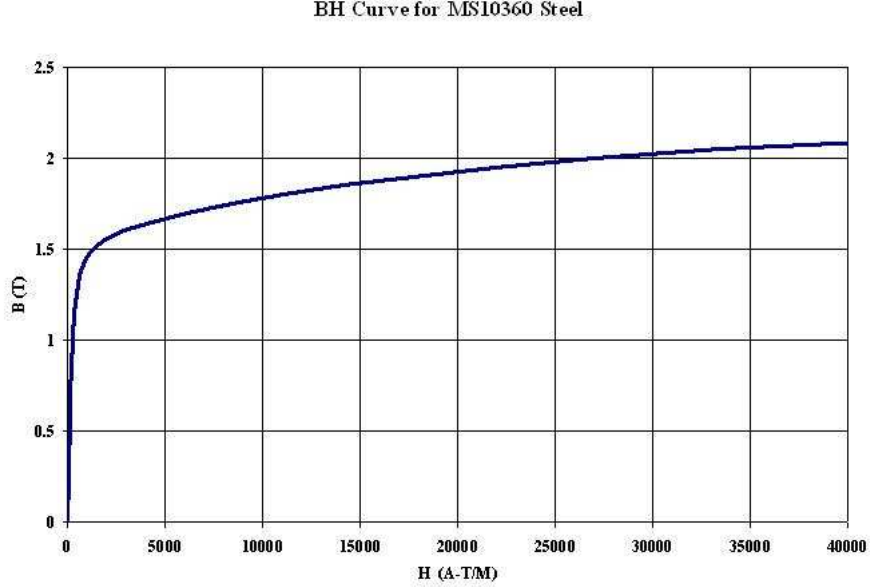


Figure 3.14: BH Curve for MS10360 Steel

The B-field magnitude in the center of the magnet (in the plane  $Z = 0$ ) is shown in Fig. 3.15. The maximum field occurs at the edge of the pole piece nearest the center, and is 3.23 T.

The variation of field along the magnet axis is shown in Fig. 3.16. The calculated central field ( $X=0, Y=0, Z=0$ ) is 1.59 T.

The value of  $\int B \times dl$  along the magnet axis ( $X=0, Y=0$ ) is 5.24 T-m. The variation of this integral along parallel paths about the magnet center is shown in Figs. 3.17 and 3.18.

### 3.3.2 Muon Toroids

A muon toroid assembly provides the bend field that enables the muon chambers to determine the momentum of energetic muons from the vicinity of the collision point, without any use of the measurements from the pixel detector or forward tracker. This capability is exploited to form a “stand-alone” muon trigger to complement, cross check, and calibrate the BTeV Detached Vertex Trigger[3]. The toroid assembly also provides the absorber material that prevents hadrons, electrons, and photons from penetrating and registering in the muon detectors. To provide both a large integrated magnetic field and enough absorption of hadrons, each toroid is constructed of a meter thick soft iron energized by a pair of coils. The toroid assembly also supports the 10’ B2 dipole, the “Compensating Dipole” (see below). Finally, the toroid structure is used to support a cantilevered plate, the Muon Filter,

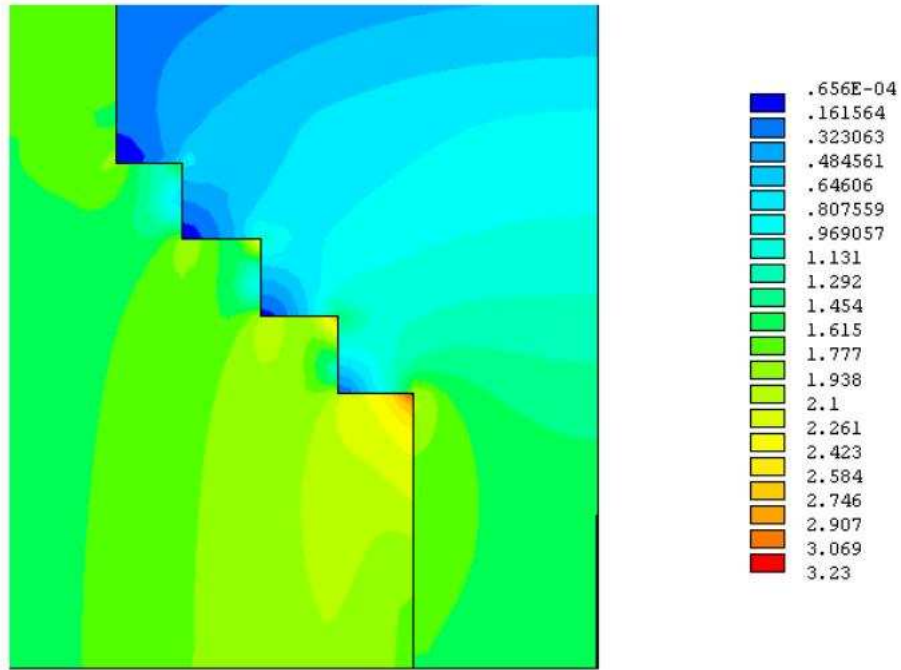


Figure 3.15: B-field at the Center ( $Z=0$ ) of the BTeV Vertex Magnet

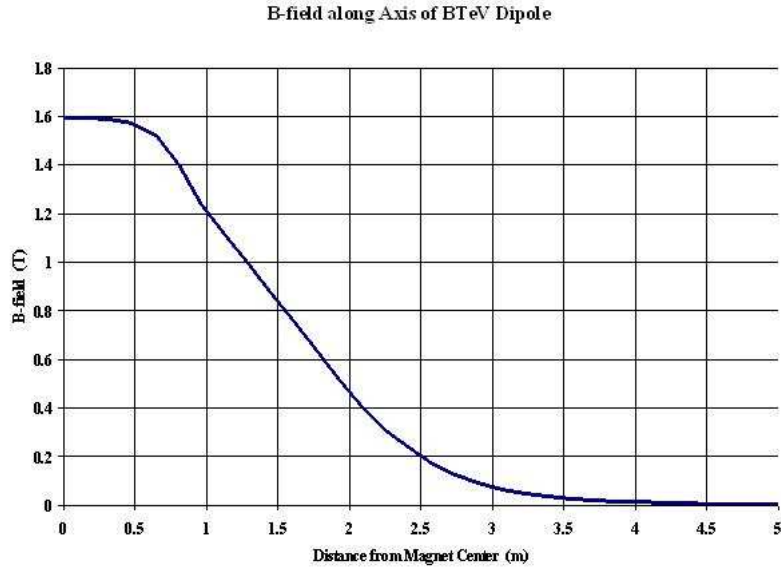


Figure 3.16: B Along the Z Axis ( $X=0$ ,  $Y=0$ ) of the BTeV Vertex Magnet

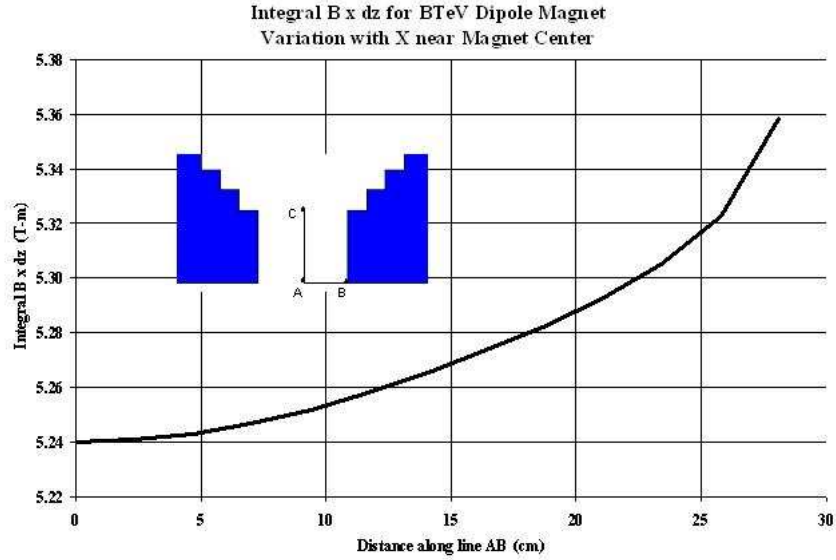


Figure 3.17: Variation with X of  $\int B \times dz$  for BTeV Vertex Magnet near the magnet center (Y=0)

which shields the final stations of the muon detector from the spray of particles hitting near apertures of the Compensating Dipole or the beampipe.

Note that a second toroid assembly will be built and located symmetrically at the south end of the Collision Hall. This is needed to support the south compensating dipole and to shield the BTeV spectrometer from radiation emanating from the south Tevatron tunnel.

It is planned to obtain the iron slabs that form the toroids from the existing SM12 magnet in the MEast Spectrometer. The SM12 magnet has 36 30-ton iron yoke blocks that can be recovered without fully disassembling the SM12 magnet. 24 of these pieces will be recovered, modified and transported to the C0 Assembly Hall. They will then be combined with other soft iron pieces to form 4 octagonal-toroid magnets. The final assembly will also include mounting points for the muon detectors on the north pair of toroids, extra absorber around the beampipe, and inserted compensation dipoles that are needed to return the Tevatron circulating beams to their original trajectories. The components' weights are given in Table 3.2.

The steps required to construct the Muon Toroids are the following:

1. Remove 24 iron slabs from the existing SM12 magnet in the Meson Area Detector Building and transport them to the C0 Assembly Hall;
2. Procure the remaining parts, including coils, additional steel slabs and other fixturing;

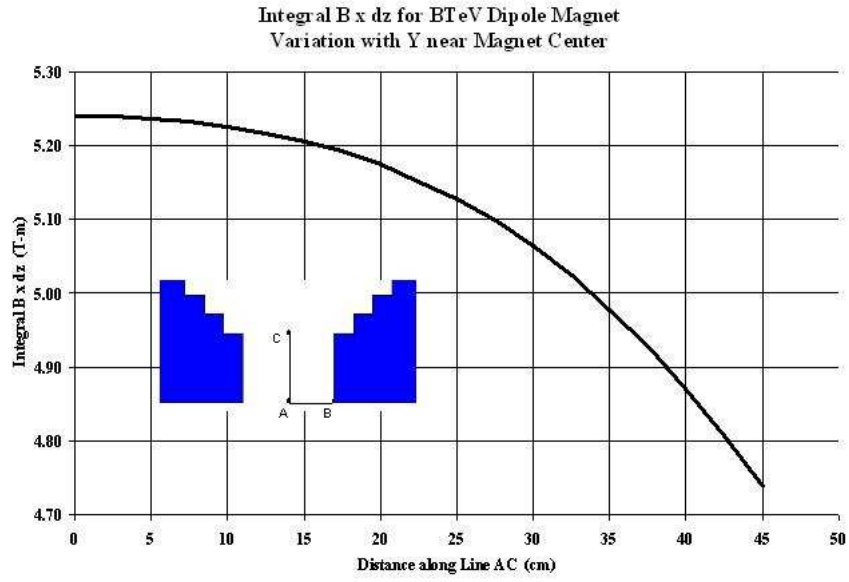


Figure 3.18: Variation with Y of  $\int B \times dz$  for the BTeV Vertex Magnet near the magnet center (X=0)

Table 3.2: The Mass and Weight of the Toroid Magnet

Item	Weight
Toroid Iron	365 tons
Muon Filter	19.5 tons
Coils	0.6 tons
Support Accessories	5.4 tons
B2 Magnet	6.2 tons
Assembled Pair of Toroids	397 tons
Assembled Toroid Pair with Moving Equipment	405 tons

3. Construct the toroids using the C0 Assembly Hall crane;
4. Roll the toroids into the Collision Hall and hook up their utilities and protection systems.

### **3.3.2.1 Recovery of Iron Slabs from the Existing SM12 Magnet and Transportation to the C0 Assembly Hall**

The Toroid Magnet (TM) parts includes: Four 198" x 198" x 40" octagonal shaped magnets, coils, a muon filter, a pair of B2 compensation dipole magnets, and some supporting structural devices needed for muon filter and muon chamber installation on the north toroid assembly only. Also, there are accessory structures for moving the two toroid-pair assemblies from the C0 Assembly Hall to the C0 Collision Hall.

The two octagonal shaped toroid assemblies in each toroid pair weigh a combined 365 tons. About 85% of the soft iron will come from salvaging iron from the existing SM12 magnet used by Experiment E866 in the Meson Lab. It will take 24 pieces of the 36 existing soft iron rectangular blocks, each with dimension 198" x 63" x 17".

The SM12 magnet is constructed identically to the SM3 magnet and hence the procedure for removing the 24 iron return yoke pieces from this magnet is also identical to step 5 in the SM3 disassembly procedure outlined in detail above. They will be stored in the Meson Detector Building and then transported to the C0 Collision Hall when needed for the toroid assembly.

### **3.3.2.2 Procurement of Coils, Additional Steel Slabs and Other Fixturing**

The toroid coils have sections that can be removed to provide access for installing Muon chambers located between the two toroids in a toroid pair. The 4 coils will have 10 turns each and will be made from existing 0.57" x 1.00" copper bus which includes a 1/4" hole for water-cooling. A new fixture will be required to form the coil segments. Each of the coil segments will have lugs welded to each end and stainless water tubes brazed at each end. The coils will be wrapped with multiple layers of kapton for insulation. The coils are spaced and mounted to the Toroid iron with G-10 brackets. A special crate that can hold 10 coil segments will be used for handling, assembly, and shipping. Since these coils will be readily accessible and easy to repair, no spare coil turns will be produced.

The toroid coils will be fabricated by the Technical Division using existing copper conductor. The coil winding, insulating and curing procedure will be identical to a procedure previously used to produce coils with this conductor. There will be 40 single turn coils produced using an existing coil winding machine at the Fermilab magnet facility.

The remaining 15% of the soft iron will be purchased. The purchased iron will be used for the 4 soft iron plates with dimensions of 198" X 99" x 2". All these parts will be appropriately fabricated into the 5 different iron sizes needed to build the two octagonal toroids.

### **3.3.2.3 Toroid Magnet Parts Description**

The Toroid construction involves a number of additional slabs of iron and some fixturing. Purchased soft iron pieces of dimension 198" x 99" x 2" complete the body of the two Toroids. These purchased pieces along with the return yoke slabs from SM12 will be flame cut and assembled as detailed below into the two pairs of large octagonal Toroids.

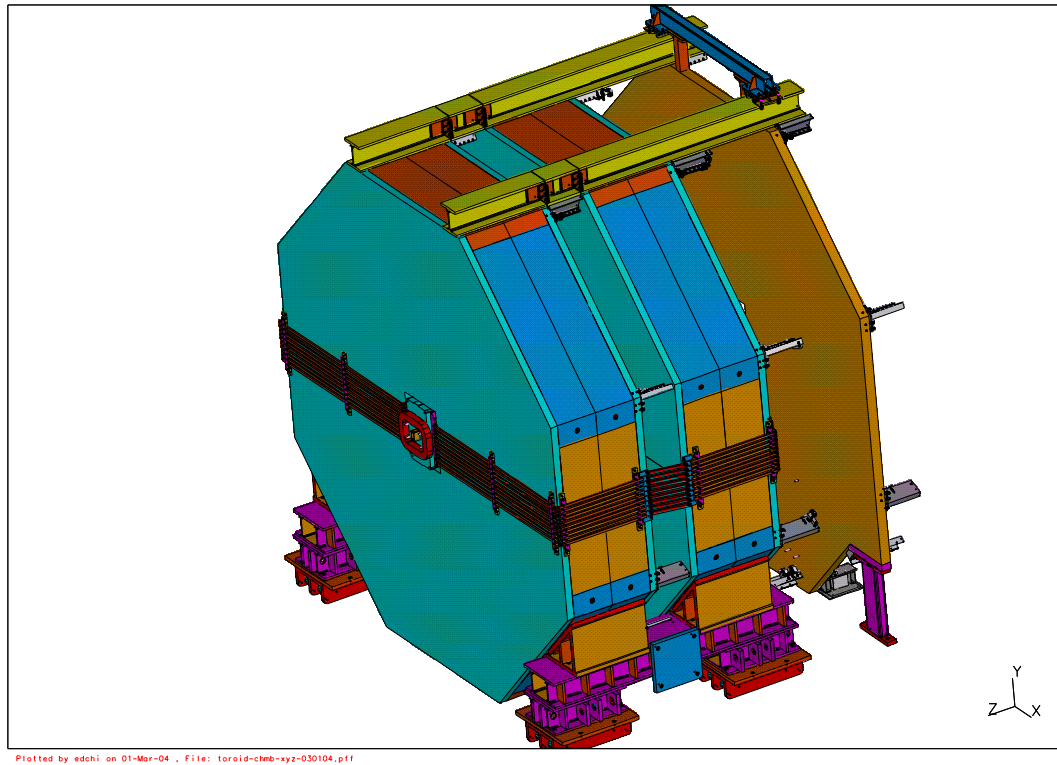


Figure 3.19: The north Muon Toroid Assembly. This view shows the north toroid assembly ready to be rolled into the Collision Hall. It includes the muon chamber support structure and filter and the roller assembly. The south toroid assembly will reuse the same roller assembly and will not have the muon chamber superstructure.

The 4 inch thick Muon Filter, located downstream of the Toroids, will be fabricated from 2 pieces of 198" x 99" x 2" steel plate. These plates are supported from the toroid. Two I-beams are mounted to the top of the Toroids. They have the following functions:

1. to provide lateral structural support and increase structural stability;
2. to create a mechanical work bench for the installation or removal of the Muon Chambers at the Collision Hall; and
3. to enable the Muon Filter to move along the beam direction (z dir.) to create extra access space for the Muon Chamber installation and other service activities.

On the north pair of toroids only, a Muon Filter will hang from a trolley (Fig. 3.20) that can run along the top of the I-beams mounted to the tops of the Toroids. It is composed

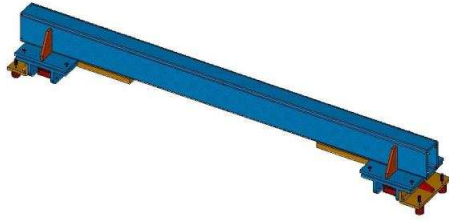


Figure 3.20: Trolley used to provide Z motion for the Muon Filter

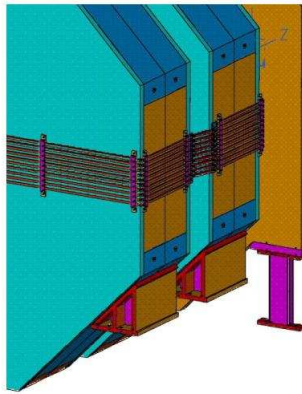


Figure 3.21: Vertical Leg used to provide support for the Muon Filter

of a rectangular steel tube, two 15 ton Hilman rollers, and 4 cam rollers to guide the direction. The device supplies the support for the filter in the vertical (Y) and longitudinal (Z) directions and enables the filter to move in the beam direction (Z) for access to the Muon chambers located on the backside of the Filter. When in the final position the weight of the Filter will be transferred to two legs that connect at the outer edges. The vertical supporting leg is shown in Fig. 3.21. The top of the Filter will remain connected to the trolley, which will be locked in position to provide longitudinal stability.

The same four 500 ton Hilman rollers, Fig. 3.22, that are used for moving the Collision Hall shield door will be used for moving the Toroid magnets into the Collision Hall. The Hilman rollers will mount under two bridge beams that connect the two Toroid magnets at the bottom. The bridge beams have locations for hydraulic cylinders for lifting the Toroid magnet pair for installation and removal of the Hilman rollers. The same hydraulic cylinders used for raising and lowering the shield door will also be used for the Toroid magnets.

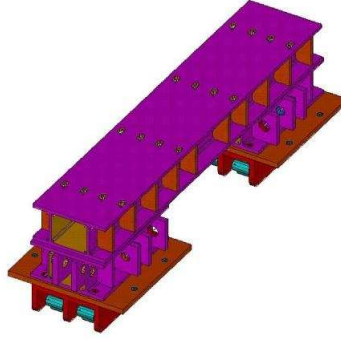


Figure 3.22: Hilman Roller assembly used to roll both of the BTeV Toroid pair assemblies and also the Vertex Magnet from the C0 Assembly Area to the C0 Assembly Hall

#### 3.3.2.4 BTeV Toroid Assembly Sequence

The steps required to assemble the Muon Toroids are summarized below and in Figs. 3.23 through 3.27. A detailed description is available elsewhere.

- Step 1: Weld two bottom slabs (4.5" thick-Slab5) together.
- Step 2: Add four trapezoidal shape slabs.
- Step 3: Add four support brackets by crane.
- Step 4: Add four middle central slabs.
- Step 5: Add eight rectangular side slabs.
- Step 6: Add four 3" thick lower part plate slabs.
- Step 7: Mount the coils.
- Step 8: Insert the B2 Compensation Dipole Magnet.
- Step 9: Add four large blocks to the top.
- Step 10: Add top side .
- Step11: Add 3"-thick top pieces.
- Step 12: Add I-beams on the top.
- Step 13: Add pre-assembled muon chamber rails.
- Step 14: Add muon filter.

After testing, the assembled 405 ton Toroid Magnet pair is then ready for moving to the C0 Collision Hall for Installation.

#### 3.3.2.5 Assembly Sequence

The optimum sequence for assembling the Vertex Magnet and the first muon toroid assembly is to build the Vertex Magnet first in the C0 Assembly Hall. It would then be moved as far east as possible so that the first toroid assembly can be built while the Vertex Magnet is being tested and measured with the Ziptrack magnetic field measuring device. The 1st toroid



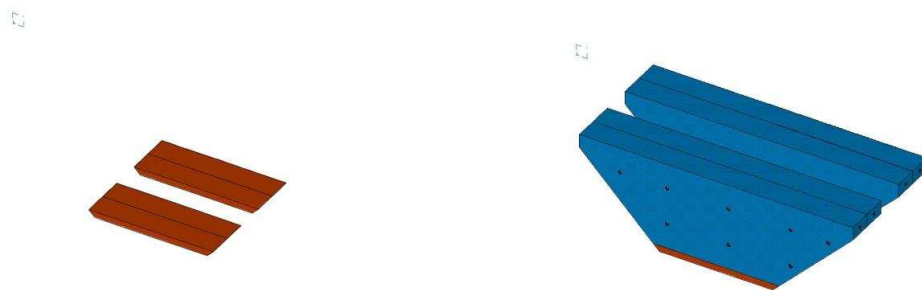


Figure 3.23: Toroid Assembly Steps 1 and 2

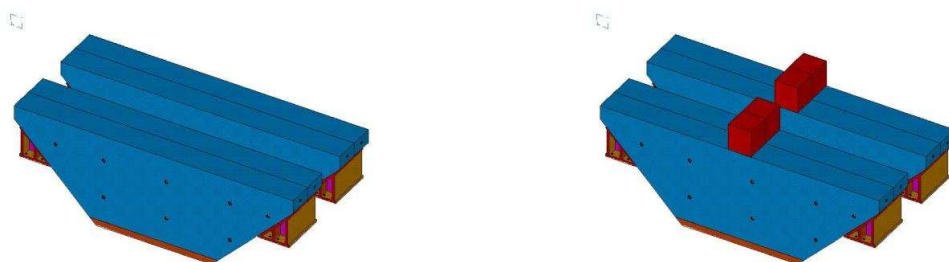


Figure 3.24: Toroid Assembly Steps 3 and 4

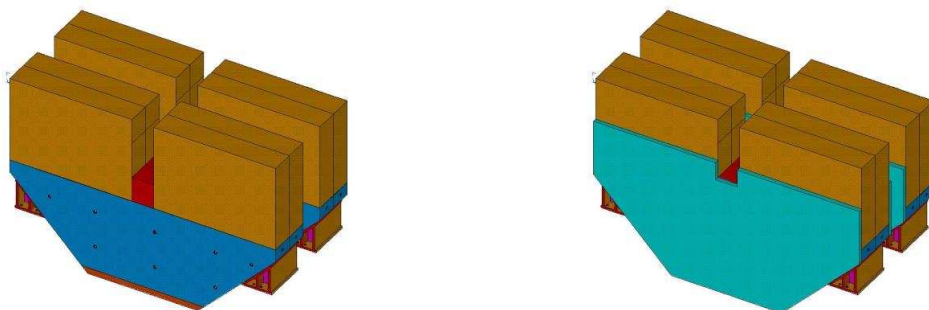


Figure 3.25: Toroid Assembly Steps 5 and 6



Figure 3.26: Toroid Assembly Steps 7 and 8

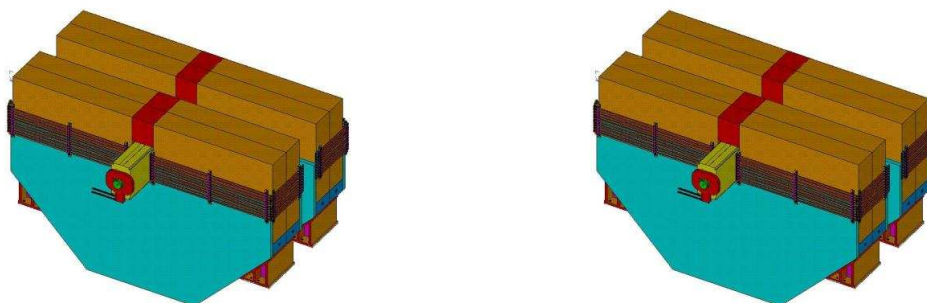


Figure 3.27: Toroid Assembly Steps 9 and 10

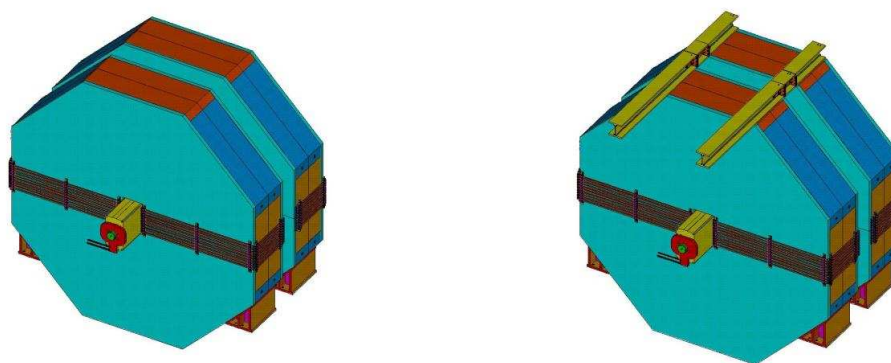


Figure 3.28: Toroid Assembly Steps 11 and 12

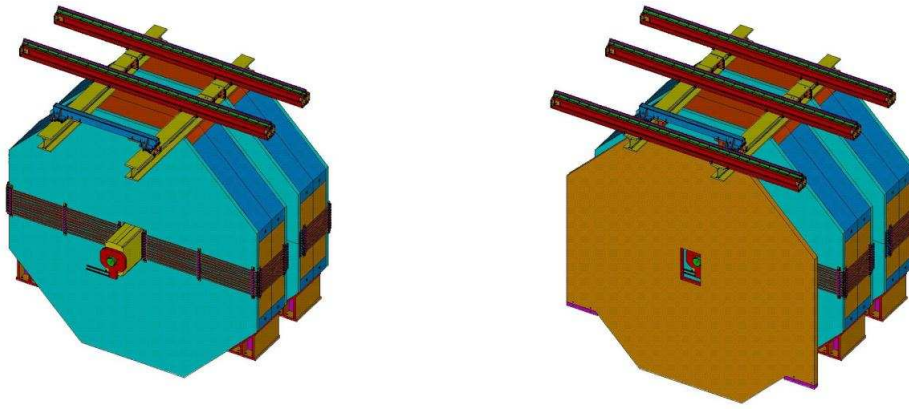


Figure 3.29: Toroid Assembly Steps 13 and 14

assembly would then be rolled into the Collision Hall during the summer 2006 shutdown followed by the Vertex Magnet. If delays occur in either the Vertex Magnet or toroid parts procurements, the assembly and installation order can be reversed. If either assembly is not ready by the last week of the summer shutdown, its installation can be delayed until any convenient 1 week shutdown that might occur during FY2007. This would cause a slight delay in the construction of the 2nd toroid assembly and in the other large spectrometer components but would most likely not jeopardise the overall completion of the spectrometer in FY2009.

### 3.3.2.6 Installation, Including Hook Up to Utilities and Protection Systems

The connection of the Toroids to the necessary power, LCW, control, and monitoring systems will be done under the supervision of Accelerator Division Electrical Department Staff. The existing ACNET control system and protocols will be employed and Accelerator Division Electrical safety standards will be followed.

The coils for both toroids are operated from one Transrex 240 KW power supply at a current of 1000 Amps. The voltage drop is 10 Volts.

### 3.3.2.7 Calculations and Analysis

Since the BTeV Toroid is installed above the floor of the C0 building, it must be designed to resist the sudden movement caused by seismic or other external forces. Since these objects are very tall with small bases, we have studied their mechanical stability. The calculations are based on the following assumptions:

- Assuming it is a #1 seismic zone. See Fig. 14 of reference 1.
- The structure is an essential facility.
- Ignoring the small additional weight of the muon chambers.

We applied the following engineering standards and texts: the ASCE Standard “Minimum Design Loads For Buildings and Other Structures” [4], AISC “Allowable Stress Design” [5], and “Foundation Analysis and Design” [6].

We have determined that the Toroid is within safety requirement for stability against overturning from seismic or other external forces.

A similar calculation has been applied to the Muon Filter. The calculated safety factor is less than 1.50 which is recommended by “Foundation Analysis and Design”. Therefore the current structural design of the filter is not stable enough and needs to be modified. There are two ways to improve the structural stability: to increase the base contact area of the filter and to install a bolt to anchor the filter with the foundation; or to add a structure such that the lateral force  $V$  will be transferred to another structure through the new structure. Studies are currently underway to address this issue, which is not viewed as a difficult problem.

Details of all of the calculations are available as a BTeV Internal Document.

### 3.3.2.8 Toroid Fields

The field in the toroid has been calculated using finite element analysis. One complication is that the “compensating dipole” magnet is placed in the bore of each pair of toroid magnets. The clearance between the outer boundary of the dipole iron and the inner boundary of the toroid iron is greater than  $\sim 2.5$  cm. There are concerns that the field of each magnet may be unacceptably distorted by the presence of the other magnet.

A 3-d ANSYS electrostatic finite element model of the toroid assembly was created to address this issue. The BH used was the same that was applied to the most recent Minos toroid studies, and is based on measurements of MINOS toroid steel. The BH curve is plotted in Figs. 3.30 and 3.31. The total NI/coil for the dipole and toroid magnets were 36333 A-t, and 24183 A-t, respectively. The results of these calculations were also incorporated in the simulation codes used to model the BTeV spectrometer. The calculations also explored various options for reducing the fringe field of the toroid assembly, especially in the region of the EmCal photomultiplier tubes.

The geometry of the inserted compensating B2 dipole and the toroid is shown in Fig. 3.32. The field in the dipole across the air gap (line A-B of Fig. 3.32) is shown in Fig. 3.34. No asymmetry of field can be observed on the plot. The vertical sextupole moment is less than 4 Units and is not a problem. Fig. 3.35 shows the field in the dipole iron. Without the toroid, this field would be symmetric top-to-bottom in the figure. But the toroid coil forces much of the dipole flux downward, producing the slight field asymmetry in the return yoke iron of the dipole.

The profile of the field in the toroid iron is shown in Fig. 3.33. The toroid field was plotted along the 0 degree and 90 degree radii. Fig 3.36 shows the field along these two perpendicular radii. Because the hole in the center of the toroid iron is not square, the iron is about 4% thicker at 0 degrees which accounts for the lower field.

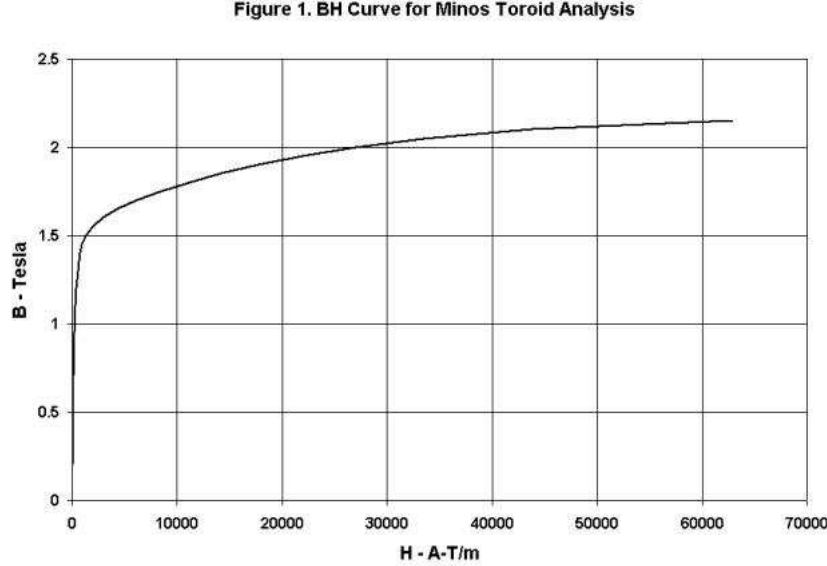


Figure 3.30: BH Curve for MINOS Toroid Steel (properties similar to steel used for BTeV)

### 3.3.2.9 B2 Dipole Modifications

Each toroid contains in its central hole a 10' B2 Dipole that compensates for the deflection of the Vertex Magnet. Together the two B2 Dipoles and the Vertex Magnet form a “3-bump” that restores the beams to their original trajectories on both sides of the IR. This is discussed below. The dipoles are mounted inside the toroids to save space along the beam direction. Figure 3.37 shows the B2 mounted inside the Muon Toroid. The B2's coil sticks above the profile of the B2's yoke. Space must be left for the coil on the detector end of the B2 to pass through the hole in the toroid in case it becomes necessary to remove the B2 to repair it. This space is filled with a steel or copper absorber plate attached to the B2's yoke, shown in the figure, in order to block the path for hadrons to reach the muon detector. A detailed plan has been developed to permit extraction of the B2, in case of failure, without moving the low beta quadrupoles just outside the C0 enclosure.

### 3.3.3 Beampipes

The beampipe provides the vacuum for, and encloses, the circulating Tevatron proton and antiproton beams. It must be able to conduct the wall current associated with the circulating beams. It must also be as thin as possible in order to minimize the reinteraction of particles emanating from the collision point.

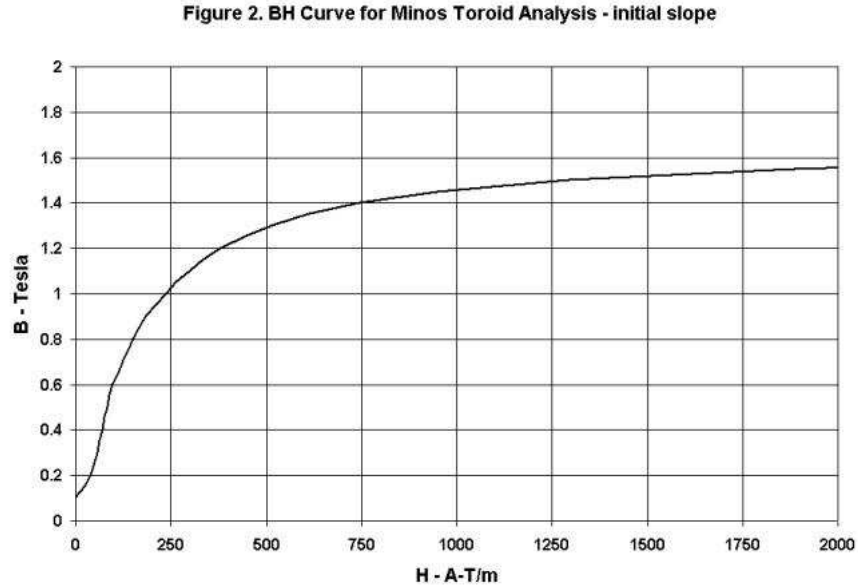


Figure 3.31: Initial Portion of BH Curve for MINOS Toroid Steel (properties similar to steel used for BTeV) showing more detail on the rise towards saturation

The plan is to construct the beampipe in sections. The 1" diameter beampipe in the region of the forward tracking chambers will be constructed by modifying the CDF Run IIb beryllium beam pipe. Design work is progressing on specifying the needed modifications.

The 2" diameter beampipe inside the RICH detector will be assembled from the existing CDF Run I beryllium beampipe. The existing pipe will be cut to the desired length and retrofit with appropriate flanges to enable it to be integrated into the spectrometer.

A third component of the beampipe assembly is the torispherical thin-walled flange/window that transitions from the 1" beampipe section onto the face of the pixel vacuum tank. It will be fabricated from spun aluminum. Special thin-walled flanges and ion pumps complete the beampipe assembly.

The torispherical window must provide a connection for attachment to the accelerator vacuum pipe. It must also terminate the pixel vacuum box while minimizing the amount of material that particles produced in the interactions must traverse before reaching the downstream detection elements of the spectrometer. To accomplish this, we have designed an aluminum formed head, following the guidelines in the ASME Boiler and Pressure Vessel Code. The head thickness of 0.023 inch (0.58 mm) is the required thickness according to the Code for a head diameter of 20 inches (508 mm). Figure 3.39 shows this window. Its relation to the interaction point is shown in Fig. 3.40.

An analysis was performed with the structure under an internal pressure of 14.7psi. The

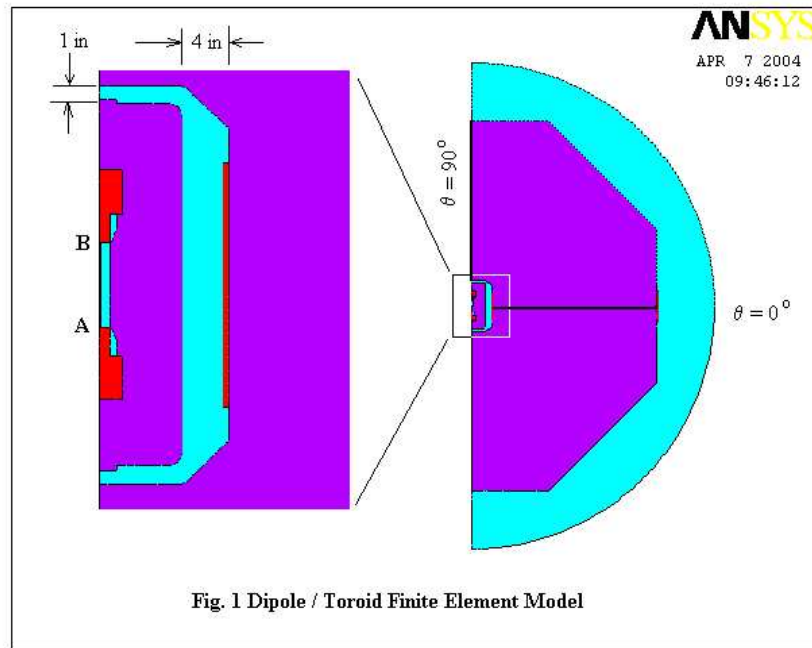


Figure 3.32: Geometry of the compensating dipole and toroid. Shown are the dipole coils, dipole iron, location of the toroid coils, and the toroid iron.

safety factor for the design is three times the yields stress of aluminum. The maximum deflection is 0.024 inch (0.61 mm). The transition to the beam pipe has a radius of 0.1 inch. When the front of the head sits at  $z=65$  cm from C0, the largest thickness through which a particle travels within the detector acceptance is 0.036 inch (0.91 mm).

The current flange design is for a metal wire seal. Research and analysis must take place to understand the best available option to seal the window to the vacuum vessel and how to fabricate the custom-made flange. We will also have to research how to best fabricate a uniformly thin-walled aluminum head with such large diameter.

### 3.4 Power Supply Summary

The BTeV Detector uses three types of high current magnets. The parameters for these magnets are listed in Table 3.3. Power supplies will be reclaimed and recommissioned from experiments and beamlines that have been decommissioned. Note that the power supplies widely known at Fermilab as “Transrex” supplies are now manufactured under the name PEI. These power supplies will be cooled by Low Conductivity Water supplied from the Tevatron tunnel.

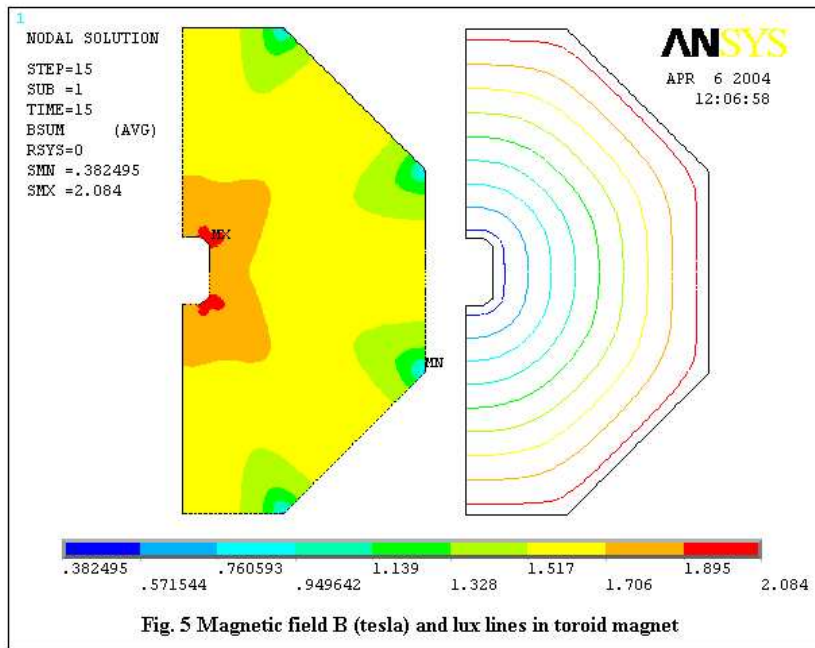


Figure 3.33: Field in the toroid iron (shown for 1/2 of the toroid).

Table 3.3: Voltage and Current Requirements and Power Supplies for Magnets

Magnet	Vertex Magnet	B2 Dipole	Toroid
Number of Elements:	1	2	1
Current(Amps):	4200	2300	1000
Voltage(Volts):	120	8	10
Power Supply Type/number:	Transrex 500KW/2	Transrex 500 KW/1	Transrex 250KW/1

## 3.5 Integration and Testing Plan

This section describes the full chain of integration and testing of the Vertex Magnet, muon toroids, and beampipes after they have been properly installed at C0. The alignment of these elements in the overall C0 alignment system is also described.



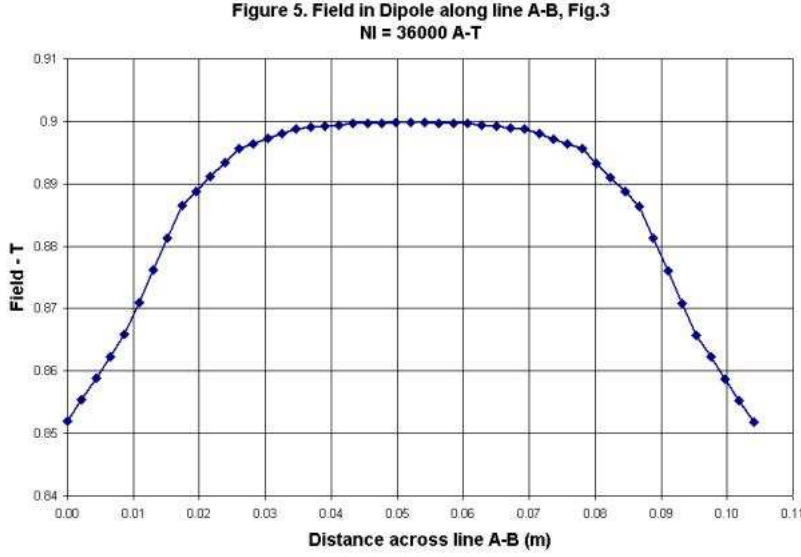


Figure 3.34: Field in the compensating dipole along the line AB of Fig. 3.32 for NI = 36333 A-T

### 3.5.1 Vertex Magnet tests and integration into the BTeV spectrometer

After assembly in the C0 Assembly Hall, the Vertex Magnet will be temporarily connected to its power supply (which also sits in the Assembly Hall). The magnetic field monitor, controls and safety connections will be installed on the magnet. The magnetic field will be extensively measured using the Ziptrack magnetic field measuring device.

After the Vertex Magnet is rolled into its final location in the C0 Collision Hall, the permanent power, control, and safety connections will be made. The remote operation, readout, and control of the magnet and its safety systems will be checked. The ability of the current in the magnet to follow the MDAT ramp of the main Tevatron magnet excitation current will be verified.

After allowing at least two weeks for any potential settling of the Collision Hall floor, the magnet will be shimmed into its exact final location with respect to the primary Tevatron tunnel survey monuments to within 1mm. Secondary fiducial marks will be mounted on the walls and floor of the Collision Hall and on the vertex magnet to facilitate continued monitoring of the survey location of the magnet, and BTeV spectrometer detector elements, during the lifetime of the BTeV spectrometer. The pixel detector vacuum tank and the forward tracking detector stations will have independent adjustments of their position with respect

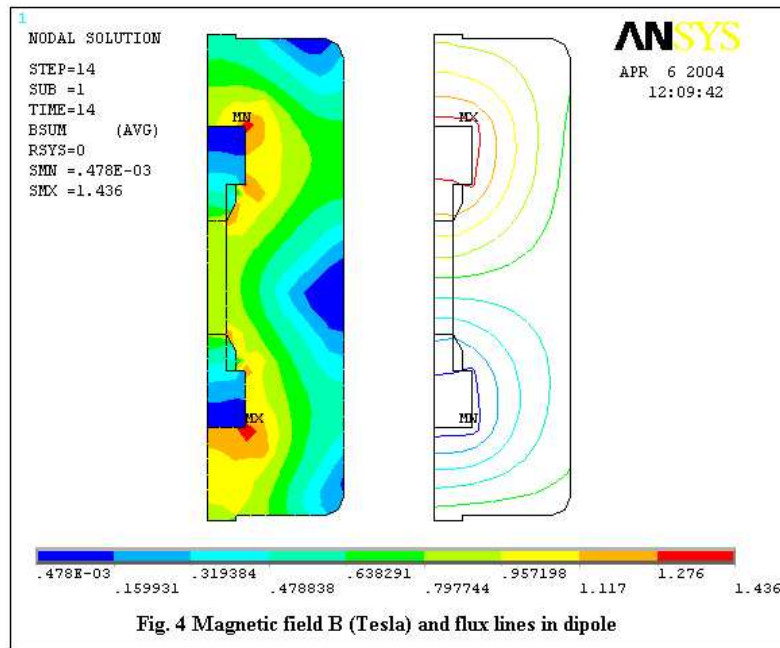


Figure 3.35: Field in the compensating dipole iron showing asymmetry in the top and bottom return yokes due to the Toroid

to the vertex magnet in order to achieve the more stringent initial alignment requirements for these detectors.

### 3.5.2 Toroid tests and Integration into the BTeV spectrometer

After assembly in the C0 Assembly Hall, the muon toroids, with their embedded compensation dipoles, will be temporarily connected to their power supplies (which also sit in the Assembly Hall). The magnetic field monitor, controls and safety connections will be installed on the toroids and compensating dipoles. The magnetic fields will be extensively measured using the Ziptrack magnetic field measuring device.

After the muon toroid assembly is rolled into its final location in the C0 Collision Hall, the permanent power, control, and safety connections for the toroids and compensating dipole will be made. The remote operation, readout, and control of the toroids and compensating dipoles and their safety systems will be checked. The ability of the current in the compensating dipole to follow the MDAT ramp of the main Tevatron magnet excitation current will be verified.

After allowing at least two weeks for any potential settling of the Collision Hall floor, the muon toroid assembly will be shimmed into its exact final location with respect to the

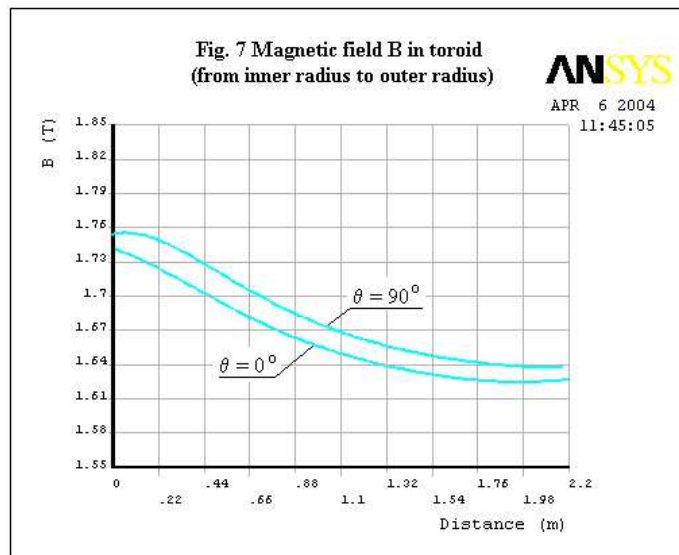


Figure 3.36: Azimuthal field in the Toroid at 0 and 90 degrees

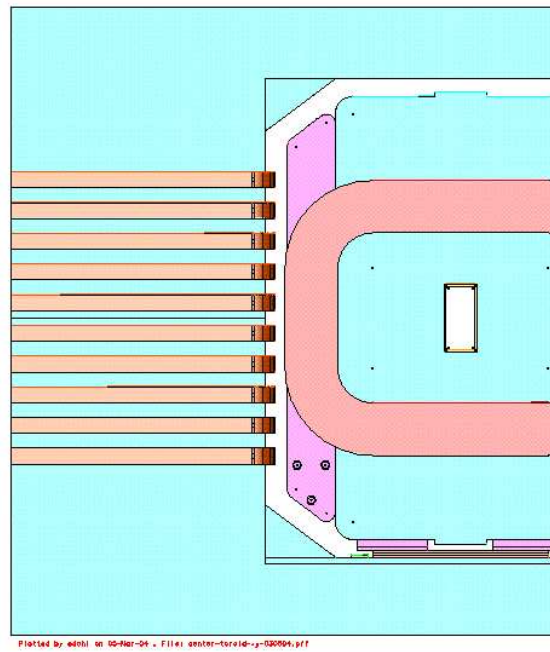


Figure 3.37: B2 as it is mounted in the hole of the Muon Toroid

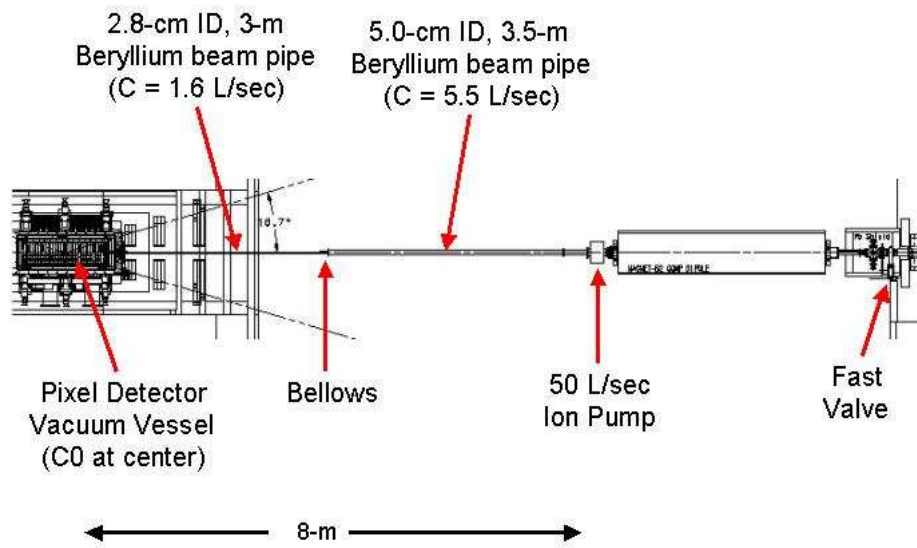


Figure 3.38: Schematic of Beampipes in BTeV

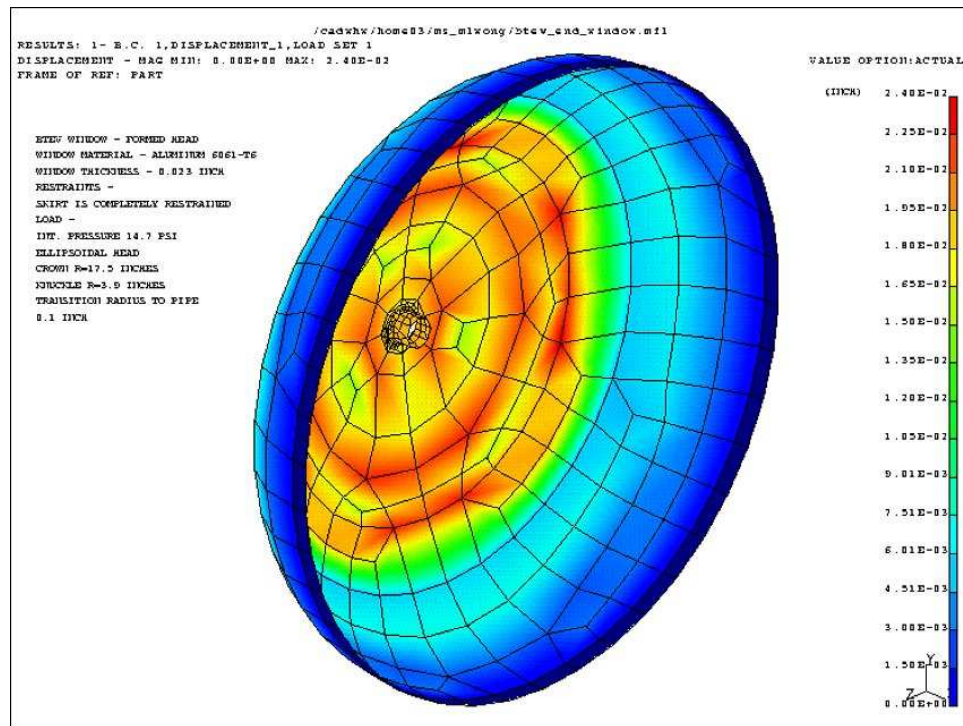


Figure 3.39: Displacement analysis of Pixel Vacuum Window

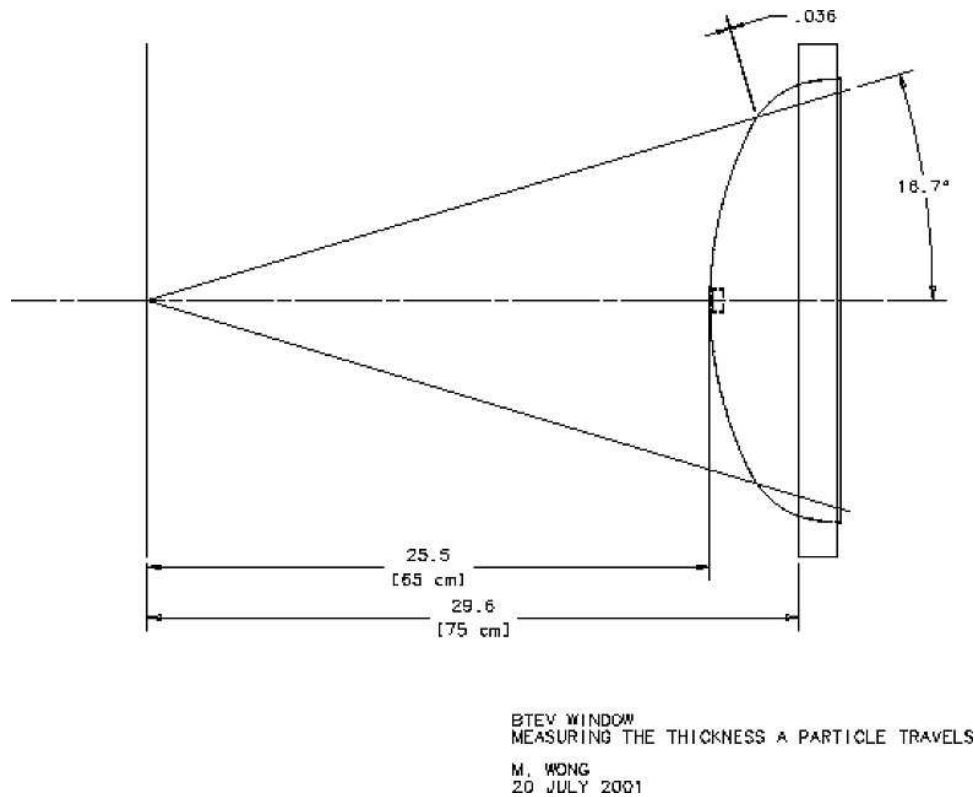


Figure 3.40: Relation of Pixel Vacuum Window to interaction point

primary Tevatron tunnel survey monuments to within 1mm. The compensating dipoles will then be adjusted, with respect to the toroids, so that they are aligned with the Tevatron beamline to within 0.25 mm. Secondary fiducial monuments will be mounted on the toroids and compensating dipole to facilitate continued monitoring of the survey location of these elements, and the BTeV spectrometer muon detectors at the 1mm level, during the lifetime of the BTeV spectrometer.

### 3.5.3 Tests and Integration of the beampipe sections into the BTeV spectrometer

The three major beampipe sections, the torispherical shaped end wall of the pixel vacuum tank, the 1" beryllium tracking chamber beampipe, and the 2" beryllium RICH counter beampipe, will be fully instrumented and tested at a location remote from C0. They will be transported to C0 at the appropriate stage of the spectrometer installation so that they can be placed in their final configuration. They will replace equivalent sections of conventional Tevatron beam pipe that will be in place during the various stages of the spectrometer installation before the final installation of the pixel detector, forward tracking chambers, and RICH counter.

After installing a beampipe section in the spectrometer, all pumping ports, flanges, and vacuum monitoring connections will be made. The vacuum must be restored to better than  $10^{-7}$  torr at each stage of the installation. The beampipe will then be survey aligned with an accuracy better than 1 mm with respect to the Tevatron centerline. The operation, readout, and control of the beampipe vacuum remotely by computer will then be checked.

In addition, a protective shield will be installed to protect the thin beryllium pipes from all accidental contact with sharp or dropped objects. The protective covering will be removed as a last step before closing the Collision Hall and preparing for beam. The beryllium beam pipe sections will be coated with a thin coat of epoxy to protect them against moisture.

The failure of a beryllium beam pipe section would be a major problem, potentially causing a protracted shutdown and repair of the Tevatron as well as the BTeV spectrometer. Because of this, operational safe guards will be put in place that severely limit any activity near the beam pipe, and protect the beam pipe with protective covers, whenever any work must be done in proximity to the beam pipe.

## **3.6 Completed and Planned R&D**

### **3.6.1 Vertex Magnet**

The Vertex Magnet is based on the existing SM3 magnet (built in 1982). The SM3 magnet was assembled by welding together, in place, various blocks of iron recovered from the Nevis Cyclotron. In order to better understand any problems that might arise during the disassembly of this all-welded magnet, a test disassembly of the magnet was undertaken in 1999. A contract was written to remove the flux plates from SM3 and also to dismount 2 of the 30-ton side iron blocks. The disassembly went well.

A search for the original assembly prints and engineering notes from 1982 was also successful. These notes and prints, as well as the disassembly test, form the basis for our estimate of the cost of the full disassembly and will form the basis of the final design of the Vertex Magnet.

Further studies with magnetostatic modeling programs are planned in order to better characterize the fringe field of the Vertex Magnet design. These fringe fields might need to be reduced with an additional small amount of soft iron shielding in order to protect the detectors from magnetic field distortion.

### **3.6.2 Muon Toroids**

It is planned to obtain the 24 large iron slabs that form the toroids from the existing SM12 magnet in the MEast Spectrometer. The SM12 magnet has 36 30-ton exterior iron return yoke blocks, 24 of which can be recovered without fully disassembling the SM12 magnet. These 30 ton pieces are identical to the sidepieces of the SM3 magnet, and are held in place with similar welds. Thus the disassembly test on SM3 in 1999 is applicable to the cost estimation and final design of the toroids utilizing these pieces. Design work is well along on

specifying the final assembly including the mounting points for the muon detectors, the extra absorbers around the beampipe, and the insertion of the compensation dipole. Magnetostatic modeling of the toroid and its embedded dipole has had an affect on the details of the final design.

### 3.6.3 Beampipes

The 1" diameter beampipe in the region of the forward tracking chambers will be constructed by modifying the existing CDF Run IIb beryllium beam pipe. Design work is progressing on specifying the needed modifications including the design of the low-mass, welded flange between this beam pipe and the 2" RICH beam pipe. The techniques for cleaning and heating this beampipe to achieve the required high vacuum must also be studied.

The 2" diameter beampipe inside the RICH detector will be assembled from the existing CDF Run I beryllium beampipe. The existing pipe will be cut to the desired length and retrofit with appropriate flanges to enable it to be integrated into the spectrometer. The flange at both end of this 2" beryllium pipe is specified to be minimum thickness. R&D is needed to develop an acceptable design.

The torispherical thin-walled flange/window that transitions from the 1" beampipe section onto the face of the pixel vacuum tank will need to be prototyped at reduced scale to understand the mechanical and vacuum properties of such a design.

The specifications of other flanges and ion pumps in the complete beampipe assembly must also be studied in order to understand the assembly, vacuum and beam impedance issues that arise. The window, the 1" beryllium pipe, and the 2" beryllium pipe are all connected via low-mass welded flanges.

## 3.7 Vertical Trajectory of Beams in C0

The BTeV Vertex Magnet is a dipole with its magnetic field oriented perpendicular to the direction of the beam. The magnet is centered in Z on the Collision point which is in the center of the Collision Hall. In order to fit the magnet into the C0 Collision Hall and for reasons related to servicing the experimental apparatus, BTeV bends particles, and the two beams, vertically.

The vertical deflection of the beams by the Vertex Magnet must be compensated by two 10 foot long B2 dipoles with fields oriented opposite to that of the Vertex Magnet and located  $\pm 9.7$  m from the Collision Point [7]. The Vertex Magnet has a vertical kick of 5.2 Tesla-m. The B2's dipoles each have a vertical kick of 2.6 Tesla-m at 980 GeV. The full apertures of the B2 magnets (inside the vacuum pipe) are 3.902" (in the B2 end plane) x 1.902" (out of B2 bend plane). The BTeV pixel detector, rather than the Vertex Magnet, will be the limiting aperture at the Collision Point [8] except during injection and ramping when the pixel detector will be retracted.

The magnets form a “3-bump” that deflects each beam up by 7.6mm at the Collision point. The beams enter and exit the C0 Collision Hall on the same trajectory they would have if there were no magnet. The geometry of the system is shown in Fig. 3.41.

These magnetic elements are all located inboard of any quadrupole magnets so their operation can be decoupled from the Tevatron Optics. Two modes are possible:

- The Vertex Magnet and the two B2 magnets can be kept off during injection, ramping, and squeezing and energized only after collisions have been established; or
- The Vertex Magnet and the B2 magnets could be programmed to follow the Tevatron ramp from 150 GeV injection to 980 GeV collision energy.

Depending on the low field behavior of the Vertex Magnet and the B2 dipoles, the aperture of the pixel detector while retracted, and any complications with controls, either mode could be chosen. Note that the toroids will not be ramped in either case. The results of the magnet measurements on the vertex dipole and the compensating dipoles will determine the best mode of operation.

Although BTeV will require the full low- $\beta$  insertion in order to take data, BTeV has requested that the C0 area be returned to a conventional straight section and the elements of the dipole spectrometer be installed earlier for apparatus testing and commissioning. The Accelerator Division has stated that the B2 apertures will not limit the separated orbits at injection or through collision for the existing (Collins straight section) configuration during BTeV testing, low- $\beta$  insertion, or CDF/D0 Run II operations. The  $\beta$  functions for the two configurations are listed in table 3.4.

Table 3.4: Typical  $\beta$  functions for various modes of BTeV running

z (m)	existing Collins Straight at collision, injection similar		John Johnstone Triplet
	$\beta_x$	$\beta_y$	$\beta_x = \beta_y$
-11.2 B49 and of B2	61.9 m	84.9 m	330 m
-8.2 C0 and of B2	63.7 m	81.2 m	200 m
0.0 C0 IP	69.7 m	72.1 m	0.35 m
+8.2 C0 end of B2	78.2 m	65.5 m	200 m
+11.2 C11 end of B2	81.9 m	63.6 m	330 m

The expected multipole field expansion for the Vertex Magnet, based on the electrostatic simulation, is small compared with any one of the superconducting bend magnets in the Tevatron lattice. Nevertheless, the multipole content of Vertex Magnet field will be measured before installation in the Tevatron. The multipole fields for the 10 foot long B2 magnets are known and are small.



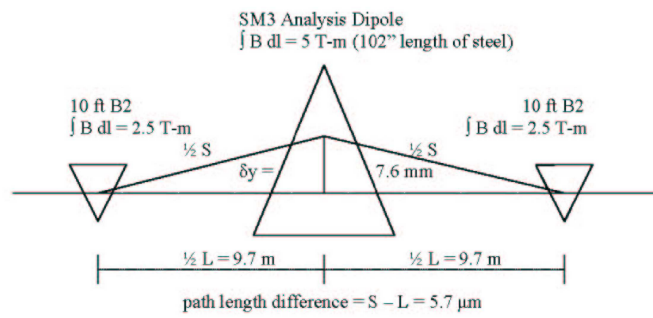


Figure 3.41: The Geometry of the BTeV Vertical Bending Spectrometer

# Bibliography

- [1] see Fermilab Beams-Doc 877
- [2] <http://ppd.fnal.gov/experiments/e907/Meetings/collab8/holger2.pdf>
- [3] See the Trigger Chapter in Part 4 for further details.
- [4] ASCE Standard "Mini. Design Loads For Buildings and Other Structures" (11/27/1990)
- [5] AISC "Allowable Stress Design" 9th Edition
- [6] "Foundation Analysis and Design" 3rd Edition by Joseph Bowles
- [7] This situation is different than for the currently running experiments in B0 and D0 whose spectrometer magnets are solenoids with their fields parallel to the beam and thus do not deflect them.
- [8] [http://www-ap.fnal.gov/~peterg/btev\\_ip\\_sept03/btev\\_1596\\_v3.pdf](http://www-ap.fnal.gov/~peterg/btev_ip_sept03/btev_1596_v3.pdf).

# Chapter 4

## The Pixel Vertex Detector

### 4.1 Introduction

The vertex detector is critical to the success of the BTeV experiment. The key goals of the vertex detector are excellent spatial resolution, ease of tracking pattern recognition, radiation hardness, material thinness, and readout of data fast enough for use in the lowest-level (L1) BTeV trigger system. To do this, very high precision space points along charged particle trajectories are required and these are provided by the pixel detector.

The pixel vertex detector is located at the center of the BTeV spectrometer, inside a 1.5T dipole magnet surrounding the interaction region. Data from the pixel detector will be used to find charged particle trajectories and reconstruct the vertices from which the tracks come. Pixel detectors are chosen because they can provide high precision space points with very few noise hits, and be quite radiation hard. Radiation hardness enables the detector elements to be placed very close to the beam (in vacuum, separated from the beam only by a few thin strips for RF shielding), minimizing track extrapolation errors.

### 4.2 Requirements

The measurement of 3-dimensional space points by the pixel detector, with very few additional noise hits, provides the necessary elements for excellent pattern recognition, allowing the reconstruction of tracks and vertices in real time, essential for triggering on events containing reconstructable heavy flavor decays. The pixel detector has to cover completely the angular acceptance of the downstream detector elements. The requirements that are listed below have been set to meet the BTeV physics goals based on detailed simulations and analyses. Furthermore, we have carried out several years of extensive R&D, including bench tests, irradiation studies and beam tests. This has led to a baseline design of the pixel system that will meet the performance required by the experiment to achieve its physics goals while being both affordable and technically achievable.

### 4.2.1 Resolution

The resolution of each pixel plane is one of the defining characteristics of the system. This resolution is determined by two things: the spatial resolution of the pixel sensors in a plane, and the amount of material in a plane. A fundamental limit on the accuracy with which tracks can be extrapolated out of the pixel detector into the beam region is given by the spatial resolution at the first two measurement planes, and by the error in the reconstructed track direction due to multiple Coulomb scattering in the first pixel plane.

- **Position resolution** The spatial resolution at each pixel plane must be better than 9 microns in the narrow pixel direction for tracks at angles up to 300mr with respect to the beam.
- **Material Budget:** Each pixel plane should have no more than 1.5% of a radiation length in the active area. Outside the active area but within the angular acceptance of the downstream detector elements, all materials that are required by the pixel system have to be minimized and must, on average, be less than the amount inside the active area.
- **Time Resolution:** Proper time resolution of the Pixel System has to be better than 50 fs.
- **Impact Parameter Resolution :** this is dominated by the closeness, material, and resolution in the first measurement point. It is related to the position resolution and the material budget. It should be good enough to achieve a rejection factor of 100 at the L1 trigger while keeping the efficiency for interesting all-charged B decays at 50% or above.
- **Two-track Resolution:** When two tracks cross a pixel plane too close to one another, the measurements associated with the two tracks can not be separated from one another. The two-track resolution must be better than  $450\mu\text{m}$ .

### 4.2.2 Efficiency

BTeV was designed to operate at a luminosity of  $2 \times 10^{32} \text{ cm}^{-2}\text{sec}^{-1}$  with a 132 ns beam-crossing interval (BCO). We can therefore operate at longer BCO as currently planned for the Tevatron, specifically at 396 ns, even with a corresponding larger number of interactions per beam crossing. In order to allow the Trigger system to use simple pattern recognition algorithms which can be implemented in hardware, the Pixel System must have very high efficiency and excellent two-track resolution. All hit data must be read out in a zero suppressed format, and spurious hit data must be minimized. The Pixel system must have high enough bandwidth so that the pixel data from every beam crossing can be read out and be provided to the Level 1 Trigger hardware.

- **Efficiency:** At design luminosity, each pixel plane must have a hit efficiency of at least 98.5% during its entire operational lifetime. This includes losses due to dead pixels, noisy pixels whose output is suppressed, and any loss of data by readout electronics or readout deadtime.
- **Noise:** The noise rate of the system must be less than  $10^{-5}$  per pixel.
- **Readout Bandwidth:** The BTeV Level 1 trigger must make a decision on every bunch crossing (396 ns). This requires a data-driven readout of the pixel system. It also means that (on average) all hit pixel data has to be read out and be available to the trigger processor every bunch crossing.

### 4.2.3 Radiation Tolerance

The anticipated radiation field at the pixel detector is expected to be dominated by high energy charged particles coming from the primary proton-antiproton interactions, and by electrons and positrons from photon conversions. The best estimate of this rate currently comes from BTeV GEANT and MARS calculations. The hottest region will be that nearest the beam for each detector element. At the closest position, planned for 6 mm from the beam line, the integrated number of minimum ionizing charged particles per ten years of running at a luminosity of  $2 \times 10^{32} \text{ cm}^{-2}\text{sec}^{-1}$  is  $\sim 10^{15}/\text{cm}^2$ , corresponding to an ionizing dose of roughly 35 Mrads. (Most of the pixels will see substantially less radiation as the radiation level falls roughly as  $1/d^2$ , where  $d$  is distance from the colliding beams.) The detector components must continue operating in this environment, with acceptable levels of signal-to-noise, operating voltages, efficiency, and spatial resolution.

- **Radiation Tolerance:** All the components of the pixel system must remain operational up to 10 years of BTeV running at the nominal luminosity.

The detector design has been guided by these high level physics driven requirements, as will be described in the sections below, where more detailed functional requirements will also be presented.

## 4.3 Overview

The pixel vertex detector provides the high resolution tracking near the interaction which is required to associate tracks with their proper vertices – primary and secondaries. The design of the pixel detector system is driven by the long interaction region at the Tevatron which has a  $\sigma_z$  of 30 cm. This forces one to have a rather long vertex detector. In addition, the detector must be placed very close to the interaction region in order to achieve good impact parameter resolution and acceptance. In practice, this is limited both by the radiation level that can be tolerated by the detector as well as the beam aperture. Furthermore, since the vertex detector information will be used in the Level I trigger, this places special requirements

on the detector and its readout. It is especially important for the trigger, which operates within strict time constraints, that the number of spurious noise hits be as low as possible. Also, the system must minimize the production of pattern recognition ambiguities or ghost tracks which would take extra time to sort out at the trigger level. The three-dimensional nature of the pixels is an enormous help in this regard.

With the planned configuration, the point resolution is expected to be between  $5\mu\text{m}$  and  $9\mu\text{m}$ , depending on the angle of the incident track. This has been demonstrated in our beam test at Fermilab in 1999 [1]. The angular resolution (without taking multiple scattering into account) is of the order of 0.1 mr. The pixel detector does quite a respectable job of measuring momentum without any assistance from the downstream spectrometer. For example, for a track which passes through ten stations, the resolution is

$$\frac{\sigma_p}{p} = 2\% \times \frac{p}{10 \text{ GeV}/c} \quad (4.1)$$

where  $p$  is the momentum in  $\text{GeV}/c$ .

The pixel detector system has 23 million pixels, each  $50 \mu\text{m}$  by  $400 \mu\text{m}$ , in order to have acceptable spatial resolution and low occupancy for the high multiplicity interactions anticipated. The BTeV pixel detector, like most pixel systems developed for high energy physics experiments, is based on a design relying on a hybrid approach. With this approach, the pixel sensor array and the readout chips are developed separately and the detector is constructed by flip-chip mating of the two together. Each sensor pixel is read out by a dedicated electronics cell, containing appropriate amplifier, discriminator, and other circuitry in an Application Specific Integrated Circuit (ASIC). A bump bond connects each sensor pixel to its readout cell. The pixel module is the basic building block of the pixel detector. Each module consists of a single sensor which is bump-bonded to a number of readout chips. Underneath the readout chips, a high density interconnect (HDI) flex circuit is glued that carries the I/O signals and power between the chip and the readout electronics. The modules come in four different sizes. In total, there will be 1380 modules and 8100 readout chips. The total active area of the detector is about  $0.5 \text{ m}^2$ .

The BTeV pixel detector has doublets of planes distributed along the IR separated by 4.25 cm. The individual planes are composed of two half-planes, each about  $5 \text{ cm} \times 10 \text{ cm}$ . There are altogether, 60 planes arranged in 30 doublets (stations). They are mounted left and right of the beam and are arranged so that a small square hole of  $\pm 6\text{mm} \times \pm 6\text{mm}$  is left for the beams to pass through (see Fig. 4.1). The two halves of the detector are displaced along the beamline by up to half-spacing between the stations to allow overlap between the two halves. A schematic of the detector is shown in Fig. 4.1.

Each half plane will have detector modules mounted on two sides of a graphite substrate with excellent thermal conductivity. On one substrate, the modules will have the narrow pixel dimension lined up in the y-direction (vertical) and the active area measures about  $5 \text{ cm}$  by  $10 \text{ cm}$ . On the other substrate, the modules will have the narrow pixel dimensions lined up in the x-direction (horizontal) with a total active area of  $3.8 \text{ cm}$  by  $7.3 \text{ cm}$ . A reasonable momentum measurement can be made using information from three or four stations. Pulse

height is read out and made available to the trigger, hence charge sharing can be used to improve the spatial and momentum resolution. The momentum information can be used to reject very soft tracks that would adversely affect the trigger algorithm because of multiple scattering.

Each half of the pixel detector will be sitting in vacuum and will be separated from the beams by a thin rf shield. To take the signal out of the vacuum vessel, we will use large feed-through boards (FTBs) made out of multilayer printed circuit boards. The vacuum system will consist of two integrated cryopumps plus additional surfaces at liquid nitrogen temperature (cryopanel) inside the pixel vacuum vessel. Nominally, the pixel detector will be placed at 6mm from the beams. During beam refill, the two halves of the detector will be moved away to about  $\pm 2$  cm from the beams. When the beam is stable, the detectors will then be moved close to the beam for data taking. A system of actuators and motion sensors will be used. To bring high voltage (HV) bias to each module, a power cable will be used. Our baseline assumes that each module will have its own HV power supply channel and that it will have separate analog and digital low voltage (LV) for the readout chips. On average, the power dissipated is about  $0.5\text{W}/\text{cm}^2$  of the active area, giving a total of 2.5 kW for the whole pixel detector system. The operating temperature of the detector is about  $-5^\circ\text{C}$ , and a cooling system is needed.

Fig. 4.2 shows a conceptual design for the stainless steel vacuum vessel for the pixel detector. The vessel is a rectangular box with a length of  $\sim 165$  cm and a height of  $\sim 60$  cm. Particles within 300 mrad traverse only the pixel stations and the 0.5 mm thick Al exit window. The graphite substrates will be attached to a support frame made out of carbon fiber composites. The position of the pixel detectors relative to the positions of the colliding beams will be controlled by a set of actuators attached to the vacuum vessel.

## 4.4 Summary of completed R&D

### 4.4.1 Introduction

Since the submission of the BTeV Proposal three years ago, we have made great progress in the development of the individual components required to build the BTeV pixel detector. The major components of the pixel detector system are the sensor, readout chip, sensor-readout-chip connection (bump bonding), high-density interconnection between the pixel readout chips and the system control elements, and the mechanical support and cooling systems. We have been designing and purchasing prototypes of these components, assembling units and testing them in beams and exposing them to intense radiation. We have also performed detailed simulation studies to understand the various design issues for the components as well as system aspects. Through these efforts, not only are we learning what is needed for BTeV, but we are gaining the necessary experience and know-how to build the actual pixel detector for the BTeV experiment. One of the highlights of this effort is the successful demonstration in a test beam during the 1999 Fermilab fixed target run of the resolution and pattern recognition power that can be achieved with a pixel detector [1]. Our R&D effort

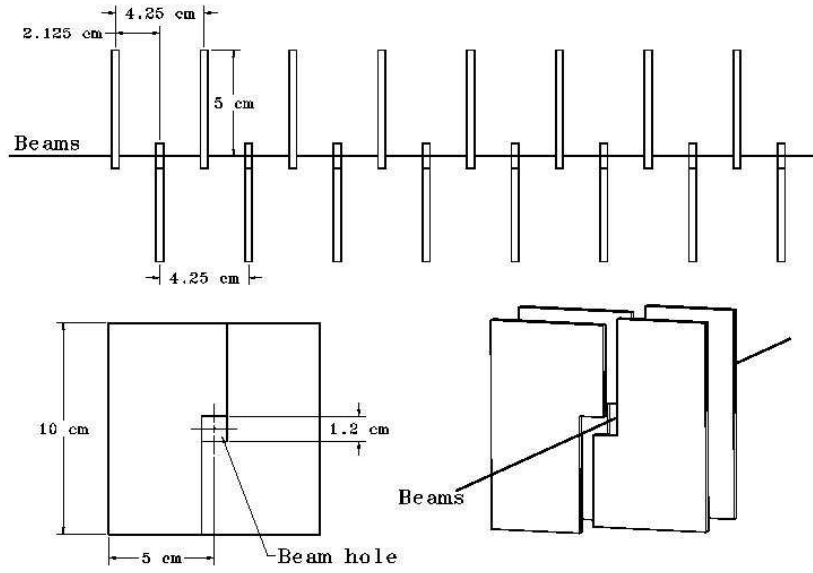


Figure 4.1: Schematic drawing of part of the pixel detector.

has also addressed the system engineering aspects. The vacuum system and RF shielding was reviewed by the Fermilab Accelerator Division in October 2003. The baseline design concept of the two systems were well received by the review panel.

Our R&D program has so far led to more than 40 publications and a large number of internal documents and reports. A complete list of all the published papers can be seen in [2]. This section summarizes the main accomplishments.

## 4.4.2 Sensor Development

### 4.4.2.1 Introduction

The dimensions of the pixel unit cell determine the hit resolution and occupancy. In turn, they affect the complexity of the system, the space available for the pixel electronics, and the demands posed on the cooling system. The sensor thickness affects the signal to noise achievable in the course of the detector lifetime, and the resolution achievable for large angle tracks that share the charge signal among several pixel cells. The overall material budget is determined not only by the thickness of the active elements in this system (sensor and readout electronics), but also by the mechanical support and cooling system.

The BTeV pixel detector will be placed very close to the colliding beams and will be exposed to a significant level of irradiation. At the full luminosity that we plan to operate,



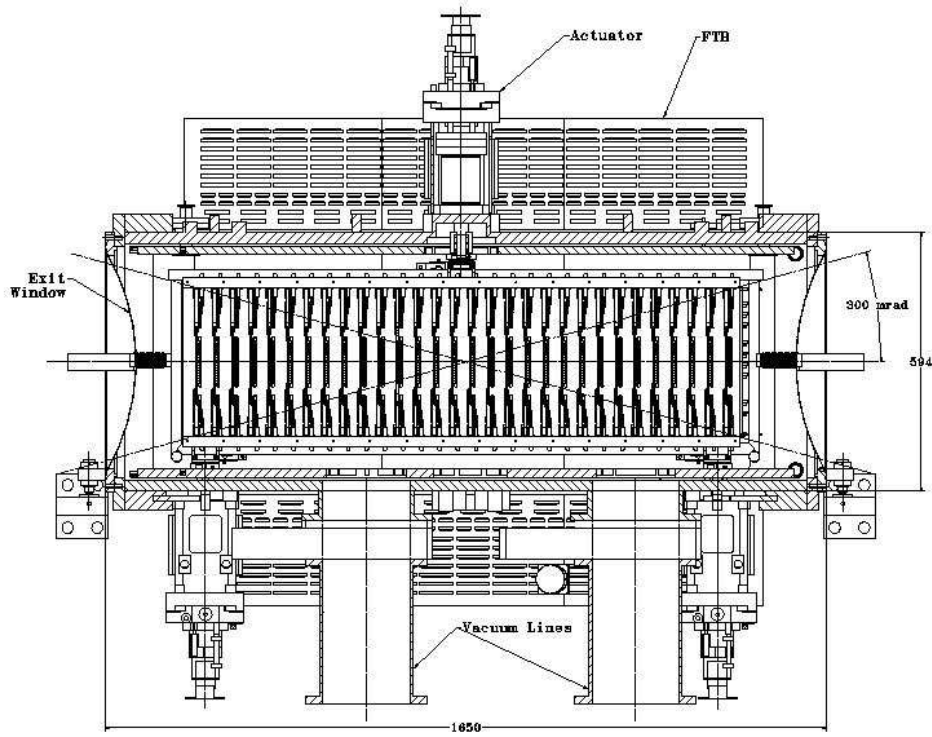


Figure 4.2: Side view of the vacuum vessel and support structure for the pixel detector. The pixel stations are mounted in two halves inside the vacuum vessel. Between the pixel stations and the colliding beams, there will be a thin RF shield. Signals are fed through the vacuum vessel via printed circuit boards with high density connectors. Also shown in the figure are actuators to move the detectors in and out of the beams for data-taking and beam refill.

it is expected that the innermost pixel detector will receive an equivalent fluence of  $1 \times 10^{14}$  particles/cm<sup>2</sup> per year of running. This will lead to radiation damage to both the surface and the bulk of the silicon pixel detectors.

#### 4.4.2.2 Sensor Design Considerations

The main challenge is to have a radiation hardened detector which will survive and remain operational after significant radiation damage to both the surface and the bulk of the silicon sensors.

Ionizing radiation leads to the charge-up of the surface, which anneals out in less than an hour at room temperature and to the formation of trapped charge both in the oxide and the interface to the silicon bulk. This charge is mainly positive and its presence results in the accumulation of an electron layer under the oxide. This leads to an increase in the interpixel capacitance with irradiation. The trapped charge density depends on the crystal orientation

because of the amount of dangling bonds available. Therefore, the crystal orientation is an important parameter in the design of the detectors. In particular, test results on silicon strips showed that the interstrip capacitance is strongly affected by radiation for  $\langle 111 \rangle$  substrate. Surface currents due to the oxide charges have been observed but they are less important than the bulk currents induced by irradiation.

The bulk damage is mainly due to the non-ionizing energy loss (NIEL) which, through the displacement of atoms in the crystal lattice, creates new energy levels, effectively acting as acceptors. Therefore the effective doping concentration will change with irradiation. For very-high-dosage irradiation, this will eventually lead to inversion of the conduction type of the bulk material (type-inversion), increases in leakage current and depletion voltage, changes in capacitance and resistivity, and charge collection losses. These are problems that need to be addressed by all the next generation hadron collider experiments. As a result, there is a worldwide effort to address these technical challenges.

In order to increase the useful operation time of the silicon sensors, operation with partial depletion has to be considered. This is more suitable for n-type pixel readout, because after type inversion the depleted region will grow from the  $n^+$  side of the junction. For this reason, the BTeV pixel sensors have  $n^+/n/p^+$  configuration. In these detectors, the charge collecting pixels are defined by the n-implants that are isolated from their neighbors. Without isolation, the accumulation layer induced by the oxide charge would short the individual  $n^+$  pixels together. We have explored two isolation techniques:

- The p-stop isolation where a high dose p-implant surrounds the n-region.
- The p-spray isolation developed by the ATLAS collaboration, where a medium dose shallow p-implant is applied to the whole n-side. To increase the radiation hardness and also the breakdown voltage before irradiation, a “grading” of the p-spray implantation (moderated p-spray) is required [8].

#### 4.4.2.3 Sensor Prototypes

Similar radiation environment is expected in the high luminosity LHC collider experiments ATLAS and CMS. As a result, there is a worldwide effort to study the various design issues affecting the radiation hardness of silicon sensors. Since our pixel size ( $50\ \mu\text{m} \times 400\ \mu\text{m}$ ) is the same as ATLAS, we have followed rather closely their development path. The design of our silicon sensors is guided by the necessity to operate the device at hundreds of volts without the risk of junction breakdown or micro-discharge. For this, a multiple guard ring structure is used to control the potential drop toward the cut edge on the p-side. These structures maintain the p edges of the sensors at the same potential as the  $n^+$ -side, which sits at the input potential of the readout chip. Finally, the hardening of the silicon itself is accomplished following the ROSE collaboration results, which developed the diffused oxygenated float-zone (DOFZ) silicon where the oxygen impurity concentration in the silicon wafer is enriched in a controlled way by a diffusion process. Our design takes advantage of all these previous results. We have signed a non-disclosure agreement with the ATLAS pixel sensor group.

Through this arrangement, we have purchased sensor wafers from them as well as gained access to their design. These wafers include both p-stop and p-spray sensor wafers. Some of these sensors were used in our test beam run in 1999 and we studied charge collection for both types of sensors.

We are also developing sensors of our own design. Our first effort was a joint development with the US CMS. We made a joint submission in Spring 1999 to SINTEF Cybernetics (Oslo, Norway). These wafers contain  $n^+/n/p^+$  sensors with different  $p$ -stop isolation geometries. This submission also included wafers from oxygen enriched silicon. In the summer of 2002, we received from TESLA (Prague, Czech Republic) a new batch of 15 pixel sensor wafers. These wafers contain sensors with the size and form factor to meet the needs of the BTeV pixel detector. For this submission, we used the moderated p-spray technology.

#### 4.4.2.4 Test Results on sensor prototypes

We have tested sensors from three vendors: the p-stop sensors are from SINTEF, the p-spray sensors are from TESLA and from CiS (Erfurt, Germany). The base material for the p-stop sensors was low resistivity (1 - 1.5 kohm/cm), 270  $\mu\text{m}$  thick  $< 100 >$  silicon. The p-spray sensors were fabricated using higher resistivity (2-5 kohm/cm)  $< 111 >$  silicon, 250  $\mu\text{m}$  thick. Some of the SINTEF and CiS wafers and all the TESLA wafers have been oxygenated. We tested three different pixel array sizes for p-stop sensors and one for the p-spray. The first p-stop array (called test-sized sensor) contains 12 x 92 cells and all these cells, except for four, are connected together. This structure was designed to study the behavior of a single cell. The second array (called FPIX0-sized sensors) contains 12 by 64 cells and it is designed to be read out by a single FPIX0 chip [10], the very first readout chip implementation for BTeV. The third array (called FPIX1-sized sensors), both for p-stop and p-spray, contains 18 x 160 cells and it is designed to be read out by a single FPIX1 chip. We have four different guard ring structures on the tested devices.

**SINTEF p-stop sensors** We have tested prototype p-stop sensors produced by SINTEF. Figure 4.3 shows the typical I-V curves measured for two of the test-sized sensors from a non-oxygenated wafer. These curves show very small leakage current and a reverse breakdown voltage of 500 V or higher (breakdown voltage is defined as the voltage for which the current increases steeply and is larger than 1 mA at room temperature). We have probed all sensors on all the wafers that we have received. To characterize these sensors before and after irradiation, we measured bulk parameters of the sensors including the bias voltage dependence of the leakage current, the full depletion voltage, breakdown voltage, and the temperature dependence of the leakage current [5]. Other parameters studied include the voltage distribution across the guard rings, effect of dicing, temperature and humidity dependence. Most of the sensors meet the specifications: leakage current less than 50 nA/cm<sup>2</sup> and breakdown voltage above 300V. Typical depletion voltage is about 180V. We have found the same results for both common and individual p-stop pixel isolation, for sensors with different guard ring layout and also between oxygenated and non-oxygenated wafers.

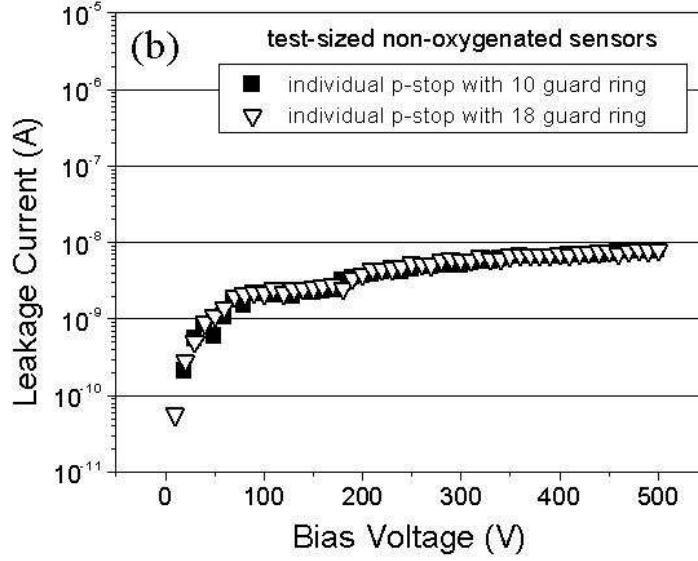


Figure 4.3: Typical I-V characteristics for non-irradiated test-sized pixel sensors

We also noticed that during wafer probing the test-sized sensors had better performance, i.e., higher breakdown voltage ( $> 500$  V) and small leakage current ( $\sim 10$  nA/cm<sup>2</sup> after full depletion). For the FPIX0-sized and FPIX1-sized bare sensors, although the current was also small, the breakdown voltage was lower (typically just above 300V). The same results were found for all the sensors that were tested. The poorer breakdown voltage performance for the bare FPIX0-sized and FPIX1-sized sensors is due to the fact that we could not bias properly all the cells on the bare sensors. Fig. 4.4 shows the I-V of a FPIX1-sized sensor before and after bump bonding to a readout chip and one can clearly see the difference. In fact, the breakdown voltage performance improved significantly and was similar to that obtained for the test-sized sensors. This was observed for all the sensors that were bump bonded to readout chips.

A few of these sensors have been exposed to a 200 MeV proton beam at the Indiana University Cyclotron Facility (IUCF). Fig. 4.5 shows the leakage current measurements before and after irradiation up to a fluence of  $4 \times 10^{14}$  200 MeV protons cm<sup>-2</sup> for a SINTEF p-stop sensor. The leakage current after irradiation increased by several orders of magnitude. However, operating at lower temperature can significantly reduce this leakage current. Fig. 4.6 shows that the leakage current decreases exponentially with temperature. Up to  $6 \times 10^{14}$  p/cm<sup>2</sup>, the sensors have a breakdown voltage higher than 500 V.

The leakage current after irradiation has a nearly linear dependence on fluence. In fact, the increase of the leakage current  $\Delta I$  (i.e. the difference between the currents measured

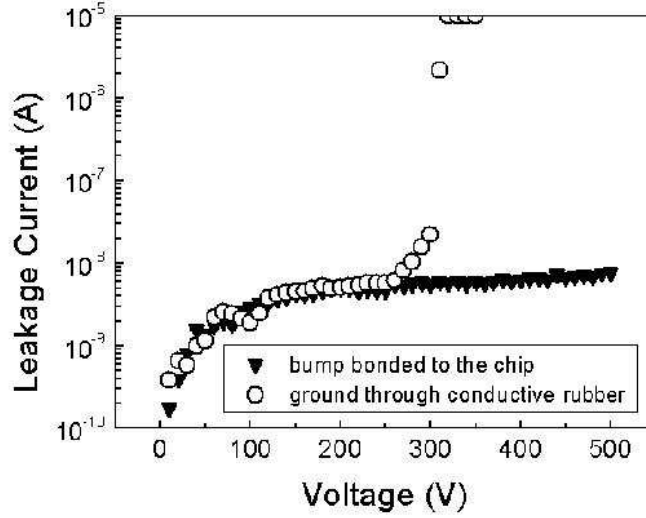


Figure 4.4: I-V characteristics for a FPIX1-sized p-stop sensor before and after bump bonding to the readout chip.

after and before irradiation) shows a linear dependence on the fluence:  $\Delta I = \alpha \Phi V$  where  $\alpha$  is the damage constant,  $\Phi$  is the fluence, and  $V$  is the sensor volume. Fig. 4.7 shows the fluence dependence of the increase in leakage current normalized to volume. We obtained a value for the leakage current damage constant  $\alpha$  of  $3.8 \times 10^{-17}$  A/cm, comparable to previous measurements [3].

The other bulk damage is the change in effective doping density which is reflected in a change in the full depletion voltage. Fig. 4.8 shows the dependence of the full depletion voltage on the proton irradiation fluence for a few p-stop sensors made from standard and oxygenated wafers. At a fluence of  $6 \times 10^{14}$  p cm<sup>-2</sup>, the full depletion voltage is still rather low, even lower than the value before irradiation. This characteristic is due to the low resistivity of the starting silicon material. This result, together with the fact that the breakdown voltage is still high compared to the full depletion voltage after irradiation, means that the BTeV pixel detector can be fully depleted without excessively high bias voltage even after a few years of operation. These tests show acceptable operation of the irradiated sensors in terms of leakage current, required depletion voltage, and breakdown voltage[5]. However, for this pixel layout there is still the problem with determining the breakdown voltage in wafer probing. In this design, it is not possible to implement a bias grid in the layout and, therefore, we cannot bias simultaneously all the cells before connection to the readout chip.

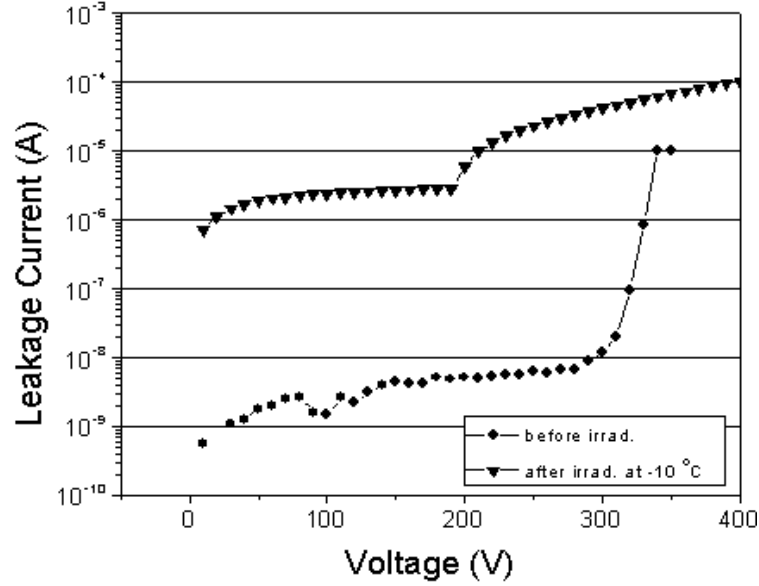


Figure 4.5: Leakage current measurements before (at room temperature) and after (at  $-10^{\circ}\text{C}$ ) irradiation to  $4 \times 10^{14} \text{ p/cm}^2$  for a SINTEF p-stop sensor.

**P-spray sensors** Several p-spray wafers from CiS and two from TESLA were tested. These were ATLAS pre-production pixel sensor wafers. Apart from a few sensors that show higher leakage current and low breakdown voltage ( $< 300\text{V}$ ), the typical I-V curves for FPIX1-sized p-spray sensors show a breakdown voltage higher than  $500\text{V}$  and a low leakage current. We have irradiated these sensors in a few steps up to a total of  $4.2 \times 10^{14} \text{ p/cm}^2$ . Fig. 4.9 shows the increase in the leakage current due to irradiation for the sensor irradiated up to  $2.3 \times 10^{14} \text{ p/cm}^2$ . The current increased by several orders of magnitude, as was the case for the p-stop sensors that we tested. We investigated the dependence of the full depletion voltage on proton fluence (see Fig. 4.10) and again we found that up to  $4.2 \times 10^{14} \text{ p/cm}^2$  the depletion voltage is still very low compared with the breakdown voltage ( $> 500\text{V}$ ). From a comparison between Fig. 4.8 and Fig. 4.10, we can see that the type inversion occurs at a lower dose for the high-resistivity p-spray sensors than for the low-resistivity p-stop sensors.

**FPIX2 sized p-spray sensors** We received in the summer of 2002 15 wafers from TESLA with the sensor layout matched to the size of the new FPIX2 readout chip (described in the next section). These are low resistivity moderated p-spray sensors. Probing tests have been completed. We have found satisfactory yield also from this batch of wafers. We plan to characterize these new sensors before and after irradiation and readout by the new FPIX2 readout chips.

Our plans for the future are to continue the radiation hardness investigation for the p-spray type of sensors. We plan to study the moderated p-spray detectors in a test beam to

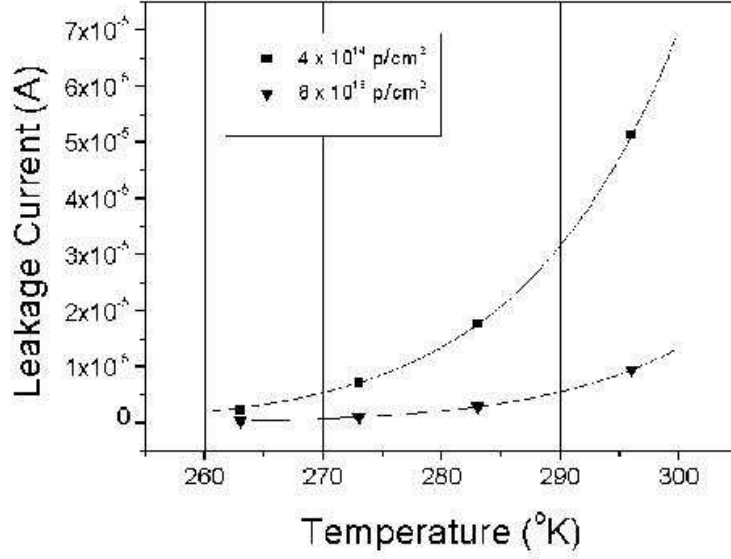


Figure 4.6: Leakage current as a function of temperature for two sensors. One was irradiated to  $8 \times 10^{13} \text{ p/cm}^2$ , and the other to  $4 \times 10^{14} \text{ p/cm}^2$ .

study the charge collection properties before and after irradiation and compare the results with the predictions from simulation. The p-stop sensors are used in a beam telescope that we have built for the test beam. Besides using these detectors to provide the beam reference, we will also check the charge collection properties and resolution of these sensors.

#### 4.4.2.5 Simulation

A detailed understanding of the factors affecting the sensor performance is crucial to its design. We have studied a number of issues through simulation. These include charge collection, radiation damage effects (including the deterioration of the noise performance due to the increased leakage current and the change in detector response induced by the change in the effective donor concentration), charge sharing, resolution achievable as function of track angle, and mapping of the electric field throughout the whole sensor. Other factors that affect the ultimate resolution achievable in this system are related more closely to the design approach and the performance of the readout electronics. In particular, the electronic noise, and the threshold that determines the minimal charge deposition that will be recorded as a signal hit, are important. The sensitivity to these parameters has been studied, as well as the tradeoff between analog and digital readout.

In order to understand these effects, we have developed a stand-alone simulation, based on a two-dimensional model of the signal formation in silicon. This program has been interfaced with the Monte Carlo software used to study our physics reach. This integration allows us to have a more realistic model of the detector occupancy, crucial in trigger simulations, and

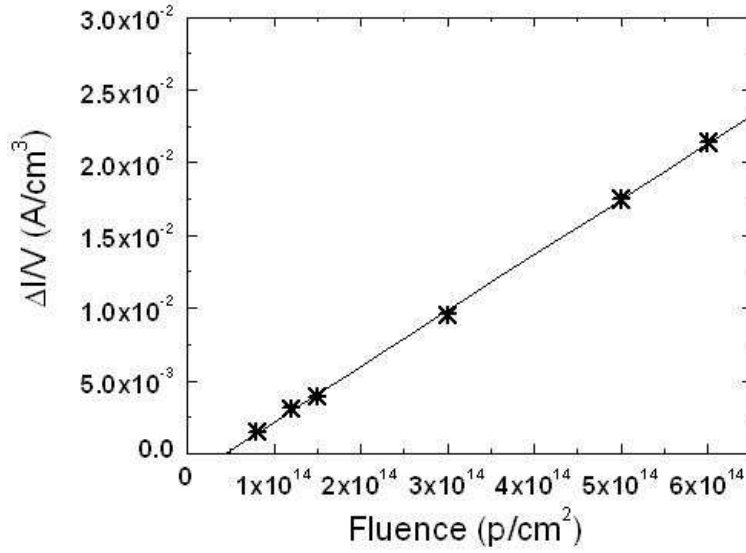


Figure 4.7: Fluence dependence of the increase in leakage current for p-stop sensors. All measurements were taken at room temperature.

also provides a more realistic implementation of the hit resolution achievable for different track angles of incidence. These studies allow us to map the achievable hit resolution for any given geometry as a function of the track incidence angle. They have also provided us with more accurate information on the hit multiplicity associated with a given track angle. We have used this more realistic information to achieve a better understanding of several key features of our detector performance.

Fig. 4.11 shows the resolution as a function of the incident beam angle for a pixel detector [1]. Two curves and data points are included in the figure: the solid line and circles show prediction and measurements done with an eight-bit ADC external to the pixel readout chip; the dashed curve and triangular data points illustrate the simulation and measurements obtained if we were only to use digital readout. The clear advantage of the analog readout is evident and for all incident angles, a resolution of better than  $9\mu\text{m}$  has been obtained.

### 4.4.3 Pixel readout chip

#### 4.4.3.1 Introduction

The use of the pixel detector data in the first level trigger means that the BTeV pixel readout chip must be capable of reading out all hit information from every beam crossing. Furthermore, the pixel readout chip should be optimized for the bunch crossing time planned for the Tevatron operation when BTeV is running. It must be radiation hard so that it can be used close to the beamline. This requires a pixel readout chip with a low noise front-end, an unusually high output bandwidth, and implementation in a radiation-hard technology.



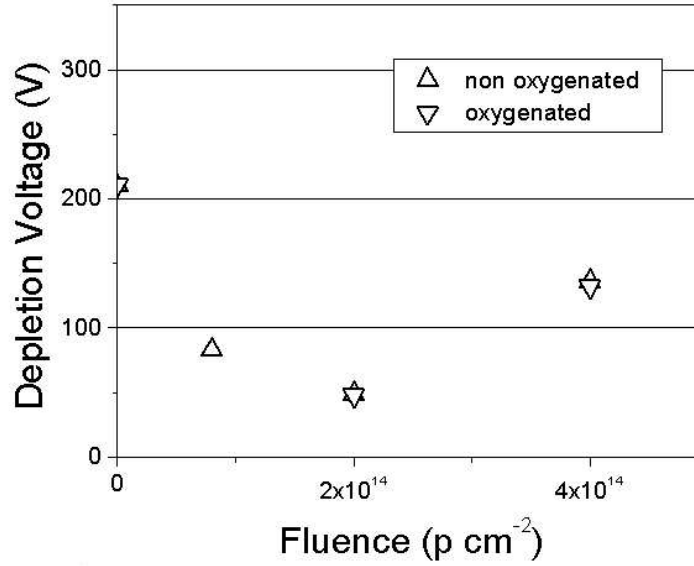


Figure 4.8: Full depletion voltage as a function of the fluences of the proton irradiation for normal and oxygenated p-stop sensors.

During the last few years, a pixel readout chip has been developed at Fermilab to meet these requirements. This has been done through several stages of chip development, each of increasing complexity [9].

As described above, the baseline BTeV design calls for  $n^+$  on  $n$  silicon sensors with appropriate guard ring structures for high voltage operation. These sensors provide adequate signals after significant radiation exposure, but also have rather large radiation-damage-induced leakage current. The BTeV pixel readout chip must be able to tolerate this leakage current at least up to 25-50 nA per pixel.

#### 4.4.3.2 FPIX0 and FPIX1

An R&D program was started at Fermilab seven years ago whose goal was the design of a pixel readout ASIC for BTeV. The program envisioned a series of prototype pixel readout chips, each with specific engineering goals. The first two prototype chips, FPIX0 and FPIX1, were designed and fabricated with the migration to a radiation hard Honeywell 0.5  $\mu\text{m}$  CMOS Silicon-On-Insulator (SOI) process in mind. Both chips have been extensively tested, both alone and bonded to a sensor. Furthermore, a beam test of pixel detectors using both chips was carried out at a test beam at Fermilab in 1999. As shown in Fig. 4.61 in the "Performance" Section, the beam test results showed that for resolution, 2-bit ADC information will be adequate[1]. We have now chosen to have a 3-bit FADC for each pixel since this gives an extra margin as well as allows for better monitoring and control of effects due to the very non-uniform radiation dosage to the pixel detectors in BTeV.

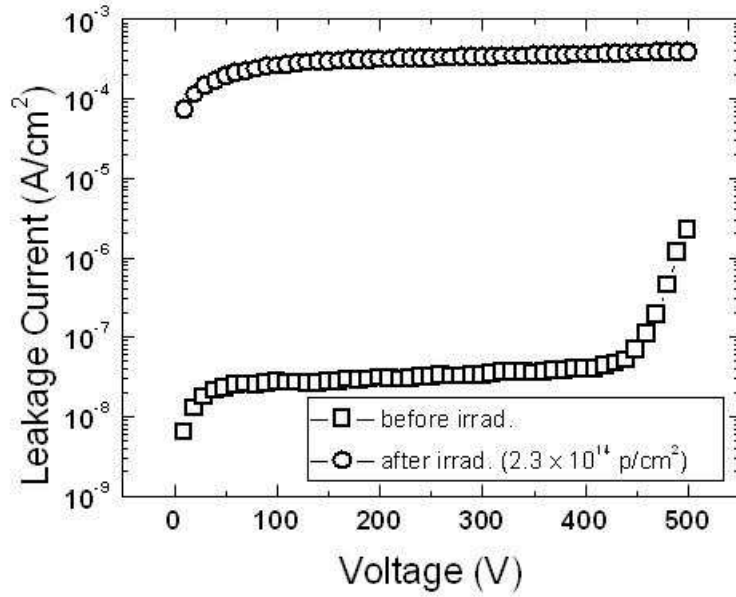


Figure 4.9: I-V curves for a FPIX1-sized p-spray sensor before and after irradiation up to  $2.3 \times 10^{14}$  p/cm<sup>2</sup>. The measurements were performed at room temperature.

The FPIX1 readout chip is the first implementation of a new column-based pixel architecture designed to meet the requirements of BTeV. The most stringent requirement is that all pixel hit information from every Tevatron crossing must be digitized and read out so that it may be used to form the primary trigger for the experiment. Simulations indicate that, with a 26.5 MHz readout clock, FPIX1 is capable of reading out an average of more than three pixels per beam crossing (BCO), assumed to be 132 ns. Relatively straightforward extensions of the FPIX1 architecture should increase the readout bandwidth by a factor of four or more.

FPIX1 was fabricated using the HP  $0.5\mu$  CMOS process. This choice was made in order to facilitate the production of a final BTeV pixel readout chip using the radiation hard Honeywell  $0.5\mu$  SOI CMOS process. This is costly and time consuming. Moreover, there is also an uncertainty about whether this process will be available when BTeV is ready for production. Thus, in May 1999, there were two outstanding issues in the design of the pixel readout chip. These were the number of ADC bits that would be needed to achieve the required resolution and the rad-hard technology. Since then, two positive developments have resulted in a much better understanding of the two issues. These two developments are the successful beam test mentioned above and the increasingly encouraging results on deep-sub-micron CMOS process for readout circuit prototypes obtained at Fermilab and other places.

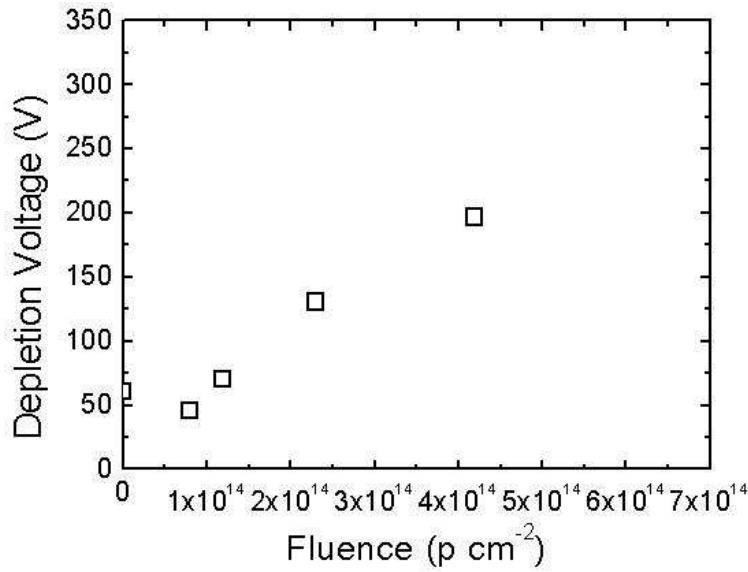


Figure 4.10: Depletion voltage as function of proton fluences for p-spray pixel sensors.

#### 4.4.3.3 0.25 $\mu\text{m}$ CMOS pixel readout chips

During the last few years, results from groups at CERN and Fermilab indicate that standard commercial deep-submicron (0.25  $\mu\text{m}$  and below) CMOS processes are even more radiation hard than military processes such as the Honeywell 0.5  $\mu\text{m}$  SOI, provided only that a set of special design rules is followed. We have chosen the 0.25  $\mu\text{m}$  CMOS process as the baseline technology for the pixel readout chip. A full prototype pixel readout chip (FPIX2), was submitted last Fall using this process. This chip follows the design philosophy developed in the earlier prototypes (FPIX0 and FPIX1), but incorporates new circuit design and implementation features appropriate for direct, radiation-hard use of the chips. The use of standard deep-sub-micron technology would allow for more rapid development cycles and reduced cost for the production quantities that we will need.

The development path of the pixel readout chip using the 0.25  $\mu\text{m}$  CMOS process included a number of submissions, implemented in two different commercial 0.25  $\mu\text{m}$  CMOS processes following radiation tolerant design rules (enclosed geometry transistors and guard rings) [4]. The preFPIX2I chip, containing 16 columns with 32 rows of pixel cells, and complete core readout architecture, was manufactured by a vendor through CERN [10]. The preFPIX2Tb chip, contains, in addition to the preFPIX2I chip features, a new programming interface and 14 digital-analog-converters (DAC) to control the operating and threshold settings of the whole chip. It was manufactured by Taiwan Semiconductor Manufacturing Company (TSMC). The last block to be tested was the high-speed data output serializer. This is needed to minimize the number of output signals, without compromising the high readout bandwidth. This was implemented in a small serializer test chip, again manufactured by TSMC.

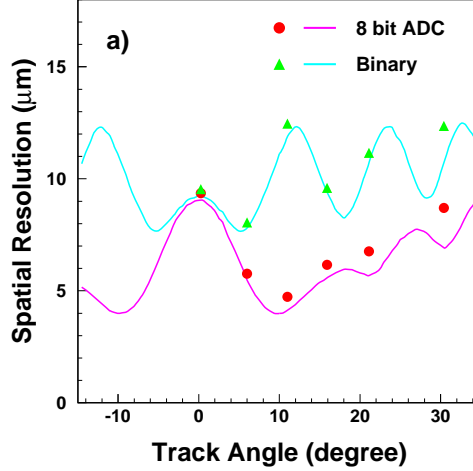


Figure 4.11: Resolution as a function of the angle of the incident beam. Data was taken with prototype pixel detectors during the 1999 Fermilab fixed target run. The detectors were instrumented with the earliest versions of the pixel readout chip FPIX0 at Fermilab. The curves represent the predicted resolution: the oscillating curve is the simulated digital resolution and the lower one assumes 8-bit charge digitization. The circles and triangles are extracted from the data.

An important feature of the preFPIX2Tb chip is the implementation of on-chip DAC's in order to minimize the number of external I/O lines. The change of the DAC behavior due to the proton irradiation has been measured and is shown in Fig. 4.12. The three curves shown correspond to the deviation from the linear fit to the unirradiated data for total dose of 0, 14, and 43 Mrad. It can be seen that the linearity and accuracy of the DAC output remains acceptable after 43 Mrad total dose.

To study total dose and Single Event Effects (SEE), samples of these prototype chips have been exposed to 200 MeV protons at IUCF. The comparison of the chip performance before and after exposure shows the high radiation tolerance of the design [6]. Chips have been exposed to as much as  $2 \times 10^{15}$  protons-cm<sup>-2</sup> (about 87 Mrad) and no evidence of catastrophic failure or deterioration of the functionality of the readout chip has been observed. In particular, no radiation induced SEE, such as Latch-Up or Gate-Rupture has been observed. After heavy irradiation, the prototype pixel readout chip shows little change in noise and threshold dispersion[6]. The comparison of the chip performance before and after exposure (Fig. 4.13) shows the high radiation tolerance of the design. Fig. 4.14 shows the time walk after 43 Mrad of irradiation. Between a threshold of 1000 e<sup>-</sup> and a threshold larger than 4Ke<sup>-</sup>, the measured timewalk is about 50 ns, certainly more than adequate even with a BCO of 132ns. We verified, at the required high speed and low power consumption, the complete functionality of our design up to total dose of 87 Mrad of 200 MeV protons. We tested all

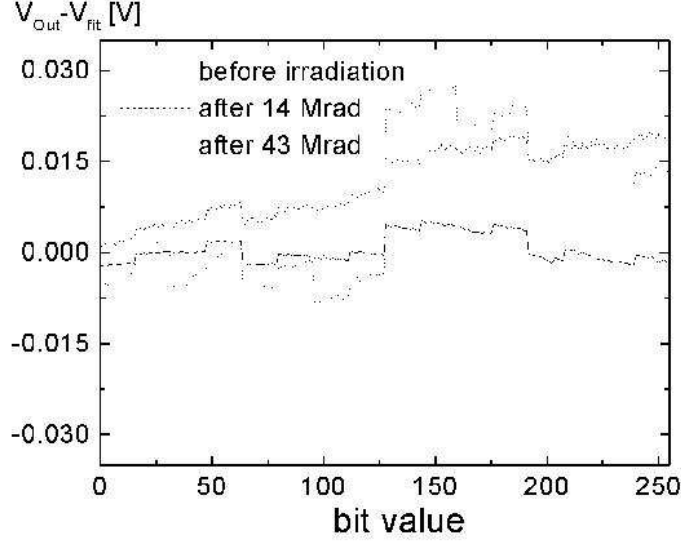


Figure 4.12: DAC analog response before and after 14 and 43 Mrad total dose exposure to 200 MeV protons. The full scale (255 counts) corresponds to about 1.7V

circuit blocks implemented in several prototype chips: the pixel cell, the data-driven and column-based readout architecture, the on-chip digital-analog converters, the programming interface, and the 140Mbit/s data output serializer. In particular, we show in Fig. 4.15 the good quality of the 140Mbit/s eye-pattern of on-chip LVDS drivers driving 50 foot cable. This implies that repeaters between the pixel detector and the data combiner boards located behind the magnet will not be needed.

In the BTeV operating environment, an intense radiation field will be present, which can induce Single Event Upsets (SEU) in the data transmission. These soft errors can result in data corruption, equivalent to digital noise, and loss of driver-receiver synchronization, introducing readout dead time. We have measured extensively the SEU cross section of the static registers implemented in the readout chip (mask and charge-injection registers, DAC registers, and serializer registers), and the radiation induced error rate of the data output serializer running at the nominal speed of 140Mbit/s. The measurements consisted of detecting bit error rates in the static registers controlling the readout chip front-end operating conditions and the pixel cell response. The single bit upset cross-section measured for the DAC's located on the chip periphery was  $(5.5 \pm 0.6 \pm 0.5) \times 10^{-16} \text{ cm}^2$  while for the mask and charge-injection registers located inside each pixel cell was  $(1.9 \pm 0.2 \pm 0.2) \times 10^{-16} \text{ cm}^2$  (where the first error is statistical and the second systematic due to uncertainty in the beam fluence) [7]. We tested and did not observe any dependence of the upset rate on the

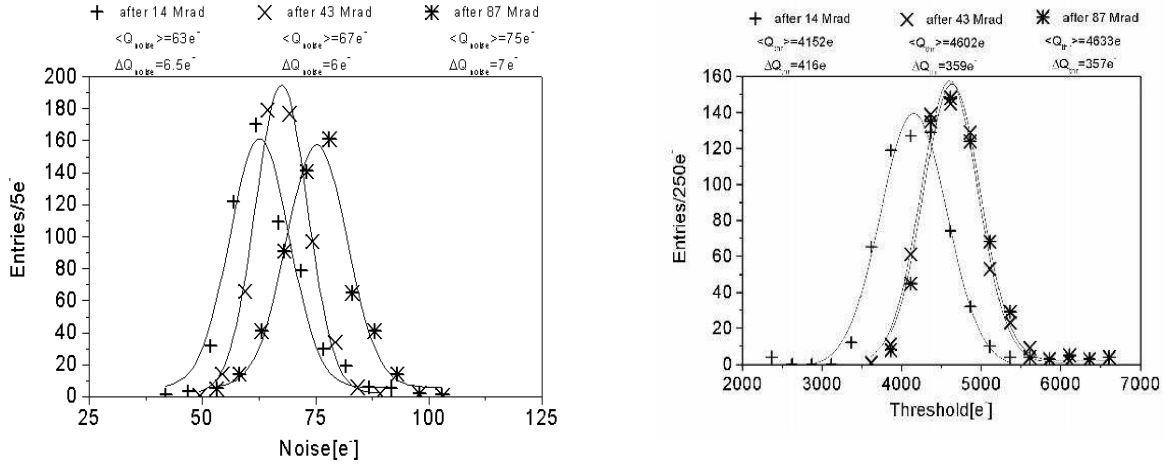


Figure 4.13: Noise and threshold distributions of BTeV prototype 0.25μm CMOS pixel read-out chip after irradiations to 14, 43, and 87 Mrad. For comparison, before irradiation, the mean noise and threshold dispersions were measured to be  $106 \pm 4\text{e}^-$  and  $345\text{e}^-$  respectively.

beam incidence angle or clock frequency up to 16 MHz. Our measurements of the SEU rate implies that the SEU bit error rate in the BTeV pixel detector operating at the nominal luminosity is small enough that it will not be necessary to design explicitly SEU tolerant registers. Rather, the SEU rate can be comfortably handled by a periodic readback of the chip configurations during data-taking and a download of the chip configuration whenever an upset is detected.

Based on the experience gained, we have moved on to a full-size BTeV pixel readout chip (FPIX2). This chip has 22 columns by 128 rows and includes all features of the preFPIX2Tb chip and the high speed data output interface which accepts data from the pixel unit cell and the column logic, serializes the data, and transmits the data off chip. We received at the end of 2002 about 20 wafers. For this submission, we had three different versions of the front-end design. Starting from Version A which is an improved and optimized (to the TSMC process) design of the preFPIX2tb, we added modifications to the discriminators (version B), and then further modifications to the second stage of the preamplifier. First results from bench tests of these chips are very impressive. All versions seem to be working fine. Fig. 4.16 shows the noise and threshold dispersion of version C of this chip. We have recently completed the probing of five wafers of the FPIX2 chip. The tests include powering up, checking of the voltage and current levels during quiet state and during operation, loading and reading back of pattern at high clock speeds using one or more serial lines. The yield is excellent, well

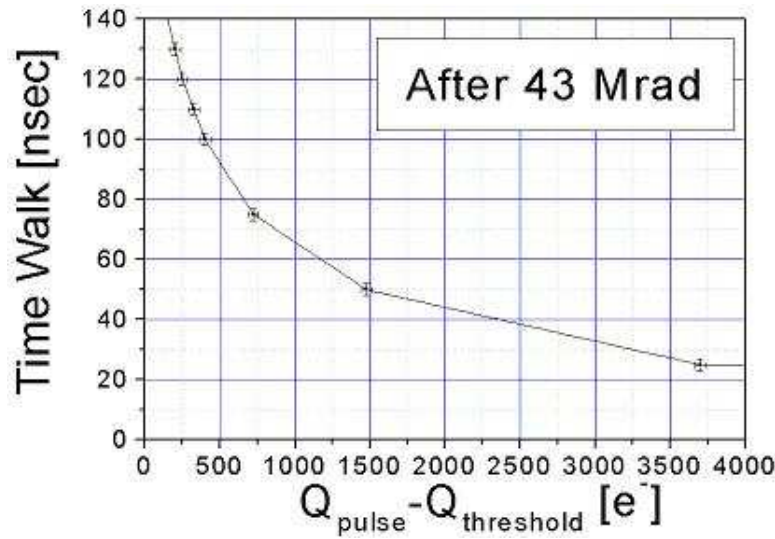


Figure 4.14: Time-walk of an irradiated preFPIX2Tb chip after a fluence of 43Mrad

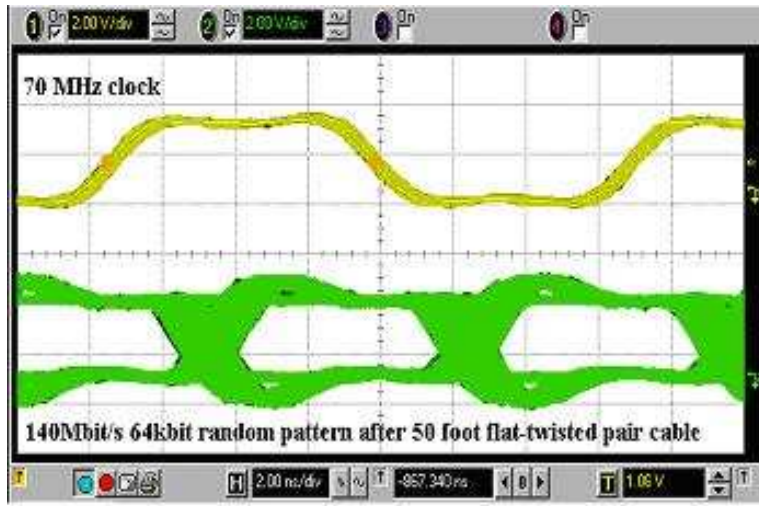


Figure 4.15: 140Mbits/s eye-pattern of on-chip LVDS drivers driving 50 foot cable

above 90%. The design appears to be acceptable for the final BTeV pixel system, pending on tests (both bench and beam test) with sensor bump-bonded to it before and after irradiation.

#### 4.4.4 Bump bonding development

The BTeV pixel detector, like all other pixel systems used in or planned for HEP experiments, is based on a hybrid design. With this approach, the readout chip and the sensor array are developed separately and the detector is constructed by flip-chip mating the two together. This method offers maximum flexibility in the development process, choice of fabrication

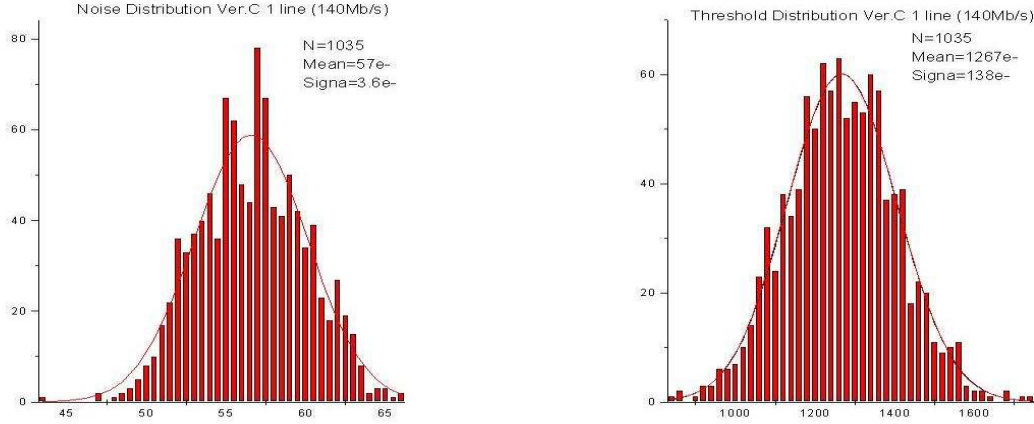


Figure 4.16: Noise and threshold distributions of BTeV FPXI2 pixel readout chip

technologies, and sensor materials. However, it requires the availability of a highly reliable, reasonably low cost fine-pitch flip-chip attachment technology. The technology has to be able to fulfill the following requirements:

- small bump - the typical bump diameter and height for our pixel detector is between  $10 - 12\mu\text{m}$ .
- fine pitch ( $50\mu\text{m}$ )
- high yield - a defect rate of better than  $10^{-3}$  is required.

We have focused our study on two options: indium bumps, and Pb-Sn solder bumps.

A series of yield and stability tests were performed on bump-bonded test structures. These tests were done with indium, fluxed-solder, and fluxless-solder bumps from a number of commercial vendors. Our tests have validated the use of indium and fluxless-solder as viable technologies. The failure rate obtained from this large scale test is about  $2 \times 10^{-4}$  which is adequate for our needs [11].

In order to check the long term reliability of the bump-bonding technology, we monitored the quality of the connectivity over a period of one year. In addition, we performed thermal cycling (exposure to  $-10^0\text{C}$  for 144 hours and  $+90^0\text{C}$  for 48 hours in vacuum). Furthermore, we irradiated some of these test structures with a  $^{137}\text{Cs}$  source up to a dose of 13 Mrad. The typical failure rate of both types of bumps under these stringent tests was found to be a few  $\times 10^{-4}$ . These results show that both techniques are highly reliable [12].



One of the remaining concerns is thermal stress on the bumps due to the coefficient of thermal expansion (CTE) mismatch of the bump material, silicon, and the substrate material on which the detector is placed. Questions still remain on the long-term reliability of the bumps due to thermal cycle effects, sensitivity to low temperatures, attachment to a substrate with a different CTE, and radiation.

We have carried out studies on effects of temperature changes on both types of bump bonds by observing the responses of single-chip pixel detectors and a five-readout-chip pixel detector assembly exposed to a  $^{90}\text{Sr}$  source. After going through  $60^\circ\text{C}$  thermal cycles, the hit maps, the responses of the single-chip pixel detectors to a radioactive source as a function of temperature indicated that basically all channels remain active after many thermal cycles. There is indication that a small number of pixels (about 0.3%) become slightly more noisy after thermal cycling for detectors using indium-bumps. With solder bumps, we have not observed any change.

We have also studied the strength of the bumps by visual inspection of the bumps bonding silicon sensor modules to dummy chips made out of glass. There, the bumps were clearly visible and we could observe any deformation of the bumps after thermal cycles and irradiation (figs. 4.17 and 4.18). While we have not observed any shorts or bridges, we do see changes in both indium and solder bumps at the level of 0.3% and 0.5% respectively. We are still investigating with the vendors on the possible causes of the changes observed and their significance [13]. In summary, both indium and Pb-Sn solder bumps are viable technologies and we have qualified three vendors.

The other uncertainty is wafer thinning. For material budget reasons, we would like to have the readout chip wafers thinned down to  $200\text{ }\mu\text{m}$ . One challenge to the bumping process is wafer thinning. After the CMOS fabrication sequence, the wafers may be reliably thinned to  $100\text{ }\mu\text{m}$  or even lower, before the bumping process. There has been a lot of experience in this with the SVX chips which are thinned down to  $300\text{ }\mu\text{m}$ . However, the bumping of thinned wafers is technically very difficult. There is significant risk of damage to the thinned wafers during the multi-processing steps required for wafer bumping. Also, the thinned wafers may pose processing challenges during photolithography. This is particularly true in our cases where fine pitch and small bumps are required. There are two approaches to solve this problem.

The first approach is to process the thinned wafers through the bumping sequence by temporarily attaching them to a wafer carrier with an appropriate polymer (adhesive). The risks associated with this method are basically solvent attack on the polymer layer during any of the process steps.

The second approach is to thin the wafers after bumping. This requires protection of the bumped surfaces during the thinning process. We are currently working with three bump-bonding vendors to test both approaches. A large scale qualification program is underway and we expect results will be available some time during 2004.

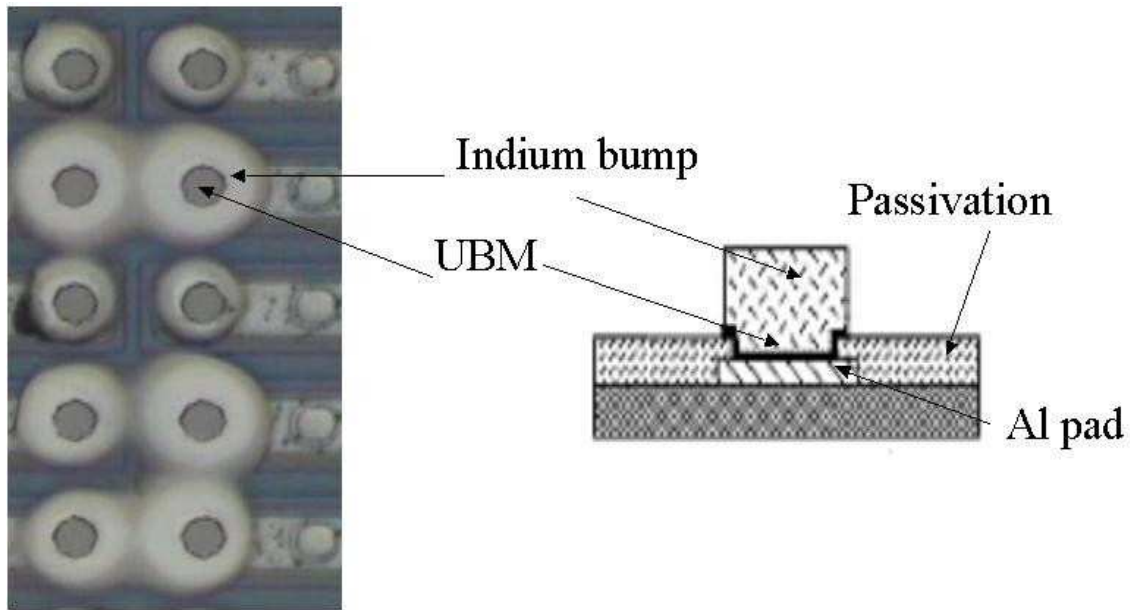


Figure 4.17: Sketch showing cross-section of indium bumps on the right. On the left is shown a picture under optical microscope of a region of the glass-Si module where the bumps are clearly visible.

#### 4.4.5 Multichip Module

Each pixel readout chip includes a high density of control and data output lines at the periphery. These lines need to be connected to the back-end electronics. A full set of pads is available on the readout chip for these interconnection purposes. This is achieved through a high density, low mass flex circuit wire bonded to a number of readout chips to form a multichip module.

Each pixel half-plane will be made up of a number of these multichip modules. The module is the basic building block of the pixel detector system. Each pixel module is composed of three layers. One of the layers is formed by the readout integrated circuits (ICs) which are flip-chip bump-bonded to the pixel sensor. A low mass flex-circuit interconnect is glued either on the top of or underneath this detector assembly, and the readout IC pads are wire-bonded to the flex-circuit. Fig. 4.19 shows the pixel module with the HDI glued to top of the detector assembly.

##### 4.4.5.1 First prototype

Figure 4.20 shows a picture of the first prototype of the pixel module. It is composed of a pixel sensor bump-bonded to five FPIX1 readout chips and a four layer high density flex circuit made by Fujitsu Computer Packaging Technologies (FCPT, San Diego). This flex circuit has line traces of  $20\ \mu\text{m}$  in a  $40\ \mu\text{m}$  pitch, copper line thickness of  $5\ \mu\text{m}$ , vias spaced by  $200\ \mu\text{m}$ , via cover pads of  $100\ \mu\text{m}$  and average via hole diameter of  $26\ \mu\text{m}$ . In this

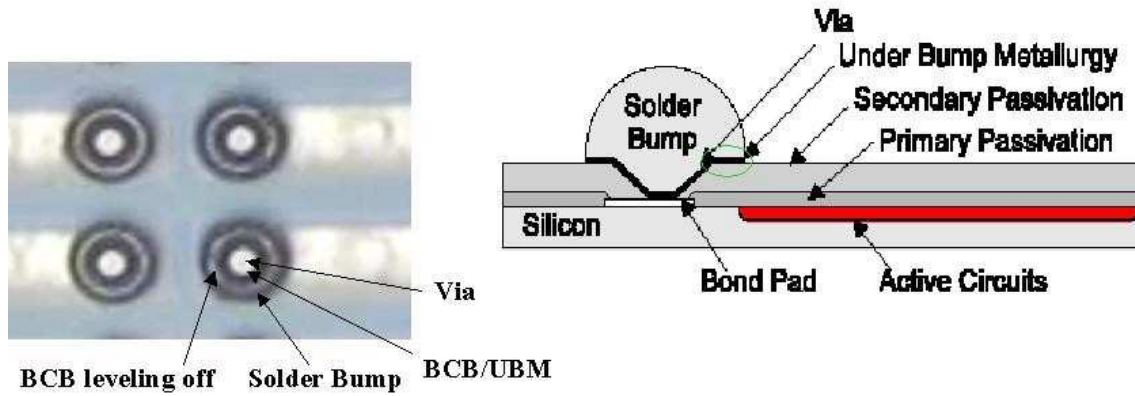


Figure 4.18: Sketch showing cross-section of solder bumps. On the left is shown in detail a few bumps as seen under the microscope of a glass-Si module.

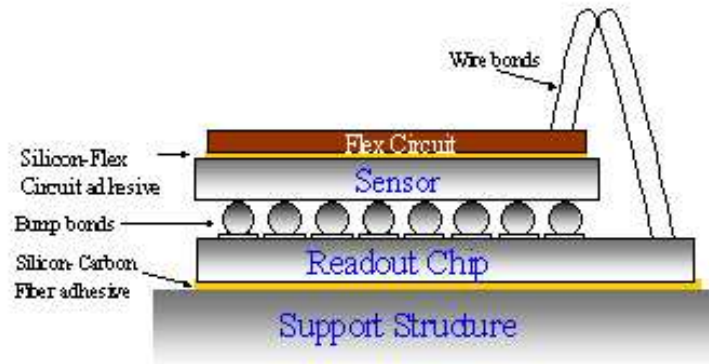


Figure 4.19: Sketch of the second pixel multichip module stack

prototype the flex interconnect is located on the side of the readout chips instead of on the top of the sensor or underneath the readout chips (as in the baseline design described below). The pixel sensor used is oversized; it can be bump-bonded to a total of 16 readout chips.

The threshold and noise characteristics of this pixel module have been studied. These characteristics were measured by injecting charge in the analog front end of the readout chip with a pulse generator and reading out the hit data through a logic state analyzer. The comparison of these test results with the results of a single FPIX1 chip shows no noticeable degradation in the noise and threshold characteristics of the chip. Furthermore, tests with a deadtimeless mode, where the charge injected into the front end is time-swept in relation to the readout clock also does not reveal any degradation in performance, indicating no crosstalk problems between the digital and analog sections of the FPIX1 and flex circuit.

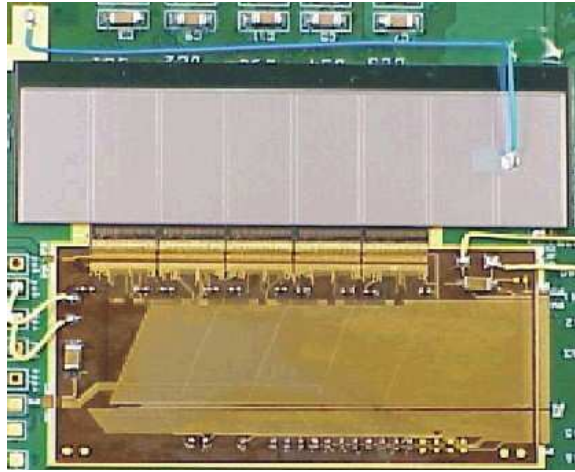


Figure 4.20: The first prototype pixel 5-chip module

#### 4.4.5.2 Second prototype

This prototype is composed of the three layers as described in Fig. 4.19. It also used the FPIX1 chips. The goals for this development were to assess the electrical and mechanical performance of such assembly, as well as to acquire insights into the construction process and yield. The prototypes built include four five-chip modules (two with sensors and two without). We have also tested the HDI by comparing the performance of single chip detectors read out using the HDI and a standard printed circuit test board.

The FPIX1 interface with the data acquisition system was not optimized to reduce the number of interconnections. The large number of signals in this prototype imposes space constraints and requires aggressive circuit design rules, such as  $35\mu\text{m}$  trace width and trace-to-trace clearance of  $35\mu\text{m}$  and four metal layers. A circuit with such characteristics is very difficult to obtain and very few places have such manufacturing expertise. The Engineering Support and Technical Division at CERN manufactured the FPIX1 interconnect flex circuit. Fig. 4.21 shows a picture of the flex circuit. Several design strategies to minimize electrical noise and guarantee signal integrity were incorporated in the layout and are being evaluated.

The interface adhesive between the flex-circuit and the pixel sensor has to compensate for mechanical stress due to the coefficient of thermal expansion mismatches between the flex circuit and the silicon pixel sensor. For this prototype phase, we chose to use a conductive silver epoxy. Figure 4.22 is a picture of a five-chip module that we have assembled and tested.

These modules were characterized for noise, threshold dispersion and their variances. These characteristics were measured by injecting test charge into the analog front end of the readout chip with a pulse generator. The results for various thresholds are summarized in Table 4.1 and 4.2 [15]. These results are comparable with previous characterization results of single readout IC mounted on a printed circuit board. No crosstalk problem has been observed among the digital and analog sections of the readout chip and the flex circuit.

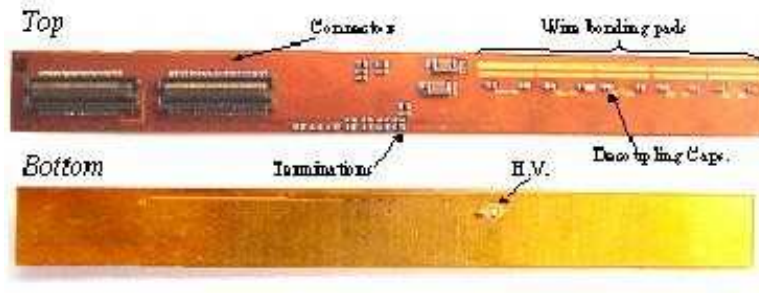


Figure 4.21: Picture of the flex-circuit made by CERN.

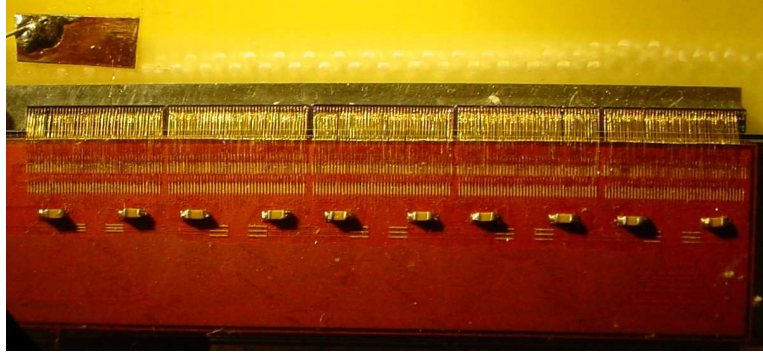


Figure 4.22: The second prototype pixel 5-chip module

The connectivity of the bump-bonds was tested by shining a radioactive source ( $^{90}\text{Sr}$ ) onto the sensors, while the absolute calibration of the modules is achieved using X-ray sources. Figure 4.23 shows the hit map of a five-chip module using a  $^{90}\text{Sr}$  source. This figure shows that most of the bump-bonds in the module are functioning, although chip 3 has a bad column (traced to be a digital control logic defect in this particular readout chip), and chip 5 has several broken bump-bonds. However, for this prototyping phase, none of the chips were tested before the flip-chip mating process. We plan to do wafer probing and use only known-good-dies for all future assemblies including production. For this prototype module, the threshold dispersion is  $380e^-$ , while the noise mean is around  $260e^-$ . These results are comparable to the single chip with no sensor used as a benchmark in these tests.

#### 4.4.5.3 Third Prototype

This prototype is designed for the pixel modules using the FPIX2 chips. Based on the experience of the first two prototypes, we realized that placing the HDI on top of the pixel module would pose serious technical challenges to the design of the HDI and the assembly of the module. In this design concept, the width of the HDI is limited to a little narrower than the width of the sensor module (8.4 mm). This in turn means narrow line width and spacing and rules out the possibility of having one HDI for an 1x8 pixel module. For the assembly, with the HDI on top of the sensor module, we have found that it is difficult to



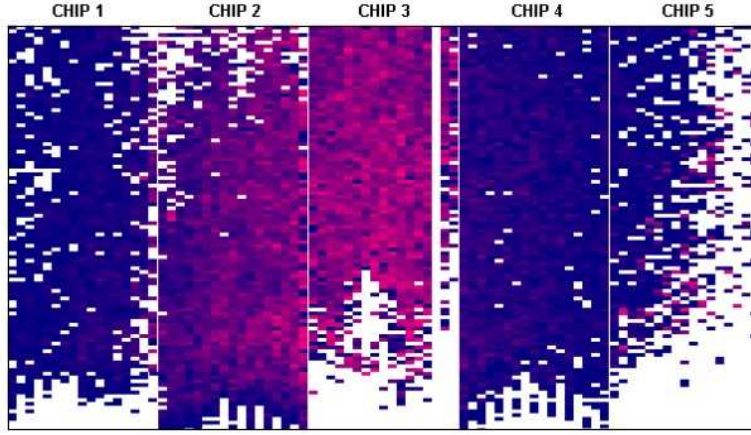


Figure 4.23: Hit map produced by a radioactive source moved from spot to spot.

<i>Single bare chip</i>				<i>Single chip with sensor</i>			
$\mu_{Th}$	$\sigma_{Th}$	$\mu_{Noise}$	$\sigma_{Noise}$	$\mu_{Th}$	$\sigma_{Th}$	$\mu_{Noise}$	$\sigma_{Noise}$
7365	356	75	7	7820	408	94	7.5
6394	332	78	12	6529	386	111	11
5455	388	79	11	5500	377	113	13
4448	378	78	11	4410	380	107	15
3513	384	79	12	3338	390	116	20
2556	375	77	13	2289	391	117	21

Table 4.1: Performance of the one-chip FPIX1 module without and with sensor. All numbers are given in equivalent electrons. There is no significant increase in noise and threshold dispersion with the sensor attached.

connect the HV bias to the sensor since the bias pad would be covered by the HDI. Also, wire bonding of the HDI to the readout chips is potentially dangerous to the bump bonds holding the sensor to the readout chips. Lastly, our experience with pixel modules based on FPIX1 chips showed that for stable operation, the chips would need to be sitting on top of a ground plane. With this design, the chips will be sitting on the substrate and a solid ground plane may not be easily achievable.

These concerns lead us to a new alternative design which puts the HDI on the bottom of the readout chips. In so doing, all the previous concerns will be removed. The HDI can now be wider (up to 11 mm), making the design less challenging and feasible for an 1x8 pixel module. The readout chips will now be sitting on the HDI which has a solid ground plane as the top layer. Assembly of the module will also be much simpler. One of the remaining issue is that the part of the HDI which sticks outside the readout chip is not wide enough to provide space for both the wire bond pads and the fast decoupling capacitors. This is usually desirable to provide high frequency filtering (low inductance connection) for the low voltage

Chip 1		Chip 2		Chip 3		Chip 4		Chip 5	
$\mu Th$	$\mu Noise$	$\mu Th$	$\mu Noise$	$\mu Th$	$\mu Noise$	$\mu Th$	$\mu Noise$	$\mu Th$	$\mu Noise$
$7204 \pm 352$	$267 \pm 17$	$8241 \pm 396$	$226 \pm 28$	$7328 \pm 388$	$215 \pm 20$	$7324 \pm 395$	$181 \pm 10$	$7146 \pm 391$	$240 \pm 24$
$6760 \pm 381$	$307 \pm 23$	$7123 \pm 400$	$232 \pm 18$	$6253 \pm 403$	$217 \pm 20$	$6226 \pm 383$	$184 \pm 11$	$6150 \pm 404$	$250 \pm 26$
$5364 \pm 359$	$262 \pm 19$	$5900 \pm 412$	$225 \pm 19$	$5250 \pm 400$	$230 \pm 19$	$5124 \pm 380$	$181 \pm 12$	$5020 \pm 420$	$243 \pm 24$

Table 4.2: Performance of the five-chip FPIX1 module. All numbers are given in equivalent electrons.

supplies to the chips. Characterization tests with the pixel module prototypes will determine if such capacitors are indeed necessary, since the HDI has a power and a ground plane that will act as a capacitor ( $\sim 800$  pF) and the HDI has decoupling capacitors located near the connector. Nevertheless, if necessary, the extra capacitors will be located at a "mezzanine" flex circuit assembled on top of the sensor, as shown in Figure 4.24. The first prototype pixel module with this stack concept has a connector to interface the pixel module to the PIFC (fig. 4.25). Future prototypes will connect the HDI to the PIFC via wire bonds. This new HDI will be available for testing in Spring 2004. The corresponding PIFC (both data and power flex cables) have been designed, submitted for fabrication, and will be available for testing soon.

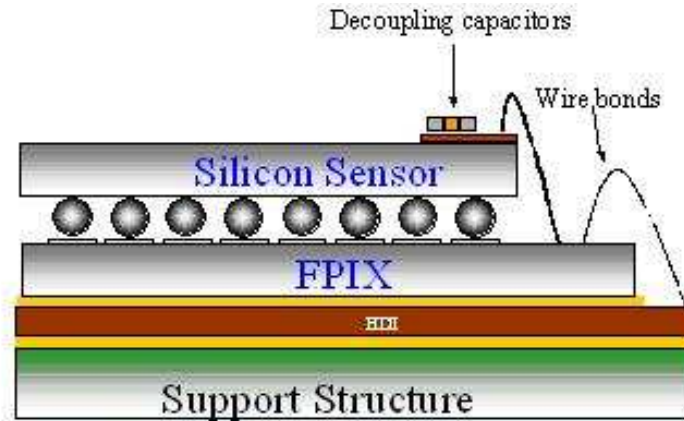


Figure 4.24: New design for the third prototype pixel multichip module

#### 4.4.6 RF shielding issues

The pixel detector will be installed inside the beam vacuum enclosure in the C0 interaction region. This raises concerns both for the operation of the pixel detector, and for the operation of the Tevatron collider. The bunched Tevatron beam could potentially excite microwave resonances in the pixel vacuum enclosure. If high Q resonance modes exist, they could destabilize the circulating beams. High microwave power in the vacuum box might also interfere with the operation of the pixel detector.

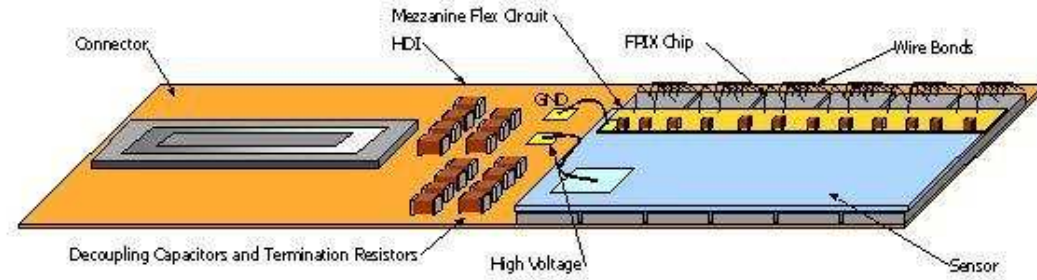


Figure 4.25: Sketch showing the new 6-chip module prototype

#### 4.4.6.1 Beam simulator test

In order to better understand these issues, we have built an apparatus to simulate the pixel vacuum vessel in the Tevatron (see Fig. 4.26). The basic structure of the test apparatus is a rectangular box made out of aluminum with two narrow diameter pipes at either end. The box and the two pipes are simplified full size models of the pixel vacuum vessel and the beam pipes outside the pixel region. In the center of the setup, a thick wire (8 mil Cu/Be) or an Aluminum tube was strung through the whole length of the box and pipes. A series of strong rf pulses, which mimic the Tevatron bunches, can be sent down the central wire or tube and the resonance structure of the apparatus can be measured with a network analyzer.

As is shown in Fig. 4.27, a series of strong resonances exist at frequencies above 1 GHz. These resonances are suppressed by more than three orders of magnitude by the addition of eight 5 mil Cu/Be wires surrounding the central wire. These test results have been reviewed by the Fermilab Accelerator Division. The reviewers concluded that a set of wires similar to those used in the test apparatus would be sufficient to ensure that resonances in the pixel vacuum vessel would not limit the Tevatron performance. The review panel also noted that the BTeV pixel vacuum vessel will contain a large amount of dielectric material (cables, etc.) that was not included in our test apparatus. This material will also tend to de-Q resonance modes and reduce the potential for problems[16][17].

We will continue to investigate various shielding configurations. We will also test the operation of prototype modules using this setup.

### 4.4.7 Mechanical support, cooling and vacuum system

#### 4.4.7.1 Introduction

The mechanical support design for the BTeV pixel detector system is dominated by the dual needs to have a stable and repeatable set of detector positions and to keep the amount of material to a minimum. These requirements are motivated by the consequences for the physics goals of BTeV of resolution smearing in both space and mass. The former of these is the most critical, since it influences many elements in the final capability of BTeV: separation





Figure 4.26: Picture showing the beam simulator. The inset on the top right corner shows the central wire and the ring of surrounding wires.

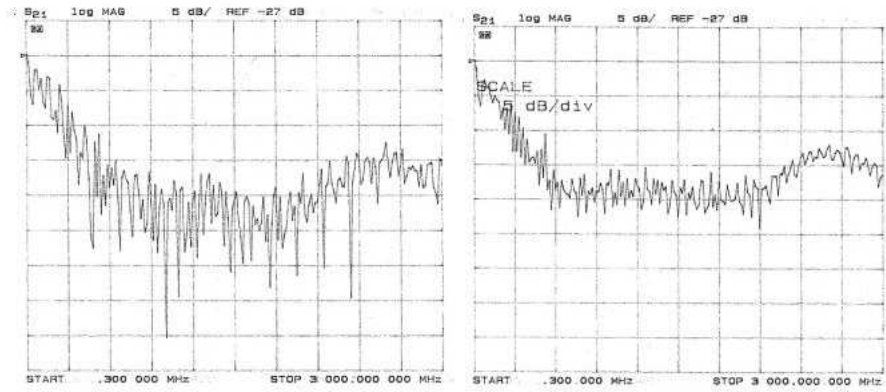


Figure 4.27: Results of the measurements with no wires (left) and with 8 thin wires shielding the central wire carrying the signal from the network analyzer.

of decay vertices from interaction vertices, trigger efficiency and enrichment, signal to background levels, proper time resolution, and sensitivity to multiple interactions per crossing. The mass resolution is also important, but mostly influences just the signal to background quality of BTeV data.

The pixel detector should be as close to the beam as possible to minimize the extrapolation distance from the first measured hit to the primary vertex. The pixel modules will be precisely placed on a support substrate which will also provide cooling to the detectors. The substrate will have a notch built in to allow the beam to pass through. The pixel detector needs to be retractable to a distance of  $\pm 2$  cm from the beam while the collider is being

filled and until the beams are brought to their final stable configuration. For this, a set of actuators and position sensors are required. Because of this dynamic aperture (separation) between the beams and the detector, the pixel stations will be placed inside a vacuum vessel. For the data, control and power signals I/O, we need to have a large number of vacuum feed-throughs. Significant progress has been made on the engineering design of the overall mechanical support, the vacuum vessel, motor drive assembly, and the individual substrates on which the pixel modules will be mounted. In some cases, early prototypes have been made and evaluated.

Major assembly steps have been worked out for the current baseline design. The mechanical stiffness of all the important elements such as the substrate mounting brackets, C-fiber support cylinder, and vacuum vessel were checked with finite-element-analysis (FEA) calculations to make sure that any deflections and stresses under load are acceptable.

Work has also started on the vacuum system design. One of the first tasks is to understand the gas load. We have built a 5% mock-up pixel system using as close as possible the same material as the real detector and measured the outgassing rate as a function of operating temperature. Prototype printed circuit boards for signal feed-through in and out of the vacuum vessel have been tested and the results validate our conceptual design. To check the robustness of the high density flex circuits after multiple flexes due to the movement of the pixel detector in and out the beam, cable flexing tests have been carried out including tests at low temperatures and after heavy irradiation. Initial results show the cables can withstand a large number of flexes (10,000 times) without any deterioration in performance.

#### **4.4.7.2 Carbon support structure**

The pixel stations require a very lightweight and rigid support structure, constructed to tight mechanical tolerances. Furthermore, the structure should have no long term deformations and can keep the alignment precision over a long period of time. Carbon fiber composite provides the best combination of low density and rigidity along with ease of manufacturability. To verify the FEA calculations, the manufacturing process, and assembly procedure, prototype support half-cylinders and support brackets were made using carbon fibers. Dummy aluminum substrates were then mounted (see Fig. 4.28) to the cylinder using the brackets on a coordinate measuring machine table. Known loads were then applied to the substrate and the deflection of the brackets were measured. Good agreement with the FEA results were obtained. To check the long term deformations and creep effect caused by small temperature gradients, we have studied using novel techniques such as Electronic Speckel Pattern Interferometry (ESPI), Fiber Bragg Grating (FBG) methods the displacement of the prototype carbon support structures.

A few ply lay-ups have been checked to identify a lay-up with highest possible modulus of elasticity and smallest coefficient of thermal expansion. Finally a 6-layer [0/45/90/90/-45/0] lay-up was chosen for building a full scale support structure prototype. To build this prototype, the material used is 76  $\mu\text{m}$  thick K139/BT250E-1 55 gsm prepreg (carbon fiber pre-impregnated with epoxy) made by BRYTE Technologies, Inc. This prototype has been



Figure 4.28: Picture shows aluminum dummy substrates supported by brackets made out of carbon fiber on to a carbon support frame.

completed. We are now working on a mounting fixture and a program to test the structure. This prototype will be mechanically and thermally tested to check whether the measurements are consistent with FEA predictions.

The mechanical stability of the pixel station can be monitored by use of FBG sensors. FBG sensors are optical fiber sensors acting as strain gauge, with unrivalled long-term stability, electromagnetic field insensitivity, mass lightness and radiation hardness. Use of FBG sensors can provide, during data acquisition, real time monitoring of the deformations occurred by the mechanical structures that hold and keep in position pixel detectors.

Use of FBG sensors and ESPI was adopted to test the carbon support half-cylinder structure reduced-size prototype. The measurements were intended to test the structural behaviour of the half-cylinder with respect to both thermal and mechanical stressing, thus characterizing both structural design and the production materials. The results would then be used to plan extended tests on the full-size prototype, with the aim of developing a complete system based on FBG sensors that will provide real-time monitoring of the final support half-cylinder structure during the operation and running of the experiment. The results obtained from the first set of tests show that detector position monitoring can be efficiently worked out by supporting structure deformation analysis [18, 19]. Specific investigations will show the feasibility of embedding FBG sensors in the composite materials

of BTeV mechanical structure. Such an option will be considered as a valid alternative to gluing the FBG sensors on the surface of the structure.

#### 4.4.7.3 Substrate

Each pixel half-station is assembled on two substrates, with the pixel modules placed with a small overlap on both surfaces of the substrate to provide complete coverage of the active area. For a number of years, the baseline design was to use a substrate made out of a novel material called "fuzzy carbon" with a number of embedded cooling tubes made out of glassy carbon. However, fuzzy carbon is very fragile and is made by a proprietary process owned by a single vendor. More importantly, such a design will have a large number of cooling joints and pipes containing coolants placed inside a vacuum system. The reliability and the risk of a leak in the system is a subject of grave concern. On another front, the outgassing tests of a 5% model of the pixel detector at various temperatures suggested that the use of a cryogenic panel at  $-160^{\circ}\text{C}$  might provide sufficient pumping to achieve the required vacuum level. The presence of the cryogenic panels and liquid nitrogen lines inside the pixel vacuum vessel provides a convenient heat sink. Cooling for the pixel substrate can now be done by conduction without the need of flowing coolant through the substrates. We will then have a joint-free and leak-tight cooling system. A material with very high thermal conductivity is needed for this kind of heat transfer mechanism in order to minimize the temperature gradient across the substrate. After some preliminary study among carbon-carbon, carbon-fiber reinforced plastics, carbon foam, flexible pyrolytic graphite sheet (PGS) and thermal pyrolytic graphite (TPG), TPG was chosen because of its outstanding thermal properties and low radiation length. To avoid any stresses due to the difference in CTE amongst the various materials that will be used (e.g. TPG, carbon fiber,  $\text{LN}_2$  tubes, cooling blocks), the more flexible and light weight PGS will be used to connect the TPG substrate to the cooling blocks. TPG is a unique form of pyrolytic graphite manufactured from the thermal decomposition of hydrocarbon gas in a high temperature, chemical vapor deposition reactor. Pressure and thermal annealing are then performed in order to enhance its thermal properties as desired. The thermal conductivity of TPG, after this sort of annealing, can be as high as  $1,700 \text{ W/m}\cdot\text{C}$  at room temperature. This property is temperature dependent, and it even surges to a peak of about  $3,000 \text{ W/m}\cdot\text{C}$  at  $-160^{\circ}\text{C}$ . TPG is currently used by the ATLAS SCT barrel modules and outer forward silicon modules. It has also been used by HERA-B and AMS and is proven to be a good candidate for such a substrate design.

The fundamental heat removal mechanism in this design is conduction. The conceptual design of the TPG substrate is shown in Fig. 4.29 and Fig. 4.30. The pixel modules are placed in an alternative stagger pattern on both surfaces of the TPG substrate to provide full coverage. The TPG substrate can be divided into two working areas. The first is the active or heat source area in the middle of the substrate where the pixel modules are placed. The second is the extended area that provides the needed channel between the active area and the heat sink.

Material budget is always minimized in the substrate design. TPG has a radiation length

of about 18.9 cm while for the flexible PGS, it is about 42.7 cm. The thinner the material, the higher the temperature gradient across the substrate will be. Since temperature gradient will generate thermal stresses and displacements in turn, the TPG substrate cannot be too thin and these stresses and displacements should be kept within acceptable limits. The work on the TPG is divided into four key areas:

- Thermal/structural modelling
- Study of Material properties
- Substrate design issues
- System issues and manufacturability

The goal in the thermal/structural modelling and substrate design is to identify the thickness of the substrate based on the balance of material budget and thermal performance, and to verify whether the corresponding thermal displacements and stresses are acceptable. Finite Element Analysis (FEA) was used as a design tool to investigate the different configurations and to study possible temperature stability control methods.

Based on the material budget requirement, the thickness of the substrate is the key parameter in the substrate design. Through the FEA calculations, we have established that a configuration with cooling at two ends of a TPG substrate arranged vertically with a uniform thickness of 0.38 mm (corresponding to 0.20%  $X_0$ ) would meet our needs. This is shown schematically as in Fig. 4.29. This would generate a temperature gradient across the active area of the X and Y-measuring planes of about 15.1°C and 8.4°C respectively [20].

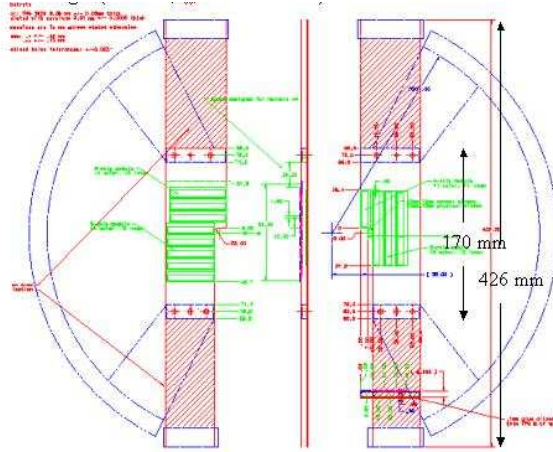


Figure 4.29: Layout of the TPG substrate

After the basic configuration has been established, a complete FEA model with multichip modules placed on both surfaces of a TPG substrate (fig. 4.30) was made. The temperature dependence of the thermal properties of the TPG was included in the model. A uniform heat

load density of  $0.5\text{W}/\text{cm}^2$  was assumed to be generated from the readout chips. Displacement restraints were applied to those nodes representing the precision hole and slot (used for station assembly and thermal stress relief purposes) where only in-plane displacement was allowed. The thermal profile across the substrate and modules are shown in Figures 4.31 to 4.34. In addition, thermal stresses and displacements were checked and they appeared to be acceptable[21].

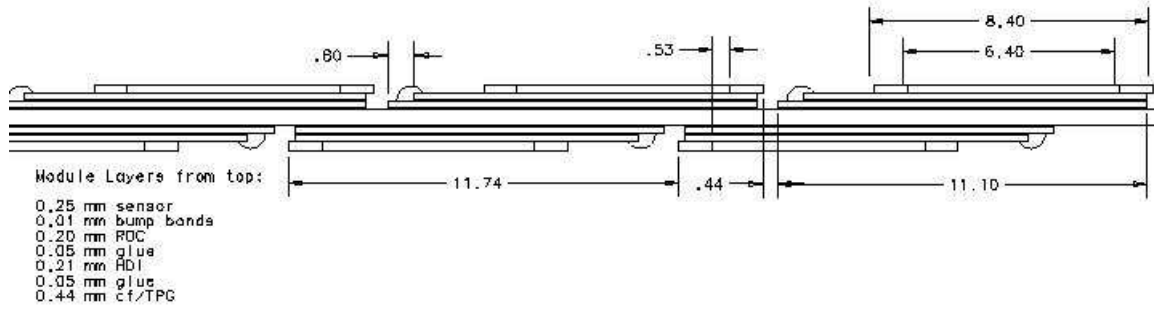


Figure 4.30: Layout of the multichip modules on the TPG substrates

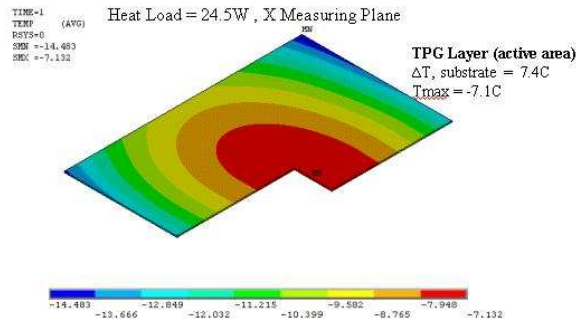


Figure 4.31: Thermal profile of TPG substrate within the active area in the x-measuring plane

We have recently changed our pixel module configuration so that the HDI will be placed underneath the pixel readout chips, directly on top of the TPG substrates. A preliminary FEA was done to compare the thermal performance of this design against the previous design which had the HDI placed on top of the sensor. The result showed little difference in the thermal uniformity across the substrates but the temperature of the readout chips would be up to  $5^{\circ}\text{C}$  higher in the new design. This can be compensated by keeping the ends of the TPG substrates at a slightly lower temperature.

Referring to Figure 4.35, there are three possible configurations of attaching the substrate to the heat sink. Configuration A, which is similar to the Atlas SCT Barrel module design that uses spring clips to keep the TPG in contact with the cooling block and allow a thermal in-plane sliding, is foreseen inappropriate in our complicated 3-D environment.

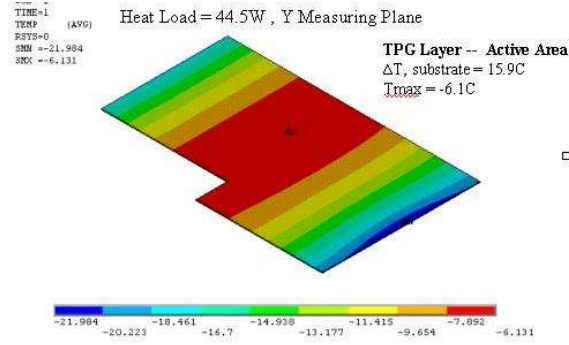


Figure 4.32: Thermal profile of TPG substrate within the active area in the y-measuring plane

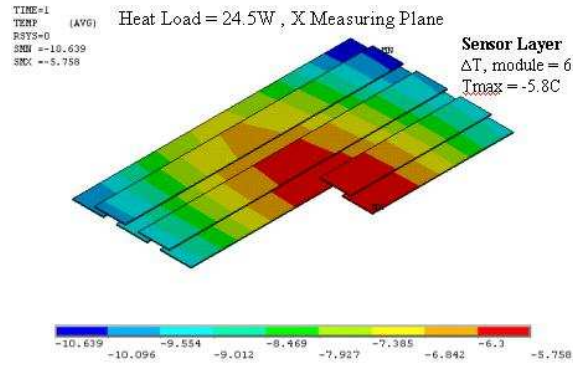


Figure 4.33: Thermal profile of sensors in the x-measuring plane

Configurations B and C, which use PGS as a flexible coupling, were studied carefully. The only difference between B and C is the location of the flexible joint. PGS in configuration B is directly attached to the heat sink beyond the extended TPG substrate, while the PGS in configuration C is placed immediately beyond the core of the TPG substrate and another piece of TPG is used to attach to the heat sink. In this study, the basic joint structure is a PGS-TPG-PGS sandwich with an overlap in each joint of 12 mm. Both TPG and PGS were modeled with temperature-dependent thermal properties.

It was found that configuration B always needed larger dimensions than Configuration C to achieve this. Moreover, with configuration B, we will need a much longer piece of TPG. After careful consideration of the manufacturing difficulty and the issue of handling, configuration C has been chosen for further studies and prototyping.

The future and final step in the FEA study will be to check the performance of the TPG substrate with additional heaters which will be used in order to achieve the needed temperature stability. A number of power outage or spike scenarios will be assumed. In



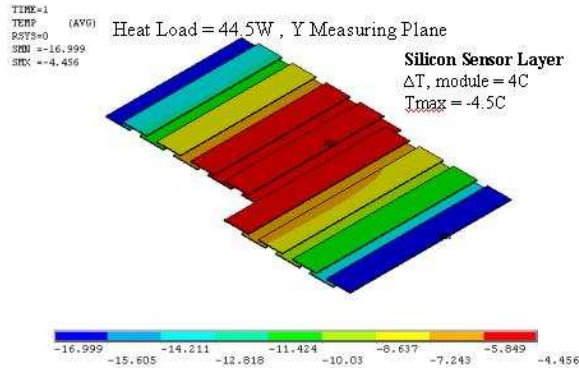


Figure 4.34: Thermal profile of sensors in the x-measuring plane

addition, thermal radiation effects, even though expected to be very small, will be included in the simulation.

The study of material properties of TPG and PGS include the measurement of the coefficient of thermal expansion, thermal conductivity, and elastic modulus as functions of temperature down to liquid nitrogen temperatures. Possible effects due to magnetic field and radiation have also been investigated. Fig. 4.36 shows the measured thermal conductivity of TPG and PGS as a function of temperature. One can see the strong temperature dependence for TPG. In contrast, the thermal conductivity of PGS is rather stable within the range of temperatures that are of interest to us.

TPG is intrinsically friable and delaminates rather easily. Moreover, since sensitive pixel readout chips will be placed on top of it, we are concerned about carbon dust that it may generate. The surface needs encapsulation and we have tried several encapsulation techniques. Due to the material budget constraints, however, choices for the encapsulation material is limited. These include a thin coat ( $\sim 10\mu\text{m}$ ) of parylene, epoxy, and carbon fiber. We have tried to encapsulate by using one ply of carbon fiber about 30 micron thick. Before the encapsulation, a pattern of perforated holes are drilled on the TPG substrate. By doing so, hundreds of resin bonds interconnecting the top and bottom layers are formed. Since getting fracture across the wider cross section of area is unlikely to happen, carbon fiber is only added along the long side to stiffen the much vulnerable smaller cross section area as needed. The carbon fiber lamination strengthens the TPG significantly and addresses the concerns with routine handling of the substrate.

Other tests include the flatness measurement of TPG and outgassing studies before and after encapsulation. The outcome of these tests show that TPG with the carbon fiber sheets laminated to the surfaces are robust enough for handling and modules placement. We are currently working out quality assurance issues.



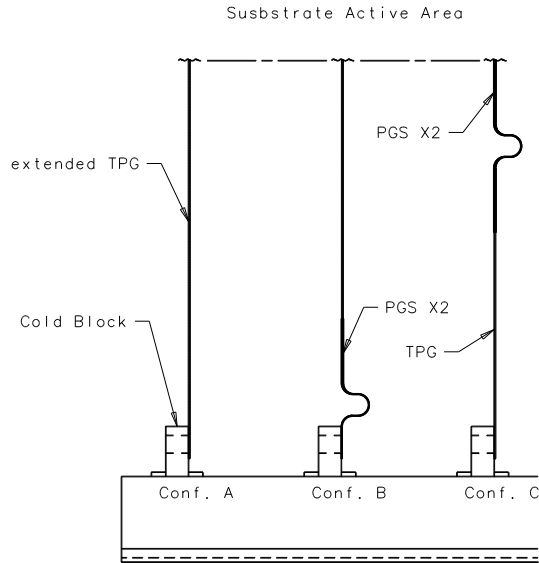


Figure 4.35: Joint Configuration in the extended area

#### 4.4.7.4 Feed-through Board

The feed-through board (FTB) is primarily dedicated to bring signals from and the power to the pixel modules. The huge number of lines and tight space available do not allow the use of commercially available feed-throughs. The solution to this problem is to use a custom made multilayer printed circuit board as the feed-through core element.

The preliminary specification of the FTB has been completed [23]. Based on this, a full layout has been done, and suitable connectors have been chosen. The board is very complicated and in order to realize this, there are quite a few issues which need to be addressed:

- The potential pitfalls of making such large size thick multilayer board. Each board measures 27.5" by 17". The current layer count is 36 because of the numerous numbers of signal and power traces that will be needed. On the other hand, the board cannot be too thick because of geometrical constraint due to the magnet and to the depth of the connector that can be placed on the board. A potential problem is board warping

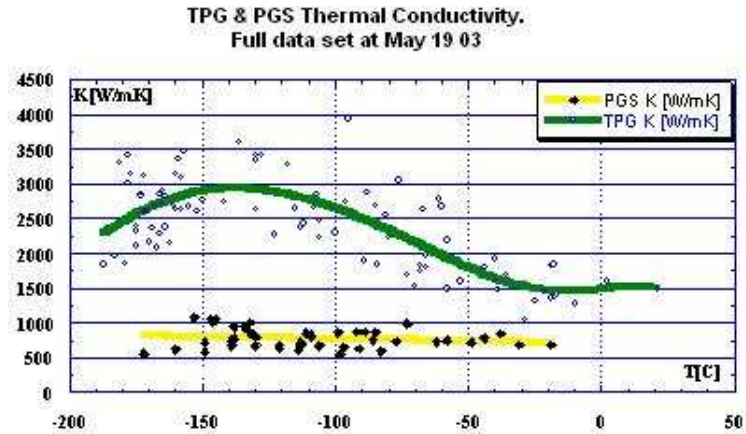


Figure 4.36: Thermal conductivity of TPG and PGS as a function of temperature

during the assembly. Another problem is impedance matching and the fine trace width and spacing. There are only a few vendors for such complicated boards.

- The possibility of making a vacuum tight board. With so many layers and different connectors and slots on the board, it will be challenging to make such a board that can hold the required vacuum level.
- Robustness of the board and the fine traces during assembly and operation and effect of irradiation.
- Reliability of vacuum tight joint in between boards and aluminum plates.

For the first three questions, a full scale board prototype has been designed. Fig. 4.37 shows a schematic of the full-sized feed-through board prototype. We have contacted a few vendors on fabrication issues such as material selection, thickness, insertion of connectors, and the possibility of warping. A couple of these prototype feed-through boards have been ordered and will be available for testing in 2 months' time. We are also looking into ways of simplifying this board. Small test boards will be built to test new design concepts and layout ideas. These test boards will be made using two materials of different dielectric constants. We will perform tests to check the outgassing and dielectric properties before and after irradiation. To answer the last question, a mechanical FTB prototype was built. Multilayer boards were substituted by regular fiberglass plates of the correct thickness. Then they were joining together by gluing on the aluminum plates. The assembly was checked and no leak

found. A load was next applied to the ends of the board. Even after the FTB was bent (Fig. 4.38) no leak through the joints was detected.

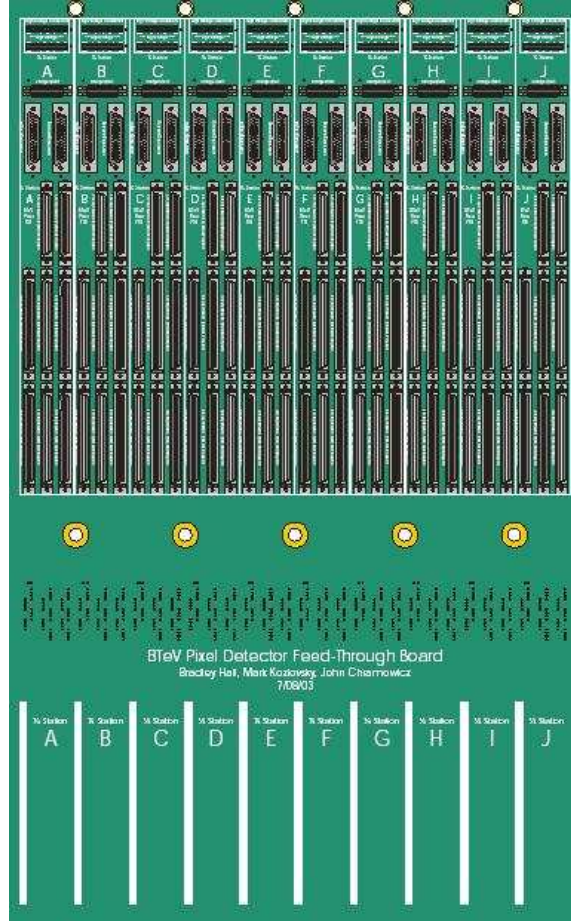


Figure 4.37: Front view of the Feed-through Board now being layout and reviewed.

#### 4.4.7.5 Outgassing test and 5% model test

A model comprised of about 5% of the BTeV Pixel Detector (in terms of surface area) was built for the purpose of measuring its gas load due to outgassing and to understand how the gas load affected the ultimate vacuum pressure of the chamber. The model consisted of six substrates with dummy modules. A carbon-fiber shell supported the substrates. Kapton strips simulated the electrical flex cables. An aluminum plate served as a cable strain relief plate and a heat sink. The test was set up so that the model and the cable strain relief plate/heat sink was each cooled independently. Fig. 4.39 and Fig. 4.40 show the model.

When the model and heat sink were at room temperature, the vacuum pressure was  $3.4 \times 10^{-7}$  torr and the gas load was  $5.2 \times 10^{-4}$  torr-L/sec. Cooling the model and heat sink



Figure 4.38: Prototype feed-through board being tested for vacuum properties.

to  $-10^{\circ}\text{C}$  cut the gas load and the vacuum pressure in half. By cooling the heat sink to  $-160^{\circ}\text{C}$ , the vacuum pressure was brought down to  $1.0 \times 10^{-8}$  torr. Analyzing the residual gas analyzer (RGA) readings at each temperature, it was found that water vapor was the main load and that cooling the heat sink to  $-160^{\circ}\text{C}$  resulted in the heat sink acting as a cryo-panel that pumped water at a rate of 19,000 L/sec [22]. Thus, using the cryo-panel in conjunction with other pumps such as turbopumps or cryogenic pumps can result in the pixel vacuum vessels ultimate pressure to be  $< 10^{-8}$  torr, which is the minimum acceptable pressure in the beam regions.

Several tests need to be run to fully understand the ramifications of having a cryo-panel in the vacuum vessel. To address question of the cables passing a very cold heat sink, the effects of cold temperature on the electronic flex cables have been tested. A prototype signal cable and a power cable were completely immersed in liquid nitrogen. The ends of these cables were then repeatedly flexed for a distance of about 3 cm while having current run through them (10 mA for signal cable, 1.5 A for power cable). The voltage of each cable was recorded. The flex test ran for 100,000 flex cycles. The cables continued to show consistent voltages, indicating that the cold temperature did not have an effect on the structural integrity or performance of the cables. Future testing will include measuring the position and temperature of the support structure and the substrates when the cryo-panel is cooled and understanding the long-term effects of the cryo-panel, such as ice buildup and

structural effects. We will also do a complete FEA model of the temperature profile of each of the main elements inside the vacuum vessel.

One of the implications of the results from the 5% model outgassing test is that by using cryo-panels inside the detector vacuum vessel, we no longer need any separation between detector and beam volumes. This means that we will not need big rectangular bellows that appeared in earlier designs. Furthermore, we can choose to split the two halves of the pixel detector either vertically or horizontally. The test results gave us a few new ideas on how we can improve the reliability of the BTeV pixel detector. A major concern of our baseline design is that we will have numerous joints, connections and manifolds filled with coolant inside a high vacuum vessel. Any leak in such a system will have significant impact on the operation of the Tevatron. Based on the results of the outgassing test and the presence of cryopanel inside the vacuum vessel, as discussed before, our substrate and cooling system has been changed to a joint-free design based on liquid nitrogen lines and the high thermally conductive TPG substrate.



Figure 4.39: 5% model of the BTeV pixel detector, with dummy silicon modules assembled on six Al substrates.

#### 4.4.7.6 Positioning system

The positioning system will provide precise independent motions of half-detectors in both  $x$  and  $y$  direction (where  $z$  is beam direction). The pixel detector has to be moved out of the beam during beam refill and returned precisely to its original position once stable beam is established. Because of possible variation of beam position from store to store, we have to be able to adjust the detector position to correct for long term beam position drift. While the nominal beam hole is fixed at 12 mm, we may want to change the beam hole for various



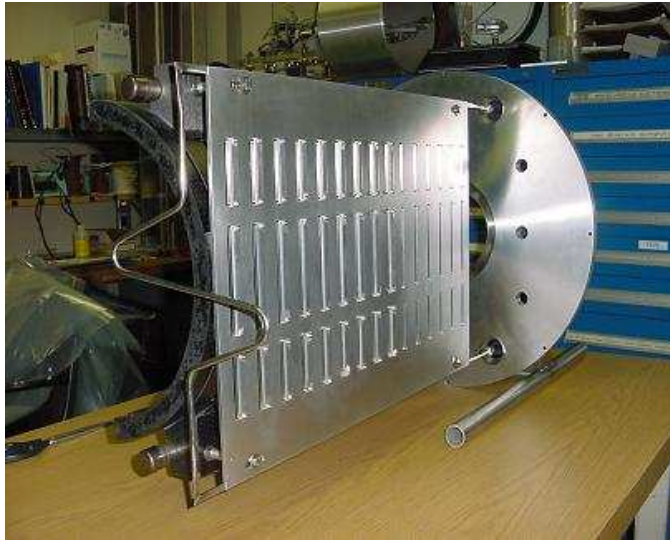


Figure 4.40: 5% model of the BTeV pixel detector, with cable strain relief/heat sink and its cooling channel.

reasons. The design of the positioning system is driven by these requirements. We would like to achieve a precision of  $2\ \mu\text{m}$  or better for the movement and the position of the whole system should be repeatable to better than  $50\ \mu\text{m}$ .

The positioning system consists of two major components:

- actuators: the elements that move the half-detectors; and
- sensors: these define the actual position of the half-detectors and are used to direct the movement of the actuators.

**Actuator** Progress has been made in design of the pixel positioning system. We have built a prototype air-actuated motion device (Fig. 4.41) This prototype contains a carbon steel gearbox, feed screw and slides, which is of a concern when operated in a magnetic field, Results of testing this prototype are summarized as follows:

- Incremental step motion of under 1 micron level precision is achievable with the chosen design;
- The actuator is robust and can withstand the design load without excessive deformation;
- The pneumatic indexer is not sufficiently reliable. It broke after the actuator had made about 100 motion cycles;

- Independent checking of the harmonic gearbox used in the actuator showed that when operating in a magnetic field, the power required to rotate the gearbox is about 6 times higher than the power required when there was no magnetic field. Extensive wear of the gearbox parts was noticed after about 20 hours of operation inside the test magnet;
- No significant effect of the magnetic field on feed screw mechanism was found.

These results lead to the following design changes:

- a. The pneumatic indexer will be replaced by a conventional electromotor installed outside the magnet, at an easily accessible location. A long flexible shaft will be used to transmit motor rotation to the actuator;
- b. A gearbox built of non-magnetic components will be used in the actuator;
- c. Non magnetic slides will be used.

Special attention was paid to design of attachment of the detector to actuators. The most important requirement to the attachment design is that there should be no backlash. In the near future, we are going to build a prototype of these attachments and test them mechanically and thermally. We have also started to look into the use of piezoelectric actuators. A key question to be answered is the effect of radiation on the piezoelectric actuators, in particular, neutron radiation. This will be studied in the next few months.

**Position Sensors** These sensors are used to measure the position of the pixel half-detectors after each movement during the beam refill. The sensors have to be operated inside a magnetic field and in vacuum. The required precision is about  $1\ \mu\text{m}$  or better and the sensors have to be very robust and reliable. For these reasons, capacitive sensors have been chosen as the primary candidates. Tests on capacitive sensors are currently under way.

## 4.5 Technical Description

The technical design of the BTeV pixel detector is based on the results and experience that we have acquired during the last few years of R&D as summarised in the last section. The design for the mechanical support, vacuum system, and RF shielding have not been finalized, but will follow closely the results obtained and the anticipated results from testing of our prototypes.

### 4.5.1 Pixel Detector Specifications

The baseline pixel vertex detector consists of a regular array of 30 “stations” of “planar” silicon pixel detectors distributed along the interaction region sitting inside the 1.5T SM3 dipole magnet. Each station contains one plane with the narrow pixel dimension vertical,

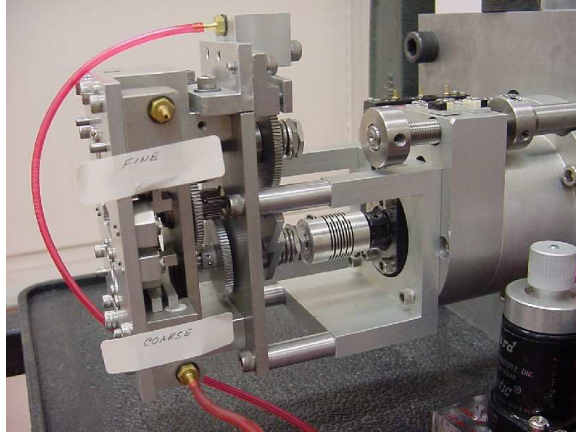


Figure 4.41: Sideview of the prototype actuator.

and one with the narrow dimension horizontal. The stations are split, having a left half and a right half. Each half-station contains one (approximately)  $5\text{ cm} \times 10\text{ cm}$  precision vertical-position-measuring half-plane, and a smaller, (approximately)  $3.8\text{ cm} \times 7.3\text{ cm}$  horizontal-position-measuring half-plane. The left half-stations are positioned at regular intervals along the beam, and the right halves are similarly positioned, but midway between the left-half stations. This allows for possible overlap of half-planes with a variable-sized, small hole left for the beams to pass through. Table 4.3 summarizes the properties of the pixel detector.

The vertex detector contains  $\sim 30 \times 10^6$  pixels, each  $50\text{ }\mu\text{m} \times 400\text{ }\mu\text{m}$ , and covers a total active area of  $\sim 0.5\text{m}^2$ . Each sensor pixel is read out by a dedicated electronics cell. The sensor pixel and the readout cell are connected by a “bump bond.” The basic building block of the detector is a pixel module which is a hybrid assembly consisting of a sensor, a number of readout chips, and a flexible printed circuit (a high-density interconnect, HDI) which carries I/O signals and power. The sensors are variously sized to accept variable numbers of readout chips to make the required half-plane shape. Each readout chip is “flip-chip” mated to 22 columns of 128 rows of pixels on the sensors, corresponding to 2,816 active channels per readout chip. Each readout chip covers an active area approximately  $0.64\text{ cm} \times 0.92\text{ cm}$ . To avoid any dead space between adjoining read out chips, the pixels on the sensors corresponding to the edge of the readout chip (first and last column) are extended to  $600\text{ }\mu\text{m}$ . These pixel modules are supported by a movable carbon substrate that allows the pixel sensors to be positioned a safe distance away from the beam-line until stable conditions have been established in the Tevatron, at which point they are moved as close to the beam-line as radiation damage considerations will allow. This substrate also provides cooling through conduction for the readout electronics. To minimize the material, the pixel half-detectors sit in vacuum, separated from the beams by only a set of rf shielding wires or strips.



Table 4.3: Pixel Vertex Detector Properties

Property	Value
Pixel size	rectangular: $50\ \mu\text{m} \times 400\ \mu\text{m}$
Outer Plane Dimensions	$10\ \text{cm} \times 10\ \text{cm}$
Central Square Hole (adjustable)	nominal setting: $12\ \text{mm} \times 12\ \text{mm}$
Total Planes	60 (each splits into left and right half)
Total Stations	30 (split into left and right half-stations)
Pixel Orientations (per station)	one with narrow pixel dimension vertical & the other with narrow dimension horizontal
Separation of Half-stations	4.25 cm
Staggering of the two half-detectors	offset by half of the station separation
Sensor Thickness	$250\ \mu\text{m}$
Readout Chip Thickness	$200\ \mu\text{m}$
Total Station Radiation Length (incl. rf shielding)	3.0%
Total Pixels	$2.3 \times 10^7$
Total Active Area	$\approx 0.5\text{m}^2$
Readout	analog (3 bits)
Trigger	Signals are used in Level I trigger.
Rate Requirements	Time between beam crossings is 396 ns 132 ns BCO also fully supported
Noise Requirement	desired: $< 10^{-6}$ per channel/crossing required: $< 10^{-5}$ per channel/crossing
Resolution	better than $9\ \mu\text{m}$
Radiation Tolerance	$> 6 \times 10^{14}$ particles/cm <sup>2</sup>
Power per Pixel	$\sim 60\ \mu\text{Watt}$
Operating Temperature	$\sim 5\ ^\circ\text{C}$

### 4.5.2 Front-end chip

The pixel electronics must not only satisfy the efficiency requirement as outlined in the Requirements section, and provide charge sharing information to allow the position resolution requirement to be met, but also must be robust and easy to test, and must facilitate testing and monitoring of the pixel sensors. The pixel readout chip has to satisfy the following requirements:

- **Dynamic Range:** The dynamic range of the front-end amplifier should cover up to the mean charge as deposited on the sensor by a normally incident minimum ionizing particle.

- **Noise of Front-end:** The design of the system shall be such that before irradiation, the front-end electronics noise should be less than 200 equivalent electrons and this should not increase significantly after irradiation to a fluence equivalent to 10 years of BTeV operation.
- **Leakage Current Compensation:** as silicon sensors get damaged by radiation, their leakage current will increase. Each pixel must compensate for this increase in leakage current up to 100nA per cell.
- **Threshold and Dispersion:** Each pixel input shall be compared to a settable threshold. This analog threshold of each readout-chip shall be settable via digital control. Typical settings shall be from 2000 to 6000 equivalent electrons at the input. Threshold dispersion must be low enough that the chip can be operated stably and efficiently at 2500 electrons threshold setting. With a  $250\mu\text{m}$  thick sensor which roughly gives a signal size of 20K electrons, this gives a ratio of signal/threshold of 8. Typically, the threshold dispersion should be comparable and not significantly larger than the noise of the front-end during its entire operational lifetime. The threshold overdrive should also be low enough so that signal just above the threshold will be correctly time-stamped.
- **Analog Information Availability:** Analog information from each pixel cell shall be available. This helps in improving the spatial resolution, but more importantly, it helps in monitoring the performance of the sensors. After careful study including beam tests and simulation, we conclude that a 3-bit ADC will be adequate both for resolution and monitoring.
- **Masking: Kill and Inject:** Each pixel channel must be testable by charge injection to the front-end amplifier. By digital control, it shall be possible to turn off any pixel element from the readout chain.
- **Cross-talk:** A tolerable cross-talk is such that at no time shall it exceed the threshold. We require the cross-talk to be less than 5%.
- **Power Consumption:** The total power consumption of the readout chip must be no more than  $0.5\text{W}/\text{cm}^2$ . This roughly corresponds to about  $60\mu\text{W}$  per pixel.
- **Time Stamp:** Each pixel hit must be given a correct timestamp which identifies the beam crossing number.

The pixel size will be  $50\mu\text{m}$  by  $400\mu\text{m}$ . Each FPIX2 pixel readout chip will read out an array of 22 columns by 128 rows of pixels. Fig. 4.42 shows the FPIX2 layout. The chip consists of five functional sections: the pixel array, the end-of-column logic the command interface, the programmable registers and digital to analog converters(DAC), and the data output interface. The pads located on the top edge of the chip in figure 4.42 are for debugging

purposes only and will be removed for the production version. Connections to the chip are made by using a single row of 70 wire-bond pads located at the bottom edge of the chip.

The pixel unit cells, each of which contains an amplifier and a 3-bit flash ADC, the end-of-column logic associated with each column of pixels, and core logic, which controls the flow of data from the core to the data output interface are together referred to as “the core”. The rest of the chip is referred to as the “periphery”. The programming interface accepts commands and data from a serial input bus, and, in response to commands, provides data on a serial output bus. The programmable registers are used to hold input values for the DACs that provide currents and voltages required by the core, such as the discrimination threshold and the threshold levels for each of the FADC bits. The data output interface accepts data from the core, serializes the data, and transmits it off chip using a point-to-point protocol operating at 140 Mbps. All I/O (except the test signal inject) is differential and uses Low Voltage Differential Signaling (LVDS). Since the average number of hits per crossing is very non-uniform across the whole half station, the required output bandwidth also varies greatly. To account for this fact, each FPIX2 chip can be programmed to use 1, 2, 4, or 6 serial output links. The only supply voltages required are 2.5V and ground; all other bias voltages, currents, and threshold settings are generated internally by the programmable DACs.

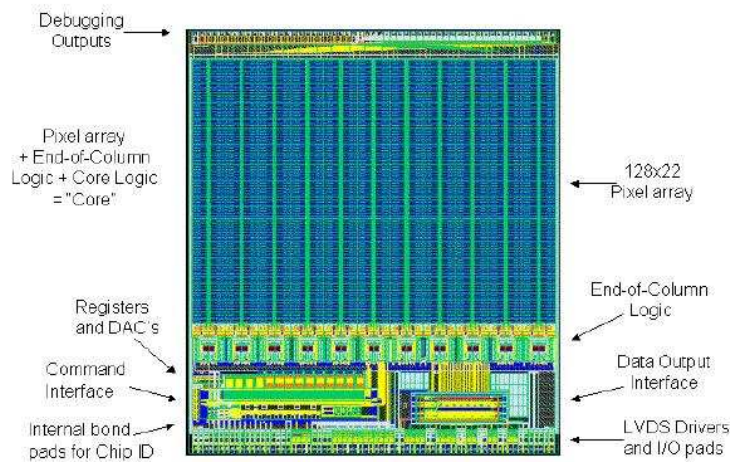


Figure 4.42: FPIX2 layout.

### 4.5.3 Sensor

The BTeV pixel cell size is  $50\text{ }\mu\text{m}$  by  $400\text{ }\mu\text{m}$ , where the small dimension is dictated by the needed spatial resolution. The technology chosen is  $n^+/n/p^+$ . Because of the accumulation layer induced by the oxide charge, the individual  $n^+$  cells would be shorted together unless some electrical insulation is provided. Various isolation techniques have been developed

for silicon pixel sensors. We have explored two techniques: p-stop and moderated p-spray. Both techniques seem to give good results before and after irradiation based on electrical characterization results. The final choice depends on the results of the charge collection and efficiency studies of both types of detectors before and after irradiation. Recent results from CMS have shown that the p-stop sensors had significant charge losses around the corners of the p-stop region, particularly after heavy irradiation [24]. On the other hand, the charge loss observed in the p-spray sensors were a lot less and this was found to be around the bias dot region [24],[25]. We plan to confirm these results in a test beam starting Spring 2004.

Another major issue is on testing the sensors before bump bonding. We have discussed in previous section that wafer probing of p-stop sensors do not give the correct breakdown voltage. This is due to the fact that not all the pixels are biased properly. In the p-spray technique, a bias grid structure can be implemented which allows the testing of the sensors under full bias before assembly. This structure is very important for quality control during mass production. Moreover, in case of missing bonds, this bias grid acts as a safety feature during operation, maintaining the unconnected  $n^+$  electrode potentials close to ground. The bias grid connects every pixel via an equally sized punch-through gap, preventing excessive potential on any individual pixel. For this reason and because of the charge loss problem observed on the p-stop sensors, the p-spray sensors will be used as our baseline technology for the final production.

The sensors will be fabricated on 4" wafers of n-type silicon. Each wafer will consist of sensor modules of different sizes. We will discuss with the vendors on the optimal layout to maximize the yield. In addition, there will be a few single chip sensors, test structures, gate-controlled diodes, and MOS capacitors for quality control purposes. All wafers will be oxygenated.

The following geometrical tolerances need to be met:

- Misalignment of  $p^+$  implant,  $n^+$  implant and metal layers  $\pm 2\mu\text{m}$ ,
- Mask alignment precision between front and back side  $\pm 5\mu\text{m}$ ,
- thickness  $250\ \mu\text{m}$ ,
- uniformity of wafer thickness (wafer to wafer)  $\pm 10\mu\text{m}$ .

The following electrical specifications need to be met:

- Operating voltage  $V_{op}$  at  $20^\circ\text{C}$ : 200V or 1.3x full depletion voltage, whichever is greater;
- Leakage current at  $20^\circ\text{C}$   $\leq 50\ \text{nA}/\text{cm}^2$  at  $V_{op}$ ;
- Current slope measured at  $20^\circ\text{C}$ :  $I(V_{op})/I(\text{Depletion voltage}) \leq 2$ ;
- Bulk resistivity 1.0-2.5  $\text{K}\Omega\text{-cm}$ ;
- Breakdown voltage  $\geq 300\ \text{V}$  or  $1.5\ V_{op}$  whichever is greater
- Detector current shall increase by no more than 25% after 12 hours of operation in dry air at  $V_{op}$

#### 4.5.4 Bump Bonding

Both indium and solder bumps are viable technologies to meet our requirements. Over the years, we have qualified three vendors. These are AIT (Hong Kong), MCNC (North Carolina), and VTT (Finland). Solder bumps are used by all three companies while only AIT can provide indium bumping. Besides these three companies, we have kept in contact with the LHC experiments about their plans and qualified vendors. The choice of the technology and vendor will depend on the availability and capacity of the vendors as well as QA plans and issues. Solder bumps have a few advantages over indium:

- Mechanically more robust
- Process can be fully automated and handle large volume
- Mainstream in industry and cheaper for large production
- More vendors available

For these reasons, in our base estimate, we have used solder bumps as the baseline technology with indium as a viable alternative.

#### 4.5.5 Modules

The main components of the pixel module are:

- Pixel readout chips
- Silicon sensor bumped bonded to the readout chips
- High density interconnect HDI flexcircuit with surface mount components
- Two Pixel interconnect flex cables (PIFC): one for the power and the other for data and control signals. These will be connected to the HDI with the connection technology still being studied. Options include small, fine pitch connectors, wire bonding, solder pads, and the use of a fine-pitch z-axis conductive film.

The pixel multichip module is built as a three-layer stack. The bottom layer is the high-density interconnects (HDI) circuit, to which all FPIX chips are wire-bonded. The bottom of the FPIX chip is mounted on top of the HDI, while the top of the FPIX chip is flip-chip bump bonded to a silicon pixel sensor. The bottom of the FPIX chip is in electrical contact to the ground plane on the top metal layer of the HDI. The HDI also provides low voltage (2.5V) to the FPIX chip and high voltage (up to 1000V) to bias the pixel sensor.

The modules come in four different sizes: 1x4 (with one long piece of silicon sensor bump-bonded to 4 readout chips arranged in a linear array), 1x5, 1x6 and 1x8. The HDIs will accordingly come in 5 different sizes, with the 1x4s having two versions, one being the

mirror image of the other one. The PIFC's will come in 4 different sizes to match the corresponding HDIs.

The pixel detector design is severely bounded by several constraints which impacts on the choices of high density interconnect (HDI) cables. These constraints include readout speed, material budget, outgassing, distribution of the high voltage for detector bias, radiation environment, reliability, and cost.

The circuit density of the HDI is highly associated with the read out speed of the pixel chip. All data generated inside the pixel chip has to be readout for the lowest level trigger decision. In order to accommodate reasonable read out throughput, several readout buses will have to be routed for the data serializers on the pixel readout chips. Based on the space available for routing, one can see that very high density circuits need to be used. Several factors impact the amount of data that each readout chip needs to transfer: readout array size, distance from the beam, and the data format. Further details of the data structure and throughput are given in the Chapter on Electronics.

Since the pixel detector will be placed inside a strong magnetic field, the flex circuit and the adhesives cannot be ferromagnetic. The pixel detector will also be placed inside a high vacuum environment, so the multichip module components must have a low outgassing rate. The severe radiation environment and planned operating temperature (-5 to -10°C) also impose severe constraints on the pixel multichip module packaging design.

Another important constraint of the HDI is the ability to distribute the high voltage for detector bias. The pixel detector receives different radiation levels depending on the distance from the beam and therefore, it has to be biased with different high voltages to obtain the optimal performance and account for different detector degradation with radiation. The circuit interconnect will have to reliably deliver the high voltage to different points of the pixel plane and avoid high voltage breakdowns that may short circuit the high voltage traces with signal traces or power and ground.

The HDI will be made out of low-mass flex-circuit interconnect. This approach will effectively meet all the constraints outlined. The baseline design for the interconnect is to glue the HDI directly to the TPG substrate, with the pixel modules placed on top of it. In this way, a solid ground plane can be provided by the HDI to the back side of the readout chips. The HDI will consist of the following four layers of flex-circuit:

- one layer for the ground plane.
- two layers for signal interconnects,
- one more layer for power and other signals.

These layers are quite thin and can be kept within 18  $\mu\text{m}$  of copper thickness or less. The PIFC consists of a power flex and a data flex. Each of these flex cables has two layers and uses standard flex circuit design rules. We are also investigating the use of Aluminum for the power flex cable to reduce mass.

### 4.5.6 Readout and control

The success of the experiment relies critically on the quality of the data provided by the pixel system to the Level 1 trigger. The trigger imposes the following readout requirements on the readout of pixel system:

- **Data Sparcification:** The data output from the pixel detector shall be only of those cells that are above the settable threshold.
- **Pixel output data content:** The pixel hit data must include the beam crossing number, chip identification number, and the pixel hits for that beam crossing. The pixel data must have row and column numbers, and pulse height information for each hit.
- **Minimum Data Rate Capability:** The data output from each pixel readout chip shall be data driven, and capable of continuous readout at a minimum rate of 4 hit pixels per beam-crossing time.
- **Graceful Degradation above rate capability:** The data output from the pixel system may be lost for rates well above the minimum rate specified above. However, the loss should be in a fashion that when the burst in data rate is passed, the system shall return to normal operation without external intervention.
- **Readout Abort:** The system must have a means of recognizing and aborting the readout of any chip that has an unusually high volume of data output (e.g. due to oscillation).

The readout architecture is a direct consequence of the BTeV detector layout. The BTeV pixel detector covers the forward direction, with an angular acceptance of 10-300 mrad, with respect to both colliding beams. Hence, the volume outside this angular range is outside the active area and can be used to house heavy readout and control cables without interfering with the experiment. The architecture takes advantage of this consideration.

The Data Combiner Board (DCB) located approximately 10 meters away from the detector remotely controls the pixel modules. All the controls, clocks and data are transmitted between the pixel module and the DCB by differential signals employing the Low-Voltage Differential Signaling (LVDS) standard. Common clocks and control signals are sent to each module and then bussed to each readout IC. All data signals are point to point connected to the DCB. This readout technique requires the design of just one rad-hard chip: the pixel readout chip. The point-to-point data links minimize the risk of an entire module failure due to a single chip failure and eliminate the need for a chip ID to be embedded in the data stream. Simulations have shown that this readout scheme results in readout efficiencies that are sufficient for the BTeV experiment.

In order to maximize the data throughput, the FPGAs on the DCB latch the signals on both the rising and falling edges of the 70MHz clock. The 24-bit long hit data (5 column-number bits, 7 row-number bits, 3 pulse-height bits, 8 timestamp bits, and 1 word mark bit)

are serialized onto 1, 2, 4, or 6 programmable serial links. The serializer-FPGA synchronization is established and maintained by sending a Sync/Status word when no data are to be sent and just before each time the Token-Pass signal is launched to the first pixel column. More details will be given in the Electronics Chapter.

## 4.5.7 Mechanical Support

### 4.5.7.1 Introduction

One of the main requirements of the mechanical support structure for the BTeV pixel detector is to keep the amount of material to a minimum. Counter to the material budget requirement are the needs for reproducible, stable position-determining supports, to remove significant amounts of heat directly from the active sensor areas, to move the detectors back from the interaction region during injection and machine-study periods, and to reposition the detectors reliably and accurately for physics data-taking. The detector needs to be retractable to a distance of  $\pm 2$  cm from the beam while the collider is being filled. When stable beams are established, the detector will be moved back with good precision to its nominal position. Because the pixel information will be used in the Level 1 trigger, the pixel detector needs to be aligned fairly quickly and easily (using tracks from data obtained by a short interaction trigger run) to a precision which is necessary to obtain the required spatial resolution of  $9\mu\text{m}$  or better for all tracks and remain stable during data-taking. Note that for the current RUN II, the typical store time is between 12-24 hours and the refill time is up to 4 hours. It is envisaged that when BTeV comes online, the store and refill time will be significantly reduced.

### 4.5.7.2 Requirements of the Mechanical support system

Since the pixel detector will be installed close to the Tevatron beam, it must meet the requirements of the Beams Division. The following criteria have to be met:

- **Beam Conditions at other IR:** The presence of the detector must not degrade the beam conditions at other IR's by parasitic RF coupling.
- **Tevatron Operation:** Static and dynamic pressure effects inside the vacuum vessel must be low enough so that it will not affect the operation of the Tevatron.
- **Vacuum Loss:** A detailed vacuum loss and failure mode analysis has to be performed to safeguard the operation of the Tevatron and avoid potential damage to the Pixel System.

To achieve the physics goals of BTeV, the mechanical support system of the pixel detector has to meet the following requirements:

- **Acceptance:** The Pixel detector mechanical support structure should have low mass within the geometrical acceptance ( $300 \times 300 \text{ mrad}^2$ ) of the spectrometer so that the performance of the other systems in the spectrometer not be compromised;



- **Alignment:** The pixel system must be alignable during each of the the assembly stages by suitable inclusion of alignment marks;
- **Effect on the Spectrometer dipole magnet:** The whole detector will be placed inside the aperture of a dipole magnet with a field strength of 1.5 T; it should not have any effect on the local magnetic field strength;
- **Effect of the dipole magnet:** Between stores, the dipole magnet may be ramped down. After the refill, the magnet will be ramped up from 0 to 1.5T. All support and motion control structures for the pixel system should not be damaged or affected by this ramping or by tripping of the magnet. Furthermore, the alignment of the pixel stations must not be influenced by the magnetic field by more than 20  $\mu\text{m}$  and must have a ramp to ramp stability better than 10  $\mu\text{m}$ .
- **Operating Temperature:** The design must take into account that the operating temperature of the detector will be in the range between -10°C and -5°C. Thermal stress must be considered so that the mechanical stability of the system will not be affected.
- **Pressure:** The goal for the pressure inside the pixel vacuum box is  $10^{-8}$  torr.

All alignment requirements are given in terms of the narrow pixel direction.

- **Initial Alignment on Half-Planes - Narrow Pixel Direction:** The individual sensor subassemblies shall be mounted on their half-plane support to an accuracy of 5 microns, and measured to an accuracy of 2 microns before the substrate is mounted on its frame.
- **Initial Alignment of Half-Planes on Frame:** The individual half planes must be mounted with a precision of 20 microns or better, and the positions known to 10 microns before the half-planes are inserted in the vacuum container.
- **Alignment of the Two Halves:** The two halves of the detector must be positioned with respect to each other with an accuracy better than 50 $\mu\text{m}$  in x and y, and 200 $\mu\text{m}$  in z (longitudinal direction).
- **Offset:** the left and right halves of the detector should be staggered in the longitudinal direction to allow for minimal dead space;
- **Retractability:** The detector has to be retracted to a distance of 2 cm away from the beam and after each refill, the detector has to be moved into position for data-taking. The reproducibility should be better than 50 $\mu\text{m}$  and the position sensors must be read out with a precision of 1-2  $\mu\text{m}$ .
- **Centering the Assembly on the Beams:** The full assembly must be such that the full detector can be centered on the nominal location of the Tevatron beams.

- **Alignment Monitoring:** The System must include some means of alignment monitoring online to a precision of better than  $50\mu\text{m}$  for each station;
- **Stability:** the system should be stable to within  $2\mu\text{m}$  during each store for data-taking;
- **Direction of motion:** the two halves can be moved in x and y independently so that we can accommodate the beam if it is not positioned exactly as expected, and so that we can operate with a square beam hole which is either larger or smaller than the nominal value.

#### 4.5.7.3 Substrate

The pixel modules will be placed on a supporting substrate made out of thermalized pyrolytic graphite (TPG). The thermal conductivity of TPG at room temperature is about  $1700\text{ W/mK}$  in-plane with roughly a  $-0.4^\circ\text{C}$  change, reaching a maximum of about  $3000\text{ W/mK}$  at  $-180^\circ\text{C}$ . Its thickness is  $380 \pm 15\mu\text{m}$ .

The TPG material, is however, intrinsically friable and easily delaminates in the out-of-plane direction. In addition, some trace of graphite dust exists and TPG therefore must be encapsulated. It will be encapsulated on each surface with a single ply of prepreg (carbon fiber with epoxy)  $\sim 30\mu\text{m}$  thick. Before the encapsulation, a matrix of perforated holes are planned to be laser-drilled on the substrate. During the lamination of the carbon fiber sheets to the TPG substrates, hundreds of epoxy bonds interconnecting the top and bottom layers of the CF are formed and hence the overall stiffness of the substrate is greatly improved.

Each substrate will have an extended region outside the active area to allow the placement of fiducials, brackets mounts (to the carbon support cylinder), and temperature control and sensing elements. It is L-shaped and measures  $170\text{ mm} \times 65\text{ mm}$  at the widest region. Pixel modules will be placed on both sides of the TPG substrate to form a half-plane. To provide mechanical stability, an x-measuring half-plane and a y-measuring half-plane will be bolted together to form a half-station. Figure 4.43 shows in detail the pixel modules assembled on the substrate.

With FEA as the chief design tool, we have chosen a substrate based on  $0.38\text{ mm}$  thick TPG with a simple, vertical 2-end cooling configuration. This will be adequate to remove the  $60\text{ W}$  of heat that will be generated by the pixel modules. As shown in Fig. 4.44, the substrate is thus a long piece of TPG consisting of a core area, which houses the modules, and an extended area, which channels the heat to the heat sink that is kept at cryogenic temperature. In the extended area, a pair of precision hole-and-slot washers is glued. These washers, together with the precision pins extended from the Carbon Fiber Reinforced Plastic (CFRP) brackets, are to determine the alignment of the substrate to the CFRP cylinder. In addition, this hole-and-slot arrangement will facilitate the thermal displacement of the substrate with respect to the CFRP brackets without creating any additional unwanted thermal stresses and distortion. Temperature control and sensing elements will be placed here also to dynamically control and monitor the operating temperature of the modules in case different operating conditions and failure scenarios arise. A flexible thermal coupling made of

PGS is glued to both ends of the TPG core substrate. This is needed to provide mechanical decoupling of the precisely assembled and aligned substrates from the less accurately made (brazed) cold blocks (see section of Cooling). Extensive FEA and experimental tests are ongoing to optimize the length and width of each component of these thermal joints.

The X- and Y- measuring half-plane substrates are both made in this way. They are glued together with CFRP hollow spacers in between. This spacer is made hollow so that those HDI cables inside the substrate can be led through for outer connection.

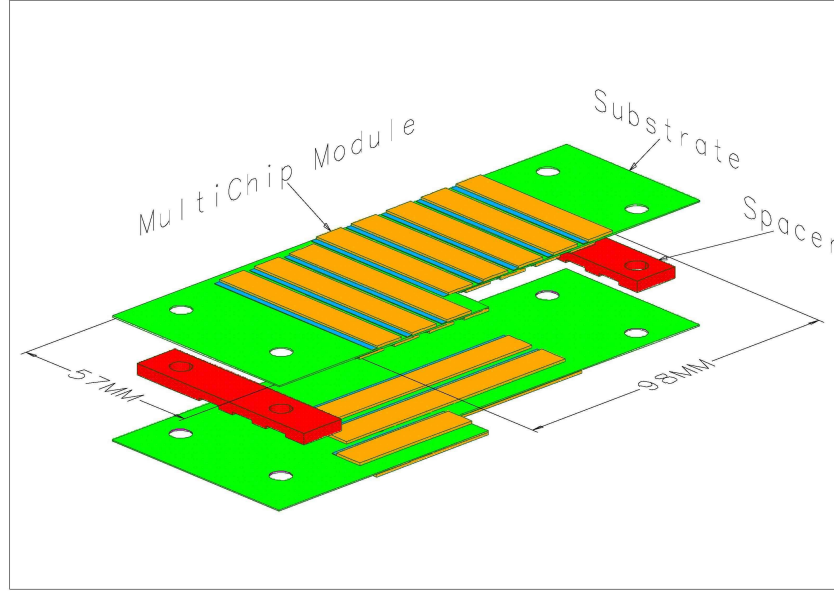


Figure 4.43: Schematic drawing of pixel modules assembled on the TPG substrates.

#### 4.5.7.4 Assembly of modules

The modules are planned to be placed on the both sides of TPG alternatively to provide full coverage of the tracking area. To ensure a successful tracking, 0.53 mm of overlapping of the adjacent modules is allowed. The accuracy of the module placement with respect to the half-plane TPG substrate is within  $5\text{ }\mu\text{m}$  in the X-Y pixel plane. Some precision fixture is needed to achieve this goal. As there are 120 half-plane substrates in the pixel detector, the ultimate goal of this fixture assembly is to produce all these substrates identically so that they can be placed in any CFRP bracket location.

The assembly process starts with gluing a couple of precision hole and slot washers on the half-plane substrate. A gluing fixture can be used so that all the half-plane substrates are made in the same way, and the accuracy of this gluing process is to be good to within  $5\text{ }\mu\text{m}$ . This half-plane substrate is then placed on the module placement fixture assembly as

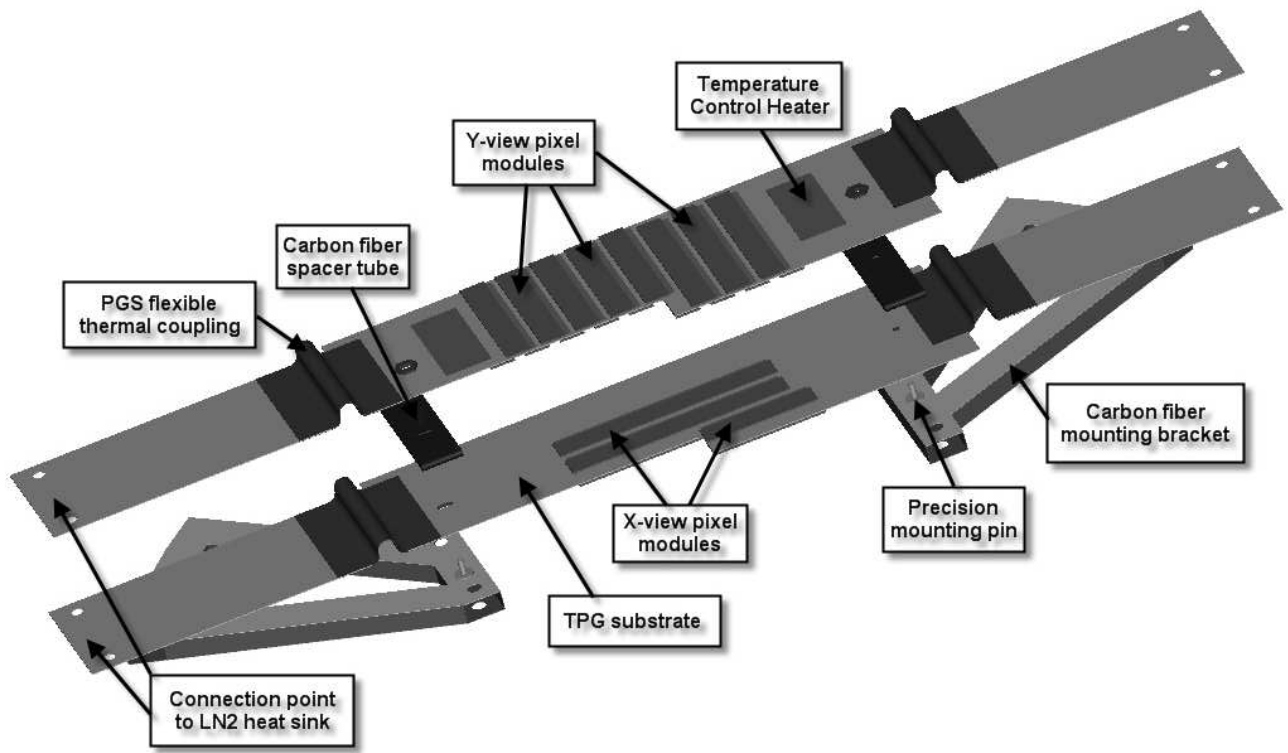


Figure 4.44: Schematic drawing of two TPG substrates to form a pixel half-station.

shown in Figure 4.45. This module placement fixture assembly consists of several flat tooling plates and has a space in the middle to be allowed for the exchangeable plate. Two precision pins and two fiducials are made in the fixture. Since their locations are fixed, the reference to each other is thus locked and hence all the data with respect to either pin or fiducial reference system are transferable. The half-plane substrate will be engaged with the pins of the fixture assembly through the precision washers. After the application of a uniform layer of 0.075 mm-thick glue to the pixel module by means of another glue dispensing fixture, the module is held by a module holder which is mounted on 3 translational stages and has 1 angular moving capability. The module is then oriented and positioned with reference to the fiducial marks. Slight pressure is applied on the module to accomplish this gluing process. To take this slight loading pressure off the TPG substrate, there will be a supporting plate underneath the TPG. To ensure the placement of this set of modules matching the set of modules on the other side, a couple of targets that can be visible from either side will be placed on the substrates for checking the placement precision.

The same module placement fixture assembly will be used for fixing the CFRP bracket position so that the same precision pins reference system will be used for the whole assembly process. Template stations will be built on the same fixture to be used for CFRP bracket installation (see the following section).

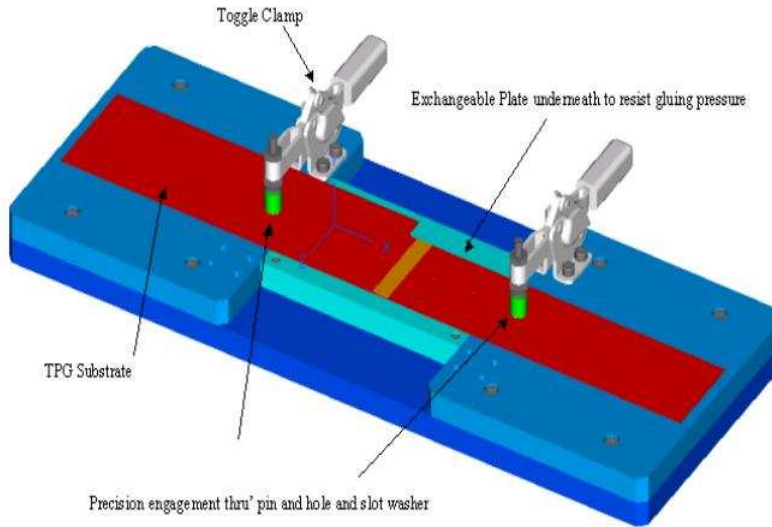


Figure 4.45: Schematic drawing showing the fixture used to assemble the pixel modules on the substrate.

#### 4.5.7.5 Carbon support structure

The support structure for the pixel half-planes consists of inner and outer shells connected to each other by a number of ribs. Shells and ribs are made of carbon fiber laminates of 12 and 6 carbon fiber plies respectively. Figure 4.46 shows the design of the support structure for the pixel detector. Each pixel half-station will be attached by CFRP brackets to a C-shaped support structure. Fig. 4.47 is a technical drawing showing details of the carbon fiber support structure. Using the Template station, discussed in the previous section, the CFRP brackets will be positioned to  $20\ \mu\text{m}$  of their ideal locations within the support structure and bonded in place. This assembly method ensures that all station mount locations be identical.

Use of FBG sensors has been successfully tested for real-time and long-term monitoring of tracking detector structures. Monitoring directly provides the deformations due to either thermal or mechanical loads, and allows for working out the position displacements of the detector hold by the deformed structure. Resolution of  $1\ \mu\text{Strain}$  for deformation measurements and 1mm for displacement measurements have been obtained. FBG sensors were used glued on metallic and CFRP structures, thus allowing their usage on already engineered structures. FBG sensors were also embedded in CFRP components thus providing the possibility of planning detector supporting structure with built-in structural monitoring system.

We will use two arrays of FBG sensors to monitor both the mechanical stability and the relative position of the carbon support structures. The first FBG array will be installed on the support structure to monitor its mechanical stability with respect to both thermal

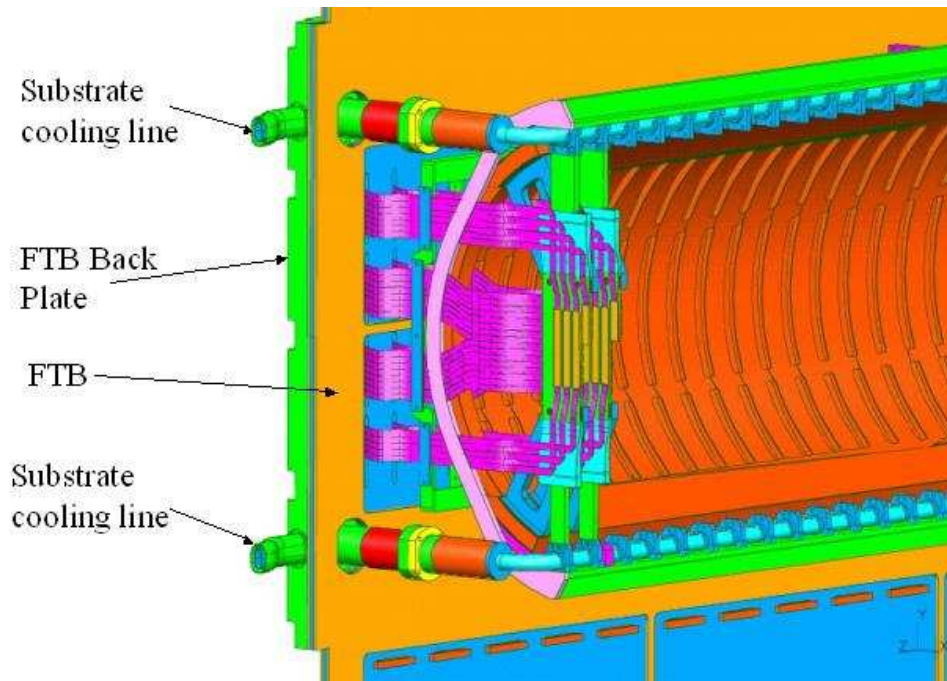


Figure 4.46: Side view of the support structure for the pixel detector. Also shown in the figure are a few pixel half-stations with flex cables coming off the pixel modules and feeding through slots on the feed-through board. The main cooling line and cooling blocks are also shown.

and mechanical loads. The second FBG array will be installed on the positioning system as an extra and independent check to precisely monitor the repositioning of the pixel detector after each movement during the beam refill. Figure 4.48 shows a schematic view of the FBG monitoring system proposed for the Pixel Cylinder Support structure and positioning system. A total of 48 FBG sensors fibers are installed on each half-cylinder structure: sensors are arranged in 12 strings of 4 sensors each; sensor strings are bounded in three bundles of 4 fibers each; each bundle is connected to a fiber optic ribbon cable to deliver to the optical switch. A total of 16 FBG sensors are installed on the positioning system of each half-cylinder structure: sensors are arranged in 4 strings of 4 sensors each; each sensor string is directly connected to an optical fiber to deliver the signal to the optical switch. The optical signal of the sensors is delivered to the Optical switch by use of fiber optic patch cords and vacuum connectors. The Optical Switch selectively address (time multiplexing) the signal of all the sensor strings to the Interrogation System, that both feeds coherent light to the FBG sensors and performs the analysis of the optical signals provided by the FBG sensors. The Optical Switch and the Interrogation System are both controlled by the Local Controller; the Local Controller is connected to remote systems for controll, data analysis and data storage.

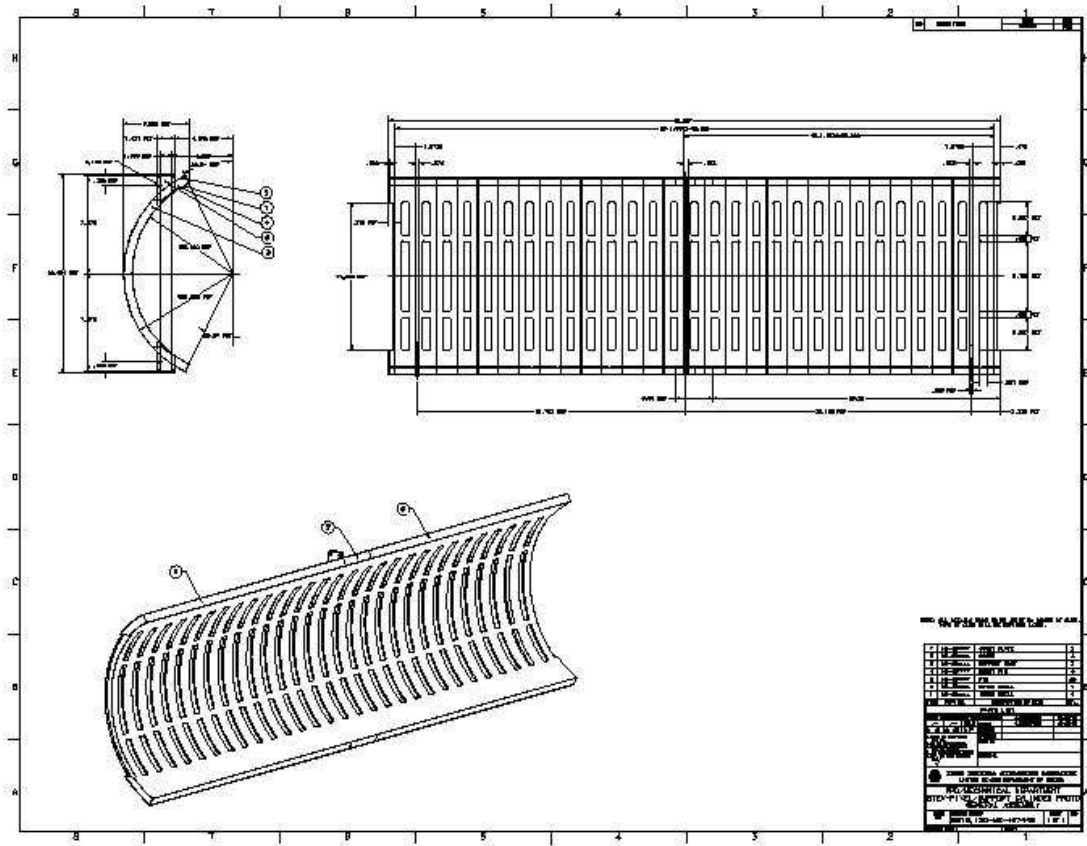


Figure 4.47: Side view of the support structure for the pixel detector.

#### 4.5.8 Vacuum vessel

The whole pixel detector will be placed inside a vacuum vessel. Figure 4.49 shows a conceptual design of the vacuum vessel. The vessel is a rectangular box with a length of 165 cm and a square cross-section of 59.5 cm on a side. The vacuum vessel has a number of penetrating holes. Those holes are needed to provide the connections to the beam pipe, vacuum, cooling and positioning systems. The design of the vacuum vessel is driven by its functional requirements:

- Because of the presence of a strong magnetic field of about 1.5 T and the vacuum requirement, stainless steel 316L will be used;
- The body of the vessel should be vacuum tight;

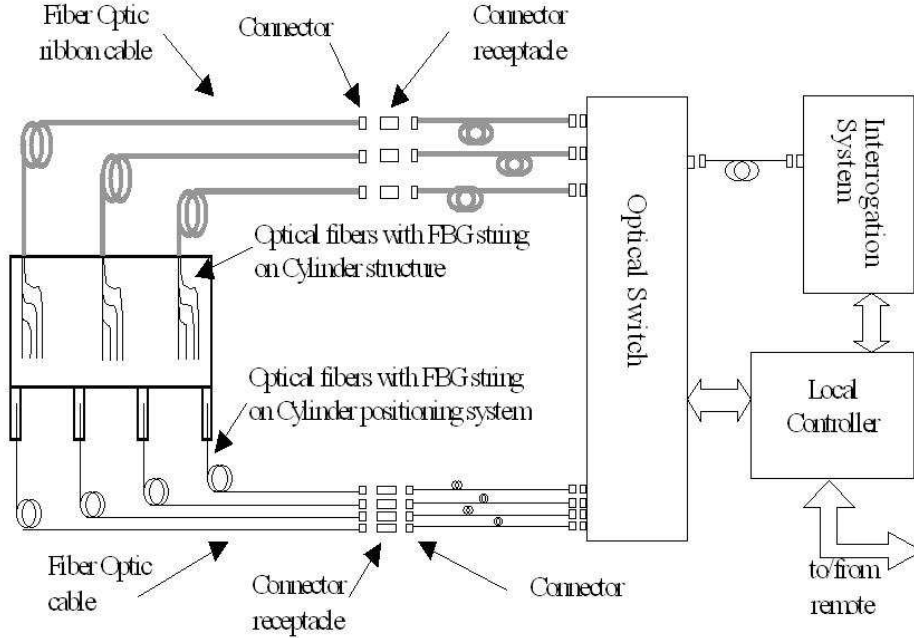


Figure 4.48: Schematic of the FBG system.

- The vacuum vessel has to be mechanically stiff enough to maintain position of the pixel planes to within  $20\ \mu\text{m}$  during data taking.

FEA is used to calculate distortion of the vacuum vessel under different loading conditions. As a result of this calculation, we will use 1 and 1.5 inch thick stainless steel plates to build the vessel. The final number of penetrating holes, as well as their diameters and positions, are not yet fixed because of uncertainties about final configuration of vacuum, cryogenic and detector positioning systems. When all these systems are finalized, we will perform another round of FEA calculation and complete the detail engineering drawings.

#### 4.5.9 Cooling

The full heat load is dominated by the readout chip. This heat load is expected to be  $\sim 0.5\ \text{W}/\text{cm}^2$ . A much smaller load comes from the sensor leakage current. This latter heat load will grow with radiation damage, from about a few  $\mu\text{W}/\text{cm}^2$  to up to few tens of  $\text{mW}/\text{cm}^2$  after a few Mrad of irradiation. The pixel device is expected to operate at temperatures from  $-10$  to  $-5^\circ\text{C}$ . Maintaining these temperatures even when the devices are not in use minimizes the effects of radiation damage. Thus, a cooling system must be designed for these temperatures. The maximum operating temperature of all the pixel sensor modules



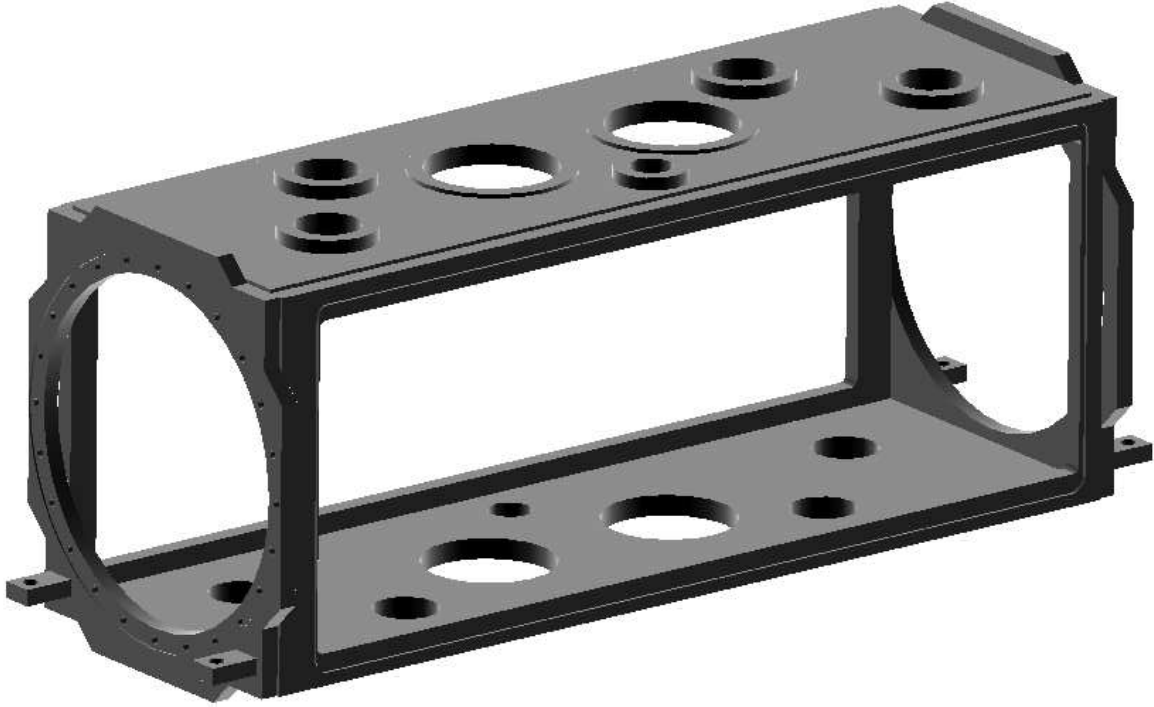


Figure 4.49: Schematic showing the pixel vacuum vessel.

shall not exceed  $0^{\circ}\text{C}$ . To avoid any excessive stress on the bumps, the minimum operating temperature of the pixel sensors shall be above  $-15^{\circ}\text{C}$ .

The alignment precision of the modules has to be kept to a high precision. Thus, the temperature must be controlled and reproducible. Since the operation is well below the temperatures at which the devices will be assembled, the coefficients of thermal expansion must be considered in the mechanical designs. Thermal uniformity across the substrate is determined by the potential thermal warping due to mis-match in CTE between substrate and silicon, (hence loss in alignment accuracy) and by the thermal stress on the bump bonds (leading to damage and possible dead channels). The thermal uniformity shall not create any thermal stress on the substrate, the bumps, and the epoxy layers which may lead to the loss in alignment precision of the modules. The maximum temperature excursion, once equilibrium is reached, shall not exceed  $\pm 3^{\circ}\text{C}$  on any sensor module, and the deviation from the median temperature for different areas on the whole substrate shall be kept to a minimum so that no thermal stress and distortion of the substrate will be created.

Cooling of the pixel detector is done by conduction using the excellent thermal conductivity property of TPG. The vacuum system will have cryopanel and liquid nitrogen lines placed inside the vacuum vessel. We take advantage of this and use the liquid nitrogen lines as a heat sink. Fig. 4.50 shows the design of the cold block assembly placed inside

the vacuum vessel which consists of a liquid nitrogen tube and copper tabs. The tube is made of 5/8" diameter (outer) stainless steel and will carry liquid nitrogen at a pressure of 8 bars. To spread heat coming from the pixel modules on the half-stations and to allow attachment of the TPG substrates to the tube, copper tabs will be brazed to the tube to serve each half-station. To accommodate the movement of the detector during beam refill, bellows will be added to the tube at both ends. Each half-detector will have two cold blocks assemblies. The whole assembly will be placed outside the geometrical acceptance of the pixel detector. Control heaters will be attached to the substrates to maintain the stability of the temperature under various conditions.

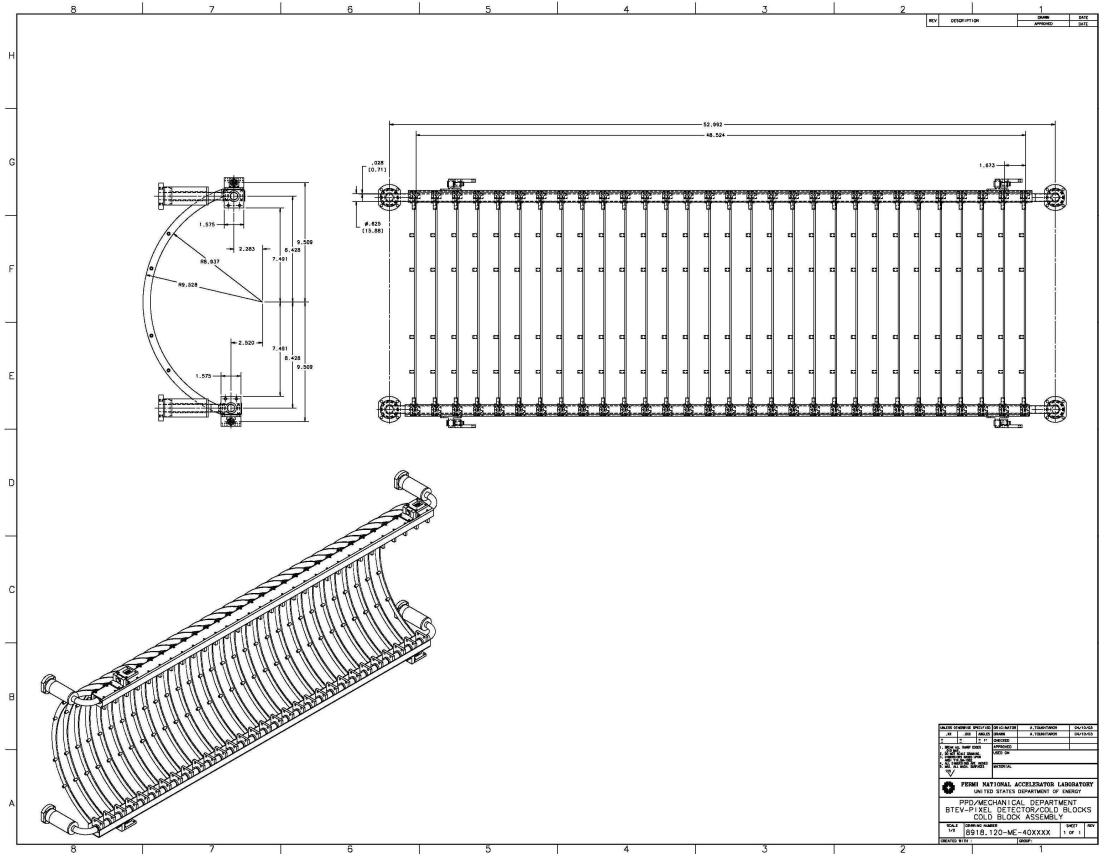


Figure 4.50: Drawing showing the liquid nitrogen cooling line inside the vacuum vessel.

#### 4.5.10 Vacuum system

The design goal of the vacuum system is to have a pressure of  $1 \times 10^{-8}$  torr inside the pixel vacuum vessel, especially in the region where the colliding beams will go through. The pumping requirement for the BTeV Pixel Detector is based on the gas load measurements

of the 5% model. The outgassing rate of the model at room temperature was measured to be  $5 \times 10^{-4}$  torr-L/sec. The main component was water with the next component being nitrogen which was present at the level of 1% of the total. For the entire pixel detector, at room temperature, the expected gas load due to outgassing is roughly  $10^{-2}$  torr-L/sec. The vacuum pumping system will consist of surfaces that are cryogenically cooled. The amount of cold surfaces required to pump water and to pump nitrogen is calculated considering the density and flow of the particles inside the vertex detector.

The vertex detector vacuum specification of  $1 \times 10^{-8}$  torr requires a gas density of  $5.3 \times 10^{-10}$  mole/m<sup>3</sup> regardless of the temperature. A gas load of  $10^{-2}$  torr-L/sec at room temperature is equivalent to a particle flow released inside the vertex detector of about  $5 \times 10^{-7}$  mole/sec. At this molecular flow rate, we have calculated that with a cryogenically cooled surface area of 5.4 m<sup>2</sup>, the required gas density is achievable.

#### 4.5.10.1 Description of the Vacuum System

The vacuum system is made up of two integrated "cryopumps" plus additional surfaces at liquid nitrogen (LN<sub>2</sub>) temperatures within the vacuum vessel [26]. A set of liquid helium cooled surfaces will pump gases such as nitrogen and hydrogen that are not condensable on a surface at the LN<sub>2</sub> temperature. A set of liquid nitrogen cooled surfaces will pump water vapor. The major pumping components are shown in Figure 4.51. The cryopumps, shown in Figure 4.52 and 4.53 have LN<sub>2</sub> cooled copper surfaces surrounding a set of surfaces cooled by gaseous helium (GHe) to about 20°K and inside those a set of about 4°K liquid helium (LHe) cooled tubes covered in charcoal. The innermost, and coldest surfaces are primarily for pumping hydrogen. The 20°K surfaces are for pumping nitrogen and the large LN<sub>2</sub> cooled surfaces are for pumping water. The cryopumps are located along the top and bottom walls of the vacuum vessel. The water pump is made of several components. Besides the LN<sub>2</sub> surfaces in the two cryopanel, the cold block assembly in the pixel cooling system and the cable strain relief bars provides additional LN<sub>2</sub> surfaces for pumping water vapor.

Figure 4.54 shows the details of the layout of the piping for the vacuum and cooling system. Each LHe cryopump is supplied by its own dewar. Liquid helium enters the pixel vacuum vessel in the cryopump at 4°K. Helium gas leaves the cryopump at 20°K. A cold block assembly and the thermal shields for a LHe cryopump share a LN<sub>2</sub> dewar. For conservation, liquid nitrogen is pumped from a phase separator back to the inlet. When the BTeV vacuum vessel is brought up to atmospheric pressure, nitrogen coming from the phase separator is used.

**Pump for non-condensable gas** The option of using commercial cryopumps has been investigated. Due to the limited space around the vacuum vessel inside the magnet, the conductance any piping leading from the vacuum vessel to a remotely located cryopump is not adequate to remove the non-condensable gas. This leaves the requirement that the cryopump be located directly on the vacuum vessel. However, after installation of the vessel inside the magnet, the cryopump is not accessible for maintenance. As a result, it is not

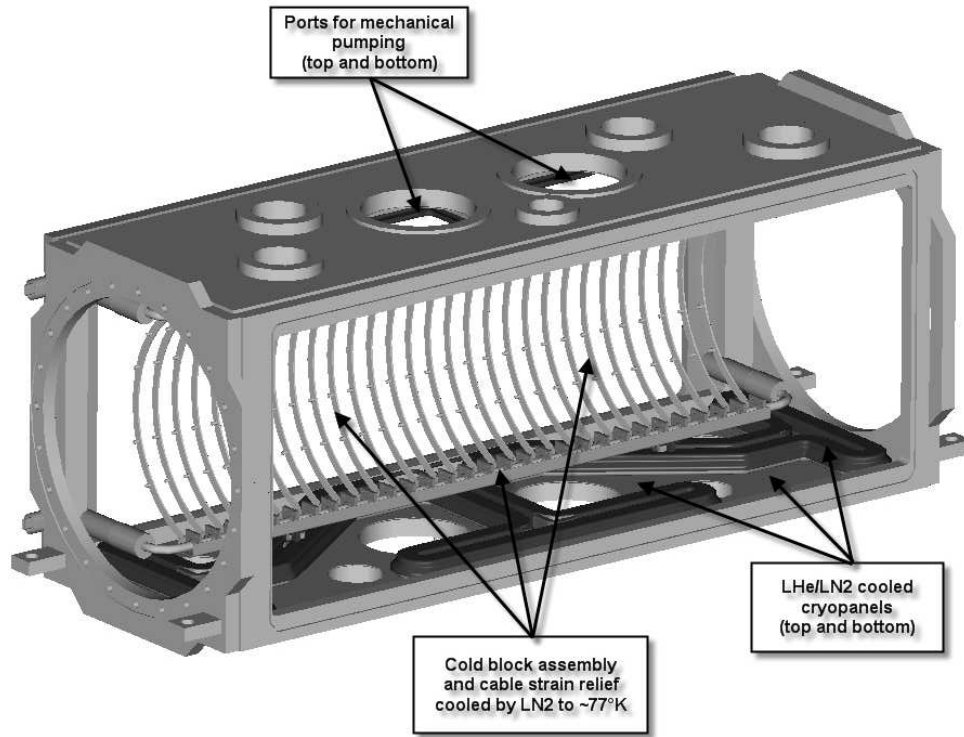


Figure 4.51: Components of the vacuum system for the pixel detector.

possible to use commercial cryopumps because they require maintenance service every 10,000 hours. Also, the commercial cryopumps need to be magnetically shielded so they can operate in a magnetic field of less than 300 gauss. The required magnetic shield will not fit in the space that we have. As a result, it is not possible to use commercial cryopumps.

To pump non-condensable gases such as nitrogen and hydrogen, we will install inside the pixel vacuum vessel two liquid helium cryopumps as shown in Fig. 4.53. Figure 4.52 shows the thermal shields layout on top of the vacuum vessel wall. Figure 4.53 shows the cross section of the thermal shields and the piping within the cryopump. The central part of the pump is made of 4-mm stainless steel pipes carrying liquid helium ( $\sim 4^\circ\text{K}$ ). They are covered by charcoal to pump hydrogen. The charcoal capability to be degassed at room temperature is very important for this application. The gaseous helium boil-off ( $\sim 20^\circ\text{K}$ ) cools a set of thermal shields that surround the charcoal-covered pipes. The copper shields, each having a thickness of about 1 mm are thermally coupled to these helium gas pipes. The warmest stage of the cryopump is the set of copper radiation shields that are cooled by liquid nitrogen. The decreased liquid nitrogen temperature reduces the power going to the liquid helium lines so that less liquid helium needs to be supplied to the cryopump. The liquid nitrogen flows through the 6-mm inner diameter pipes. The full cryopump assembly takes up a space of 130 cm by 45 cm by 4.7 cm. The overall pumping speed of these two cryopumps



Figure 4.52: Thermal shields of the cryopump.

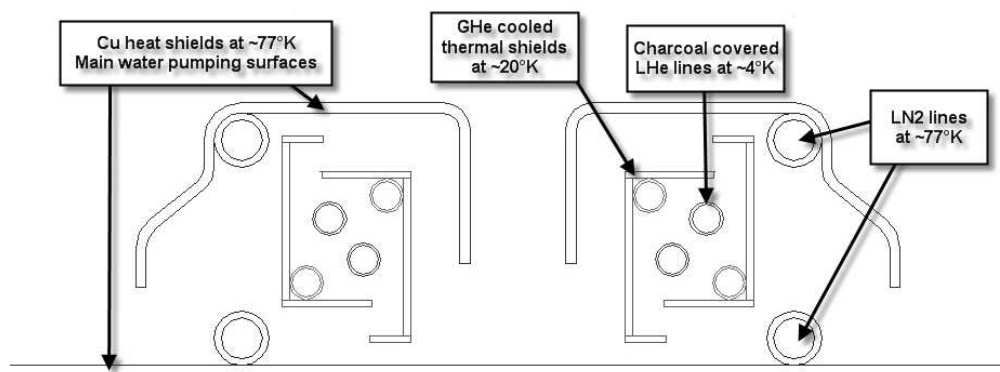


Figure 4.53: Cross-section of the three-stage LHe cryogenic pump. As LHe is heated, the GHe flows through the lines that cool the inner thermal shields to 20°K. The LN<sub>2</sub> shield sits 3 mm away from the room temperature vacuum vessel wall.

for hydrogen depends on the charcoal temperature; it changes from about 500L/sec at 5°K (hydrogen condensation coefficient on the charcoal about 0.05) to more than 5000 L/sec at less than 3°K (when the condensation coefficient should be about 1).

The liquid helium system will require equipment for the LHe transfer and production. This makes the system rather complicated and costly. We are also currently exploring the option of using Titanium Sublimation Pumps (TSP) to pump on non-condensable gases. This is at least an order of magnitude less expensive and much simpler than the LHe system. In this option, two TSPs will be located on the top and bottom surfaces of the vacuum vessel.

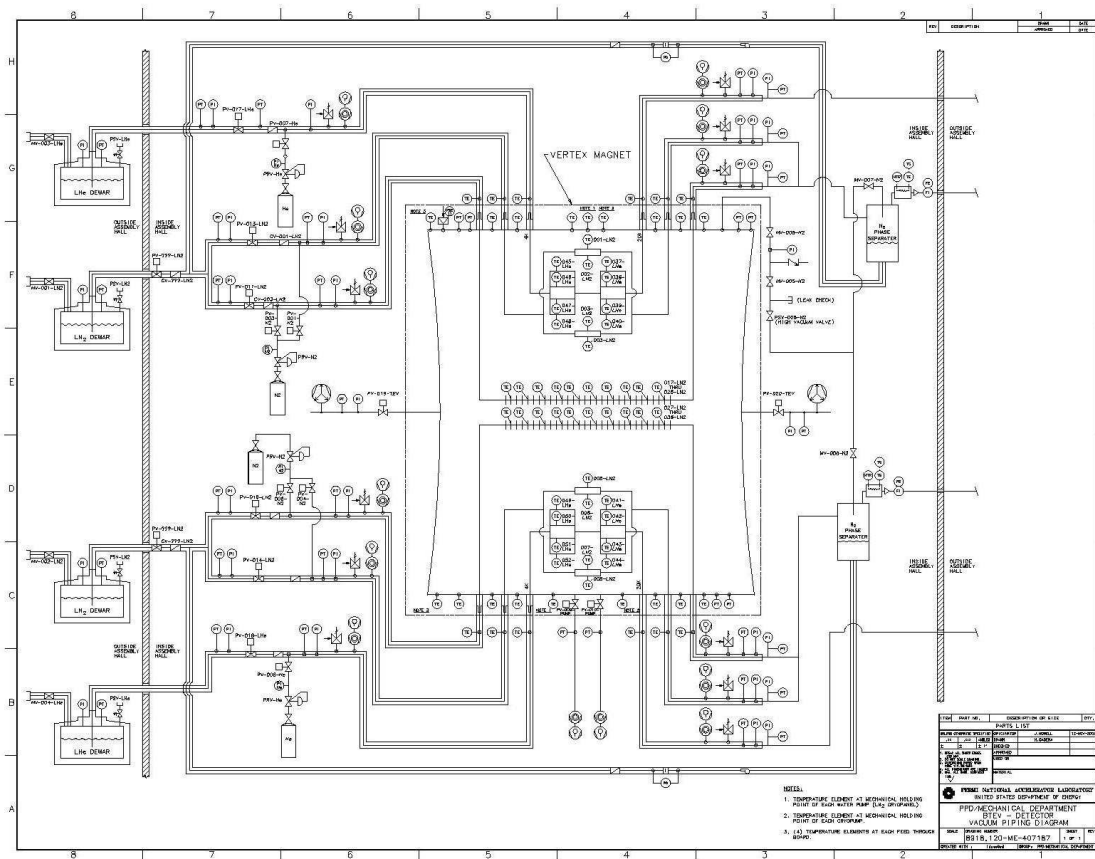


Figure 4.54: Layout of the vacuum system for the pixel detector.

The two TSPs are connected to the pixel detector vacuum by four rectangular apertures. The total pumping speed for nitrogen from the two TSPs is expected to be higher than 5000 L/sec. However, the TSPs do not pump noble gases and methane. These latter gases are pumped only by the mechanical pumping system

**Water Pump** There are several parts to the water pump: the cold block assembly, the cable strain relief structure, and the radiation shields of the cryopumps. The cold block assembly is the heat sink for the substrate temperature control system (see "Cooling" section). For each half of the detector, there are 60 tabs (copper cold blocks) that are the thermal connections from the substrates to the liquid nitrogen heat sink. Liquid nitrogen flows through two tubes passing through tabs (copper cold blocks). The surfaces of the cold block assembly that are readily exposed to the pixels, namely the channels and the tabs, are cold enough to act as water pumps with a total surface area of 5200 cm<sup>2</sup>.

Each of the two cable strain relief structures consists of 30 aluminum C-shaped plates. The aluminum structures are thermally connected to the heat sink. The thermal conductance

of the aluminum makes the temperature in the structure range between  $-195^{\circ}\text{C}$  and  $-139^{\circ}\text{C}$ , if the heat sink is at a temperature of  $-195^{\circ}\text{C}$ . Note that a secondary benefit of the cable strain relief structure is that it acts as a radiation shield around the sides of the pixel detector, thus reducing the temperature of the detector and helping to reduce outgassing. The surface area of one plate is  $170\text{ cm}^2$ . Thus the total surface area of the strain relief structure as shown in Fig. 4.55 that pumps water is  $5000\text{ cm}^2$ .

Another large contribution to the water pumping comes from the thermal shields of the two liquid helium cryopumps. The total effective area of the cold block assembly, the cable strain relief structure, and the shields of the liquid helium cryopumps is  $5.4\text{ m}^2$  and a water pumping speed of  $800,000\text{ L/sec}$ . Note that in all the calculations, we have used the outgassing rate measured at room temperature and not considered the significant reduction of this rate at the low temperature of the pixel detector and with the elapsed time under vacuum.

The layout of the vacuum system is as follows: two liquid helium cryopumps will be placed directly inside the vacuum vessel. On the top and bottom plate of the vacuum vessel, there will be vacuum ports with vacuum lines leading from the vessel out to the roughing pumps, which are located remotely outside the magnet. The expected conductance through the lines is on the order of  $10\text{ L/sec}$ . An isolation valve is placed in the line between the vessel and each of the roughing pumps. A safety valve is also placed in the system to prevent the vacuum vessel to build up pressure if there is a power failure.

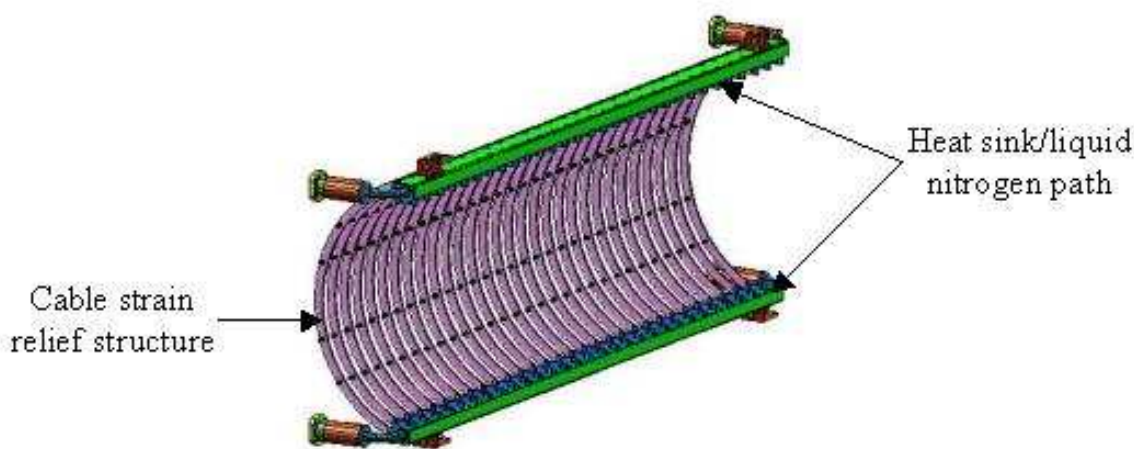


Figure 4.55: Drawing showing the cold block inside the vacuum vessel.

#### 4.5.10.2 Regeneration of cryopanel

The long-term capacity of a cryopanel cooled with a liquid nitrogen was measured to understand how long it can pump before regeneration is needed. The test showed that the cryopanel pumped for an equivalent of 44 weeks of detector operation without any degrada-

tion in performance [27]. This was a lower limit because the test was ended only because our supply of liquid nitrogen ran out. This means that we can operate the detector for one full year of running without regeneration. The test also verified that the water condensation coefficient on the cryopanel was about one. Thus the expected pumping speed of  $5.4m^2$  of the liquid nitrogen cooled surface is 800,000 L/sec for water vapor. This is enough to bring the detector pressure to about  $10^{-8}$  torr for a gas load of 0.01 torr-L/sec.

#### 4.5.10.3 Pump down procedure

The proposed sequence to pump down the pixel vacuum system is:

1. At room temperature, use roughing pumps to bring the vacuum to  $1 \times 10^{-3}$  torr at speeds of greater than 10 L/sec. This pumping speed depends on the number and dimension of the pipes connecting the fore vacuum port of the cryopumps to the turbo. The larger this pumping speed is, the lower the vessel pressure at which we start the cool down procedure will be.
2. Slowly feed liquid nitrogen to bring all the water pump surfaces to the  $LN_2$  temperature and wait until the pressure and temperature become stable. The substrate temperature is kept stable by balancing the heat applied to the control heaters on the substrate and by flowing cold nitrogen gas through the cold block assembly. The pressure will be brought to the  $1 \times 10^{-5}$  torr scale.
3. Change the setting of the substrate temperature control heaters and adjust the liquid nitrogen flow rate through the cold block assembly to reach the working temperature ( $-10^\circ C$ ). Then turn on the pixel modules and continue to adjust the control heaters and the liquid nitrogen flow rate to keep the pixels at the desired working temperature.
4. Send the liquid helium to the two cryopumps and wait until the pressure and temperature becomes stable. The vacuum pressure should become about  $1 \times 10^{-8}$  torr at the end of this cool down phase.

#### 4.5.11 Feed-through board

The flex cables will bring signals from the pixel modules to connectors sitting inside the vacuum part of the feed-through boards. From there, the signals will go through copper traces inside the board, and will be taken to the part of the board which is outside the vacuum vessel. Connectors sitting on the part of the board outside the vacuum vessel will be used to bring the signals to external data cables. Because of complication in fabricating large size multilayer printed circuit boards, the complete FTB will consist of six (three top and three bottom) 17x27.5 inches boards. To make vacuum tight joints between the boards and to make the FTBs stiffer, aluminum plates will cover both sides of the board leaving free space for inner and outer connectors and other on-board components. Fig. 4.56 is an engineering drawing of the feed-through board assembly.



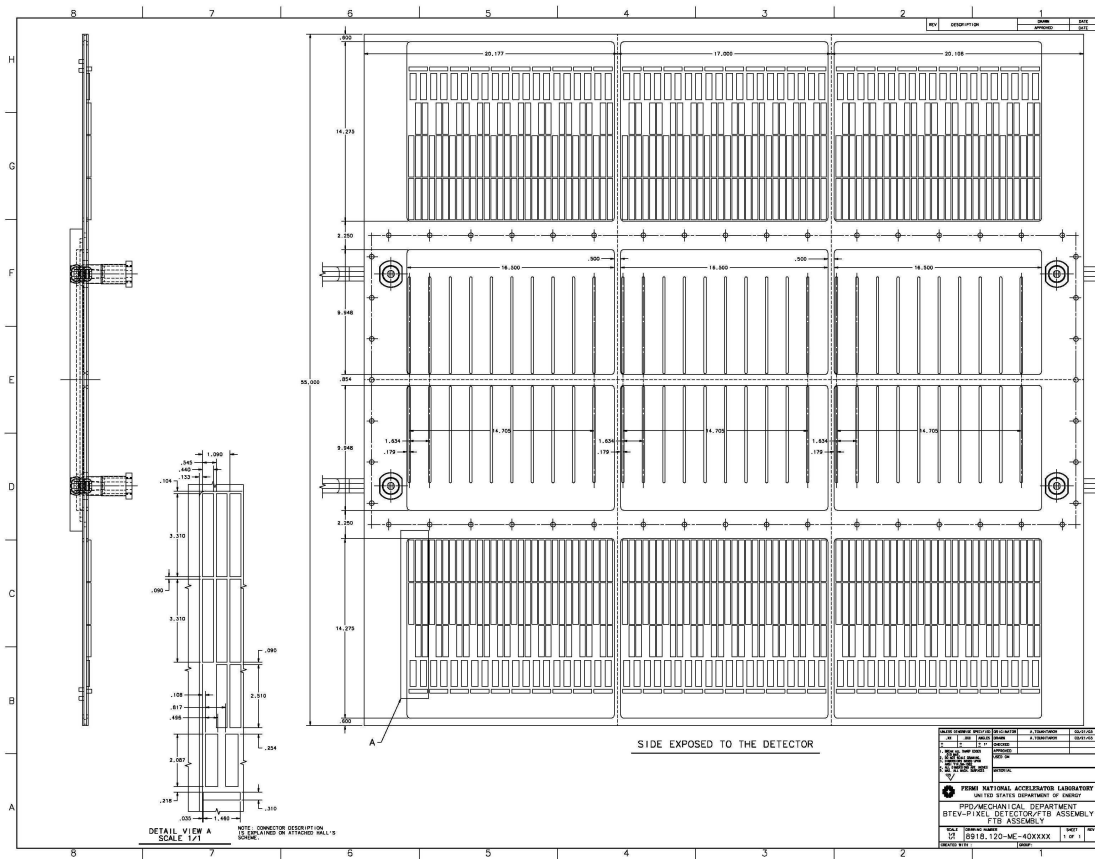


Figure 4.56: Engineering drawing of the complete feed-through board assembly. Signals are fed through the vacuum vessel via these printed circuit boards with high density connectors.

#### 4.5.12 Actuators

Four actuators (two at the top and two at the bottom, see fig. 4.57) will be attached to each of the half-detectors. The bottom actuators will be attached to the cold blocks assembly and to the carbon fiber support structure. The top actuators will be attached to the cold block assembly, a third support of the support structure will be created by attaching to the cold block assembly (see Fig. 4.58). This detector supporting scheme is chosen for the following reason. Each cold block assembly has two inlets and two outlets for liquid nitrogen, with each inlet and outlet having bellows to accommodate movement of the detector in and out of the beam. Any difference in the bellows behavior will create excessive forces. These forces, in the case of a three-actuators supporting scheme (e.g. two at the bottom and one on top) will create extra motion of the cold block with respect to the carbon support structure. This extra motion in the worst case scenario can be as large as 5 mm, which is more than acceptable. The solution to this problem is to attach four actuators to the cold block assembly in close proximity to the bellows. At the same time, we have to keep the

carbon support structure attached to the actuators at only three points. In other words, we have to provide a kinematic supporting scheme.

Capacitive position sensors will be permanently attached to the inner surface of the vacuum vessel and the metallic targets will be attached to the half detectors. A couple of sensors will be installed on each measuring point, one for  $x$  and the other for  $y$  measurement. Special attention has been given to the choice of location where the sensors will be placed. Our current plan is to place four pairs of sensors per half detector. They will be mounted close to the end window openings. Final alignment and sensor calibration will be done after the detector halves have been installed inside the vessel and attached to the actuators. This design has quite a lot of redundancy (since only 5 sensors will be enough to define the detector position), but it is conservative and will reduce risk in case of sensor malfunctioning. With this scheme, any distortion in the pixel detector support structure will be detected.

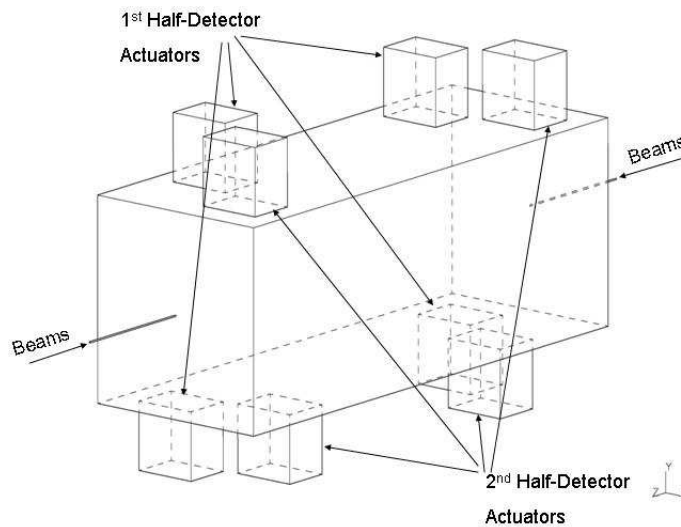


Figure 4.57: Schematic drawings showing the locations of the actuators

### 4.5.13 RF shielding

The performance and readout of the pixel detector should not be unduly perturbed by the presence of the circulating beams. On the other hand, the presence of the detector must not affect the operation of the Tevatron or degrade the beam conditions at other IR's by parasitic coupling. An rf shield design is needed to suppress the wake-field and beam instabilities. We are currently exploring the use of a number of CuBe wires of  $125\ \mu\text{m}$  in diameter or four thin ( $\sim 50\ \mu\text{m}$ ) but wide strips made out of stainless steel. In either case, the wires or strips will extend beyond the length of the vacuum vessel and the exit windows by as much as 4 meters on both ends. Their distance to the beam axis is adjustable between 20 mm (for injection) and 5 mm for data-taking. This can be done by either having a separate set of actuators or by coupling their radial movements to those of the pixel detector stations.

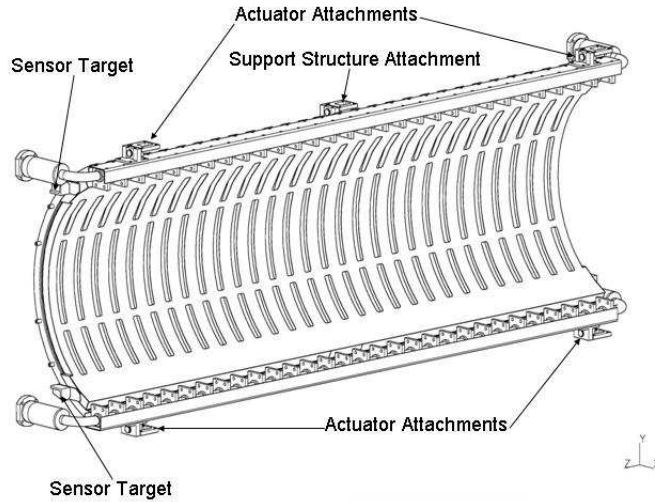


Figure 4.58: Locations of the actuator attachment and sensors on the pixel half-detector

#### 4.5.14 Power distribution

The power supplies to the pixel detector must provide:

- Low voltage for the electronics
- High voltage bias for the silicon sensors
- Power for the various accessories for the operation of the detector. These include position control system, cooling system, and the temperature control system.

We envision two options for the location of the power supplies: outside and inside the experimental hall. The first option simplifies the design and procurement of power supplies, but imposes restriction on the distribution cables. The cables can act as EM pick-up elements conducting noise into the detector or generating conductive paths between the different layers of the detector.

The second option imposes more challenges due to the need of locating DC-DC converters near the detector to break conductive paths and decrease the EM pick-up. The pixel detector will be subject to strong magnetic field, which does not allow any magnetic material in the design of such converters. Experience at CDF also showed that radiation effects would be significant inside the enclosure.

Our baseline design will have the HV power supplies installed in the catwalk that will be located just outside the experimental hall. The LV power supplies will be located inside the experimental hall, near the walls of the enclosure. A power distribution system will be developed, tested, and installed.

#### 4.5.15 Control and Monitoring

The BTeV Pixel system requires continuous and careful monitoring in order to ensure safe and continuous operation during its long lifetime. It also needs a system which can be used to actively control the many inaccessible and complex pieces of hardware that make up the detector. Finally, a system to continuously record critical parameters is needed to watch for drifts in the many parameters so that problems can be diagnosed and corrected before they become critical.

The pixel monitoring needs can be divided into the following distinct groups:

- Cooling system
- Temperature control system
- Low and High Voltage power supply system
- Radiation Monitoring
- Vacuum system
- Actuators and position sensor
- Rack protection

These systems include the monitoring of a wide variety of parameters including pressures, temperatures, positions and flow rates. In addition, the complex vacuum system require active feedback and control of critical parameters. For less time critical monitoring appropriate limits will be set and an alarm will be issued should such limits be exceeded. In some cases, the alarm should automatically initiate a turn-off sequence to prevent any major damage to the system. For example, any signs of failure of the vacuum or cooling system should automatically trigger a mechanism to turn off all HV power and interface with the appropriate Tevatron alarm/interlock systems. Earlier this year, during the preparation for the pixel beam test at Fermilab, we implemented and tested a slow control and monitoring system based on APACs hardware and IFIX software. This is a system used by CDF and MINOS and is commonly found in American and European industry. We have successfully used the system to control the HV to the pixel sensors, LV to the readout chips, and monitor the temperature of the pixel detectors and coolant reservoir. We continuously monitor the current drawn by the sensors and the readout electronics and remotely control the position and angle of the mechanical box holding the detectors. This gives us valuable experience in testing the APACS hardware and IFIX software systems. In addition, this system is being expanded to include the BTeV RICH test beam monitoring system and will be further integrated with additional BTeV test setups as they are installed in the testbeam. Based upon these experiences, we will work together with the DAQ group and the relevant Fermilab departments to design and develop a system that is capable of meeting our needs and those of BTeV as a whole.

## 4.6 Ongoing Prototyping Efforts

Prototype substrates made out of TPG have already been received. A complete half-station is currently being assembled using mechanical grade silicon modules. This will give us experience in testing assembly of modules on the TPG using prototype fixtures. Once assembled, our plan is to test the thermal performance, check the thermal profile, and to study any thermal stresses and displacements at different operating temperatures.

One issue that still needs to be addressed is how to optimize the thermal connection of the heaters (which are needed for temperature control of the system) to the substrate, thus confirming the effective CTE of the assembly. Testing of a prototype control system will measure the time constant of the system. The time constant of the substrate temperature control system will be sufficiently short during the power failure. The temperature transient will not experience overshoot. The temperature change during the transient, in case of failure in the pixel power supply, will not exceed  $15^{\circ}\text{C}$ , as shown in a thermal modelling calculation[28]. This assumes that we will have uninterrupted power supply to feed the heater power in the pixel detector[29].

We have already made a full-size stainless steel cooling tube carrying  $\text{LN}_2$  with copper cold blocks brazed to it (see Fig. 4.59). Tests of the prototype cooling tube will begin soon. We will check the thermal profile at various places along the tube as a function of flow rate and applied heat load. The measurements will then be compared with our calculations. Possible vibration caused by the liquid nitrogen flow will also be studied. The design of the vacuum system is very advanced and we will test prototypes of the cryopumps this year.

Another critical area that needs to be addressed is the shielding from EMI effects due to the circulating beams. We have done first measurements using the rf shielding test setup to study the effect on the noise and threshold of a FPIX1-instrumented pixel detector. These measurements will continue with rf amplifiers of much high power to mimic the Tevatron beams.

We are ready to produce full-sized feed-through board prototypes. Once received, these boards will be tested both electrically and mechanically. Effects such as cross-talk, signal integrity, high voltage performance will be studied under normal and vacuum conditions. We will also study outgassing and check whether the boards are leak tight.

We plan to do a series of beam tests using the MTEST facility at Fermilab. The goals of the tests are to study charge collection and efficiency of the p-spray sensors before and after irradiation. We will also study the performance of the 5-chip FPIX1 modules, and the performance of the new FPIX2-instrumented pixel detectors.

A moderate scale module assembly is also under way. We will assemble up to 50 FPIX2 modules of different types using a new HDI design. We hope that all the assembly and testing issues of the pixel modules will be fully understood after this round of prototypes and we can head into pre-production. Concurrently, a large scale wafer thinning program has started and we will work with industry to fully master the technique of thinning 8" wafers with bumps put on.

Lastly, we will continue to study system issues. From our test beam experience, as well

as operational experience from other large experiments, systems issues such as power supply, grounding, cabling, and connectors are potentially the most problematic areas. A system demonstrator will be built to test the cooling system, the temperature control system, the vacuum system, the electronics readout system, and gain experience of operating the pixel detectors under conditions that will be close to the final BTeV experiment. The test will include one or more half-stations with working pixel modules fully assembled on it, a full size support structure, feed-through boards, control heaters, and the cold block assemblies. The gas load of the full sized model will be measured to better understand the total outgassing rate of the materials used in the detector assembly. Various operating conditions will be studied to test the temperature control system. Figure 4.60 shows a sketch of the test setup. This demonstrator program will be carried out early in the construction phase of the project. Another critical issue that we will need to address is the effect on the pixel detector during unforeseen beam incidents in which the pixel detectors may see a large particle flux in a very short time. We plan to study this with a few pixel modules in the Booster irradiation facility some time next year.

To understand and address more complicated system issues, we plan to assemble a 10% pixel system after the demonstrator test. With such a system, we can also carry out a thorough investigation of a complete electrical, mechanical and cooling system. This will also enable us to operate a small system in the real C0 environment. This system will be placed outside a normal beam pipe. Issues such as grounding, shielding, and fast readout coupled to a prototype trigger processor can be studied in detail there. At the same time, it will allow us to understand the yield at the various steps of production, as well as how to assemble reliably the full scale pixel system. We will use parts that are procured during the preproduction phase for this system test.

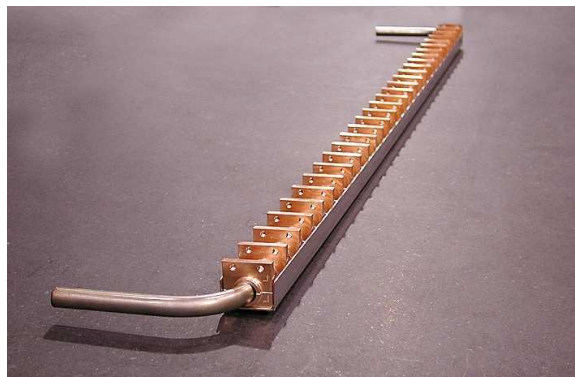


Figure 4.59: Prototype liquid nitrogen cooling line with copper tabs brazed to the stainless steel tube.

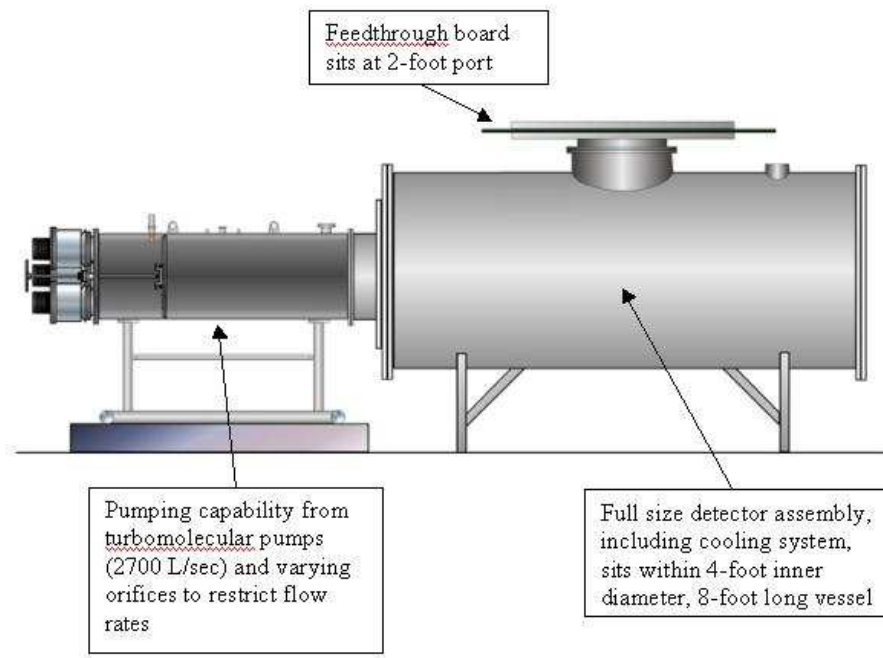


Figure 4.60: Schematic of the system demonstrator setup.

## 4.7 Production - QA and Testing

### 4.7.1 Overview

The key to keeping the project on schedule and on budget is the extensive testing and qualification of the components and of the product at each step of the assembly. The basic building block of the pixel detector is a module, which is composed of a pixel sensor bump-bonded to a number of pixel readout chips. Underneath the readout chips on the module, a high density flex cable (HDI) will be glued. The readout chips will be wire-bonded to the HDI and the latter will carry all the signal, control, and power lines from the pixel module to the DAQ system. The HDI will in turn be attached to a pixel interconnect flex cable (PIFC). All of these individual components will be tested before assembly. A few of the groups involved in the pixel project will be equipped with probe stations that can test the sensors, HDI, and flex cables. Furthermore, a common PCI-based test-stand will be used at all sites for hardware checks and software development and debugging. Databases will be used extensively so that all production and testing information will be readily accessible at all sites. We also do cross checks and calibration so that the same high quality testing procedure and standard can be maintained at all sites. Lastly, we intend to have specifications documents, detailed quality control planning, vigorous test procedures established with commercial vendors for critical components to ensure that only products that passed our acceptance criteria will be delivered. To ensure this, we intend to do a lot of testing at the vendor sites. We have already

gained good experience with one sensor vendor during our latest submission. These quality control plans and procedures will be developed as the project moves to the construction phase.

The assembled pixel modules will undergo initial functionality tests followed by burn-in testing. The modules that pass the burn-in testing will then be mounted on a support substrate to form a pixel half-station. Next, all modules on a half-station will be fully tested for electrical and readout problems. Before assembly, each substrate will be tested for mechanical tolerances and thermal conductivity. A separate cooling test will be performed to insure that the pixel half-station achieves the designed operating temperature. During this process, all assembly and alignment parameters will be recorded in a database.

The pixel stations will next be mounted to a carbon support shell to form a half-detector. During this step, the position of each pixel half-station will be measured and the information will again be recorded in a database. Once the half-detector is fully assembled, each half-station will be tested and read out. This testing will be repeated after the half detector is inserted into the vacuum vessel at SIDET.

When both half-detectors are inserted and all cables and connections inside the vacuum vessel are properly installed, connected, and tested, the vacuum vessel will be closed. Before transporting the vessel from SIDET to C0, a number of additional tests will be performed. These include:

- **Vacuum test:** the vessel will be pumped down to check for possible leaks
- **Cooling test** - Leak tightness and temperature performance will be checked with the vessel under vacuum and then the modules fully powered.
- **Electrical test** - the modules will be powered up to check for continuity
- **Readout test** - all modules on a half station will be readout simultaneously
- **Actuator test** - the half detectors will be moved closer and further apart and the read-back sensors calibrated.

When the pixel detector has passed all these tests, it will be ready for installation.

### 4.7.2 Sensor Tests

To ensure high quality of the pixel sensors, we plan to have a series of quality assurance(QA) checks to be performed by the vendors and by the pixel group. Fermilab will serve as a central distribution and control center with dedicated testing and coordinating (with the vendors and other institutes) tasks. There will be one or more other testing sites set up and the QA program will be carried out in a consistent manner at all places.

The vendor is required to perform checks and tests to ensure the wafers will be selected and processed according to our specification and their design rules. Consistency of the processing will be checked by the vendor using Process Control Monitors (PCM) of their



choice. Information on the consistency of the alignment and processing will be provided to us. I-V and C-V measurements are to be performed on the diodes, single chip devices, and the modules.

All the delivered sensor wafers will be tested at Fermilab and other testing sites. These include visual inspection, I-V measurement and C-V measurements on all modules and single chip devices. A subset of the wafers will also be subjected to additional tests. These include:

- Leakage current stability over time
- Flat band voltage measurements on MOS test structure
- Current measurement as function of gate and reverse bias for gate controlled diodes
- Sensor thickness and warping
- Irradiation test on selected single chip sensors and test structures

For consistency, cross-checks will be performed on some detectors and wafers to make sure that measurements at various sites agree with each other.

### **4.7.3 Pixel Readout chips**

All the received wafers of the pixel readout chip will be probed at Fermilab. We have already acquired some experience of testing the first batch of FPIX2 wafers. These tests include powering sequence, checking of the voltage and current levels during quiet and operation mode, loading and reading back of a test pattern at high clock speeds using one to all of the serial lines. We may also do more detailed checks such as determining the noise and threshold performance of all pixels. The chips that pass the criteria will be marked and the known-good-die (KGD) map will be sent to the bump bonding vendors. One or more wafers will be diced up so that we can carry out characterization tests to check on functionalities and performance. Chips from these wafers will also be irradiated to check their performance after irradiation. Test stands will be set-up at various sites to study the performance and operational characteristics of the chips and pixel detectors.

### **4.7.4 Bump Bonding**

The tested sensors and readout chip wafers will be sent to one or more bump bonding companies to be flip-chip mated to produce the pixel detector modules. We would like to have the readout chips thinned down to 200 microns. Thinning will be done in another company. A database is necessary to keep track of all the shipment of the wafers. We are currently discussing with the prospective vendors on a detailed QA plan. Tests will be performed by the vendor to check on the quality of bump deposition and the strength of the bump-bonds. These tests include visual inspection, automatic checking of the bumps on the wafer using a profiler, and scanning electron microscopy. Pull tests will also be performed

randomly on test structures to check the quality of the mating. After hybridization, the integrity of the mating will be checked by several means. Some of the modules will be X-rayed at Fermilab and a record of all the X-ray images will be kept. Some single chip detectors will also be made, and these detectors will be tested to study their performance. We also plan to do probing tests of all the modules. I-V and C-V measurements will be carried out on the sensor of each module to compare its behavior before and after bump bonding. These tests will be performed at Fermilab. The equipment needed will be the same as for probing the sensors. A small complication in the process flow is the issue of thinning. At this point, we assume that thinning will be done after the bumps have been put on the readout wafers. Note that the sensor wafers will be delivered to us at the thickness we specified, since the sensor fabrication uses a double-sided process. If needed, the inspection and testing of the bumped-readout-chip wafers after thinning will be done at Fermilab.

#### **4.7.5 HDI and interconnect flex cable**

The HDI will come in 5 different types, one type for each module type(size), with the ones for the 1x4 module having right and left-hand versions. All together, there will be 5 types of HDIs. Including factors due to production and assembly yield, extra quantities etc, we will need about 2000 HDIs in total. Each HDI has to be tested for shorts, broken lines, open vias, and bad wire bond pads. Surface mounted components have to be assembled on the HDIs. Each HDI will need to be bonded to a Pixel Interconnect Flex cable. The joint technology to be used is still being evaluated. Options include wire bonding, small connectors, solder pads, and z-axis conductive adhesive. The bonding and the line integrity have to be rechecked afterwards. Tests will need an optical microscope and simple probe station (due to the fine line spacing and width). Assembly of components on the HDIs will be done in industry. Tests of the assembled HDIs will be done at Fermilab, Iowa, and Wayne State University. The PIFC will be used to connect the pixel module (the HDI) to the feed-through boards. The two cables, HDI and PIFC need to be joined together. Testing of the PIFC will be done at Fermilab, Iowa and Wayne State University. The joining of the HDI to the PIFC needs a special fixture. This design and fabrication will be done by Fermilab.

#### **4.7.6 Substrate**

The pixel modules will be assembled on a TPG substrate. Each substrate will form the mechanical support for a half-plane. There will be 120 substrates in total. The substrate will need to be encapsulated before the placement of pixel modules on them . All substrates will be produced by industry. Encapsulation will be done at Fermilab. At the two ends of the substrate, a flexible part made from Pyrolytic Graphite Sheet (PGS) will be glued. The substrates will need to be checked after delivery. They will be visually inspected for any defects and non-uniformity. They have to be measured for flatness, dimensions, and be checked for thermal performance. The substrates will then be machined to the right size.

Precision alignment pins or fiducial marks will be placed on the substrate. The testing and machining will be shared between FNAL and Iowa.

#### **4.7.7 Substrate support structure**

Fermilab will be responsible for the fabrication and testing of the substrate support structures. This structure will come in two halves. Pixel stations will be mounted to the substrate support structures using mounting brackets. Frascati will be responsible for checking the stability tests on the support structure. They will also be responsible for performing a feasibility study on the in-situ checking of any long term deformation or creeping of the structure during operation.

#### **4.7.8 Feed-through board**

The feed-through board is a very complicated multilayer printed circuit. These boards are needed to bring the signal, control, and power cables from outside the vacuum vessel to the pixel modules inside the vessel. It will be manufactured and assembled by industry. The boards will be tested electrically by the manufacturer and only boards which pass the tests will be sent to us. At Fermilab, these boards will be tested mechanically for outgassing and vacuum leak-tightness. Electrical tests will be repeated under vacuum conditions. Six of these boards will then be glued together with aluminum support frames to form one side of the vacuum vessel. The glued joints will be checked for vacuum properties.

#### **4.7.9 Database**

The amount of information that we have to keep track of during the production and assembly of the BTeV pixel detector is enormous. This includes the various parameters from the large number of components that need to be tested, the assembly and alignment parameters, voltage and threshold settings, current limits, and various monitoring information such as temperature and pressure. Furthermore, there will be a number of vendors involved for the components and at various stages of the assembly. We will have to keep track of the inventory and the parts flow at each step of the process. Finally, a number of institutes will participate in the testing of the components and we need to maintain a stringent and uniform quality control for the testing of the components. For these reasons, we need a production and testing database to store all the information.

We will learn as much as we can from the experience of the Tevatron (CDF and D0) and LHC experiments (ALICE, ATLAS, and CMS). Together with the Fermilab Computing Division, we will design and develop a relational database to track and identify each piece of all the components. The database will consist of:

- Detector construction database: this keeps track of all the components and their detailed test results

- Electronics manufacturing database: this keeps track of the shipping of all the different wafers (readout chips, sensors) from one place to the other and the processing task that has been performed at different places (e.g. bumping, thinning, wafer probing)
- Detector Configuration database: this keeps track of all the alignment parameters of the pixel modules placement on the substrates, the pixel half stations and the pixel half detectors at different stages of the assembly process
- Detector calibration database: this keeps tracks of the calibration results using radioactive source, laser, and test pulses. Besides keeping a record of bad (dead or noisy) channels, detailed performance parameters such as noise, threshold, and gain will be recorded for each pixel in the system. All information pertinent to the performance of the detector, such as voltage and current settings, limits, operating temperatures, vacuum conditions will also be kept.

## 4.8 Performance

### 4.8.1 Spatial Resolution

BTeV test beam studies, performed with prototype sensors and readout having pixel sizes of  $50\text{ }\mu\text{m}$  by  $400\text{ }\mu\text{m}$ , have demonstrated a spatial resolution between 5 and  $9\text{ }\mu\text{m}$  in the narrow dimension, depending on the track angle of incidence (see Fig. 4.61). The solid line shows the resolution function (Gaussian) used for the Monte Carlo studies presented in the BTeV proposal. (The MC simulations also included non-Gaussian tails in the resolution distributions as measured in the test beam.) The figure shows both the resolution obtained using 8-bit charge information directly, and also the resolution obtained by degrading the pulse height to 2-bits of information. This result confirms the prediction of our simulations: that excellent resolution can be obtained using charge sharing, even with very coarse digitization. Based on these results, it has been decided that the BTeV readout chip will have a 3-bit FADC in each pixel cell. This will provide excellent spatial resolution. In addition, the actual pulse heights may be used to indicate the presence of  $\delta$ -rays or  $\gamma$  conversions.

The single hit resolution is made possible by the choice of pixel size and a relatively low threshold for readout (approximately 2500 input electrons equivalent compared to about 24000 electrons for a minimum ionizing track at normal incidence for the devices tested). Relatively low dispersion of the thresholds across the chip and low noise in each pixel make the low readout threshold possible. Given the relatively long beam crossing interval of the Tevatron (compared with the 25ns at LHC), time slewing in the chips will not be a problem. Mounting stability and the necessary pixel alignment, using actual tracks in the final location, will be important to avoid serious degradation of this good resolution.

While single hit resolution is important, it is not the whole story. We have worked to minimize the multiple scattering due to the material in all the components of the system (see Table ??). The pixel detector will sit in a vacuum with only a set of wires or a few strips

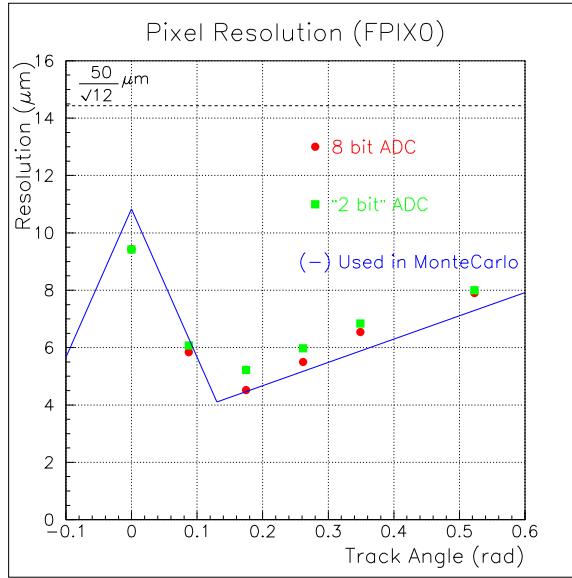


Figure 4.61: Resolution as a function of the angle of the incident beam for both 2-bit and 8-bit ADC readouts. The lines are piecewise linear fits to a simulation of the resolution.

between the beam and the detectors. The very close proximity to the interaction region and the spacing between pixel planes is kept to a minimum to reduce the extrapolation distances to vertices, both primary and secondary. All these parameters have been optimized using detailed (MCFast and GEANT) simulations of our experiment and representative physics measurements.

### 4.8.2 Pattern Recognition Capability

The early choice of pixel technology for the BTeV vertex detector was based, in part, on the space point information that it provides which will help in pattern recognition. Fig. 4.62 comes from a beam test of BTeV prototype pixel detectors, and shows the power of space points in reconstructing high density tracks. There, an interaction in a carbon target a few mm upstream of the first pixel plane leads to seven tracks reconstructed in much less than  $1 \text{ cm}^2$ , a density an order of magnitude more than typical for BTeV.

The pattern recognition capability benefits enormously from the low occupancy, averaging slightly above 1 track per  $B$  event in the highest rate readout chip. In addition, the stretching of edge pixels and the overlap of pixel modules mounted on opposite sides of the substrate provide complete coverage within the nominal plane acceptance. The regular spacing of planes along the beam also eases the job of the Level 1 trigger.

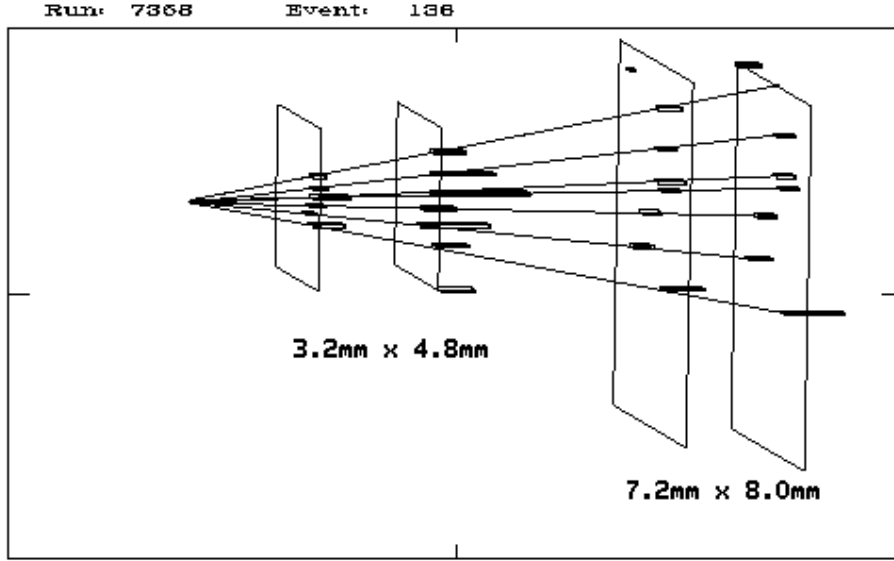


Figure 4.62: Multiparticle interaction observed in Fermilab beam test. The length of each hit is proportional to the pulse height. The straight lines represent fits to the outgoing tracks.

### 4.8.3 Radiation Hardness

We have done a detailed simulation of the expected radiation levels for the whole BTeV detector and the experimental area. The luminosity used in the simulation was  $2 \times 10^{32} \text{ cm}^{-2} \text{ s}^{-1}$ . The Pythia generator was used to generate minimum bias events which served as input particles for the MARS code. The full BTeV geometry file was used, including the location and amount of material in the various subsystems of the detectors, the dipole magnet, and the compensating dipoles. The charged hadron fluence distribution in the pixel region is plotted in Fig. 4.63. We have also looked at other particles such as neutrons, gammas, electrons, and muons. In the pixel active region, the fluences due to these latter particles are more than an order of magnitude less than that from the charged hadrons. As one can see from Fig. 4.63, it is expected that the innermost region of the pixel detector will receive a fluence of  $1 \times 10^{14} \text{ particles/cm}^2/\text{year}$ .

The significant radiation environment in which we plan to operate our detector means that all components of the pixel system have to be radiation hard. Our irradiation studies showed that both the sensors and the readout chips are radiation hard enough to remain operational for at least 10 years of BTeV running.

These irradiation results will be augmented with charge collection and other tests in a test beam at the Fermilab Meson Test Beam Facility as soon as it is available. Finally, we have started and will continue to test all components (bump bonds, high density interconnects, adhesives, etc.) in high radiation environments before final certification for use in the pixel detector.

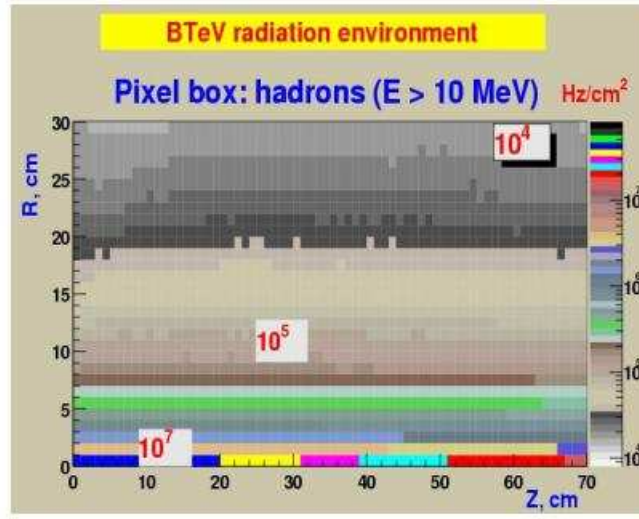


Figure 4.63: Charged particles distribution in the BTeV pixel detector

#### 4.8.4 Material Thickness

In order to prevent multiple scattering from decreasing the utility of our precision spatial resolution, we are keeping the material budget as low as possible. The sensors are 250 microns thick and the readout chips are thinned to no more than 200 microns thick. The high-density interconnects have four Cu layers. Signal and power flex-cables are decoupled and the materials in each can be separately optimized. We are currently investigating the use of power cables using Al instead of Cu. For rf shield, we are still investigating the options of using four Al or stainless steel strips, each 5 mm wide by 50 microns thick or a set of Cu/Be wires of 125 $\mu$ m in diameter. Our estimate is that in the active area covered by both precision-x measuring pixels and precision-y measuring pixels, there will be approximately 3.3% of a radiation length of material per station, and in the active area covered by precision-y measuring pixels only, there will be approximately 2.5% of a radiation length of material. The average over the entire active area will be slightly less than 3% per station.

#### 4.8.5 Readout Speed

Our pixel readout is data-driven. That is, the readout occurs as soon as data is ready on the readout chip. The token passing from row to row, which is an important part of the potential readout speed, is very fast (0.125 ns per row), and this starts in parallel in all columns. The readout rate allows us to move all the data off chip with negligible loss of data, even if the amount of data is three times that projected for our nominal luminosity

of  $2 \times 10^{32} \text{ cm}^{-2}\text{s}^{-1}$ . Data output is serialized, but uses a number of parallel readout paths selectable for each readout chip. The bandwidth of each serial path is 140 Mbps. The chips located closest to the beam are read out using 6 serial paths (840 Mbps total). Other chips are read out using 1, 2, or 4 serial paths. Most of the readout chips in the pixel system require only 1 serial output path. The readout bandwidth summed over the entire pixel detector is approximately 2 Tbps (terabits per second). The data coming off the chip is already highly sparsified, since only pixels above threshold are read out. Sorting out the data and assembling events is done external to the detector in large buffer memories.

### 4.8.6 Physics Capability

Figure 4.64 shows the momentum resolution as a function of track momentum using the pixel hits only. Figure 4.65 shows the distribution of  $L/\sigma(L)$ , which is the normalized detachment between the primary vertex and the  $B$  decay vertex, for reconstructed decays  $B_s \rightarrow D_s^- K^+$ , where,  $D_s^- \rightarrow \phi \pi^-$  and  $\phi \rightarrow K^+ K^-$ . The mean value is 44 standard deviations! Figure 4.66 shows the L-resolution and the proper time resolution for the  $B_s$  decay. The resolution in proper time is 46 fs even for this complex multibody decay containing a tertiary vertex (the  $D_s^-$  decay). This can be compared with the  $B_s$  lifetime of  $\sim 1500$  fs or the  $B_s$  mixing period of  $\sim 400$  fs if  $x_s$  is about 25. It is clear that the BTeV vertex detector has abundant resolution to carry out detailed time-dependent analyses even if the  $B_s$  were to have a surprisingly high oscillation frequency.

## 4.9 Cost, schedule and Risk analysis

### 4.9.1 Cost

The construction cost for the pixel detector is estimated to be \$15.5M with a contingency of \$6.2M to give a total cost of \$21.7M. These figures includes fringes and overheads. Most of the estimates are based on budgetary quotes from industry or recent requisitions of prototypes. A few are based on experiences with other projects on similar items (e.q. data cable used by CDF).

### 4.9.2 Schedule

The overall work schedule covers the whole construction period for the BTeV detector. This is based on a fully resource-loaded schedule. It is planned to ensure that the pixel detector is installed well before the start of the data-taking. A 10% detector is envisaged to be built and tested in CZERO using parts from the preproduction run and will be operational in 2007.



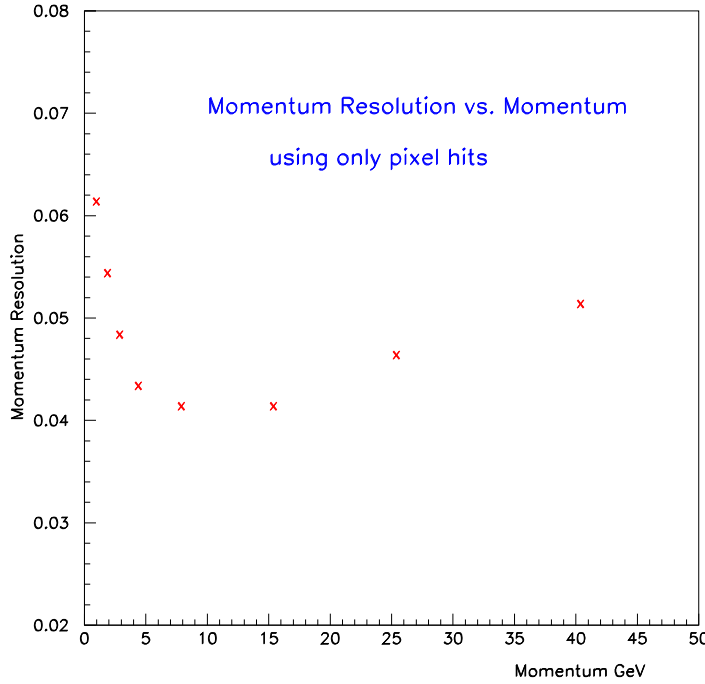


Figure 4.64: Momentum resolution as a function of track momentum using just the pixel hits

### 4.9.3 Production Risk Analysis

A risk is a situation that has the potential to cause a wanted or unwanted change in the project. Here, we focus on risks to the BTeV pixel detector that are unwanted. Risks can affect the schedule, cost, scope (what the project finally has in it) or technical success of the project.

A measure of the severity of risk is Severity ( $S$ ) = Probability of occurrence ( $P$ )  $\times$  Impact ( $I$ ) if it occurs. Following the guidance as outlined in [30], we have done an analysis of the pixel detector and identified the "risk events" as outlined below during the construction phase. Only events that have a Severity above 0.15 are listed. We also give our risk mitigation plan.

**Sensor** Currently, all vendors that we have contacted are using 4" technology. However, at some future dates, vendors may choose to move from 4" technology to 6" technology. Past experience showed that it would take a long time for the vendors to understand the process and improve the yield. The potential impact is on the schedule because the vendor may take a long while to ramp up the production capacity. We assign a severity factor of 0.15 to this based on a probability of 0.3 and an impact of 0.5. Our mitigation plan is to work with multiple vendors and keep in close contact with vendors to understand their future plans.

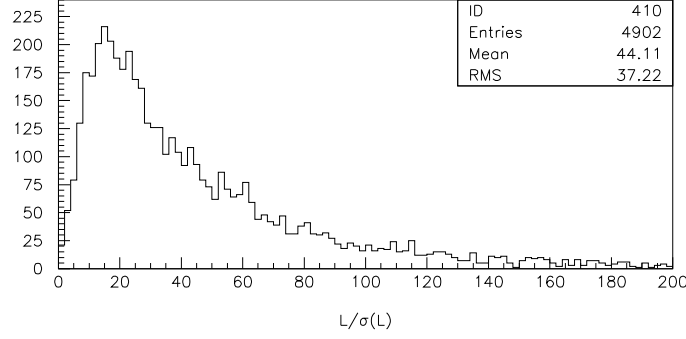


Figure 4.65: Normalized detachment,  $L/\sigma(L)$ , between the primary vertex and the decay vertex for the decay  $B_s \rightarrow D_s^- K^+$ .

**Bump bonding** Our current bump bonding vendors may not be available to us in the future or have unacceptable yield. Since we need more or less state-of-the-art technology for this, there is not a lot of experience for the vendors with large scale production (P=0.5). The impact of this will be high (0.8) as it will lead to severe cost increase and project slippage. Our plan is to identify more vendors and to keep close contact with ALICE, ATLAS, and CMS about their schedules and vendors.

**Readout chip** The pixel readout chip is based on a  $0.25 \mu\text{m}$  CMOS process. Since the trend in industry is a move towards processes with finer features, there is a probability (0.25) that the process would disappear before we go into production. The impact will be high (0.8) as it will mean re-design of the chip using a different process. The best solution is to start production as soon as funding is available.

**HDI** The risk (0.3) is that none of the vendors can produce the multi-layer flex cables with acceptable yield; or the couple of vendors are too busy with orders from other HEP experiments. While minimal technical problems are expected, we do not know what the yield of large scale production will be. The impact (I=0.5) will be high as it will lead to overall project slippage and increase in cost. We need to identify other vendors and keep abreast with all the developments in electronic packaging. We have to follow the industrial trend but not lead it.

**TPG substrate** TPG substrate is a quite fragile material and has a very poor tensile strength and a very low elastic limit in the out of plane direction. Any excessive loads

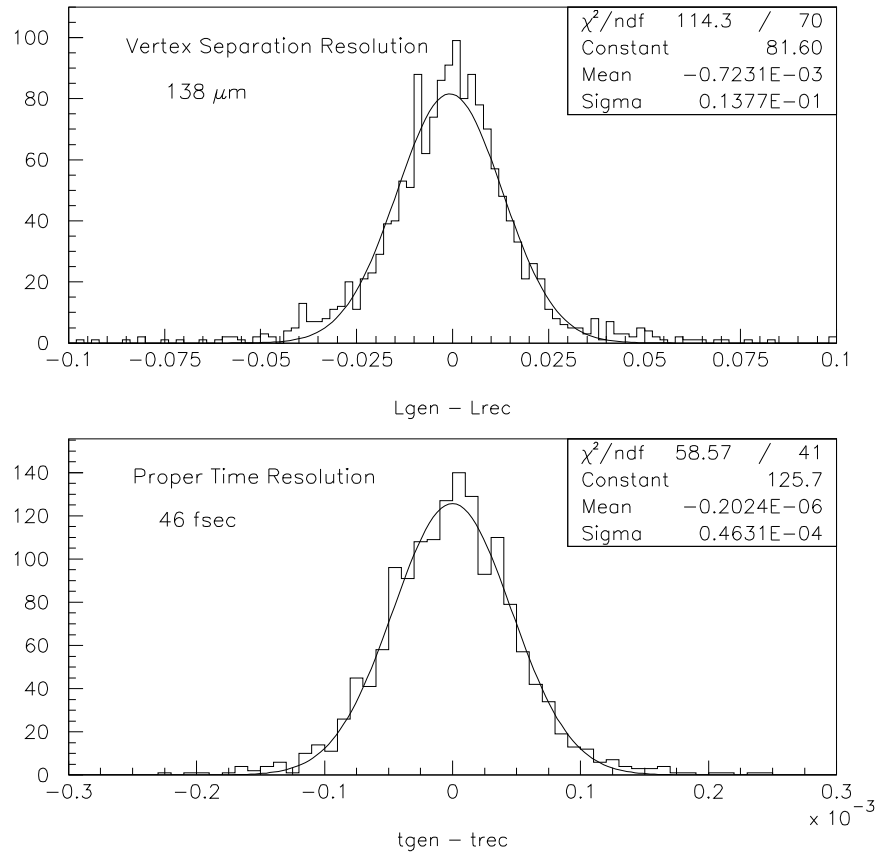


Figure 4.66: Top) The resolution in L, the separation between the primary and secondary vertex. The quantity plotted is the difference between the Monte Carlo generated separation  $L_{gen}$  and the reconstructed separation  $L_{rec}$ , for the  $B_s \rightarrow D_s^- K^+$  decay. The X- axis is in cm. The L resolution is 138  $\mu m$ ; and bottom) resolution in proper time. The quantity plotted is the Monte Carlo generated proper time  $t_{gen}$  minus the reconstructed proper time,  $t_{rec}$  of the  $B_s$  decay. The X-axis is picoseconds ( $10^{-3}$  nanoseconds). The proper time resolution is 46 fs.

that come from improper handling, installation (like gluing pressure of module on TPG), or operation (thermal stresses due to thermal gradient and CTE mismatch) can make the TPG substrate yield or deform permanently. Probability of failure is moderate (0.3), and the impact factor is high(0.5). The best mitigations are to develop proper procedures to handle the TPG with great care, to conduct more tests to understand its behavior so that undesirable stresses will not be generated, and to go through a series of real module placement

as early as possible to expose any troubles. We have recently made good progress on the encapsulation which has addressed a lot of the handling issues and concerns.

#### 4.9.4 Operation Risk Analysis

The mechanical system of the BTeV pixel detector is a very complicated system which must be integrated to the Tevatron machine vacuum without excessive risk. We have carried out a preliminary risk analysis to address failure scenarios, and to provide a basis for further discussion and any design modifications that may be necessary. A number of precautionary measures to mitigate these risks have been looked into and these have been included in the baseline design of the BTeV pixel system.

The critical parts of the system which have been analysed include the vacuum, cooling, rf shield, actuators, and the magnet. The detailed risk analysis is presented in [29]. This preliminary analysis will be developed further as the project progresses to the construction phase. By working together with the relevant department at Fermilab and learn from the experience of CDF and D0, most of these failure scenarios could be mitigated. As an example, we will work together with the Acceleration Integration Department to understand machine-related radiation loads for beam accidents and also to study impact of BTeV operation on the machine. It should be borne in mind, however, that since the pixel detector is placed inside a vacuum vessel which in turn will be located inside the analysis magnet, it will be hard to access should any problem occur. Routine maintenance or repairing of the detector elements that are placed inside the vessel *in-situ* will not be possible. To remove the vessel out of the magnet for repair will require a downtime of the machine for at least one month. This implies a robust system with minimum and long time in between maintenances. We have designed our system with this condition imposed as a boundary condition.

# Bibliography

- [1] J.A. Appel et al., *Nucl. Instrum. Meth.* A485 (2002) 411.
- [2] <http://www.btev-fnal.gov/public/hep/detector/pixel/status/pixel-papers.shtml>.
- [3] F. Lemeilleur et al., 3<sup>rd</sup> RD48 Status Report, CERN/LHCC 2000-009.
- [4] P. Jarron et al., 3<sup>rd</sup> RD49 Status Report, CERN/LHCC 2000-03; D.C. Christian et al., *Nucl. Instrum. Meth.* A473 (2001) 152.
- [5] M.R. Coluccia et al., IV and CV curves for irradiated prototype BTeV silicon pixel sensors, FERMILAB-Conf-02/148E; M.R. Coluccia et al., Characterization of prototype BTeV silicon pixel sensors before and after irradiation, FERMILAB-Conf-01/344E.
- [6] G. Chiodini et al., Radiation tolerance of prototype BTeV pixel detector readout chips, FERMILAB-Conf-02/147E.
- [7] G. Chiodini et al., Single event effects in the pixel readout chip for BTeV, FERMILAB-Conf-01/369E.
- [8] ATLAS Pixel Detector Technical Design Report, CERN/LHCC 98-13.
- [9] D.C. Christian et al., Development of a pixel readout chip for BTeV, *Nucl. Instru. Meth.* A435 (1999), 144.
- [10] J. Hoff et al., PreFPIX2: Core Architecture and Results, FERMILAB-Conf-00/260E.
- [11] S. Cihangir et al., Characterization of indium and solder bump bonding for pixel detectors, *Nucl. Instru. Meth.* A476 (2002), 670.
- [12] S. Kwan et al., A Study of Thermal Cycling and Radiation Effects on Indium and Solder Bump Bonds, FERMILAB-Conf-01/377E.
- [13] S. Cihangir et al., Study of Bump Bonding Technology, FERMILAB-Conf-03/310E.
- [14] S. Zimmermann et al., Development of high data readout rate pixel module and detector hybridization at Fermilab, *Nucl. Instru. Meth.* A465 (2001), 224.

- [15] S. Zimmermann et al., Development of a High Density Pixel Multichip Module at Fermilab, FERMILAB-Conf-01/247E. et al.
- [16] V. Shiltsev et al., BTeV IP Review Closeout Report.
- [17] A. Burov, BTeV Impedances.
- [18] M. Caponero et al., Use of Fiber Bragg Grating Sensors for detector position monitoring, BTeV-doc 1297
- [19] M. Caponero et al., Composite Materials for FBG, BTeV-doc 1064.
- [20] C.M.Lei, FEA on cold-finger TPG substrate, BTeV-doc-1416; Update on FEA, BTeV-doc-1431.
- [21] C.M. Lei, Phase 2 detailed FEA on TPG substrate, BTeV-doc 1560; Phase 3 FEA, BTeV-doc-1587.
- [22] C. Kendziora, M. Marinelli, M. Ruschman, and M. Wong, Results of 5% Model of Pixel Detector, BTeV-doc 767.
- [23] B. Hall and M. Turqueti, BTeV Pixel Detector Feed-through Board Specification, BTeV-doc 1730.
- [24] T. Rohe, Comparison of Charge Collection Properties of different p-stop designs, talk presented at the CMS Tracking week, February, 2004.
- [25] R. Klingenberg, private communication.
- [26] C. Kendziora, M. Marinelli, and M. Wong, Vacuum System for Pixel Detector, BTeV-doc 2415; Liquid Helium Cooled Cryopump, BTeV-doc 2511.
- [27] C. Kendziora, M. Marinelli, M. Ruschman, and M. Wong, Loaded Cryopanel test results, BTeV-doc-2374.
- [28] J. Howell, C. Kendziora, CM Lei, M. Marinelli, Z. Tang, and M. Wong, Status of the Substrate Temperature Control System, BTeV-doc-2880.
- [29] Preliminary Risk Analysis of the BTeV Pixel Detector Operation, G. Jackson, S. Kwan, M. Marinelli, and M. Wong, BTeV-doc 2039.
- [30] J.N. Butler, Risk Analysis and Mitigation Procedures, BTeV-doc 1112.

# Chapter 5

## Charged Particle Identification System

### 5.1 Introduction

Charged particle identification is an absolute requirement for a modern experiment designed to study the decays of  $b$  and  $c$  quarks. The forward geometry is well suited for a Ring Imaging Cherenkov detector (RICH), that provides powerful particle ID capabilities over a broad range of momentum. Even with the excellent mass resolution of BTeV, there are kinematic regions where signals from one final state will overlap those of another final state. For example,  $B_s \rightarrow D_s K^-$  signal must be distinguished from  $B_s \rightarrow D_s \pi^-$  background in order to measure the CKM phase  $\gamma$ . These ambiguities can be eliminated almost entirely by an effective particle identifier. In addition, many physics investigations involving neutral  $B$ -mesons require “tagging” of the flavor of the signal particle by examining the properties of the “away-side.” Our studies show that kaon tagging is a very effective means of doing this. “Same-side” kaon tagging is also very effective for  $B_s$  mesons.

The RICH detector is located downstream of a 1.6T dipole magnet surrounding the interaction region. It consists of two independent systems. The main system has a 3 m long  $C_4F_8O$  gas volume. Charged particles radiate Cherenkov light in this medium. The light is focused with a segmented mirror onto an array of photodetectors sensitive to light between 280 – 600 nm. These photodetectors can either be multi-anode photomultiplier tubes (MAPMT) or hybrid photodiodes (HPD). The MAPMT is a square device approximately 1” on a side with 16 channels, while the HPD is circular in cross-section with a diameter of about 6.8”. All costing is done assuming MAPMTs that have recently been upgraded. HPDs provide a competitive alternative. Both systems yield about the same number of Cherenkov photons, but currently the MAPMTs are less expensive due to changes in the exchange rates over the last year, and are easier to operate. Therefore we have adopted the MAPMT based system for our baseline.

The second system, used mainly for separating kaons and protons below 10 GeV/c, consists of a liquid  $C_5F_{12}$  radiator, approximately 1 cm thick, placed in front of the gas

volume. Cherenkov photons generated in this medium exit the sides of the gas tank and are detected in an array of 3" diameter photomultiplier tubes. The liquid is contained by the front face of the RICH tank and a 3 mm thick quartz window. There is a 40 cm<sup>2</sup> hole around the beam pipe to avoid radiation from fast particles.

## 5.2 Requirements

### 5.2.1 Physics Requirements

The following requirements describe the RICH detector performance goals dictated by the physics goals of BTeV. The momentum range over which excellent hadron identification is required is between 3 and 70 GeV/c. The low momentum hadron identification optimizes flavor tagging, whereas the high momentum range will enable us to separate  $\pi$ 's and K's from two body B-meson decays. Excellent identification should be provided in the full BTeV solid angle (10-300 mrad). Besides providing excellent hadron identification, the RICH detector is also an integral part of the lepton identification system in the solid angle between 200 and 300 mrad. It is the only detector element available to distinguish  $e$ ,  $\mu$  and hadron species, as the muon detector and the electromagnetic calorimeter have smaller solid angle coverage.

#### 5.2.1.1 Cherenkov Angular Resolution per Track

The separation of charged hadrons into different species will be accomplished in the data analysis by characterizing each charged track with a set of probabilities for being an electron, muon, pion, kaon, or proton. From a knowledge of the distribution of Cherenkov angular resolutions per track such probabilities can be derived.

It has proven useful to specify RICH detectors by their average Cherenkov resolution per track, and we shall do so here. For example, the difference in emission angle of Cherenkov photons from pions and kaons at 70 GeV/c (the upper range for which we require excellent particle identification performance) is 0.44 mrad, so achieving a resolution per track of 0.11 mrad would give a separation of 4 standard deviations. Separation improves dramatically as momentum decreases. Furthermore, the average Cherenkov resolution per track can be understood in terms of the average Cherenkov resolution per photon and the number of photons. A separation of at least  $4\sigma$  for  $\pi$ ,  $K$  and  $p$  in the momentum range of 3-70 GeV/c (or from their Cherenkov photon threshold to 70 GeV/c) is required.

#### • Requirements for Gaseous RICH

- **Average Cherenkov Resolution per Track:** The average Cherenkov angle resolution per track shall be better than 0.12 mrad. This requirement may be met with the following set of parameters:
  - \* The distribution of Cherenkov photons about the correct Cherenkov angle should have an r.m.s. deviation of no more than 0.85 mrad.



- \* The number of Cherenkov photons per track should average at least 50 for tracks in the plateau region.

- **Requirements for Liquid RICH**

- **Average Cherenkov Resolution per Track:** The average Cherenkov angle resolution per track shall be better than 1.9 mrad. This requirement may be met with the following set of parameters:
  - \* The distribution of Cherenkov photons about the correct Cherenkov angle should have an r.m.s. deviation of no more than 6.5 mrad.
  - \* The number of Cherenkov photons per track should average at least 12 in the plateau region.

## 5.2.2 Radiation hardness

The highest radiation in the RICH detector occurs at the entrance and exit windows. Fortunately these are not active components. The MAPMT array is shielded by the magnet and only  $\sim 20\%$  of the photomultiplier tubes in the liquid system see any significant radiation. These are in a narrow cone at the top and bottom of the detector where the magnetic field sweeps slower charged particles. The window containing the liquid is made of quartz, a radiation hard material and doesn't exist in the highest radiation area due to the hole near the beam.

## 5.2.3 Geometrical Requirements

- **Size of RICH Detector:** The RICH detector must subtend at least  $\pm 300$  mrad both horizontally and vertically with respect to the beam axis.
- **Alignment:** The RICH system must be mechanically stable. The mirrors must be aligned so the aberration does not degrade the resolution. Furthermore, the MAPMT position with respect to the mirror focus must be determined to better than  $1/10$  of the MAPMT pixel width.
- **Thickness:** The RICH detector must be of minimal material thickness. The total number of radiation lengths allowed less than 20% of a radiation length.

## 5.2.4 Mirror Requirements

The RICH-mirror system should be designed so that its effect on the total Cherenkov angle resolution per track is not significantly increased for reasons stated in Section 5.2.1. The mirror system consists of segmented mirrors put together to form two big mirrors, each one having a mean radius of curvature  $R_{mean} = 697$  cm and an aperture of 220 cm x 440 cm. One of them will be positioned in the positive  $x$ -direction and tilted by 261 mrad clockwise

and the other one will be positioned in the negative  $x$ -direction and tilted by 261 mrad counter-clockwise. The mirror system requirement can be divided into three categories, namely:

- **Material requirement:** We require the radiation length to be  $< 2\%$  at normal incidence to the mirror. A protective coating for the mirror is also required. This coating should have 99 % transmission at 280 nm.
- **Geometrical requirement:** The mean radius of all mirror tiles must lie within  $697 \pm 3$  cm. The maximum shift of any tile from the mean is allowed to be  $\pm 3$  cm. The surface smoothness must be less than 2.8 nm.
- **Optical requirement:** We define a quantity called spot-size which is the diameter of the circle where 95% of the light reflected from the entire mirror is focused. From simulation, we determine that the spot-size must be less than 2.5 mm.
- **Reflectivity:** The mirror must reflect 90% of the light averaged over the entire surface for wavelengths larger than 280 nm.

### 5.2.5 Electronics Requirements

The baseline photosensitive device MAPMT associated with the gas RICH poses stringent requirements on the electronics in terms of the data rate and throughput at least in the highest occupancy region. The backup HPD system also depends critically on low noise. The expected signal level in the MAPMT's has an approximately flat distribution from threshold up to about  $10^6$  electrons, while the expected signal level from the HPDs is about 5,000 electrons. Thus, we require very low noise front-end electronics for the HPDs, while for MAPMTs, an increase in noise will just reduce somewhat the level of signal photons. Although the average occupancy of the BTeV RICH detector is very small (0.75% hits/pixel), in the hottest MAPMT the number of hits in an event can be as high as 9, with 11% of the events having more than 4 hits per tube, according to a Monte Carlo simulation based on an average of 6 interactions per crossing.

- **Noise of the front end:** The equivalent noise charge of the front end electronics when connected to the MAPMT will be less than or equal to 1000  $e^-$ , or 500  $e^-$  if the backup HPD system is used.
- **Speed:** The analog signal should have a peaking time of about 75 ns and a fall time (10 % of the peak) of 200 ns.
- **Event rate:** All the building blocks of the front end electronics (preamplifier and shaper, gain stage, discriminator, digital architecture) need to be able to process event at a rate of 7.5 MHz without degradation of the performance.

- **Data rate:** The front end electronics will provide digital information of the MAPMT pads hit by a photoelectron within the beam crossing when the event was originated.
- **Threshold uniformity:** Each front end electronics ASIC will have a global threshold, settable by an external DAC that spans the whole dynamic range of the chip (0-6000  $e^-$ ). Moreover a fine tuning of the individual channel threshold will be built within the chip. This fine tuning needs to maintain the threshold dispersion below 200  $e^-$  per chip.
- **Masking out bad channels:** It should be possible to mask out bad channels by digital control.
- **Electronics calibration:** It is necessary to be able to inject a calibration charge on each individual channel to characterize the ASIC performance with the expected signal level.
- **Chip initialization and readback of the downloaded information:** The mode of operation of the chip (calibration/data taking, individual thresholds, active channel mask) needs to be initialized with a serial bit pattern. The downloaded information needs to be available to be read back for diagnostic purposes.
- The hybrids need to have a dead channel count below 1% (at most 1 dead channel per hybrid).

### 5.2.6 Readout Requirements

The success of the experiment relies critically on the quality of the data provided to the data acquisition system.

- **Data Sparsification:** The data output from the detector includes only those cells that are above a settable threshold.
- **RICH output data content:** The hit data must include the beam crossing number, chip identification number, and the addresses of all hit pixels for that beam crossing.
- **Data Rate:** The noise level should be such that the maximum data rate should not exceed an average of 4% of the  $\sim 154,000$  channels.
- **Readout Abort:** The system must have a means of recognizing and aborting the readout of any chip that has an unusually high volume of data output (*e.g.* all the channels lit up).
- **Remote programming of local FPGA's:** All the FPGA's located in the front end devices must be remotely re-programmable from the slow control lines if necessary.

### 5.2.7 Electrical and magnetic interference

The readout chip must be shielded electronically from external noise (MAPMT HV, sensor bias ... ). Common mode noise arising from the experimental environment should be kept well below the intrinsic noise performance of the front end electronics. Adequate shielding of the analog front end should be part of the final packaging of the devices.

### 5.2.8 Mechanical Properties of the front end hybrids

For the baseline MAPMT system, the 128 channel hybrids must fit within the profile of the 8 tubes (4x2 array) that they are connected to. For the backup HPD system, the front end hybrid should be composed of a rigid component (hyb-A) hosting the analog front end devices, connected via a flex portion (flex) to a rigid component including the logic periphery (hyb-B).

- **Mechanical clearance of hyb-A:** In the case of the HPD, the component hyb-A must be small enough to fit inside the mu-metal shield surrounding the HPD and have holes in locations specified in accordance with the overall HPD support structure.
- **flex mechanical properties:** In the case of the HPD, the flex component of the hybrid must maintain signal line integrity upon the tight bend required to fit into the HPD mechanical structure.

### 5.2.9 Cooling System

Both the gas and liquid system will require active cooling. In the gas RICH, the baseline MAPMT system we need to cool both the readout chips and the bases. For the backup HPD system, the heat load is dominated by the readout chips. The liquid RICH will also require cooling of the bases and the readout chips.

### 5.2.10 Gas and Liquid Systems

The gas and liquid systems both recirculate their respective fluids. Since neither system operates below 280 nm, purity is not an issue in terms of the photon yield. However, the changes induced by impurities to the index of refraction can be a problem, thus we specify that the purity is monitored in both systems. Moreover both systems are cleaned with appropriate techniques to maintain the purity specified below.

- **Gas System Purity:** The  $C_4F_8O$  system shall recirculate gas. By means of standard filtering techniques, the gas purity shall be maintained at better than 99%.
- **Liquid System Purity:** The  $C_5F_{12}$  system shall recirculate liquid. By means of standard filtering techniques, the purity shall be maintained at better than 99%.

- **Gas System for HPD:** The HPD array shall be provided a separate gas system that is resistant to electrical breakdown, necessary because of the 20 kV required by the HPD's. This gas may be sulphur-hexafluoride. This is not required for the baseline MAPMT system.

### 5.2.11 Power Supplies

The MAPMTs are run close to 900 V. There are 3 separate high voltages to be supplied to the HPD's: 20 kV, 19.89 kV, and 15.6 kV. In addition there is a low voltage of  $\sim 60$  V supplied to the silicon sensor inside the HPD. The PMTs system requires 1000 V.

- **Ripple:** The high voltage supplied to the MAPMT must have a ripple on the voltage low enough not to increase the gain variation by more than 25% or the electronic noise by more than 10%.

All high voltages to the HPD must have a ripple on the voltage sufficiently small over the entire frequency range so not to increase the electronic noise by more than 5%. This may be accomplished by either using a very low ripple power supply, or by using an RC filter close to the detector.

- **Voltage reference/grounding:** All low and high voltage power supplies will be floating. Each RICH photosensitive element assembly will have one well-defined local ground and defined isolation (resistive and/or capacitive) from other grounds. The design must take safety of equipment and personnel as well as ground loop avoidance and other noise prevention into consideration.

### 5.2.12 Monitoring

#### Monitoring of the RICH

To check the performance and the safe operation of the RICH System, we need to monitor several items:

- **Temperature & Humidity Monitoring:** The RICH monitoring system should check temperature at  $\sim 16$  individual points in the gas, and in the liquid. We will also monitor the temperature in the collision hall. Each hybrid will be monitored by a thermistor. The humidity in the HPD array must be measured and kept below 5% to avoid corona discharge. For the baseline MAPMT system, the humidity should be kept below 40%.
- **High Voltage & Low Voltage Monitoring:** All voltages and currents must be read back from the detectors and their values displayed. All currents must also be monitored.

- **Alarms:** Appropriate limits should be set on the parameters that are being monitored and an alarm will be issued if these limits are exceeded. In some cases, the alarm should automatically start a turn-off sequence to prevent any major damage to the system. In other cases, it will provide a warning.

### 5.2.13 Electrical Requirements

The hardware that is designed and built, or purchased to implement the RICH system will consist of digital electronics. This hardware must comply with the *BTeV Digital Electronics Standards* document. This document contains requirements, standards, and recommendations that apply to all digital electronics in BTeV. The subjects that are addressed in the document include interfaces, grounding, EMI, shielding, infrastructure, safety, reliability, and maintainability.

### 5.2.14 Electronics Protection

BTeV will have a committee to review component electronics protection proposals. BTeV management will provide documents defining acceptable electronics protection procedures. The RICH System should observe all safety rules and regulations as detailed in the BTeV Safety Requirement Document. A series of interlocks and alarms should be in place.

### 5.2.15 Functional Requirements

In order to fully exploit the photodetector capabilities and achieve the required resolution on the Cherenkov ring, the mirror panels need to be carefully aligned with respect to each other and with respect to the MAPMT planes.

- **Mirror Alignment:** The mirror panels will be aligned in the experimental hall with accuracy consistent with the geometrical requirements described in Section 5.5.4.
- **MAPMT Alignment:** The MAPMT position in the detector will be aligned with respect to the mirror surface with accuracy consistent with the geometrical requirements described in Section 5.5.4.
- **Access:** It should be possible to access individual MAPMT (or HPD) modules, PMT modules and Mirror panels for adjustment or repair.

### 5.2.16 Requirements on Rest of BTeV

- **Stray Magnetic fields:** The magnetic field in the region of the MAPMT and PMT arrays must be enclosed in a shield adequate to keep the magnetic field below 10 Gauss, without individual shielding of the devices. (Mu-metal shields then will reduce the field below our level of sensitivity).

- **Beryllium Beam Pipe:** The beam pipe between the magnet and the end of the RICH detector needs to be made of thin Beryllium to minimize the radiation lengths in order to keep the backgrounds at an acceptable level.
- **Tracking:** Tracking must be provided before and after the RICH detector. The current requirements for the Straw and Silicon systems are adequate for our purposes.
- **Operating Temperature:** The operating temperature of the detector must be kept below 28°C, otherwise the liquid radiator will become gaseous. The temperature variation should be kept within  $\pm 2$  °C. The temperature need not be uniform across the entire detector.

## 5.3 Technical Description

The RICH detector consists of two separate subsystems that share the same space along the beam line, as shown in Fig. 5.1. The main system consists of a 3 m long  $C_4F_8O$  gas radiator, a focusing mirror and a photon detector consisting of arrays of multi-anode photomultipliers (MAMPT) or hybrid photo-diodes (HPD) that have pixilated elements approximately 6 mm x 6 mm in size. An example of simulated Cherenkov rings detected in the gaseous RICH is shown in Fig. 5.2. The second system consists of a 1 cm thick  $C_5F_{12}$  liquid radiator and an array of standard 3" photomultiplier tubes placed on the sides of the gas radiator tank. Cherenkov rings created in the liquid radiator are directly projected onto the photomultiplier arrays (so called "proximity focusing"). An example of simulated Cherenkov rings detected in the liquid radiator RICH is shown in Fig. 5.3. In this section we discuss the motivation for the technology choices and then we describe each of the major components of the RICH.

### 5.3.1 Selection of RICH Radiators

Because of the large particle momenta there is really only one choice of detector technology: a gaseous ring-imaging Cherenkov detector. Pions and kaons can be separated in the required momentum region with a single gas radiator (see Fig. 5.4). Initially we chose  $C_4F_{10}$  (the heaviest RTP gas) and assumed an index of refraction of approximately 1.00138 in the visible range [5]. This gas has been used by DELPHI (endcap) [1], HERA-B [2] and HERMES [3]. It was also the choice for one of the LHCb RICH detectors [4].

Unfortunately, the main manufacturer of  $C_4F_{10}$ , the 3M company, recently stopped producing this gas. Although still available, the price has risen by a factor of five and we do not believe that the source is stable. To determine a replacement we needed to measure the refractive index of different gases to determine if they were suitable. Fig. 5.5 shows our measurements of refractive indices as a function of wavelength for three different gases, the original  $C_4F_{10}$ ,  $C_4F_8O$  and  $C_4F_8$ . The measurements were obtained with light interference technique. The curve is the one we have been using in our simulations; it is contained in a HERAb thesis and appears to be an extrapolation of DELPHI measurements that were done

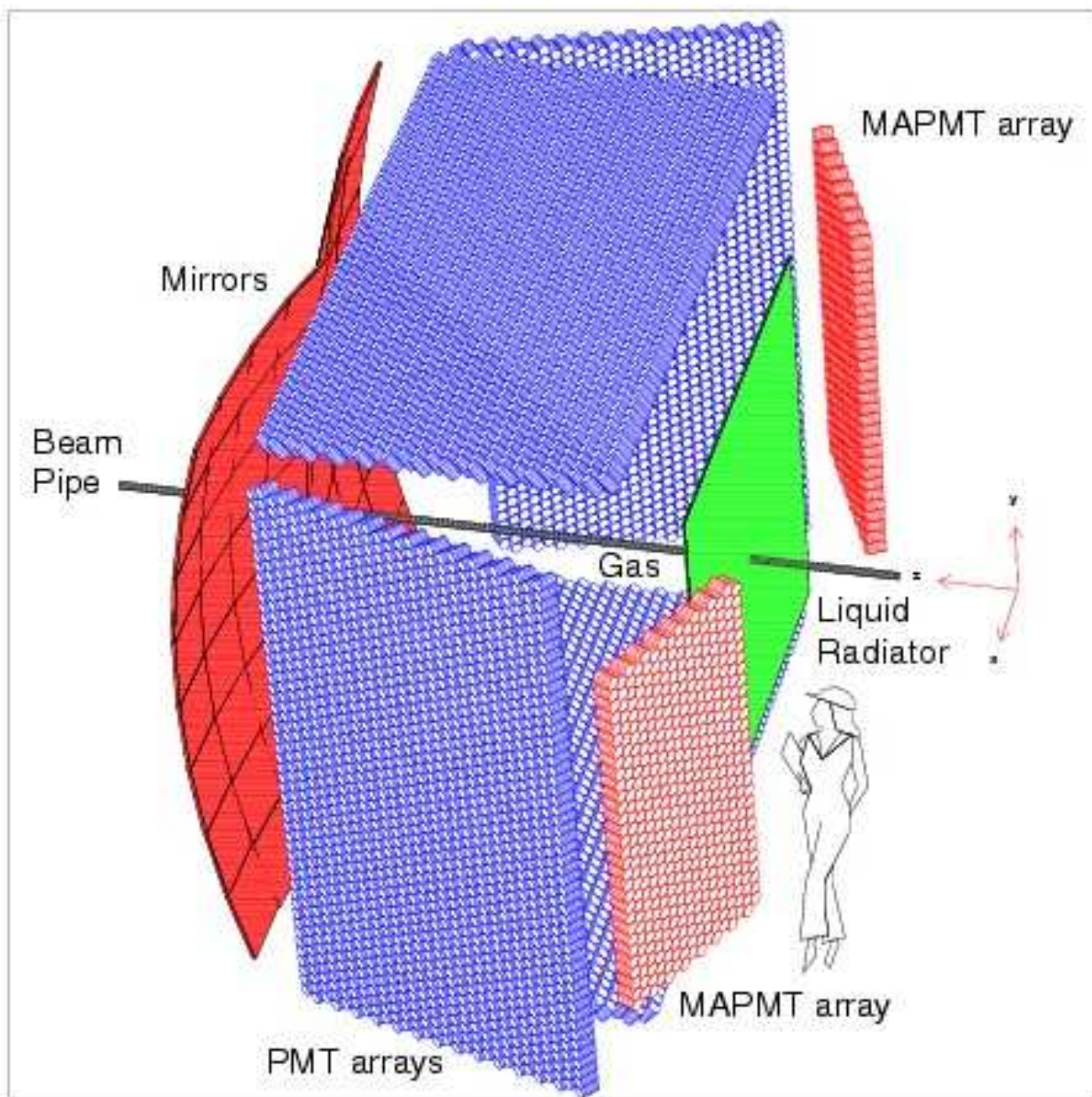


Figure 5.1: Outline of the important RICH components.



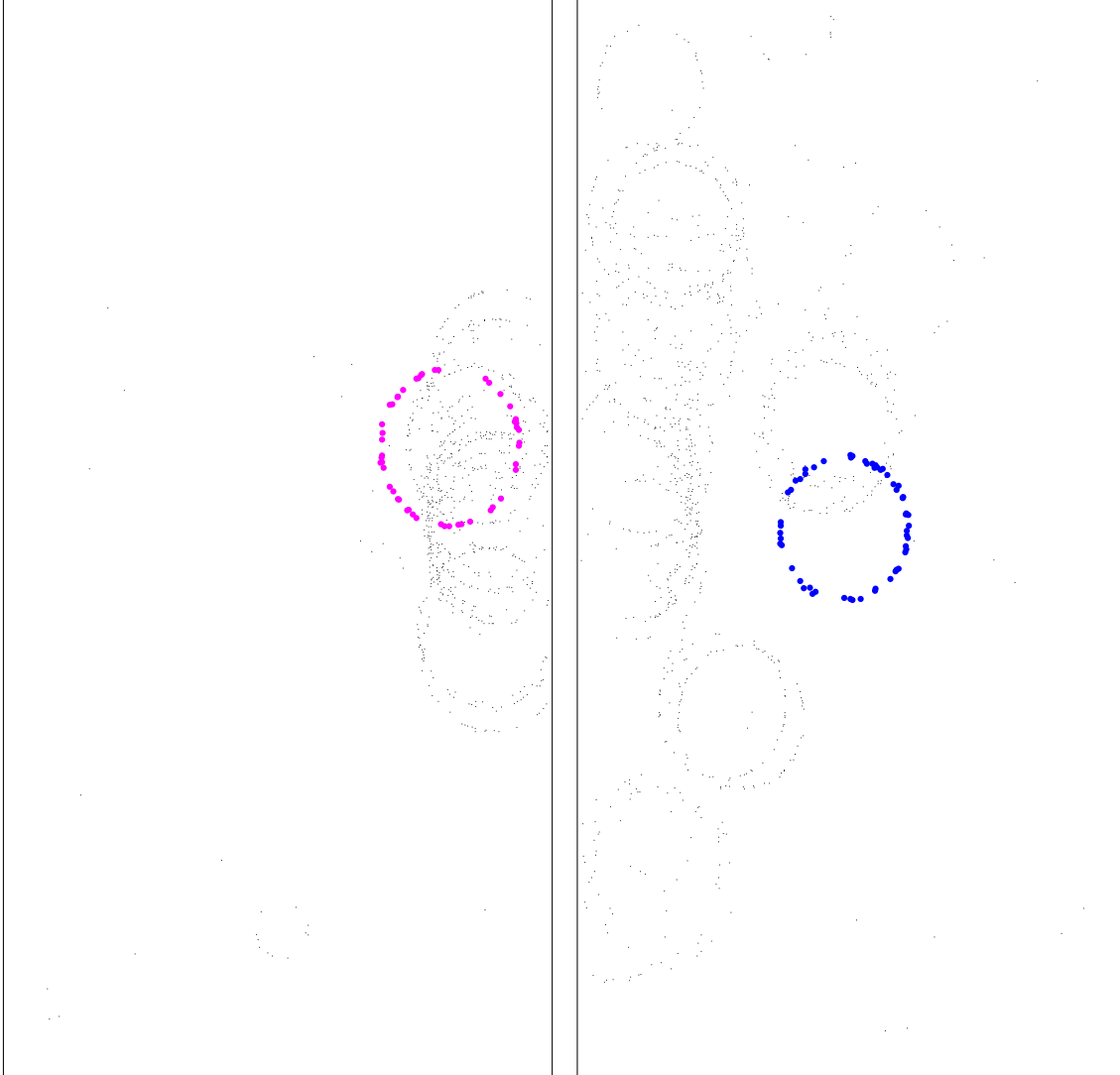


Figure 5.2: Cherenkov rings from the gas radiator detected in the MAPMT arrays as simulated for a  $B \rightarrow \pi^+\pi^-$  event with two minimum bias interactions in the same bunch crossing. The Cherenkov hits for the pions from the  $B$  decay are highlighted.

in the UV. Fortunately the  $\text{C}_4\text{F}_8\text{O}$  falls right on the curve and use of this gas will therefore provide identical performance to that of the initially simulated  $\text{C}_4\text{F}_{10}$ . The 3M company produces  $\text{C}_4\text{F}_8\text{O}$  and has told us that there are no plans to discontinue its production. We also note that using  $\text{C}_4\text{F}_8$  would only marginally change the physics performance, by reducing the high momentum particle separation between kaons and pions, for example, by  $\sim 1$  GeV/c. Recently, we tested  $\text{C}_4\text{F}_8\text{O}$  in the test beam of the RICH prototype (Section 5.4.1.5) and confirmed its suitability.

Below  $\sim 9$  GeV, no gas can provide  $K/p$  separation since, for these momenta, both  $K$  and  $p$  are below radiation threshold. In this case, the RICH operates in a threshold mode for ( $K$  or  $p$ ) vs.  $\pi$  separation (except that it has much better noise discrimination than a normal

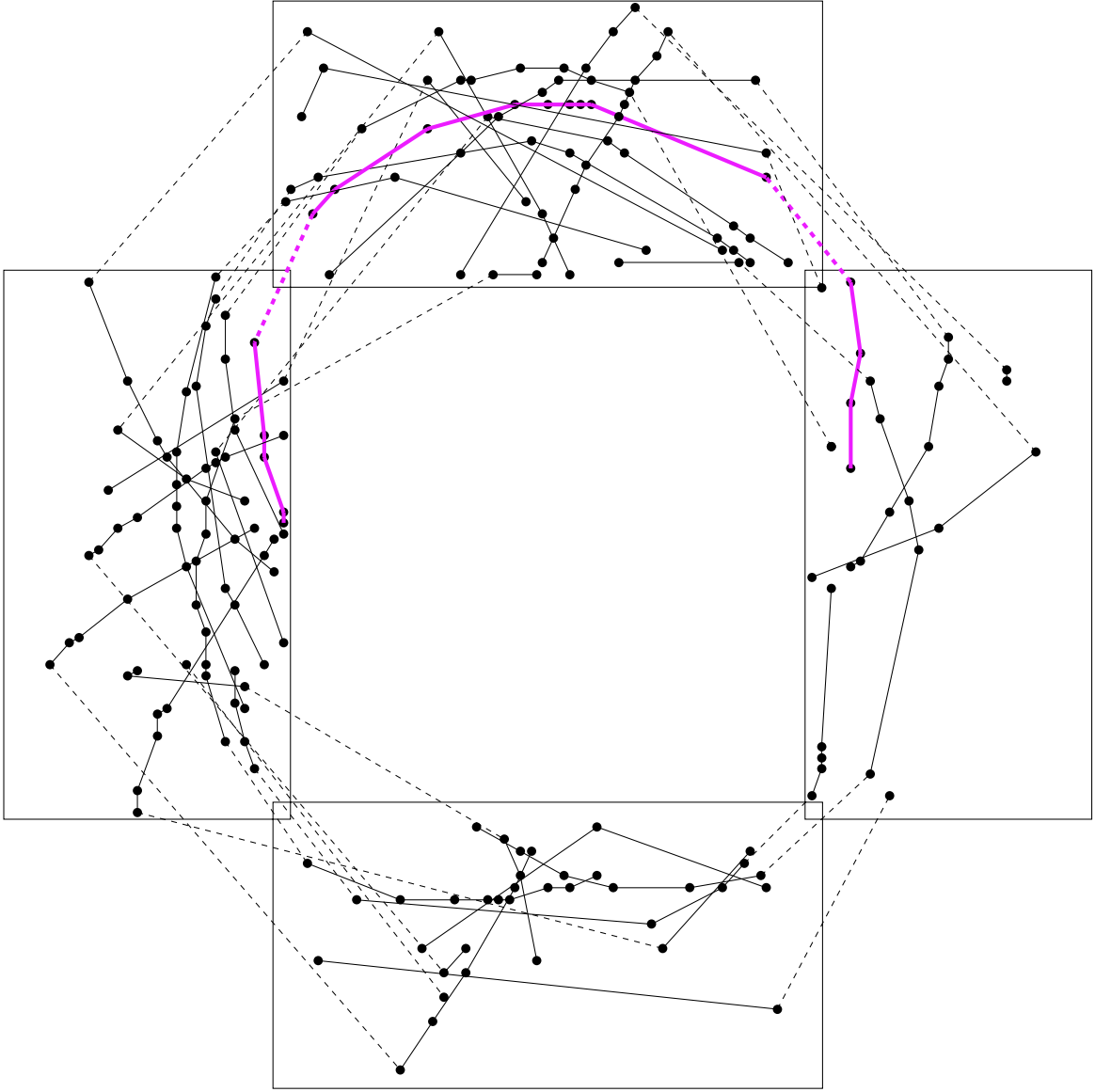


Figure 5.3: Cherenkov rings from the liquid radiator detected in the PMT arrays as simulated for a kaon tagged  $B$  event with two minimum bias interactions in the same bunch crossing. Hits belonging to the same track are connected. The Cherenkov hits for the tagging kaon are connected by a thick line.

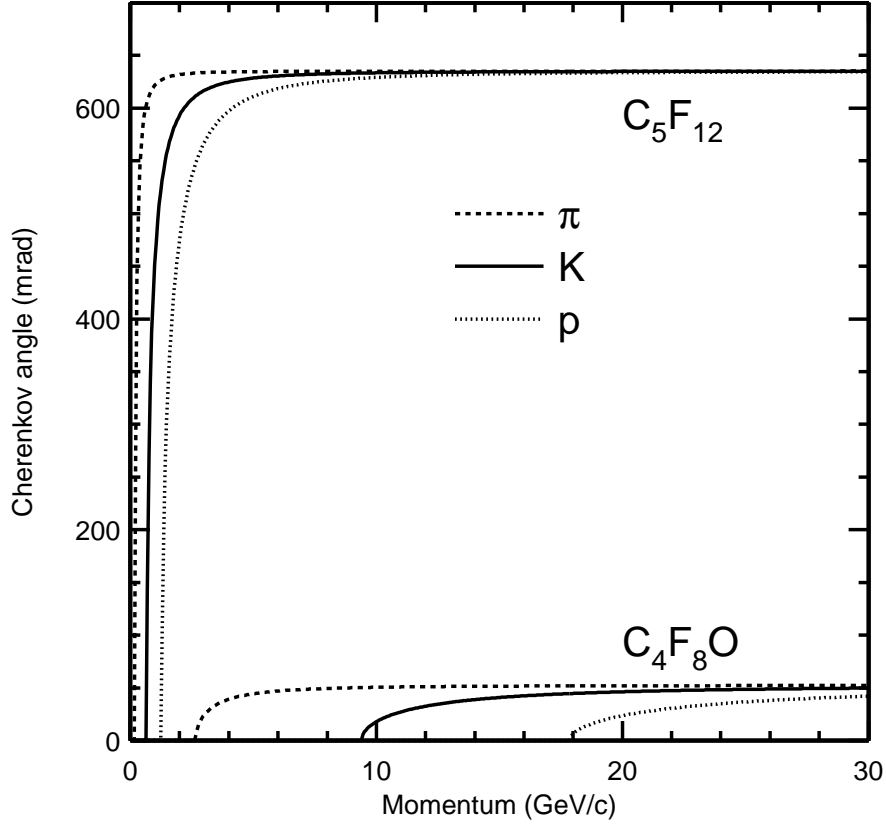


Figure 5.4: Cherenkov angles for various particle species as a function of particle momentum for  $C_4F_8O$  ( $n = 1.00138$ ) and liquid  $C_5F_{12}$  ( $n = 1.24$ ) radiators.

threshold counter because it still measures a Cherenkov ring for pions). Separation of kaons from protons turns out to be important for  $b$ -flavor tagging. In the case of the  $B_s^0$ , we use a positively identified kaon for both “same side” and “away-side” tagging. For the  $B_d$ , only the “away-side” case requires kaons. In the “same side” tag, there is a strong correlation between the sign of the fragmentation kaon and the flavor of the  $B_s$ . However, the tagging fragmentation kaon comes from the primary vertex which also contains many protons that can cause false tags. In “away-side” tagging, the lack of  $K/p$  separation prevents one from distinguishing kaons from  $p, \bar{p}$ , which occurs  $\sim 8\%$  of the time in  $B$  meson decays. Decays of  $\Lambda_b$  baryons produce  $p, \bar{p} \sim 50\%$  of the time, but their production rate is suppressed relative to  $B$  meson production. These low momentum protons lead to a reduction in the purity of tagged kaons.

Originally we planned to improve identification of low momentum particles by inserting a thin ( $\sim 4$  cm) piece of aerogel ( $n = 1.03$ ) at the entrance to the gas RICH, as proposed by LHCb [6]. The Cherenkov rings were focused by the mirrors of the RICH and were detected

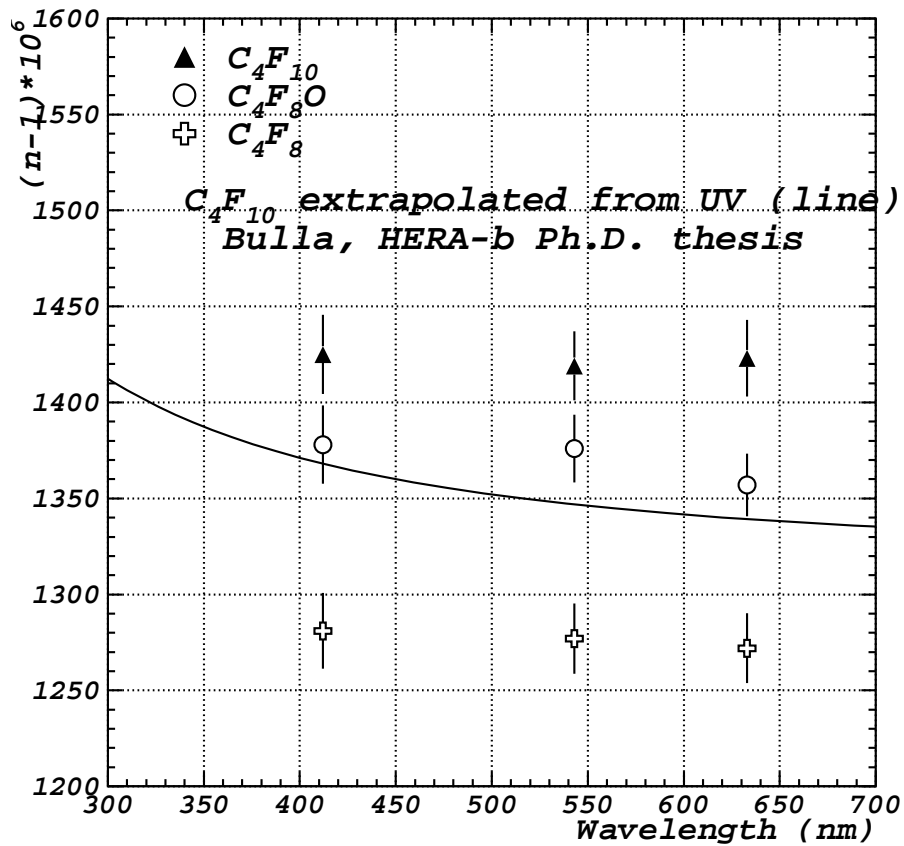


Figure 5.5: Syracuse measurements of refractive indices of various gases as a function of wavelength compared with the curve from HERAb for  $C_4F_{10}$  [5].

using the same photon detector array (somewhat enlarged) as the gas photons. A study using detailed reconstruction of the Cherenkov rings showed that the relatively low light yield from the aerogel, combined with confusion from the larger number of overlapping rings from higher momentum tracks radiating in the gas, resulted in very little particle discrimination.

We now plan to use a liquid  $C_5F_{12}$  radiator which has an index of refraction of 1.24 and produces relatively intense, large radius Cherenkov rings, even with only 1 cm of liquid. The  $C_5F_{12}$  radiator has been successfully used in other experiments (e.g., DELPHI). The rings hit the side walls of the RICH gas containment vessel (see Fig. 5.1), which are instrumented with standard 3 inch photomultiplier tubes. Moreover, the small-angle Cherenkov photons produced in the gas radiator almost always intercept the RICH mirror and rarely intercept the side, top, or bottom walls. Thus, the two main limitations of the aerogel scheme, the low amount of Cherenkov light and the confusion between aerogel photons and  $C_4F_8O$  photons, are eliminated. At the same time, the refractive index of  $C_5F_{12}$  is low enough that kaon and proton rings have very different radii, even at 9 GeV, and can be distinguished (Fig. 5.4).

### 5.3.2 Liquid Radiator

A 1-cm thick liquid radiator will be mounted at the entrance to the RICH vessel. The mechanical design of the liquid radiator is shown in Fig. 5.6. The radiator is about 2.5 m  $\times$  2.5 m in size and will cover the entire RICH entrance window. To suppress unwanted Cherenkov radiation in the liquid by higher momentum tracks, a 40 cm  $\times$  40 cm section of the radiator is removed around the beam pipe. The cut-out helps also the gaseous RICH and ECAL since it reduces a number of photon conversions in the high particle flux area. The liquid is contained in a carbon fiber box with a 3-mm thick quartz exit window. We chose quartz for its radiation hardness. To reduce the static head pressure of the liquid on the window, the radiator is segmented vertically into 4 separate volumes (vessels). There are also a number of reinforcement posts distributed throughout the window, with decreasing spacing towards the bottom of each volume. The total amount of material in the liquid radiator, including its support structure, corresponds to 8.7% of a radiation length.

A liquid re-circulation system is used to provide pure thermally-stable liquid  $C_5F_{12}$  to the four liquid radiator vessels. The total system volume is approximately 20 gallons. A particulate filter, pump, and temperature-regulating heat exchanger are used to circulate and condition the fluid. This single circuit (see Fig. 5.7) services all four vessels. A manifold, however, cannot be used to supply the fluid to the vessels since the increased static head on the lower vessels would exceed the critical breaking stress of the quartz window. Therefore, all vessels are connected in parallel via a switching unit. Also, to prevent any additional stress on the quartz, the chambers are open to atmospheric pressure at both the inlet and outlet. The fluid is collected in a reservoir for recirculation. A PLC-based control system regulates the temperature of the reservoir and the flow-rate of the fluid. Temperature control is necessary to avoid evaporation of the liquid ( $T < 28^\circ\text{C}$ ).

### 5.3.3 Gas Radiator

The gas radiator ( $C_4F_8O$ ) fills the entire tank volume and adds 8% to the radiation thickness of the detector. The average Cherenkov radiation path in the gas is about 2.9 m.

The front and rear windows of the tank are made of carbon fiber; 0.05 inches thick at the front (0.6% r.l.) and 0.04 inches thick at the rear (0.5% r.l.). The seal around the beam-pipe is achieved using a polyurethane bellows and a flange for each window (Fig. 5.8).

The radiator gas circulation system is used to provide pure  $C_4F_8O$  gas to the RICH vessel. The total system volume is approximately 2,000 cubic feet. A simplified flow diagram of the system is shown in Fig. 5.9. The major components of the system are a metal bellows pump, a molecular sieve to remove water vapor and particulates, a parallel purification arm to remove nitrogen, oxygen and other gases, and a passive expansion volume to compensate for external atmospheric pressure changes. The purification arm may be switched in as needed, and contains a compression pump that condenses the  $C_4F_8O$  gas to approximately 3 atmospheres. The impurity gases that do not condense are vented through a relief valve which is set at a pressure just above the condensation pressure of  $C_4F_8O$ . The pure liquefied  $C_4F_8O$  is then vaporized and re-enters the system through a regulator valve set just below

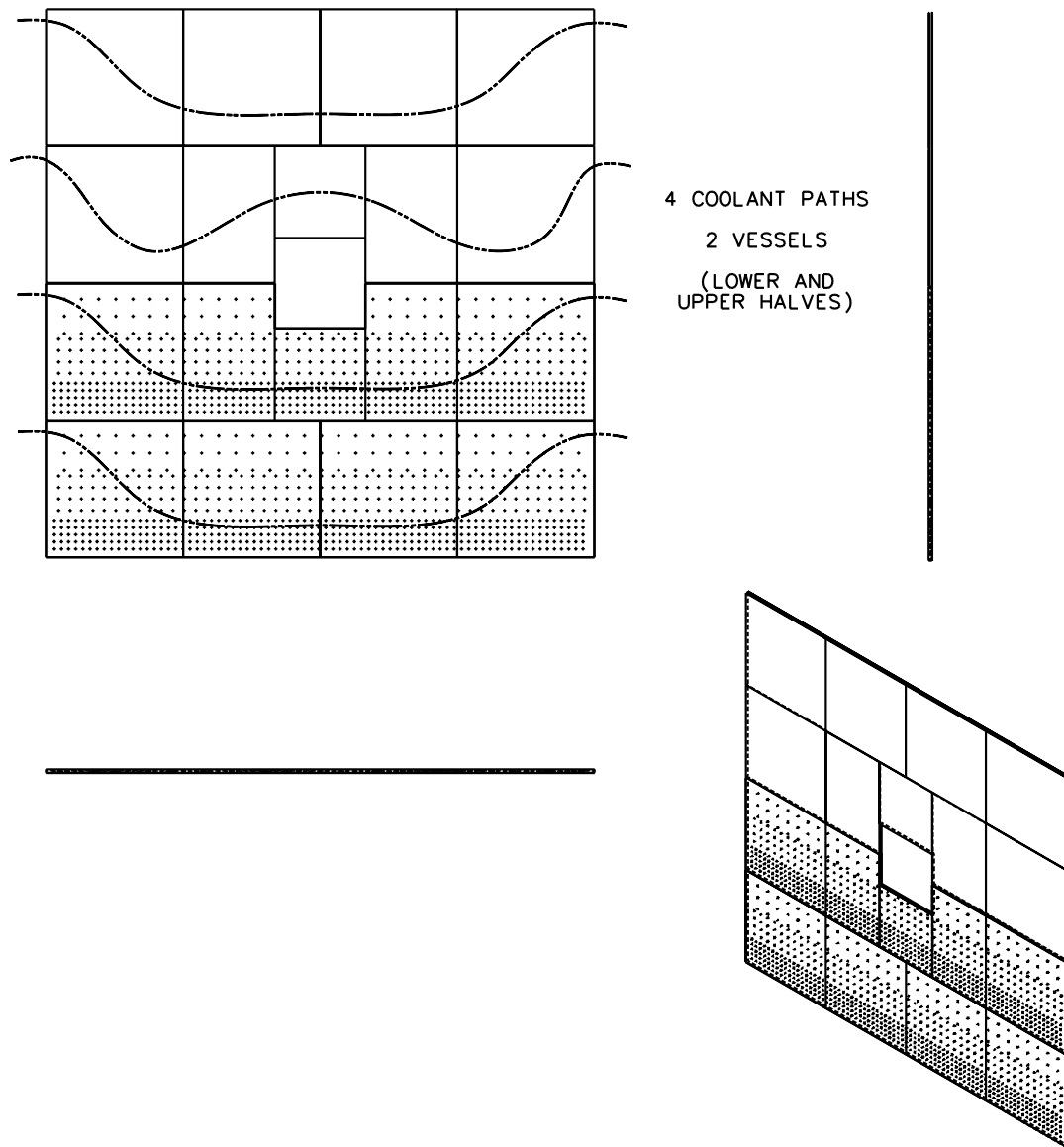


Figure 5.6: Mechanical design of the liquid radiator. The top left figure views the radiator face-on. Side views are also shown. In the figures, the carbon-fiber support posts are only shown on the lower two vessels. The same support scheme will also be used on the upper two vessels.

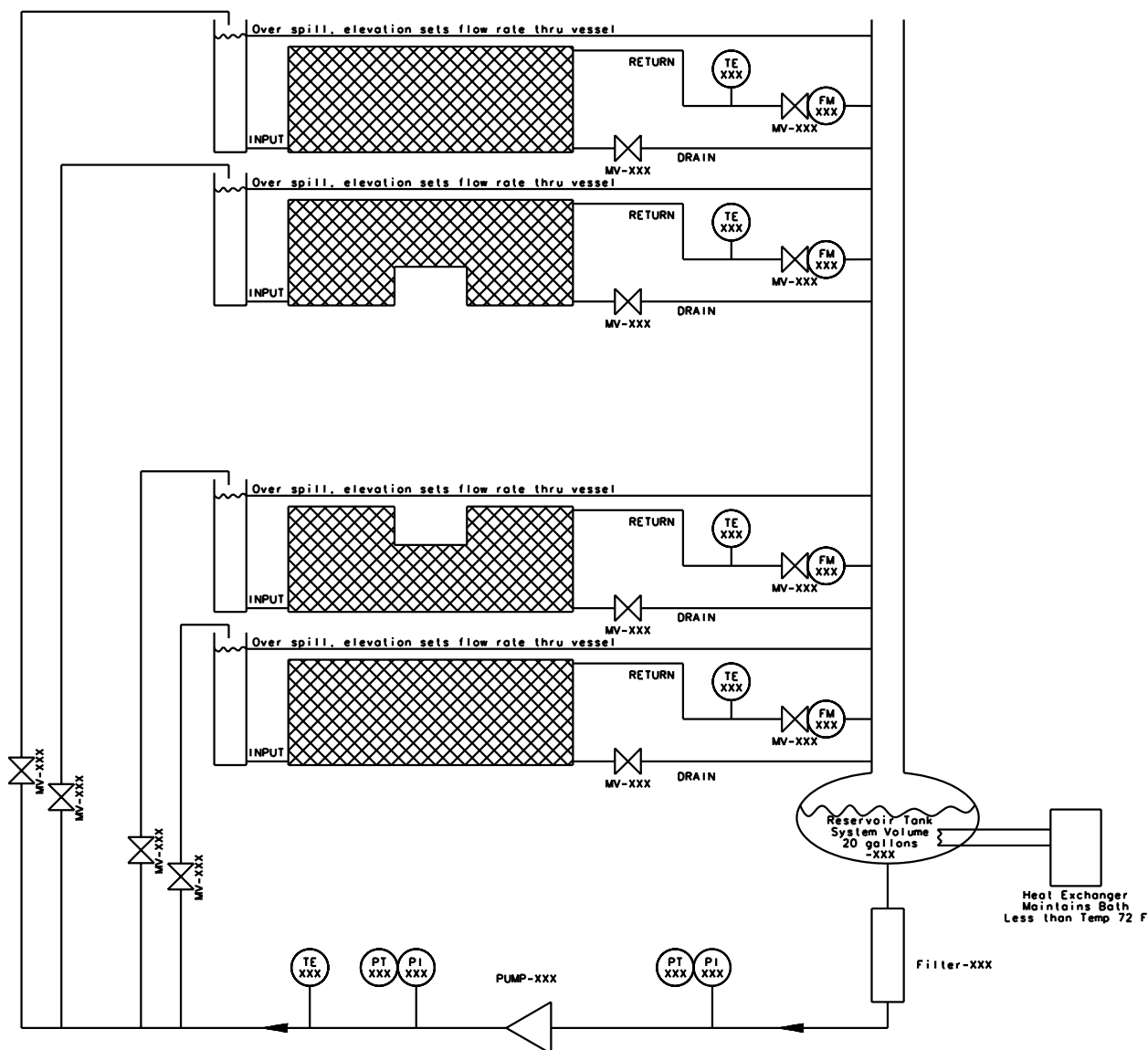


Figure 5.7: Simplified flow diagram of the  $C_5F_{12}$  liquid recirculation system for the RICH.

the gases critical condensation pressure. A PLC-based control system regulates the pumping speeds to maintain an internal vessel pressure equal to atmospheric pressure. The expansion volume is designed to be about 10% of the total gas volume. The concern is that even a small differential between the interior and atmospheric pressures will cause large deflections and stresses in the entrance and exit windows for this heavy gas. Space constraints near the windows prohibit large deflections. A monitoring system will record temperatures and pressures.

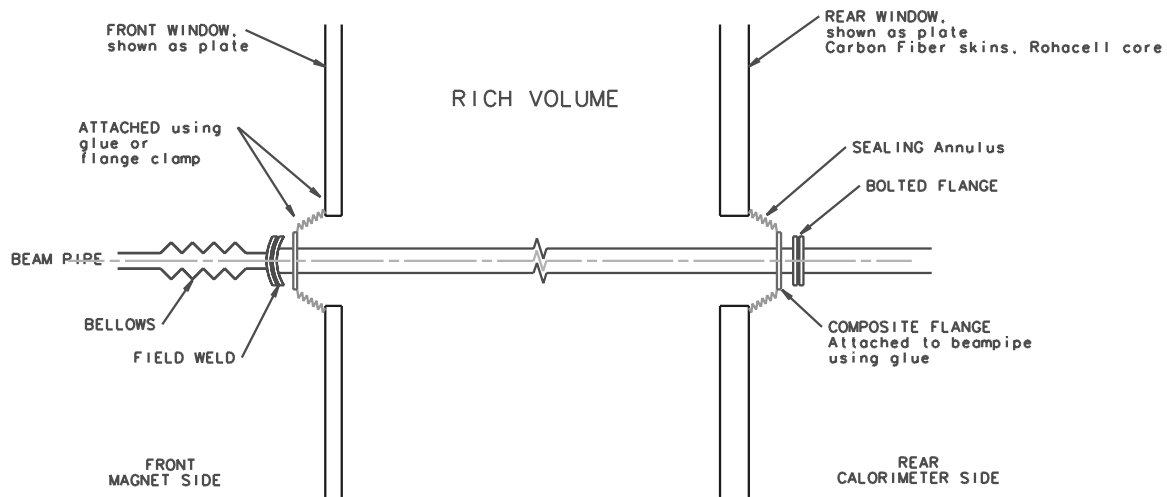


Figure 5.8: Beam-pipe to window seal at the front and rear of the RICH.

### 5.3.4 Mirrors

Spherical mirrors at the end of the gas volume reflect Cherenkov photons radiated in the  $C_4F_8O$  and focus them into rings at the photodetection surface. The mirrors are tilted allowing the photodetectors to be out of the spectrometer acceptance and to be shielded by the magnet. Since the geometric aberrations due to the mirror tilt are significant for the gas radiator, we plan on the longest RICH detector we can accommodate within the space limitations. This also maximizes the photon yield from the gaseous radiator, again improving the resolution of the device.

This mirror system consists of two large mirrors each with a mean radius of  $R_{mean} = 697$  cm, and an aperture of 220 cm x 440 cm. They can be broken down to any number of tiles and shapes to optimize cost and performance. A hole (probably circular in shape) of 3 cm radius is needed in the center of the mirror system to allow the beam pipe to go through, as shown in Fig. 5.10.

Because of the high precision  $PbWO_4$  calorimeter just behind the RICH, we require that the radiation length of the mirror system is less than 2% at normal incidence. This can easily be satisfied if composite mirrors are used.

For performance and cost reasons, it is more practical to handle smaller mirror tiles. Therefore, we divided each of the two big mirrors into arrays of full and half hexagons for an initial design. One possible design is shown in Fig. 5.10. It would consist of 19 full hexagons (64.2 cm side-to-side), 4 half hexagons and 7 hexagons missing one edge-triangle. Once these mirror tiles are produced by the vendor and tested at Syracuse, we will ship them to Fermilab where they will be assembled.

Subsequently we approached different vendors with these preliminary designs. The CMA company of Tuscon, Az has proposed using larger square tiles that has several nice features for us. There design is shown in Fig. 5.11.

In this design there are only 16 mirror for the entire system leading to a much easier task



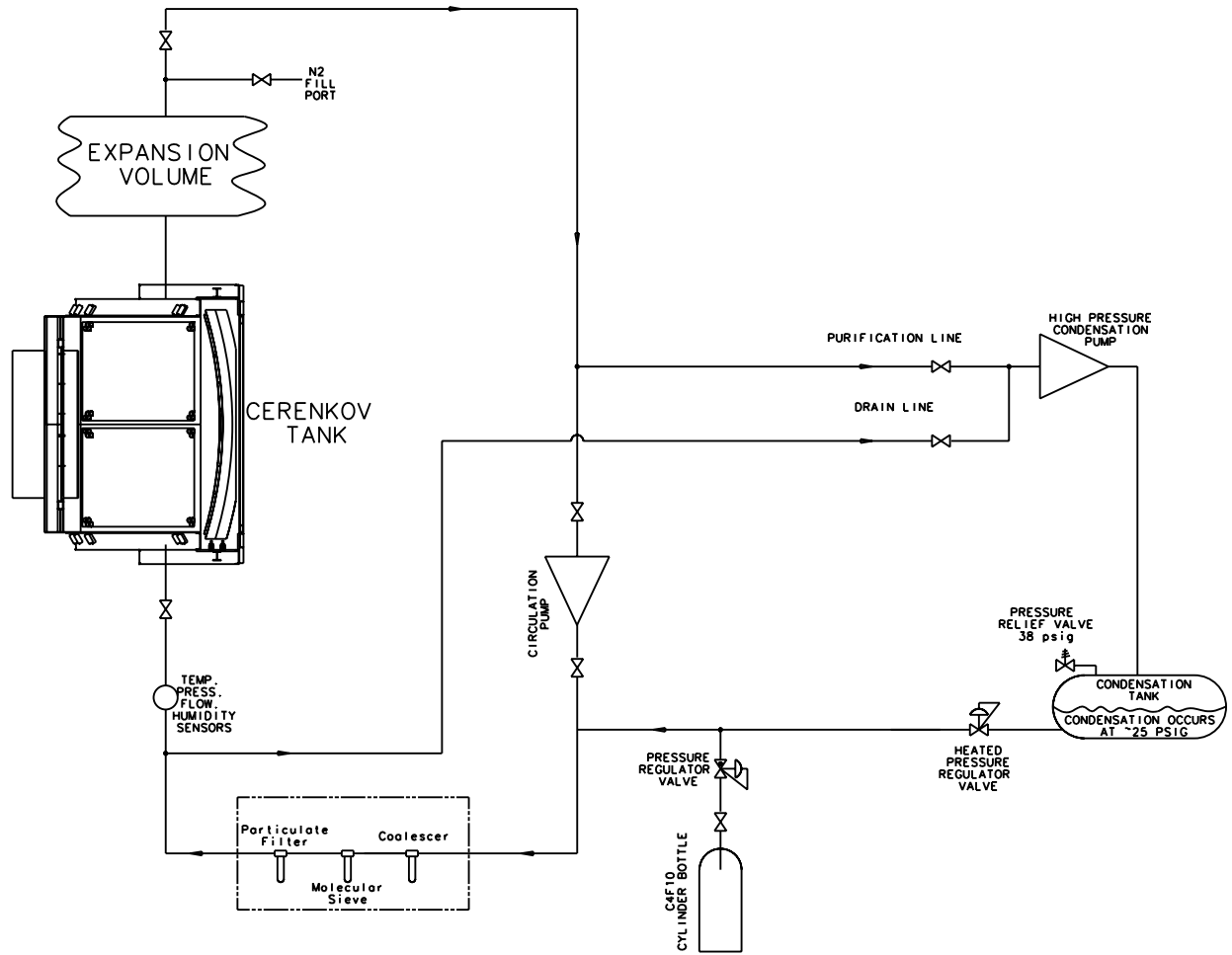


Figure 5.9: Simplified flow diagram of the  $C_4F_8O$  gas recirculation system for the RICH.

of assembling and aligning the segments. These mirrors are made from composite materials and have a thickness  $< 2\%$  r.l. [7].

The mirror support structure, which is integrated with the rear window, is shown in Fig. 5.12. Each mirror tile is supported by a 3-point kinematic mount attached to a large flat support panel, which is made of two carbon fiber skins of each 0.51 mm thick containing between them 7.62 cm of foam. The total radiation length is 2.6%. The size of the support panel is 447 cm x 447 cm made in four strips, one for each vertical column of mirrors. The panels have 48 circular holes with a diameter of 10.16 cm, from which we extend carbon fiber cylinders to the mirror mounts for easy access. These cylinders are attached to bellows which are themselves attached to the rear window. The deflections are computed to be  $\sim 0.4$  mm when the tank is filled with gas.

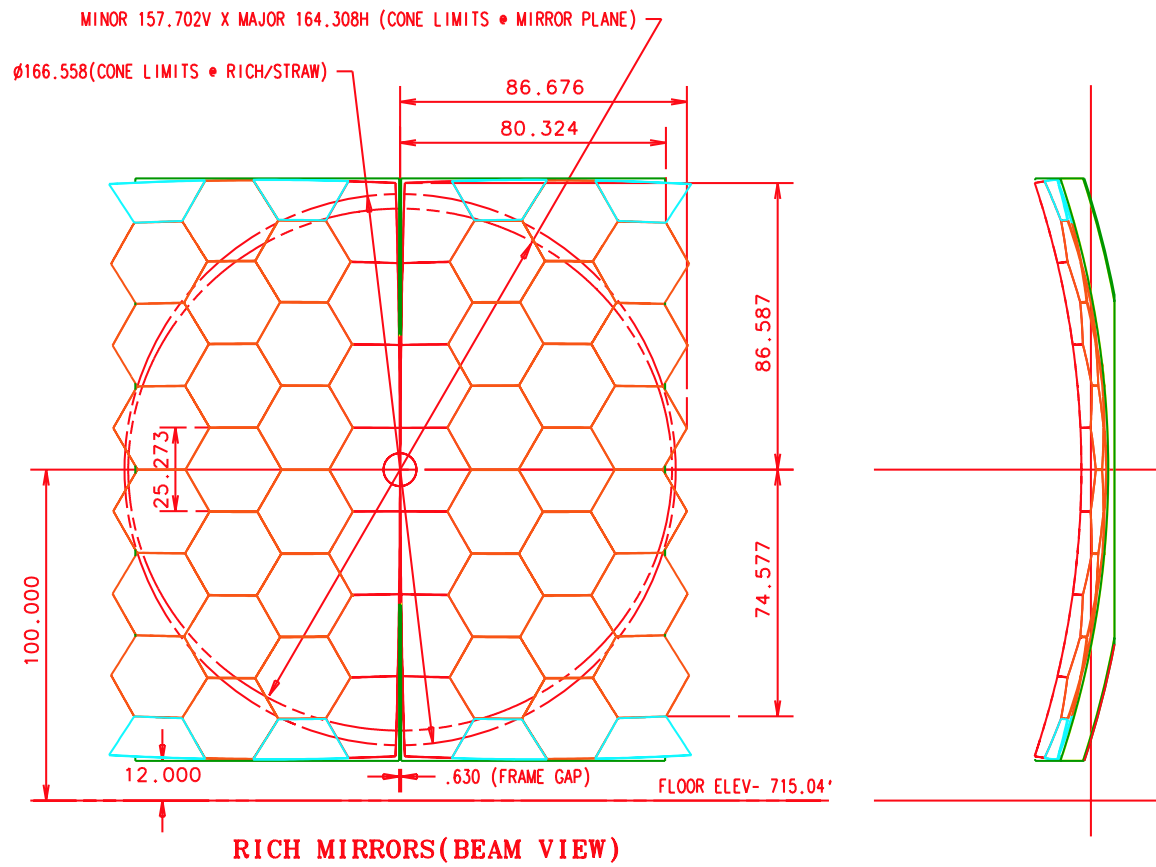


Figure 5.10: The original RICH mirror system (units are in inches).

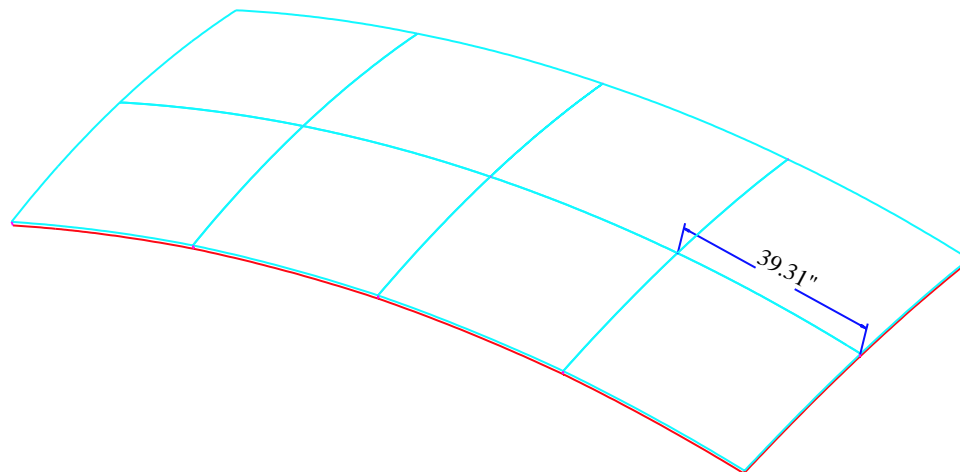


Figure 5.11: Sketch of one-half of the CMA proposed mirror array (units are in inches).

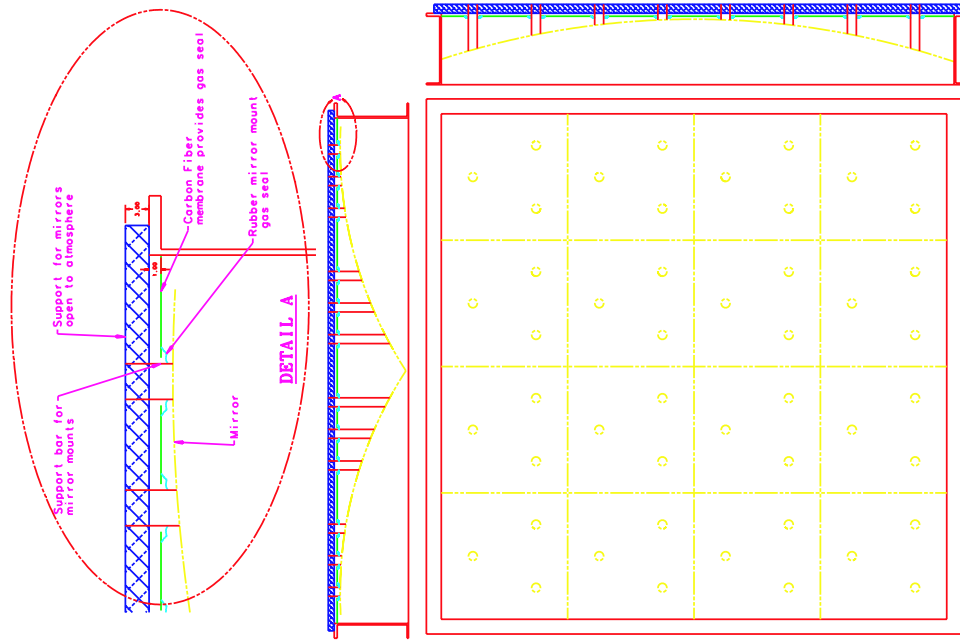


Figure 5.12: Drawing of the mechanical support for the CMA mirrors.

### 5.3.5 Photodetector Planes and Tank Structure

The size, optimal position and orientation of the photodetection surface for the  $C_4F_8O$  Cherenkov photons were determined using a ray tracing Monte Carlo. Even though the true focal plane of a spherical mirror is not planar, non-planar surfaces do not improve the resolution significantly and are difficult to realize in practice. We therefore use a flat photodetector plane whose position and tilt (442 mrad) was optimized using simulation. Since the actual emission point along the track for Cherenkov photons is unknown, the Cherenkov angle reconstruction assumes emission at mid-point of the RICH vessel. The emission point error, which contributes to Cherenkov angle resolution, is magnified by the mirror tilt from 0.2 mrad to 0.53 mrad. This error imposed by geometrical considerations sets the scale for the other two major contributions to the Cherenkov angle resolution: chromatic error and photodetector segmentation error (called also photon position error) to be discussed in Section 5.3.6.1.

The photons generated in the liquid radiator ( $C_5F_{12}$ ) pass through the quartz window and enter the  $C_4F_8O$  gas volume. Most of the photons reach the sides of the RICH gas containment box. The sides, top, and bottom of the box are instrumented with arrays of 3" diameter photomultipliers to detect these photons. The tilt of the PMTs is also determined by simulation.

The photodetectors for each system (MAPMT or HPD for gas system, and PMT for liquid system) are each shielded using a mu-metal tube to minimize the impact of the main dipole's fringe field on the performance of the tubes. Additional external shielding of the

magnetic field will be needed for the MAPMTs (or HPDs) and is provided by the steel-walled enclosure. The major detector elements (front and back windows, liquid radiator, mirrors and photodetector boxes) will be attached to the tank superstructure, which consists of massive beams (see Fig. 5.13), which will also support the tank walls and acrylic windows which seal the gas volume in front of the photodetectors. The superstructure is segmented to decouple mechanical loads due to the different components.

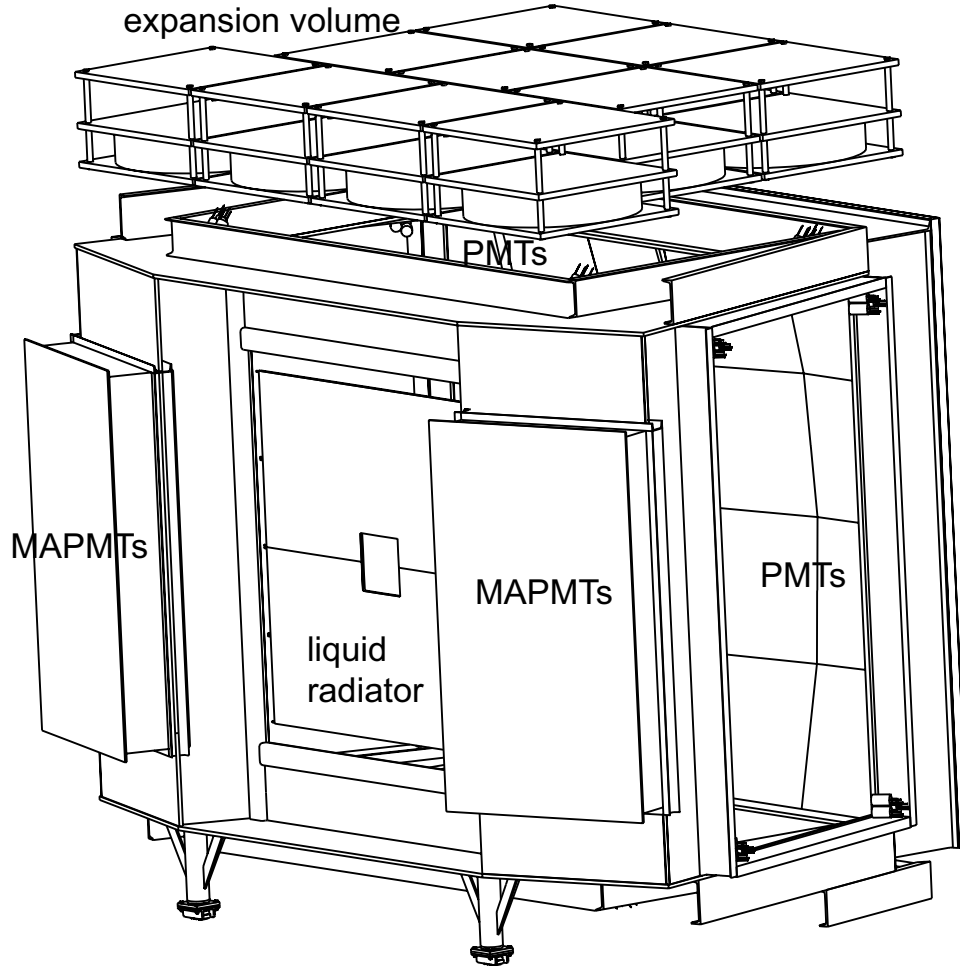


Figure 5.13: Tank support beams and location of the major components. The PMTs arrays are not shown except for their locations.

### 5.3.6 Photodetectors for the $C_4F_8O$ radiator

We choose to work in the visible wavelength region above 280 nm to minimize chromatic aberrations that arise because the index of refraction varies with wavelength. Because of the open geometry of the forward spectrometer and the availability of space to install shielding to

protect detection elements from the fringe field of the BTeV analysis magnet, arrays of multi-anode photomultipliers (MAPMT) or hybrid photo-diodes (HPD) can be used. Currently the MAPMTs are the baseline solution with the HPDs being a viable alternative.

### 5.3.6.1 MAPMT Photodetectors

Mult-Anode Photo-Multiplier Tubes are the baseline choice for the photon detector of the gas radiator system. In a MAPMT, the dynode structure is transversely segmented creating many independent channels within a single PMT enclosure. The initial R5900 multi-anode tubes developed by Hamamatsu were 30 mm  $\times$  30 mm in cross-section and were segmented into four (R5900-M4), sixteen (R5900-M16) or sixty-four (R5900-M64) separate anodes. The main drawback of these tubes was a large dead area around the photocathode. The active area of these tubes was only about 36%. Some type of light focusing system in front of the PMTs was needed to recover the dead area. The R5900-M16 and R5900-M4 tubes were used in the HERA-B RICH detector [2]. The HERA-B system used a two-lens system providing a demagnification by a factor of two. In the HERA-B solution the tubes are not closely packed, reducing the cost of the detector but allowing the segmentation error to dominate the achievable resolution. Furthermore, the photon yield is reduced due to reflective losses at each lens surface. The LHCb group, which is considering MAPMTs as a back-up system for their own version of PP0380 HPDs<sup>1</sup>, developed a different demagnification system consisting of a single convex-plano lens [6] to work with a closely packed array of R7600-M64 tubes. These tubes are 26 mm  $\times$  26 mm in cross-section, as the outer flange was eliminated increasing the active area to about 48%. The light recovery factor by the lens is 1.55 [12], resulting in an effective active area of 74%. Our initial modeling of the MAPMT system consisting of closely packed R7600-M16 tubes with convex-plano lenses showed somewhat worse performance than HPDs [13].

Hamamatsu has recently developed a new multi-anode tube - R8900. The focusing of the photo-electrons onto the first dynode was redesigned to provide a much larger active area of 85% in a 26 mm  $\times$  26 mm form-factor. Consequently, no lens system is needed. Moreover, the square geometry minimizes the geometrical losses, except for a possible magnetic shield. In bench studies, we have determined that the R8900 tubes can be adequately shielded from the fringe fields of the BTeV dipole magnet (see Section 5.4.1) using a 250  $\mu$ m thick mu-metal shield. We have simulated a system of MAPMTs assuming a 1 mm gap between tubes and find a geometrical acceptance of 79% (compared to 62% for the HPDs). The quantum efficiency of MAPMTs is likely to be at least 15% higher than for HPDs since photo-cathode quality is easier to control over the small area. While photo-electron collection efficiency is very high for HPDs, about 1/3 of the photo-electrons are expected to be lost in R8900 tubes, failing to multiply on the first dynode. Putting the geometrical, quantum and collection efficiencies together we expect to obtain about the same photon yield from both the MAPMT and HPD systems (see Tables 5.1 and 5.6). The R8900-M16, with 6 mm  $\times$  6

---

<sup>1</sup>Finer pixels and faster readout are required in LHCb, thus the readout electronics had to be integrated with the diode chip.

Table 5.1: Expected performance of BTeV RICH system. The photon yield and the resolution per track given here do not take into account any reconstruction losses due to overlap of Cherenkov rings from different tracks in the same event. The gaseous RICH performance given here corresponds to the baseline option (MAPMTs). The HPD solution produces very similar numbers (see Table 5.6).

	$C_4F_8O$ , $n = 1.00138$	$C_5F_{12}$ , $n = 1.24$
emission point error	0.50 mrad	0.4 mrad
segmentation	0.51 mrad	5.3 mrad
chromatic error	0.49 mrad	3.7 mrad
total error per photon	0.83 mrad	6.2 mrad
number of photons	52	12.4
total error per track	0.11 mrad	1.8 mrad

mm anode pixels (Fig. 5.14), has the right segmentation for our application producing the segmentation error which is well matched to the emission point and the chromatic errors (see Table 5.1). The tubes are equipped with a standard bialkali photocathode on a borosilicate glass window. A UVT acrylic will be used to separate the gas and the MAPMT volumes. Wavelength coverage of the borosilicate glass and of the UVT acrylic are very similar (see Fig. 5.50). Since MAPMTs require a single  $\sim 1$  kV voltage to operate and provide a gain of  $10^6$ , the technical aspects of the readout and HV distribution are much easier to manage than for the HPDs. The current price of R8900 tubes is lower per unit area than that of the PP0380AT HPDs from DEP (described in Section 5.3.6.4). Therefore, the MAPMT system is used for the baseline design and the HPD system is maintained as a viable alternative.

A system with 9016 MAPMTs approaches the full geometrical coverage limit. With 16 pixels per tube, the detector would have 144,256 electronic channels.

After successful bench tests of the first two R8900-M16 prototypes (see Section 5.4.1), we received additional 52 tubes, which were characterized on a bench and later used in the test beam of the RICH prototype (see Section 5.4.1.5).

### 5.3.6.2 MAPMT Readout Electronics

To minimize development cost and effort, MAPMT readout is closely related to the HPD readout electronics, which is described in Sec. 5.3.6.5. Since a single photoelectron produces as many as 1,000,000 electrons in the MAPMT (vs. 5,000 in the HPD), gain of the VA\_BTEV chip originally developed for the HPD (see Sec. 5.3.6.5) is reduced and noise requirements are less stringent. Design of the digital part is shared with the HPD hybrid. The MAPMT tubes will plug into a mating board, which will contain HV divider and connectors to the MAPMT hybrid board. Unlike for the HPD option, no flex-rigid technology is required making the MAPMT hybrid board cheaper and more reliable. The layout of the first prototype MAPMT

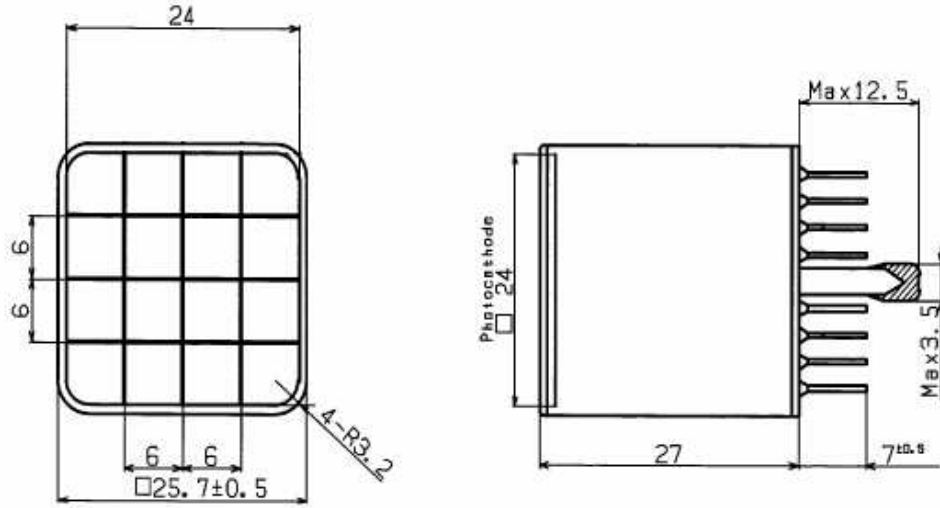


Figure 5.14: Dimensions of the prototype R8900-M16 MAPMT from Hamamatsu.

VA\_BTeV front-end hybrid is shown in Fig. 5.15. One hybrid has 2 VA\_BTeV chips and serves 8 MAPMTs (128 channels).

We received and bench tested 16 MAPMTs hybrids. Later they were successfully used in test beam of the RICH prototype (Section 5.4.1.5).

### 5.3.6.3 MAPMT Mechanical Support

The mounting arrangement for the MAPMTs is sketched in Fig. 5.16. Conceptually the detector plane is segmented vertically into groups four tubes high. The tubes are plugged into circuit boards containing the bases (“baseboards”) that are attached to a box channel beam which runs across the entire width of the detector. The MAPMTs are cabled to hybrid boards attached to box channel via standoffs. Each hybrid has 128 channels and is cabled to 8 tubes. The hybrids then go to a multiplexer board as shown. The box channels which provide the mechanical strength are screwed in at the ends to a rigid frame. Cooling lines are attached to the box channel. Prototype of this mechanical support was used in the test beam (Section 5.4.1.5).

### 5.3.6.4 HPD Photodetectors

HPDs are commercially available from DEP (Delft Electronic Products B.V.) in the Netherlands. For BTeV, we have collaborated with them in developing a 163-channel HPD with an outer diameter of 81 mm (PP0380 tube, see Fig. 5.17) The active diameter of the HPD is about 74 mm. A photon entering this device is focused by a spherical quartz window onto a photocathode deposited on the inner surface of the window. Photoelectrons are then accelerated by  $-20$  kV through a drift region with electrostatic focusing onto a segmented



Figure 5.15: Photograph of the first MAPMT hybrid board. Compare with the HPD hybrid board shown in Figs. 5.19-5.20.

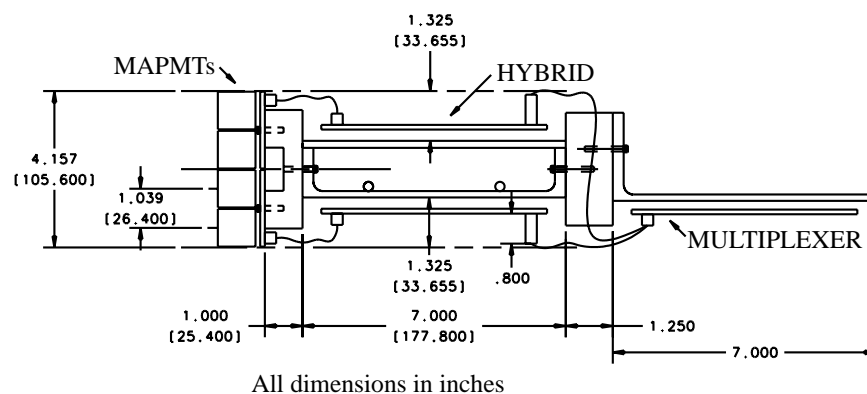


Figure 5.16: Drawing of prototype mounting scheme of MAPMTs.



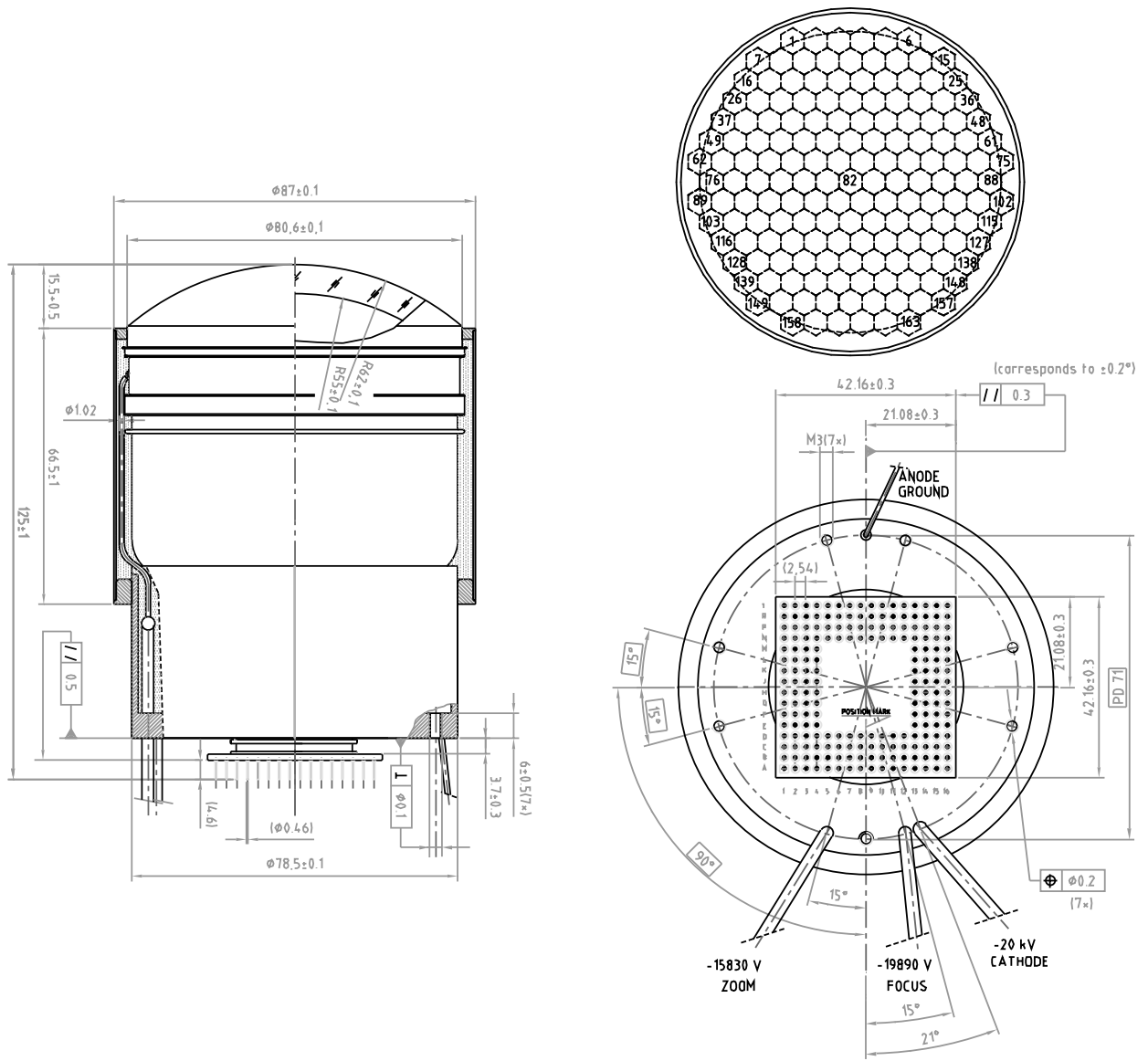


Figure 5.17: BTeV HPD (DEP PP0380AT). The outer dimensions are outlined on the left. The bare tube diameter is 83 mm. The insulated tube diameter is 87 mm. Silicon pixels (163 channels) on the cathode are shown in the upper right drawing. Pin layout is illustrated in the lower right picture.

silicon diode where they produce a signal of  $\approx 5000$  electrons. In addition to  $-20$  kV, the HPD requires voltages of  $-19.89$  kV and  $-15.83$  kV for focusing and demagnification onto the silicon pixel array. The charge collection time from the silicon depends on the bias voltage and is well below 100 ns. The focusing used in the PP0380 HPDs was developed by DEP in collaboration with the LHCb group [8]. The segmentation of the diode array into pixels has been adjusted to match our spatial resolution requirements. The effective pixel size at the HPD front-face is 5.7 mm side-to-side, corresponding to a photon position error of 0.45 mrad, which is slightly smaller than the 0.53 mrad contribution from the emission point

uncertainty. A 163 pin-grid array connects the pixel elements to readout electronics residing outside the tube.

About 80% of the bare tube area is active. However, the HPDs require 2 mm thick insulation and 2 mm thick magnetic shields which add to the inactive area. Closely-packed tubes cover 91% of the area they occupy. Thus the overall geometrical light collection efficiency is  $\sim 62\%$ .

The last major factor impacting the RICH performance is the wavelength coverage, which is determined by the photo-cathode and window material. The wavelength sensitivity determines chromatic error and is a major factor in the number of Cherenkov photons detected per track. Quartz windows are a standard feature in the HPD tubes as they can easily sustain the high voltage on the photo-cathode. High quality quartz extends the wavelength coverage from the visible range down to 160 nm. Such a large wavelength coverage results in a large chromatic error of 1.4 mrad per photon and in a large number of detected photons per track ( $\sim 162$ ). When the wavelength coverage is limited, the photon yield drops but the chromatic error per photon improves. These two effects offset each other. The simulations show that a shallow optimum in Cherenkov resolution per track is reached when the wavelengths are limited to about 280 nm. UVT acrylic used in the vessel window will produce such a wavelength cut-off. This results in a chromatic error of 0.50 mrad per photon with a photon yield of  $\sim 50$  photons per track. The total intrinsic Cherenkov angle resolution is therefore 0.84 mrad per photon and 0.11 mrad per track, which is comparable to the MAPMT performance (see Table 5.6). A system with 944 HPDs approaches the full geometrical coverage limit. With 163 pixels per tube, the detector would have 153,872 electronic channels.

We have received 15 BTeV-HPDs which were extensively tested on a bench [9].

### 5.3.6.5 HPD Readout Electronics

A single photoelectron, when accelerated through 20 kV, produces a signal of about 5000 electrons in silicon. In collaboration with IDE AS Norway, we have developed low noise electronics to operate with the HPD. The Syracuse group previously worked with this company on development of a custom-made ASIC called VA\_RICH and its associated front-end hybrid boards that were used in reading out the CLEO-III RICH detector. The pulse-height spectrum for the PP0380AT HPD obtained with VA\_RICH electronics is shown in Fig. 5.18. Peaks due to one, two, and three photo-electrons are easily seen.

In BTeV, the RICH readout will be binary. The readout must also be much faster than with VA\_RICH. Therefore, a different adaptation of the VA chip family has been produced for the BTeV HPD. We refer to this new ASIC as VA\_BTeV. The VA\_BTeV chip comprises 64 processing channels, including an analog section, a comparator and a digital section. The analog section consists of a RC-CR preamplifier-shaper unit with gain tuned to the low expected signal. It has a fast peaking time of 72 ns that is substantially shorter than the Tevatron bunch crossing time of 396 ns. The fall time is 200 ns, so the process signal is completely finished by the time of the next bunch crossing. If the Tevatron were to go to 132 ns crossing time there would be a small loss of hits due to the low overall occupancy.

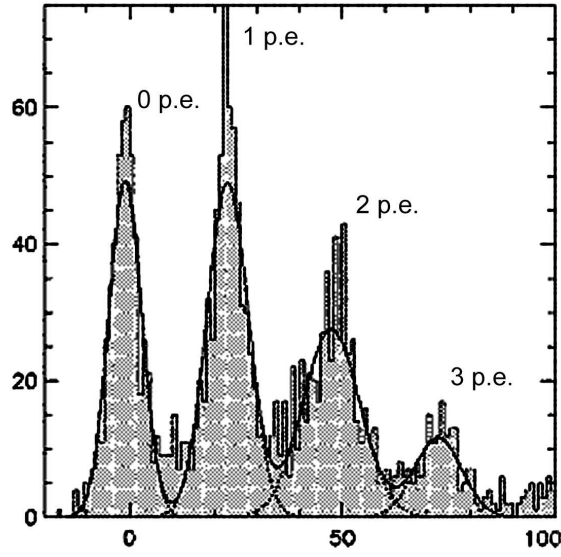


Figure 5.18: Pulse-height spectrum obtained for a single channel of the BTeV HPD with VA\_RICH readout. The pedestal peak is positioned at zero. The subsequent peaks corresponds to one, two and three detected photo-electrons. The peaks are separated by  $\sim 5000 e^-$ .

An optional gain stage that can be switched off is included to enable it to operate at slightly higher thresholds. The chip architecture features parallel input and parallel output for fastest delivery of the output information. Since each chip has 64 channels, a front-end board will house three ASICs. They will be connected to the HPD output pins via a small mating board. This analog part of the front-end hybrid will be well-isolated from the digital part for the best signal to noise performance. Binary signals for each channel are fed in parallel into the digital part housing an FPGA, which serializes the output, encodes the channel address and attaches a time stamp.

The layout of the first prototype VA\_BTeV front-end hybrid is shown in Fig. 5.19. The first prototypes were tested on a bench. Satisfactory noise performance was obtained. The next iteration of the design features a flex circuit to make a right angle bend between the analog part (mounted directly on the HPD end) and the digital part to allow for closely packed arrays of HPDs. A number of improvements to the hybrid design have also been implemented (see Fig. 5.20). A batch of 16 hybrids was procured and bench tested at Syracuse.

#### 5.3.6.6 HPD Mechanical Support

The mechanical support of the HPDs and their electronics is illustrated in Fig. 5.21. Each tube is supported on three mounting rods screwed into the HPD back flange. The mounting rods for six HPDs, together with the support frame for their readout electronics create a single mechanical unit, called a “hexad”, which can slide in and out of the mu-metal tubes.

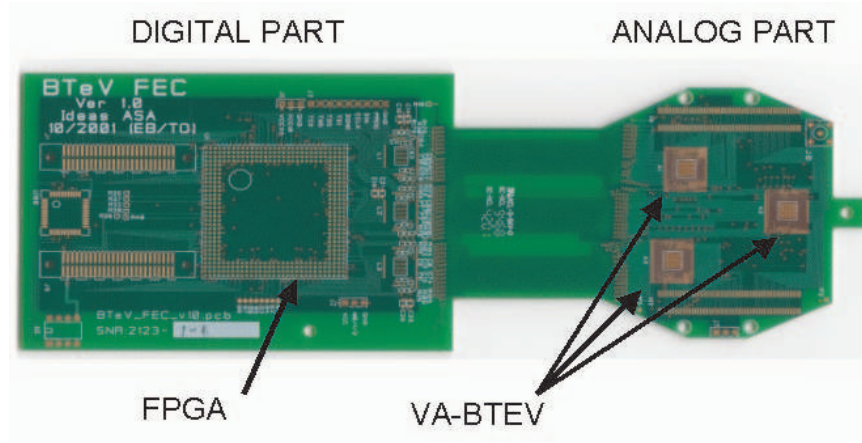


Figure 5.19: Layout of the first prototype of the BTeV RICH front-end hybrid board.

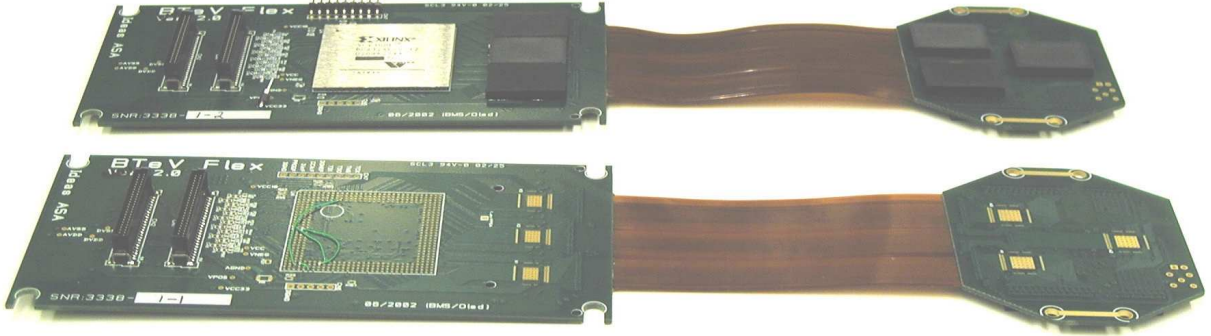


Figure 5.20: Photograph of the new flex hybrid board which will be used to read out an HPD.

This allows modular replacement, as well as testing, of the HPDs. The mating board with a ZIF socket attaches to the HPD pins. The analog part of the front-end hybrid plugs into the mating board with the help of connectors. The flex part of the front-end board creates a 90 degree angle. The digital part of the front-end electronics rests on one of the support plates.

### 5.3.7 Photodetectors for the $C_5F_{12}$ Liquid Radiator

Cherenkov photons generated in the 1 cm thick liquid radiator pass through the quartz window, undergoing refraction at the liquid-quartz and quartz-gas interfaces, and travel at large angles towards the PMT arrays. The PMTs are tilted to match the average angle of incidence of the radiated photons. The Cherenkov images at the PMTs are not simple rings since they are distorted by light refraction at the interfaces of the various media and by the orientation of the RICH's walls. The chromatic error for  $C_5F_{12}$  is 3.7 mrad per photon. The

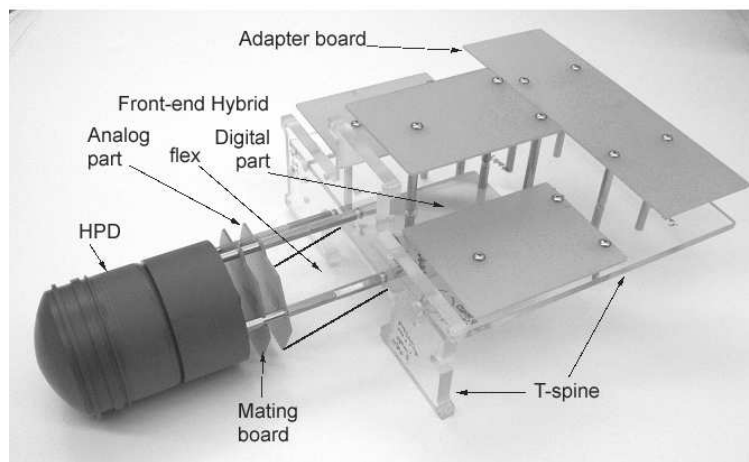
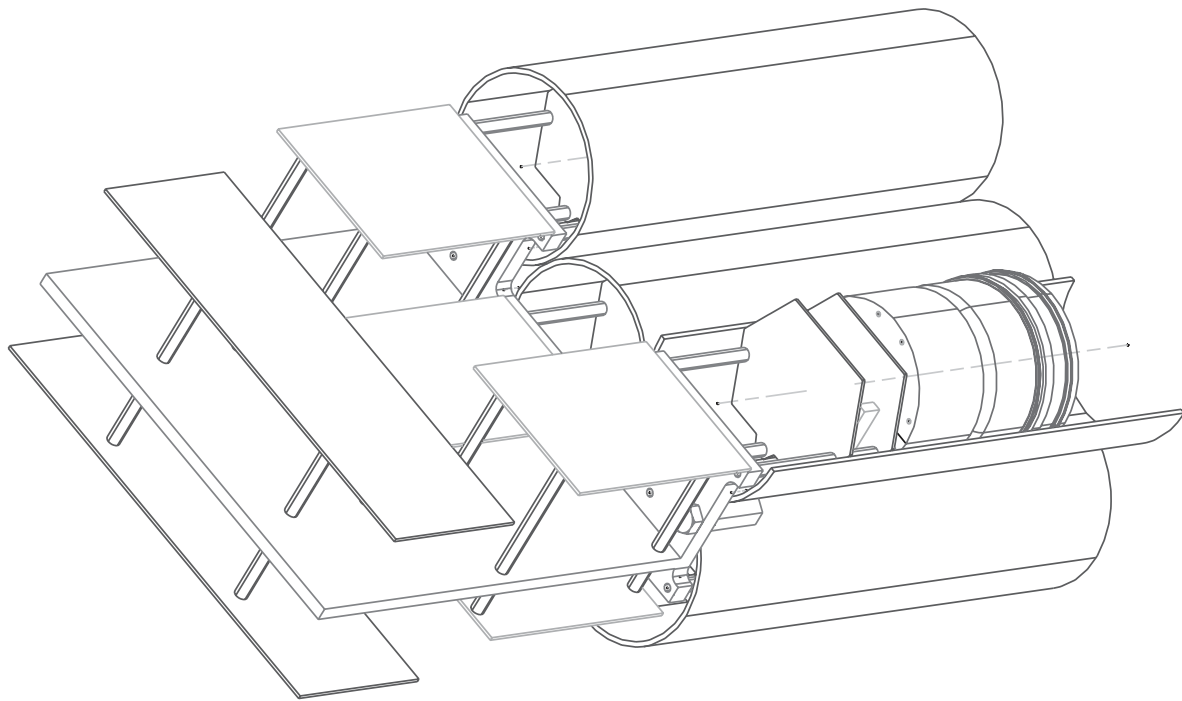


Figure 5.21: Mechanical support of HPDs and their electronics. Drawing of one mechanical unit(“hexad”) with 6 HPDs inserted into magnetic shielding tubes is shown in the upper part. Photograph of a mechanical mockup of such unit is shown in the lower part.

emission point error is negligible. The photon position error is determined by the size of the photomultiplier tube. Three inch PMTs produce a photon position contribution to the Cherenkov angle resolution of 5.3 mrad. The total error is then 6.2 mrad. Two inch PMTs improve the resolution by about 20%, however they approximately double number of tubes and cost of the PMT array. The current design has about 5000 3" PMTs covering the most illuminated portions of the two RICH side walls, as well as the top and bottom walls. While most of these tubes will be equipped with a borosilicate glass window, 500 PMTs located in radiation hot-spots (see Sec. 5.4.5) will have UV glass windows for increased radiation hardness. With this system, we expect to detect 12.4 photoelectrons/track, resulting in a per-track resolution of 1.76 mrad (see Table 5.1). Since at 9 GeV/c, kaon and proton Cherenkov angles differ by 5.34 mrad, the separation would be about 3 standard deviations. Separation improves substantially for lower momentum tracks.

Several manufacturers produce 3" tubes which satisfy our requirements. Further details on these tubes are discussed in Section 5.4.4.

### 5.3.8 Power Supplies

The MAPMTs require a 1 kV power supply. We plan to use the same power supply as adopted for the pixel detector (CAEN A 152N). The same power supplies can be also used for the PMTs in the liquid radiator RICH subsystem.

The power supply system for the backup HPD option is more complicated, since it requires much higher voltages (-20 kV, -19.89 kV and -15.8 kV). Because of the low level signal from the HPDs ( $\sim 5000 e^-$ ), it is very sensitive to any noise on its high voltage lines. We plan to use three separate power supplies, instead of using a voltage divider. Groups of tubes will be ganged together to reduce the number of power supplies. The peak-to-peak ripple on each supply is required to be less than 10 mV. On a test bench, we have used a power supply from Acopian with a  $\sim 1$  V p-p ripple combined with a HV RC filter close to the tube. Noise studies were performed with VA\_RICH readout electronics (see Sec. 5.4.2.8) and the performance was found to be satisfactory. This extra filtering close to the detector may not be practical due to limited space near/in the HPD enclosure. Furthermore, the stored energy in the 20 kV capacitors may be a safety concern.

We have also acquired 3 Matsusada power supplies (PS), each capable of delivering up to 30 kV with a p-p ripple of  $\sim 5$  mV. These PS are currently being used in bench tests of the HPD (using VA\_BTeV electronics). Their noise performance is excellent. They require a control and monitoring system to set the high voltage and to monitor the high voltage and the current output. The HV control system is shown schematically in Fig. 5.22. A prototype system with remote control through Labview has been developed and is being used in bench tests of the HPD system.

Other options which are being explored includes the acquisition of a CAEN SY1527 universal HV mainframe and a CAEN SY3527 HV supply to be used with the MAPMT sensor configuration. This will give us the opportunity to experiment with the CAEN HV supplies

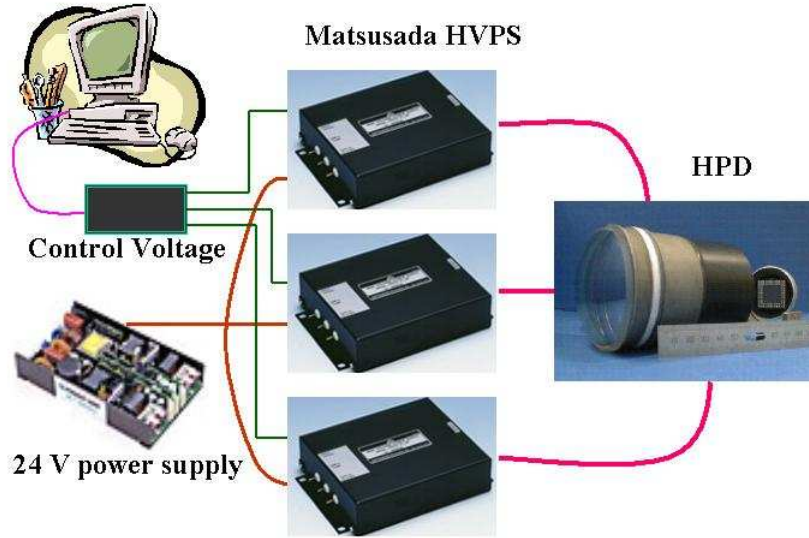


Figure 5.22: Block diagram of the HPD high voltage distribution system.

and control software which are considered a candidate for the integrated implementation of the high voltage distribution system for BTeV.

Finally, we are planning to acquire a Wiener low-ripple low voltage supply to benchmark the low voltage implementation in our system. In addition to the three high voltage supplies, the HPD also needs a power supply of  $\sim 60$  V to bias the silicon pixels.

All high voltages (20 kV and 1-2 kV) and low voltages ( $\sim 60$  V) will be controlled by setting the voltage of an individual channel or group of channels. Each channel will provide power to a group of HPDs or MAPMTs. The power supply grounds are floating and defined locally at the detectors that are being powered.

The applied voltages and current draws are monitored for every channel by the RICH monitoring system. Ranges of acceptable values for each power supply will be determined. Voltages or currents which fall outside the prescribed range will send a warning/alarm to the fast control system (*i.e.*, a PLC) and the slow control system (such as iFix).

### 5.3.9 Monitoring

The windows and container vessel of liquid and gas radiator can be broken or deformed if the proper pressure is not maintained. The monitoring system will watch the temperatures and pressures at various points in the gas and liquid volume. Depending on the condition, a fast response can be provided by a PLC, or a warning provided by the slow control system. Other properties that will be monitored include: the purity of gas and liquid which could also affect the index of refraction, the temperature of each front end electronics hybrid, and the humidity inside and outside the MAPMT enclosure.

The critical sensors will be watched by a commercial PLC, and will provide a fail-safe shutdown in extreme cases and an alarm or warning in other non-critical cases. All monitored sensors will also be interfaced to the slow control system (iFix) which also can produce alarms, historical data collection and retrieval, and graphical displays. Fermilab has a great deal of experience with iFix, which is being used throughout the lab for slow controls.

## 5.4 Completed R & D

In this section, we discuss the R&D progress on the various RICH detector components.

### 5.4.1 Development of MAPMT System for the Gas Radiator

Multi-anode PMTs provide an excellent technology for detection of Cherenkov photons with fine segmentation in visible wavelengths. We have recently received prototypes of the  $4\times 4$  segmented tube, the R8900-M16, and have studied various features of these redesigned tubes (see Section 5.3.6.1). An outline of the tube is shown in Fig. 5.14. Particular attention was directed toward studying the most important features of the device, namely, the pulse height spectra from individual channels, the effective area, and the magnetic field sensitivity. These aspects were studied by illuminating the MAPMT using a pulsed LED source connected to an optical fiber. The optical fiber was a single-mode fiber which produced a spot size of  $\approx 100\ \mu m$  on the face of the MAPMT. The test setup allowed us to look at the pulse height spectrum from individual channels as well as the integrated number of counts above a set threshold. Signal distributions were obtained by taking the difference between readings with light on and off. A photograph of the test setup is shown in Fig. 5.23.

#### 5.4.1.1 Pulse Height Spectra

For each channel, we measured the pulse height spectrum using the system described above. The pulse height distribution (in ADC counts) for each of the 16 channels in one tube is shown in Fig. 5.24. We find the distributions to exhibit well defined single photon peaks. The variation in gain from channel to channel is of order  $\pm 20\%$ , which is acceptable, since we are only interested in whether the channel had a hit or not (binary readout).

#### 5.4.1.2 Active Area Measurement

For this measurement, we scanned the face of the MAPMT in steps of  $\approx 300\ \mu m$ . We scanned through the center of the rows and columns, going beyond the end of the physical device in order to measure the drop-off in active area at the periphery of the tube. Figure 5.25 shows the results of the scan across the four columns. In each of the four plots, we show the total signal count (solid curve) and the contributions from the individual cells (dashed) in each column. The cell numbers are provided at the top of each figure. Several observations are made from these data.



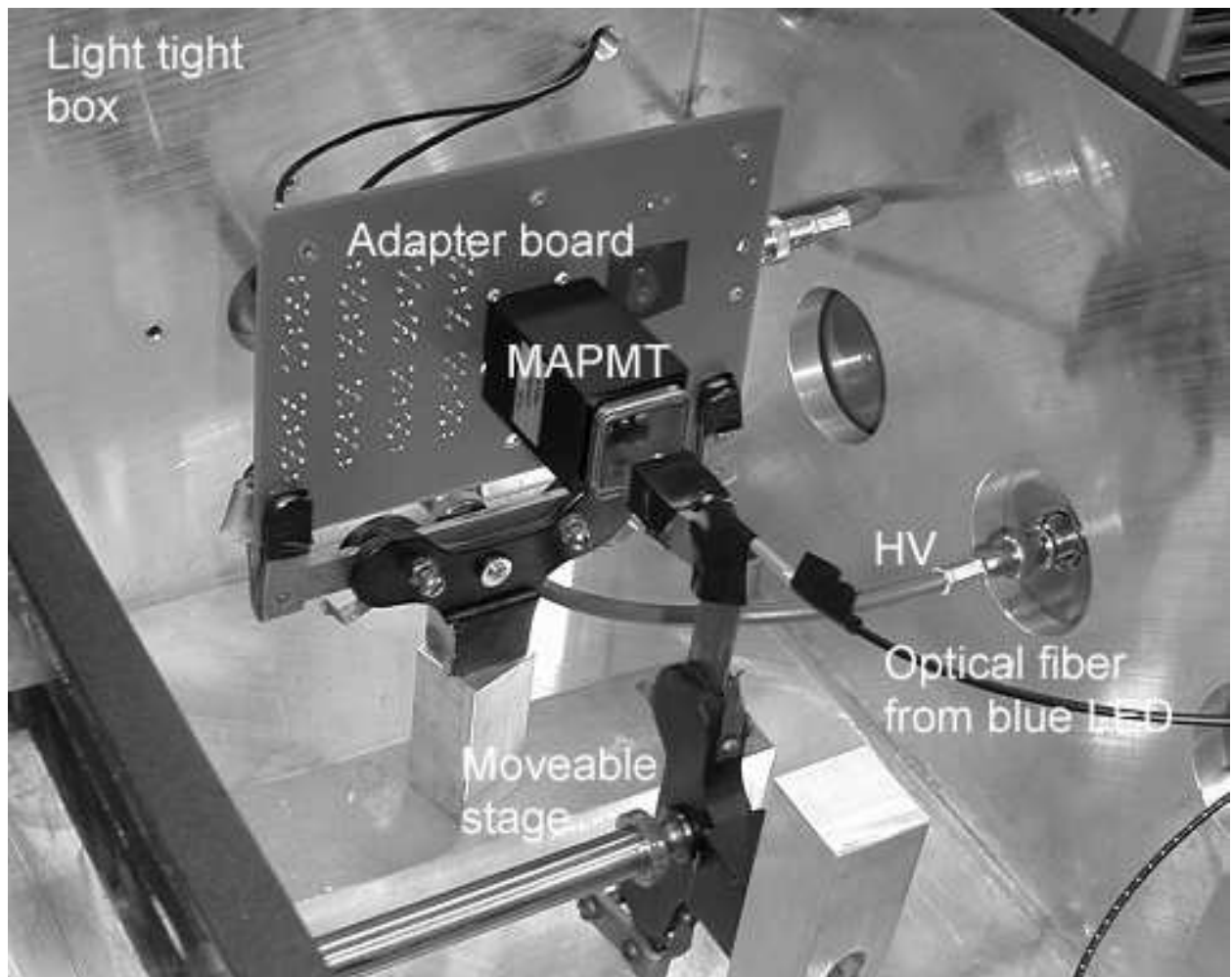


Figure 5.23: Photograph of the MAPMT test set-up at Syracuse. The prototype R8900-M16 tube from Hamamatsu is illuminated here by blue LED light which is delivered by a single-mode optical fiber. The optical fiber is mounted on a movable stage.

- The relative response is roughly flat across the face of the tube
- There efficiency near the edges of the tubes begins to falloff at approximately 1.5 mm from the physical edge.
- The effective area of a cell has Gaussian-like tails which extend beyond the physical dimension of the cell. This *broadening* of the cells effective active region was one of the tradeoffs in achieving a larger total active area for the MAPMT.

In Fig. 5.25, it is observed that cells 1, 5 and 9 have a higher relative response than the other three columns. Because this study was primarily concerned with measuring the active area, the thresholds were not tuned to account for gain differences between channels. We

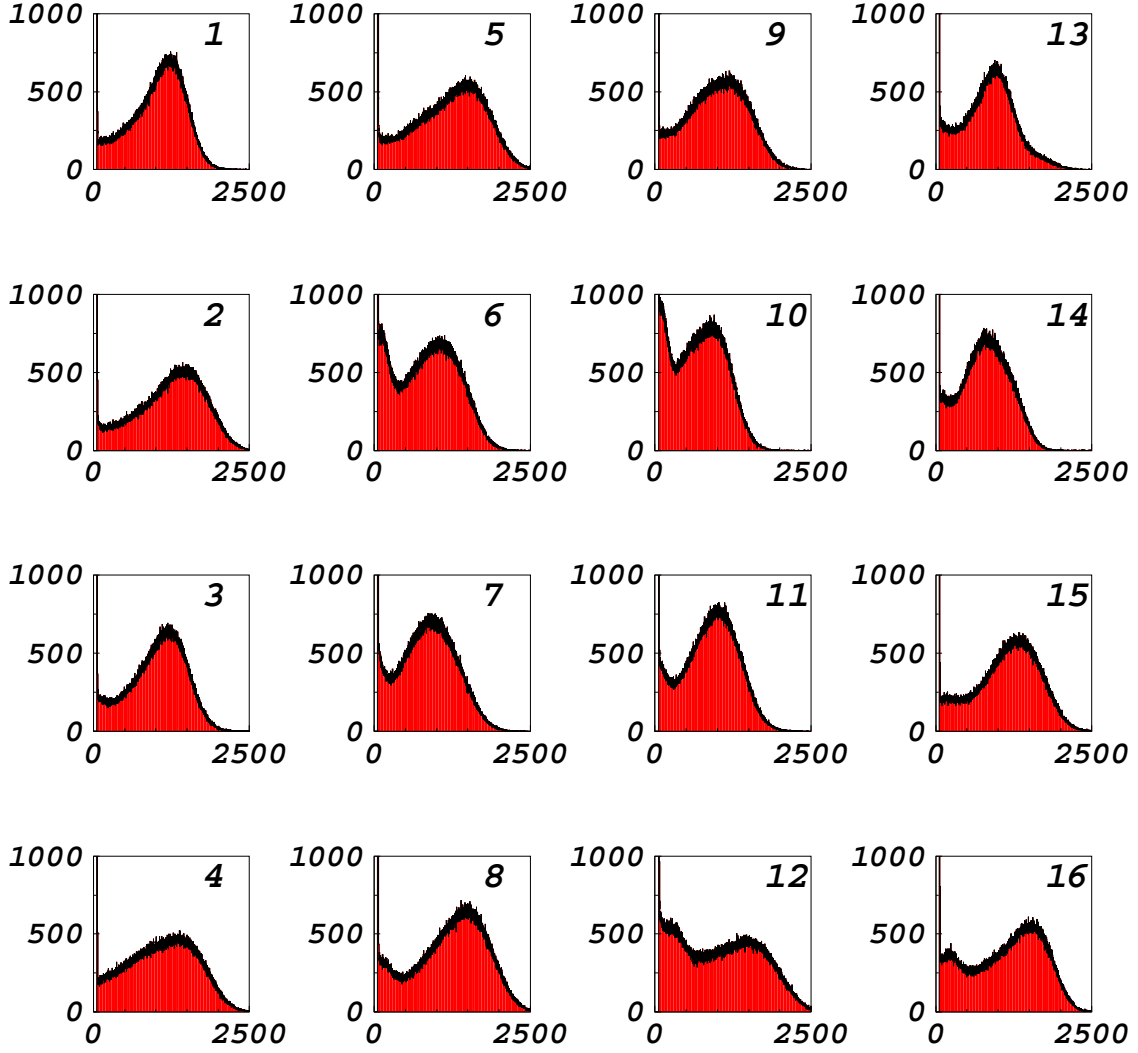


Figure 5.24: Pulse height distributions for the 16 channels of one of the prototype R8900-M16 MAPMTs. The number inset in each plot is the MAPMT channel number. The layout on this page is the same as viewing the tube head-on.

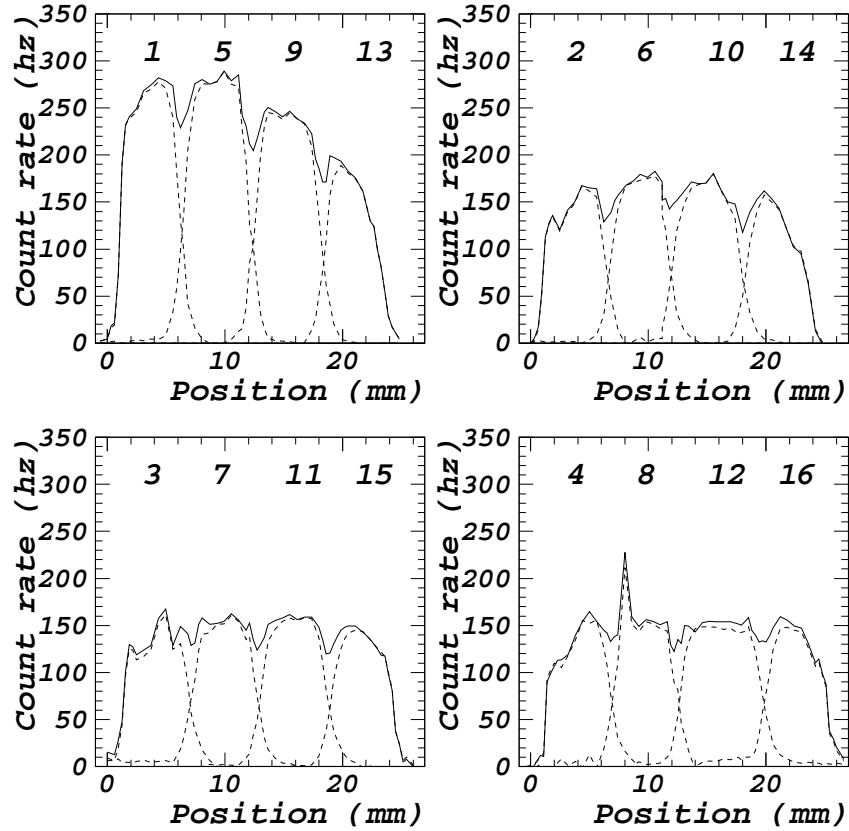


Figure 5.25: Scan along the four columns of the first R8900-M16 MAPMT prototype using a blue LED and an optical fiber. Shown are the background-subtracted count rates as a function of position for each cell along columns (dashed), and the sum of all four cells (solid).

have also studied in detail the falloff of efficiency in the corners of the MAPMT, and find that the falloff begins about 2 mm from the corner along the diagonal. The test performed here on this device, as well as on a second MAPMT, suggest that Hamamatsu has indeed been successful in producing a MAPMT with large active area. Using these data, and defining the width as the point at which the efficiency drops off by 50%, we find that  $\approx 22.5$ -23 mm of the maximum 24 mm is active. These effects have been included in the simulations of the BTeV RICH discussed in Section 5.7.1.2 and used as a benchmark for evaluation of the test beam results (Section 5.4.1.5).

Similar scans of 52 MAPMTs obtained for the test beam show improved uniformity of the response, even without fine tuning of the discrimination thresholds. An example is shown in Fig. 5.26. According to Hamamatsu, this is due to improved precision of positioning of the wires in the focusing grid between the photocathode and the first dynode.

04/05/19 12.38  
MAPMT Tube na0008 Y Slices, Voltage = 800V

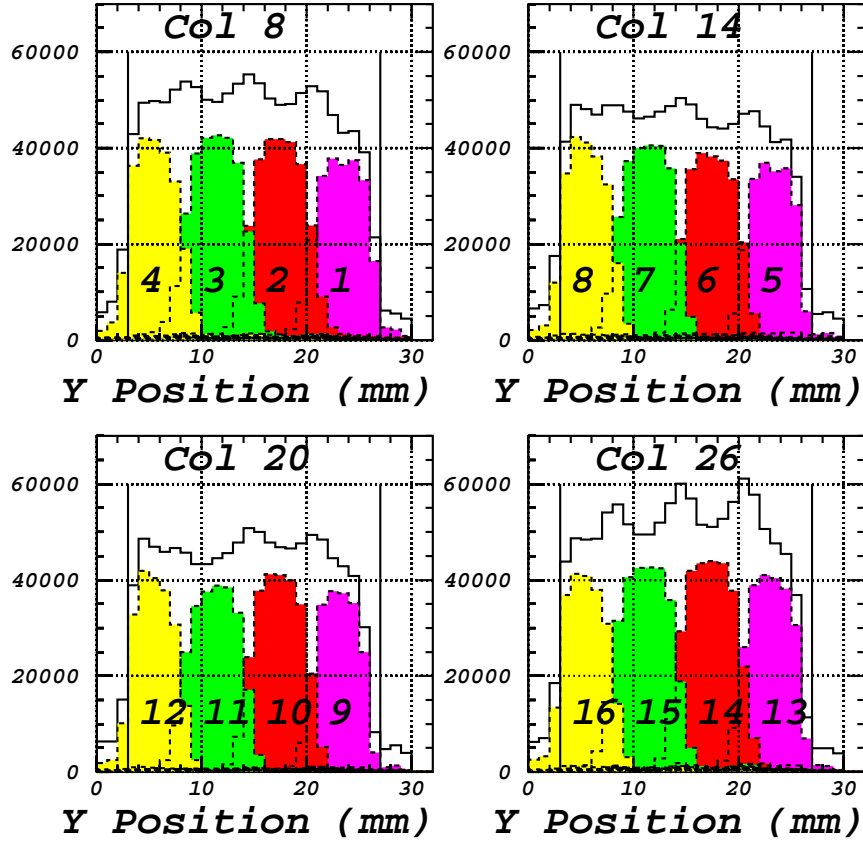


Figure 5.26: Scan of an improved R8900-M16 MAPMT used in the test beam. See Fig. 5.25 for explanation and comparison.

#### 5.4.1.3 Magnetic Field Studies

Another important aspect of the tube is its resistance to magnetic fields. The photon detectors will be located just outside the main dipole analysis magnet where a non-negligible fringe field exists. The photon detectors will be in an iron/mu-metal box which is required to reduce the magnetic field inside the box to a maximum of 10 Gauss. Since it is difficult to predict the direction of the field inside the box, we require that the photon detectors do

not suffer a significant loss of efficiency in either a longitudinal or transverse magnetic field of 10 Gauss.

To test the performance of the tube, we placed the MAPMT in a solenoidal magnetic field such that field was aligned either in the longitudinal or transverse direction with respect to the direction of the dynode chain. The performance of the tube was first studied without a shield, and then with a 250  $\mu\text{m}$  thick mu-metal shield extending a distance  $d$  beyond the edge of the tube. In the transverse field configuration, we found that the metal casing of the MAPMT provided sufficient attenuation of the field (loss in average efficiency less than 5%). On the other hand, the longitudinal field ( $B_{LONG}$ ) produced a significant loss in collection efficiency and thus the MAPMT must be shielded. To effectively shield the longitudinal component of the field, we found that the shield must extend about 1 cm beyond the front face of the MAPMT. In Fig. 5.27 we show the collection efficiency as a function of the applied longitudinal field. The vertical axis has been normalized to the response at  $B_{LONG}=0$ . We show the effect on three of the four corner channels (ch#1, #13, and #16), one edge channel (ch #3) and one center channel (ch#10). The corner channels are observed to be more sensitive to longitudinal fields than the other channels. In fact, we observe that for some of the channels, the relative collection efficiency actually improves, whereas for one of the corner channels (ch#13) the collection efficiency is degraded by  $\approx 20\%$  with respect to  $B_{LONG}=0$ . We have confirmed that indeed ch#13 was the worst channel in this geometrical configuration. If the tube is rotated by  $90^\circ$  (about the  $B_{LONG}$  direction), the worst channel becomes a different corner channel, but the magnitude of the efficiency loss is about the same for the “new” worst channel. Averaging over all 16 channels, we find that the net loss in efficiency is  $<5\%$ , for the case where the full field is longitudinal, which is unlikely to be the case. If part of the field is transverse, the average loss in collection efficiency is lower.

#### 5.4.1.4 MAPMT Electronics

We have been working with IDE AS to produce a modified version of the VA\_BTeV chip/hybrid which will accommodate the MAPMT signal of  $\sim 10^6$  electrons. The chip is required to have a large dynamic range ( $10^5 - 10^7$  electrons). A 2-chip hybrid with a new analog front end tuned to the expected MAPMT signal has been produced and delivered to Syracuse. An additional benefit of this modified chip is that in addition to the normal digital channels, there is a dummy channel with an analog output. This aids in the testing of this readout chip. These hybrids have been successfully tested on a bench and later used in the test beam run (next section).

#### 5.4.1.5 Test Beam of Gas Radiator RICH Prototype

A prototype of the gas radiator RICH was constructed at Syracuse and tested using a high momentum proton beam in the MTEST area at Fermilab in June 2004. The tank (see Fig. 5.28) employed a full-length radiator arm with a single spherical mirror tile tilted by the nominal angle. The mirror focuses Cherenkov light onto an array of MAPMTs placed at the end of the other arm of the vessel. The hexagonal glass mirror from IMMA, Turnov (see

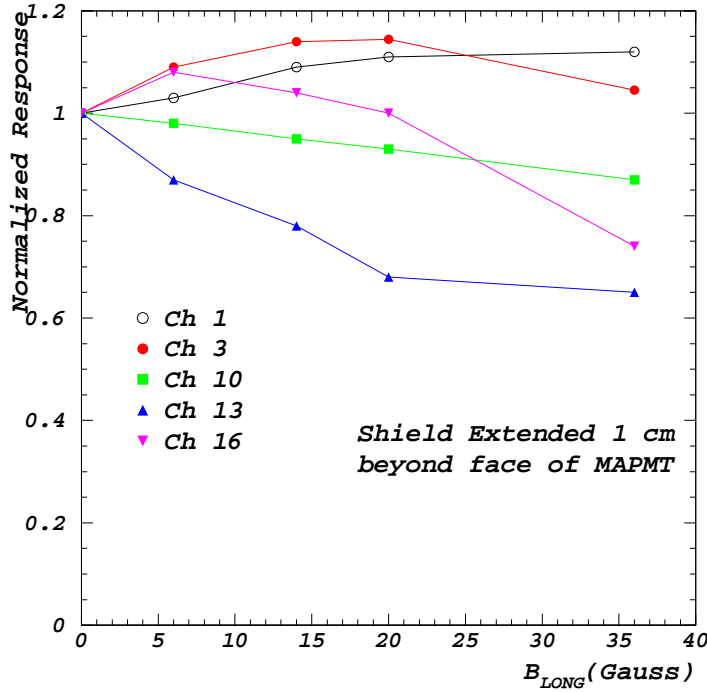


Figure 5.27: Relative collection efficiency for a prototype R8900-M16 MAPMT as a function of the applied longitudinal magnetic field. The vertical axis is normalized to the value at  $B_{LONG}=0$ .

Fig. 5.37 and Section 5.4.3) has a radius of curvature of 659cm, which is a bit shorter than the nominal design value (697cm), thus the MAPMT array is positioned 19 cm closer than in the nominal detector design. The spot size measured for the mirror (see Section 5.4.3.1) is about 3 mm, which is slightly larger than the 2.5mm spot size specification which we set for the mirror manufacturers.

The MAPMT array is shown in Fig. 5.29. The R8900-M16 tubes were initially exposed to Cherenkov photons using air as a radiating medium and orienting the tubes in double-row geometry (see top photo). Later, all 52 tubes were distributed along the ring expected from the  $C_4F_8O$  radiator (bottom picture). The MAPMTs were mounted on the first prototype baseboards. The baseboards host 16 MAPMTs, with each MAPMT having its own resistive HV divider to supply the dynodes with appropriate voltages. The baseboards also route the MAPMT anode pins to a standard header, which interfaces to the FE hybrid via four short cables. A small gap between the tubes allows for insertion of mumetal magnetic shields (which will be necessary for operation at C0). The mumetal shields were not installed for the first round of test beam studies, but are expected to be tested in a subsequent test beam in Jan. 2005. The baseboards are supported by box channels beams (see Fig. 5.16 and Section 5.3.6.3), which also support the Front End readout hybrid boards (see Fig. 5.15 and Section

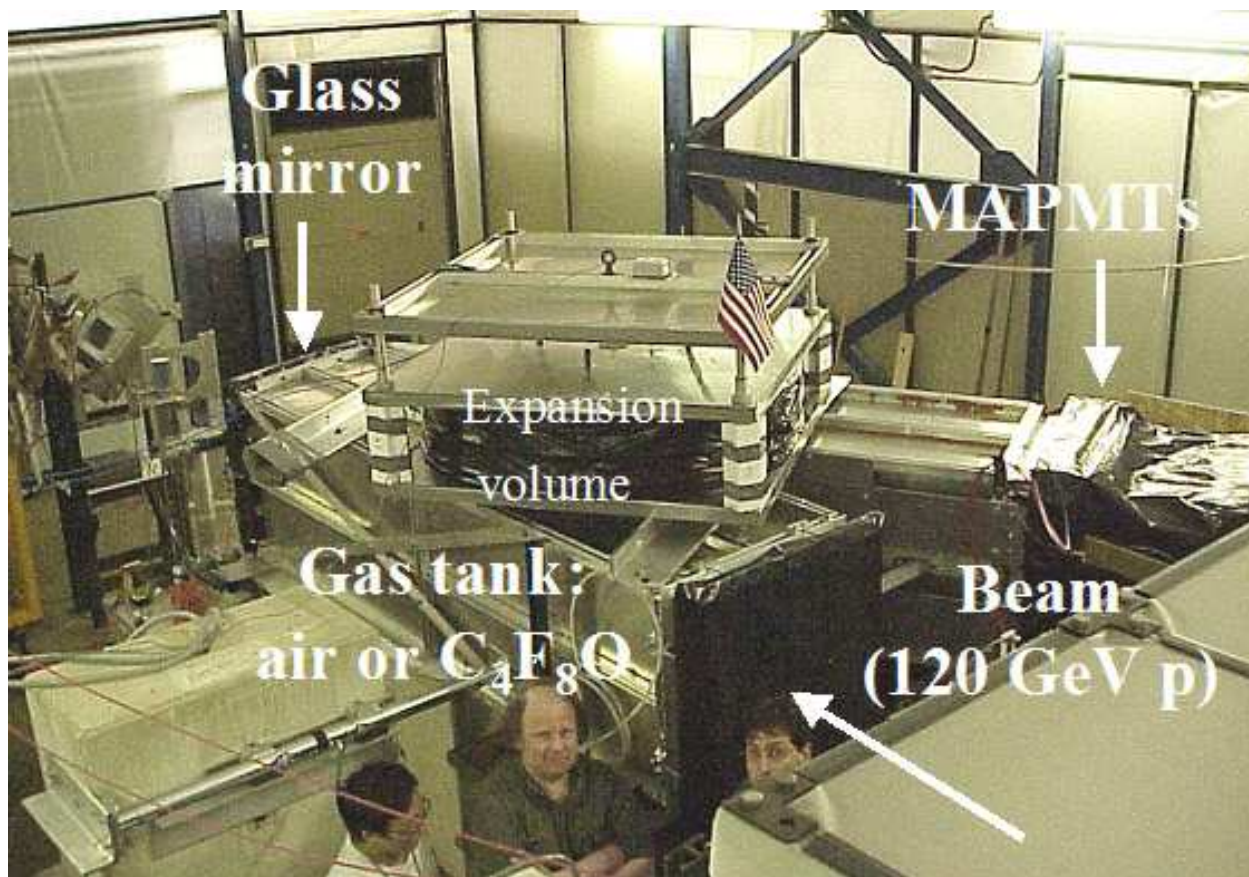


Figure 5.28: Gas RICH prototype in MTEST area.

5.3.6.2) The MAPMTs, baseboards, FE hybrid boards and the mechanical support represent advanced prototypes of the designed system.

Further components of the readout system in the first round of the test beam were less mature and were adopted from the bench set-up for testing FE boards. Only one FE board could be read out at a time, limiting the data taking to 8 MAPMTs (128 channels). Also, this readout system could not be triggered on individual tracks. We acquired data asynchronously with respect to the beam using a 4-8 kHz gate generator which produced a trigger window which was typically open for  $1\mu s$ . The latter time is about 5 times longer than intended for nominal data taking, since we had to rely on the random coincidences between the trigger window and the track arrival. In this setup most of the triggers did not contain any particles passing through the radiator, enhancing electronic noise over the Cherenkov light signal. Fortunately, the number of such noise hits was small, as measured using data taken in anti-coincidence with the beam spills. Electronic noise events rarely produced more than one hit. Thus, events with no beam particle in the detector were rejected by requiring two or more hits. For higher beam intensities, accepted events would often contain more than one beam particle passing through the RICH. In most cases, this is of no consequence



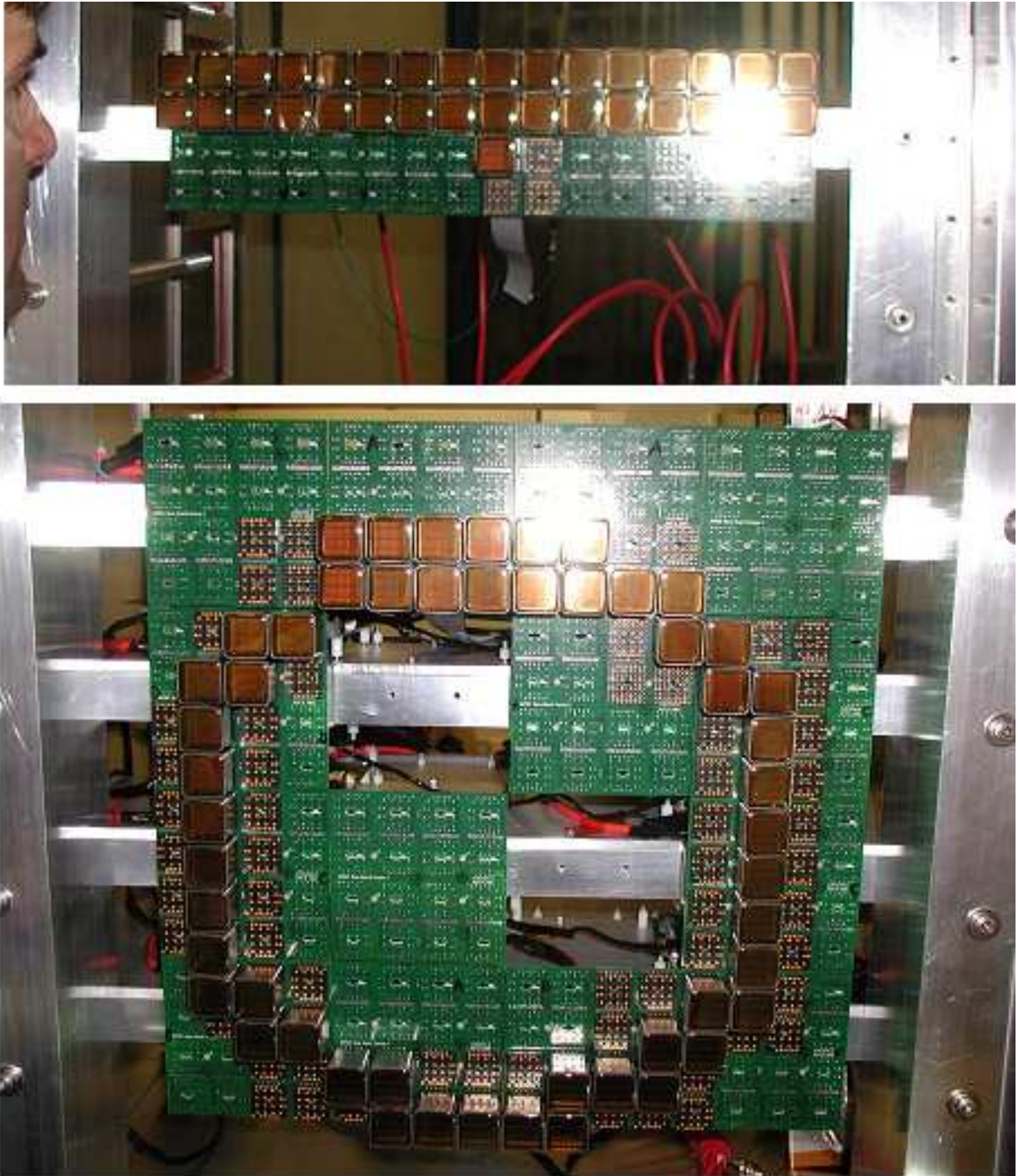


Figure 5.29: MAPMT arrays used in the test beam prototype. (top) Configuration used with air as radiator. (bottom) Configuration used with  $C_4F_8O$  radiator.



because the angular divergence of the beam was small compared to the Cherenkov angle resolution, which produces rings which are imaged at the same location in the photodetector array. However, some fraction of events contained secondary particles from upstream beam interactions, which produced Cherenkov rings in different locations, contributing a smooth background under the Cherenkov ring produced by the proton beam.

The hardware and much of the firmware for a more advanced prototype readout chain now exists. The addition of multiplexer boards will allow many FE hybrid boards to be read out at the same time. Triggering on individual tracks will also be possible, eliminating contamination from multi-track events and secondary particles. Firmware and DAQ software development for this system are progressing well and is expected to be ready for the test beam in January 2005.

Meanwhile, we present results from the first round of test beam runs. Initial data were taken with air inside the RICH tank. The mirror tilt was adjusted to maximize the fraction of the ring captured within a single  $4 \times 2$  array of MAPMTs. The hit intensity in each pixel, integrated over many triggers, is shown for the data in the top portion of Fig. 5.30. The ring radius matches the expectation well, as illustrated by the Monte Carlo generated distribution shown in the bottom portion.

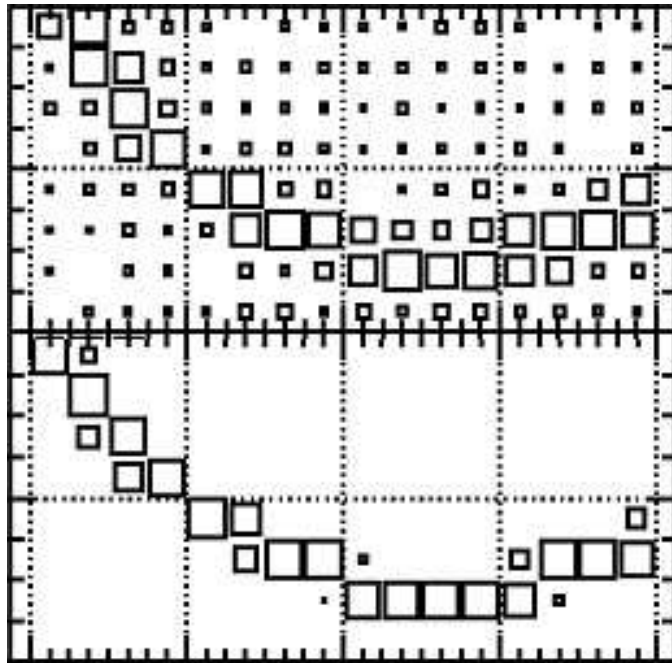


Figure 5.30: Cherenkov ring produced with air as radiator in the  $4 \times 2$  array of MAPMTs (outlined with the dashed lines) for the test beam data (top) and test beam MC (bottom). The Monte Carlo simulation does not include particles from upstream beam interactions, thus it lacks the background hits extending beyond the image produced by the primary beam particles.

The Cherenkov image presented above was obtained using 700 V applied to the MAPMTs,

which is at the on-set of the plateau region as illustrated in Fig. 5.31. At this HV setting no significant electronic cross-talk was observed as checked with the LED pulser. For higher HV settings we observed a coupling of the signal to neighboring electronics channels. We eliminated this cross-talk in the analysis software by counting neighboring hits as one photon. This procedure induces some inefficiency for photons striking neighboring channels. This inefficiency increases as the cross-talk hits spread to the next-to-nearest neighbors for even higher HV settings. This is observed as a slight decrease in the photon yield as observed in the data taken with the highest HV settings (see Fig. 5.31).

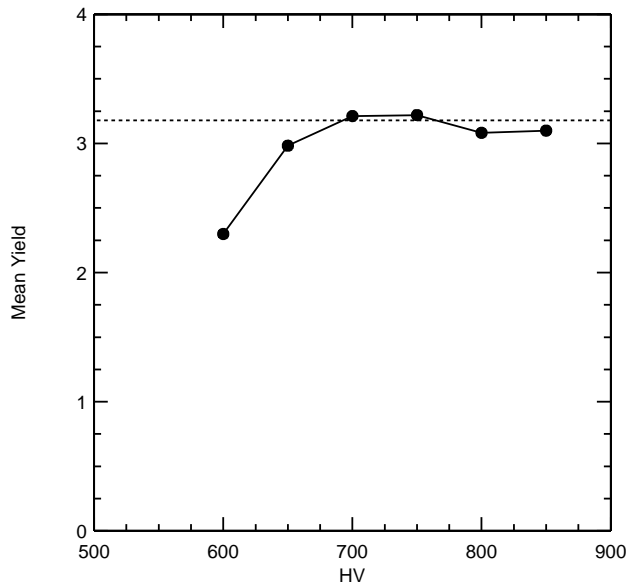


Figure 5.31: Average number of Cherenkov photons reconstructed in the  $4 \times 2$  array of MAPMTs for the air radiator as a function of HV, for fixed discrimination threshold. Only events with 2 or more hits were used to reject electronic noise events (see the text). The dashed line represents the yield predicted by Monte Carlo.

The plateau region free of cross-talk effects was rather narrow ( $\sim 50$  V) for the FE board settings used in the test beam runs. We are currently studying on a test bench ways to reduce the cross-talk, and therefore broaden the acceptable range of operating voltages. The cross-talk appears to be related to saturation of the VA\_BTEV ASIC for very large pulse heights. The dynamic range of the ASIC will be better matched to the MAPMTs pulse heights in the next iteration of the FE hybrids.

The dashed line in Fig. 5.31 represents the photon yield predicted by the Monte Carlo simulations. The simulation includes an average particle multiplicity per event of 1.12, as measured using scintillation counters during data taking. The Monte Carlo also simulates

the average quantum and collection efficiencies for the MAPMTs. The latter was assumed to be 70%, which is on high end of the range predicted by Hamamatsu for these devices in the plateau region. The Monte Carlo assumes no further losses in the FE electronics. Agreement between the data and MC in 700-750 V range is remarkable. This is the first experimental verification of the assumptions encoded into our Monte Carlo, which was used to predict the physics performance of the final BTeV RICH detector. In other words, the first test beam of the R8900-M16 tubes and of the FE electronics based on VA\_BTEV chip indicates that these devices work according to expectations.

The data taken with the  $C_4F_8O$  radiator are shown in Fig. 5.32, where they are compared to Monte Carlo simulation. The refractive index was scaled in Monte Carlo to reproduce the Cherenkov ring size observed in the data. The refractive index, averaged appropriately over wavelength, is determined by this procedure to be 1.001295, which is lower than the value obtained using a Michelson Interferometer, indicating that the vessel contained a mixture of  $C_4F_8O$  and air. The fraction of air was determined to be  $(8 \pm 2)\%$  by weighing a fixed volume of gas extracted from the tank. Correcting the previous result for the air fraction and for the pressure and temperature dependence, we determine the average refractive index of  $C_4F_8O$  at RTP to be  $1.00432 \pm 0.000071$ . The  $n - 1$  value is 3.4% higher than the nominal value assumed in our Monte Carlo. It is also higher, but within the errors, as compared to our optical measurements obtained with the light interference technique (see Fig. 5.5). The relative change in the Cherenkov radiation momentum thresholds is half of the  $n - 1$  variation, thus the uncertainty in the measured refractive index has no impact on the expected detector performance. In fact, larger changes of  $n$  will be induced by variations in atmospheric pressure. Our test beam represents the first use of the  $C_4F_8O$  gas as a Cherenkov radiator. These results demonstrate that, in fact,  $C_4F_8O$  is a suitable replacement for  $C_4F_{10}$  for detectors operating in visible wavelengths.

The data shown in Fig. 5.32 are a superposition of 10 different runs taken over the period of 2 days, as we could not read out more than 8 MAPMTs at a time with the June 2004 testbeam readout system. Thus, the photon yield for the entire Cherenkov ring could not be directly measured. Furthermore, the fraction of multi-track events was high (around 2.1) for these data and not measured independently. A measurement of the Cherenkov photon yield per track will be performed in a test beam in January 2005 using a more advanced DAQ capable of selecting single-track events and reading out all 52 tubes simultaneously.

The Cherenkov angle resolution per single photon is determined to be 0.94 mrad from the fit illustrated in Fig. 5.33. It is 9% higher than the Monte Carlo value, however, the Monte Carlo assumes negligible beam divergence. This is a likely cause for the disagreement. Better tests of the angular resolution will be obtained with the individual track trigger to be implemented during the next test beam run.

## 5.4.2 Development of HPD System for the Gas Radiator

Hybrid Photo-Diodes provide a competitive technology to the MAPMTs for detection of Cherenkov photons with fine segmentation. We have developed a 163-channel HPD together

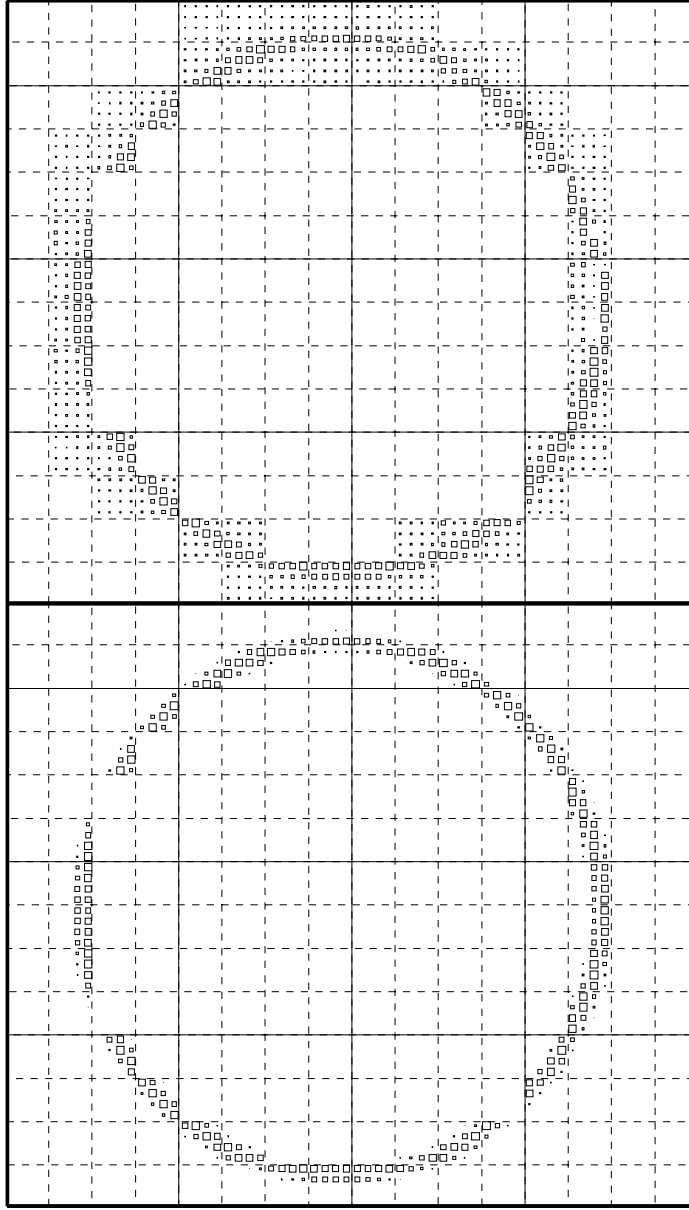


Figure 5.32: Cherenkov ring produced with  $\text{C}_4\text{F}_8\text{O}$  as radiator in the array of MAPMTs (outlined with the dashed lines) for the test beam data (top) and test beam MC (bottom). Only the dashed squares with hits were instrumented with MAPMTs. The solid lines represent individual baseboard boundaries. The Monte Carlo simulation does not include particles from upstream beam interactions, thus it lacks the background hits extending beyond the image produced by the primary beam particles.

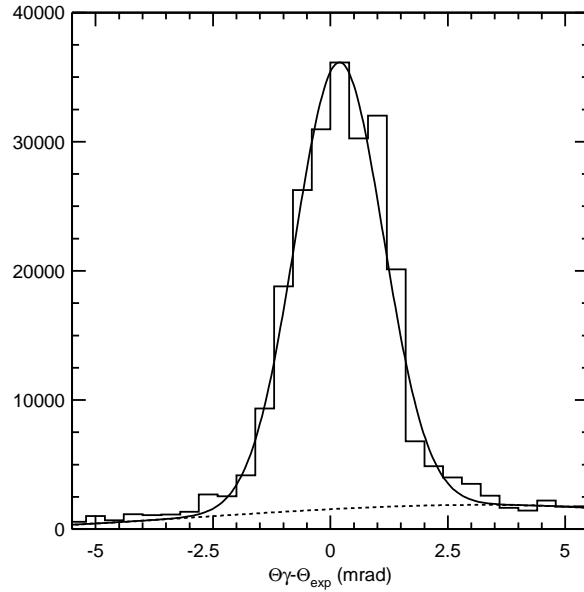


Figure 5.33: The difference between the measured and expected per-photon Cherenkov angle in mrad. The solid line represents the fit of a Gaussian on top of a polynomial background. The dashed line represents the background contribution alone.

with DEP which meets our specifications on position resolution. A picture of this redesigned HPD is shown in Fig. 5.17. Two initial tubes of this type were manufactured by DEP and successfully tested at Syracuse. We have also recently received 15 additional tubes which will be used in the 2004 testbeam run. The pulse-height spectrum for one of the HPD channels, obtained with low intensity LED light and VA\_RICH readout electronics (adopted from the CLEO III RICH) is shown in Fig. 5.18. Peaks due to one, two, and three photoelectrons reaching the same pixel within the integration time are observed, demonstrating good single photoelectron detection capability (in RICH operations we will detect one photoelectron at a time). A number of other baseline tests have been performed and are discussed below.

#### 5.4.2.1 Measurements of the Active Area

An important parameter of the HPD is the active area of the tube, as presented to the incident Cherenkov radiation. The active area of the HPD has been measured, by scanning a collimated light source across the diameter of the HPD using a linear motion stage. The LED light source had a beam spot of 1 mm diameter at the HPD window, and was pulsed to produce an average of one photoelectron during the integration time of the electronics. The mean number of photoelectrons was determined as a function of radius. An active area

diameter of 74 mm was obtained, consistent with the DEP specs of a 72 mm photocathode deposition and the expected refraction through the spherical quartz window.

#### 5.4.2.2 Measurements on the Electrostatic Focusing

As discussed previously, the HPD electrostatically focuses photoelectrons produced in the photocathode onto a pixelated silicon detector. Measurements were made to determine the best electrostatic focus of the HPD. Using a collimated LED light source, the position and RMS of the spot was determined as a function of the three voltages, UK (cathode), UF (focus), and UZ (zoom). The results were consistent with electrostatic simulations made by DEP, for the optimum high voltage setting. Of practical importance, it was found that the focus has a weak dependence on the values of UK and UZ, but a strong dependence on UF. Consequently, the value of UF should be set to nominal within 10 V (i.e., 0.05%).

#### 5.4.2.3 Relative Quantum Efficiency

The previous tests also yield a measurement of the efficiency of the HPD across the tube face. This is a relative measurement, referenced to the quantum efficiency of the tube at the center of the window. We find a reduction in efficiency as a function of radius, with a maximum loss of about 10% at the very edge of the active area of the tube. This is consistent with expectations based upon discussions with DEP.

#### 5.4.2.4 Shielding of HPDs from Magnetic Field

Measurements by the LHCb group [10] showed that the PP0380 HPD shielded by 0.9 mm mu-metal tube can be exposed to fields up to 30 Gauss, but would require software corrections due to significant distortions of the photoelectron trajectories. Our goal is to reduce the field inside the HPD to a level at which no software corrections will be needed.

Measurements of magnetic field effects on HPD performance were made by placing the HPD in a pair of Helmholtz coils, having better than 5% field uniformity in the central region. The point spread function (PSF) is the image of a LED through a pinhole in a screen placed at the window of the HPD. The pinhole was moved to various locations and the position of the PSF spot was reconstructed by a centroid method. The photoelectron trajectories are distorted by the applied field, thus the centroid moves across the pixel array, as illustrated in Fig. 5.34. The HPD was shielded by a tube of CO-NETIC AA foil, arranged in four layers of 0.25 mm each, with the HPD recessed 5 cm inside the tube. Both transverse and longitudinal applied fields were varied. Typical results for the displacement are shown in Fig. 5.35. The applied field required to displace the PSF a single pixel is about 45 Gauss for longitudinal field. and a factor of two higher for transverse field.

ANSYS calculations of the fringe field from the BTeV dipole analysis magnet predict that the field in the HPD region will be in the range of 50-150 Gauss. By surrounding the HPDs and their electronics with a shielding box (0.25" iron + 0.25" air gap + 0.125" mu-metal) the total field is reduced to a maximum of 10 Gauss. Even if this field is mostly longitudinal,

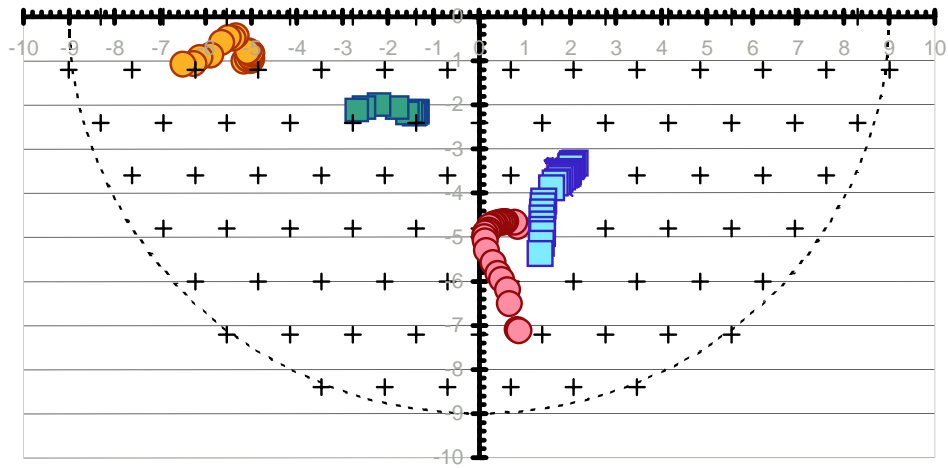


Figure 5.34: Images of the pinhole light source in the plane of the HPD diode (series of circles or squares). The scale is in mm. The crosses indicate the centers of individual hexagonal pixels. Different points within the series show displacement of the image under the influence of the magnetic field. The HPD was shielded as described in the text. The external magnetic field was longitudinal and it was varied from 0 to 55 Gauss.

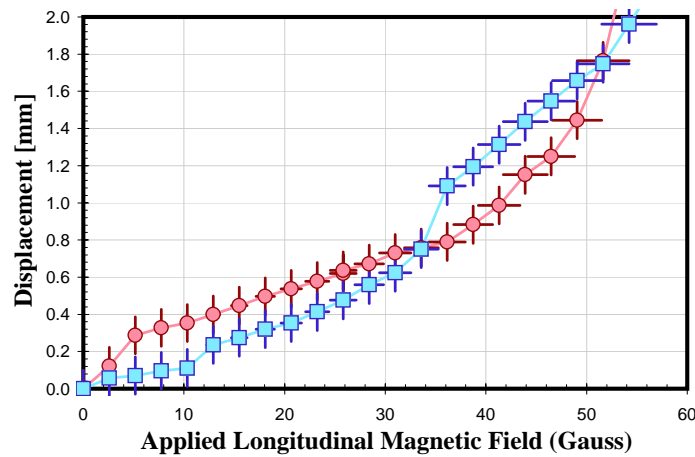


Figure 5.35: Typical displacement of the images in the plane of the HPD diode under the influence of longitudinal magnetic field. The pixel size is 1.4 mm. The two curves correspond to the outer image locations from Fig. 5.34.

such fields will result in image distortions which are a fraction of the pixel size as illustrated in Fig. 5.35.

A beehive of magnetic shields to be used in the beam test box is under construction. Unlike in the final detector, these prototypes are made of Aluminum, since magnetic shielding is not necessary for the test beam. The procedure for constructing the beehive has been established, using a mechanical jig to precisely align the shields. Since the hexads must be interchangeable, the corresponding sets of shields in the beehive must be well aligned in position and angle. Relevant thermal and mechanical tests of the various components have been carried out.

#### **5.4.2.5 HPD Insulation**

In the initial design, the upper electrodes of the PP0380 HPD were not insulated and the 20 kV voltage was supplied by a lead wire running along the tube (see Fig. 5.17). Such HPDs work well when operated at a sufficient distance away from any other metal objects. However, we discovered that we could not operate them reliably inside magnetic shields, which, for practical reasons, must be grounded. Painting the HPD with corona-suppressant material and using layers of kapton did not cure the HV breakdowns. We were able to eliminate them only by potting the entire gap with insulating material. This led to a slight redesign of the HPD. All tubes are now required to have an insulating layer to cover the upper part of the HPD. The 20 kV wire is completely encased inside the insulator layer. Fifteen tubes with this encapsulation have recently been delivered to Syracuse University and tests show that the potting has eliminated the HV breakdown.

#### **5.4.2.6 Characterization of HPDs**

A total of 15 HPDs have been delivered to Syracuse University. Each HPD delivered has been tested for high voltage behavior, pixel diode performance, mechanical tolerance, and optical characteristics. A characterization database is kept on all HPDs, which includes the DEP measurements of quantum efficiency and leakage current per pixel. All HPDs are tested at 20 KV, in contact with a magnetic shield, as required by the system design. All HPDs are flashed by an LED light source at two intensities to confirm basic pixel operation (no dead channels have been found). The mechanical dimensions are also measured. All HPDs are within specification except for the outer diameter which is slightly larger than specified due to the eccentricity in the insulation material. This has been compensated for in the mechanical design of the mu-metal shields.

#### **5.4.2.7 High Voltage Distribution**

See Section 5.3.8 for details on the HV system design.



#### 5.4.2.8 HPD Front End Readout

We have obtained 15 VA\_BTeV hybrids. Their basic functionality has been tested. The intrinsic noise of the ASIC is also within specifications, as indicated by a pulse height scan of the channels (see Fig. 5.36). We have also performed initial tests where we pulse the HPD with an LED light source which is tuned to produce an average of 1 photo-electron per pulse. The response of the tube indicates that it is sensitive to single photons. Additional studies of the hybrid are in progress.

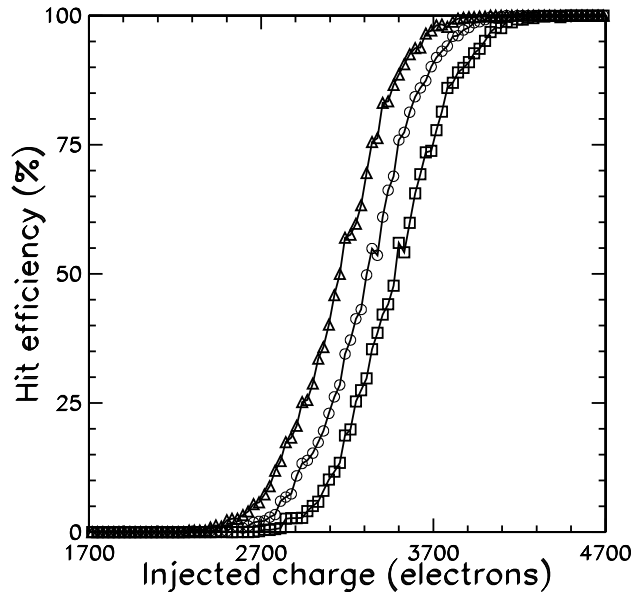


Figure 5.36: Threshold scan with the calibration pulse of one of the channels on the first BTeV RICH front-end hybrid board. The three curves correspond to three different settings of the discriminator threshold. From these curves we measure the electronic noise to be  $\sigma = 300$  electrons.

#### 5.4.3 Mirrors

We have developed techniques for investigating the optical qualities of mirror segments. We have obtained two mirror prototypes, each with a diameter of 60 cm and a radius of curvature of 660 cm, which is similar to the required radius for the BTeV RICH. One of the mirrors is made out of 6 mm thick Simax glass (4.7% of  $X_0$ ) and the other one of a thinner 2.2 mm glass substrate reinforced by two carbon fiber shells with a foam core (2.4% of  $X_0$ )<sup>2</sup> (see

<sup>2</sup>The foam width is irregular and goes from 0 mm (at the edge) to 20 mm (in the center).

Fig. 5.37). These mirrors were studied at Syracuse, and both mean radius and spot size measurements were performed. The details of these measurements are discussed below.

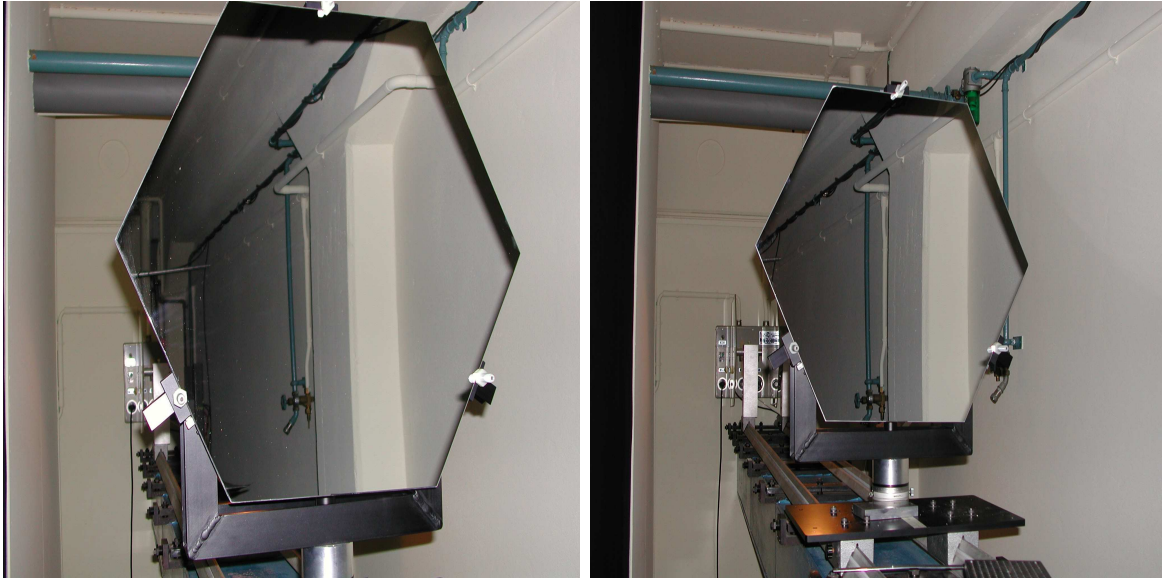


Figure 5.37: Two photographs, side-by-side, of the Turnov mirror prototypes (60 cm in diameter, 6.6 m in radius). The glass mirror is shown on the left. The glass-carbon fiber mirror is shown on the right. These mirrors will be used in the RICH beam test next spring.

#### 5.4.3.1 Measurement of Radius of Curvature and Spot Size

The mean mirror radius can be measured using the basic optical equation for the spherical mirrors, which is given in terms of the radius of curvature  $R$ , mirror-object distance ( $s$ ) and the mirror-image distance ( $s'$ ):

$$\frac{2}{R} = \frac{1}{s} + \frac{1}{s'}, \quad (5.1)$$

A test-stand which included an optical bench, a three-point mirror holder, and a point light source, was developed to measure the radius of curvature and spot size. The point source illuminated the mirror and the reflected light was collected by a digital camera. To facilitate the measurements, the camera and the point source were put on the same plane perpendicular to the optical axis (see Fig. 5.38).

To measure the mean radius  $R_{mean}$ , we adjust the separation between the point source and camera until the spot image is at its minimum size. At this point, the mean radius  $R_{mean} = s = s'$ . The minimum size of the spot image is called the spot size. Figure 5.39 shows the spot image for the glass mirror.

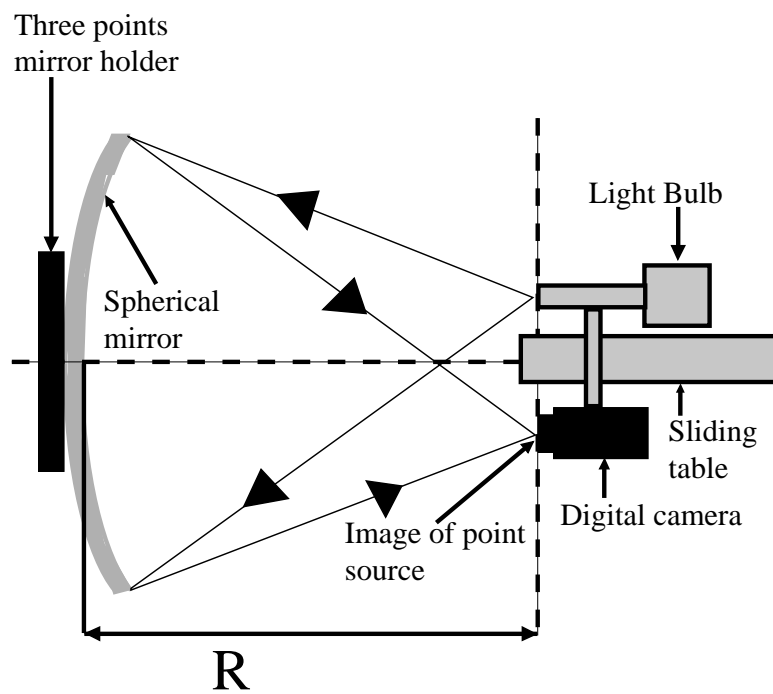


Figure 5.38: Procedure to measure the spot size.

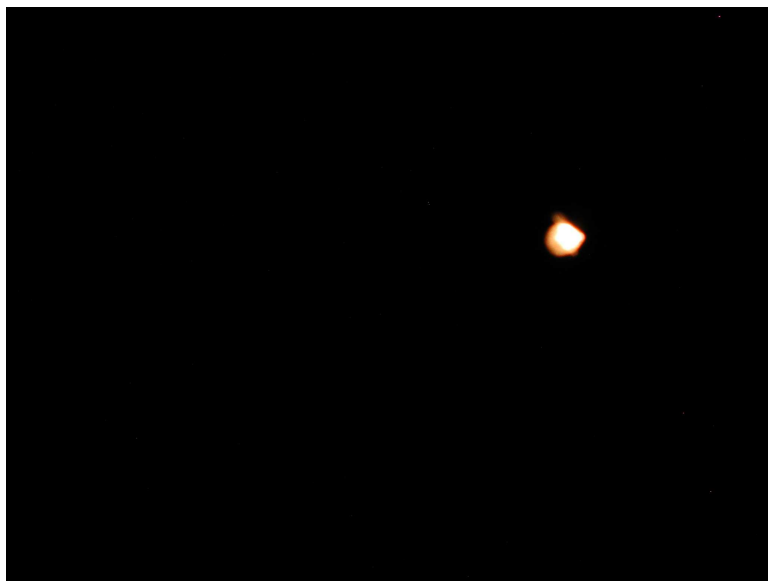


Figure 5.39: Spot image from the glass mirror. The visible diameter is  $\sim 3$  mm.

The intensity  $I(x, y)$  (in ADC counts) detected in each of the  $N_x \times N_y$  pixels is used to construct a quantity,  $P_D$ , defined as the percentage of the reflected light into a circle of diameter  $D$  with respect to the total measured light. The radius of the image at which  $P_D = 0.95$  is the aforementioned spot size, hereafter referred to as  $D_{95}$ . The center of the image is computed using an intensity weighted average of the  $x$  and  $y$  pixels' positions (the so-called "center of gravity").

Neither the center of gravity nor the spot size can be determined reliably if the pixels are saturated. The pixels saturate when the light intensity is too high. On the other hand, it is necessary to have sufficient intensity in order to accurately measure the tails of the intensity distribution. To account for saturated pixels, we developed an algorithm to merge four spot images taken at different light intensities into a single image.

We have applied this technique to both prototype mirrors. Here we show the results for the glass mirror only. Figure 5.40 shows the contribution of each one of the four images to the total one (left), and pixel values distribution across one row (right). Figure 5.41 shows the percentage of the focused light as a function of the spot diameter  $D$ . This method of merging the four images was demonstrated to converge by taking a fifth image at a higher intensity and merging it with the other four images. The resulting  $D_{95}$  value came up consistent with the previous measurement using four images.

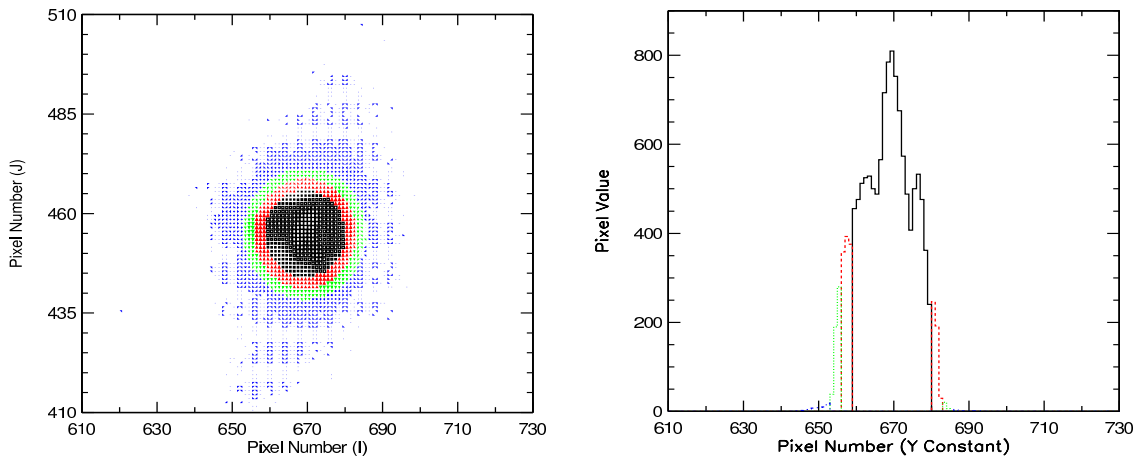


Figure 5.40: Four images merged into one. Two-dimensional spot image (left), pixel value distribution across one row (right). The different images are shown with different line styles.

Using this measurement process, we studied the glass and CF mirrors by measuring the mean radii and spot sizes. The results are summarized in Table 5.2.

The spot-image of the composite mirror (CF) showed 6 spikes (see Fig. 5.42), which are an odd feature not observed with the glass mirror. These spikes could be removed by masking off an  $\sim 5$  cm annulus near the edges of the mirror. Thus, we concluded that the mirror edges had been distorted.

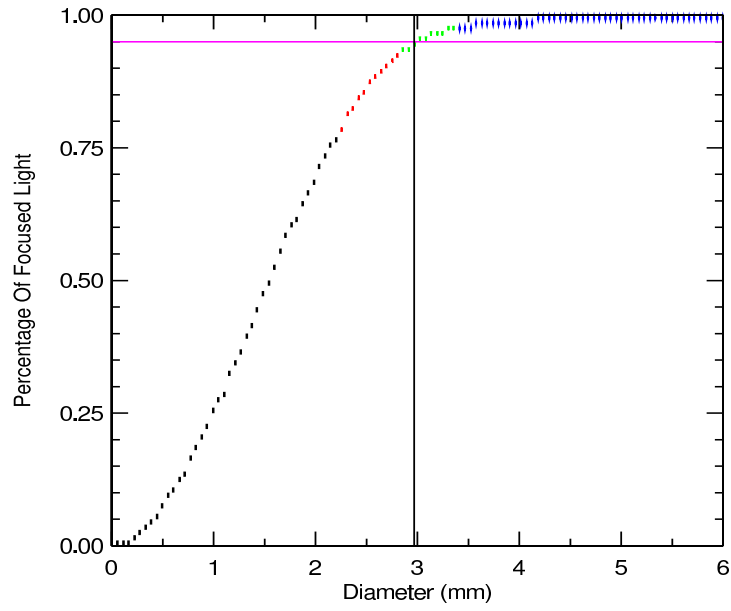


Figure 5.41: Percentage of focused light ( $P_D$ ) as a function of spot diameter..

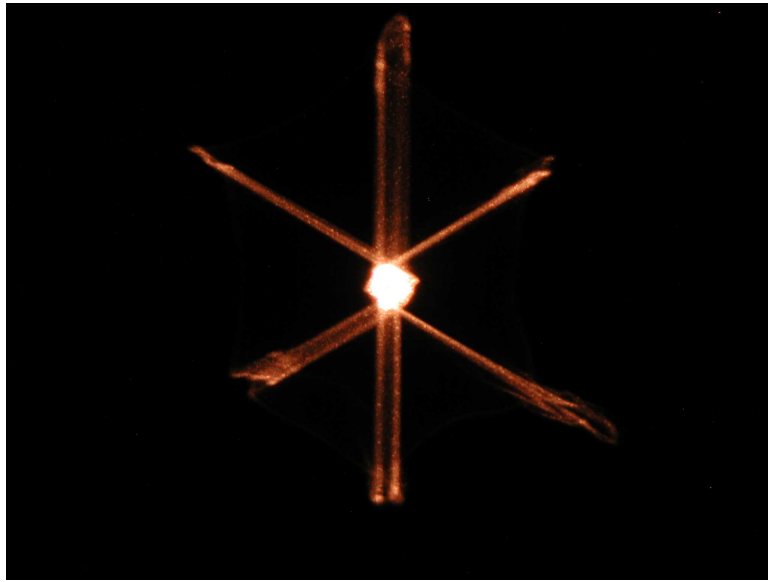


Figure 5.42: Spot image from the composite mirror without hiding the edges.

Table 5.2: Mirror test results.

Firm	Spot size (mm)	Mean radius (cm)
IMMA (Glass)	2.97	659
IMMA (CF)	4.10	648

Similar tests were also performed at a test setup developed by the CERN-TA2 group. The measurements for the glass mirror agree very well, however, for the composite mirror, there seems to be some defects which developed either through some aging effect or through the mishandling of the mirror. Some changes had already been noticed even before their shipment to Syracuse. The glass mirror was used in the test beam of the RICH prototype (Section 5.4.1.5).

#### 5.4.3.2 Mirror Mechanical Support

We currently plan to attach the mirrors to a panel using three kinematic mounts attached to three points. One of these points will be a fixed mount, a second will act as a free mount, and the third will allow pivotal motion (see Fig. 5.43). Table 5.3 shows the composition of each mount.

Table 5.3: Basic mirror mount information.

Components	Material	Fixed Mount	Free Mount	Pivot
Spherical bearing housing	Polycarbonate	✓	✓	✓
Spherical bearing	Polymer	✓	✓	✓
Threaded rod	Aluminum	✓	✓	✓
Nuts	Aluminum	✓	✓	✓
Fixed tap insert	Polycarbonate	✓	x	x
Pivot block	Polycarbonate	x	x	✓
Split pivot block housing	Polycarbonate	x	x	✓
Dowel pin	Polycarbonate	x	x	✓

Prototype mirror mounts have been machined at Syracuse and tests have been done to check the adjustment of all three mounts. We have checked that the positions can be adjusted to the required level of 0.004" and that there is minimal cross-talk. That is, when adjusting one mount point, the other two do not migrate significantly from their set position. A summary of the tests performed is given in Table 5.4. The uncertainty on the mirror mount adjustments and the cross-talk measurements is of the order of the dial indicators precision.

This mounting scheme was successfully used in the test beam of the RICH prototype (Section 5.4.1.5).

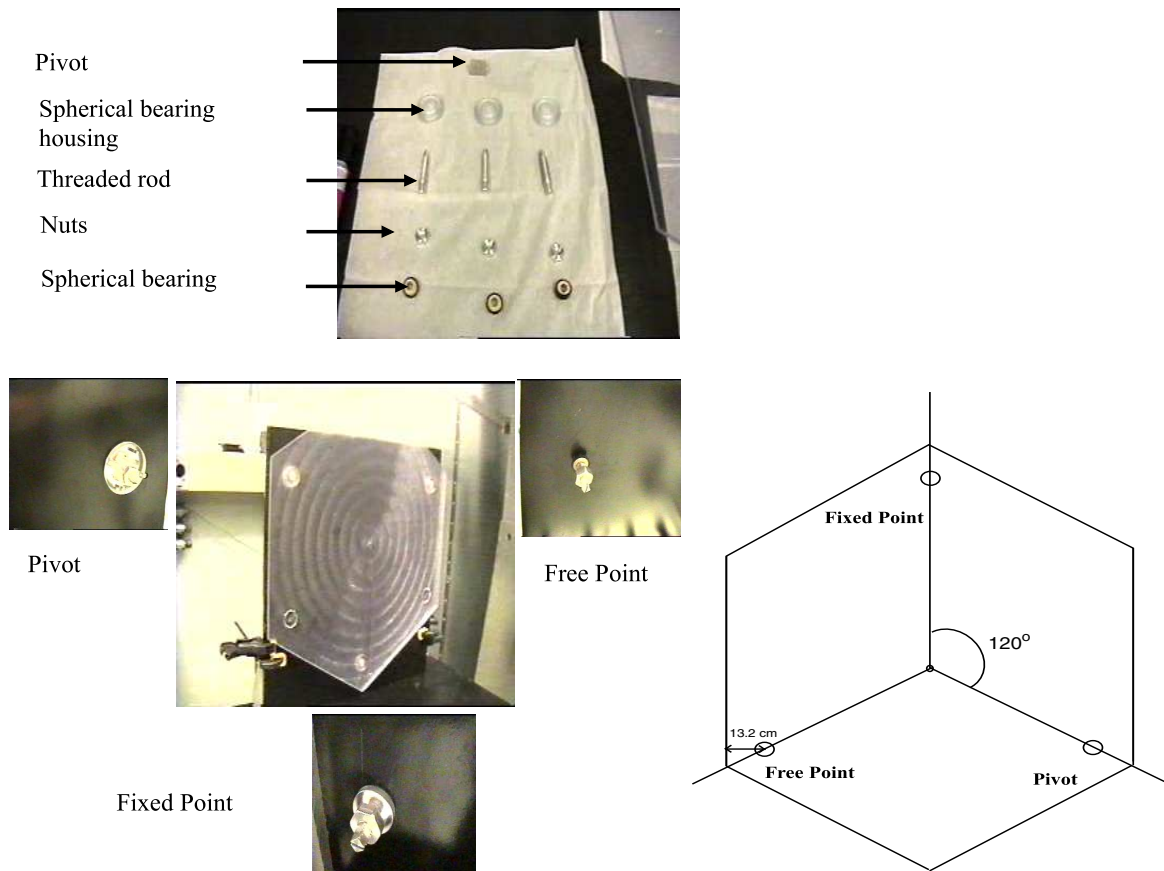


Figure 5.43: Mirror mount components and locations.

Table 5.4: Tests performed on the prototype mirror mount.

	Pivot (A)	Free Mount (B)	Fixed Mount (C)
Adjustment to 0.004"	✓	✓	✓
Cross-talk ( $10^{-3}$ "	Move A by 0.24" $\delta B=3$   $\delta C=2.2$	Move B by 0.3" $\delta A=3.5$   $\delta C=1.2$	Move C by 0.28" $\delta A=-6.0$   $\delta B=-7.0$

#### 5.4.3.3 Ronchi Test Of The Test Beam Mirrors

To probe the mirror quality, we performed a Ronchi test. We used a point source, placed approximately at the center of curvature of the spherical mirror, and a Ronchi grating of 50 lines/inch was used. It was positioned near the focus and in the path of the reflected light. The outcome of this test is a combination of fringes with a shape dependent on the mirror aberrations. These fringes would appear straight if the mirror were perfectly spherical. Any deformations of fringes is the result of deviations from an ideal spherical shape. This test

was done for both testbeam mirrors, where the recorded pictures are shown in Fig. 5.44. For the glass mirror, the image shows clear zonal features (concentric rings), presumably associated with the grinding and polishing of the mirror. Aside from the zonal features, spherical aberration and possibly coma seem to be predominant. For the composite mirror, the aberrations seem to be somewhat irregular with the edge not clearly defined (odd features near the edges are also apparent when looking at the spot image). A spherical aberration is the most likely explanation for this observed Ronchi pattern.

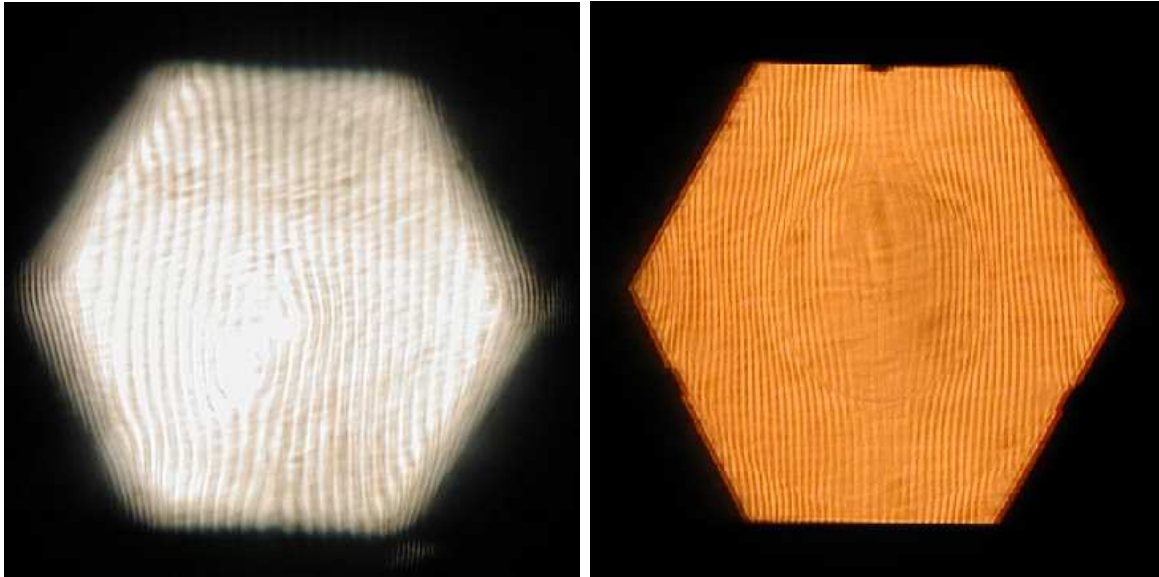


Figure 5.44: Ronchi test for the CF composite mirror (left) and the glass mirror (right).

## 5.4.4 Liquid Radiator

### 5.4.4.1 Liquid Radiator Versus Aerogel Radiator

As discussed in Section 5.3.1, we have determined from a detailed simulation that an aerogel radiator provides poor separation of kaons from protons below kaon radiation threshold (9 GeV/c). The initial simulations of the aerogel radiator neglected backgrounds from minimum bias events and from photon conversions in the BTeV detector components (beam pipe, tracking system, RICH radiators). While an aerogel radiator has been successfully used in the HERMES experiment, their events typically contain only  $\sim 1$ -2 charged tracks as compared to  $\approx 80$ , on average, for the BTeV RICH. Thus, the positive experience with an aerogel radiator in HERMES was found not to carry over into the BTeV event environment. We therefore replaced the aerogel radiator with a  $C_5F_{12}$  liquid radiator. Photons are detected using conventional 3" PMTs which cover the side walls and top and bottom of the vessel (see Fig. 5.1). It should be noted that although some liquid photons do reach the mirror



(about one third), they are imaged outside the instrumented area of the MAPMT planes and therefore do not contaminate the gas ring images.

To determine whether a  $C_5F_{12}$  liquid radiator system could provide adequate  $K/p$  separation, we simulated a RICH consisting of a 1-cm thick radiator and 3" PMTs on the side, top and bottom walls. Simulations of the liquid radiator performance for a sample of low momentum ( $< 9$  GeV/c) kaons and protons are compared to the simulations of the aerogel radiator in Fig. 5.45. For aerogel (top picture) the distribution of protons in the particle identification variable (see Section 5.7.2) is essentially indistinguishable from the distribution obtained for kaons. For the same sample of events and tracks, the liquid radiator (bottom picture) produces a meaningful separation of these two particle species.

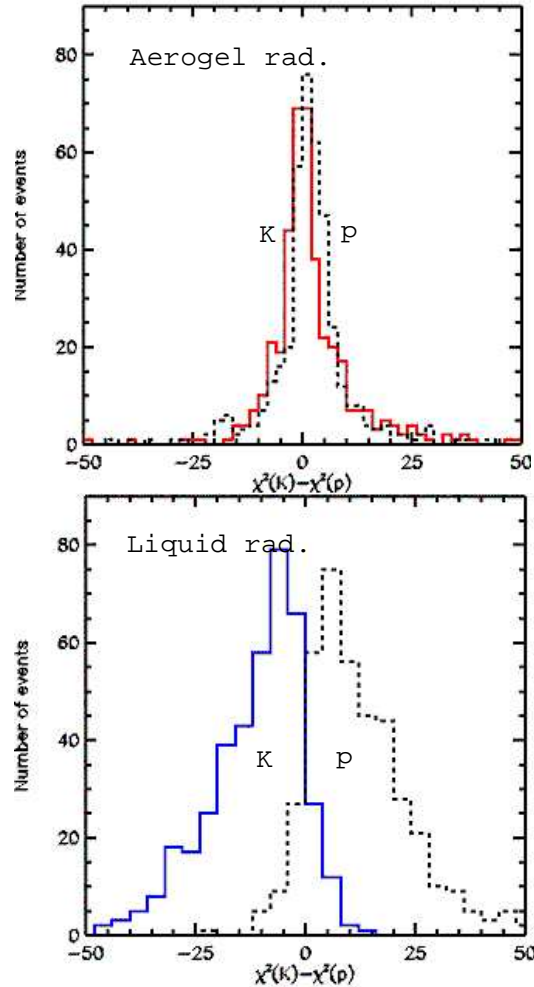


Figure 5.45: Performance of the RICH detector with an aerogel (top) and liquid  $C_5 F_{12}$  (bottom) radiator on a sample of low momentum (4-9 GeV/c) tracks. The events include one  $b\bar{b}$  event and an average of two minimum bias events. Solid histograms show the kaon distribution and dashed histograms show the proton distributions.

We also simulated 2" diameter PMTs which would improve the photon position resolution, but would cost  $\sim 50\%$  more with only a 20% improvement in the total Cherenkov angle resolution per track (5.3 mrad for 2" tube versus 6.0 mrad for a 3" tube). Since the separation is  $\geq 3$  standard deviations using the 3" tubes, they are taken as our baseline choice.

#### 5.4.4.2 Selection of PMT Manufacturer



Figure 5.46: Photograph of 3" 8-stage PMTs from Hamamatsu and Burle.

Because of the large number of PMTs needed, minimizing the cost per PMT is essential. The cheapest PMTs with single photoelectron capability are conventional head-on tubes, with an 8-stage box dynode structure which are produced in large quantities for use in medical applications (Gamma Cameras). With a HV around 1 kV, their gain is on the order of a few times  $10^5$  and they have a collection efficiency well above 90%. A standard bialkali photocathode with a borosilicate glass window provides a peak quantum efficiency around 30%. The dark count rate is orders of magnitude below the level that would impact RICH performance.

At present, we are in contact with four different manufacturers which make such phototubes in a 3" size: Burle, Electron Tubes, Photonis and Hamamatsu (for examples see Fig. 5.46). We have tested sample PMTs from these manufacturers in order to establish single photoelectron detection capability and efficiency loss in a weak magnetic field. All tested tubes showed good separation of the single photoelectron peak from the pedestal in the pulse-height distribution, as illustrated in Fig. 5.47.

A possible mounting scheme using injection-molded fixtures to position a PMT inside the mu-metal shield is shown in Fig. 5.48. We are also considering integration of the mounting fixture with the HV divider board.

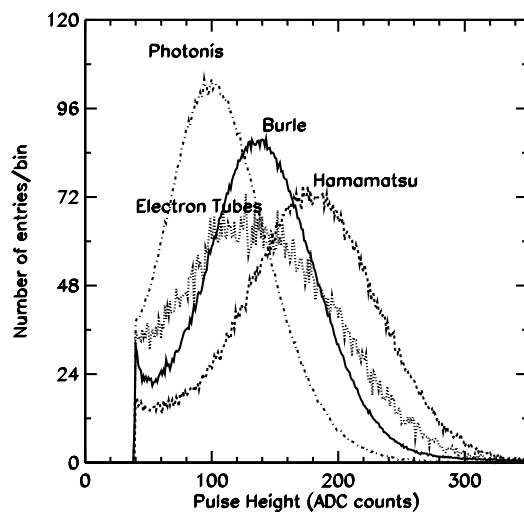


Figure 5.47: Pulse-height spectra obtained with various 8-stage 3" PMTs which are exposed to an attenuated LED light source. The single photoelectron peak is clearly visible for each, with a good peak-to-valley ratio.

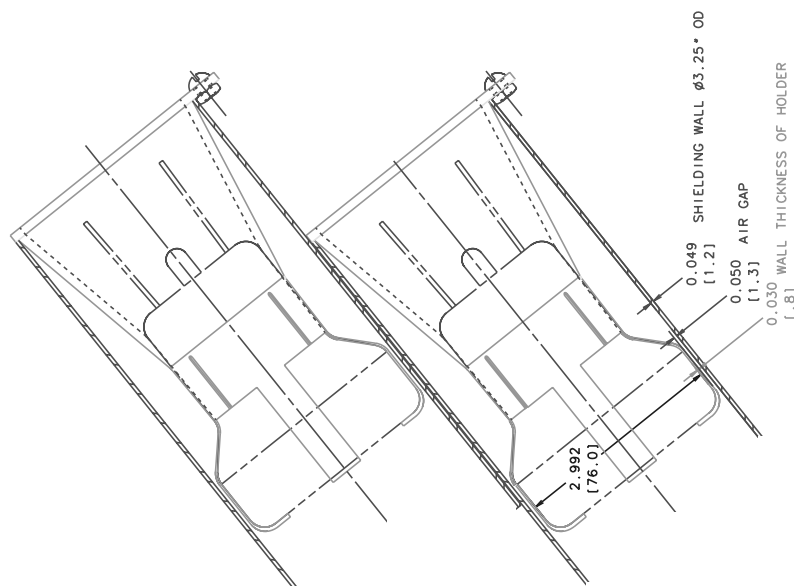


Figure 5.48: Possible mounting scheme for 3" PMTs in their magnetic shields.

Calculations of the fringe magnetic field of the BTeV dipole analysis magnet predict fields up to 14 Gauss in the PMT region. The transverse component of the magnetic field can be easily suppressed by placing the PMTs inside 1 mm thick mu-metal tubes. Shielding of the longitudinal component is more difficult. Simulations were used to determine that we can extend the shielding tubes only as far as 2 cm beyond the photocathode without substantial light loss. Some tubes show more sensitivity than the others, as illustrated in Fig. 5.49. Since cross-calibration of the counting rates between different PMTs has not been done yet, we are not ruling out use of any of these tubes at this point.

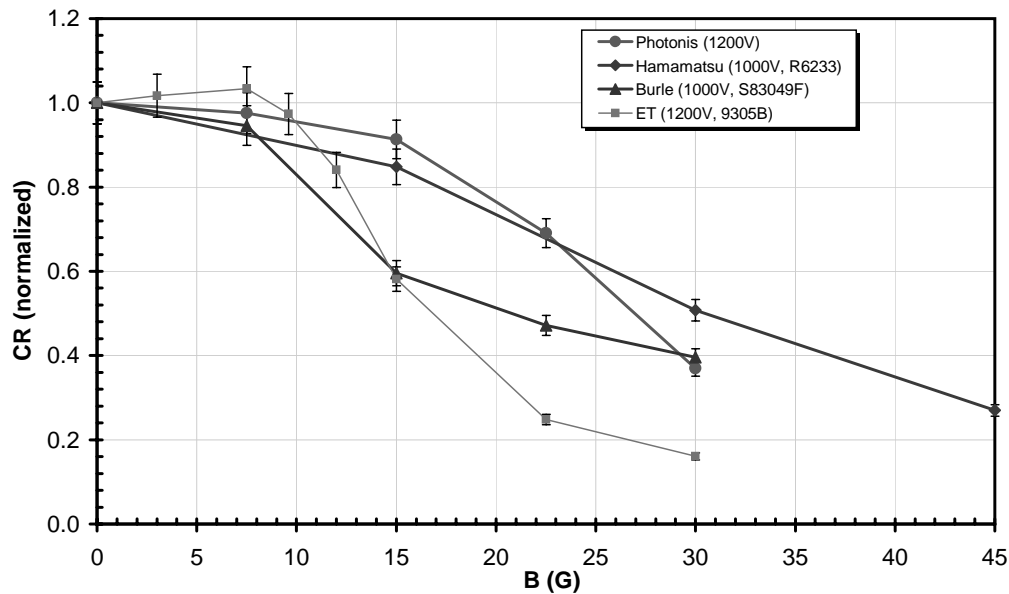


Figure 5.49: Dependence of the counting rate of 3" 8-stage PMTs from various manufacturers on the longitudinal magnetic field, shielded by 1 mm mu-metal tubes extending 2 cm beyond the photocathode. All counting rates were normalized to 1 for no magnetic field applied.

It will be important to compare various PMT models in their single photon counting efficiencies, which factor in the quantum and the collection efficiencies. Since tube-to-tube variation is expected even from a single manufacturer, such studies need to be performed on a large sample of phototubes. We plan to order about 16 PMTs from each vendor, test them on a bench, and later, construct an array that together with the liquid radiator prototype will be studied in a test beam.

We are also exploring with the manufacturers various options for the PMT package. In one scenario, PMTs would be delivered with flying leads. We would develop our own HV divider boards and mechanical support mechanism. It is likely, however, that we will have the manufacturer deliver the tubes already integrated and tested with the HV divider boards.

Another possibility is that the mechanical support would be built into these boards. More interactions with the manufacturers are needed to determine the most cost effective solution, which may be different for different vendors.

#### 5.4.4.3 PMT Readout Electronics

Since the output signals from the liquid radiator PMTs and the MAPMTs considered for the gas radiator will be very similar, we plan to adopt the MAPMT readout architecture (see Sec. 5.4.1) to readout the PMTs as well. One front-end board is likely to serve 64 PMTs, with signal cables soldered on both ends (to minimize costs associated with connectors). A different layout of the input traces to the analog part, or a dedicated interface board will need to be developed.

#### 5.4.5 Radiation Damage Studies

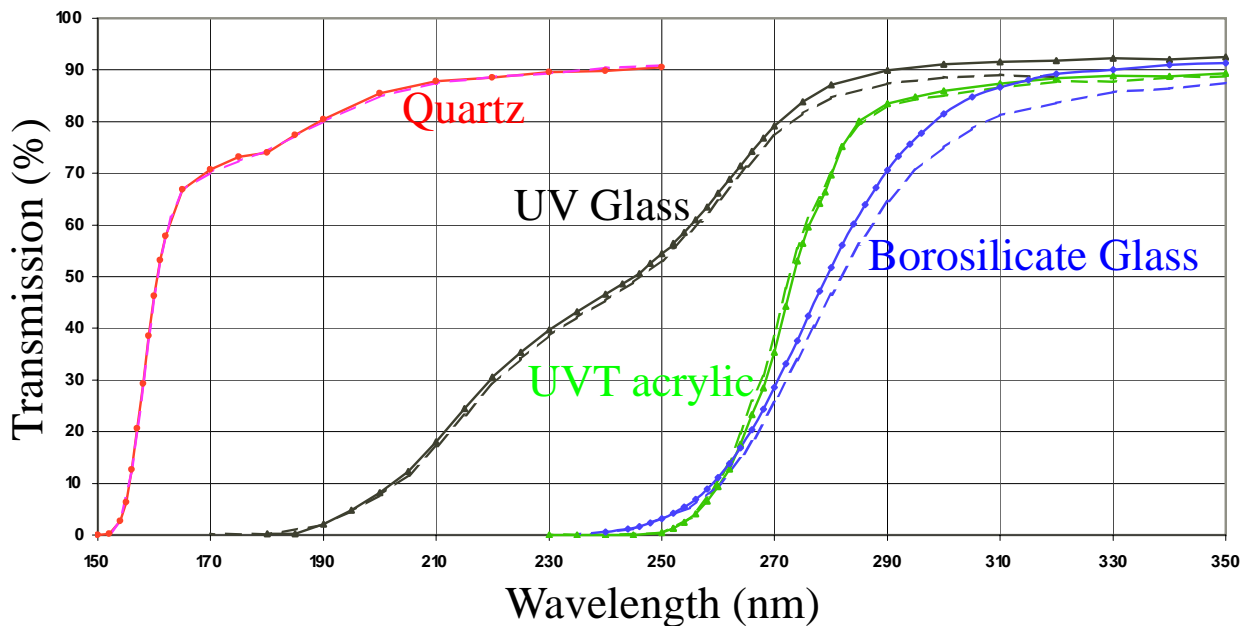


Figure 5.50: Transmission measurements for various samples of window materials for photodetectors before (solid lines) and after (dashed lines) 10-15 krad of radiation. The quartz sample was supplied by Electron Tubes. The UV glass and borosilicate glass window samples came from Hamamatsu. The borosilicate glass from Burle and Photonis gave similar results (not shown).

The photon detectors and their readout electronics are situated beyond the aperture of the detector, and therefore are shielded from the interaction point by the dipole magnet elements. Our simulations indicate that the flux of slower particles bent by the magnet

onto the PMT array will produce a delivered dose of up to 1 krad/year in the hottest spot. Radiation levels in the HPD area will be lower by a factor of 20. We are conducting our own radiation damage studies for PMT windows and materials that we are considering for the gas vessel window (e.g. UVT acrylic). Transmission curves measured at Syracuse for various materials provided by prospective vendors are shown in Fig. 5.50 (solid lines). The samples were exposed to a radiation dose of 10-15 krad by spray from the Tevatron Booster. This dose is equivalent to about 10 years of PMT exposure in the hottest locations (200 years for MAPMT arrays). The spray consists of a mix of moderate energy (an MeV to a few GeV) protons, neutrons and gammas. The transmission curves have been remeasured (dashed lines). The borosilicate glass shows a few percent loss of light (the sample developed a visible tint). A smaller deterioration is observed for the UV glass (the sample from Hamamatsu). No change in transmission properties of UVT acrylic have been detected. The quartz also shows no deterioration, as expected. The samples will be exposed to a higher radiation dose and their transmission will be again remeasured.

## 5.5 Planned R&D

Many of the technical challenges of the RICH have been addressed over the last several years through extensive R&D. Individual components and subsystems of the RICH have been tested on a bench and function in accordance with the design specifications. System integration and tests in realistic beam conditions were initiated with the test beam of the gas RICH prototype, which started in June 2004 (Section 5.4.1.5). Another round of data taking is scheduled for January 2005. A beam test of the liquid radiator system is expected to occur later in 2005.

### 5.5.1 Further Beam Test of the Gas Radiator RICH

A beam test of the gas RICH system, including the gas radiator, a mirror tile and photodetectors started in June 2004. In addition to the system integration, the beam test goals include verification of our calculations for the expected light yield and Cherenkov angle resolution. The initial test beam results are described in Section 5.4.1.5. The first test beam data demonstrated that the MAPMTs with the FE hybrids deliver the expected Cherenkov photon yield. The  $C_4F_8O$  was demonstrated to be suitable gas radiator. The multiplexer boards have not yet been tested in beam conditions. The readout chain, which includes the multiplexer boards is being now programmed and bench tested at Syracuse. It will be tested in a beam in January 2005. Further optimization of the FE hybrid boards to broaden the operating point is also in progress. The next round of data taking will facilitate simultaneous readout of a larger number of MAPMTs and a much improved triggering scheme. Thus, achieved Cherenkov photon yield and angular resolution will be tested with improved sensitivity. The other ongoing R&D effort is focused on the exact design for the mumetal shielding for the MAPMTs.

An alternative HPD-based system has been also developed. We have enough HPDs and FE readout boards in hand to proceed with an HPD test beam if necessary. All elements were tested on a bench and performed well. The HPD test-beam array consists of 15 HPDs. The simulated test-beam data are shown in Fig. 5.51. Only locations along the Cherenkov ring are filled with photodetectors. The HPD mechanical support structure for the test beam has been fabricated and will fit the existing test beam enclosure. Given limited beam access time, we are concentrating on testing and optimizing the MAPMT-based system. If the baseline choice of photodetectors changes, we can resume HPD testing without much delay.

## 5.5.2 Beam Test of the Liquid Radiator RICH

The Syracuse group has dealt with liquid radiators in the R&D work for the CLEO III RICH. Some equipment and radiator prototypes from that work will be adopted for initial studies of the  $C_5F_{12}$  liquid.

The design of the liquid radiator is discussed in Section 5.3.2. One module of the liquid radiator (Sec. 5.5.2) and an array of PMTs (Sec. 5.4.4.2) will be exposed to a test beam in 2005. They need to be connected by a light-tight arm, which does not need to be hermetic since the medium inside can be air. A test box which will support the liquid radiator and the PMTs will need to be designed. The readout electronics will use the same architecture as the MAPMTs, except for the details of the lead connections from the PMTs to the analog front end of the readout chip. These aspects will be addressed in the upcoming year.

In addition to the nominal separation and orientation of the radiator and the PMT array, we will also investigate much larger lever arms to confirm the size of the chromatic effects. Since the test array will contain a much smaller fraction of the Cherenkov image than the full size PMT array, Monte Carlo methods will be used to extrapolate the test beam results to the full detector design.

## 5.5.3 R&D on Mirrors

The design and specifications for the RICH mirrors are discussed in Section 5.3.4. As part of our R&D effort, we are investigating various technological choices. One relatively cheap and well established technology choice is to use a glass mirror. Typical glass mirrors would introduce about 5% of a radiation length ( $X_0$ ) in front of the EM calorimeter. They would also require a heavy support structure. We are therefore investigating alternative mirrors which use lower radiation length materials, such as carbon fiber. Carbon fiber (CF) mirrors as thin as 0.8% of  $X_0$  can be built [14].

To this end, we contacted several US companies (CMA, COI, Hextek, Opticon, GMO) and international companies (St Petersburg Research Institute for Space Optics (Russia), IMMA (Czech Republic)) which are well known to produce both composite mirrors and/or glass mirrors. Price quotations for the full mirror system were obtained from several vendors. The decision of which technology choice is driven by cost and tests performed on sample mirrors obtained from competing vendors. The tests include the spot size and radius of curvature

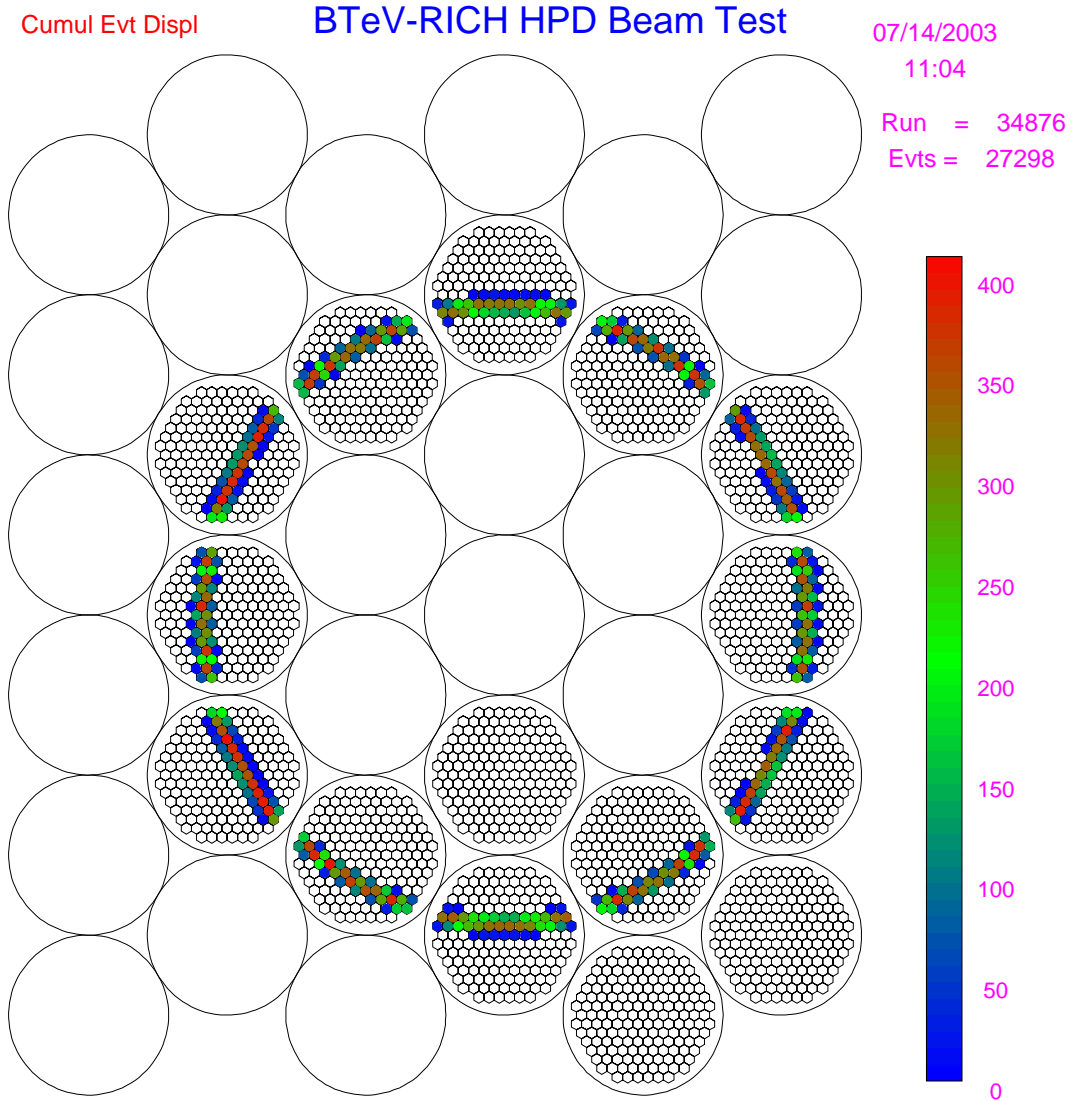


Figure 5.51: Cumulative display for many simulated events for the HPD test beam prototype. Individual pixel location for the deployed HPDs are shown. Filled pixels represent light intensity integrated over a large number of overlapping Cherenkov rings from beam particles. Compare to the test beam data obtained with the MAPMT system shown in Fig. 5.32.



measurements, a Ronchi test, reflectivity, and response to humidity. We will also expose the sample mirrors to radiation at levels of 1 times and 5 times their expected dose, and repeat the above tests. Tests of prototype mirrors from IMMA are described in Section 5.4.3. The glass mirror from IMMA was used in the test beam (Section 5.4.1.5). A prototype CF mirror with smaller radius of curvature than the design value has been recently fabricated for us by CMA. It will be soon tested at Syracuse. If these tests are successful, we will proceed with ordering a full size mandrel and a few mirror tiles with the nominal dimensions.

#### 5.5.4 Mirror And MAPMT Plane Alignment

Proper alignment of both mirrors and detection plane is a complicated task which is important to achieve the required Cherenkov angle sensitivity. In the current design, we have two arrays of spherical mirrors each one having 19 full hexagons (64.2 cm side-to-side), 4 half hexagons and 7 hexagons missing one edge-triangle. These segments will be attached to individual support panels using three kinematic mirror mounts (see Section 5.4.3).

There are two aspects which need to be considered with respect to alignment. First, there is the initial alignment of the mirror array when the detector is installed, and the second is the continuous monitoring of the alignment during the life of the experiment. The initial alignment will depend on whether the pixel system and the straws upstream of the RICH are already installed in the spectrometer. If they are not, we will be able to locate the mirrors in the RICH vessel and align them in their final position. If the upstream detector components are installed prior to the RICH, alignment in place is more difficult.

For the initial alignment, we first mount the mirror array and allow the system to settle (due to its own weight). The LHCb RICH group observed that the main relaxation of their system, especially the screws, occurs during the first 5 days. Of course this depends on the rigidity of the system and if heavy glass or lightweight carbon fiber mirrors are used. The position of the array can be monitored to see when it has finished settling. After it has settled, we first perform a visual alignment of each individual segment followed by a fine adjustment. We envisage two scenarios depending on when the RICH would be installed.

If the RICH is installed prior to the pixel system and upstream straws, the mirror-to-mirror alignment can be done by placing a collimated light source at the interaction point and minimize the spot image off to the side of the magnet. A layout showing the ray optics is shown in Fig. 5.52. Two rays segments, originating from the interaction point, and focused at the radius of curvature, are indicated in the figure. Once the detection plane is installed we can do a global alignment and fine adjustment after installing the monitoring system which is described later in this section.

If the RICH is installed after the pixels and straws, we will likely have to perform the mirror-to-mirror alignment outside the C0 hall inside the RICH box, and then perform a global alignment after moving the whole structure to the C0 hall. In this case the mirror will be put in a thin mylar bag to keep them dry. The fine mirror adjustments can be done after installing the monitoring system, which is described later in this section. For the mirror-to-mirror alignment, we have considered two possible alignment schemes. Both

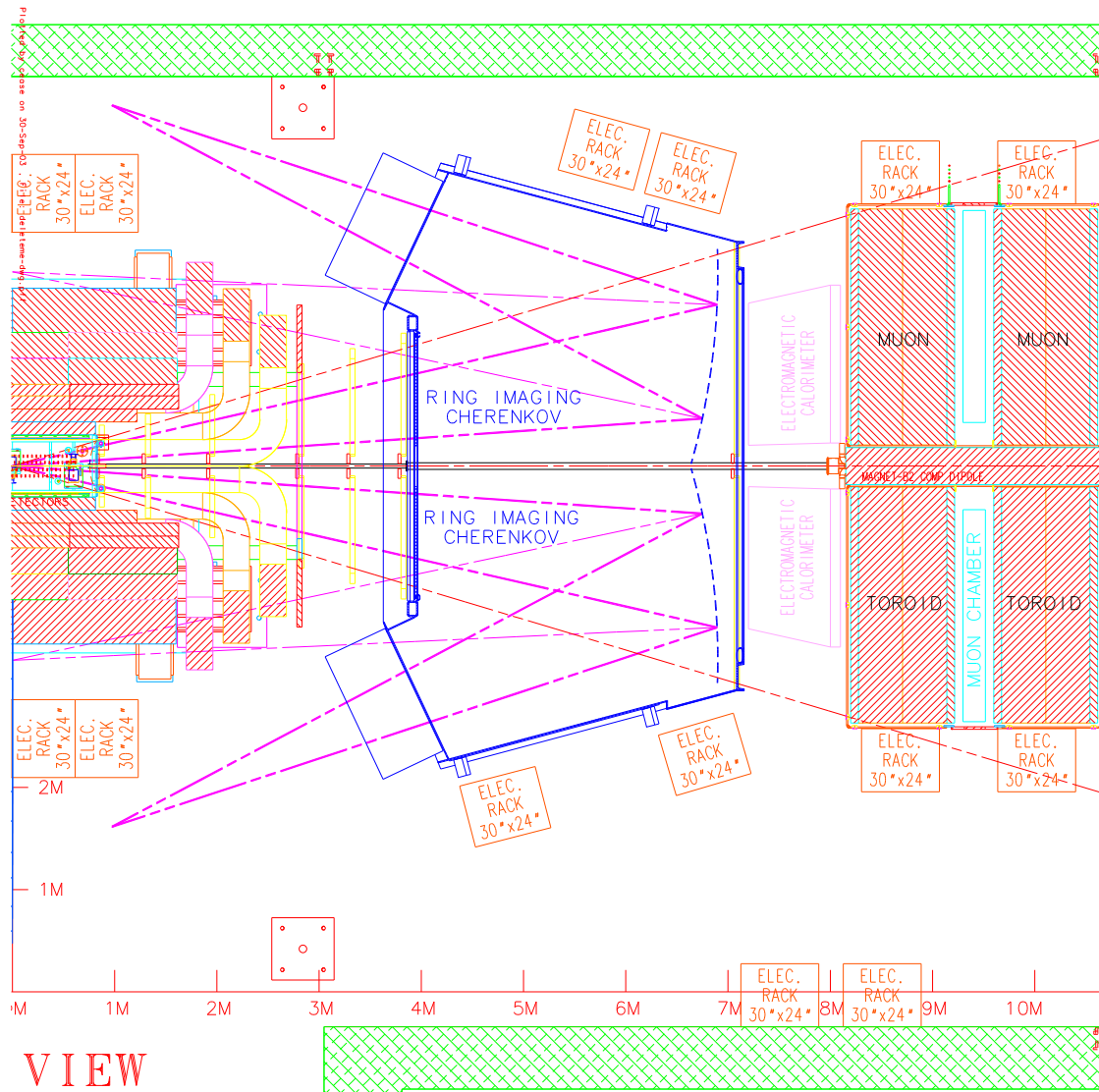


Figure 5.52: Plan view of detector showing optical ray traces which can be used to align each mirror tile.

require roughly 7 meters perpendicular to the mirror plane. The first method requires a point source and a CCD camera. These two will be used for mirror quality testing prior to the installation. As shown in Fig. 5.53, a theodolite will be employed to determine the desired center of curvature of the mirror to be aligned. The center of the point source and the CCD camera are then sited at this point. If the mirror is perfectly aligned, the image of the laser point source will be at the center of the CCD screen. By visual inspection, one can determine the displacement to the order of 1 mm, corresponding to a tilt angle of the mirror of about 0.1 mrad. The alignment can be greatly improved by using an online program which computes the center of gravity of the image. This method provides a continuous view during adjustment. It also allows for monitoring over longer periods of time to check for any possible long-term migration.

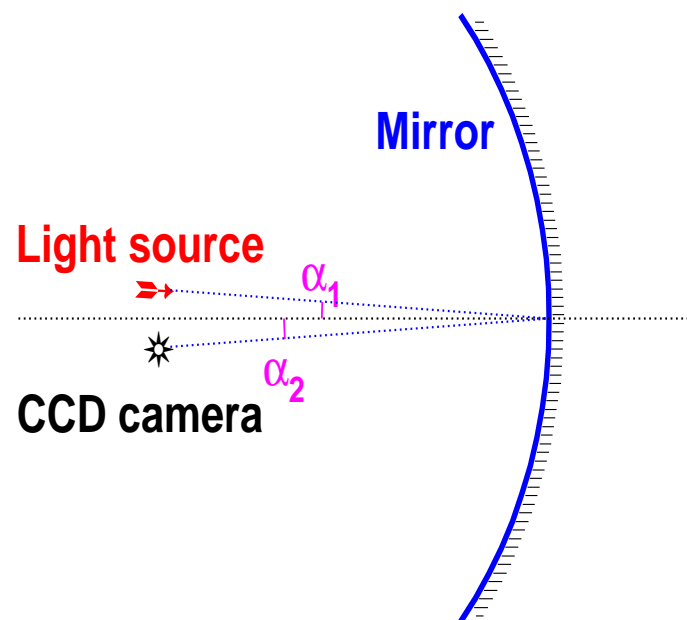


Figure 5.53: Mirror alignment using point light source and CCD camera.

The second method is to use a theodolite directly with the function of “auto-collimation” as shown in Fig. 5.54. This method was used by the COMPASS experiment [15]. The auto-collimation function is for the perpendicular alignment of a plane mirror. It works in a similar fashion for a spherical mirror, since we can place the theodolite at the desired center of curvature. The observer brings a projected reticule into alignment with the standard reticule. Misalignment of the mirror causes the reticules to be displaced with respect to one another. The method could provide much superior precision than the first method.

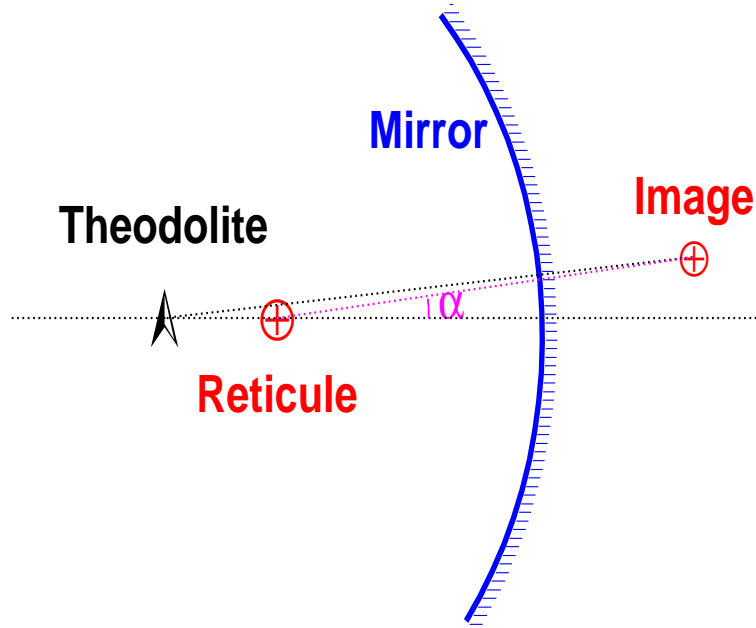


Figure 5.54: Mirror alignment using a theodolite.

Because the alignment of the mirror system is a critical to achieving the required Cherenkov angle resolution, the mirror positions will be monitored throughout the life of the experiment using an online monitoring system.

We can use collimated light sources for each mirror segment and the reflected light can be read out using the MAPMTs (or HPDs). From an optical point of view, the best position of the light source would be at the entrance window. On the other hand we have to minimize the radiation length of material in the detector volume. Another possibility is to attach optical fibers on the corners of the mirrors, and have them directed toward the MAPMT plane so that they mimic reflected photons.

Figure 5.55 shows a possible better solution. This solution entails mounting collimated light sources on the top and bottom of the front window. Simulations show that it is possible to place these LED's in predefined positions and directions so that mirror tiles can be aligned individually. The light source could be an array of LEDs with suitable collimators. The collimation could be achieved using a set of holes drilled into a plate and the angles of the holes could be chosen to illuminate specific mirrors. The hole could be made relatively small to create a relatively narrow beam of photons. In this model, the light hits the mirrors at more of a glancing angle.

Using the readout from the photodetectors, one can track changes in alignment of both the mirrors and MAPMT's. To determine which system has moved (in the case that a

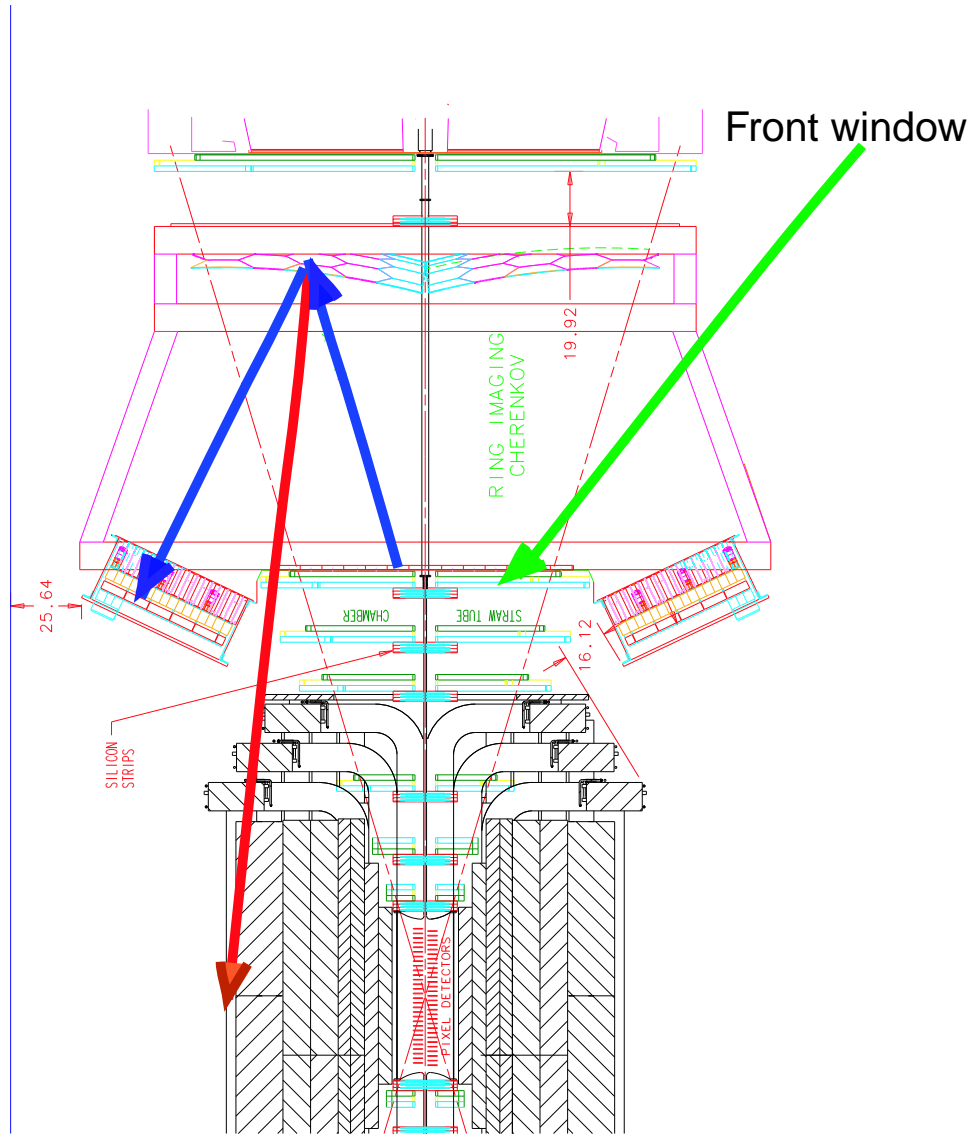


Figure 5.55: Alignment scheme using collimated light sources mounted on the top and bottom of the front window. The arrow originating from the front window represents a focused LED ray which reflects off a given mirror segment and is detected in the photodetection plane.

relative motion is detected), we can have separate light sources for monitoring the MAPMT arrays position. Alternately, we can rely on alignment of the MAPMT plane with the same method as alignment monitoring of support structure described above. The main difficulty of this method is to ensure the direction of the light source is as stable as the detector.

## 5.6 Production Quality Assurance and Testing

The RICH detector is a critical component of the BTeV detector, and it is important that all the major components are thoroughly tested. In some cases, components will be tested at several stages in the fabrication process. In this section we describe the quality assurance and testing which will be done for the primary components of the RICH. In particular, we discuss:

- Photon Detectors for gas system (MAPMTs or HPDs)
- Photon Detectors for liquid system (PMTs)
- Readout Electronics
- Mirror Tiles and Array
- Liquid and Gas Radiators
- Power Supplies
- Cabling
- Cooling System

### 5.6.1 Photon Detectors for Gas System

The single most costly item for the RICH are the photon detectors, and it is therefore critical to ensure their long-term success. In the RICH design, we will be prepared to use either Multi-anode Photomultiplier Tubes (MAPMTs) or Hybrid Photodiodes (HPDs) for detecting photons from the gas radiator. We therefore present both scenarios below. The QA program will progress from basic functionality tests toward a configuration which resembles true detector operation. The tests will be performed at Syracuse University, which will have several areas equipped with small to large dark-boxes which will be used for these tests. If necessary, additional test-stands can be constructed and commissioned within a matter of a few weeks.

#### 5.6.1.1 MAPMT Testing

The MAPMT tests will utilize three test stations, two for certification and one for long-term stability. The two stations for certification should reduce potential bottlenecks in the certification process. The basic MAPMT multiplet consists of 16 MAPMTs connected to a voltage divider base board, which is in turn connected to two VA\_MAPMT hybrids. The hybrids are connected to a multiplexer board which interfaces to the PC through a custom PCI interface. MAPMTs are grouped initially according to the measured average gain provided by Hamamatsu. The various test boxes are light-tight and contain the MAPMTs,

hybrids and multiplexer(s) (MUX). Several feedthroughs are used for various cables including low voltage power, MAPMT high voltage, fiber light source and digital I/O cables.

In this first QA station (#1), we illuminate the MAPMTs uniformly using a pulsed LED light source which is connected to a leaky optical fiber. We measure the response of each channel as a function of high voltage (the so-called plateau curve). Fig. 5.56 shows a cartoon of the setup. The PC controls the HV supplies, the LED pulsing system, the DAQ readout and information on the LED current. The LED voltage is tuned to provide about 1 photoelectron on average per 500 ns into each MAPMT channel. The data are immediately analyzed to determine the plateau region for each channel from which a suitable operating point for the multiplet is determined. Assuming the gains provided by Hamamatsu are accurate, the tubes should all plateau within  $\sim \pm 20$  V of one another. Tubes which do not plateau near a common voltage are removed, replaced and retested. All data and summary plots are saved to an electronic logbook. Our initial tests of 52 MAPMTs provided by Hamamatsu showed a clear correspondence between their measured gains and the plateau voltage. We expect this test to take about one hour.

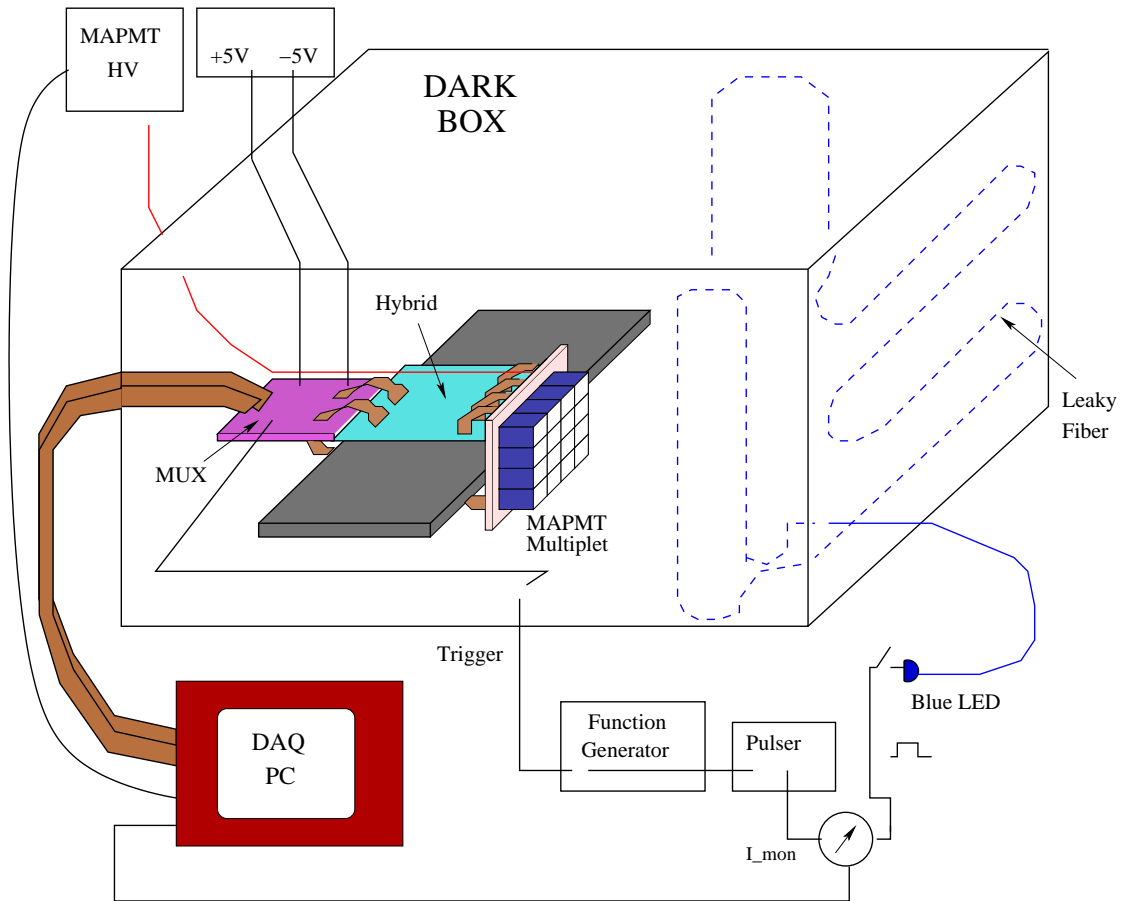


Figure 5.56: Cartoon of MAPMT QA Certification Test Station #1.

In the second QA station, we perform an XY scan to test the uniformity of response across the MAPMT multiplet. QA Station#2 is similar to QA Station #1, except it is equipped with a controllable XY stage to which a single mode fiber and collimator is attached. The LED voltage is set to provide one photoelectron per 500 ns, on average, and the spot size of the fiber on the face of the MAPMT is about 100-200  $\mu\text{m}$ . With the HV and threshold fixed, we measure the response of all channels using a scan grid of 32x32 points. Using a pulse rate of 10 kHz, 500 ns width, and a 5 second sampling time gives a response of around 20,000 counts. An offline program will provide quick feedback on the uniformity of the MAPMT multiplet. All data and summary plots are saved in the electronic logbook. The time required at QA Station#2 is about 3 hours, which includes an hour of setup and breakdown. We therefore estimate a total of 4 hours for the certification testing.

In the long-term testing (ie., burn-in), we form a larger multiplet, which consists of a  $49 \times 4$  array of MAPMTs. Prior to attaching the MAPMTs/baseboard assembly, the hybrids, MUX's and cooling lines are attached to the channel. The entire assembly is about 5 feet long and is placed in a large darkbox containing feedthroughs for the low and high voltages, communication cables, cooling and the light pulsing system. The entire array is illuminated using a leaky optical fiber and read out via the DAQ PC. We monitor the LED current and the response of all channels as a function of time over the course of about 2 weeks. The average and RMS count rate are monitored for stability with respect to the LED current (and hence light output), which may vary slightly with time. A change in the LED light output is also characterized by an increased response of all channels, and is therefore straightforward to diagnose. Once the array has passed the burn-in test at QA Station#3, it is stored with all of its associated electronics in a designated storage area. Tubes which do not exhibit stable behavior are replaced with spare tubes which have passed certification testing, and the channel is retested.

#### 5.6.1.2 HPD Testing

The issues for the HPD testing are similar to the PMTs. The initial tests of the HPD will be performed on each device as a single unit. The data from each step will be recorded in an electronic logbook for ease of tracking the testing history for each tube. The initial tests on the HPD include:

- **High Voltage and Silicon Bias Checkout:** In this first test, the HPDs will be placed in a mu-metal shield and the 3 high voltages (20 kV, 19.89 kV and 15.8 kV) and the silicon bias voltage will be applied. The current draw on each supply will be monitored to make sure it's stable and within specification. The HV supplies are expected to draw almost no current, and the silicon bias typically draws 10 nA of current, and should not exceed 20 nA.
- **Photocathode Sensitivity Test:** Here, we want to demonstrate that the photocathode is sensitive to single photons. The HPD face is illuminated using a blue LED located precisely 6 in. from the front face and centered at radius  $R=0$  with respect to the



center of the tube. The current through the LED will be set to a predetermined value and the current drawn in the silicon bias supply and the hit pattern will be recorded.

- Focusing Test: The goal here is to demonstrate that the electrostatic focusing is working properly. This test will consist of an XY scan of the face of the HPD using a blue LED and optical fiber. A total of 163 points are used in the scan, and each point should illuminate (primarily) a single pixel. An offline program quickly analyzes the data to check that the inferred position of the light source based on the responses of the pixels is consistent with the position provided by the readback of the XY stage. The program will also compute the RMS spread in positions of hits and this should be consistent with the expected spread.

The aforementioned tests will be carried out in the Quality Assurance Test Station shown in Fig 5.57. We expect these certification tests to take about 3-4 hours per tube.



Figure 5.57: HPD Quality Assurance Test Station.

Once the tubes have passed these single tube tests, a HEXAD, consisting of six HPDs in a hexad structure will be produced and tested (see Fig 5.21). The hexad will be in its mu-metal beehive mounting structure by this point. The hexad is mounted in a burn-in test box. The burn-in test-stand will be equipped with the VA\_BT<sub>e</sub>V readout electronics and controlled using LabView. The six HPDs will be each pulsed with a blue LED and read out. This test will run continuously for 2 weeks, and we will monitor the following quantities:

- Current through each LED
- silicon bias current

- current draw on HPD high voltages
- Count rate per pixel
- RMS variation in count rate per pixel

The data for these runs will be stored in a file which will be retrievable through the electronic logbook.

### 5.6.2 Single Anode PMT Tests for Liquid System

The single anode PMTs are used for the liquid radiator system. The QA tests are analogous to those for the MAPMTs, except we expect that a single test box for certification will be sufficient. If we need to parallelize the certification testing, we can implement a second test box within a month. For the certification test box, we use two separate LEDs, one connected to a diffused light source and a second connected to a single mode optical fiber on an XY stage, each selectable via an external switch. Thus, we are able to provide either a diffused light source, or a narrow point source for XY scanning. The mechanical unit for the 3" PMTs consists of an 8×8 array of PMTs, which are grouped according to the manufacturers measured gain. The array is pre-assembled with the PMT HV leads connected to a local HV distribution and the signal cables already route to a 64-channel hybrid. The array will be mounted in the vertical orientation and illuminated using one either the diffuse light source for plateauing the tubes or the collimated source for XY scanning. The readout follows the same scheme as the MAPMTs, except each MUX accomodates up to four hybrids, instead of two. As with the MAPMT, we first measure dark-count subtracted response as a function of HV and confirm that all the tubes in the group of 64 plateau at a similar voltage (within  $\sim \pm 20$  V). Once the tubes are plateaued, we switch to the second LED and perform an XY scan. The grid will provide 14 points per tube, for a total of 896 scan points. As with the MAPMT array, we expect this to take about 4 hours for this certification testing.

### 5.6.3 Readout Electronics

The Syracuse group is responsible for developing the front-end readout for the photo-detectors, up to, but not including, the data combiner board. The Syracuse group has been collaborating with IDE AS Norway to produce readout chips for the MAPMTs, HPDs, and most recently for the single-anode PMTs. Each board received from IDE AS Norway will undergo a set of functionality tests at Syracuse. The tests will be performed at frequencies of 7.5 MHz and 2.5 MHz, corresponding to 132 ns and 396 ns crossing times of the Tevatron. A database will be established which holds the information on all the boards/channels in the system ( $\sim 165,000$  channels). A photograph of the electronic test station is shown in Fig. 5.58

The QA tests for MAPMT (or HPD) and PMT electronics include:

- Noise test: For each board we perform a noise versus threshold scan. At the nominal threshold, with no photodetector attached, the noise should be zero. Noisy channels are flagged and saved in a database.
- Dead channels: To determine the number of bad channels, if any, we perform a coarse pulse height scan. For the MAPMTs and single anode PMTs, the scan consists of first injecting charge ranging from  $\sim 20,000$  to  $200,000$  electrons in steps of  $20,000$  electrons, and then we inject a charge of  $1$  million electrons. All channels should turn on at a similar level of injected charge, with the exact value depending on the threshold setting. Bad channels are flagged according to whether they fail to turn on at  $2 \times 10^5$  or  $1 \times 10^6$  electrons. The number of dead channels is required to be less than  $2\%$ . The list of dead channels for each board will be stored in an electronic logbook so that we can track each board's history. For the HPD option, a scan range of  $1000$ - $5000$  electrons is used, which covers the signal region of the HPDs.

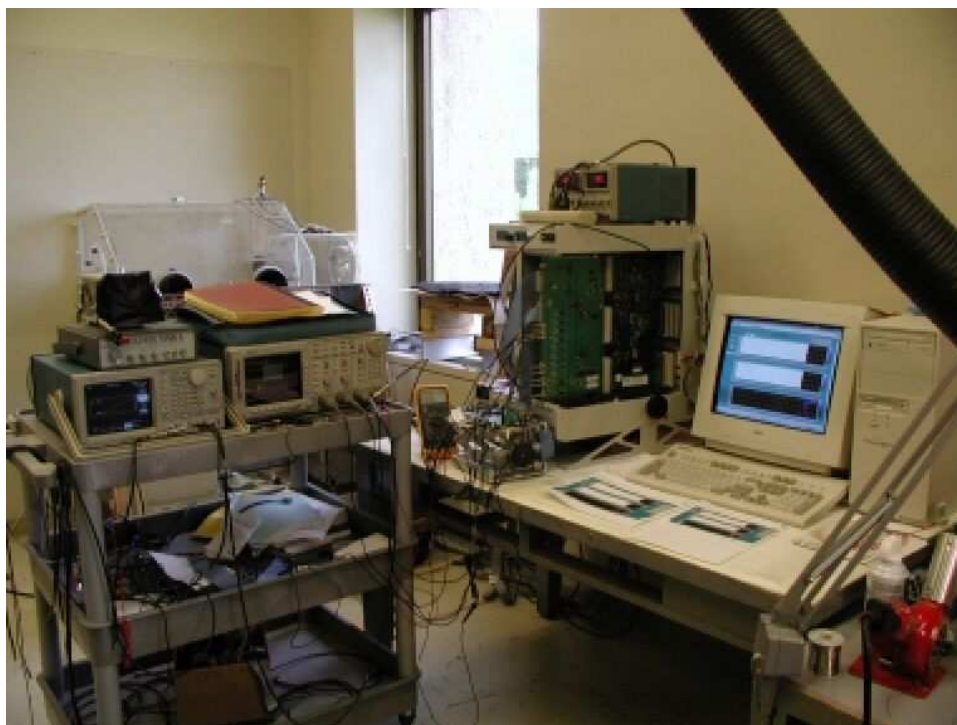


Figure 5.58: Test-stand at Syracuse University for testing front-end electronics.

We expect the testing to take about 40 minutes per hybrid.

### 5.6.4 Mirror Tile testing

The critical tests of mirror quality are that the radius of curvature and spot size are within specifications. A description of these tests are given in section 5.4.3. The mean radius of all mirror tiles must lie  $697 \pm 3$  cm, and the maximum shift of any tile from the mean is allowed to be within  $\pm 3$  cm. We also demand that the spot size is less than 2.5 mm. Simulations show that with this spot size requirement, the loss in Cherenkov angle resolution is less than 5%. For each mirror, we will also perform a Ronchi Test, as described in section 5.4.3. As shown in Fig. 5.44, an undistorted mirror will yield an image of the mirror with a vertical pattern. Lines bowing inward or outward indicate that the mirror is parabolic or too flat. A visual inspection of the Ronchi pattern will be performed and a digital image will be recorded for each mirror tile and stored in an electronic database. We may also choose to perform a Shack Hartman test on each tile, which can be used to measure the small mirror distortions. In our request for quotations, we have asked that each mirror tile be tested using a Shack Hartman sensor. These measurements can then be used in RICH simulations and Cherenkov angle reconstruction.

We also require that the mirror to have an average reflectivity of  $\geq 90\%$ . The average reflectivity will be measured by scanning a collimated light source over the surface of the mirror and comparing the light yield collected by a PMT to the value obtained in the absence of the mirror.

### 5.6.5 Liquid and Gas Radiators

Syracuse University and Fermilab will be responsible for the design, procurement, assembly and testing of the gas and liquid radiators. This includes all the accessories, including monitoring devices and controls. Syracuse will be responsible for all aspects of transmission tests on samples from several vendors. Syracuse University has available a spectrophotometer which is capable of transmission measurements down to  $\sim 150$  nm, well below our sensitive region (see Fig 5.59). The custom-built system consists of a Hamamatsu Deuterium lamp, Oriel chopper, McPherson monochromator, Varian vacuum pump, vacuum-tight sample volume with provision for x-y movement of the sample and readout electronics. The system is driven by a Labview-based DAQ. Fermilab will provide the necessary engineering expertise for design of the vessels and the recirculation systems. The system will be reviewed by physicists and engineers from Fermilab.

### 5.6.6 Testing of High and Low Voltage Power Supplies

The power supplies will also need to be put through some rudimentary tests to ensure their reliable operation. These tests will be the responsibility of Fermilab. The power supplies will be tested using a passive-load board which will provide resistive loads which are comparable to the loads they will experience during data taking. Separate boards will be produced for the low voltages ( $\sim 5$ V), the MAPMT/PMT voltages ( $\sim 1000$ V), and the HPD high voltages if

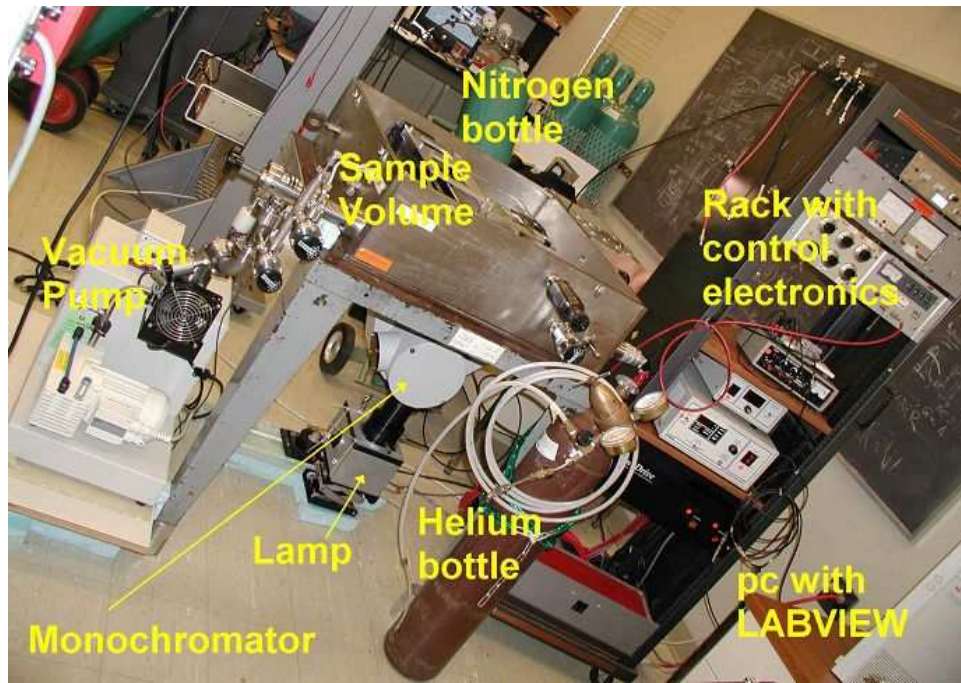


Figure 5.59: Transmission measurement setup.

necessary ( $\sim 20$  kV). These board will have jumpers or switches which will allow for different loads to be connected to the power supply. Two additional resistors,  $R_{alarm}$ , and  $R_{trip}$ , will be used to provide loads which, in the first case, should cause the power supply to go into an alarm state, and in the second, cause a power supply (PS) trip. The following tests will be performed:

- Measure the actual voltage versus the set voltage. Confirm that  $V_{set} = V_{actual}$ .
- Confirm that the readback (monitored), voltage ( $V_{mon}$ ) also agrees with  $V_{set}$ .
- Measure the current as a function of applied voltage (confirm that it's linear over the full range of the PS), *i.e.*, no sagging of the PS.
- Measure the readback (monitored) current  $I_{mon}$  as a function of the actual current ( $I_{actual}$ ).
- Confirm that the PS alarm circuitry is working properly by connecting in  $R_{alarm}$ .
- Confirm that the PS trip circuitry is working properly by connecting in  $R_{trip}$ .
- Check that the PS reset circuitry is operating properly. The reset circuitry re-enables the PS so that it may be turned back on after a trip.

- For silicon bias supply (HPD option only), measure the ripple on the 60V PS and make sure it is within specifications.
- Check that the PS is floating. The power supplies will likely be required to be floating with an optional jumper to connect the V- to ground.
- Confirm that the power supplies ramp up to the set voltage properly.
- Check that the ripple on the HPD 20 kV PS is within specification.
- Each PS will then be connected to a load board for 1 week and the output voltages and currents will be monitored for stability. The PS voltages and currents are required to be stable within specification.

### 5.6.7 High and Low Voltage Cables

The integrity of the high and low voltage cables will be established by Fermilab. Briefly, the concerns are:

- Low voltage Cabling: The primary concerns are shorted or broken lines. After terminating the cables, we will have an automatic cable-tester which indicates open or shorted lines.
- High Voltage Cabling: After cables ends are terminated we will test them at 125% of operating voltage. We will make sure there is no current draw on the cable when it is unterminated at the far end.

### 5.6.8 MAPMT and PMT Electronics Cooling System

The VA\_BTeV electronics generate enough heat that water cooling will be necessary. For MAPMTs, the voltage dividers will also need to be cooled. The single anode PMTs will also need to be water cooled. Syracuse University and Fermilab will be responsible for the design, procurement, assembly and testing of the cooling system and all the accessories, including monitoring devices, cooling lines, and insulation. Fermilab will provide the necessary engineering expertise. The system will be reviewed by physicists and engineers from Fermilab.

## 5.7 Expected Performance of the RICH

Detailed simulations were performed to determine specifications of various detector components as well as the expected physics performance. These various simulations are discussed below.



### 5.7.1 Detector Simulations

Simulations play an important role in developing specifications for various detector components. Both the mirror system and the photodetector systems have used a simulation of the RICH detector to develop specifications and determine the expected performance. Simulation of events are generally handled using a version of GEANT (BTeVGeant) which incorporates the BTeV geometry [19]. The RICH simulation takes from GEANT the list of particles produced and generates photon hits in the photodetectors. The RICH simulation accounts for geometrical losses due to acceptance, photo-conversion and collection efficiencies of the photodetectors, optical characteristics of the radiating medium, and reflectivity of the mirrors.

Results from this simulation were used to determine that an aerogel radiator would fail to provide acceptable  $K/p$  separation, whereas a  $C_5F_{12}$  liquid radiator provides  $\geq 3\sigma$  separation (see Section 5.4.4.1). Here we discuss the usage of this simulation in developing specifications for the mirror system as well as its use in comparing different photodetector options.

#### 5.7.1.1 Mirror Simulations and Specifications

The Cherenkov angle resolution which will ultimately be achieved will depend critically on the mirror system. Each of the mirror tiles need to be uniform at a level such that all the tiles together truly focus to at the focal plane. Any errors introduced as a result of the mirrors being imperfect must not contribute significantly to the Cherenkov angle uncertainty.

The requirements on the mirror radius have been investigated by simulating an imperfect mirror system. In particular, we simulate the effects of variations in the mirror radius within a given mirror tile, as well as variations in radii between neighboring tiles. In the latter case, differences in radii can be mostly corrected for in the reconstruction by using the track's momentum and the photon's hit position to determine the most likely mirror from which a photon reflected. By using this particular mirror's radius of curvature in the particle ID likelihood (see Section 5.7.2.1), we in part take out mirror-to-mirror radius variations. Large differences in radius from the nominal value will cause the photons to be imaged in front of or behind the photodetection plane. These effects have been studied using the RICH simulation. In the results presented here, unless otherwise noted, we use the “most likely” mirror radius in the Cherenkov angle reconstruction.

In the first study, we changed the radius of curvature to a fixed value that differs from the nominal value by an amount  $\pm\delta R$ . Figure 5.60 shows the effect on the Cherenkov angle resolution as  $\delta R$  is increased from 1 to 10 cm. The degradation in Cherenkov angle resolution does not become an issue until  $\delta R \geq 3$  cm because  $\sim 75\%$  of the time we are able to determine the correct mirror from which the photon was reflected and assign the correct radius of curvature. Beyond 3 cm, the degradation worsens because the photodetector is far from the focal plane of the mirror. These simulations lead to the requirement that the variation in mirror radii is less than  $\pm 3$  cm. A 4 cm shift variation in the nominal radius produces about a 5% change in the Cherenkov angle resolution per track.

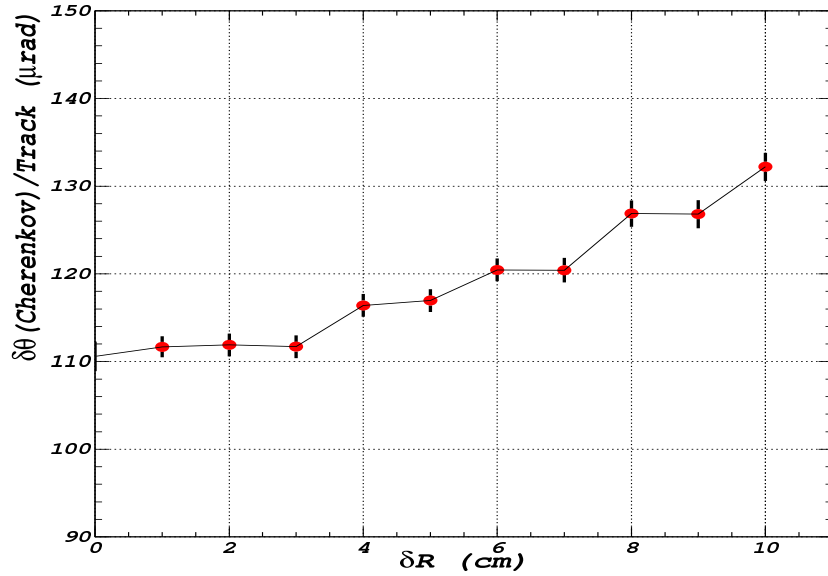


Figure 5.60: Dependence of the Cherenkov angle resolution per track on deviations of the radius of curvature  $\delta R$  from the nominal radius of 697 cm.

The effect on the Cherenkov angle resolution due to variations between neighboring tiles has also been investigated using two different methods. In the first method, we uniformly distribute tracks in a circle of radius 58 cm, so that Cherenkov photons are shared among 7 tiles (based on the default value of the hexagon side) as shown in Fig. 5.61. We then simulate random variations in mirror radii by randomly varying, event by event, the radii of the struck tiles within  $\pm\delta R$ . The effect on the Cherenkov angle resolution is shown in Fig. 5.62.

The worst case scenario occurs, when a track radiates photons which are shared by three mirrors. To probe this case, we generated tracks which pass through one of the corners of mirror #1 (corner A) as shown in Fig. 5.61. We then set the mirror radii as follows:

- Mirror #1 is held at the nominal radius  $R_{nom}$ .
- Mirror #2 is held at  $R_{nom} + 1$  cm.
- We vary the radius of mirror #3 by the amount  $+\delta R$ .

The effect on the Cherenkov angle resolution is shown in Fig. 5.63 (left). The first curve (squares) shows the variation of the Cherenkov angle resolution when varying the radius by an amount  $+\delta R$ , but assuming the nominal radius in the reconstruction. The second curve (circles) shows the same variation when we use the radius of the mirror which was determined by ray-tracing. It is clear that using the proper radius is extremely important.

To understand how quickly the resolution degrades when a track shares its photons with 3 mirror tiles with different radii, we simulated more extreme variations among the mirror tiles. In particular, we simulated the following configurations:



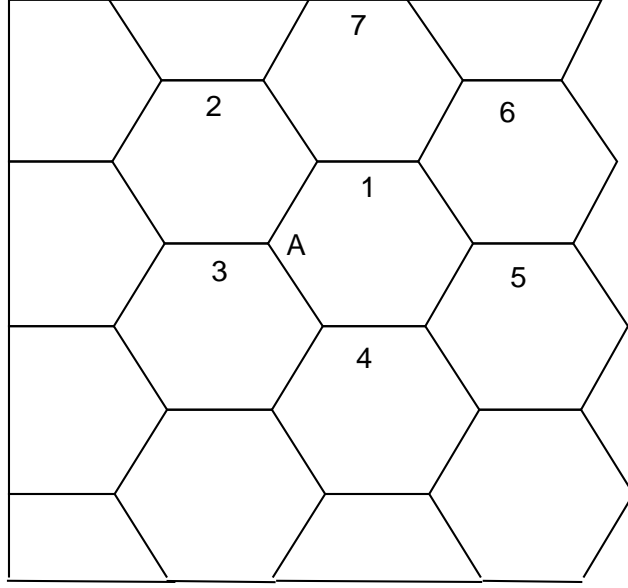


Figure 5.61: The mirror configuration used in the simulation.

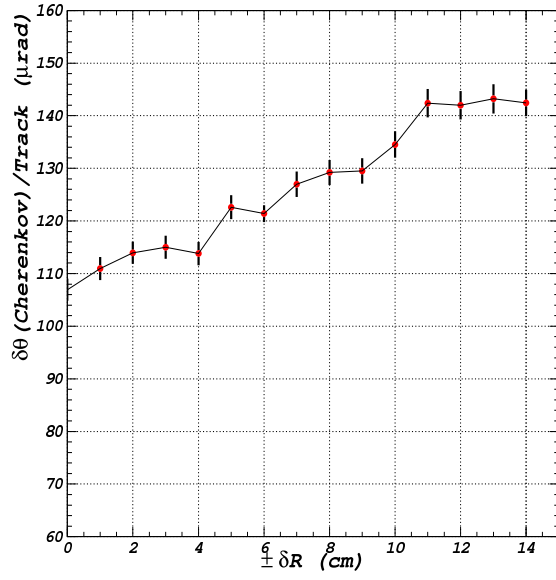


Figure 5.62: Variation of the Cherenkov angle resolution per track for a random variation of the radii of curvature for the 7 tiles.

- Variation #1 (see Fig. 5.63 (right))
  - Mirror #1 is held at the nominal radius  $R_{nom}$ .
  - Mirror #2 is held at  $R_{nom} \pm 3 \text{ cm}$ .
  - We vary the radius of mirror #3 by the amount  $+\delta R$ .
- Variation #2 (see Fig. 5.64 (left))
  - Mirror #1 is held at the nominal radius  $R_{nom}$ .
  - Mirror #2 is held at  $R_{nom} \pm 4 \text{ cm}$ .
  - Radius of mirror #3 is varied by the amount  $+\delta R$ .
- Variation #3 (see Fig. 5.64 (right))
  - Mirror #1 is held at the nominal radius  $R_{nom}$ .
  - Mirror #2 is held at  $R_{nom} \pm 5 \text{ cm}$ .
  - Radius of mirror #3 is varied by the amount  $+\delta R$ .
- Variation #4 (see Fig. 5.65 (left))
  - Mirror #1 is held at the nominal radius  $R_{nom}$ .
  - Mirror #2 is held at  $R_{nom} \pm 6 \text{ cm}$ .
  - Radius of mirror #3 is varied by the amount  $+\delta R$ .
- Variation #5 (see Fig. 5.65 (right))
  - Mirror #1 is held at the nominal radius  $R_{nom}$ .
  - Mirror #2 is held at  $R_{nom} \pm 7 \text{ cm}$ .
  - Radius of mirror #3 is varied by the amount  $+\delta R$ .

In each of these cases, we use the radius of the mirror inferred by ray-tracing in the particle ID likelihoods. Based upon these studies, we require that all the mirror tiles have an average radius of curvature which within  $\pm 3 \text{ cm}$  of the nominal value.

We also investigated requirements on the *spot size*. The spot size is defined to be the diameter of the circle in which 95% of the light reflected from the entire mirror is focused. Unfortunately, a requirement on the spot size may not guarantee that the mirror's distortions can be neglected. In particular, the effect on the Cherenkov angle resolution will depend on whether the distortions are random or correlated. For instance, point-to-point correlations may degrade the Cherenkov angle resolution more than similar magnitude random variations. We therefore have studied how various aberrations contribute to the spot size. In this study, we simulate the spot size the same way we measure it, that is, on-axis. The effect of

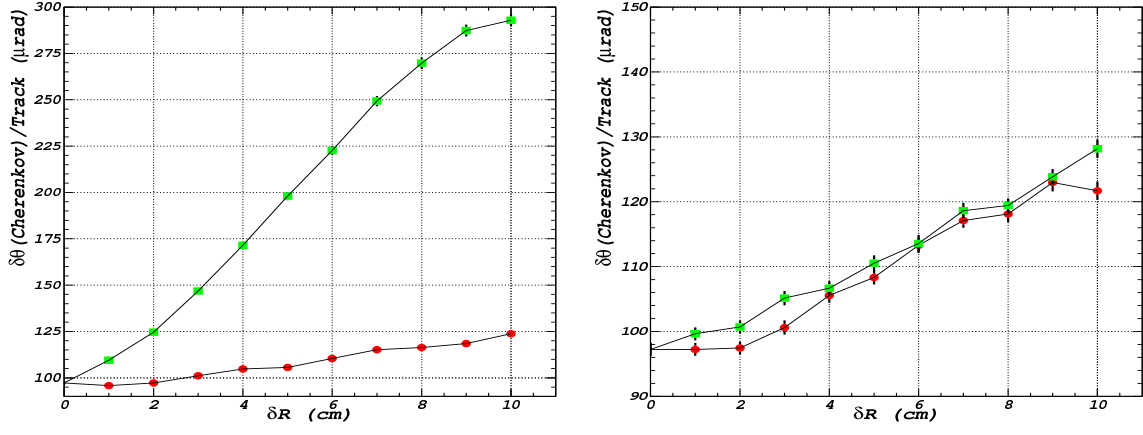


Figure 5.63: Left plot shows the variation of the Cherenkov angle resolution per track for different radii of Mirror#3. Squares show the results if we use the nominal radius (697 cm), and circles show the results when we use the inferred radius of the struck mirror tile. The right figure shows a comparison in the Cherenkov angle resolution for +3 cm (circles) and -3 cm (squares) shifts in the nominal radius (but using radius of inferred mirror tile in the reconstruction).

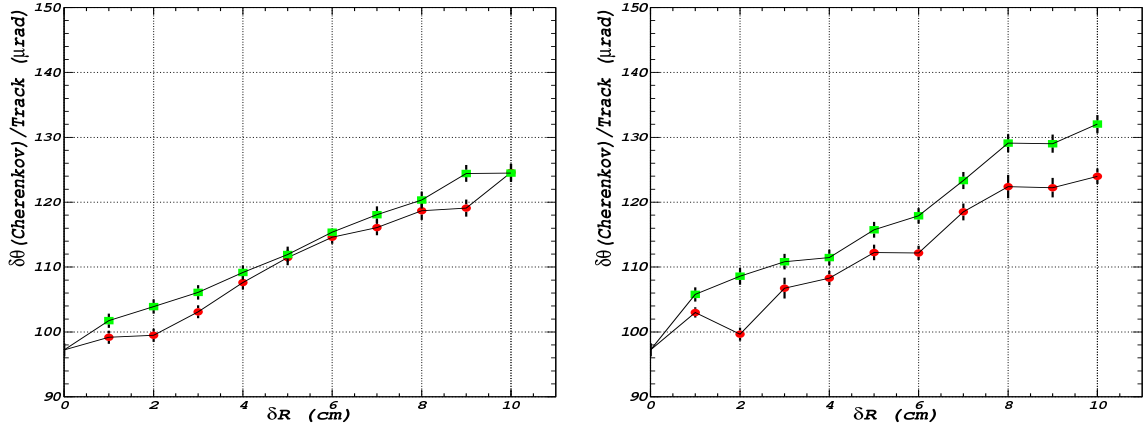


Figure 5.64: Same as in Fig. 5.63 (right), except we shift mirror #3 by  $\pm 4$  cm (left) and  $\pm 5$  cm (right).

the aberration is then propagated off-axis to simulate the effect on the Cherenkov angle reconstruction.

We generate a spot image using a wavefront expansion,  $W(x_m, y_m)$ , which is defined to be the difference between the real surface and the perfect spherical surface, in terms of Zernike polynomials. If we define the normalized coordinates,  $x_m$  and  $y_m$ , of the photon hit on the mirror as shown in Fig. 5.66, the deviations  $\Delta X_D$  and  $\Delta Y_D$  (see Fig. 5.67) of the photon hit on the detection plane from its ideal position (if the mirror surface was perfect) are then proportional to the derivatives of the wavefront  $W(x_m, y_m)$  via the following equations:

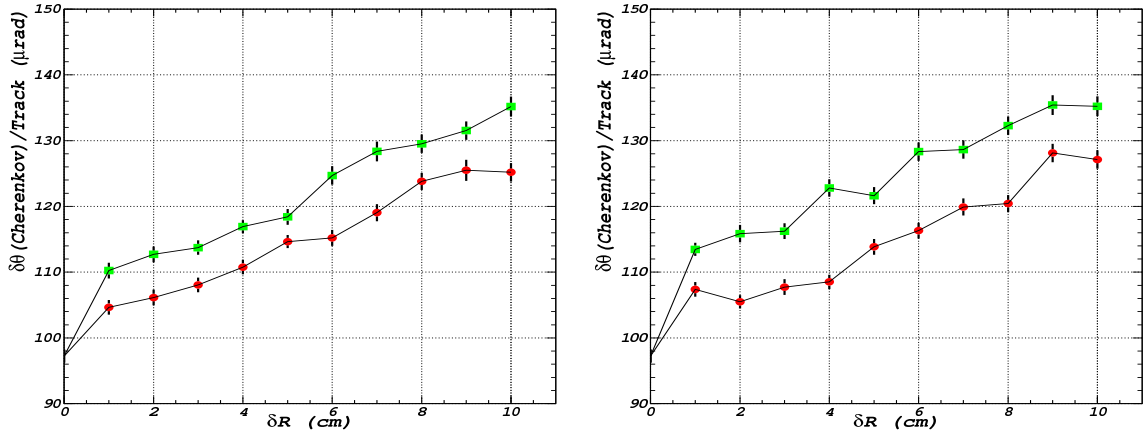
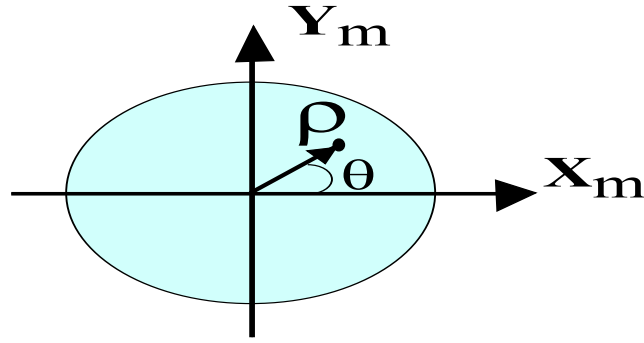


Figure 5.65: Same as in Fig. 5.63 (right), except we shift mirror #3 by  $\pm 6$  cm (left) and  $\pm 7$  cm (right).

$$\begin{aligned}\Delta X_D &= -d \cdot \frac{\partial W(x_m, y_m)}{\partial x_m}, \\ \Delta Y_D &= -d \cdot \frac{\partial W(x_m, y_m)}{\partial y_m}.\end{aligned}\tag{5.2}$$

Here,  $d$  is the distance between the detection plane and the mirror. These deviations are used to measure both the spot size and the Cherenkov angle resolution.



**Mirror Plane**

$$\begin{aligned}\mathbf{X_m} &= \rho \cdot \cos(\theta) \\ \mathbf{Y_m} &= \rho \cdot \sin(\theta)\end{aligned}\quad \text{where,} \quad \begin{aligned}0 &< \rho < 1 \\ 0 &< \theta < 2\pi\end{aligned}$$

Figure 5.66: Definition of the normalized photon hit coordinates on the mirror.

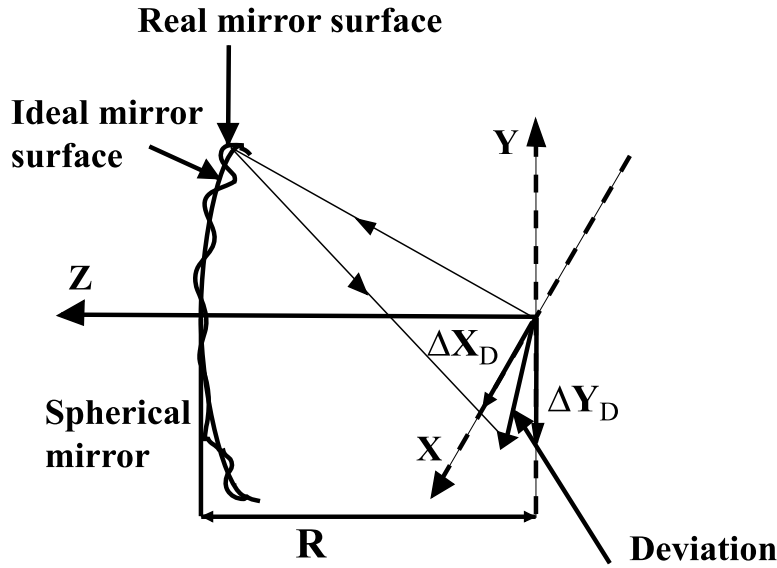


Figure 5.67: The deviations,  $\Delta X_D$  and  $\Delta Y_D$  from the ideal image position as a result of an imperfect spherical mirror.

The generation of the spot image using this wavefront can be done either as a random variation of the reflection angle or as a function of some specific aberrations. Figure 5.68 shows the variation of the Cherenkov angle resolution per track for different spot sizes. For random variations (filled points), there is a nearly linear correlation between Cherenkov angle uncertainty and spot size. We also show in Fig. 5.68 the simulation results of the first few Zernike terms that have non-negligible contribution to the Cherenkov angle resolution per track, see table 5.5 for a list of the Zernike terms. Shown are the effects from (mis)focusing and spherical aberration (top left), effects of coma (upper right) and secondary astigmatism (bottom). It is observed that these correlated aberrations degrade the Cherenkov angle resolution per track more than random variations. In each figure we also show the effect of random variations. We therefore conclude that for a given spot size, random variations generally give an optimistic Cherenkov angle uncertainty. Correlated aberrations produce a significantly larger error in the Cherenkov angle for a given spot size. Although other aberrations contribute to the spot size, their effect on the Cherenkov angle resolution per track is found to be negligible. To ensure that the correlated aberrations do not degrade the Cherenkov angle resolution by more than 5%, we require that the spot size is below 2.5 mm. If the spot size is larger than 2.5 mm further analysis is required to understand the types of aberrations which exist and their contributions to the spot size. This can be done by analyzing the wavefront and determining the magnitudes of the Zernike coefficients.

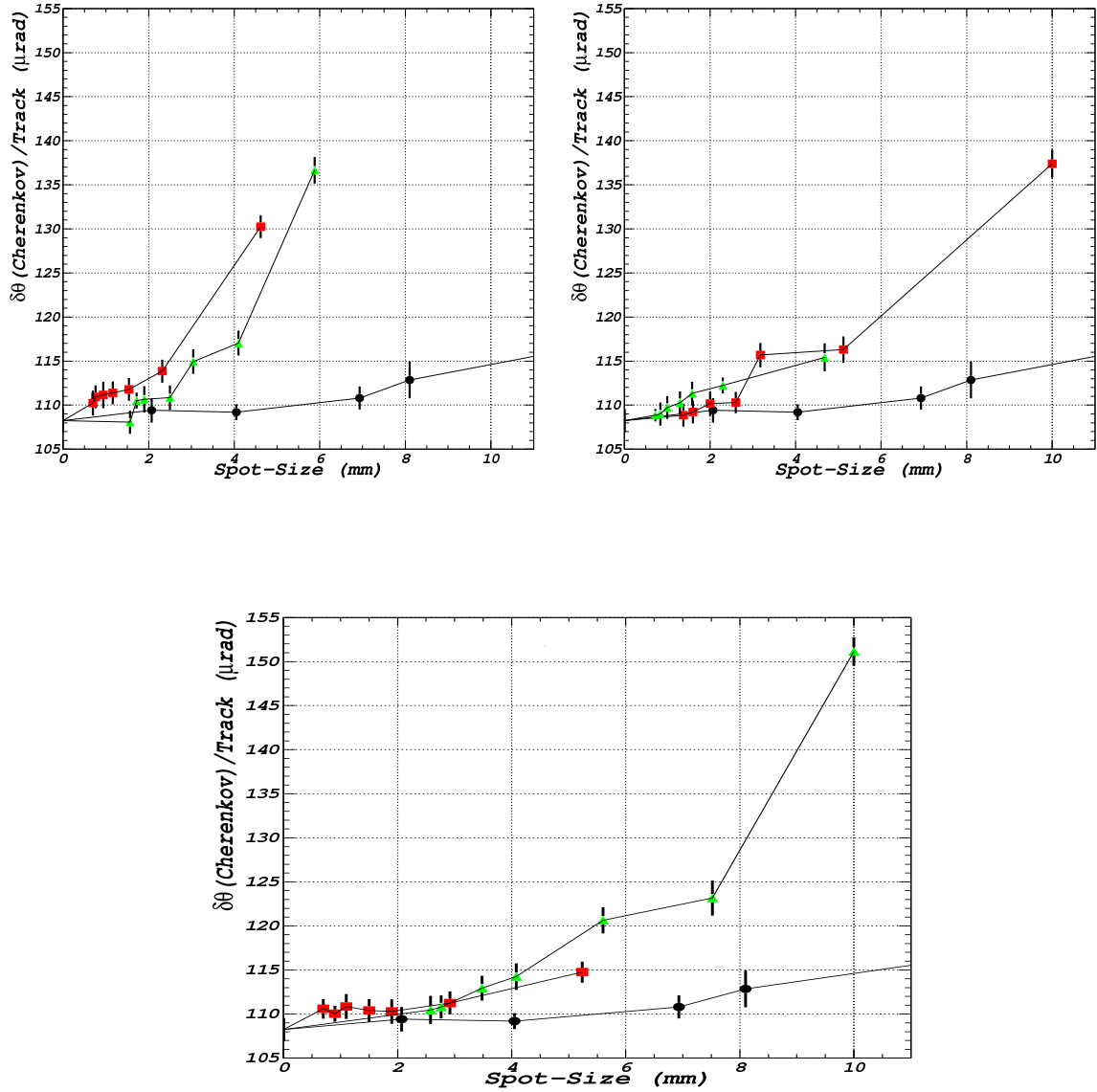


Figure 5.68: Variation of the Cherenkov angle resolution per track for different spot sizes (mm) and different aberrations. The upper left plot shows the effects of the focus term  $Z_4$  (squares) and primary spherical aberration term  $Z_9$  (triangles). Upper right plot shows the effects of the coma<sub>x</sub> term  $Z_7$  (squares) and coma<sub>y</sub> term  $Z_8$  (triangles). Bottom plot shows the effects of the secondary astigmatism<sub>x</sub> term  $Z_{12}$  (squares) and secondary astigmatism<sub>y</sub> term  $Z_{13}$  (triangles). In all plots, the circles correspond to random variations.

### 5.7.1.2 Photon Detector Simulations

The choice of photodetector (MAPMT or HPD) depends very much on performance, ease of implementation, and cost. We have simulated the BTeV RICH using both MAPMT and HPD photodetector configurations. The simulation includes all geometric effects, quantum efficiency, collection transmission and reflection. In addition to simulating both the MAPMT and HPD systems, we also considered using or not using an acrylic window in front of the photon detectors. The acrylic window absorbs UV photons which would otherwise pass through the HPD's quartz window. Since UV photons suffer from large chromatic error, this degrades the resolution per photon. Even though the Cherenkov resolution per track is compensated by the increase in the number of detected photons, the pattern recognition becomes more difficult, so it is advantageous to reject the large number of poorly measured UV photons. Table 5.6 shows that the two systems provide comparable Cherenkov angle resolution (bottom line of the table).

### 5.7.1.3 Occupancy of the gas RICH photon detectors

The RICH electronic readout has to be designed keeping in mind the expected data rates in the different regions. In particular, we need to be able to read out the expected high rate of data in the most intense regions close to the beam pipe. This puts strong demands on the electronics and the speed of the readout. In the following, we simulate the expected number of photons in the FE hybrid boards for beam crossings containing 1  $b\bar{b}$  event and either 2 or 6 minimum bias events per crossing. Since the pixel size and number of channels per FE hybrid board are similar for the MAPMT and for the HPD options, the results are representative for both systems. These numbers of minimum bias events correspond to the mean numbers expected at an instantaneous luminosity of  $2 \times 10^{32} \text{ cm}^{-2} \text{ s}^{-1}$  for 132 ns and 396 ns operation of the Tevatron.

Figures 5.69(a) and 5.69(b) show the mean number of hits per bunch crossing for each FE hybrid board. Each tower corresponds to a single FE Hybrid.

Figures 5.70(a) and 5.70(b) show the distribution of the number of hits in a bunch crossing summed over the 10 hottest FE hybrid boards. The FE boards have a mean of 17.5 photons per bunch crossing with an RMS of 16.6 and a maximum of 97 photons, when the luminosity corresponds to 2 interactions per bunch crossing. The same numbers at a luminosity corresponding to 6 interactions per bunch crossing are 51.2, 23.9 and 130 photons per bunch crossing.

Figures 5.71(a) and 5.71(b) show the distribution of the number of hits in a bunch crossing summed over the 10 FE hybrids with “medium” activity. Here, we define “medium” as an average of one-third the mean activity of the hottest hybrids. These FE hybrids have a mean of 5.9 photons per bunch crossing with an RMS of 7.2 and a maximum of 58 photons, when the luminosity corresponds to 2 interactions per bunch crossing. The same numbers at a luminosity of 6 interactions per bunch crossing result in a mean of 16.9 photons, an RMS of 11.8 photons and a maximum of 78 photons per bunch crossing.

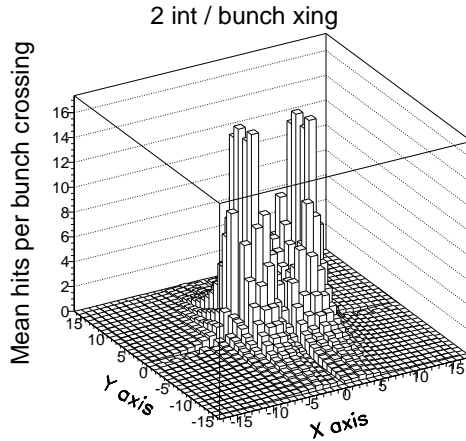
Zernike Coefficients	Radial	Angular
$Z_1$	1.0	1.0
$Z_2$	$\rho$	$\cos(\theta)$
$Z_3$	$\rho$	$\sin(\theta)$
$Z_4$	$2\rho^2 - 1$	1.0
$Z_5$	$\rho^2$	$\cos(2\theta)$
$Z_6$	$\rho^2$	$\sin(2\theta)$
$Z_7$	$(3\rho^2 - 2)\rho$	$\cos(\theta)$
$Z_8$	$(3\rho^2 - 2)\rho$	$\sin(\theta)$
$Z_9$	$6\rho^4 - 6\rho^2 + 1$	1.0
$Z_{10}$	$\rho^3$	$\cos(3\theta)$
$Z_{11}$	$\rho^3$	$\sin(3\theta)$
$Z_{12}$	$(4\rho^2 - 3)\rho^2$	$\cos(2\theta)$
$Z_{13}$	$(4\rho^2 - 3)\rho^2$	$\sin(2\theta)$
$Z_{14}$	$(10\rho^4 - 12\rho^2 + 3)\rho$	$\cos(\theta)$
$Z_{15}$	$(10\rho^4 - 12\rho^2 + 3)\rho$	$\sin(\theta)$
$Z_{16}$	$20\rho^6 - 30\rho^4 + 12\rho^2 - 1$	1.0
$Z_{17}$	$\rho^4$	$\cos(4\theta)$
$Z_{18}$	$\rho^4$	$\sin(4\theta)$
$Z_{19}$	$(5\rho^2 - 4)\rho^3$	$\cos(3\theta)$
$Z_{20}$	$(5\rho^2 - 4)\rho^3$	$\sin(3\theta)$
$Z_{21}$	$(15\rho^4 - 20\rho^2 + 6)\rho^2$	$\cos(2\theta)$
$Z_{22}$	$(15\rho^4 - 20\rho^2 + 6)\rho^2$	$\sin(2\theta)$
$Z_{23}$	$(35\rho^6 - 60\rho^4 + 30\rho^2 - 4)\rho$	$\cos(\theta)$
$Z_{24}$	$(35\rho^6 - 60\rho^4 + 30\rho^2 - 4)\rho$	$\sin(\theta)$
$Z_{25}$	$70\rho^8 - 140\rho^6 + 90\rho^4 - 20\rho^2 + 1$	1.0
$Z_{26}$	$\rho^5$	$\cos(5\theta)$
$Z_{27}$	$\rho^5$	$\sin(5\theta)$
$Z_{28}$	$(6\rho^2 - 5)\rho^4$	$\cos(4\theta)$
$Z_{29}$	$(6\rho^2 - 5)\rho^4$	$\sin(4\theta)$
$Z_{30}$	$(21\rho^4 - 30\rho^2 + 10)\rho^3$	$\cos(3\theta)$
$Z_{31}$	$(21\rho^4 - 30\rho^2 + 10)\rho^3$	$\sin(3\theta)$
$Z_{32}$	$(56\rho^6 - 105\rho^4 + 60\rho^2 - 10)\rho^2$	$\cos(2\theta)$
$Z_{33}$	$(56\rho^6 - 105\rho^4 + 60\rho^2 - 10)\rho^2$	$\sin(2\theta)$
$Z_{34}$	$(126\rho^8 - 280\rho^6 + 210\rho^4 - 60\rho^2 + 5)\rho$	$\cos(\theta)$
$Z_{35}$	$(126\rho^8 - 280\rho^6 + 210\rho^4 - 60\rho^2 + 5)\rho$	$\sin(\theta)$

Table 5.5: Wavefront expansion in terms of Zernike's coefficient.

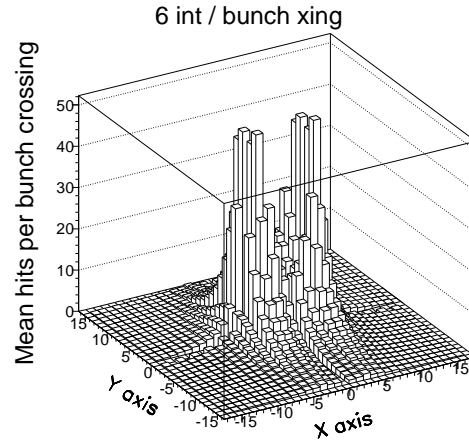


Table 5.6: Results on the Cherenkov angle resolution (in mrad) from simulations of the MAPMT and HPD systems. We consider two cases: on the left we show the scenario where we use an acrylic window in front of the photon detectors (baseline) and on the right we show the results when the acrylic window is absent.

Resolution Type	Resolution (mrad) with Acrylic Window		Resolution (mrad) without Acrylic Window	
	HPD	MAPMT	HPD	MAPMT
Total $\sigma_\theta$ per photon	0.84	0.83	1.46	0.88
Segmentation Error	0.45	0.51	0.45	0.51
Chromatic Error	0.52	0.44	1.42	0.51
Emission Point Error	0.49	0.49	0.49	0.49
Recon #Photons/Track	50.3	52.0	161.8	61.8
Total $\sigma_\theta$ per track	0.118	0.115	0.116	0.111



(a)



(b)

Figure 5.69: The mean number of hits per bunch crossing in FE hybrid.

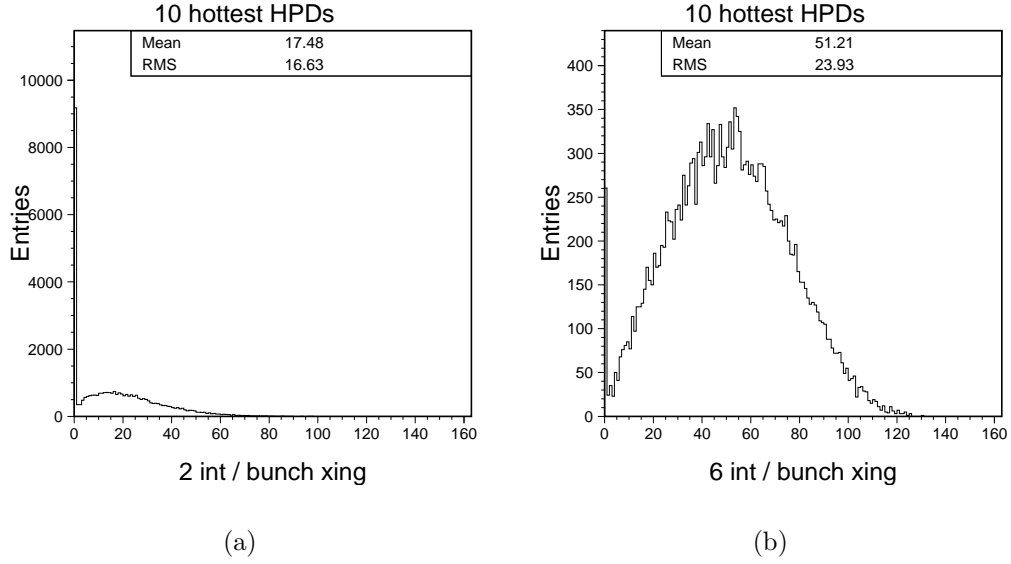


Figure 5.70: The distribution of the number of hits in a bunch crossing summed over the 10 hottest FE hybrids.

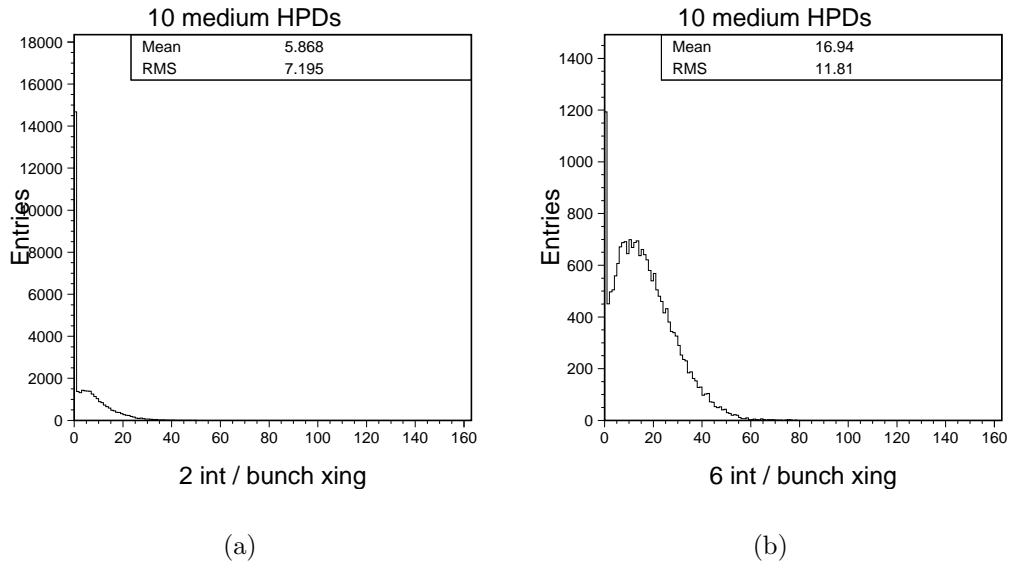


Figure 5.71: The distribution of the number of hits in a bunch crossing summed over a set of 10 FE hybrids with “medium” activity. These have an activity of 0.33 times the average activity of the 10 hottest FE hybrids.

#### 5.7.1.4 Simulations of Data Readout

The RICH MAPMTs are mounted to 23 supporting bars on each side. Signals from 8 MAPMTs in  $4 \times 2$  array are collected by one front end hybrids (FEH) and passed to a Front End Multiplexer (FEM) board. Each FEM board serves up to 4 FEHs (a group of 32 MAPMT). The digitized data are transmitted  $\sim 10$ -20 meters to a Data Combiner Board (DCB) via copper cables.

The high event rate requires that these cables transfer data at very high speed. The baseline design uses high speed point to point differentially driven serial lines. Each cable contains 4 twisted pairs. They provide for a reference clock (refclk) of 7.5 MHz, a beam crossing time and control data line (T/C link), and two pairs for event data. Each pair transfers data at 63.6 MByte/s and the data is encoded in the 8B10B format to balance the current.

The expected occupancy of the MAPMT has a strong dependence on location in the detector. We simulate the occupancy using BTeVGeant with two interactions per bunch crossing. The highest occupancy 32-MAPMT group registers  $\sim 39.1$  hits per bunch crossing on average, whereas the mean number of hits per group is 3.4. The electronics of the MAPMT readout is expected to have a noise level below 1%. Assuming a 1% noise occupancy, the mean numbers of hits are 43.8 per bunch crossing for the highest-occupancy group and 8.5 when averaged over all groups.

The total number of bits to be transferred includes 18 bits per hit to uniquely identify a MAPMT channel and 2-3 additional words to indicate the event ID or bunch crossing number. The non-uniformity of the occupancy distribution across the detector implies a location-dependent number of readout cables. Some areas may require as few as 2, whereas the highest-occupancy areas may require as many as 8. Taking into account data transfer speeds, we estimate that 534 of such cables are needed to move data in the RICH MAPMT system, which includes a 20% overhead.

With this cable arrangement, we study the data flow between the FEMs and DCBs. We randomly pick up events from of a pool of 14,000 events fully simulated using BTeVGeant (with 1% noise). Each FEM is assumed to have an 128-Kbit FIFO memory chip. We simulated 10 million successive bunch crossings and observe no memory overflow. The final size may be much bigger than this if necessary.

Since the Tevatron accelerator will continue to run with 396 ns between beam crossings (mean of 6 interactions per crossing at  $\mathcal{L} = 2 \times 10^{32} \text{ cm}^{-2}\text{s}^{-1}$ ), we simulated this scenario as well. This reduces the burden on data transfer, assuming the noise level remains at 1%. For some of the low occupancy groups, 1 readout cable per group will be enough to transmit the data in a single crossing. In total we estimate that we will need 428 such cables for the RICH MAPMT system.

### 5.7.2 Signal Simulations

Simulations of detector design must ultimately feed into simulations of physics signals. Here we present studies that have been performed to demonstrate the effectiveness of the RICH

detector. For further physics simulations, see Part 2 in the BTeV Proposal Update [16]. For historical reasons, all simulations are run at 2 interactions/crossing. For one of the critical decay modes, we compare the RICH performance at 2 and 6 interactions per crossing. It should be realized that 6 interactions/crossing is only the starting value, with the average rate closer to 3 interactions/crossing.

### 5.7.2.1 Tagging Performance

In addition to the issue of resolution, the performance of the RICH will depend on other details such as occupancy and the degree to which Cherenkov rings overlap. A realistic simulation of efficiency and fake rates must take into account ambiguities in track-photon assignment. Since photons from the liquid radiator and the gas radiator fall on separate sensor arrays, the Cherenkov rings from the two radiators do not produce additional ambiguity in the pattern recognition.

We have analyzed simulated data with an algorithm which could be applied to real data. The reconstruction is performed in two steps. In the first pass, all hits within  $\pm 3\sigma$  of a mass hypothesis are included in the per track average, excluding those hits which are within  $\pm 3\sigma$  of the pion hypothesis for any other track. The second pass is essentially the same except that instead of assuming that all tracks are pions in the hit exclusion, the most likely mass hypotheses based on the first-pass results are used. To discriminate between two mass hypotheses for the same track (e.g.  $K$  or  $\pi$ ) we compute the likelihood ratio expressed as a  $\chi^2$  difference:

$$\Delta\chi_{K\pi}^2 = -2\log(L_\pi/L_K) \quad (5.3)$$

with,

$$L_h = P(N_h|N_h^{exp}) G(\theta_{trk\ h}|\theta_h^{exp}). \quad (5.4)$$

Here  $P(N_h|N_h^{exp})$  is the Poisson probability for observing  $N_h$  photons within  $\pm 3\sigma$  of this hypothesis when  $N_h^{exp}$  are expected, and  $G(\theta_{trk\ h}|\theta_h^{exp})$  is the Gaussian probability density for obtaining the Cherenkov angle (per track)  $\theta_{trk\ h}$  for given mass hypothesis  $h$  when  $\theta_h^{exp}$  is expected. The expected photon yield includes acceptance corrections and losses due to the Cherenkov ring overlaps. For a given cut value on the  $\Delta\chi_{K\pi}^2$  we obtain values for efficiency and fake rate.

To illustrate the performance of the C<sub>4</sub>F<sub>10</sub> system we show in Fig. 5.72 (left) the simulation of  $B_d \rightarrow K^\pm \pi^\mp$  background rejection as a function of  $B_d \rightarrow \pi^+ \pi^-$  efficiency, and in Fig. 5.72 (right) the efficiency for detecting the  $K^-$  in the decay  $B_s \rightarrow D_s^+ K^-$  versus the rejection of the  $\pi^-$  in the decay  $B_s \rightarrow D_s^+ \pi^-$ . These simulations include photon conversions and other backgrounds. We see that high efficiencies can be obtained with excellent rejection rates.

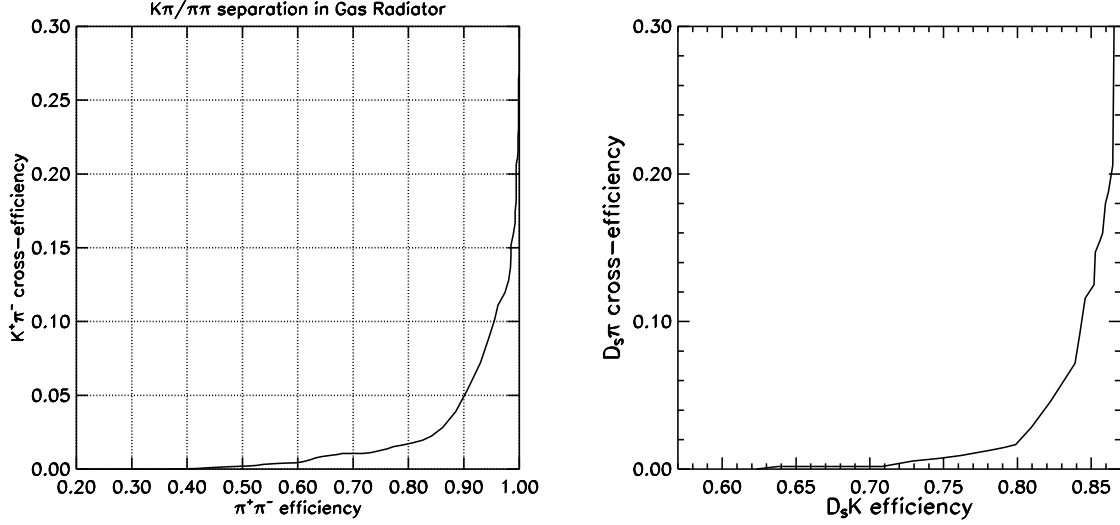


Figure 5.72: (left) Cross-efficiency of particle identification system for  $B_d \rightarrow K^\pm \pi^\mp$  as a function  $B_d \rightarrow \pi^+ \pi^-$  PID efficiency. (right) The efficiency to detect the fast  $K^-$  in the reaction  $B_s \rightarrow D_s^+ K^-$  versus the rate to misidentify the  $\pi^-$  from  $B_s \rightarrow D_s^+ \pi^-$  as a  $K^-$ . The efficiencies are defined relatively to number of events with both tracks entering the RICH detector. The Monte Carlo simulation included on average two minimum bias interactions in addition to the  $b\bar{b}$  production.

The gas radiator will also play a significant role in lepton identification as electrons below 22 GeV/c and muons below 15 GeV/c are separated by more than  $4\sigma$  from pions. Since the RICH acceptance is much larger than the calorimeter and muon system a great deal of efficiency is added.

To demonstrate the performance of the liquid radiator, we have analyzed Monte Carlo samples of  $b\bar{b}$  events to determine the efficiency and misidentification probability for kaons with momenta less than 9 GeV/c. These are significant in kaon flavor tagging because of the large number of protons which are produced at the interaction point. Background cross-efficiency, in this case the identification of a proton as a kaon, is plotted as a function of kaon efficiency in Fig. 5.73. Again, we find that high efficiencies are obtained with relatively low fake rates.

### 5.7.2.2 Simulations at 2 and 6 Interactions per Crossing

Simulations in the original BTeV proposal [13] were done assuming a luminosity of  $2 \times 10^{32} \text{ cm}^{-2} \text{ s}^{-1}$  with a 132 ns bunch crossing interval, which corresponds to a Poisson mean of 2 interactions per bunch crossing. Current plans are [17] that the Tevatron will run with a bunch spacing of 396 ns, corresponding to 6 interactions per bunch crossing. Examples

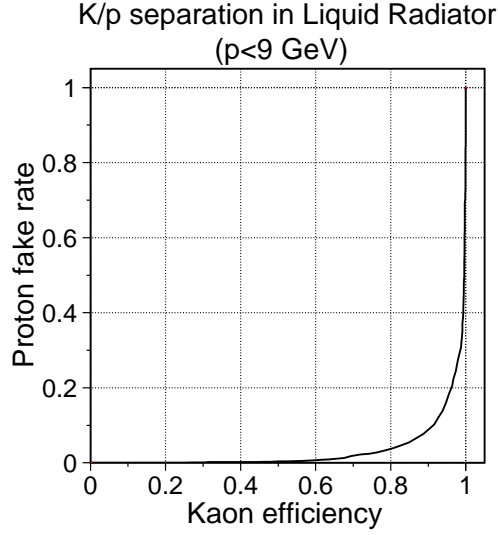


Figure 5.73: Proton fake-rate as a function of kaon identification efficiency for tracks with momenta  $< 9$  GeV/c.

of detected Cherenkov images for 6 minimum bias events added to a  $b\bar{b}$  event are shown in Figs. 5.74-5.75. The effect of this change in running conditions has been simulated and compared to the original assumption of 2 interactions per bunch crossing.

To investigate this, we considered the decay  $B_S \rightarrow D_S^\pm K^\mp$ ,  $D_S \rightarrow \phi\pi$ ,  $\phi \rightarrow K^+K^-$  as a benchmark physics state needing good performance from the RICH for  $K - \pi$  separation to measure the CKM angle  $\gamma$  (and possible time-dependent CP violating effects).

This decay has three charged kaons and one charged pion in the final state. We require positive identification of the kaon from the  $B_S$  and at least one of the two kaons from the  $\phi$  decay. The analysis is identical to that in the proposal [13], with the addition of the charged particle identification by the RICH.

We generated signal and minimum bias events using Pythia [18]. The only requirements for the signal events were that the 4 tracks (3 kaons and 1 pion) were in the BTeV detector acceptance ( $10 \text{ mrad} \leq \theta < 300 \text{ mrad}$ ) and the  $D_S$  decay length was greater than 1 cm. These events are then passed through the BTeVGeant detector simulation package. Different simulations corresponding to exactly 0, 1, 2,  $\dots$ , 10 minimum bias events per signal event were performed, and each was analyzed separately.

We look to quantify the change in the RICH performance in going from a mean of 2 interactions per crossing to 6 interactions per crossing. One important measure is to compare the difference in the negative log-likelihoods for the kaon and pion hypotheses ( $\chi_K^2 - \chi_\pi^2$ ) for the kaons and pions in the decay  $B_S \rightarrow D_S^\pm K^\mp$ . These log-likelihoods are shown in Fig. 5.76(a) for 0, 1, 2 minimum bias events per bunch crossing and Fig. 5.76(b) for 7, 8, 9 minimum bias interactions per bunch crossing.

It is clear that separation between kaons and pions is degraded as the number of minimum bias events becomes large. The above chi-squared plots can be converted into an efficiency vs fake rate curve as shown in Fig. 5.77. In addition, a few of the other distributions were

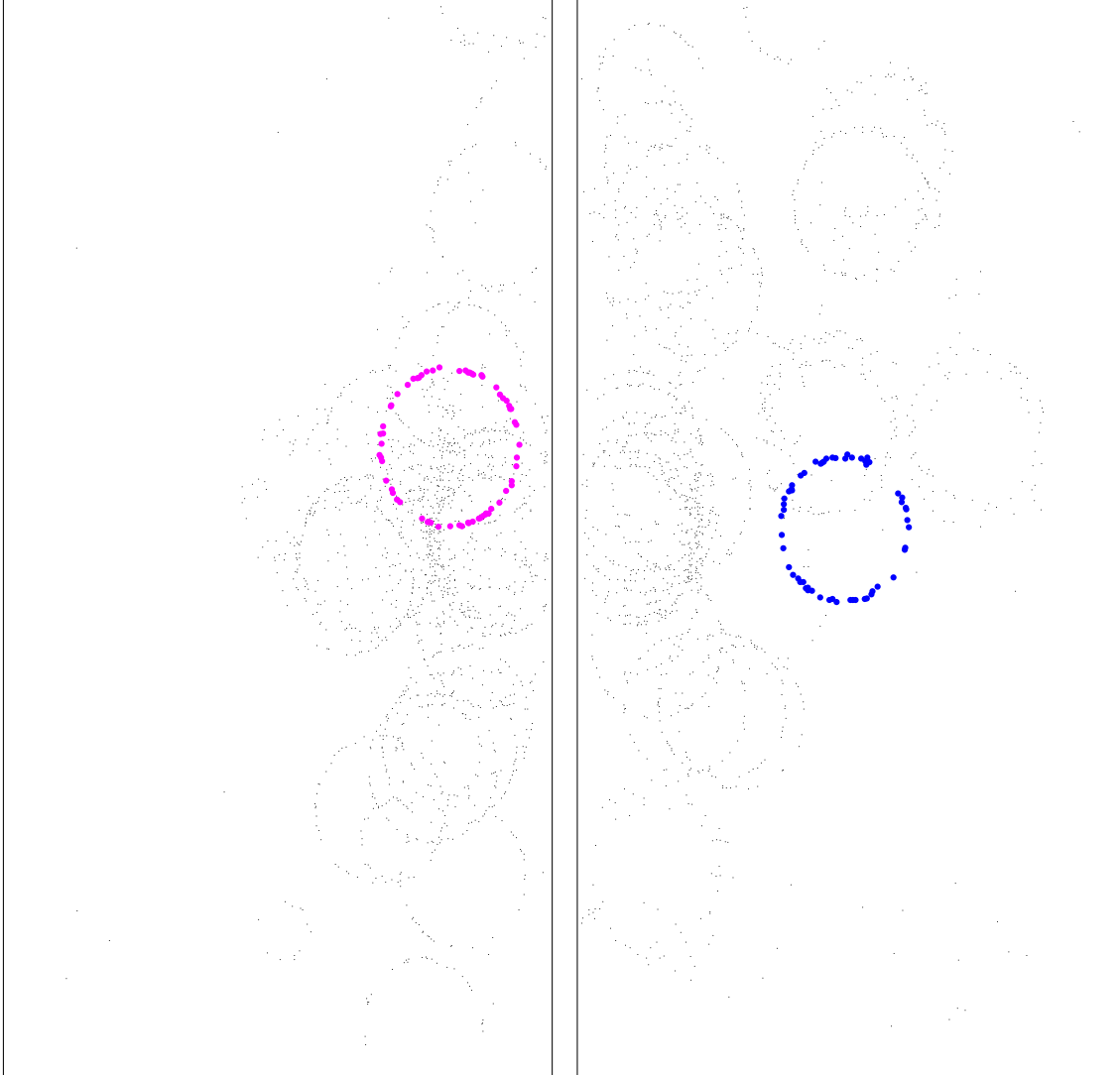


Figure 5.74: Cherenkov rings from the gas radiator detected in the HPD arrays as simulated for a  $B \rightarrow \pi^+\pi^-$  event with six minimum bias interactions in the same bunch crossing. The Cherenkov hits for the pions from the  $B$  decay are highlighted. Compare with Fig. 5.2 for two minimum-bias interactions.

studied and two of them – the reconstructed  $B_S$  and  $D_S$  masses are shown in Figs. 5.78(a) and 5.78(b).

To determine the effect on the RICH tagging, we weight the events containing different numbers of minimum bias events according to Poisson distributions with means of 2.0 and 6.0 interactions per bunch crossing. Let us define  $\epsilon_{imin}$  to be the efficiency for tagging both the kaon from the  $B_s$  decay and at least one of the kaons from the  $\phi$  decay for a given value of  $imin$ , the number of minimum bias events per signal event in the sample. These efficiencies are normalized to the case of  $imin = 0$ . The distribution is then fit to an exponential function

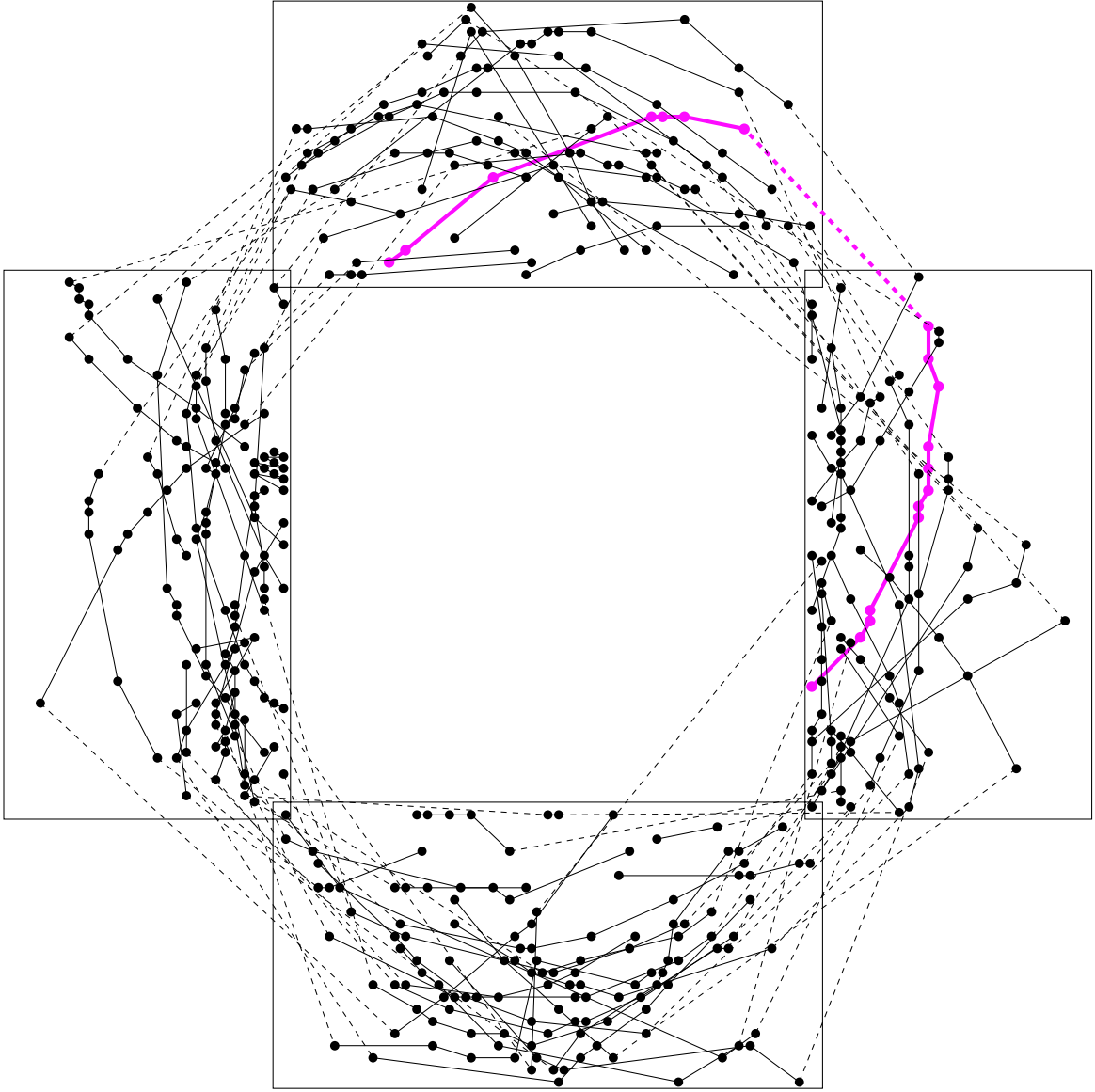


Figure 5.75: Cherenkov rings from the liquid radiator detected in the PMT arrays as simulated for a kaon tagged  $B$  event with six minimum bias in the same bunch crossing. Hits belonging to the same track are connected. The Cherenkov hits for the tagging kaon are connected by a thick line. Compare with Fig. 5.3 for two minimum-bias interactions.



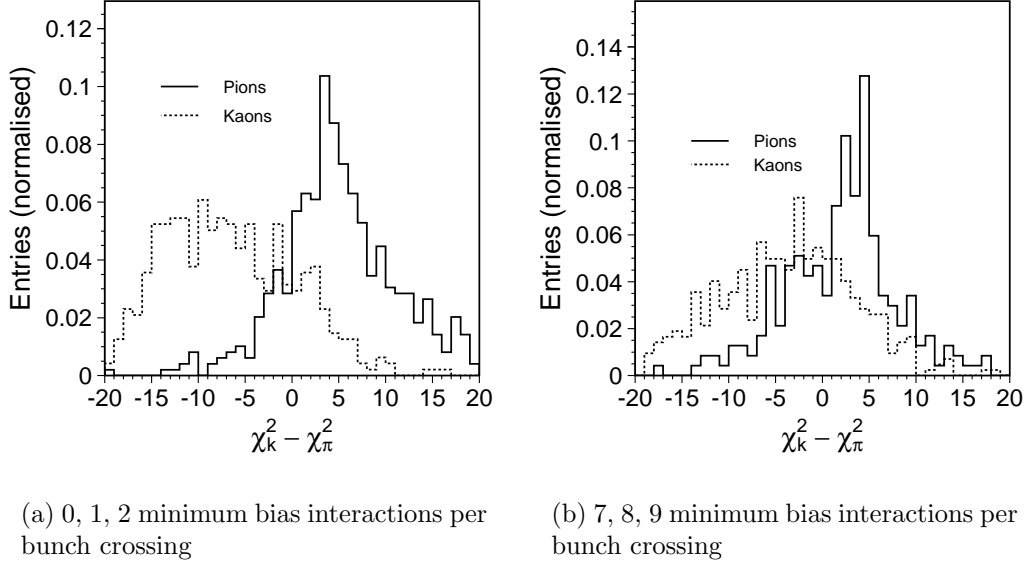


Figure 5.76:  $\chi_K^2 - \chi_\pi^2 \rightarrow$  The difference in the negative log-likelihoods for the kaon and pion hypotheses.

(of the form  $\exp(\text{constant} + \text{slope} \times x)$ ) to obtain values for  $\epsilon_{imin}$  at each value of  $imin$ . The distributions for  $\epsilon_{imin}$  are shown in Fig. 5.79(a) and Fig. 5.79(b).

To obtain efficiencies for averages of 2 and 6 interactions, we convolute  $\epsilon_{imin}$  with corresponding Poisson distributions having these mean values. Since we are primarily concerned with the change in performance in going from 2 interactions to 6 interactions per crossing on average, we compute a relative efficiency,  $\epsilon_{rel}$ , defined by:

$$\epsilon_{rel} = \frac{\sum \epsilon_{imin} * \text{Poisson}(6.0, imin)}{\sum \epsilon_{imin} * \text{Poisson}(2.0, imin)}$$

where,

$$\text{Poisson}(\mu, n) = \frac{\mu^n \exp(-\mu)}{n!}$$

After convolution, we find  $\epsilon_{rel} = 0.90$  if we require only one of the kaons from the  $\phi$  to be tagged. If we require both kaons to be tagged, we find  $\epsilon_{rel} = 0.76$ . Hence, even with a tight tagging requirement, a mean of 6 interactions per crossing still yields 76% of the value obtained for 2 interactions per crossing. We therefore conclude that the RICH will effectively separate kaons from pions, even at 6 interactions per bunch crossing. The performance is  $\sim 25\%$  better at 2 interactions per bunch crossing. Again, it is important to note that we will only be running at 6 interactions per crossing at the beginning of the run; the average will be closer to 3 interactions per crossing, in which case we only lose 5% in relative tagging

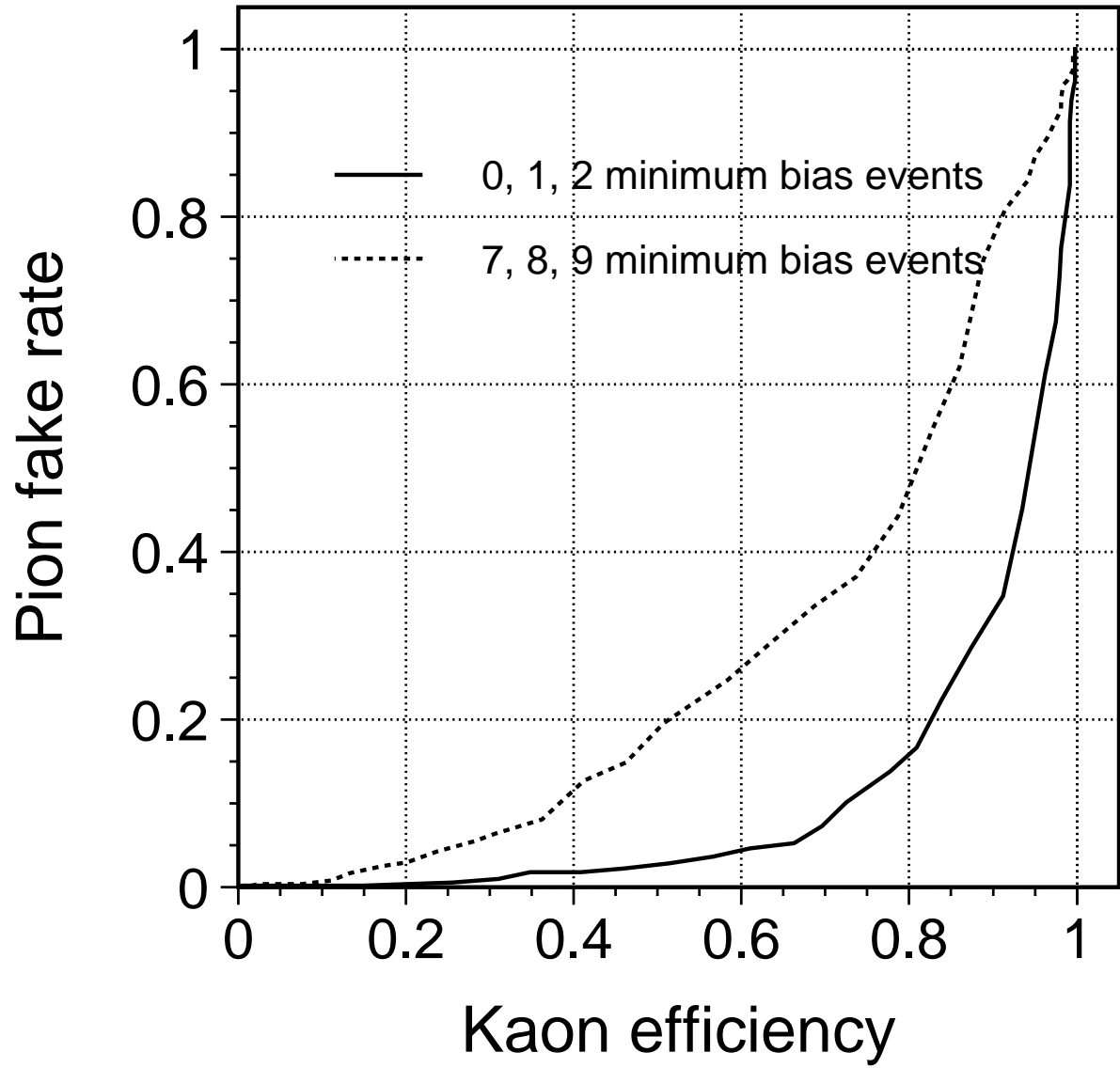


Figure 5.77: Curve for the kaon efficiency versus pion fake rate, for kaons and pions from  $B_S$  decays.

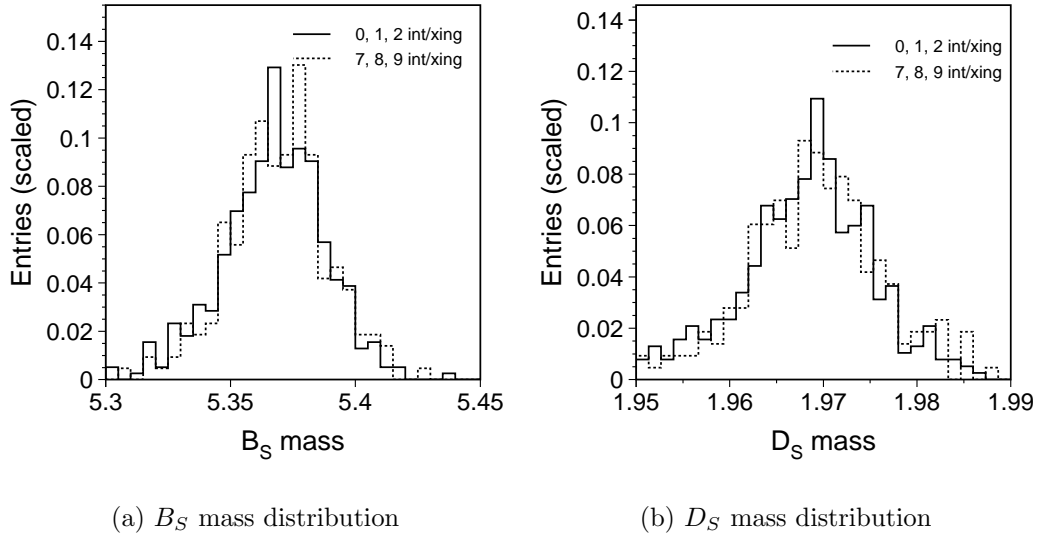
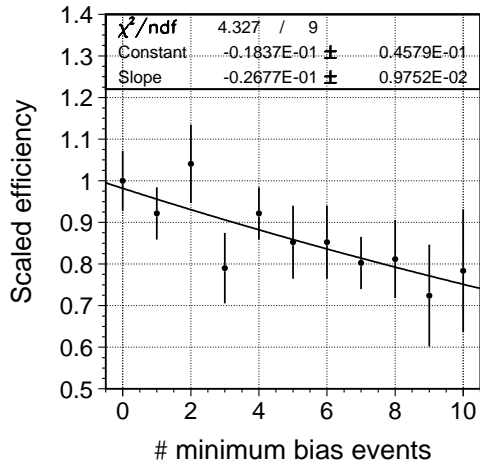
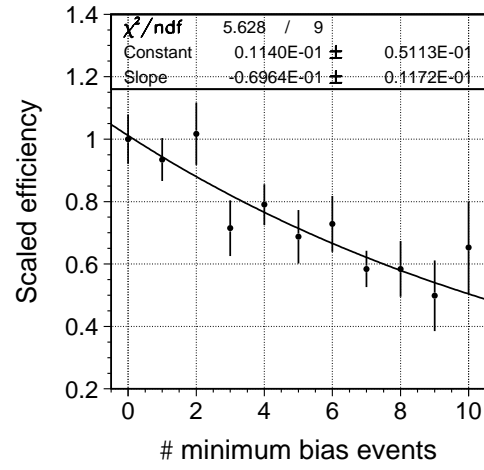


Figure 5.78: The  $B_S$  and  $D_S$  mass distributions for the selected events, after the full event reconstruction.

efficiency for the default analysis. Even with the more stringent requirement that both kaons from the  $\phi$  decay (as well as the kaon from the  $B_s$ ) be identified, we only incur a 12% relative loss in efficiency.



(a) At least one tagged kaon from  $\phi$  decays



(b) Both kaons from  $\phi$  decays are tagged

Figure 5.79: The scaled efficiency ( $\epsilon_{imin}$ ) distributions, both fitted to exponentials as mentioned in the text.

# Bibliography

- [1] W. Adam *et al.*, Nucl. Instrum. Meth. **A343**, 60 (1994).
- [2] I. Arino *et al.*, Nucl. Instrum. Meth. **A516**, 445 (2004).
- [3] Y. Miyachi, HERMES Collaboration, Nucl. Instrum. Meth **A502**, 222 (2003); Y. Sakemi, HERMES Collaboration, Nucl. Instrum. Meth **A453**, 284 (2000); Y. Sakemi, HERMES Collaboration, Nucl. Phys. Proc. Suppl. **78**, 366 (1999); P. Carter, “Proposal for Dual Proceedings of the Third International Workshop on Ring Imaging Cherenkov Detectors, Weizmann Institute of Science, Ein-Gedi, Dead Sea, Israel, Nov. 15-20, 1998; E. Cisbani *et. al.*, HERMES Internal Note 97-005.
- [4] LHC-B: RICH Technical Design Report, CERN-LHCC-2000-037; LHC-B Technical Proposal, CERN LHCC 98-4, LHCC/P4, 1998.
- [5] Hera-b gives the index of refraction as function of photon energy as

$$n - 1 = 0.0013178 + 1.723x10^{-7}E_{\gamma} + 5.495x10^{-6}E_{\gamma}^2 \quad . \quad (5.5)$$

See A. Bulla, “Die Entwicklung eines ringabbildenden Cerenkov-Zählers für den Detektor HERA-B,” Ph.D. thesis (1997). This formula is an extrapolation of measurements made at Delphi in the ultraviolet wavelength region. See E. Fokitis *et al.*, Nucl. Phys. Proc. Suppl. **B44**, 246 (1995); E. Fokitis *et al.*, Nucl. Instrum. Meth **A371**, 255 (1996).

- [6] R. Forty, CERN-PPE/96-176, Sept. 1996. Published in Proceedings of the Fourth International Workshop on B-Physics at Hadron Machines, Rome, Italy, June (1996), F. Ferroni, P. Schlein (Eds.), North-Holland, 1996.
- [7] The mirrors will be fabricated as composite sandwich structure, 12 to 25 ply facesheets and a CFRP (Continuous Fiber Re-enforced Plastic) core material. CFRP prepreg is referred to as M46J/EX-1515 material, produced from Torray M46J fibers (63 msi tensile modulus and near zero CTE) and Bryte Technologies EX-1515 cyanate ester polymer matrix.
- [8] E. Albrecht *et. al.*, “Performace of Hybrid Photon Detector Prototypes with 80% Active Area for the RICH Counters of LHCb”, Nucl. Instrum. Meth. XXXX; See also GLAS-PPE-1999-22 (hep-ex/0001053) and Nucl. Instrum. Meth. Phys. Res. **A433**, 159 (1999).

- [9] R. Mountain, for the BTeV Collaboration, “Development of a Hybrid Photodiode and its Front End Electronics for the BTeV Experiment”, Presented at the Fourth International Conference on RICH Detectors, Pylos, Greece, June, 2002; Nucl. Instrum. Meth. **A502**, 183 (2003).
- [10] LHCb RICH Technical Design Report, CERN LHCC 2000-037.
- [11] M. Artuso *et. al.*, Nucl. Instrum. Meth. **A502**, 91 (2003).
- [12] F. Muheim, “Multi-Anode Photo Multipliers as Photo Detectors for Ring Imaging Cherenkov Detectors”, presented at the 4th International Workshop on Ring Imaging Cherenkov Detectors, Pylos, Greece, 5-10 June 2002.  
See <http://www.nestor.org.gr/rich2002/list/participants.htm> .
- [13] The BTeV Proposal (2000).  
See: <http://www-btev.fnal.gov/DocDB/0000/000066/002/index.html> .
- [14] J. Friese, “A New Carbon based VUV Mirror of High Radiation Length for the HADES RICH” presented at the 4th International Workshop on Ring Imaging Cherenkov Detectors, Pylos, Greece, 5-10 June 2002.  
See <http://www.nestor.org.gr/rich2002/list/participants.htm> .
- [15] E. Albrecht *et. al.*, Nucl. Instrum. Meth. A **502**, 236 (2003).
- [16] The BTeV Proposal Update (2002).  
See: <http://www-btev.fnal.gov/cgi-bin/public/DocDB/ShowDocument?docid=316>
- [17] S. Stone and J. Butler, BTeV Internal document, BTeV-doc-1571.
- [18] T. Sjostrand and L. Lonnblad, Pythia 6.2, hep-ph/0108264, August 2001.
- [19] P. Lebrun *et. al.*, BTeV Internal document, BTeV-doc-113.

# Chapter 6

## Electromagnetic Calorimeter

### 6.1 General Overview

The decision to use a high-performance crystal electromagnetic calorimeter in BTeV was driven by the physics goals of the experiment, that generally are to make complete studies of CP violation and rare decays of  $b$ -flavored hadrons. This chapter describes general requirements arising from these physics goals, design of the calorimeter and its rationale. The design is supported by several years of R&D activities carried out by the Electromagnetic Calorimeter (EMCAL) Group of the BTeV Collaboration.

A thorough investigation of  $B$  decays requires not only the ability to track and identify charged particles, but also the ability to reconstruct photons. To address many of the physics issues we are interested in studying, we need to disentangle various isospin components of the decays. This inevitably involves decay modes containing  $\pi^0$ 's. Detection of neutral pions is critical, for example, in extracting the  $\alpha$  angle of the unitary triangle using  $B \rightarrow \rho\pi \rightarrow \pi^+\pi^-\pi^0$  or  $B \rightarrow \rho^+\rho^- \rightarrow \pi^+\pi^-\pi^0\pi^0$ . It is also crucial to detect  $\eta$ (') $s$  and isolated photons. The decay mode  $B_s \rightarrow J/\psi\eta^{(\prime)}$  used for the determination of the angle  $\chi$  involves either  $\eta \rightarrow \gamma\gamma$ ,  $\eta' \rightarrow \pi^+\pi^-\eta$  or  $\eta' \rightarrow \rho\gamma$ . Other important decays involving direct photons are  $B \rightarrow \gamma K^*(\rho \text{ or } \omega)$ . Thus, since much important physics depends on the calorimeter, our goal is to optimize its performance while keeping costs under control.

Total absorption shower counters made of scintillating crystals have been known for decades for their superb energy and spatial resolutions. The crystals act as both the shower development media and scintillation light emitter. Since the entire calorimeter is used to measure the energies of photons, the resolution can be excellent. Lead tungstate ( $\text{PbWO}_4$  or PWO) crystals are distinguished by their high density ( $8.3 \text{ g/cm}^3$ ), short radiation length ( $0.89 \text{ cm}$ ), small Moliere radius ( $2.2 \text{ cm}$ ) and short relaxation time ( $15 \text{ ns}$  for the major component) as well as its tolerance of radiation. The light output, of 10 photoelectrons per MeV into 2-inch PMT with a standard bialkali photocathode, is modest compared to many other scintillation crystals, but adequate. These characteristics are a good fit to the BTeV calorimeter. Since BTeV will operate in a very high particle density environment, it is very important that signals from two particles do not overlap in space and time very often. The

smaller the Moliere radius, the more compact are the showers created by photons, and the less frequently do two of them overlap in space. The shorter the scintillation signal, the less likely that two of them overlap in time. (However, there is no particular benefit of having the signal shorter than the time between bunches, as all the particles from a particular bunch crossing are in time.)

The space for the EMCAL is limited in the BTeV experimental hall. The dense nature of the PWO crystals makes it possible to construct a compact calorimeter. The shorter calorimeter gives hadron showers less room to spread out when their parent hadrons interact in the calorimeter, making them less likely to overlap with photon signals. In general, scintillation crystals are radiation sensitive, and the high-radiation environment of BTeV makes it impractical to use them. However, years of R&D studies, much of them done by people in CMS, show that PWO crystals are an exception. Finally, PWO crystals are one of the most economical scintillation crystals, and pure enough crystals which are radiation tolerant can be produced more cheaply than regular (not radiation tolerant) CsI or BGO crystals. These are the major reasons why an electromagnetic calorimeter made of PWO crystals has been selected as the baseline for the BTeV experiment. The CMS [1] and ALICE [2] experiments at the CERN LHC have chosen these crystals for their electromagnetic calorimeters for similar reasons. The EMCAL will consist of about 10,000 crystals, each  $28 \times 28 \text{ mm}^2$  in cross section in the back and 220 mm in length. They are slightly tapered in shape so that they can be in a projective geometry where all the crystals are pointing to a place near the interaction point. The projective geometry will secure better resolutions, in particular, position resolution, especially in the outermost area of the calorimeter. In order to avoid lining up gaps between crystals with potential paths of photons, the convergence point is displaced from the IP by 10 cm both in the horizontal and vertical directions.

Unlike CMS or ALICE, the BTeV EMCAL is not situated in a high magnetic field, so we can use photomultiplier tubes (PMTs) rather than avalanche photodiodes or vacuum phototriodes. Fringe field from the toroid gives up to 40 Gauss in the phototubes. Our default assumption is that the field can be significantly decreased by having an 1-inch steel plate backed up by a thin sheet of  $\mu$ -metal right next to the toroid. Fringe field from the upstream vertex magnet is up to 15 Gauss in the phototubes. A thin sheet of  $\mu$ -metal can be placed in front of EMCAL to shield phototubes against this field. The use of PMTs give better resolutions at low energies. We expect that approximately 5000 photoelectrons will be produced in a 1-inch diameter bialkali photocathode PMT at 1 GeV. Hereafter we assume that the maximal quantum efficiency of the mentioned phototubes is 25%. Note that for quality assurance (QA) purposes, we refer to photoelectron yield for 2-inch PMT's, that covers the entire end of a crystal being measured, while in the context of crystals being used in the BTeV experiment, we refer to photoelectron yield for 1-inch PMT's; the latter are slightly smaller than the crystals and thus collect less light.

Signals from PMTs will be digitized using FNAL QIE technology, which has evolved from that used in the KTeV, CDF, CMS hadron calorimeters and in MINOS. FNAL is working



on the design of BTeV QIE. It will have a quasi-constant fractional digitization resolution of less than 0.3%, covering a dynamic range of almost  $10^5$ .

Our choice of the PWO technology and our approach to the EMCAL operation over the lifetime of BTeV are supported by an extensive R&D program. These studies yielded many important results, some of them unique. We have good understanding of how crystals will behave over time and whether their light output will fluctuate, for example, due to radiation environment or due to temperature variations. We have designed systems to carefully monitor possible changes. We have also carried out extensive MonteCarlo study to establish EMCAL daily calibration scenario that will employ particles produced in physics data.

In the following sections we will describe each EMCAL component in terms of the requirements, the current design and what we have learned in our R&D studies. Section 2 will list the basic EMCAL requirements set by our physics goals, and the requirements on the PWO crystals. Section 3 will cover the properties of PWO crystals and what we have learned from our test beam and source studies at IHEP, Protvino. Section 4 will describe the PMTs and electronics. This is followed by results from a calibration and monitoring system using actual data as well as precision light pulsers in section 5. The mechanical support structure is covered in Section 6. The assembly procedure, installation in the C0 Hall and integration with other components of BTeV are given in Section 7. Simulation studies of the BTeV EMCAL are given in Section 8. In Section 9 we discuss the R&D studies we still need to do. Finally, we will present our estimate of the cost and schedule in Section 10 and conclude with the EMCAL group organization in Section 11.

## 6.2 Basic Requirements

The following are the requirements set by the physics goals of BTeV on the performance of the electromagnetic calorimeter. The resolution of the calorimeter is one of the defining characteristics of the system.

- **Detector size:** The system has to provide acceptance for photons of more than  $1.3 \times 10^{-2}$  steradians. In terms of the radius of the calorimeter this corresponds to 1.6 m. The choice was made to reduce the cost by a factor of about 2, while the loss in signal for most final states will be only 20%.
- **Energy Resolution:** The energy resolution of photon showers as a function of the energy is better than  $\sigma_E/E = 2\%/\sqrt{E} \oplus 1\%$ .
- **Position Resolution:** The position resolution of photon showers as a function of the energy must be better than  $\sigma_x = 4\text{mm}/\sqrt{E} \oplus 1\text{mm}$ .
- **Radiation Tolerance:** After an integrated dose of 10 Mrad (100 kGy), energy and position resolution should not deteriorate by more than a factor of 2.

Table 6.1: Properties of PWO crystal

Property	value
Density	8.28 g/cm <sup>3</sup>
Radiation length	0.89 cm
Molière Radius	22 mm
Interaction Length	22.4 cm
Light Decay Time	5 ns (39%) 15 ns (60%) 100 ns (1%)
Refractive Index	2.30
Maximum of emission	440 nm
Light Output(LO)/NaI(Tl)	1.3%
LO Temperature Coefficient	-2 %/C
Light Output (into a 2" PMT)	10 p.e./MeV
Hygroscopic	No
Brittle	Yes

The resolution of this kind of calorimeter is determined by the following factors: the size of the crystals, speed of the signal, and the amount of inactive material between and in front of the crystals. We have requirements on these aspects:

- **Size:** The cross sectional area (the area that the crystals present to incoming photons from the IP area) must be no larger than  $28 \times 28 \text{ mm}^2$  to take full advantage of small Molière radius (22 mm for the PWO crystal).
- **Signal Duration:** Signal should decay in 132 ns.
- **Thickness of Inactive Material:** The thickness of inactive material as well as space between crystals must be no more than 1 mm. The inactive materials between crystals and in front of EMCAL should be made of low- $Z$  materials as much as possible.

### 6.3 Lead Tungstate Crystals

Some of the properties of PWO crystals are listed in Table 6.1.

The crystal-related requirements necessary to accomplish the above general requirements are

- **Light Output:** 10 photoelectrons/MeV into 2-inch PMT with bialkali photocathode.
- **Light Output Nonuniformity:** less than 1%/cm between 3 and 10 cm from the front of the crystal.

- **Signal Duration:** The amount of signal within the first 132 ns must be more than 98% of the signal one collects in  $1\mu s$ .
- **Size:** The cross sectional area of the crystal is  $27.2 \times 27.2 \text{ mm}^2$  in the front and  $28 \times 28 \text{ mm}^2$  in the back with a tolerance of  $^{+0.00}_{-0.10} \text{ mm}$ . The length is  $(220 \pm 1) \text{ mm}$ .

In the last decade, the production technology of PWO crystals has made significant progress and at least three vendors are now capable of producing them for BTeV. The CMS collaboration has been working during the last several years with the Bogoroditsk Techno-Chemical Plant (BTCP) in Tula, Russia. At present, about 30,000 crystals have been produced by BTCP for CMS. CMS has also been in contact with the Shanghai Institute of Ceramics (SIC) in China in order to develop methods to mass-produce high-quality PWO crystals. SIC has already provided over one thousand PWO crystals for the PRIMEX experiment at Jefferson Lab. In addition, the ALICE experiment has been working with Northern Crystals at Apatity, Russia, to mass-produce PWO crystals. At present about 2/3 of the total 10,800 crystals have already been produced. Beijing Glass Research Institute (BGRI) also has provided a few PWO crystals to BTeV. The three vendors that we are confident can produce the BTeV crystals are BTCP, Apatity and SIC. (It should be noted that SIC produced thousands of CsI(Tl) crystals very successfully for BaBar.)

We have studied sample crystals from these four potential vendors to

- compare their light outputs with the nominal value of 10 photoelectrons/MeV for 2-inch PMT.
- demonstrate that we can obtain the expected energy and position resolutions for photons (or electrons) using these crystals.
- check if their crystals are sufficiently radiation hard to survive the BTeV-like radiation environment (3 krad as a minimum up to 20 Mrad as a maximum over 10 years of BTeV operation as was estimated).
- check if the change in light output can be monitored well enough so that we can maintain good energy and position resolutions over a long period of time in a BTeV-like radiation environment.
- check if these crystals sustain more serious radiation damage when they are exposed to a hadron beam compared with radioactive sources.
- measure radiation tolerance of wrapping materials and glue to join crystals and PMTs.
- decide what is the best way to specify the quality of production crystals based on radioactive source measurements.

Many of these studies have been done at IHEP, Protvino using their test beam facility, which runs twice a year for about a month, once from March to April and once from November

to December. Our Russian collaborators led the program for these studies that included designing and constructing a beam line, measuring the properties of the beam including the momenta of individual particles, constructing the trigger and data acquisition systems and analyzing the data. In addition, IHEP, Minnesota and Syracuse have test benches that were used to measure light outputs of crystals both before and after the beam tests.

From previous studies by CMS collaborators and others, we learned that typical PWO crystals produce about 10,000 photoelectrons per 1 GeV when instrumented with a large enough PMT to cover one of its ends entirely. The stochastic term of the energy resolution arising from statistical fluctuation in the number of photoelectrons will then be  $\sigma(E)/E = 1.45\%/\sqrt{E}$ , where  $E$  is in units of GeV. The effects of shower transverse fluctuations will result in additional 0.84% contribution in the stochastic term. Overall, one expects the stochastic term of  $(1.68 \pm 0.07)\%/\sqrt{E}$  at 10,000 photoelectrons per 1 GeV. There is an additional term in the expression for  $\sigma(E)/E$  that is independent of energy, therefore called the “constant term” that becomes dominant at high enough energies. This is caused by (1) shower fluctuations, mostly rear leakage, (2) crystal light collection non-uniformity and (3) calibration precision. Our Monte Carlo studies show that (1) contributes 0.23%. For a typical non-uniformity of our sample crystals (0.5 %/cm in the front part), (2) contributes 0.27%. The issues associated with calibration accuracy is very involved and addressed in Section 5 in detail. For physics simulations we set the total constant term to be 0.55%, somewhat worse than that obtained by KTeV (0.45%).

We also learned from previous studies that

1. current PWO crystals do not sustain permanent radiation damage when they are exposed to photon and electron irradiation (we observed crystal recovery at least up to 98% of the original signal level).
2. PWO crystals suffer less from radiation than most other scintillation crystals [7], and
3. when they are exposed to radiation at a constant rate, the damage does not accumulate indefinitely, but rather the deterioration in light output saturates; i.e. the light output decreases to a lower level but stays constant at that level.

These observations can be explained as follows. Damage occurs in the transmission of scintillation light in the crystal when valence electrons are trapped in metastable states around crystal defects. When this happens, color centers that absorb scintillation light are created because these electrons, which are in higher energy states than the valence band, jump across the band gap by absorbing visible light. The lifetimes of most of these color centers are modest (hours). The color centers disappear when the trapped electrons fall down to the lower-energy states. The lifetimes are quite temperature dependent. This is one of the strengths of PWO crystals and explains observation (1) above. When the rate of new damage production (which is presumably proportional to the dose rate) equals natural recovery rate (which is proportional to the density of damage among other factors), the damage density will reach a plateau, which explains observation (3). When crystals have only a few defects, they are radiation tolerant since as most of the crystal defects are activated

and become color centers, there will be no additional damage no matter how intensive the radiation. Observation (2) is explained by a room-temperature recovery mechanism and low defect densities in the current production PWO crystals. Current mass-production crystals are grown with targeted purification processes to reduce color-center causing defects and with various doping materials to compensate for the effects of lead and oxygen vacancies. (Note that although Molybdenum does not appear to form color centers, it does introduce a long relaxation time ( $\approx 1 \mu\text{s}$ ) scintillation component and is thus one of the major targets for removal.)

Despite these consistent sets of observations and explanations, we were worried that when these crystals are exposed to hadrons, including neutrons, they may suffer different kinds of damage and thus not survive the BTeV-like environment. Since charged hadrons and neutrons can interact with nuclei and change them to different elements, they can produce new crystal defects. A recoiling particle from the interaction can displace many atoms and produce a cluster of defects. On the other hand, for the crystal defect density created by hadrons to be comparable to that of the typical intrinsic defect density after 10 Mrad of absorbed dose, one must create one crystal defect for every 1 keV of energy deposit. This presumably led some researchers in the past to decide that the difference between hadrons and electron/photon radiation would be minimal. Nevertheless we wanted to test experimentally that hadrons and neutrons will not produce accumulating radiation damage. A significant part of our test beam studies of PWO crystals was focused on this issue. The study we carried out with extremely high dose rates (2-3 Mrad in 12 hours), where natural recovery from radiation damage was negligible, showed us that accumulation of damage was still tolerable. The effects of the electron irradiation and the pion irradiation on the overall light output change were quite similar at the same dose rates. This gives us confidence that PWO crystals will be useful over the life of the BTeV experiment.

### 6.3.1 Test Bench Measurements

Using radioactive sources,  $^{60}\text{Co}$ ,  $^{137}\text{Cs}$  and  $^{22}\text{Na}$ , we have measured the light output of sample crystals. These crystals were wrapped with Tyvek. Since most of the crystals were sent to IHEP for test beam studies, many of these measurements were done there, but some of them were done at Minnesota and Syracuse.

The pulse-height distribution of one of the Beijing crystals is shown in Fig. 6.1. The spectrum shown as the dashed line was obtained using an LED light pulser whose intensity was adjusted so that only some of the time one photoelectron is emitted by the photocathode of a Quanticon phototube, which is optimized to observe a single-photoelectron peak. The narrow peak near channel 50 is the pedestal and the next peak near 90 is due to one photoelectron. The spectrum shown as the solid line is obtained with 0.66-MeV photons hitting the crystal from a  $^{137}\text{Cs}$  source. The average peak pulse-height corresponds to 4 photoelectrons, but one can see separate peaks due to 1 to 4 photoelectrons. The peaks for 1 and 2 photoelectrons have contributions from the dark-current background of the phototube. Assuming that the average peak position is about 4 photoelectrons/0.66 MeV gamma, we

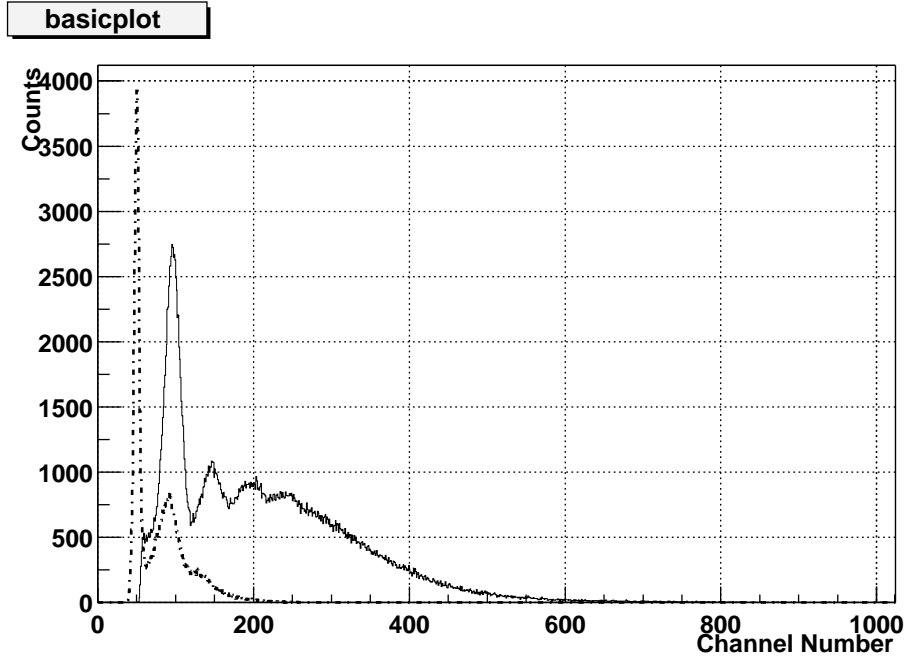


Figure 6.1: Pulse height distribution from a sample crystal using 0.66 MeV photons from a radioactive Cs source. Pedestal, one-photoelectron peak and signal peak are visible. The description of the dashed line is given in the text.

derive that the light output of this crystal is slightly less than 8 pe's/MeV into a 2-inch PMT.

The crystal light yields for some sample crystals from Beijing, Shanghai and Bogoroditsk are shown in Fig. 6.2. The mean is 7.9 pe's/MeV. We found about a 10% variation when we repeated these measurements, and attribute this to the temperature dependence of the background under the single-photoelectron peak. These measurements show that our sample crystals are as good as typical CMS production crystals.

Since the reliability of source measurements will be important in the acceptance testing of crystals, we have solved this problem by using a  $^{22}\text{Na}$  source, which produces a pair of 0.511 MeV photons back-to-back. We place a plastic scintillator on one side of the source, opposite from the test PWO crystal and trigger on the signal in the plastic scintillator when we measure the pulse height in the PWO crystal. This virtually eliminates the dark-current background in the large single-photoelectron peak and thus the time variation due to this background. Fig. 6.3 shows the triggered  $^{22}\text{Na}$  spectrum measured for one of our sample crystals at Minnesota. The whole spectrum is due to 0.511 MeV photons from the Na source. The prominent peaks due to one and two photoelectrons are consistent with the expectation for a Poisson distribution with an average of 2.8 photoelectrons per absorbed photon. Fig. 6.3 shows the result of a fit assuming that we observe 2.8 photoelectrons from the Na gamma rays. This method provides a significantly more reliable measurement

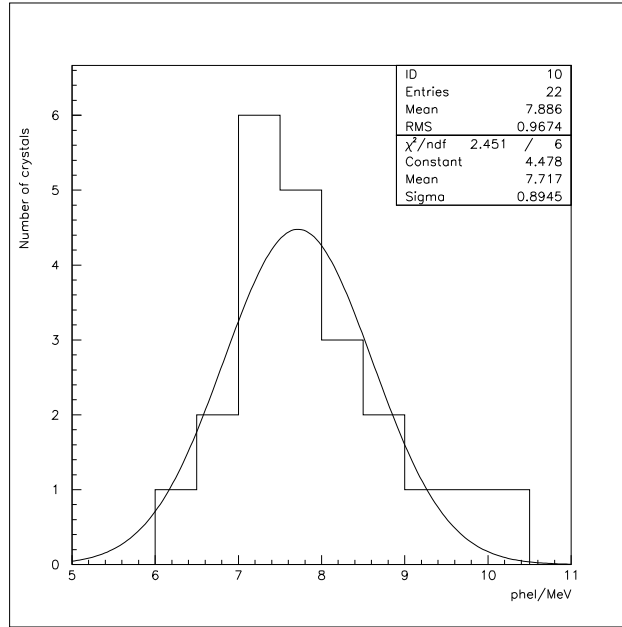


Figure 6.2: Photoelectron yields/MeV for the sample crystals.

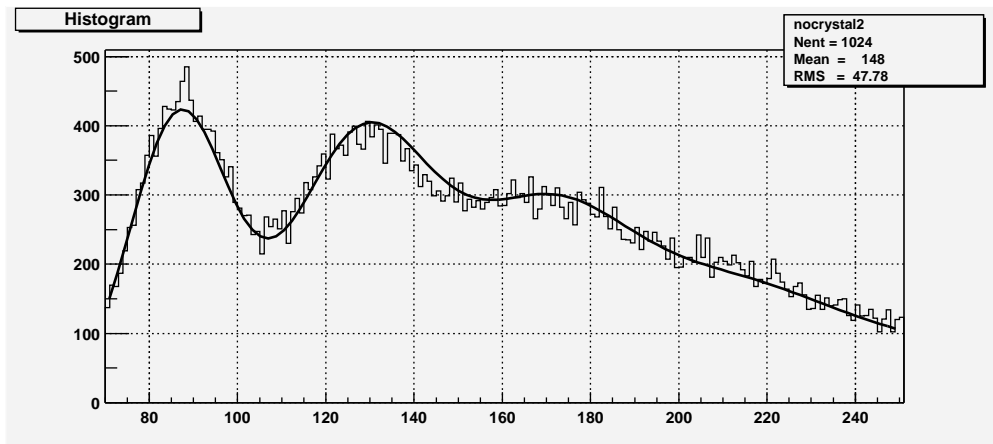


Figure 6.3: Pulse height distribution obtained with a radioactive  $^{22}\text{Na}$  source. The solid line is the result of a fit to the spectrum assuming that the average number of photoelectrons due to the Na gamma ray is 2.8.

Table 6.2: Radiation Tolerance of Optical Glues. Change in transmission after 11 Mrad of irradiation.

Glue	Change	comments
Epo-Tek 302	No change	
Meltemont light	No change	Heat to un-cure
Ock 451	No change	
NOA 81	No change	
NOA 61	No change	
Dow Corning	No change	
Histomont	No change	
Meltemont dark	-1%	Heat to un-cure
Ock 433	-3%	
Epo-Tek 301	-6%	
Epo-Tek 301-2	-7%	
Epo-Tek UVO	-10%	Only 1 Mrad

of the photoelectron yields of the PWO crystals. The difference between the sodium and cesium/cobalt sources is critical when the light output of the crystal is reduced in crystal-quality assurance operations, because here we want to avoid using optical grease to increase the coupling between a tested crystal.

With a source moved along the crystal we measured the light-output uniformity as a function of the distance along the crystal to the phototube end. Most of our test crystals are uniform enough (less than 1%/cm variation over the whole length of the crystal with no tyvek on the both small sides) not to degrade the energy resolution at high energies. Uniformity was also measured at the IHEP test-beam facility using a muon beam passing through the crystals transversely.

In addition to the crystals, the wrapping material should not deteriorate after radiation. Nor should the glue, used to join the crystals and PMT's, lose transparency. We tested three candidate wrapping materials: Teflon, Tyvek and aluminized mylar. Sample materials were used to measure the reflectivity at various incidence angles before and after 10 Mrad of irradiation using a Cs source. We did not observe any measurable changes. The uncertainty of the measurements was estimated to be about 5%.

Similar tests were done with 11 glue candidates. We glued two thin quartz plates with sample glues and measured transparencies using an LED light source and a PMT. We used a control sample, which was not irradiated, to check the stability of the setup. Table 6.2 shows the results of these measurements. Most of the glue samples lost very little transmission.



### 6.3.2 IHEP Test Beam Facility

Much of R&D studies on PWO crystals have been carried out at the IHEP test beam facility [3] [4]. The main facility provides both electron and pion beams. The energy range of the electron beam is from 1 to 45 GeV, while the pion beam was operated at 40 GeV. The maximum intensity of the pion beam is  $10^6$  pions/s allowing us to radiate crystals at a rate up to 60 rad/hour. The maximum electron beam intensity is at 27 GeV and was  $10^5$  electrons/s allowing radiation rates up to 30 rad/hour for the crystal directly hit by the beam. Each beam spill lasted about 1.5 sec of the full accelerator cycle of 9 sec.

The electron beam was used to study energy and position resolutions in addition to electron irradiation studies. The pion beam was used to irradiate crystals at high intensities. This beam has a significant number of muons that were used to monitor the light output changes. An LED based light pulser system was used to monitor PMT gain changes and to study and monitor crystal light loss [11]. A red LED was used to monitor the former while a blue LED was used for the latter, since the crystal transmission for red light is much less sensitive than for blue light.

Since the momentum spread of the electron beam is too large to study the energy resolution of the calorimeter, we installed drift chambers and an analyzing magnet to measure the momentum of each electron.

The BTeV ECAL testbeam setup consisted of a  $5 \times 5$  array of PWO crystals coupled to ten-stage photomultiplier tubes. Fig. 6.4 shows the inside of the temperature-stabilized ( $\pm 0.1^\circ\text{C}$ ) light-tight box with its cover removed.

The dimensions of the 25 Bogoroditsk, 25 Shanghai and 12 Beijing test crystals were  $27 \times 27 \text{ mm}^2$  in cross section and 220 mm in length, similar to the final BTeV size of  $28 \times 28 \text{ mm}^2$  by 220 mm. The dimensions of the four Apatity crystals were  $22 \times 22 \text{ mm}^2$  and 180 mm in length (ALICE specifications). All the crystals were wrapped with a  $170 \mu\text{m}$  thick Tyvek. Light from each crystal was measured by a 10-stage 1-inch diameter Hamamatsu R5800 PMT. For resolution studies, we used optical grease to improve optical transmission from crystals to PMTs but for radiation studies, we left an air gap between them because we did not want the issue of optical grease radiation tolerance to complicate our studies. Note that the real BTeV EMCAL will use optical glue between the crystals and the PMTs, and the glue's radiation tolerance has been studied separately.

### 6.3.3 Resolutions

In the following section we describe briefly our studies of the energy and position resolution of the small PWO calorimeter, using the IHEP test beam. A more detailed description is found in [5].

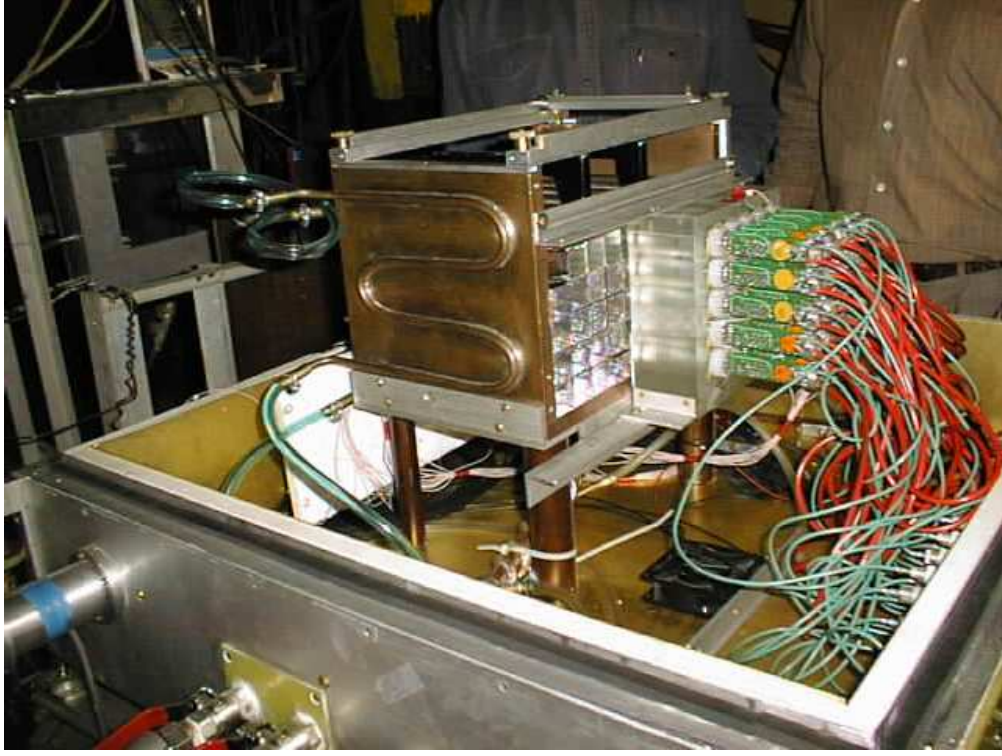


Figure 6.4: View of one of the crystal arrays tested at Protvino. The left half of the crystals have yet to be instrumented. The right half have the PMT's attached as well as the electronics.

### 6.3.3.1 Energy resolution

We measured the energy resolution of electrons as a function of energy by summing the light outputs of the  $5 \times 5$  array of crystals. The energies of the electron beam were 1, 2, 5, 10, 27, and 45 GeV.

The energy resolution,  $\sigma_E/E$ , is plotted as a function of  $E$  for the  $5 \times 5$  array of crystals in Fig. 6.5. The data were fit to the function

$$\sigma_E/E = \sqrt{a^2 + \frac{b^2}{E} + \frac{c^2}{E^2}} = a \oplus b/\sqrt{E} \oplus c/E, \quad (6.1)$$

where  $E$  is in GeV,  $a = (0.33 \pm 0.02)\%$  represents the constant term arising from calibration errors, shower longitudinal leakage, and non-uniformity in the light collection efficiency along the length of the crystals. This agrees very well with our expectation of 0.35%. The stochastic term,  $b = (1.8 \pm 0.1)\%$ , arises from photon statistics variations and the transverse leakage of shower outside the  $5 \times 5$  array of crystals. This also agrees very well with the expectation of  $(1.68 \pm 0.07)\%$ , as calculated assuming 10,000 photoelectrons per 1GeV. The term  $c = (2.4 \pm 0.2)\%$  arises from the momentum measurement errors due to multiple scattering of the electrons in the beam line upstream the prototype.

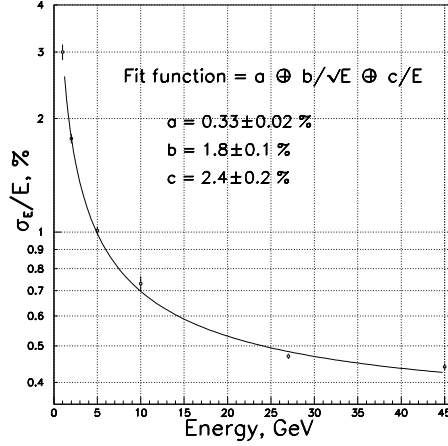


Figure 6.5: Measured energy resolution of the  $5 \times 5$  crystal matrix. The curve shows a fit to our experimental results (see text).

We studied the energy resolution for Bogoroditsk crystals and Shanghai crystals by using them in the center of the array, and they performed equally well, given no significant differences in their photon yield and non-uniformities.

The energy resolution shown in Fig. 6.5 was obtained for electrons incident within a small area at the center of the matrix of crystals. If we account for events with the beam hit anywhere within the central crystal of the  $5 \times 5$  crystal array, including gaps or nearby, the energy resolution  $\sigma_E$  degrades by about 20% at each energy. Increased fluctuations of an energy leakage outside the  $5 \times 5$  crystal array also contribute to this number. This observation is consistent with MC predictions.

The energy resolutions was also studied as a function of the incident angle.

The prototype was rotated by 5, 10 and 15 degrees relative to the normal. Data were taken with the electron beam of 10 and 27 GeV for each angle.

Both energy and position resolutions as a function of the angle of incidence are given in Figure 6.6. Energy resolution does not degrade significantly until the angle reaches beyond  $10^\circ$ . Effect on position resolution is discussed in the subsection below.

### 6.3.3.2 Position resolution

From the same data we used to study energy resolution, we obtained position resolution as a function of electron energy. The position of the electron was calculated from the weighted average of crystal positions in the shower, the center-of-gravity (COG), where the weight is proportional to the energy deposit in each crystal. Then it is compared to the position predicted by the beam-telescope drift chambers. The well-known bias in the COG was corrected on a statistical basis. The results are shown in Fig. 6.7. The MC prediction is represented in the figure by the curve that corresponds to  $\sigma x = a \oplus b/\sqrt{E}$ , where  $a = (0.17 \pm 0.01) \text{ mm}$

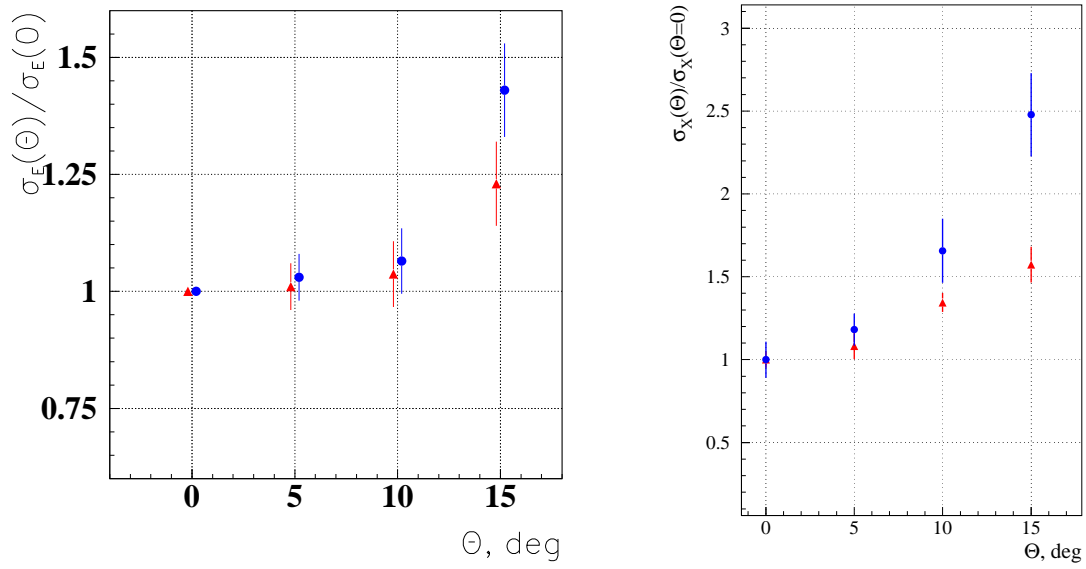


Figure 6.6: Energy (left) and position (right) resolution dependence on the angle of electron incidence. Resolution along the Y-axis is normalized to the resolution at  $0^\circ$ . Circular points correspond to 27 GeV measurements while triangles are for 10 GeV.

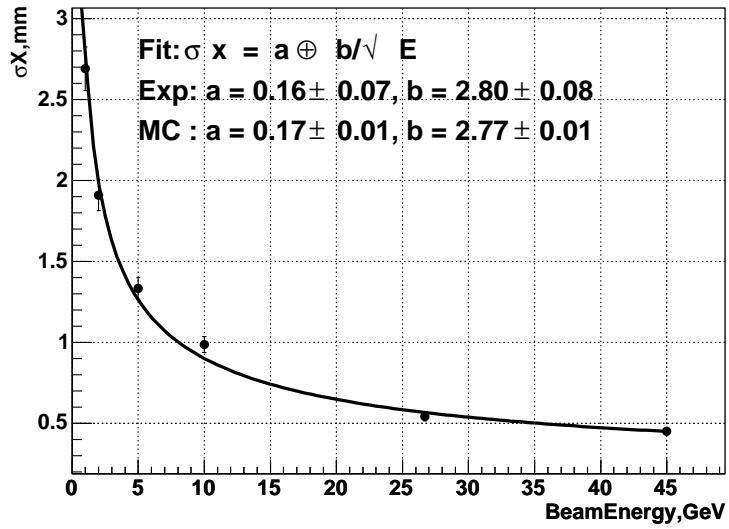


Figure 6.7: Position resolution vs energy. Dots represent the experimental data, and the curve represents Monte Carlo prediction.

and  $b=(2.77\pm0.01)\text{mm}$ . A fit of the experimental data to the same function results in  $a=(0.16\pm0.07)\text{mm}$  and  $b=(2.80\pm0.08)\text{mm}$ . This demonstrates that experimental results are in a very good agreement with the predictions.

Position resolution also strongly depends on where the electron hits the matrix of crystals. The  $\sigma_x$  ranges from  $\sim 0.28\text{mm}$  near the boundary between two crystals to  $\sim 0.71\text{mm}$  at the center of the crystal. The effect arises from equal sharing of energies between the two crystals in the former case and minimum energy sharing by the surrounding crystals in the latter.

As mentioned in the previous subsection, we also measured the position resolution as a function of the angle incidence. The results are shown in Fig. 6.6. A significant degradation in the position resolution is evident, especially at angle of  $10^\circ$  or higher. This would include a negative effect on the  $\pi^0$  mass and energy resolution at high energies, and in turn would affect the  $B$ -mass resolution in the decay modes that involve high-energy  $\pi^0$ 's. These studies justify that the projective geometry of the calorimeter was the right choice, especially given there is no appreciable additional cost to that.

### 6.3.4 Light response non-uniformity

GEANT [6] simulations show that a good light response uniformity along the length of the crystal is a key to achieving excellent energy resolution. The non-uniformity of the light yield (LY) along the crystal length contributes to the constant term of the relative energy resolution.

To measure the LY uniformity with the beam, the  $5\times5$  crystal matrix was rotated by  $90^\circ$  around the vertical axis and crystals were scanned using a muon beam in 1 cm steps. The position of the muon track going through the crystal was reconstructed using the drift chambers. Pulse-height distributions collected for each of the 1 cm intervals along the crystal lengths were fitted with a modified Landau distribution to obtain a peak position.

The peak position of the energy loss distribution for a minimum ionizing particle as a function of the distance to the PMT is shown in Fig. 6.8. The PMT position is at  $X = 0$  cm. The data were fitted in the region of the expected shower maximum (3 to  $10 X_0$ ) to a straight line in order to determine the slope of the LY uniformity. The LY values were normalized to the value of LY at  $X = 11$  cm. The distributions crystal to crystal look quite different because of difference in the crystals.

A distribution of the slopes of the LY uniformity was obtained for crystals from Bogoroditsk and Shanghai. The results are shown in Fig. 6.9. No difference between the Bogoroditsk and the Shanghai crystals was observed.

#### 6.3.4.1 Temperature dependence of the crystal light output

We made measurements of the temperature dependence of the PWO crystal light output. They were made at electron energies of 10 and 27 GeV. The rate of the temperature change was about  $1^\circ\text{C}/\text{hour}$  both during the warm up and the cool down periods. The temperature inside the box was measured using a 24 thermistor array. Their average value was used as

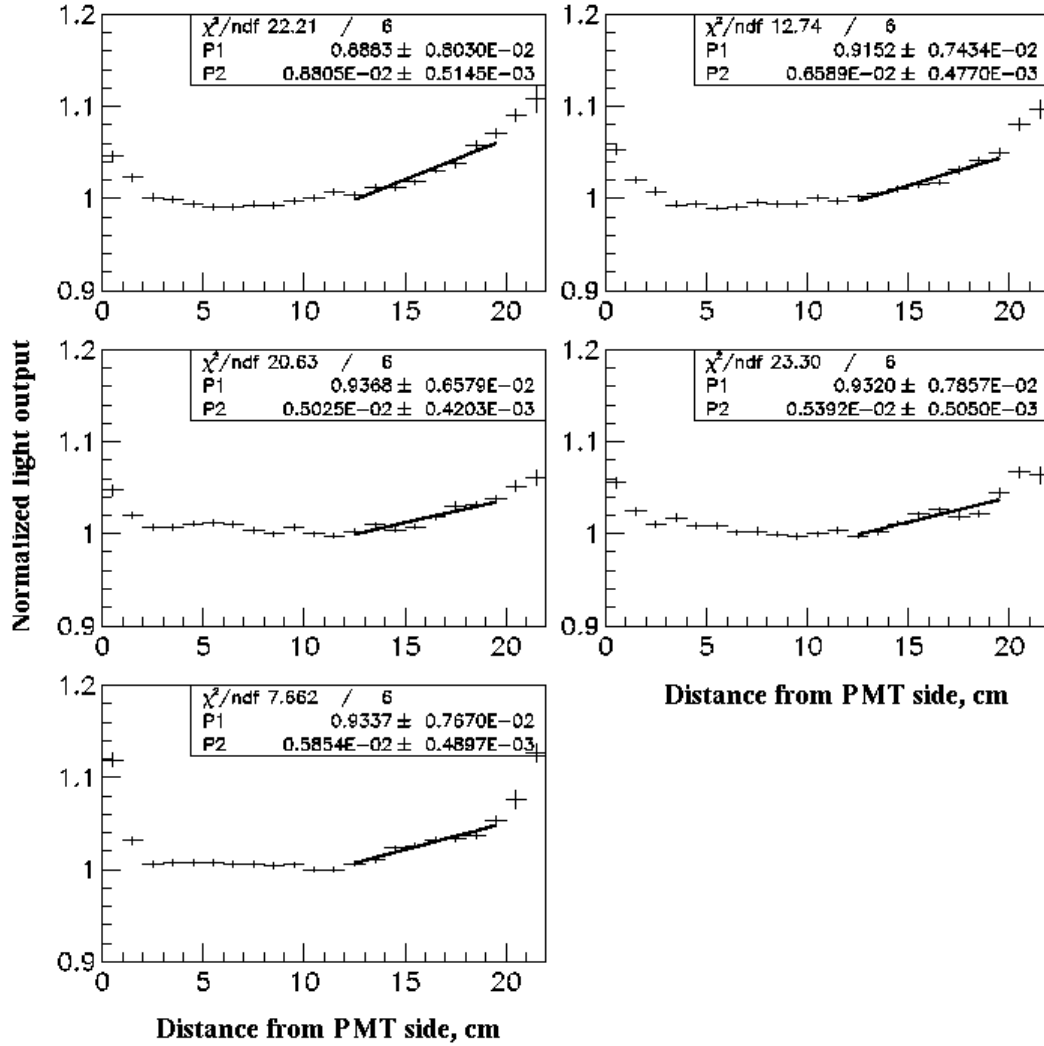


Figure 6.8: Fit results for the energy loss distributions of 5 crystals as a function of the position along the crystal for region 3-10 radiation lengths from the end of the crystal where the electron enters. The PMT position is at X=0 cm. Rise-up at the opposite to the PMT crystal side is due to internal reflection from tyvec. Light yields shown on the vertical axis were normalized to the LY at X=11 cm. Each plot corresponds to one crystal.

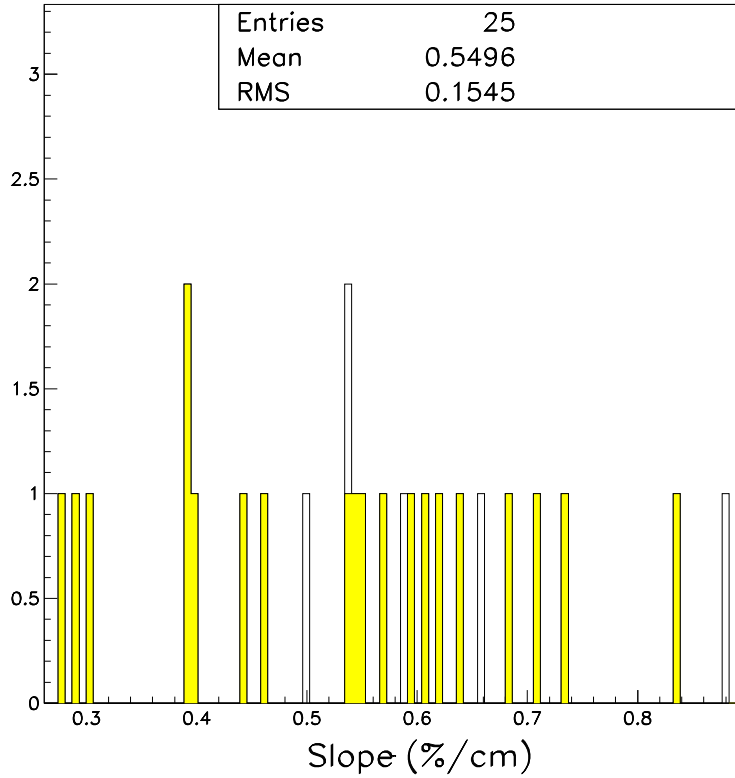


Figure 6.9: The distribution of the LY uniformity slope. The shaded histogram corresponds to 20 Shanghai crystals. The open histogram corresponds to 5 Bogoroditsk crystals.

the “crystal temperature.” The temperatures were measured once every spill (approximately 0.1 Hz). The slope of the change in the vicinity of 18 °C was found to be about -2.3% per C, in agreement with previous measurements. Figure 6.10 shows our measurements with 10 and 27 GeV electrons.

#### 6.3.4.2 Study of Potential Scintillation Mechanism Damage

Since no one has evidence of damage to the scintillation mechanism in PWO crystals after irradiation by a gamma-source [7], we have generally assumed that there is none. However, in one of our test-beam studies, we estimated its possible effects by a method suggested by Zhu [8].

We irradiated a small portion of several crystals using a 34-GeV pion beam. The pion beam was directed transverse to the length of the crystals. To estimate the effect of the radiation on the scintillation mechanism, we measured the light-output uniformity with a muon beam, also crossing the crystals in the transverse direction. If only the light-attenuation length (LAL) of the crystal suffers from radiation, the loss of light collection will not be

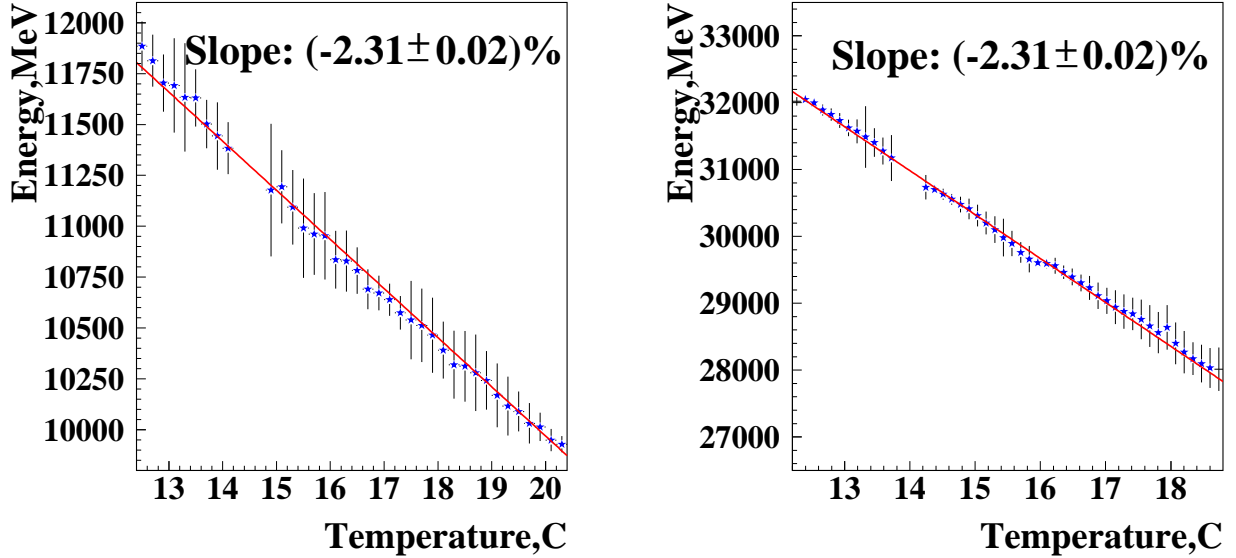


Figure 6.10: Temperature dependence of light output for one of the crystals. Temperature in  $^{\circ}\text{C}$  is along the  $x$ -axis. Light output in terms of ADC counts is along the  $y$ -axis. Measurements were done with 10 GeV (left) and 27 GeV (right) electrons.

localized in the damaged area, since light from other parts of the crystals will also suffer the loss. On the other hand, if the scintillation mechanism (SM) is damaged, only scintillation light produced in the damaged section will suffer. A difference in the measured light uniformity along the crystal length can then allow us to separate the two radiation-damage mechanisms.

For this study, the  $5 \times 5$  crystal matrix was rotated by  $90^{\circ}$  around the vertical axis and crystal light outputs were measured using a muon beam before and after irradiation by the pion beam. Two upper layers of the crystal matrix were irradiated by a 34 GeV negative pion beam. The pion beam size was approximately 2 cm horizontally by 6 cm vertically. The beam hit the centers of the crystals along their lengths. The crystals were irradiated for 28 hours with a beam intensity of  $6 \times 10^6$  particles/spill. This corresponds to an average dose rate of  $\sim 10$  rad/h, for a total of 300 rad.

To measure the light yield along the crystals, the position of each muon track going through the crystal was reconstructed using the drift chambers. Then the pulse-heights from the crystals were recorded, along with the position of the muon. Fig. 6.11 shows the results for a crystal for muons crossing the area of the crystal which was damaged by radiation. One can see clearly that the pulse-height decreased after irradiation. The pulse-height distribution for each crystal was fit for the peaks of the modified Landau distribution in bins of position.

Fig. 6.12 shows the average (peak) light output along the length of one of the crystals, both before and after irradiation. The ratio of the light outputs before and after the irra-



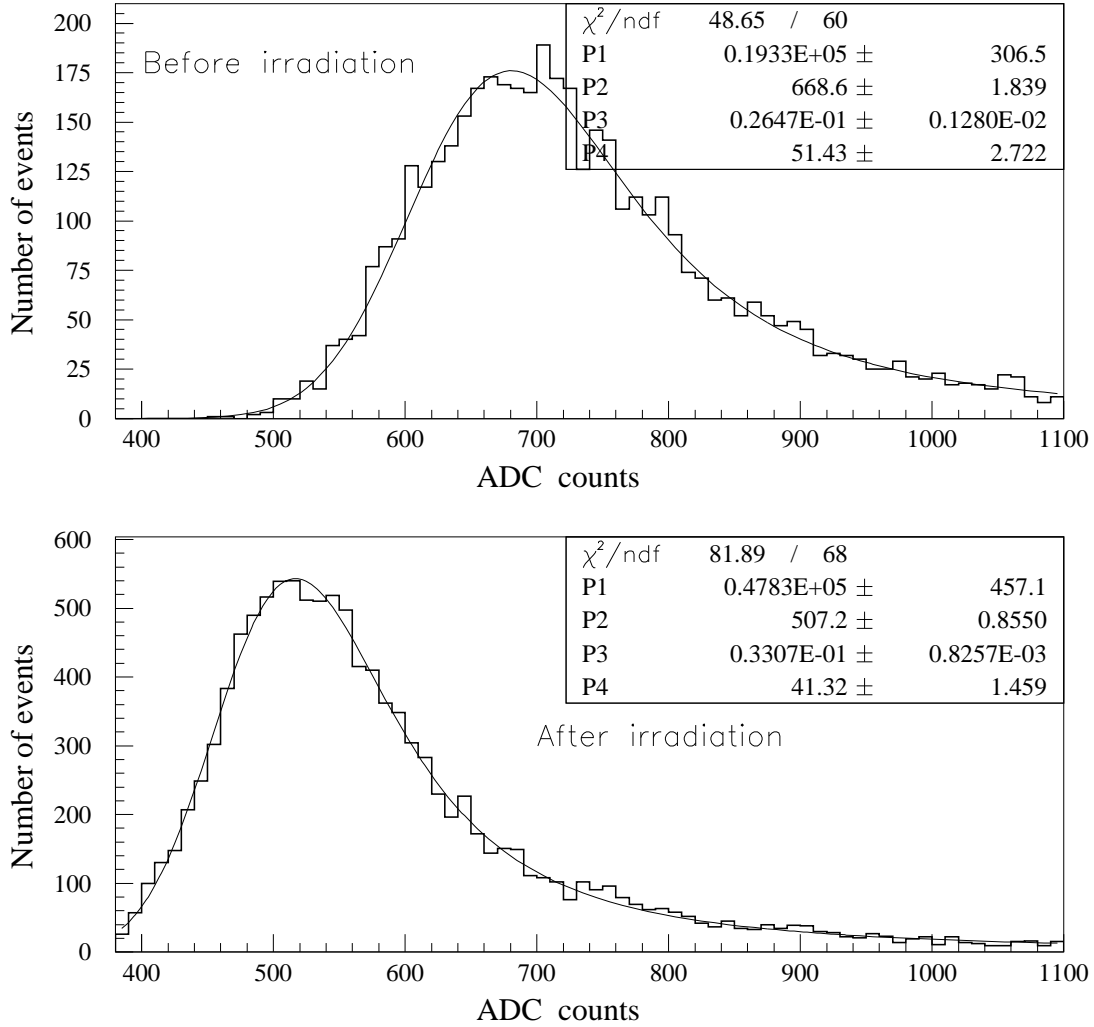


Figure 6.11: The energy-loss distributions and our fits to determine the peak positions for a single crystal, both before and after irradiation.

diation as a function of the longitudinal position is shown in the bottom of Fig. 6.12. The irradiated area is indicated by an arrow. We observe no significant additional light loss in this area, which would indicate damages in the scintillation mechanism. We computed the fractional light loss in the irradiated area relative to the rest of the crystal by calculating the ratio:

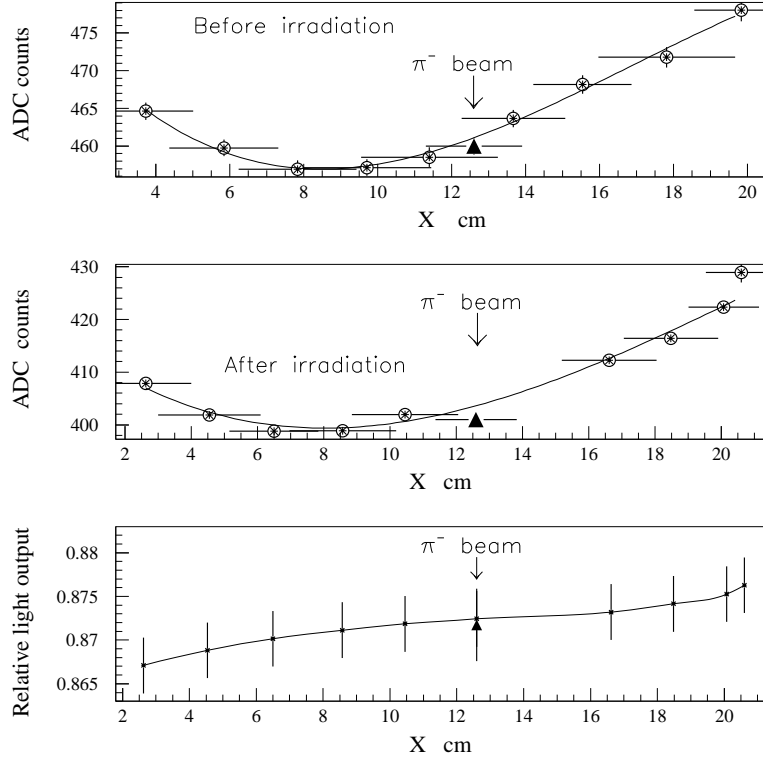


Figure 6.12: The light response non-uniformity before and after irradiation. The last plot shows the ratio of light yields before and after irradiation. Maximum intensity for the irradiating pion beam is at the  $X=12.6$  cm. The PMT position is at  $X=0$  cm.

$$rs = \frac{LO^a(x_\pi)}{LO_f^a(x_\pi)}, \quad (6.2)$$

where the numerator is a Light Output at the pion-beam position  $x_\pi$  measured after the crystal irradiation, and the denominator is the Light Output evaluated from a fit. Index  $a$  refers to quantities obtained after irradiation. If  $rs$  is unity, there is no localized loss, and any value less than 1 indicates a loss. The values of  $rs$  are shown in Fig. 6.13. They show that within our  $\sim 1\%$  accuracy we observed no change in the scintillation mechanism.

### 6.3.5 Radiation Hardness

In this section, we summarize what we learned about the effects of radiation on PWO crystals. We will start with our estimates of the radiation level PWO crystals receive at

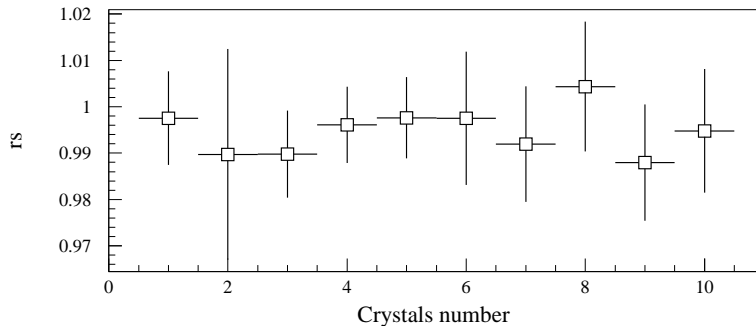


Figure 6.13: The intrinsic scintillation component of the light output change for ten crystals. The first five crystals are from Bogoroditsk and the second five crystals are from SIC and are tapered.

different locations in BTeV, and also at the IHEP test facilities. This study was based on simulations using the MARS code [9]. Then we will discuss results obtained at various radiation facilities: modest dose studies at the test-beam facility with both electron and pion beams, high dose studies at the facility near the U70 accelerator, and radioactive source studies. A more detailed description of the radiation hardness study is given in Ref. [10].

Note that Tyvek wrapping has been shown to withstand the radiation dose delivered in this study. The same applies for the PMT windows, since even regular borosilicate glass does not lose transparency up to at least 10 krad, and quartz glass is unaffected up to 1 Mrad, both within an error of 1%. Six quartz-window PMT's were used for a part of our test beam study, and the rest were borosilicate-window PMT's.

### 6.3.5.1 Simulation of the radiation environment

The BTeV EMCAL extends outward from the beam line to a radius of 1.6 m. The crystals near the beam pipe receive the highest dose. At the outer radii, the level of radiation is smaller by more than three orders of magnitude. In addition, because the dipole magnet around the primary interaction region sweeps most of the charged particles in the vertical directions, there is much more radiation directly above and below the beam line compared to other parts of the calorimeter. In order to estimate the level of radiation in the crystals we performed calculations using the MARS code. The estimates of the absorbed dose rates expected in BTeV are shown in Fig. 6.14. The  $\eta$  (pseudo-rapidity) shown here reflects the coverage of the BTeV EMCAL, where  $\eta$  of 4.45 is at the extreme inside near the beam and  $\eta$  of 2.27 is on the extreme outside. Note that the dose was calculated near the “shower maximum” 5-7 cm from the front of the crystals. The fraction of crystals receiving various doses is given in Table 10.9.

Table 6.3: Fraction of crystals with given absorbed doses and dose rates at the maximum of the dose profiles inside the crystals in BTeV (100 rad = 1 Gy)

Relative number (%)	Absorbed dose (krad/year)	Dose rate (rad/h)
11	0.3 - 1	0.11 - 0.36
22	1 - 2	0.36 - 0.72
27	2 - 5	0.72 - 1.8
12	5 - 10	1.8 - 3.6
16	10 - 50	3.6 - 18
6	50 - 100	18 - 36
3	100 - 200	36 - 72
2	200 - 500	72 - 180
0.4	500 - 1000	180 - 360
0.2	1000 - 2000	360 - 720

In the testing facility, we tried to emulate various aspects of the BTeV conditions as much as possible. Both a 27 GeV electron beam and a 40 GeV  $\pi^-$  beam were used to irradiate the crystals with moderate dose rates of 1 to 100 rad/h. Electron and pion dose profiles in the crystals are different; see Fig. 6.14 (c-d). The crystals receive radiation from pions almost uniformly along their length starting from a distance of 5-7 cm from the front. For electrons the absorbed dose rate at shower maximum is two orders of magnitude higher than the dose near the crystal ends.

The difference in the radiation profiles between pions and electrons explains the difference in the radiation profiles in BTeV between crystals near the vertical and horizontal planes. Around the vertical plane, since many charged hadrons are swept into this region by the IP magnet, there are more hadrons. Meanwhile, in the horizontal plane, most of the radiation is due to photons from  $\pi^0$  decays, so there are not as many hadrons entering this area. As a result, radiation at the rear end of crystals in the horizontal plane is a few orders of magnitude smaller than at the shower maximum. In the vertical plane, meanwhile, much radiation is from hadrons, and radiation at the rear end of the crystals is still substantial. This is one of the reasons why we used both electron and pion beams to study radiation damage of the crystals. We also wanted to verify our assumption that there is no substantial difference in the radiation damage due to electrons and hadrons.

### 6.3.5.2 Moderate dose irradiation - electron beam

We irradiated an array of crystals for Bogoroditsk, Shanghai, and Apatity with the 27-GeV electron beam for one week. The beam intensity was  $10^5$  particles/s most of the time during the irradiation. Transverse profile of the beam was bell-shaped, where 90% of the particles

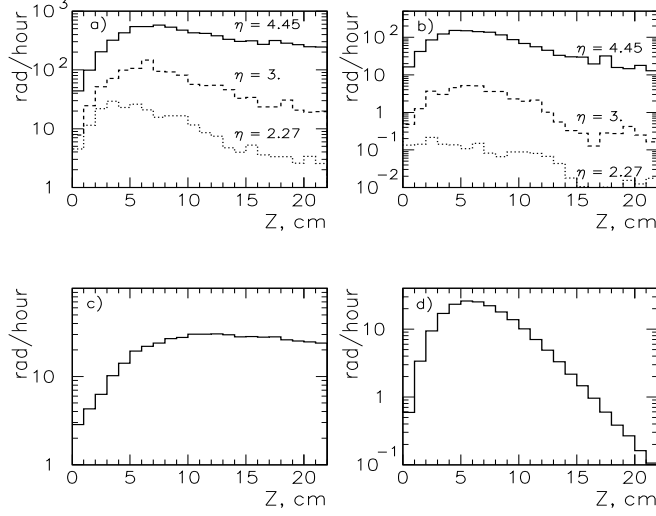


Figure 6.14: Longitudinal profiles of the absorbed dose rate (a) at the vertical plane, and (b) horizontal planes of the BTeV EMCAL at different rapidities, and at IHEP testbeam with (c) 40 GeV pions, and (d) 27 GeV electrons. The length of the crystal is 22 cm. The electron profile is calculated for  $10^4$   $e^-$ /sec, and the pion profile by  $10^5\pi$ /sec.

were within a spot of 8 cm horizontally and 6 cm vertically. This means that at a given time a set of 6 crystals received a significant dose, between 12rad/h and 22 rad/h, which corresponds to the dose rate that 80% of BTeV crystals will receive. Other 19 out of 25 in this study received a much smaller dose. We irradiated two sets of 6 crystals one after another, spending about 85 hours at each set, by pointing the beam at different places in the array.

Fig. 6.15 shows typical changes in the light output from a crystal under irradiation, at the average dose rate of 15rad/h. The top plot shows the light output changes over 85 hours. The dose rate profile vs time is shown in the middle plot. The bottom plot shows cumulative dose, which reached 1.2 krad for this crystal. Light output degrades at a faster rate at the beginning of the irradiation; degradation slows down with time and clearly exhibits tendency to plateau, due to self-annealing.

In this study, light output loss in the state of saturation is estimated in the range from  $\sim 5\%$  to  $\sim 12\%$ . In general, it is a function of the dose rate and not of the integrated dose; however at a given irradiation intensity it may also vary somewhat from crystal to crystal.

Light output degradation under irradiation of constant intensity fits well to the function

$$f(t) = N(1 - a(1 - \exp^{-bt})) , \quad (6.3)$$

where  $a$  represents fractional light loss and  $1/b$  is the characteristic time that light loss reaches saturation, and  $t$  is the time in units of hours.

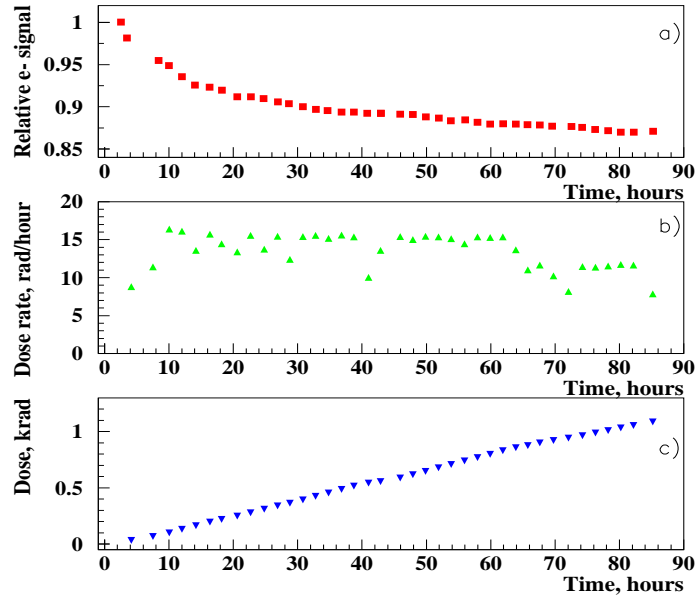


Figure 6.15: (a) Electron signal in a Bogoroditsk PWO crystal (B14) over 85 hours while being irradiated by 27-GeV electrons. (b) Dose rate. (c) Cumulative absorbed dose.

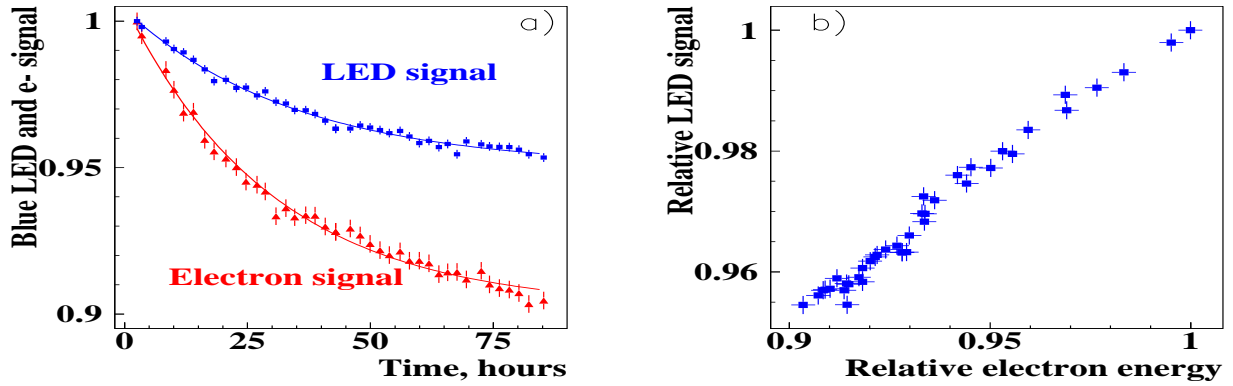


Figure 6.16: (a) Blue LED and electron signal correlation for Shanghai crystal S22, which was irradiated by 27-GeV electrons with a dose rate of 16 rad/hour. (b) Blue LED-electron correlation for the same crystal.

Changes can be monitored by blue LED (wave length 470nm); response to the electron beam and to the blue LED scale well, as shown in Fig. 6.16 for a crystal from Shanghai.

### 6.3.5.3 Moderate dose irradiation - pion beam

We also studied effect of irradiation by hadrons, with 40GeV pion beam. We wanted to know whether or not :

1. there was a significant difference between effects by hadron, electron or photon irradiation, at the same dose rate;
2. there was a significant damage at higher dose rates since the rate provided by electron beam was limited to 22 rad/h

Crystals were irradiated by the 40GeV pion beam for 4 days. As in the electron irradiation, the transverse profile of the beam was bell-shaped, roughly 8 cm horizontally and 6 cm vertically, with 90% of the particles within this area. The study was done as a series of runs. Each run lasted for 6 hours. Six crystals were irradiated with a dose rate ranging from 10 to 60 rad/h while other 19 crystals received less than a few rad/h. Irradiation runs alternated by low intensity 27GeV electron beam exposures to measure the light output degradation. We also used pure muon beam to measure the light output, as a cross-check.

We found that, qualitatively crystals behave in a similar way under electron or pion irradiations. They clearly exhibit tendency to saturation at a given dose rate, due to self-annealing. As in the case of electron irradiation, the degree of signal degradation measured in the state of saturation is a function of the dose rate and not of the absorbed dose; also, an exact amount of light output loss in a given crystal is a property of the crystal.

Changes of signal can be monitored by either blue LED, electron beam, or MIP. Response of two crystal to MIP vs absorbed dose is shown in Fig. 6.18(a) and (b). Correlation between response to the electron beam and to the blue LED during pion irradiation is shown in Fig...; pion irradiation data are represented by dots and agree well with the linear fit. As a reference, this figure also includes similar data taken during electron irradiation, represented by open triangles, that agree well with both data under pion irradiation and the predictions of the linear fit. This plot demonstrates that crystals behave in a similar way under electron or pion irradiation.

We also studied whether the irradiation induced any changes in the response along the crystal. The array of crystals was rotated by 90° with respect to the beam direction and was scanned with the muon beam. The test was done before and right after the pion irradiation. No significant changes in the response along the crystals were found, up to the dose rate of 60rad/h (accumulated dose of up to 4krad), even if the irradiation caused light output loss up to 30% in some cases.

This implies that the energy resolution of the crystals will not suffer from radiation-induced non-uniformity.

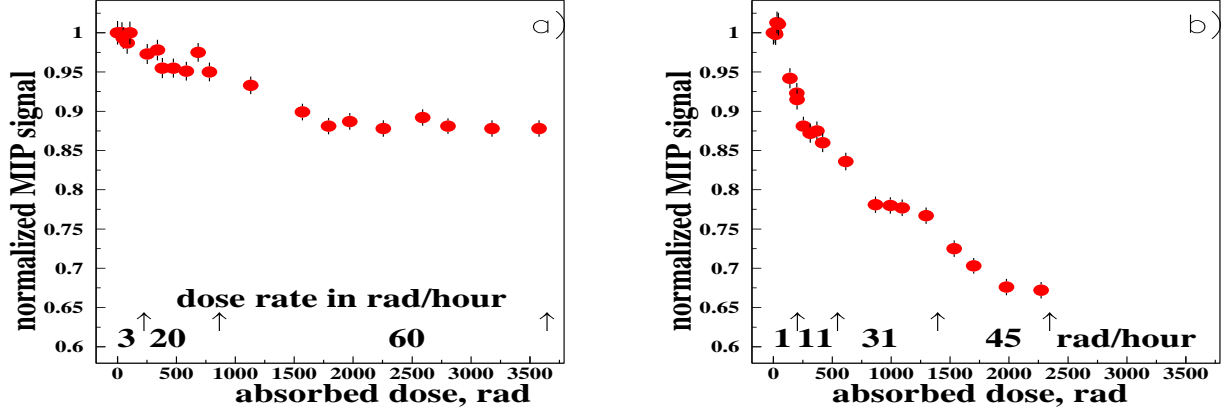


Figure 6.17: Normalized MIP signal vs absorbed dose for Shanghai crystals S16 and S20

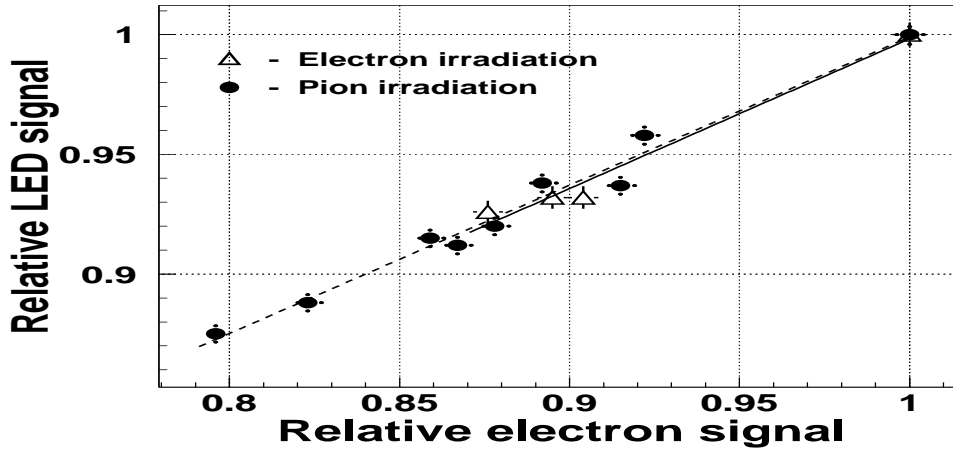


Figure 6.18: Correlation between blue LED signal and electron signal under pion (dots) and electron (open triangles) irradiation.

#### 6.3.5.4 Gamma irradiation - $^{137}\text{Cs}$ source

WE have also done studies to compare crystals light output change under pion and gamma irradiation [12].

Six of the crystals previously irradiated by 40-GeV pion beam with dose rates (30-60) rad/hour were left to recover for over a year at room temperature. Then these crystals were irradiated using  $^{137}\text{Cs}$  gamma source at the dose rates (20-100) rad/h. The dose rate profile along the length of the crystal was the same for both irradiation procedures.

Light output loss as a function of an absorbed dose for one of the six crystals under pion and gamma irradiation is presented in Figure 6.19. The behavior of the crystal under two different types of irradiation is similar. Dependence of a signal loss on the absorbed dose under only gamma irradiation for two other crystals is presented in Figure 6.20. Signal



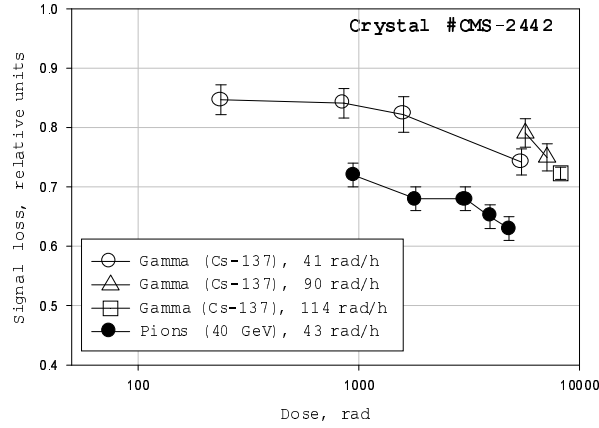


Figure 6.19: Light output loss for the crystal CMS-2442 under pion and gamma irradiation.

degrades rapidly with the absorbed dose up to 100-200 rad, then degrades at a significantly lower rate until the saturation level is reached. Saturation levels are different for different crystals. The same dependence under pion irradiation looks similar.

Ratios of pion/gamma signal losses at the state of saturation caused by irradiation at the same dose rate profiles, for the six crystals are shown in Figure 6.21. These ratios are close to each other and are in the region between 0.8 and 1. One may conclude that pion and gamma irradiation at the same dose rates affect lead tungstate crystals in a similar fashion.

#### 6.3.5.5 Super-intensive beam irradiation

Six crystals from Bogoroditsk and Shanghai were irradiated by secondary particles coming directly from the internal target of the Protvino U-70 accelerator. Two of them, Bogoroditsk B21 and the Shanghai S25, were irradiated at a dose rate of 100 krad/h, and four others, at 1 krad/h. The radiation profile along the length of crystals as well as the composition of charged hadrons, photons/electrons and neutrons in this radiation facility is fairly close to those we will encounter in the BTeV calorimeter. Note also that the cumulative dose of crystals exposed to the higher dose rate of 100 krad/h is comparable to the yearly dose of those few BTeV crystals at the high end of the dose rate range, and to the dose of 10 years worth of running for the top 3 per cent of crystals.

The dose rate was calculated using MARS program and estimated to be accurate to 30%. The calculations were tested by Thermal Luminicent Dosimeters (TLD) and by the ionization chamber measurements at various locations near the crystals. The accuracy of the absorbed dose measurements was estimated to be 30% each. These measurements were in general agreement with the results of the MARS calculations; in the worse case, they differed by a factor of 1.5. The dominant systematic error of the calculations was attributed to the accuracy of the irradiation facility geometry.

These crystals were exposed to radiation in 5 separate rounds, and after each round, we measured the light output of these crystals in the electron beam. Light output losses vs

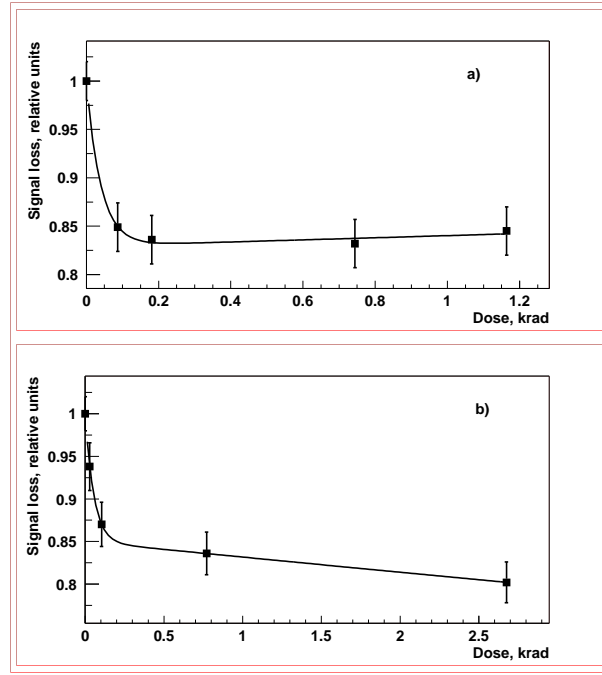


Figure 6.20: Dependence of a signal loss on the absorbed dose under gamma irradiation with a dose rate of 29 rad/h for the two crystals : (a) CMS-2443 and (b) - Bogo2313. Both crystals were produced in Bogoroditsk.

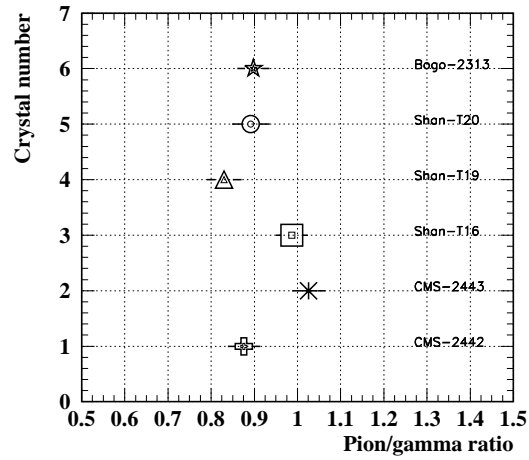


Figure 6.21: Ratios of the two signal losses at their saturation levels, under pion and under gamma irradiation for the same dose rates (30-60 rad/h) for the six crystals.

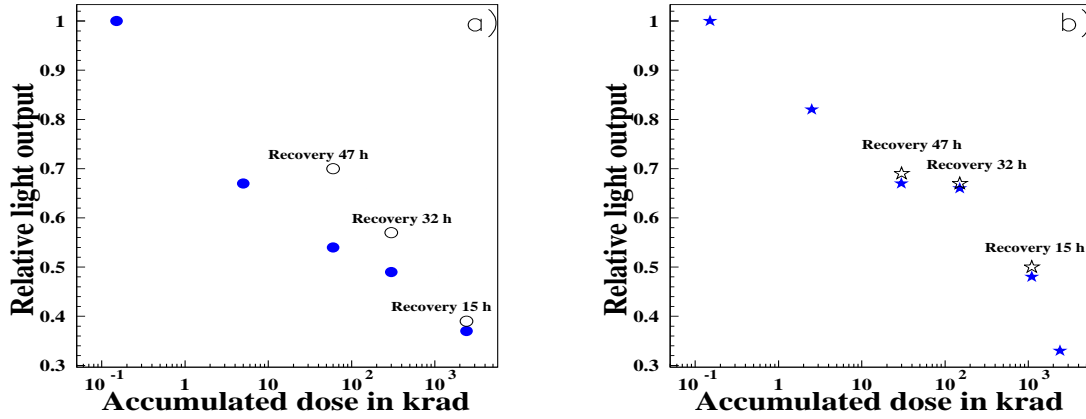


Figure 6.22: Light output changes in the Bogoroditsk crystal B21 (a) and in the Shanghai crystal S25 (b) versus absorbed dose (in krad). Dots represent data taken in the 27 GeV electron beam after immediately after irradiation (100 rad = 1 Gy). Open circles represent signal recovery after specified period of time.

absorbed dose for two crystals, one from Bogoroditsk and one from Shanghai, are presented in Fig. 6.22. Plots include results on signal recovery as well.

One of the most important conclusions is that even after an integrated dose about of 3.1 Mrad and 1.6 Mrad, both crystals remained usable. Even though they lost 2/3 of their light, these severely damaged crystals would form a very respectable calorimeter compared to a calorimeter of any other technologies choice. Note again that we expect only 0.1% of the crystals to receive this much dose in a year and 3%, in 10 years. Most likely, even these few crystals will not suffer radiation damages nearly as severe as these sample crystals since they will have a year to 10 years to recover from the damages while being irradiated.

### 6.3.5.6 Crystals recovery

After the irradiations by electrons and pions were completed, the HV was kept on the PMT's, to study crystals recovery for  $\sim 100$  days. Crystals behaviour was monitored with the LED signals. Crystals were found to re-gain their light output, at the level of  $(98 \pm 1)\%$  of the signal as it was before the irradiation started. Again, no difference between Bogoroditsk or Shanghai crystals were observed during the recovery. Typical changes of the light output from crystal during the recovery is shown in Fig.6.23, as a function of the recovery time.

### 6.3.5.7 Conclusions from the test-beam based radiation hardness studies

From this experience we learned several important lessons.

Light output from the crystals degrades under irradiation, at dose rates of 1 rad/h and above. This happens due to formation of so called color centers that affect crystals transparency, as valence electrons get trapped around crystal defects.

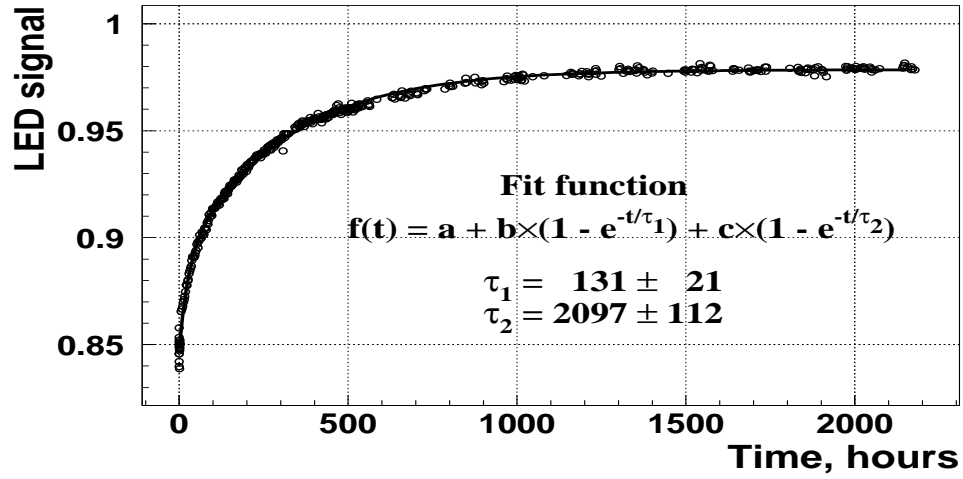


Figure 6.23: Blue LED signal of the Apatity 1434 crystal which was irradiated by 40 GeV pions for 100 hours and then recovered during the next 400 hours (a). LED damage recovery of the same crystal (b). We see that after 400 hours, the crystal recovered 90% of its light output loss.

Since the color centers are metastable states of varying lifetime and “potential barriers”, crystals are able to recover from the damage (self-annealing), if no longer irradiated or even under irradiation. Because of this, at the beginning of irradiation light output degrades at a fast rate. Then, if the dose rate is constant, self-annealing starts reducing the number of previously created color centers, gradually slowing down light output loss, until at a certain point damage and recovery processes balance each other, thus crystals reach so called saturation. While reaching saturation is a function of the dose rate, an absolute amount of light loss by a particular crystal, as measured in the state of saturation, is also a property of the crystal. This will be taken into account during detector operation.

If left to rest for an extensive period of time, crystals re-gain their light output almost to the level of what it was before the irradiation, i.e.  $(98 \pm 1)\%$ .

Note that crystals behave in a similar way under either pion or electron irradiation. No damage in the scintillating mechanism due to hadron irradiation was found.

It should also be noted that crystals remained usable even after super-intensive irradiation with the dose rates several orders of magnitude heavier than expected in BTeV.

Monitoring changes in the signal with the blue LED demonstrated that the response to it scales well with the response to an electron beam; linear approximation is good enough to determine the scale between those responses.

However, fluctuations in the light output from crystals during detector operation, as well as some variations in the crystals intrinsic properties, bring up two important issues. First of all, good continuous calibration of the crystals is required. It will be done mainly with electrons produced in physics data. Light monitoring system based on LED’s will be used in-between obtaining enough physics data for electron calibration and during shutdown periods.

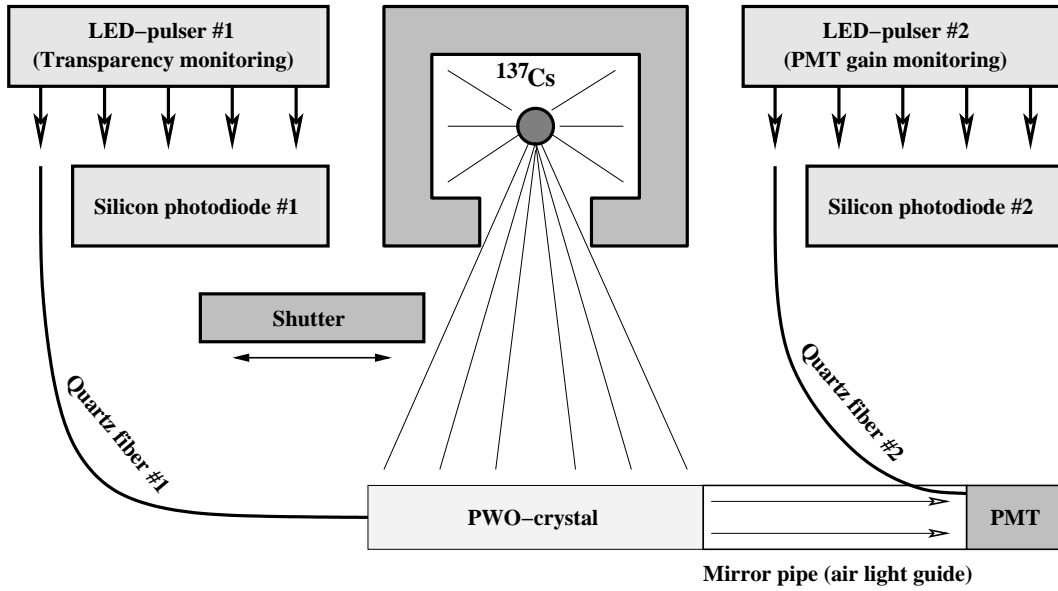


Figure 6.24: Block diagram of the GIF prototype.

Details will be given later in this chapter. Second, good quality control and estimate of the crystals characteristics before their installation into the calorimeter will also be very useful. Taking into account that pion and gamma irradiation at the same dose rates affect lead tungstate crystals in a similar fashion, it is planned to do this with the gamma-irradiation facility, rather than with the beam, to reduce the cost.

#### 6.3.5.8 IHEP Gamma Irradiation Facility

Gamma irradiation facility (GIF) is a part of the Quality assurance system. The GIF prototype was designed and installed at IHEP in May 2004. It provides continuous measurements of crystal transparency and light output changes under irradiation using a  $^{137}\text{Cs}$  gamma source [12].

The schematic view of the prototype is shown in Fig. 6.24. It consists of the collimated radioactive source with a shutter and a monitoring system, including LED-pulsers, silicon photodiodes, PMT and thermo sensors (not shown) measuring temperature of the crystal, PMT, LED-pulsers and air at the place of irradiation.

The radioactive source has an activity of  $5 \times 10^{12}$  Bq that allows one to irradiate crystals with a dose rate up to 110 rad/hour depending on a distance between the crystal and the source. To avoid unnecessary irradiation of the phototube, a mirror pipe is used as a light guide between the crystal and the PMT photocathode window. Gammas cause intense scintillations in the crystal resulting in permanent photocathode illumination and, thus, a DC anode signal proportional to the crystal's light output. This current is measured in a 1  $\mu\text{sec}$  gate using an integrating ADC.

The crystal transparency change is monitored using the LED-pulser #1. It provides 100 ns light pulses averaged at 470 nm wavelength. The LED-pulser #2 with an LED of 450 nm average wavelength and the same pulse duration is used to track any possible change of the PMT gain. The correction on this signal allows one to extract pure crystal response on the irradiation. The stability of the light pulse intensities is monitored using the silicon PN-photodiodes.

Light from the LEDs is transmitted respectively to the crystal and to the PMT window through the quartz radiation hard optical fibers. The LED-pulsers are triggered alternatively by a DAQ program. The PMT anode signals from the both LEDs appears at the ADC input in sum with the signal from gamma source. The same duration gate is used for the combined signals charge integration, so the pure PMT response on the LED flashes can be easily obtained in an offline analysis by subtracting a separately measured source signal as a pedestal. The measured source signal itself contains pure pedestal. Its value can be obtained in a dedicated measurement with a closed shutter each time before irradiating a new crystal and then subtracted, assuming that pedestal is stable during the whole irradiation time. It is foreseen nevertheless a remotely controlled blind to be placed in front of the PMT window in a real GIF in order to measure pedestals during the irradiation. The instability of the monitoring system is found to be better than 0.2% over the week.

The GIF prototype operation is illustrated in Fig. 6.25. The crystal CMS2442 with known radiation hardness properties produced by Bogoroditsk Plant [12] was irradiated using dose rates of 25 rad/h and 100 rad/h. The first 20 hours interval shows the decrease of the crystal light output (Fig. 6.25 a)) and transparency (Fig. 6.25 b)) under dose rate of 25 rad/h. The next 28 hours shows the further signals degradation at the higher (100 rad/h) dose rate. One can see the recovery process over the last  $\sim 20$  hours when the crystal was exposed to irradiation at 25 rad/h again.

38 crystals (mainly from Apatity) were irradiated with the GIF prototype in the summer 2004. Their light output degradation after 20 hours of exposition at 100 rad/h dose rate is shown in Fig. 6.26.

### 6.3.6 Crystal Specification

Table 6.4 shows our current idea of PWO crystal specifications. Ideally, we want to measure all the production crystals at a test beam facility to measure the light output, its uniformity along the crystals, the speed of the signal, and the radiation hardness under BTeV-like conditions. The first three are actually easy to measure on a test-bench setup using  $^{22}\text{Na}$  source. We will not have enough time to measure the radiation hardness for every crystal using a test beam. So we want to measure various characteristics of crystals from these manufacturers using the test beam facilities at IHEP and FNAL as well as test-bench measurements. From these studies, we expect to be able to find the most sensible specifications for the crystals.

The crystal manufacturers will measure: the crystal dimensions, the absolute light output, the fraction of light in the first 130 ns, the uniformity of light along the crystal, and that the crystal light output does not change more than 5% after exposure to a 15 rad/h source for

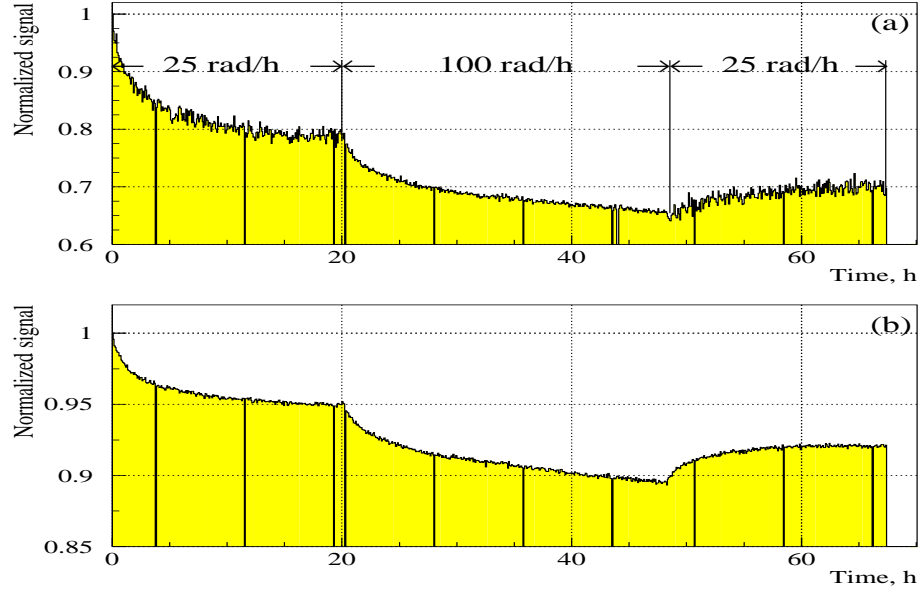


Figure 6.25: Crystal CMS2442 under irradiation with different dose rates: a)light output change; b)transparency change.

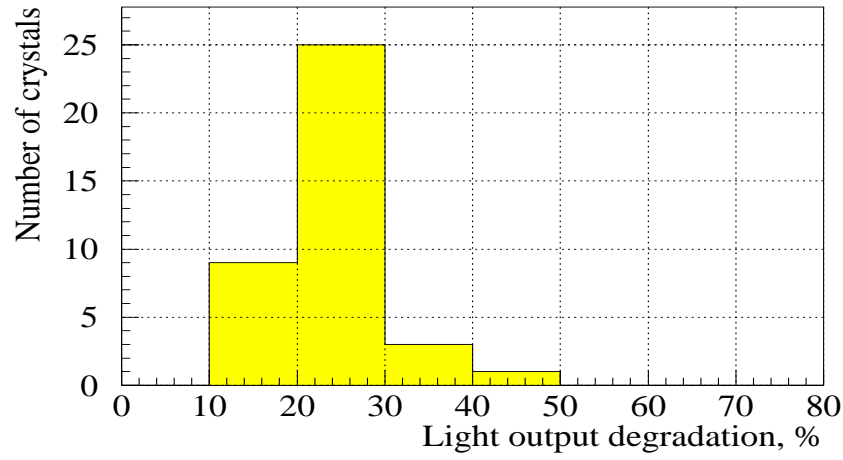


Figure 6.26: Relative light output loss for the 38 set of crystals after 20 hours of irradiation at the dose rate of 100 rad/h.

Table 6.4: PWO Crystal Specifications

Average light output	8 photoelectrons/MeV	measured with 2 in PMT with bialkali photocathode
Light uniformity	$< 1\%/cm$	3 to 10 cm from front
Fraction of signal in the first 130 ns/1 $\mu s$	98%	
Radiation tolerance	$< 5\%$ change in light output	exposed to 15 rad/hour from $^{137}Cs$ or $^{60}Co$ , photons uniformly over the length for 120 minutes
Dimensional tolerance	$+0 - 100 \mu m$ relative to the nominal size	

two hours. BTeV institutions, most likely IHEP in Russia and Nanjing in China will test all of the crystals to make sure that they agree with the manufacturers measurements. Any significant differences need to be quickly resolved.

## 6.4 Photodetectors and Read-out Electronics

### 6.4.1 Photomultipliers

The BTeV electromagnetic calorimeter is not in the magnetic field. A shielding for fringe fields from the toroid and the vertex magnet is foreseen. Therefore photomultiplier tubes can be used as photo-detectors to detect and measure the amount of scintillation light from individual crystals. The quantum efficiency of the photocathode is one of the most important parameters that affect the performance of the calorimeter. Another important property is how stable the phototube gain is so that we don't have to rely too heavily on the calibration system to correct for these changes. Phototubes must have very low dark current, a few nA. They must be relatively stable. They should have insignificant gain changes when the current changes. They have to be of one inch in diameter to be smaller than the crystal and leave sufficient room for assembly. Photocathode windows have to be tolerant to irradiation.

All the phototubes need to be tested before being used in the calorimeter. The quantum efficiency of the photocathode (cathode sensitivity) and gain (anode sensitivity) will be measured using a standard-intensity light source. The PMT manufacturers will provide these measurements. BTeV institutions will re-measure the same quantities and perform some long term tests on smaller samples. We require 10,350 PMTs including spares.

The PMT must be stable over the life of the experiment and radiation tolerant. Values of the absorbed dose in the phototubes glass windows obtained using the MARS program are presented in Fig. 6.27 and Fig. 6.28.



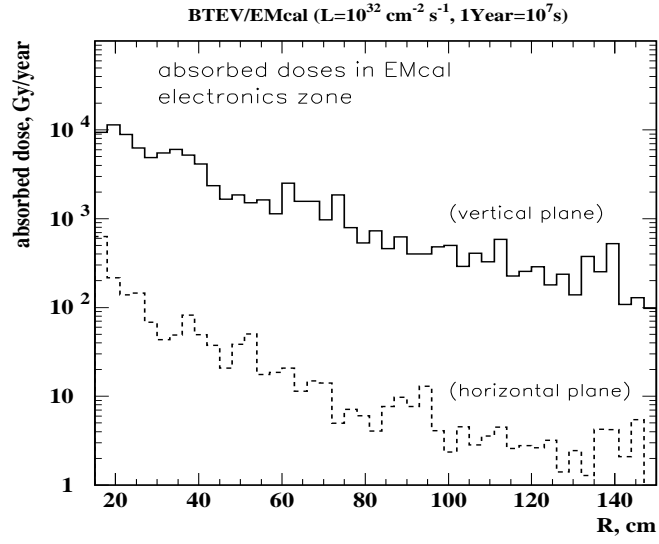


Figure 6.27: Absorbed doses in the phototube quartz front window as a function of the calorimeter radius in both the horizontal and vertical plane.

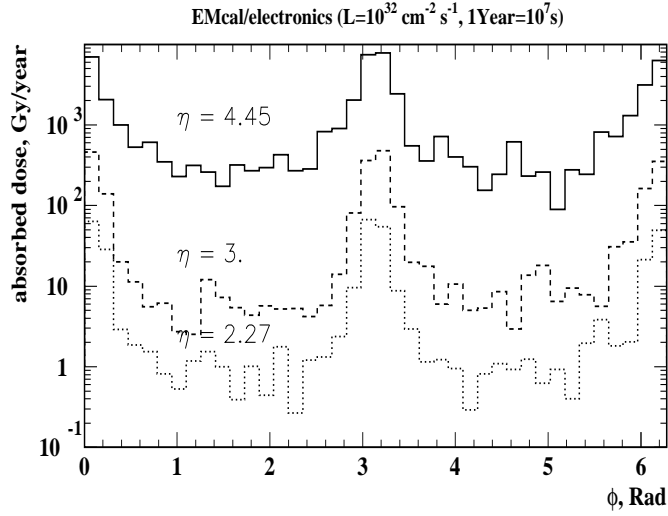


Figure 6.28: Azimuthal profiles of the absorbed dose in the phototube quartz windows. The  $\phi$ -angle is given relative to the vertical axis.

We will run the phototubes at an average output current below  $30\ \mu\text{A}$ . Each phototube must meet the following requirements:

- The gain of each PMT must be between 3,000 and 10,000 and uniform over all  $\sim 10,000$  phototubes to  $\pm 25\%$  when run at the nominal voltage.
- The dynamic range of each PMT must be from 20 photoelectrons up to  $10^6$  (2 MeV to 100 GeV).
- The gain of each PMT must have a non-linearity less than 2% within the dynamic range of  $5 \times 10^4$ .
- The gain of the each PMT over several hours must be stable to 0.1% given that the HV is stable to  $10^{-4}$ .
- The gain of each PMT over a month must be stable to 0.3%.
- The gain of each PMT over the life of the experiment must be stable to 30% given that the total charge collected by the anode is no more than 100 Coulombs.

There are four potential manufacturers: Burle, ETI, Hamamatsu Photonics and Photonis. They all have long histories of producing quality phototubes. Hamamatsu, for example, produced the R5380 model, that was successfully used by the KTeV experiment, which had very similar requirements on its PMTs as BTeV. ETI and Photonis delivered several sample tubes. So far, we have found no significant quality difference among these three manufacturers, except that some of the ETI tubes exhibited larger gain variations when the signal rate varies.

## 6.4.2 PMT gain variations and monitoring

When we started our test beam studies, we did not have a red light pulser to calibrate the gains of PMTs since the KTeV experience suggested that the Hamamatsu PMTs are very stable once the initial burn-in stage is over. (Recall that radiation damage to the crystal will effect blue light transmission but will have virtually no effect on red light.) However early test beam data showed non-trivial gain variation, particularly when the average signal rate changed, for example, when the accelerator went down.

We first investigated this problem at test benches at IHEP and Minnesota. In later test-beam runs, we installed a red LED light pulser system so that we could calibrate the PMT gain continuously.

At the dedicated stand, we studied the PMT gain behavior of pulsed light while varying the average anode current using a DC light shining on the PMT photocathode. Fig. 6.29 shows a sketch of the set up at IHEP.

The setup consisted of a high quality reference PMT (Hamamatsu R5900), a pulsed blue LED with a driver, a DC LED and a PMT that was being tested. LED light was injected into

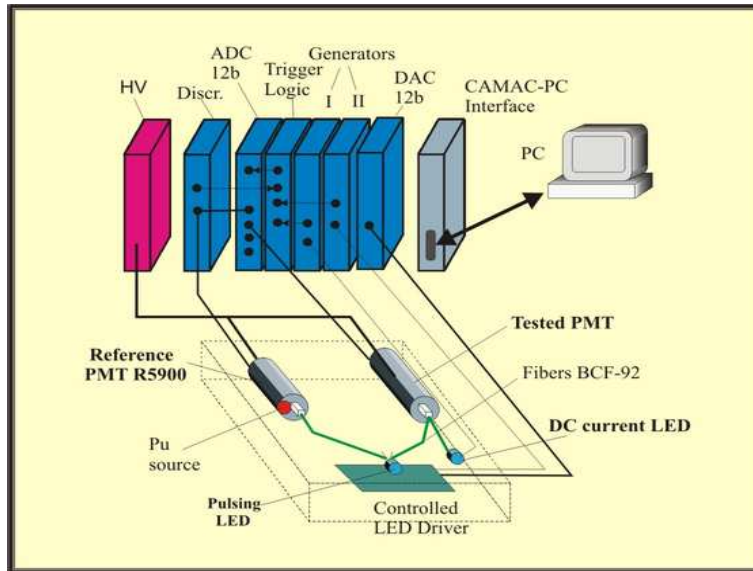


Figure 6.29: Sketch of the PMT gain stability measurement setup.

the test PMT through an optical fiber. The stability of the pulsed LED was monitored by a reference PMT with a Pu radioactive source implanted in a YAP crystal and mounted at the photocathode. The read-out and control electronics were placed in a CAMAC crate which had an interface to a PC. The average anode current was chosen for each test PMT to be about the same as what we had at the test beam. The anode current was measured directly by an ammeter. The average pulse heights from the pulsed LED were measured twice every two minutes. Each measurement contained 2,000 events and took 20 seconds. There was a 10-second time interval between the two measurements. The data from a radioactive source were collected during the remaining 70 seconds. This 2-minute cycle was then repeated. This system allowed us to make long-term PMT gain stability measurements with a precision of 0.2%.

The behavior of PMT 743 is presented in Fig. 6.30. We see a signal loss in the figure when the additional the DC green LED was turned on to produce an anode current of  $5 \mu\text{A}$ . The PMT gain changes due to average anode current variation of several  $\mu\text{A}$  were measured for all the PMTs and were found to be less than 3%. Note that some PMT gains increased when the DC light was turned on while many went down. Also, the time dependence of the change varied from one to the next. So it was not possible to correct earlier test beam data reliably for PMT gain changes using these test bench measurements. They were taken into account as a systematic error for our crystal radiation studies of the first two test-beam runs.

Details of PMT gain stabilities and gain monitoring during our test beam studies are described in the Calibration Section in 6.5.2.4. Clearly the behavior shown in Fig. 6.30 is unacceptable. We have been in contact with Hammamatsu and they are confident they can fix this problem. Tubes from other manufacturers have not shown this problem.

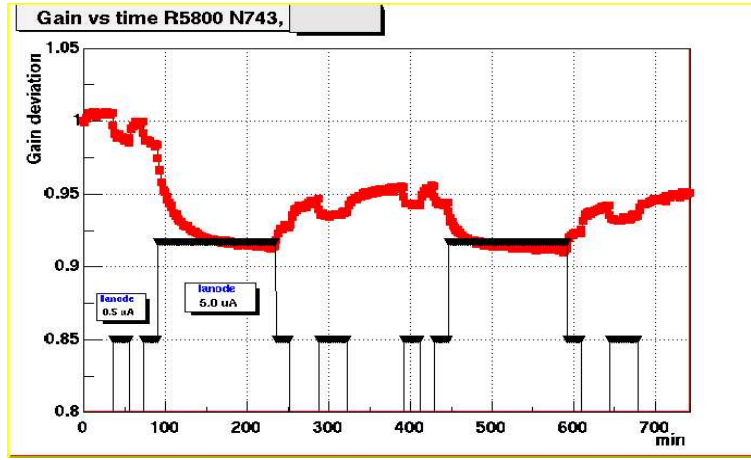


Figure 6.30: The behavior of PMT 743 at the dedicated stand for PMT gain variation measurements. (See text for details.)

### 6.4.3 High Voltage Distribution System

The HV system must be able to supply stable voltages and sufficient current capacity. It needs to be separated into multiple channels so that we can control the voltages individually, and monitor the currents to detect various abnormalities. Crystals will be combined in several groups with the same high voltage value for the whole group. Currently, we are assuming that we will have 100 or so HV channels, each serves about 100 PMTs.

Since we are using 6 stage tubes, we can afford to supply 7 separate voltages (including photocathode) and avoid having current drawing voltage dividers. However, cathode through dynode 3 draw much smaller currents than the other 3, we supply HV to them using conventional voltage divider circuit without increasing power dissipation significantly. We will, then, supply 4 separate voltages and generate the remaining three with a divider.

The requirement of the short-term stability of the HV system is that the output voltage must be maintained to  $10^{-4}$  over a week. The Medium-term stability requirement is that the output voltage must be stable over a month to  $10^{-3}$ . Long-term stability demands that the output voltage must be stable over the life of the experiment to 5V. We need to be able to monitor the output voltage of the HV supply to 0.1 V and current draw to 1% of the maximum current.

### 6.4.4 Front-End Electronics

Analog signals from photomultiplier tubes are sent via copper cables to custom electronics located in 20 electronics sub-racks positioned in racks near the calorimeter. Each Analog-to-Digital Converter (ADC) card, built with the Eurocard 9U x 400 mm form factor, has 32 channels of electronics and there are 16 ADC Cards per sub-rack. ADC cards reside in the front side of the ADC sub-rack and are paired with Cable Transition cards that reside in the back side. PMT signals are received by the Cable Transition Card and are passed to the

associated ADC Card via dedicated backplane connector pins. This set of electronics digitizes the analog signals from the PMT's and performs zero suppression on the data. The analog-to-digital conversion is accomplished with a QIE9 full-custom application-specific integrated circuit (ASIC) that is a new version in a series known as the QIE (charge Integrating and Encoding) chip developed at Fermilab.

Data generated by the ADC Cards is sent to Data Combiner Boards which concentrate and pass the data on to the remaining portions of the data acquisition system. The Data Combiner Board also provides synchronization signals to the ADC Card and provides a path for signals implementing slow control and monitoring functions. Communication between the ADC Cards and the Data Combiner Boards is implemented with 500 Mbps serial links over copper cable. Communication between the Data Combiner Boards and the data acquisition system is implemented with 2.5 Gbps serial links over fiber optic cable. ADC Cards (variable numbers depending on the occupancies in the cards) will connect to one Data Combiner Board. The Data Combiner Boards are located in sub-racks in the collision hall.

The new version of the FNAL-developed QIE ASIC will be used to digitize signals from the PMTs. The QIE IC must be robust and easy to test, and must facilitate testing and monitoring of the crystals and PMT's.

#### **6.4.4.1 Electronics Requirements**

The following describes the requirements on the EMCAL electronics.

1. Dynamic Range

For PMT's with a gain of 3000, the signal from PMT's will be  $0.6 \times 10^5$  to  $2.1 \times 10^9$  electrons, or 10 fC to  $3.4 \times 10^5$  fC. Considering variations in the quality of crystals and PMT's, the electronics must have a dynamic range of at least  $3.4 \times 10^4$  with a preferred dynamic range being  $10^5$ .

2. Electronics Noise

The system must be designed to keep total noise well below 10 fC. This total noise must include not only intrinsic noise of the QIE IC and other circuitry, but also pick-up noise.

3. Electronics Speed

The electronics must be able to both acquire signals from PMT's and complete readout on average at the maximum beam bunch crossing rate of 132 nanoseconds.

4. Crosstalk

Crosstalk must be less than 2%.

5. Some other electronics requirements

Each calorimeter hit must be given a correct timestamp that identifies the beam crossing number. The QIE IC or Front-End Board electronics need to contain the time

stamp generator. This generator could be located further downstream, perhaps in the Data Combiner Board. All the data that can be downloaded or is set on power up or reset must also be readable. These data includes internal QIE IC capacitor identities.

## 6. Radiation Tolerance

ADC's and QIE chips in particular will be exposed to up to 5 krad of radiation over 10-year period. They must continue to operate after such radiation exposure.

### 6.4.4.2 QIE ASIC

The QIE has been designed to digitize negative going signals from phototube bases that have been transmitted over three to five meters of cable. The current pulse from the phototube is best modeled as a pulse which rises to a peak in 1.5 ns, then falls as a sum of three exponentials :

$$I(t) = A[0.39 \exp(-t/5\text{ns}) + 0.60 \exp(-t/15\text{ns}) + 0.01 \exp(-t/100\text{ns})]. \quad (6.4)$$

The specifications on the QIE are listed below.

- The dynamic range of the QIE IC must be a minimum of  $3.4 \times 10^4$  with a preferred dynamic range of  $10^5$ . If PMT's with a gain of 3000 are used, the signal from the average PMT that needs to be measured will range from  $0.45 \times 10^5$  to  $1.5 \times 10^9$  electrons, or 7 fC to  $1.9 \times 10^5$  fC. If a dynamic range greater than  $3.4 \times 10^4$  is achieved, the least count should be reduced. In order to deal with variations among crystals and PMT's, it is desirable to have minimum charge of 5 fC.
- QIE input analog signals, much larger than the range of interest, will occur at a low rate. The QIE designer must specify any off-chip protection circuitry required. The QIE must recover from very large signals in less than 1  $\mu\text{sec}$ .
- The QIE must be able to both acquire signals from PMT's and be able to be read out on average at the maximum beam bunch-crossing rate of 132 ns. The QIE must also be capable of operating at a beam bunch-crossing rate of 264 or 396 ns.
- In order to be able to measure energy resolution to less than 0.5%, the QIE IC digitization precision must always be better than 0.15%.
- All QIE IC digital input and output signals must be both differential and LVDS compatible.
- Upon power-up, the QIE IC shall be operational at the default setting once the QIE IC Clock input is active and the QIE IC reset input has been asserted.
- The QIE must be designed so that testing using a DC current source can yield a calibration that will be accurate to better than 0.3% for photomultiplier input.

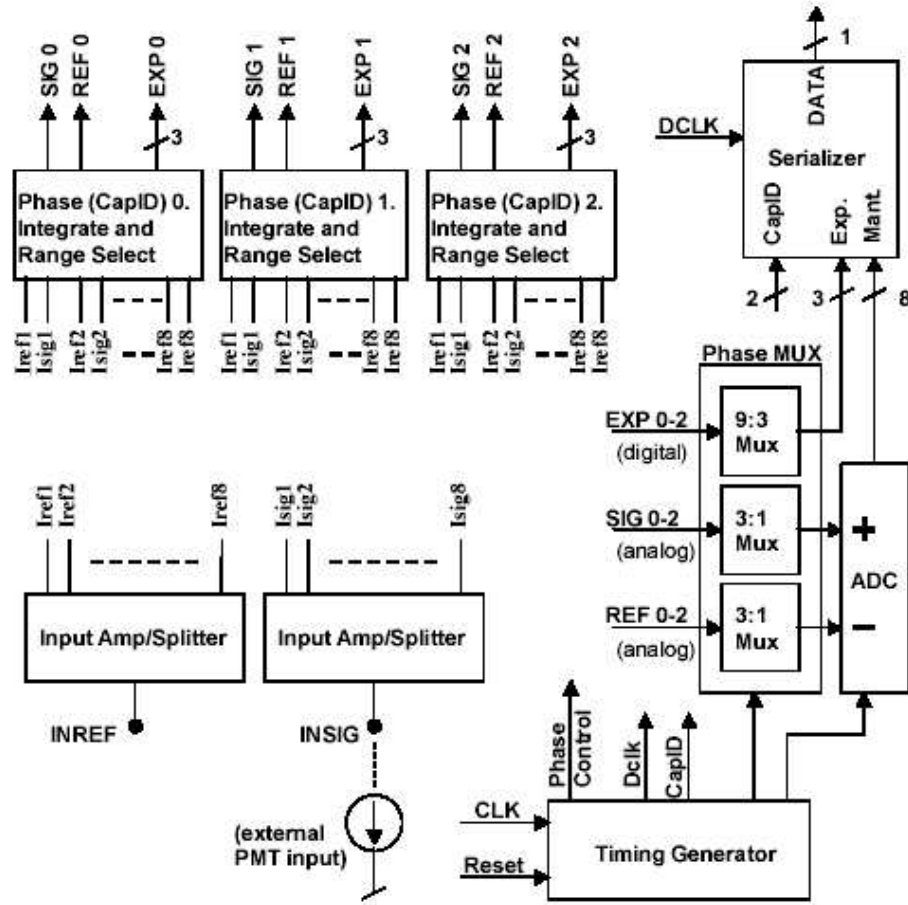


Figure 6.31: QIE9 block diagram

- At the nominal luminosity of  $2 \times 10^{32}$ , the QIE is expected to be exposed to a total dose of approximately 500 rads/year (5Gy/yr). The flux of neutrons with energy between 0.025 eV and 14 MeV is expected to be approximately  $10^5/\text{cm}^2/\text{sec}$ . The QIE must continue to operate without significant performance degradation after a total dose of 5 krad (10 years operation).
- It is strongly preferred that an ADC with an integral nonlinearity of less than 0.5%, and otherwise capable of meeting all the QIE signal acquisition and readout requirements above be included internal to the QIE.

The QIE9 chip, designed for the BTeV experiment at Fermilab, is the latest addition to a number of various QIE chips developed for high energy physics experiments. A basic block diagram is shown in Fig. 6.31

QIE9 is designed to integrate large dynamic range negative input pulses from a photomultiplier tube (PMT) in 132 ns buckets, and digitize the results with approximately constant

Table 6.5: QIE9 Range Spans

QIE9 range number	ADC count span	Input Charge (fC)	Input Charge per ADC bin (fC)	Resolution (bottom of range),%	Resolution (top of range),%
0	2-240	0 - 1190	5	—	0.12
1	2-240	1190 - 3570	10	0.24	0.08
2	2-240	3570 - 8330	20	0.16	0.07
3	2-240	8330 - 17850	40	0.14	0.07
4	2-240	17.9k-36.9k	80	0.13	0.06
5	2-240	36.9k - 75k	160	0.13	0.06
6	2-240	75k - 151k	320	0.12	0.06
7	2-255	151k - 314k	640	0.12	0.06

resolution over the entire range. It accomplishes this by simultaneously integrating a portion of each input charge pulse on 8 ranges with sensitivities that differ by factors of 2, and then selecting the one appropriate range to digitize based on the signal magnitude. The appropriate integrator output is fed to a custom on-chip 8-bit FADC which digitizes the result. Eight non-overlapping ranges combined with an 8-bit FADC yields a dynamic range of 16 bits.

In order that the QIE9 can integrate and digitize each 132 ns bucket in deadtimeless fashion, all operations are pipelined. Three identical phases of integrators (“capIDs”) exist so that digitization and reset can proceed on one phase while the others are accepting input charge. An externally applied input clock (CLK) determines the timing and period of the integrations.

The digital output is composed of an 8-bit mantissa, a 3-bit exponent (range number), and a 2-bit capID to identify which set of integrators generated the data. The data is output serially on one set of LVDS output pads (DATA). The serial output stream is controlled by an externally applied data clock (DCLK), which must be synchronized with the input clock (CLK). The frequency of DCLK should be 14 times the frequency of CLK in order to clock out 14 data bits for each integration clock period (one spare bit, 8 mantissa bits (LSB first), 3 exponent bits, and 2 capID bits). The data latency is 3 clock periods, i.e., when a given integrator phase is accepting input charge, the data that was acquired by that phase 3 clock periods ago is being read out. Table 6.5 specifies the nominal integrated charge and resolution for each of the 8 ranges.

QIE9 is a pseudo-differential device, meaning that in addition to the “signal” input (INSIG), there is also a “reference” input (INREF). A negative input signal current is applied between INSIG and ground, and INREF serves as an identical looking dummy, which helps to cancel any externally induced noise. Inside the QIE9, the outputs of the signal and



reference integrators are routed to a pseudo-differential FADC. Therefore variations in bias, temperature, etc., are a form of common mode noise and have little effect on the signal.

The input impedance of each of the INSIG and INREF inputs is desired to be 50 ohms over the entire dynamic range, in order to properly terminate a coaxial cable. For small input currents, the input impedance is determined by the internal feedback amplifier characteristics and amplifier bias current, which is set with an external resistor to the ISET pad. The ISET resistor is chosen to obtain 50 ohm nominal input impedance (the RinSel digital inputs can be used to tweak this impedance on a per chip basis if needed). For larger input currents, the feedback amplifier becomes inactive, and the input impedance is determined mostly by the resistance in series with the signal path. Thus, to keep the impedance at approximately 50 ohms for large inputs, an external resistor (nominally 47 ohms) must be added in series with the input. This resistor must be inside the amplifier feedback loop, so that its contribution is insignificant for small signals. For this reason, an input requires two pins. The signal from the cable is connected to INSIG1, and a resistor connects INSIG1 to INSIG2. The actual signal current then flows through the resistor into INSIG2. Even though the reference input does not see large currents, it uses the same input structure so that it looks as identical as possible to the signal input.

Input resistors must be added in series with the inputs in order to maintain 50 ohm impedance over a wide dynamic range of input current magnitudes. The signal input impedance value in the low current regime is governed by the ISET input amplifier bias current, set with an external resistor. The impedance in the high input current regime (greater than 1 mA) is more dependent on the value of the external series input resistor than on the ISET resistor value.

#### **6.4.4.3 Readout requirements**

The output data from the calorimeter shall be only from those cells that are above a readout threshold that can be set in software.

The calorimeter hit data must include the beam crossing number, chip identification number, and the calorimeter hits for that beam crossing. The calorimeter data must have crystal numbers, and pulse height information for each hit.

The data output from most crystals is fairly low, but those crystals near the beam pipe may have a hit in almost every crossing. The calorimeter readout chip shall be data driven, and capable of continuous readout at a minimum rate of 4 hits every group of 32 crystals per 132 nanosecond beam-crossing time.

The 32-channel ADC Card can be populated with up to 16 500 Mbps links or as few as one link. The data output from most crystals is fairly low, but those crystals near the beam pipe may have a hit every crossing. The ADC Cards connected to the crystals nearest the beam pipe will be populated with 16 links. Those servicing the crystals near the circumference will use one link.

The data output from the calorimeter may be lost for rates above certain rates. However,

the loss should be in a fashion that, when the burst of information is over, the system shall return to normal operation without external intervention.

The system must have a means of recognizing and aborting the readout of any chip that has an unusual high volume of data output (e.g. due to oscillation or noise).

## 6.5 Calibration and Light Monitoring System

There will be three kinds of calibrations in the BTeV calibration scheme. The most fundamental one is to get the energy scale of the signal, *i.e.* ADC counts to GeV conversions. We have studied, using Monte Carlo simulation, how many electrons we can collect in a given time period. The electrons momenta and thus the energy is measured by the bending in the magnetic field. As we will describe below, there will be enough electrons to calibrate the PWO crystals at least every day, and crystals near the vertical axis can be calibrated as often as every hour. The electrons come mainly from photons converted into electron-positron pairs near the interaction region and semileptonic  $B$  decays.

Note that the electron-based calibration will be mainly used to track variations of energy scale for each crystal over time, and is not the only way of determining the absolute energy scale. Additional particles, including  $\pi^0$ 's, integrated over a longer time will also be used to determine the absolute energy scale by studying the difference between photons and electrons, and the effects of photon radiation by electrons, among other subtleties.

Since our experience suggests that the gains of the PMTs may change appreciably (more than 1%) over a day, or even an hour when the signal rates varies, we need to monitor these changes using a pulser system using both red and blue light. Particle-based calibration will not have sufficient statistical sensitivity for changes over such short time scales.

Finally, since the crystal's light output also varies over a day, or even over an hour when the radiation rate varies quickly, for example when a new fill in the Tevatron starts, this change must be monitored as well, and the blue light pulser will accomplish this.

Section 6.5.1 will describe the result of our Monte Carlo studies of an electron-based calibration, and section 6.5.2 will present our ideas and experiences on light pulser systems to monitor changes in the crystal light output and PMT gains.

### 6.5.1 Energy Calibration using Electrons

We will calibrate the EMCAL using isolated electrons (and positrons) produced in data. We will rely on the  $E/p$  criteria to identify electrons and use their momenta to calibrate the energy scale of the calorimeter.

Precision on the calibration constants depends on the energy resolution of the EMCAL, momentum resolution of the tracks, and improves as  $1/\sqrt{N_e}$ , where  $N_e$  is the number of electrons per crystal used in calibration.

The detailed GEANT-based description of the BTeV detector has been used to generate simulated electron data. We processed a sample of 10,000 generic  $B$  events (generated by Pythia), which contains on the average two non-beauty background interactions per event.

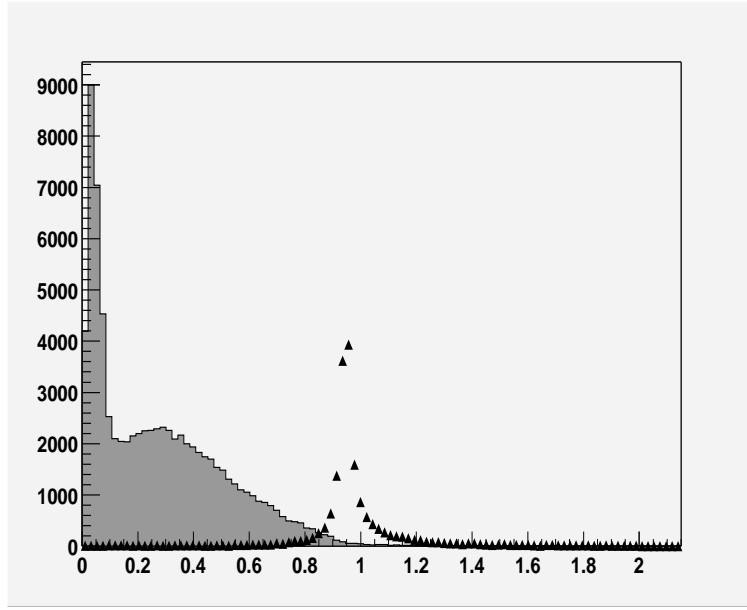


Figure 6.32: Measured ratio  $E/p$  for electrons (triangles) and for other charged tracks.

The actual number of these background interactions was fluctuated according to Poisson statistics. When we calculated the digital signal for each crystal, we took into account the energy resolution arising from a photon statistics contribution of 1.6% at 1 GeV and a constant term of 0.5%.

For this study, we selected well-reconstructed charged tracks with momenta greater than 3 GeV that entered the calorimeter fiducial volume. We further required that the projection of each of those tracks at the calorimeter matched with a reconstructed shower within 1 cm.

Figure 6.32 shows the distribution of the ratio of the reconstructed shower energy to the track momentum ( $E/p$ ) for the accepted tracks. In this figure, the points show the data for electrons and the histogram is for all other charged tracks. We used energies measured in the  $3 \times 3$  matrix of crystals centered on the crystal with the highest energy deposit.

As expected, electrons are very well separated from charged hadrons. Only a very small fraction of hadrons will pollute the electron sample. However, there is a non-Gaussian tail on the right-hand side in the  $E/p$  distribution for electrons, which indicates that there are contributions in the showers from other overlapping particles, which include radiated photons from the electrons.

We further looked at the isolation variable  $E(3 \times 3)/E(7 \times 11)$ , the ratio of the energy deposition in the  $3 \times 3$  matrix of crystals to the energy deposition in the  $7 \times 11$  matrix. The outer matrix is larger in  $y$  because the magnetic field deflects the electron and often radiated photons tangentially, producing the energy deposit pattern wider in the  $y$ -direction. Figure 6.33 shows the distribution of the isolation variable for electrons (triangles) and for other charged tracks. We required the isolation variable to be in the range  $0.92 < E(3 \times 3)/E(7 \times 11) < 1$ .

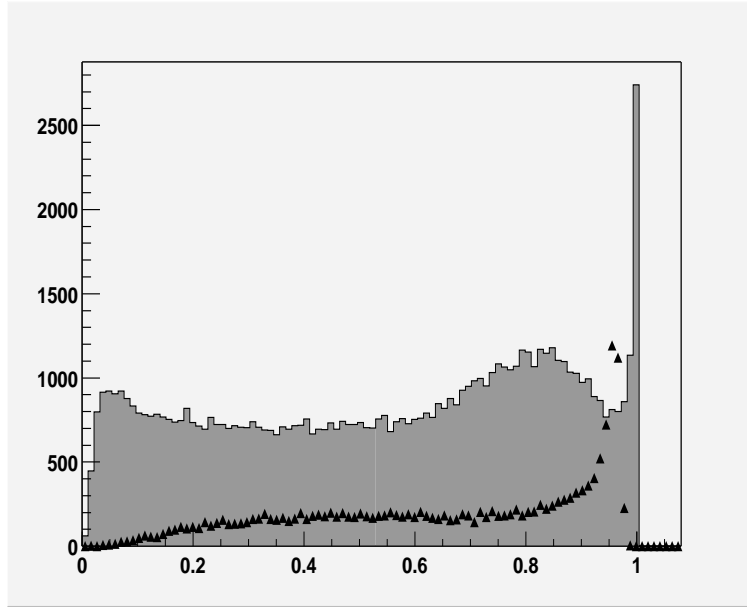


Figure 6.33: Measured ratio  $E(3 \times 3)/E(7 \times 11)$  for electrons (triangles) and for other charged tracks.

Figure 6.34 shows the  $E/p$  distribution for isolated electrons, those which passed the  $E(3 \times 3)/E(7 \times 11)$  cut. From a Gaussian fit, we obtain  $\sigma(E/p) \simeq 1.9\%$ . The statistical precision of the  $E/p$  peak position is given by  $\sigma(E/p)/\sqrt{N_e}$ , where  $N_e$  is the number of electrons available for calibration. Thus, in order to achieve 0.2% calibration precision, we will need to collect  $\sim 100$   $e$ 's per crystal.

Our electron signal can be further improved in two ways. First of all we could use a  $5 \times 5$  crystal matrix here to obtain better resolution and secondly we can identify electrons in the RICH below 22 GeV. These were not done in this study because we wanted to see how well we could do without these clean up criteria.

There are 3443 entries in the  $E/p$  distribution within  $\pm 2\sigma$  around the peak in a total of 10,000 Monte Carlo events. This means that there are  $\sim 0.34$  electron/event hitting somewhere in the EMCAL.

However, these electrons are not distributed over the calorimeter uniformly. Figure 6.35 shows the  $\phi$ -distribution of these electrons. The two clear peaks at  $\pm 90$  degrees reflect the effect of the magnetic field that sweeps charged particles in the  $y$  direction. It follows that the rate of collection of electrons useful for calibration varies by a factor of 20 between the extreme cases even at the same radius. The value of  $\sigma(E/p)$ , however, does not change from one area to another area of the calorimeter.

More detailed studies of the distributions of electrons over the calorimeter show that we will be collecting the electrons at the following rate:

- $\sim 8\%$  of crystals will receive  $\sim 1.7 \times 10^{-4}$   $e$ 's/crystal/event

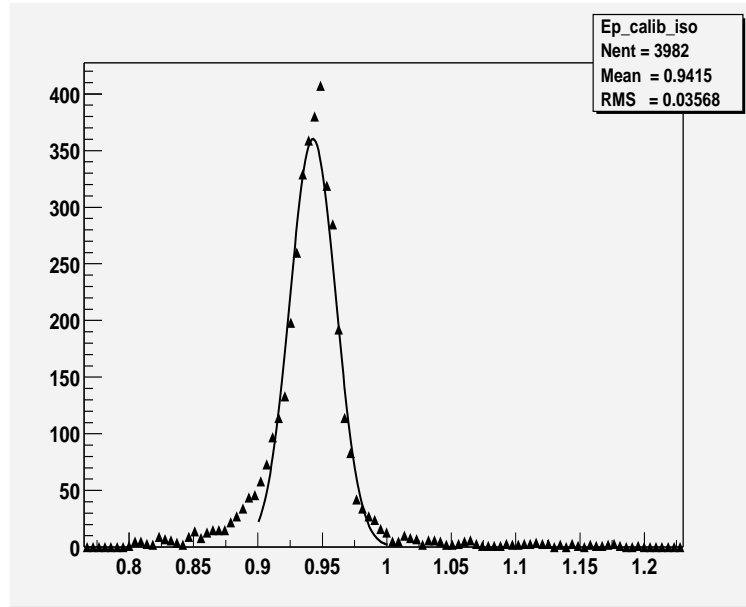


Figure 6.34: Measured  $E/p$  distribution for isolated electrons

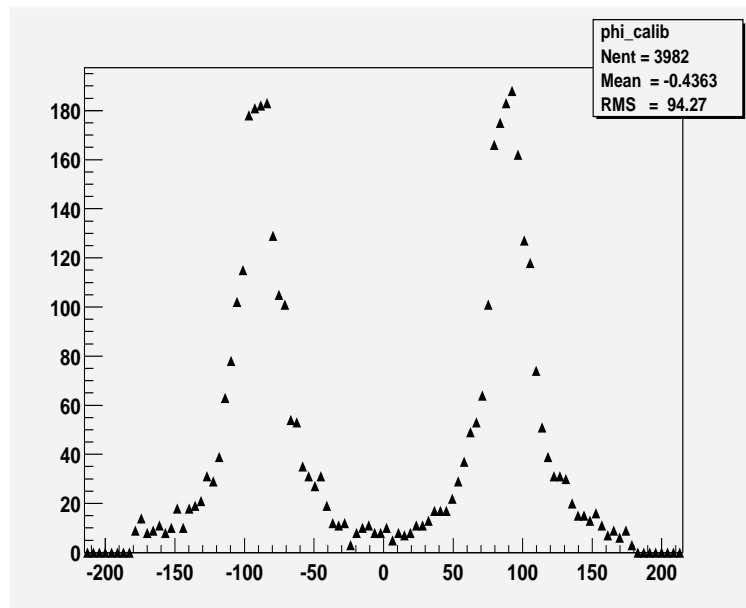


Figure 6.35:  $\phi$ -distribution for isolated electrons

- $\sim 14\%$  of crystals will receive  $\sim 1.0 \times 10^{-4}$  e's/crystal/event
- $\sim 11\%$  of crystals will receive  $\sim 5.0 \times 10^{-5}$  e's/crystal/event
- $\sim 22\%$  of crystals will receive  $\sim 2.0 \times 10^{-5}$  e's/crystal/event
- $\sim 45\%$  of crystals will receive  $\leq 1.0 \times 10^{-5}$  e's/crystal/event

The narrow area along the  $y$ -axis can be calibrated with electrons almost continuously (every hour), while for the calibration of the least covered 45% of the calorimeter, we will need to collect  $(10 - 15) \times 10^6$  events to obtain about 100 electrons/crystal. This corresponds to several hours of running at nominal luminosity.

To conclude this section, we will be able to calibrate the crystals at least once every several hours, certainly once every day, while some of the highly irradiated parts of the calorimeter could be calibrated every hour.

## 6.5.2 Light Pulser System

### 6.5.2.1 Overview

The light pulser system is used to monitor changes in the light output from the PWO crystals, and also gain changes in the PMTs. Because the PMT gain change affects the signal from the light pulser and scintillation signal in the same way, the fractional changes in these two signals will be exactly the same. In other words, the ratio in the fractional signal changes is expected to be 1. *i.e.*

$$R = (\Delta_{\text{Scint}}/S_{\text{Scint}})/(\Delta_{\text{LP}}/S_{\text{LP}}) = 1, \quad (6.5)$$

where  $S$  and  $\Delta$  represent the signal and its variation, and subscripts “Scint” and “LP” represent scintillation signal and light pulse signal. This means that correcting our scintillation light signal for the PMT gain changes using the monitoring system is straightforward. However, different PMTs have quite different  $\Delta_{\text{Scint}}/S_{\text{Scint}}$  for similar running conditions, as is clearly shown in Fig 6.36.

This is not the case for the changes in the light produced in the crystals. When the transparency of the PWO crystal deteriorates due to radiation, which is believed to be the only radiation damage mechanism in the PWO crystal, it reduces both the LED signal and particle signal. Since there are different optical paths taken by the injected monitoring light and the scintillation light, the fractional losses of the two sources of light are somewhat different. However, the relation between the two losses is more-or-less proportional as long as the absorption length is much longer than the crystal length. This suggests that the above ratio will still be a useful quantity but will not be 1. In order to find  $\Delta_{\text{Scint}}/S_{\text{Scint}}$  from  $\Delta_{\text{LP}}/S_{\text{LP}}$ , we need to know the value of  $R$  for each crystal. We will discuss how we plan to obtain the  $R$  values in section 6.5.2.5 below.

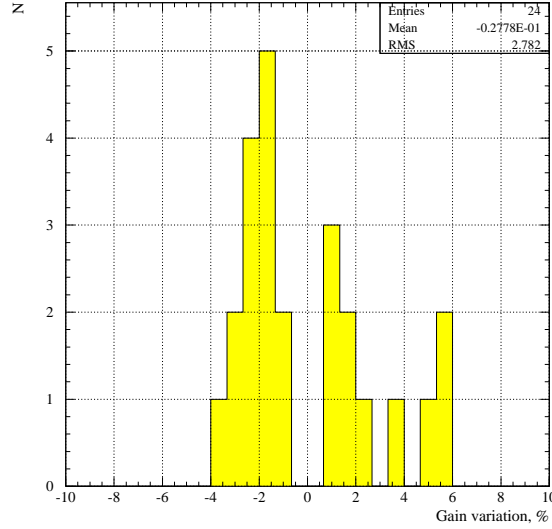


Figure 6.36: Distribution of gain variations of 6-stage Hamamatsu phototubes in the test-beam study.

Because of these differences in the values of  $R$  and variations in contributions to changes from PMT gain variations and crystal light outputs, we have decided that it is important to monitor these two changes separately.

To monitor a change in the crystal light output, we will use a blue light pulser of 470 nm wavelength close to the 430-nm emission peak of the PWO crystal. Since the signals from these blue light pulses are detected by PMTs, what we measure is the change in the product of the PMT gain and light output. In other words, the fractional change we measure is the sum of the fractional changes in the PMT gain and the crystal output. Correcting for the PMT gain change obtained in the method described below, we can separate the light output change.

If we could send calibration light pulses to PMTs directly, it would be easy to measure PMT gain changes. However, we cannot do this because each of the crystals covers the entire detection surface of the mating PMT. We chose the color of the light pulses for this task to be red, since its transmission in the crystal does not change due to radiation.

In the test beam studies, the separation of these two sources of signal variations has been crucial so that we could study the changes in the crystal properties alone. Our experience with a blue-red light pulser system at the test beam facility is described in section 6.5.2.2. This section also gives the results of our studies on the values of  $R$  for different crystals for electron and pion irradiation.

In section 6.5.2.3, we discuss our current design of the pre-production light pulser and performance results.

### 6.5.2.2 Experience at Test Beam

A LED-based light pulser system with four LEDs of different wavelengths was made for the test beam studies at Protvino to monitor gain variations of the PMTs and transmission variations of the PWO crystals. The LEDs emit at red (660 nm), yellow (580 nm), green (530 nm), and blue (470 nm) wavelengths. For the actual analysis of data, the red and the blue LEDs were most useful.

Between two accelerator spills, 10 light pulses of one color were sent to the crystals. Then in the following interval, light pulses of another color were injected in the crystals. This way, four spills were needed to collect data for all four colors. The light from all the LEDs were fed into the same set of optical fibers and they delivered the light to individual crystals. (*i.e.* there was only one fiber going to each crystal instead of having one fiber for each color LED.

In the test beam set up, the LED light was injected at the front end of the crystals. So the typical path length of LED light in the crystal approximately equals the length of the crystal. Since the light comes out of the optical fiber with a characteristic full angle spread of  $25^\circ$ , and this angle is reduced to  $11^\circ$  as the light enters the crystal from air, the path length of light in the crystal should be increased by  $1/\cos 11^\circ$ . As for the scintillation light from incident particles, half of the light travels directly to the PMT while the other half will travel towards the front of the crystal and gets reflected before it is detected by the PMT. Averaging between these two cases, the average path length of scintillation light to the PMT also equals the crystal length to the 0-th approximation. In order to estimate the 1st order correction, we need to know how much the light zigzags on its way to the PMT. The maximum angle that the light makes with respect to the crystal axis is determined by what angle the light is reflected by the side surfaces due to the total internal reflection, which is about  $64^\circ$ . This leads to many more zigzag paths than the paths for LED light. Taking into account that the scintillation light is emitted isotropically, the average  $\langle 1/\cos \theta \rangle$  factor arising from the zigzag paths is about 1.4.

The LED system monitors the transparency of the crystal at a specific wavelength (in our case, 470 nm was chosen partially due to the availability of blue LEDs) and thus does not sample the entire spectrum of scintillation light. The radiation damage effect is less severe at 470 nm than at 430 nm, the center of the PWO scintillation emission peak. From these considerations, we expect that the ratio,  $R$ , of the light loss factors for the LED signal and the particle signal is about  $1/1.4 = 0.7$  to  $1/1.6 = 0.6$ .

One of our goals in the test beam studies of the calibration system is to measure this ratio,  $R$ , experimentally, and how it varies from crystal to crystal. Naively, since this ratio only depends on the geometrical lengths of light paths for the LED and scintillation light, it should not vary from one crystal to the next. If there are variations in the shape of the absorption as a function of wavelength among crystals, the ratio,  $R$ , may vary among crystals. In addition, since the crystals will not be polished to optical flatness, actual reflections of light by the side surfaces do not follow the simple law of geometrical light reflection. This may also lead to variations of the ratio,  $R$ , among crystals. Thus we feel that it is very important to measure the variation of  $R$  values experimentally.

Since it is not practical to measure this ratio for all production crystals at a test beam



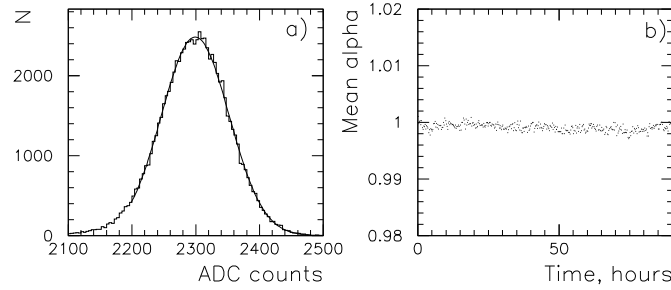


Figure 6.37: (a)  $\alpha$  energy spectrum accumulated over 1.5 hours. (b)  $\alpha$  spectrum peak position as a function of time over 85 hours. Each point corresponds to a 15-minute measurement duration.

facility (it would take too much time), we need to know if the variation, if there is one, is small enough so that we will not spoil the resolution even if we assume and use an average value of the ratio for all crystals.

### 6.5.2.3 Monitoring Systems for the Light Pulser System and Stability of Light Pulser

We built two monitoring systems to check the stability of the magnitude of the light pulses. (*i.e.* monitoring systems of the monitoring system.) One was based on a PIN photodiode, which is considered very stable even when the temperature varies. According to some literature, the temperature variation of PIN photodiodes is less than  $0.01\%/^{\circ}\text{C}$ . However, since we needed an amplifier to detect the PIN photodiode signal, the amplifier gain needed to be stabilized by housing it in the crystal box where the temperature was stable to  $\pm 0.1\text{ C}$ .

The second system used a PMT, scintillation crystal and radioactive source. The PMT (Hamamatsu R5900) monitored the LED pulser while the PMT was monitored using the stable scintillation light produced when a  $\text{YAlO}_3 : \text{Ce}$  crystal was irradiated with an  $^{238}\text{Pu}$  alpha source (YAP) [13]. The  $\alpha$  energy spectrum measured by the PMT and the peak position of this spectrum as a function of time is presented in Fig. 6.37. The width of the peak is 2.3% r.m.s. as determined by a fit to a Gaussian. The peak position was stable over 85 hours to better than 0.2%.

The measured variations (drifts) of the magnitudes of light pulses (averaged over 120 pulses) over different time periods were measured, for the periods of test beam studies. They were:

- 0.1 to 0.2% over a day;
- 0.5% over a week;
- 1% over a few months.

Temperature variations were the main cause for the variations in the sizes of pulse. When corrections based on the temperature were made in the pulse-height analysis, the long term variation significantly decreased to 0.4% over a few months and down to 0.3 % over a week. No LED ageing effects were observed after 3000 hours of operation.

The stability of this system was better than we needed to monitor the gain variations of the PMTs and the transparency variations of the crystals over the relevant time periods. For example, we were able to track the crystal transparency change with an accuracy of better than 1% over a week when we measured how much radiation damage the crystals suffered. Additionally, we were able to track the crystal transparency change with an accuracy of better than 1% over a few months when we measured the recovery process of the radiation-damaged crystals. Finally, it made it possible for us to track the PMT gain variations over a day well enough so that it did not contribute appreciably to energy resolution measurements. This last accomplishment implies that we already have a good enough system for BTeV except that we need to have a much larger system, and temperature stabilization must be considered.

#### **6.5.2.4 PMT gain monitoring**

A similar study was done when the beam intensity changed in the later test beam runs where we used a red LED light pulser system to monitor the PMT gains.

When we installed the red LED in the monitoring system, we were able to correct our data for the PMT gain changes. The blue LED signal amplitude, which measures the changes in the crystal transparencies, are shown in Fig. 6.38 as a function of time over 85 hours. The middle plot shows the raw signal from the blue LED, which shows decreases in the signal when the electron beam intensity went to zero. The beam intensity is shown in the top plot of this Figure. When these data are corrected for the PMT gain variation using the red LED data, we found much smoother results, which are shown in the bottom plot.

In our analyses of the electron beam data described in the previous sections, we corrected the signals from electrons and blue LED, using the red LED data.

#### **6.5.2.5 Crystals Light Output Monitoring**

As it was described in the section 6.3.5, crystals behave in a similar way in the radiation environments of different nature; clear correlations between electron and LED signal changes was observed. The dedicated study has been carried out to confirm that these correlations are not dependent on the type of irradiation using a particular optical monitoring scheme. To be more specific, the same crystals were calibrated with a low intensity electron beam first, then they were exposed to the highly intense electron radiation. Crystals irradiation continued with pion beam. Both electron and pion irradiations alternated with calibration runs using low intensity electron beam. Changes in the crystals transparency were monitored continuously with the use of the LED monitoring system. Linear fit of the distributions of the relative blue LED signal change vs electron signal change was done for both electron and pion irradiations. Coefficients of the linear fit are presented in Fig. 6.39

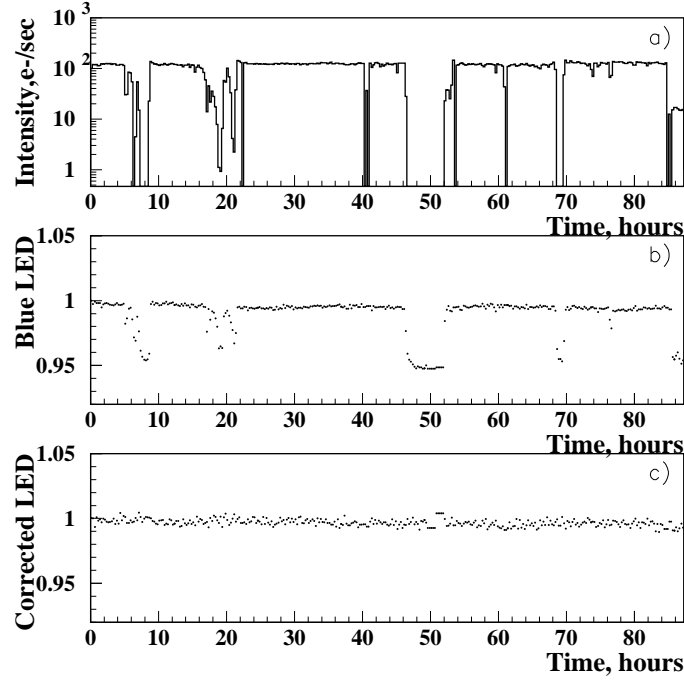


Figure 6.38: (a) Electron beam intensity in the Shanghai crystal S22 as a function of time. Blue LED behavior for this crystal (b) before and (c) after PMT gain change correction using the red LED data.

As it was expected, on average the measured coefficients are not different and are in a good agreement with the calculations for the current optical scheme. The fact that the linear approximation works well significantly simplifies the procedure of the EMCAL intercalibration that will be performed using an LED-based light monitoring system over the time intervals between two consequent in situ calibrations.

### 6.5.3 Light Monitoring System for BTeV Calorimeter

The light monitoring system, shown schematically in Figure 6.40, is designed to inject light pulses into each PWO crystal in order to measure optical transmission near the scintillation spectrum peak (430 nm). The red light pulses are used to monitor PMT gain stability. The system includes both blue and red LEDs, their driver circuits, and optical fibers to deliver light pulses to each of the PWO crystals.

We plan to use very powerful LEDs, assisted by a reflector and a light mixer so that each light pulsing system produces enough light for  $\sim 2700$  crystals, each receiving light pulses equivalent to scintillation light from 20 GeV photons. The distribution of light among the 2700 fibers should be very uniform. This is accomplished by designing a good light mixer

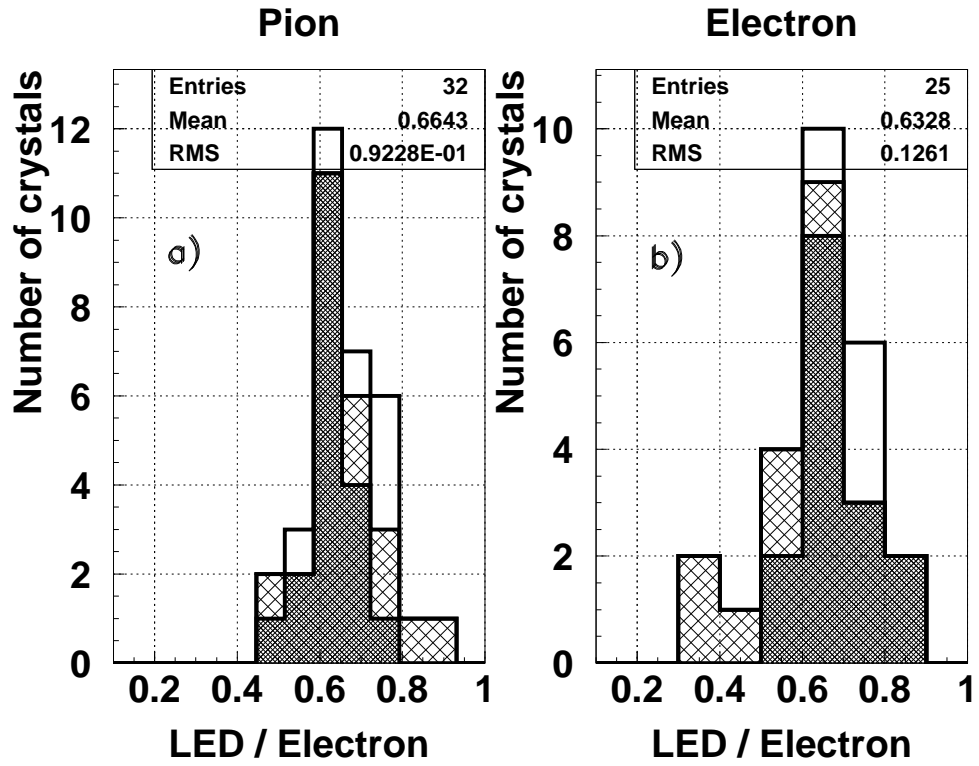


Figure 6.39: Linear fit coefficients calculated from the correlation plots of the blue LED vs. electron signal relative changes under pion (a) and electron (b) crystal irradiation.

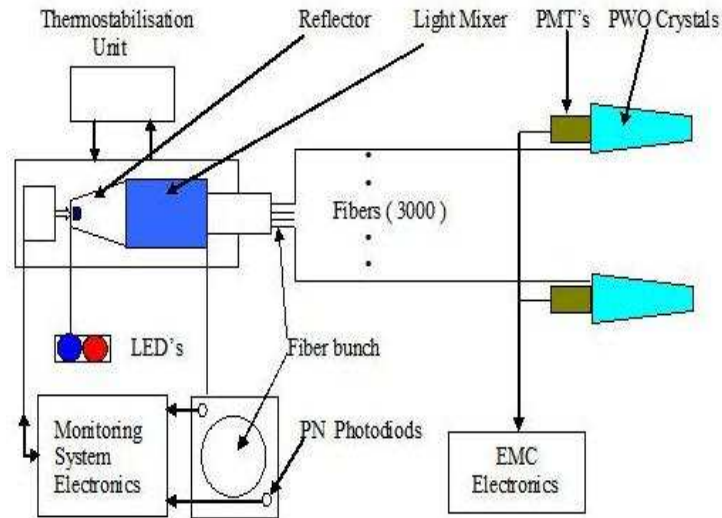


Figure 6.40: Diagram of one quarter of a light monitoring system for the BTeV calorimeter

which will distribute light uniformly across an area of  $38 \times 38 \text{ mm}^2$ . Each bunch of fibers (of about 3,000 fibers, of which 400 are spares) and two referenced PIN silicon photodiodes will be contained in this area. Four such light pulsers will serve the whole BTeV calorimeter.

The time dependence of pulse heights from the pulser is monitored by the two reference PIN photodiodes. One of the four pulser systems will be activated at any given time to limit the power requirements of the light source, the size of data transfers, as well as high and low voltages current demands.

The system is designed to continuously monitor the calorimeter in two ways:

- Continuous in-fill monitoring during  $2.617 \mu\text{s}$  gaps in the Tevatron beam structure (beam abort gaps). Less than 10% of these gaps should be sufficient to collect enough data for this purpose.
- Stand-alone monitoring runs between Tevatron fills to follow recoveries of the PWO crystals.

The principal goal of the system is to monitor short-term variation in the PMT gains and the light transmission of the crystals. The system will also be used to check out the entire crystal-readout chain during the assembly of the calorimeter. It will also permit a rapid survey of the full BTeV calorimeter during the installation or after long shutdowns. Furthermore, the light monitoring system can be used to measure the response linearity of the PWO crystal's photodetector and its readout chain. This should complement measurements with electronic charge injection at the preamplifier level which does not test the photodetector.

Some results obtained with a prototype system are presented in section 6.5.3.3.

A picture of the whole prototype system is presented in Figure 6.41. Four such boxes will be mounted on the EMCAL mechanical structure. Each of them will feed  $\sim 2,500$  PWO crystals by a monitoring light through the fibers. A led driver is presented in Figure 6.42.

### 6.5.3.1 Monitoring system components

The monitoring system will be located directly at the outer radius of the calorimeter support structure and an optical-fiber light distribution system connects the pulser to the crystals. Since the light pulser is located in a low radiation zone, its components and electronics are not required to be radiation hard. In contrast, many fibers are routed through a high radiation zone and they must be made of radiation-hard materials.

The characteristics of the LEDs we plan to use in the BTeV calorimeter monitoring system are given in Table 6.6:

Besides the exceptional luminous fluxes, we find that two additional features of the Luxeon technology are very important for our monitoring system: very long operating life (up to 100,000 hours in DC mode); and small temperature dependence of the light output ( $0.1\%/^{\circ}\text{C}$ ). The producer is Lumileds Lighting, USA. The reflector which was made at IHEP has a trapezoid shape and is made of aluminum plated Mylar or Tyvek.

The optical fibers we plan to use are produced by Polymicro Technologies, USA. Their properties are:



Figure 6.41: View of the prototype monitoring system. Inside the box there is a led driver, blue and red LEDs, a light mixer, a temperature stabilization system, and a referenced PIN-diode system. In use we have a fiber bunch coming out the far side of the box instead of the cables which are pictured; the cables are for tests only and will not go to the BTeV calorimeter. The size of the box is 370 mm x 70 mm x 60 mm.

Table 6.6: Properties of LEDs

Property	blue (royal blue) LED	red LED
Brand	Luxeon 5-W emitter	Luxeon 1-W emitter
Typical Luminous flux	30 lm (@700 mA)	45 lm (@350 mA)
Radiation Pattern	Lambertian	Lambertian
Viewing Angle	150 degrees	140 degrees
Size of Light Emission Surface	$5 \times 5 \text{ mm}^2$	$1.5 \times 1.5 \text{ mm}^2$
Peak Wavelength	470 nm (455 nm)	627 nm
Spectral Half-width	25 nm (20 nm)	20 nm
Average Forward Current	700 mA	350 mA

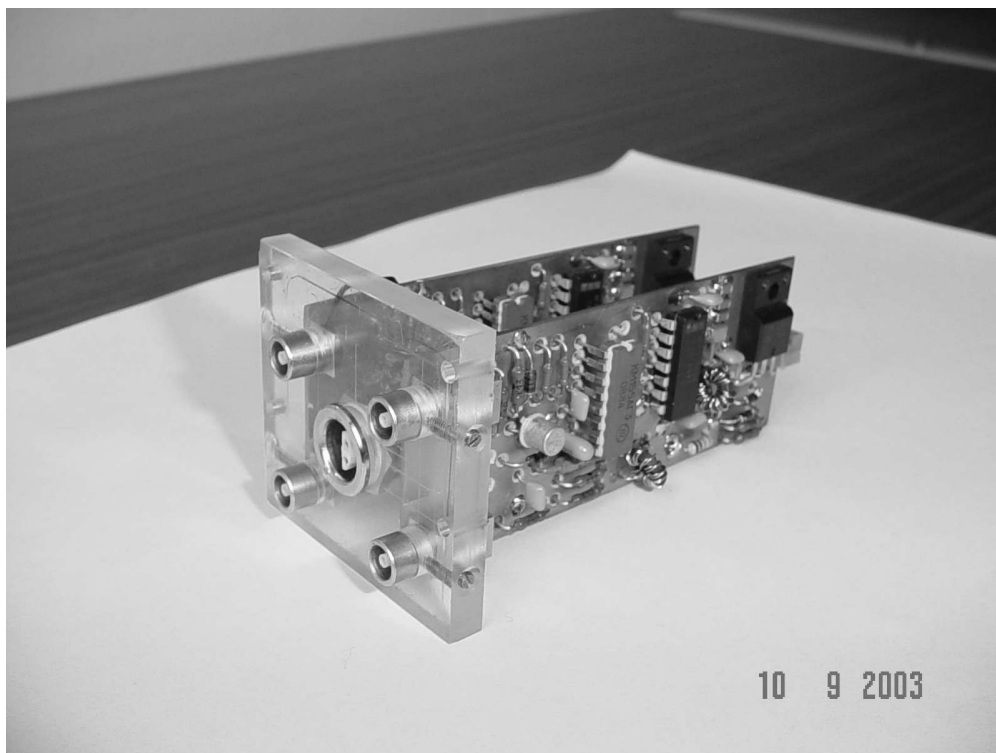


Figure 6.42: LED driver of the Prototype of the monitoring system. It will be inside the box (see the previous Figure) near the side opposite to the one with a bunch of fibers.

- Silica / Silica optical fiber
- High - OH Core
- Aluminum Buffer
- Core Diameter 270 micron
- Outer Diameter 400 micron
- Numerical Aperture 0.22
- Full Acceptance Cone 25.4 Degrees

This fiber has very good radiation hardness. According to the tests made by the CMS ECAL group, this fiber has shown no signal degradation under gamma irradiation with an absorbed dose of up to 12 Mrad.

### 6.5.3.2 Reference PIN silicon photodiodes

An essential element of the light monitoring system is a stable reference photodetector with good sensitivity at short wavelengths. PIN silicon photodiodes with a sensitive area about

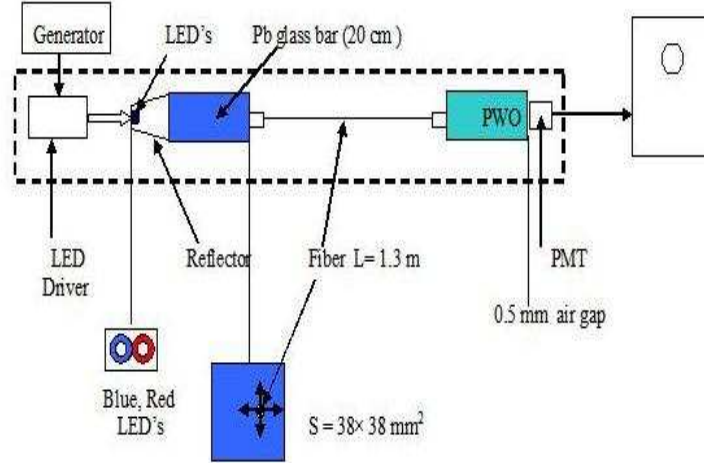


Figure 6.43: Schematic view of the light pulser prototype

6 mm<sup>2</sup> are well suited to this task. In particular, such low leakage currents are achieved with PIN diodes, due to their very narrow depletion zone resulting from heavy (p and n) doping, which is less sensitive to the type inversion than typical PIN diodes. The rather large sensitive area of this photodiode allows us to work without preamplifiers and improve the stability of the reference system itself. A PIN silicon photodiode S1226-5BQ (Hamamatsu) was used in our test measurements. It has an active area of 2.4×2.4 mm<sup>2</sup> and a dark current less than 50 pA (at 5V reverse-bias voltage).

### 6.5.3.3 Tests of the light pulser prototype

A schematic view of the light pulser prototype is shown in Figure 6.43. The light distribution uniformity was measured with a single fiber scanner. All the measurements were made with a scope and a manual scan with a step size of 2 mm. The scan area was 34×34 mm<sup>2</sup>. The result are shown in Figure 6.44 The FWHM of this pulse height distribution is 2%, and the full width is 8%. The energy equivalent is 20 GeV for the whole scan area. The average forward current in the tests was 20 mA. The maximum forward current is 700 mA. So we have a large safety factor for the amount of light. This light pulser can illuminate more than 3000 fibers.

The short-term stability of light uniformity over the area of 34×34 mm<sup>2</sup> for a day has been measured to be 0.05% and a long-term stability was 0.1% over 20 days. In spite of these encouraging results, thermostabilisation of the light pulser by means of the Peltier cell is foreseen in the design of the whole system.



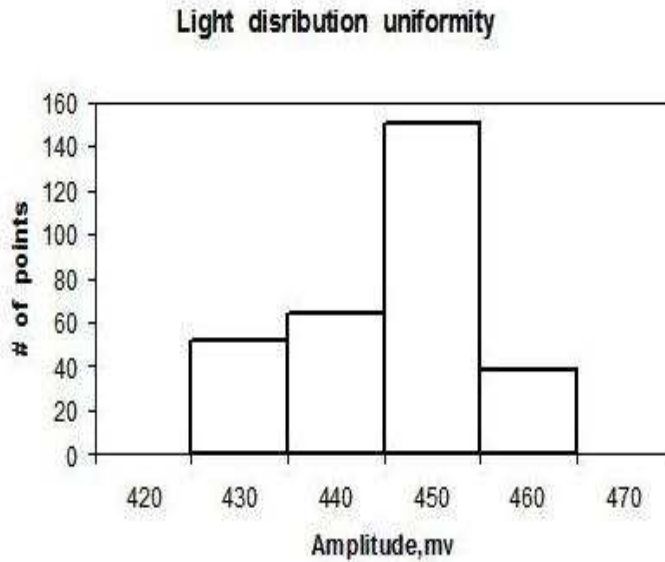


Figure 6.44: Distribution of pulse heights (in mv) measured over an area of 34x34 mm<sup>2</sup> in 2 mm steps.

## 6.6 Mechanical Structure

The mechanical support design for the BTeV calorimeter is dictated by the need to support many dense crystals with minimum amount of support materials in front and between each crystal. To achieve the physics goals of BTeV, the mechanical support system of the calorimeter has to meet the following requirements:

- The calorimeter mechanical support structure should have material with as low a radiation length as practical in front of and between the crystals so that the calorimeter energy resolution is not compromised.
- The design must take into account that the operating temperature of the detector inside will likely be between 15° and 20° C. Even though the temperature at different locations inside the calorimeter may vary a few degrees C, the temperature variations over a day at any locations must be maintained to  $\pm 0.1^\circ$  C (rms) and over a month, to  $\pm 1^\circ$  C (rms) when the ambient temperature is maintained to  $\pm 1^\circ$  C (rms).
- Thermal stress must be considered so that the mechanical stability of the system will not be affected.
- The support structure should allow us to replace PMTs or crystals.
- The support structure should be retractable to allow service of the silicon strip detectors at station 7.

- The support structure should allow partial or complete assembly of crystals in the assembly hall and transportation to the collision hall.
- The structure should also allow partial assembly in the collision hall.
- The support structure should have provisions to support electronic crates located at the periphery and to support and guide cables from PMT bases to electronic crates.
- The calorimeter holder needs to be gas tight so we can flow dry air or nitrogen in order to avoid humidity. The humidity level should be kept below 1%.
- We must be able to align the calorimeter system during the assembly stages relative to the pixel detector using suitable alignment marks. The requirement on the accuracy of the calorimeter location is 5 mm. This should be sufficient since we will have to find the position of the calorimeter relative to the pixel detector using data to determine accurate positions.
- Monitoring of the location changes should be known to an accuracy of 1 mm. Relative positions of crystals should be known within 1 mm from the nominal position of each crystal. Changes in the crystal positions relative to the “center” should be stable to 0.1 mm over a day and 1 mm over a month.

Our proposal had assumed that we will use some variant of the CMS endcap structure to support the BTeV PWO crystals. However, the carbon-fiber based cell structures that CMS will use are fairly labor intensive, and even if we produce them in Russia where this type of labor is much cheaper than in the Western Hemisphere, they would still be too expensive. Our IHEP colleagues had a different idea using aluminum strips to form these cells, similar to what was done with the CLEO CsI calorimeter. Since then, FNAL engineers took over the idea and carried out much of the engineering design work.

The overall structure in the front view is shown in Fig. 6.45. The vertical lines (label 1 in the figure) represent vertical strips which are 0.3 mm thick and 250 mm wide. The horizontal lines (position 2) represent horizontal strips of the same thickness and 40 mm in width. They run through holes in the vertical strips with interlocking notches in two places for each row of crystals. One supports the front and the other supports the back parts of the crystals. Other labeled features in this figure are as follows : 3 - top beam, 4 - lower support, 5 - Hillman roller, 6 - trolley, 18 - balance support, 19 - electronics box.

In order to get a better sense of how these strips can be assembled, and also investigate the cost of production of such a structure, we have built a prototype model. It was successfully built using parts fabricated by a commercial shop. Fig. 6.46 shows the front view of the prototype in whole and detail, which has five vertical strips hanging from the top of the frame, and three sets of horizontal strips running from one side to the other. The top set of horizontal strips are inclined at the same angles as strips near the top of the BTeV calorimeter. The middle and the bottom sets emulate those strips near the mid-height and the bottom of the calorimeter.

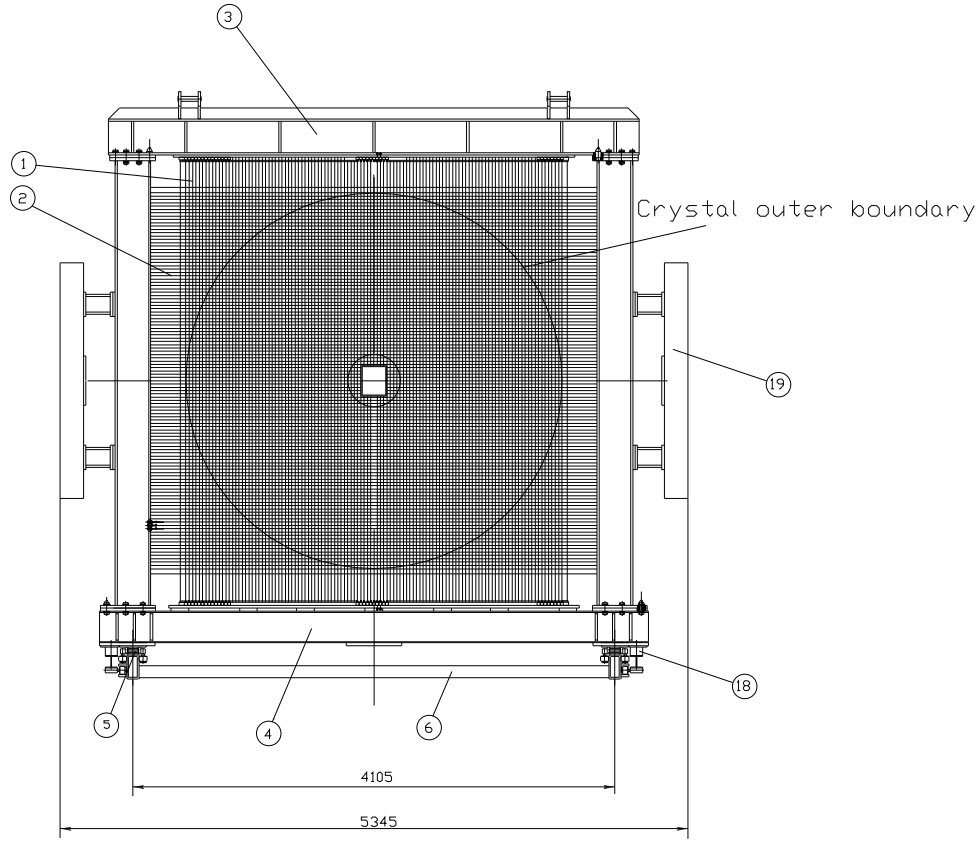


Figure 6.45: Mechanical Structure

### 6.6.1 Cooling and Humidity Control System

Since the light output depends strongly on the temperature ( $-2.3\%/^{\circ}\text{C}$ , see section 6.3.4.1), the temperature of the crystals must be stable to  $0.1^{\circ}\text{C}(\text{rms})$ . The maximum temperature deviation, once equilibrium is reached, shall not exceed  $0.1^{\circ}\text{C}$  on any temperature sensor near the crystals. The time dependence of the temperature at each monitor point shall be stable to  $0.1^{\circ}\text{C}$  over a day and  $1^{\circ}\text{C}$  over a month. When there is an access to the detector and temperatures inside the detector change, after they settle to plateau values, the temperatures should be back to the pre-access time within  $\pm 1^{\circ}\text{C}$  (rms).

The calorimeter is expected to operate at temperatures from  $15^{\circ}\text{C}$  to  $20^{\circ}\text{C}$ . Even though we would detect more light from PWO crystals at lower temperatures, we decided that this gain does not warrant the engineering complications, such as dew formation, of keeping the operating temperature below  $15^{\circ}\text{C}$ .

The current in the PMT bases and PMT's dominates the internal heat load. However, this will most likely be overwhelmed by heat flow from outside. The internal heat load comes from the power dissipation of  $30\text{ mW}$  per crystal in PMTs near the beam pipe (in the worst



Figure 6.46: Prototype Mechanical Structure

case). For the outer crystals, this drops to  $30 \mu\text{W}$ . So the performance of the cooling system has to be able to deal with the heat flow through the insulation around the detector.

We studied temperature stabilization schemes. Since the heat dissipation by the voltage dividers and the currents in the PMTs is minimal ( $20 \text{ W}$ ), our major concern was the heat flow from the ambient  $(25 \pm 1)^\circ \text{C}$  air to inside the temperature controlled environment.

We modeled the thermal properties of major components of the calorimeter, and found that when we surround the calorimeter with two 0.375 inch thick Rohacell boards and temperature-regulated air flows in 0.75 inch of space between them, we can maintain the inside temperature at  $(15 \pm 0.1)^\circ \text{C}$  [14].

Humidity must be low enough for stable PMT HV operation, thus the system will be sealed and dry air or nitrogen gas will be flowed through, in order to keep the relative humidity below 1%.

## 6.7 Detector Assembly, Installation and Integration

The calorimeter consists of PWO crystal-PMT assemblies (glued together) and PMT bases which will be inserted into a mechanical support structure. The mechanical structure is made of a strong frame to support the entire weight of the device, and interlocking vertical and horizontal strips which form cells, where individual crystals will be inserted. The mechanical structure will be surrounded by insulating layers to help reduce the thermal load on the temperature stabilizing system.

In addition, electronics racks, which hold Front-End Boards (FEB), will be mounted near or on the mechanical structure. Cable trays will also be installed on the support structure for signal and HV cables as well as optical fibers.

Optical fibers that will be used to monitor and calibrate the crystal transparencies must be attached to each crystal. They will be useful to test the functionality of each crystal in the testing phase.

The support system will be assembled either outside the C0 Hall or in the assembly area of the C0 Hall. Crystal-PMT assemblies will be inserted into the support structure as much as possible prior to moving it to the collision hall, though with the current schedule, we will not have much time to do so.

Most of the crystal-PMT assemblies will be installed in the collision hall, with some number of the assemblies being installed each time we have access to the hall. Testing of the installed crystal-PMT combination will be done on a daily basis using a light pulser to assure all crystals are functional.

When FEBs become available, we will connect the PMT outputs to FEBs and test the whole sequence up to the FEB's using a temporary DAQ system, which will read out a section of the calorimeter. A clock will be required for multiple crates but we will supply this if it is not available from the PC-based DAQ system.

When the BTeV DAQ is available, the entire connections will be made to it and the final testing will be done with whatever triggers are available at that time.

When particle-based triggers become usable, we will start checking for mis-cabling and working on alignments.

### **6.7.1 Testing Prior to Moving to C0**

The elements moved to C0 should be tested sufficiently to ensure their functioning. C0 is not intended to be a general testing laboratory. However, if some items are too large to test anywhere else, they can be tested at C0. Crystals are glued to PMT's and tested for functionality before they are inserted to the support structure. Separately, signal and HV cables as well as optical fibers for calibration will also be tested. FEBs will be tested individually and in the crates before they are brought into C0 for connections to PMT's. The mechanical support system will be tested against the specification including mechanical tolerances and integrity.

### **6.7.2 Transportation of Elements to C0**

Assuming that the mechanical structure is assembled outside the C0 hall, it will be brought to C0 by a truck. The entrance door to the C0 building is too small for the structure to pass either horizontally or vertically. A large fork lift will be required to unload the structure from the truck and tilt it to 45° for rolling through the C0 building door.

The partially crystal-filled structure will be pushed (pulled) on its wheels to the collision hall. It will be moved using a transportation cart. Standard rigging equipment along with floor/wall anchors used for the magnets will be used.

Crystal-PMT assemblies will be brought to C0 in a box. A simple lifting device (200 kg) will be used to handle this box safely.

## 6.8 Detector Performance

### 6.8.1 ECAL Simulation

The BTeV ECAL geometry has been implemented as a part of BTeVGeant, our current simulation packaged based on GEANT3.21. A detailed description of BTeVGeant is given in the Proposal.

The current version of BTeVGeant incorporates a more realistic ECAL geometry description compared to the simplified version used at the time of the Proposal, since there has been progress in the mechanical design.

Currently, the BTeV detector has one electromagnetic calorimeter, at positive Z arm. It consists of more than 10,000 Lead Tungstate ( $\text{PbWO}_4$ ) crystals. The crystals, all of the same size, are tapered; the transverse dimensions are square,  $2.72 \times 2.72 \text{ cm}^2$  at the front and  $2.8 \times 2.8 \text{ cm}^2$  at the back, with a length of 22 cm. Each crystal is surrounded by air gap of 0.02 mm on each side, to account for clearance. In between there is 0.75 mm of Aluminum for the support structure. The crystals are installed to point almost at the I.R., i.e. to point at  $x = -10 \text{ cm}$ ,  $y = -10 \text{ cm}$  from the I.R., to minimize the effect of gaps, but give the benefits of a projective geometry. The outer boundary of the ECAL is close to a 160 cm radius circle. There is an inner square hole,  $\pm 10.88 \text{ cm}$  in  $x$  and  $y$ , in the ECAL to accommodate the beam. The ECAL is positioned at 750 cm from the center of the interaction region.

GEANT3 permits users to control the thresholds and cutoffs of the many physics processes that it simulates. Low thresholds give more realistic and detailed simulations but can require a large amount of computer time. This, in turn, can make it difficult to simulate large enough samples of events to make precise statements about efficiency and background rejection. After investigating several combinations of energies below which the tracking of electrons and photons is stopped, we selected 1 MeV threshold on both. A detailed description of the cutoffs selection study is done in the Proposal (pages 158-167).

The ECAL response is simulated in a form of “hits”, where a hit is a sum of the energy deposition in a  $\text{PbWO}_4$  crystal by one or more electromagnetic or hadronic showers. The energy stored in the hit is the true energy which would be measured by a perfect device. The hits are serialized and written to the output stream, along with geometry information in the BTeV specific format, for further reconstruction and analysis.

Effects such as light collection efficiency, readout specifications and imperfections are applied in a parametric way at the reconstruction and/or analysis time. Therefore these can be varied without CPU-expensive rerunning of BTeVGeant. This approach has been used a number of projects, in particular by CMS, and has been shown to be reliable. The

data structure for ECAL hits may also optionally store information about which particles or showers contributed to the energy sum in each crystal, should a user request.

## 6.8.2 Photon and $\pi^0$ 's Reconstruction Procedure

In this section we will describe shower energy and incident position reconstruction, unfolding of overlapping electromagnetic showers, rejection of contributions from charged hadrons, and photon and  $\pi^0$  reconstruction efficiencies.

The light generated in each crystal by electromagnetic showers or other charged particles is detected and converted into a digitized signal that is proportional to the number of photons incident on the photocathode. After a calibration step these numbers represent the total amount of energy deposited in each crystal for each event. From the array of energies in the ECAL, we extract the following information:

- Shower information that includes a total energy and a position measurement.
- Matching information that connects charged particle tracks and showers.

### 6.8.2.1 Shower Reconstruction Package

Our shower reconstruction tool, the cluster finder algorithm, is designed to identify specific patterns in the calorimeter hit data. Much of the key ideas were borrowed from reconstruction packages perfected by the Crystal Ball and CLEO crystal calorimeter groups. The two defined patterns are:

- Cluster - a region of crystals with connected topology.
- Bump - a local maximum in the energy response within a cluster.

The first step in the procedure is to create clusters. A cluster is started by a single crystal with energy deposit higher than a tunable threshold called “triggering seed” (no relation to actual BTeV triggering algorithms!) and represents all connected crystals with energy deposit higher than readout related threshold called “visible hit.” Currently we use 40 MeV for the “triggering seeds” and 1 MeV for the “visible hits.” The starting crystals are selected from the list of crystals with energy deposit higher than the “triggering seed” threshold; the crystals in the list are also sorted by energy.

The shape of a cluster can vary, since it only requires crystals to be neighbors when added to the same cluster. However, a crystal can only be part of one cluster.

The next step is to find bumps in the clusters. A bump is centered around a crystal in a cluster that has the maximum energy deposit into it compared to its adjacent crystals, and thus represents a local maximum. It has a fixed shape made of rings of neighboring crystals. Crystals may belong to one or more bumps. They only need to have energy deposit larger than the “visible hit” threshold. If a crystal is a part of more than one bump, a re-weighting

algorithm will partition the energy deposit in that crystal assigning some fraction of it to each bump to which the crystal belongs.

The most important data generated for bumps are total energy, position and shape, and they are recorded along with each bump object. A program using the output of cluster finder can efficiently access those numbers from memory.

The energy algorithm assumes that a bump represents an electromagnetic showers, initiated by a photon or an electron. Due to the shape of shower propagation, most of the energy is contained in the 3x3 array centered on the crystal with maximum signal, with small leakage into further away crystals. The sum of the energy in these crystal is called E9 because it contains contributions from up to 9 crystals. To estimate total energy of a shower, we chose 5x5 array centered on the crystal with maximum signal; this energy sum is called E25.

To calculate the shower position, called center-of-gravity, the algorithm averages on the positions of all the crystals used in the 5x5 array, weighted by energy deposition in each crystal.

Various effects introduce biases into the raw results obtained using this algorithm. There are basic geometric effects and effects due to limitations on the measurements. Here is the list of important corrections:

- Correction for the leakage outside the 5x5 array of crystals and for losses due to thresholds used in the reconstruction procedure; on average, the losses total at about 2%.
- Position bias correction for the center-of-gravity, know as "S-curve correction."
- Correction for the primary vertex position.
- The clustering algorithm is written in C++ and is organized as a single stand-alone library that accepts user and simulation input data, generates the above described bump objects, and gives access to the information stored in them. The described corrections parameters were found using single photons and  $\pi^0$ 's).

### 6.8.2.2 Rejection of Contributions from Charged Hadrons

Photon showers candidates selection is based on two criteria:

Shower shape criteria relies on the fact that the transverse profile of a hadronic showers is usually wider than that of an electromagnetic one. The E9/E25 ratio is used as a shower shape criteria to test the hypothesis that the bump represents an electromagnetic shower rather than a hadronic shower. Figure 6.47 illustrates the distribution of this ratio for single photon simulated by GEANT.

Contributions from charged hadrons, as well as from electrons, are further reduced by applying the isolation criteria. Tracks are projected onto ECAL, and for each shower a distance to the nearest footprint of a charged track is calculated, then required not to exceed a certain value. An exact value of the isolation criteria depends on a particular analysis and may vary when studying one B-decay mode or another.



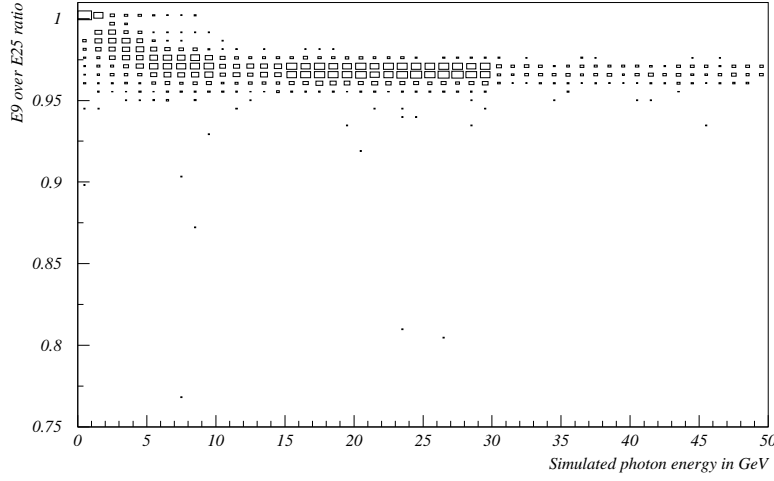


Figure 6.47: Measured ratio of E9 over E25 versus simulated photon energy.

### 6.8.3 Physics Simulation

Several studies have been done for various physics processes as reported in the proposal update. Here we reproduce one of these studies that we have continued looking at because of its importance. We report on the expected performance of the BTeV detector for the decays  $B^0 \rightarrow (\rho\pi)^0 \rightarrow \pi^+\pi^-\pi^0$  to demonstrate the usefulness of the BTeV EMCAL to detect photons. These decays are very important to study as the asymmetries in these decays can be used to measure the so-called the  $\alpha$  angle of the CP triangle, which is difficult to obtain with other decays.

Following the paper by Quinn and Snyder [15] and using their notation, the amplitude for the decay  $B^0 \rightarrow \rho\pi$  can be written as:

$$\begin{aligned} A(B^0 \rightarrow \rho^+\pi^-) &= S_3 = T^\pm + P_1 + P_0 \\ A(B^0 \rightarrow \rho^-\pi^+) &= S_4 = T^\mp - P_1 + P_0 \\ 2A(B^0 \rightarrow \rho^0\pi^0) &= S_5 = -T^\pm - T^\mp + T^{+0} + T^{0+} - 2P_0 \end{aligned} \quad (6.6)$$

Here the penguin contributions ( $P_i$ ) are identified by the isospin of the final  $\rho\pi$  state to which they contribute. Tree contributions are denoted by  $T^{ij}$ , where  $i$  and  $j$  denote the  $\rho$  and  $\pi$  charge, respectively. The amplitude for  $B^0 \rightarrow \pi^+\pi^-\pi^0$  can be written, ignoring non resonant contributions, as:

$$A(B^0) = f^+ S_3 + f^- S_4 + \frac{f^0}{2} S_5 \quad (6.7)$$

$$A(\bar{B}^0) = f^- \bar{S}_3 + f^+ \bar{S}_4 + \frac{f^0}{2} \bar{S}_5 \quad (6.8)$$

where the Breit-Wigner functions are given by

$$f^{\pm 0}(s) = \frac{\cos(\theta)}{s - m_\rho^2 + i\Pi(s)} \quad (6.9)$$

and running decay width is given by

$$\Pi(s) = \frac{m_\rho^2}{\sqrt{s}} \left( \frac{p(s)}{p(m_\rho^2)} \right)^3 \Gamma_\rho(m_\rho^2), \quad (6.10)$$

where  $s$  is the square of the invariant mass of the two pions, and  $\theta$  is the angle in the  $\rho$  rest frame between a decay pion and the line of flight of the bachelor  $\pi$ .

From eq. (6.6) it follows that

$$S_3 + S_4 + S_5 = T^{+0} + T^{0+} \equiv T \quad (6.11)$$

and, similarly,

$$\overline{S}_3 + \overline{S}_4 + \overline{S}_5 = \overline{T}^{+0} + \overline{T}^{0+} \equiv \overline{T} \quad (6.12)$$

The angle between  $T$  and  $\overline{T}$  is  $\alpha$  in the Standard Model with no ambiguities in its determination.

The amplitude  $M_+$  for tagged  $B^0$  ( $M_-$  for tagged  $\overline{B}^0$ ) is a function of the position in the Dalitz plot and of the time  $t$ .

$$M = \begin{cases} M_+ = e^{-\frac{\Gamma t}{2}} \left[ \cos(\frac{\Delta m}{2}t) A(B^0) + i \frac{q}{p} \sin(\frac{\Delta m}{2}t) A(\overline{B}^0) \right] \\ M_- = e^{-\frac{\Gamma t}{2}} \left[ \frac{q}{p} \cos(\frac{\Delta m}{2}t) A(\overline{B}^0) + i \sin(\frac{\Delta m}{2}t) A(B^0) \right], \end{cases} \quad (6.13)$$

where  $\Gamma$  is the  $B$  decay width and  $\Delta m$  is the mass difference between the heavy and light neutral  $B$  mass-eigenstates. The dependence on this quantity arises from the  $B^0 - \overline{B}^0$  mixing.

The time evolution of the physical states is shown in Figure 6.48 where we can appreciate the deviation from a pure exponential time distribution.

An example of the variation of the Dalitz plot versus time is illustrated in Figure 6.49, where the events are selected using a rejection algorithm based on  $|M|^2$  (see eq. (6.13)).

A maximum likelihood fit is performed on the generated events to determine the amplitudes and phases of eq. (6.6), and consequently  $\alpha$ .

The log-likelihood is given by:

$$\ln \mathcal{L} = \sum_i \ln \left( \left| \frac{M_i}{M_{\text{norm}}} \right|^2 \right) \quad (6.14)$$

where  $M_i$  is defined by eq. (6.13) and the normalization factor  $M_{\text{norm}}$  is given by:

$$|M_{\text{norm}}|^2 = \frac{|M_+|^2 + |M_-|^2}{2} \quad (6.15)$$

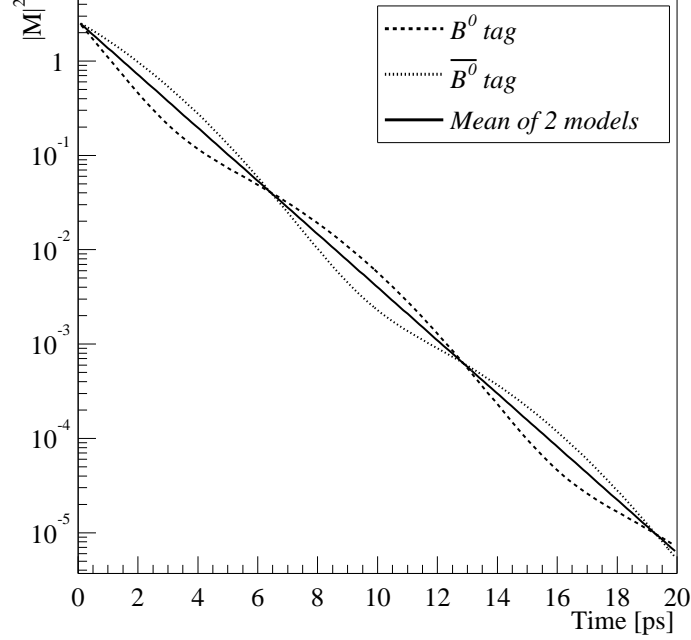


Figure 6.48: Time evolution of the physical  $B^0 - \bar{B}^0$  states.

Excellent resolution in  $\pi^0$  reconstruction and momentum will reduce the background significantly and to a manageable level, particularly near the edges of the Dalitz phase space where the  $\rho\pi$  events lie. In addition, good resolution in the proper time is also crucial to determine the angle  $\alpha$ . BTeV, with its  $\text{PbWO}_4$  crystal calorimeter, will be able to collect and reconstruct a substantial sample of  $B \rightarrow \rho\pi$  events.

The reconstruction efficiencies for  $B \rightarrow \rho\pi$  and backgrounds were studied using a full GEANT3-based simulation (see ECAL Simulation section), for  $\rho^\pm\pi^\mp$  and  $\rho^0\pi^0$ , separately. All signal and background samples were generated with a mean of two interactions per crossing. The analysis relies especially on the Kalman filter, the vertex package, and the ECAL reconstruction package.

With the use of the electromagnetic calorimeter, our aim is to find good  $\pi^0$  candidates. We select candidate “bumps” in the calorimeter using the cluster finder code (see ECAL Reconstruction section). Photon candidates are required to have minimum reconstructed energy of 1 GeV and pass the shower shape cut which requires  $E9/E25 > 0.85$ . We reduce the background rate by insuring that the photon candidates are not too close to the projection of any charged tracks on the calorimeter. For  $\rho^\pm\pi^\mp$ , the minimum distance requirement is  $> 2$  cm, while for  $\rho^0\pi^0$  we require it to be  $> 5.4$  cm. For the  $B \rightarrow \rho^+\pi^-$  events the  $\gamma\gamma$  invariant mass distribution is presented in Fig. 6.50a, for the pairs with the energy sum of greater than 5 GeV and with the vector sum of transverse momenta greater than 0.75 GeV. The  $\pi^0$  signal is very clear; the  $\pi^0$  mass resolution in this sample is 3 to 4 MeV/ $c^2$ .

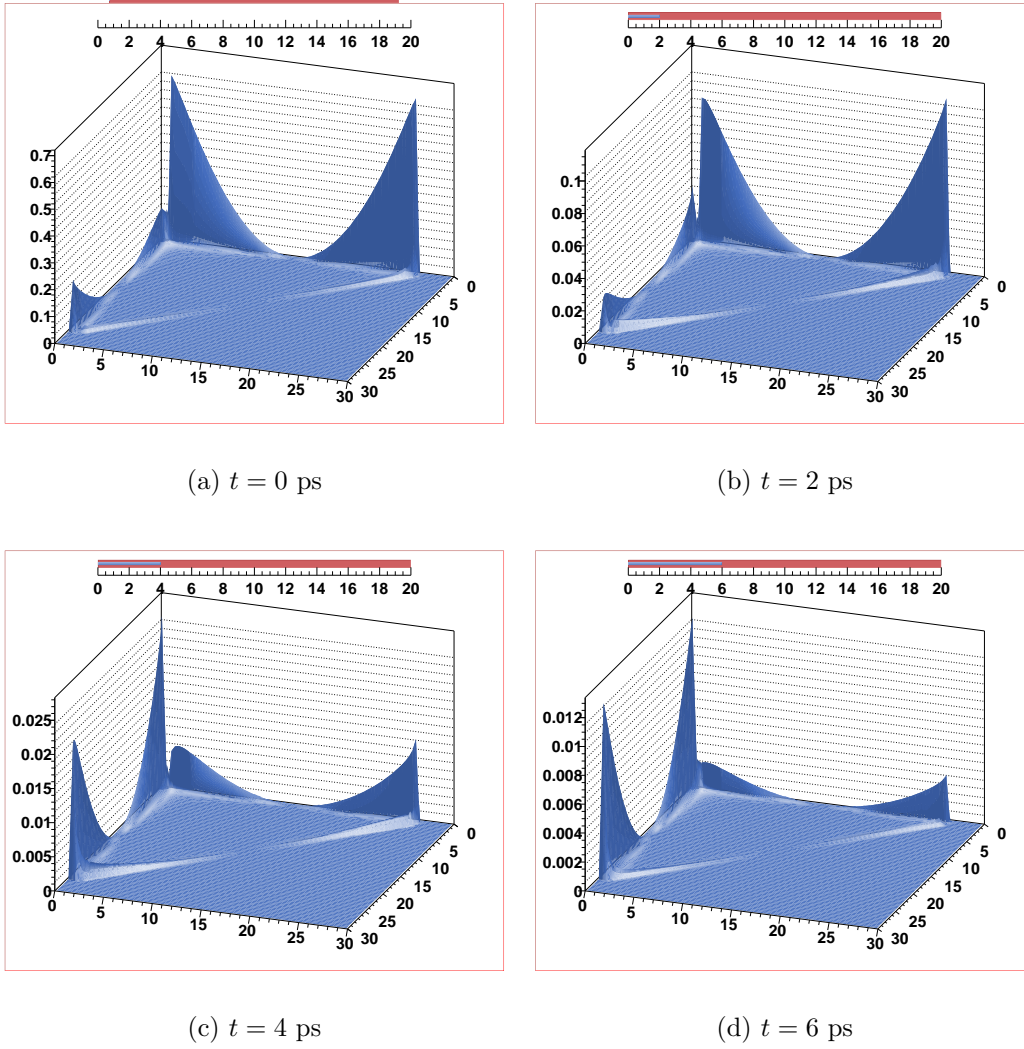
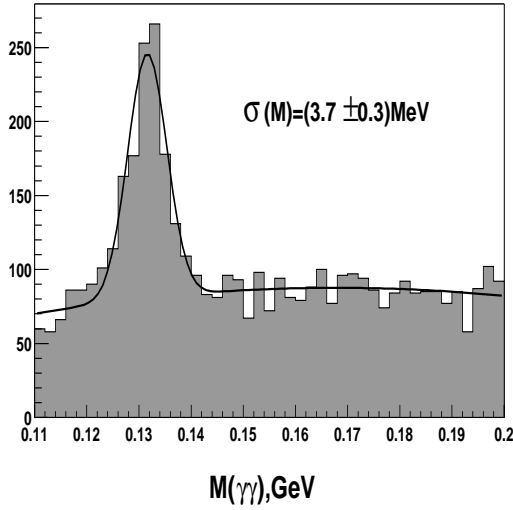


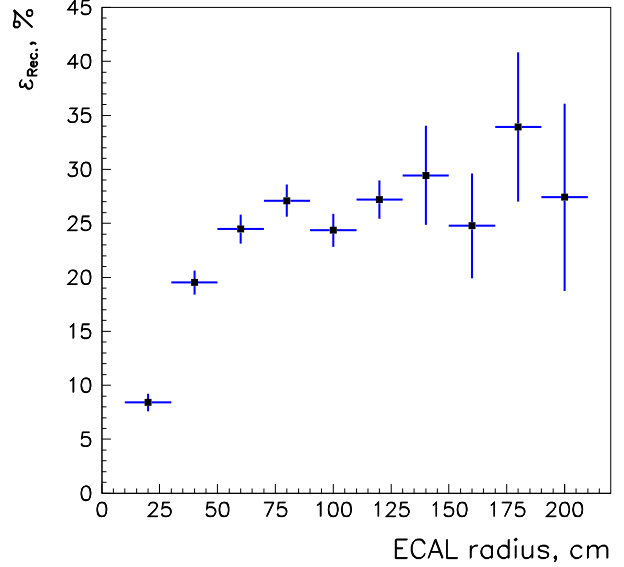
Figure 6.49: Evolution of the Dalitz plot versus time

Candidates  $\pi^0$ 's are two-photon combinations with invariant masses between 125 and 145  $\text{MeV}/c^2$ . The  $\pi^0$  reconstruction efficiency depends on the distance from beam line and is presented in Fig. 6.50b; the  $\pi^0$ 's are taken from the  $B^0 \rightarrow \rho^\pm \pi^\mp$  events. This simulation was run with a larger than proposed calorimeter so we could view the dependence on radius. (Results on sensitivities are quoted only with the actual geometry.)

We look for events containing a secondary vertex formed by two oppositely charged tracks. One of the most important selection requirements for discriminating the signal from the background is that the events have well measured primary and secondary vertices. We demand that the primary and the secondary vertices be well formed by insisting that  $\chi^2/dof < 2$  for their vertex fits. We also make a cut on the  $B$  flight significance,  $L/\sigma_L$ , greater than 4: distance between the primary and the secondary vertices divided by the



(a)



(b)

Figure 6.50: The  $\pi^0$  signal in the  $\gamma\gamma$  spectrum from  $B^0 \rightarrow \rho^+\pi^-$  events (a) and the efficiency of reconstructing the  $\pi^0$  as a function of distance from the beam line (b). Sample includes a mean of two Poisson distributed non-beauty interactions per beam crossing.

error. The two vertices must also be separated from each other in the plane transverse to the beam. We define  $r_{transverse}$  in terms of the primary interaction vertex position  $(x_P, y_P, z_P)$  and the secondary vertex position  $(x_S, y_S, z_S)$  as  $r_{transverse} = \sqrt{(x_P - x_S)^2 + (y_P - y_S)^2}$  and reject events where the secondary vertex is close to the reconstructed primary (see  $r_{transverse}$  values in Table 6.7). Furthermore, to insure that the charged tracks do not originate from the primary, we require that both the  $\pi^+$  and the  $\pi^-$  candidates have an impact parameter with respect to the primary vertex (DCA) greater than  $100\mu m$ .

When we form the invariant mass of either the  $\pi^+\pi^-$  pair or the  $\pi^\pm\pi^0$  pair, we require it to be compatible with the  $\rho$  mass, that is, between  $0.55$  and  $1.1 \text{ GeV}/c^2$ . In addition, we use several kinematics cuts which can greatly reduce the background to  $B \rightarrow \rho\pi$  while maintaining the signal efficiency. Minimum energy and transverse momentum ( $p_t$ ) requirements are placed on the three-pion system. The vector sum of  $p_t$ 's is defined with respect to the  $B$  direction which is calculated from the positions of the primary and secondary vertices. We require that  $p_t^{\text{sum}}$  divided by the scalar sum of the  $p_t$  values of all three particles,  $(p_t^{\text{sum}}/\Sigma p_t)$ , be small. We also make a cut on the  $B$  decay time requiring that the  $B$  candidate live no more than 5.5 proper lifetimes ( $t_{proper}/t_0 < 5.5$ ). The selection criteria for the two modes are summarized in Table 6.7.

The  $B^0$  mass resolution in this sample is in the range  $38\text{-}42 \text{ MeV}/c^2$ .

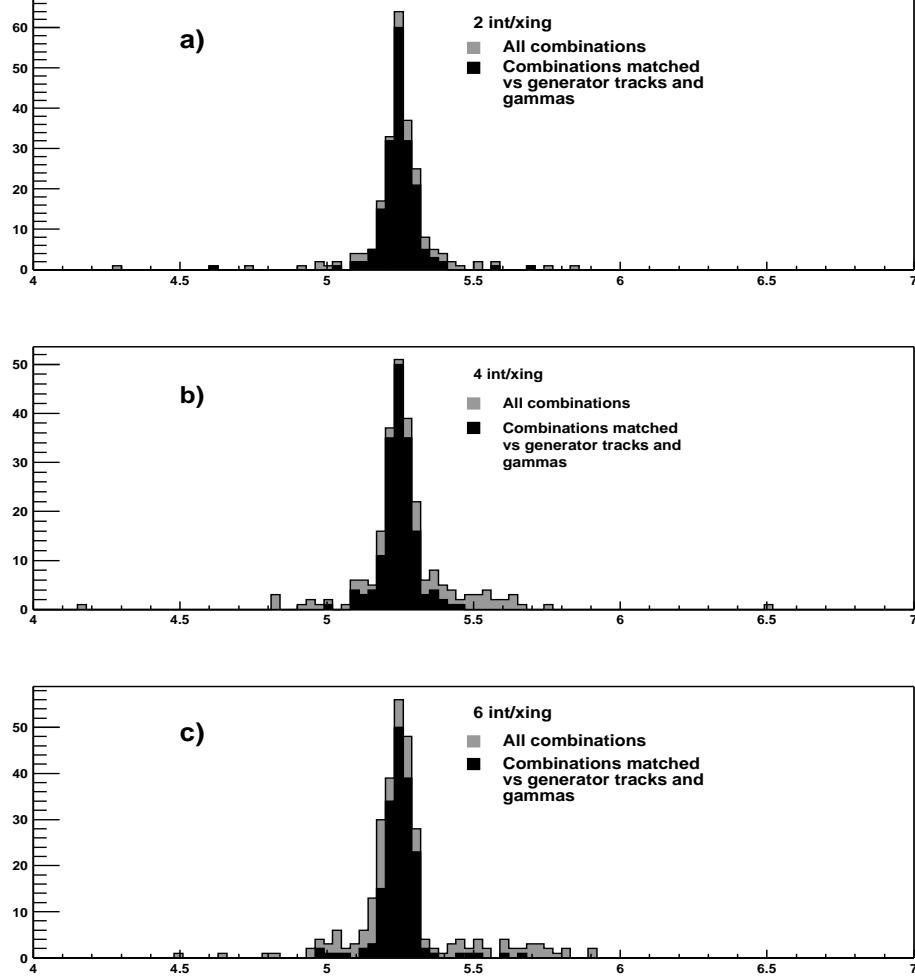


Figure 6.51: Invariant mass  $\pi^+\pi^-\pi^0$ , GeV (after cuts) matched vs generator tracks and photons, for 2, 4, and 6 interactions/crossing

The signal interval is taken as  $\pm 2\sigma$  around the  $B$  mass. The background was obtained by considering the mass interval between 5 and 7  $\text{GeV}/c^2$ .

The reconstruction efficiency is  $(0.18 \pm 0.02)\%$  for  $B^0 \rightarrow \rho^0\pi^0$  and  $(0.22 \pm 0.02)\%$  for  $B^0 \rightarrow \rho^\pm\pi^\mp$ .

Similar simulation studies were repeated to estimate reconstruction efficiency for the  $B^0 \rightarrow \rho^+\pi^-$  decay, with the assumption of four and six interactions per crossing. It was found that the ability to reconstruct  $\pi^0$ 's at six interactions per crossing does not significantly deteriorate compared to two background interactions per crossing, and the  $B$  reconstruction efficiency does not seem to be affected by more than 10%. However, the number of false  $3\pi$

Table 6.7: Selection Criteria

Criteria	$\rho^\pm\pi^\mp$	$\rho^0\pi^0$
Primary vertex criteria	$\chi^2 < 2$	$\chi^2 < 2$
Secondary vertex criteria	$\chi^2 < 2$	$\chi^2 < 2$
$r_{transverse}$ (cm)	0.0146	0.0132
Normalized distance $L/\sigma$	$> 4$	$> 4$
Distance $L$ , cm	$< 5$	$< 5$
DCA of track, $\mu\text{m}$	$> 100$	$> 100$
$t_{proper}/t_0$	$< 5.5$	$< 5.5$
$E_{\pi^+}$ , GeV	$> 4$	$> 4$
$E_{\pi^-}$ , GeV	$> 4$	$> 4$
$p_t(\pi^+)$ , GeV/ $c$	$> 0.4$	$> 0.4$
$p_t(\pi^-)$ , GeV/ $c$	$> 0.4$	$> 0.4$
Isolation for $\gamma$ , cm	$> 2.0$	$> 5.4$
$E_{\pi^0}$ , GeV	$> 5$	$> 9$
$p_t(\pi^0)$ , GeV/ $c$	$> 0.75$	$> 0.9$
$p_t^{\text{sum}}/\Sigma p_t$	$< 0.06$	$< 0.066$
$m_{\pi^0}$ , MeV/ $c^2$	125 – 145	125 – 145
$m_\rho$ , GeV/ $c^2$	0.55 – 1.1	0.55 – 1.1

combinations that would pass the cuts increases somewhat as the number of interactions per crossing may go up (see Appendix).

In addition, a check against generator level information was done in order to prove that most of the entries in the  $B^0$  mass region are true  $\pi^+\pi^-\pi^0$  combinations coming from the  $B^0$  decay, not false  $3\pi$  combinations which would mimic the signal. Figure 6.51 illustrate the results of matching against generator level information at two, four, and six interactions per crossing. It is clearly seen that most of the  $3\pi$  combinations are the correct ones.

We expect to have  $\sim 500$  effective flavor-tagged  $\rho^\pm\pi^\mp$  events and  $\sim 75$  flavor-tagged  $\rho^0\pi^0$  events per year ( $10^7$  s). The signal-to-background ratios are 4.1 and 0.3, respectively.

In terms of measuring the angle  $\alpha$  following the approach by Quinn and Snyder mentioned above and accounting for the resolutions of the BTeV detector, one would expect from simulation an uncertainty of  $\sim 1.5^\circ$  if the true value of  $\alpha$  is about  $70^\circ$ . Since multiple interactions due to different bunch crossings may slightly affect the reconstruction efficiency while the resolutions remain practically unchanged, the estimate applies to either case of two, four, or six interactions per crossing. Details about this simulation can be found in [16].

## 6.9 Schedule and Costs

### 6.9.1 Planning

The planning of the construction of the BTeV Electromagnetic Calorimeter is integrated in the overall BTeV planning. The mechanical structure is expected to be assembled in the C0 Assembly Hall. At least 50% of the Crystal-PMT assemblies will be inserted into the support structure. With our aggressive schedule, up to 90% of the crystals will be in the support structure, while when we allow possible delays in the crystal acquisition, it may be 70%. When the 2009 shutdown starts, the support structure will be moved to the collision hall. We will also place racks of Front-end Boards(FEB's) as well as the light pulsers next to the calorimeter. These electronics will be connected to DCB's and the rest of DAQ system and checked. The rest of the Crystal-PMT assemblies will be inserted into the support structure over the 2010 shutdown.

All 10,000 crystals will be produced and subjected to a quality assurance at BTeV Institutions in 2006-2009. The full calorimeter will be ready to take data for calibration at the end of 2010.

### 6.9.2 Costs

The full cost of the Electromagnetic calorimeter including contingency is \$20.762M. The present cost estimate has been developed over the last several years and the costs were an important consideration in optimizing the design presented in this Technical Design Report.

## 6.10 Organization

The EMCAL Project Manager Professor Yuichi Kubota from University of Minnesota, appointed by the BTeV co-spokespersons, heads the BTeV Electromagnetic Calorimeter project.

### 6.10.1 Participating institutes

The BTeV Electromagnetic calorimeter collaboration currently consists of the following institutions :

- Belarussian State University (BSU), Belarussia
- Fermi National Accelerator Laboratory (Fermilab), IL, USA
- Institute for High Energy Physics (IHEP), Protvino, Russia
- University of Minnesota, MN, USA
- Nanjing University, China



- University of Science and Technology of China, China
- Shandong University, China
- Syracuse University, NY, USA

### 6.10.2 Responsibilities

The work currently being done is to develop the baseline design of EMCAL. The proposed collaborative projects include the following:

- Development of detailed Monte-Carlo simulation code to help understand characteristics EMCAL and R&D results- Fermilab and IHEP
- R&D studies of PWO crystals and PMT's - IHEP, Minnesota, Syracuse and Fermilab
- Complete testing of phototubes - Minnesota and IHEP
- Light Pulser System - IHEP and BSU
- Mechanical design of EMCAL - Fermilab, Minnesota and IHEP
- Electronics - Fermilab
- Development of quality assurance systems to check the optical and radiation hard properties of mass-produced PWO crystals - Chinese institutions and IHEP

Details of the work to be done will be described in Memorandums of Understanding between Fermilab and the collaborative institutions.

The construction of the BTeV Electromagnetic calorimeter is an international project involving institutes all over the world. The construction efforts of the calorimeter are big and it has been decided to distribute the workload among the participating institutes. This organization allows institutional manpower to be engaged at their home institution and thus reduces labor and other associated costs. This strategy also ensures that existing infrastructures in the institutes can be used efficiently and thus investments for necessary laboratory installations can be minimized.

Lead tungstate crystals and phototubes of the Electromagnetic calorimeter need thorough quality control and require numerous acceptance tests. Nanjing University and IHEP will receive the crystals directly from the producers and will carry out necessary crystal quality control program. The phototubes will be tested at Minnesota before installation in the calorimeter.

Front-end electronics will be developed and produced at Fermilab.

Mechanical support will be produced either in Russia or at Fermilab and assembled at Fermilab. Cooling system will be assembled at Fermilab.

Light monitoring system will be developed and assembled in Protvino and then brought to Fermilab. Belarussian State University will participate in this project.

On-line and off-line software for the BTeV electromagnetic calorimeter will be prepared by Fermilab, IHEP, University of Minnesota and Nanjing University.

# Bibliography

- [1] CMS, The Electromagnetic Calorimeter Project Technical Design Report, CERN/LHCC 97-33, CMS TDR 4 (1997).
- [2] ALICE, Technical Design Report of the Photon Spectrometer (PHOS), CERN/LHCC 99-4, ALICE TDR 2 (1999).
- [3] T. Brennan *et al.*, “The BTeV electromagnetic calorimeter”, Nucl. Instr. and Meth., **A494**, 313–317 (2002).
- [4] V.A. Batarin *et al.*, “Development of a Momentum Determined Electron Beam in the 1-45 GeV Range”, Preprint IHEP 02-29, Protvino, 2002; e-Print Archive hep-ex/0208012; Nucl. Instr. and Meth., **A510**, 211–218 (2003).
- [5] V.A. Batarin *et al.*, “Precision Measurement of Energy and Position Resolutions of the BTeV Electromagnetic Calorimeter Prototype”, Preprint IHEP 02-34, Protvino, 2002; e-Print Archive hep-ex/0209055; Nucl. Instr. and Meth., **A510**, 248–261 (2003).
- [6] GEANT, Detector Description and Simulation Tool, Computing and Networks Division, CERN
- [7] R.Y. Zhu, “Radiation damage in scintillating crystals.” Nucl. Instr. and Meth., **A413**, 297–311 (1998).
- [8] Private communication with R.Y. Zhu. He told us to measure the uniformity of light collection after we irradiated a small portion along the crystals. If only transmission of light deteriorate in the region, since light from any parts of the crystals will pass through this area, the uniformity won’t change very much. If the scintillation mechanism is damaged, on the other hand, light collection from only damaged region will suffer.
- [9] I.Azhgirey, I.Kurochkin, V.Talanov, Development of MARS code package for radiation aspects of electronuclear installations design, in: Proc. 15th Conf. on Charged Particles Accelerators, Protvino, 22024 October, 1996, p.74.  
I.Azhgirey *et al.*, Calculation of high-energy hadron spectra at the CERN-CEC reference field facility by the MARS’95 and HADRON codes, Nucl. Instr. and Meth., **A408**, 535–542 (1998).

- [10] V.A. Batarin *et al.*, “Study of Radiation Damage in Lead Tungstate Crystals Using Intense High Energy Beams”, Preprint IHEP 02-35, Protvino, 2002; e-Print Archive hep-ex/0210011; Nucl. Instr. and Meth., **A512**, 484–501 (2003).
- [11] V.A. Batarin *et al.*, “ LED Monitoring System for the BTeV Lead Tungstate Crystal Calorimeter Prototype“, Preprint IHEP 03-32, Protvino, 2003; e-Print Archive physics/0311119; accepted at Nucl. Instr. and Meth.
- [12] V.A. Batarin *et al.*, “Comparison of Radiation Damage in Lead Tungstate Crystals Under Pion and Gamma Irradiation”, Preprint IHEP 04-03, Protvino, 2004; e-Print Archive physics/0312063; NIM, **A530**, 286-292 (2004).
- [13] V.A. Kachanov *et al.*, “Light source for energy stabilization of calorimeter detectors based on photodetectors,” NIM, **A314**, 215-218 (1992).
- [14] T. Tope, “BTeV EM Calorimeter Thermal Analysis Report,” BTeV doc 1050
- [15] A. E. Snyder and H. R. Quinn. Measuring  $CP$  asymmetry in  $b \rightarrow \rho \pi$  decays without ambiguities. *Phys. Rev.*, **D48**, 2139–2144 (1993).
- [16] M. Rovere, “Measuring  $\alpha$  with  $B^0 \rightarrow \rho \pi$  in the BTeV experiment”, BTeV-doc-3038, (2004).

# Chapter 7

## Muon Detector

### 7.1 Introduction

The BTeV muon system has two primary functions:

- Muon identification: Many of the experiment’s physics goals rely on efficient muon identification with excellent background rejection. Muon identification is important for rare decay searches, CP violation studies which require tagging, studies of beauty mixing, semileptonic decays, and searches for charm mixing.
- $J/\psi$  and prompt muon trigger: Besides selecting interesting physics (including  $J/\psi$  final states of  $B$  decays, direct  $J/\psi$  production, and rare decays), this trigger performs an important service role by selecting a large enough sample of  $b$  events on which the more aggressive and technically challenging vertex trigger can be debugged and evaluated.

We have selected a toroidal magnet design combined with fine-grained tracking elements. This design permits a “stand-alone” trigger: *i.e.* a di-muon trigger based solely on information from the muon detector. In addition, improved background rejection is possible by comparing this measurement with momentum and tracking information from the rest of the spectrometer. The system design has been chosen to reduce and distribute occupancies and to minimize confusion in pattern recognition while allowing the muon trigger system to achieve a minimum bias rejection of about 500 with a di-muon efficiency of about 80%.

### 7.2 Muon System Overview

#### 7.2.1 General design considerations

Given the objective of a stand-alone trigger and the size limitations set by the experimental hall, one can make fairly general calculations that place specific (and restrictive) constraints on the design of the system.

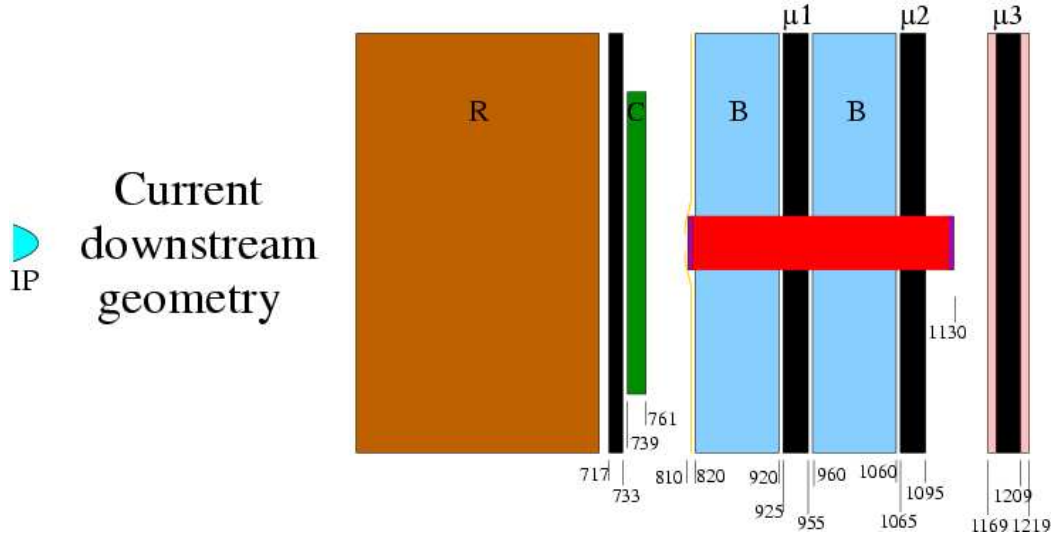


Figure 7.1: Side view of the downstream tracking elements of the BTeV spectrometer, showing the location of the two muon toroids (labeled “B”) and the three muon detector stations (labeled “ $\mu 1 - \mu 3$ ”). Also shown is the long compensating dipole in the middle and extra shielding around  $\mu 3$ . For context, the RICH (“R”), electromagnetic calorimeter (“C”), and the final tracking chamber between them are also shown. All numbers are distances in centimeters from the interaction point.

The fractional momentum resolution in a magnetic spectrometer can be parameterized as  $\sigma_p/p = \sqrt{a^2 + (bp)^2}$  where the  $a$  term depends on the bending power and multiple scattering environment of the detectors and the  $b$  term depends on the bending power and the detector layout and spatial resolution. The detector layout is constrained by the size of the experimental hall. For a multiple scattering term of  $a = 25\%$ , a trigger with a minimum momentum requirement rejects low momentum muons at  $4\sigma$ . The  $b$  term is important at high momentum, where it determines the fraction of high momentum tracks that fail a minimum momentum cut in a trigger. If  $b$  is less than 1%, the efficiency for high momentum tracks is very nearly one ( $> 99\%$ ). Above 1%, the efficiency starts to fall off rapidly, approaching 70% for  $b = 10\%$ . Monte Carlo simulations of our design predict theoretical values for  $a$  and  $b$  of 19% and 0.6% respectively.

### 7.2.2 Baseline muon system

Two toroids, approximately 1 m long with 1.5 T fields, provide the bending power and filtering of non-muons. There will be three stations of detectors, one between the two toroids and two behind the toroids (farther from the interaction point in  $z$ ), as shown in Fig. 7.1. The momentum of tracks can be measured using the two, well shielded, downstream stations and the nominal beam constraint. The station between the two toroids provides an important confirming hit for the rejection of fake tracks.



Figure 7.2: The basic building block of the muon system (plank). The inset shows an end view of the plank, and demonstrates the “picket fence” geometry of the proportional tubes. The gold colored pieces at each end of the plank are the brass gas manifolds. Visible at the end is the circuit board soldered around the edge to the brass piece.

The basic building block in the construction of the a detector station is a “plank” of 3/8” diameter stainless steel proportional tubes. There are 32 tubes in each plank, arranged in two rows of 16 offset by half a tube diameter (“picket fence” style). (See Fig. 7.2.) These are held together with aluminum ribs and by the brass gas manifolds which are glued to the end of each plank. Each plank is a sturdy, self-supporting building block which acts as an excellent Faraday cage. We want to avoid ghost tracks in the system, so our minimum requirement is that all hits from one beam crossing be collected before the next beam crossing. A mixture of Ar-CO<sub>2</sub> meets this goal. The tubes will be strung with 30  $\mu\text{m}$  diameter gold-plated tungsten wire, and the stainless steel tubes will have a wall thickness of 0.01”. The 0.5 cm wire spacing of this design has no dead regions and has an effective spatial resolution of 1.4 mm.

To minimize occupancy at small radii, twelve planks of increasing length are arranged into pie shaped octants. To minimize pattern recognition confusion, three arrangement of planks ( $r$ ,  $u$ , or  $v$ ) are used. The  $r$  views are radial. The  $u$  and  $v$  views are rotated  $\pm 22.5$  degrees with respect to the radial views and measure the azimuthal angle,  $\phi$ . A collection of 8 octants of like arrangement is called a view, and a collection of 4 views is called a station. In order to provide redundancy in the most important view in terms of pattern recognition for the trigger and momentum measurement, the  $r$  view is repeated in each station. The whole muon detector is three stations located at the end of the BTeV experiment, interspersed between and after magnetized iron toroids and shielding. A schematic of this arrangement is shown in Fig. 7.3.

The octants are the basic installation unit of the system. During the run, octants will be swapped in and out when the system requires maintenance. Bad planks in an octant will then be swapped out and fixed.

For a one-arm muon system, the 3 detector stations, with 4 views per station, 8 octants

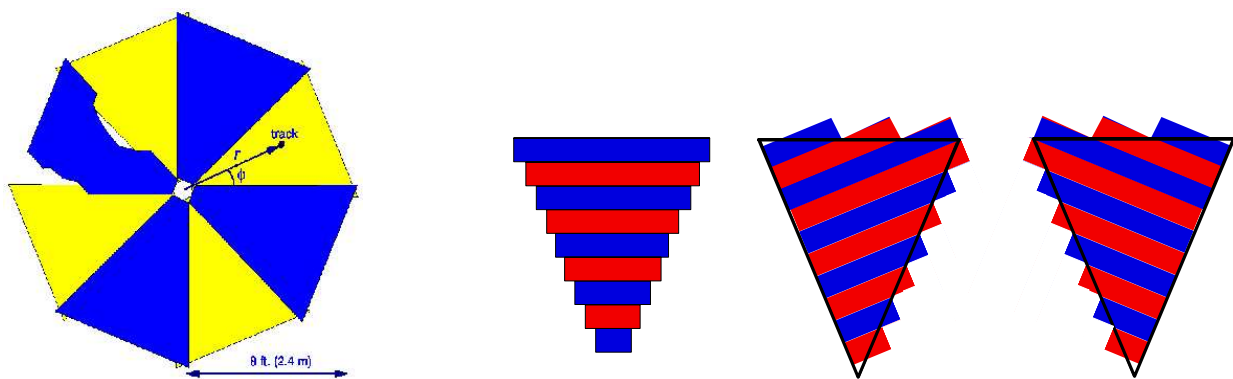


Figure 7.3: (left) Beams-eye view of one muon station (eight overlapping octants arranged in two layers). (right) Arrangement of planks to form each of the four views in an octant ( $r$  view is repeated). There will be 12 planks per octant (more than shown).

Item	Number
Stations	3
Views/station	4
Octants/view	8
Planks/octant (one view)	12
Tubes/plank	32
Total channels	36,864

Table 7.1: Channel and item counts for the BTeV muon system.

per view, and 12 planks per octant add up to a total of 1,152 planks or 36,864 tubes and electronics channels. (See Table 7.1.) The 8 octants in a view are mounted on two wheels, as described in Section 7.4.3. We will build one complete view (8 octants, 96 planks, 3,072 tubes) during the pre-production stage (which we will use to shake down and evaluate our production lines and methods). We will also make two additional views worth of planks to use as spares. These additional planks must be made at the same time to minimize the cost of the necessary parts and labor.

### 7.3 Requirements for the BTeV Muon System

The considerations that have gone into determining the requirements for the muon system include:

- The physics goals of the experiment
- The characteristics of both the events of interest and background events



- The physical size of the C0 hall and other detector components
- The robustness of the detector technologies
- Environmental, Safety, and Health (ES&H) issues

### 7.3.1 Physics requirements

These requirements are determined by the physics goals of BTeV.

1. **Luminosity:** The muon system must be able to operate at any bunch crossing time of 132 to 396 ns with a maximum luminosity of  $4 \times 10^{32}(\text{cm}^2\text{s})^{-1}$ .
2. **Lifetime:** The muon system must operate consistent with its design goals over the maximum lifetime of the experiment (10 years).
3. **Momentum resolution:** The “stand alone” momentum resolution of the muon system must be better than  $\sigma_p/p = \sqrt{0.25^2 + (0.01p)^2}$ .

### 7.3.2 Toroid requirements

1. **Bending power:** There should be two toroids in the (single) muon arm, each with a minimum field of 1.4 T and minimum thickness of 0.8 m.
2. **Magnetic field map:** The magnetic field must be known everywhere in the toroids to 1%.
3. **Magnetic field uniformity:** The magnetic field in each toroid must be uniform to 5%.

### 7.3.3 Proportional tube performance requirements

1. **Timing resolution:** The collection time for all proportional tube hits should be less than the beam crossing rate.
2. **Occupancy:** The maximum rate in any single proportional tube should be less than 200 kHz.
3. **Efficiency:** The typical efficiency of each proportional tube should be 98% or greater.
4. **Efficiency over lifetime:** The muon system efficiency over the lifetime of the experiment must be consistent with the BTeV physics goals. Currently it is thought that any aging effects will be negligible.
5. **Spatial resolution:** The position resolution of the proportional tube planks must be 2 mm or less.

### 7.3.4 Detector installation and support requirements

1. **Position reproducibility:** The position of the octants should be reproducible to 0.25 mm in  $x$ ,  $y$  and  $z$  after they are moved (*e.g.* for maintenance).
2. **Removal/exchange:** The muon octant plates should be readily removable for maintenance. It must be possible to remove an octant during two 8 hour shifts, and replace an octant in two 8 hour shifts.
3. **Internal survey:** The coordinates of the individual muon proportional tubes within each octant needs to be known a priori to a level such that it does not contribute to the expected resolutions (2 mm) of the muon proportional tubes.
4. **External survey:** The coordinates of the station fiducials with respect to the BTeV absolute coordinate system needs be known a priori and maintained over the lifetime of the experiment. Final alignment transverse to the beamline and station position monitoring will be performed via software. The location of each station along the beamline ( $z$ ) with respect to the experiment center must be determined within 2.3 mm over the face of the detector. The station to station alignment, in terms of rotations about the beam axis, must be matched to within a milliradian (about a 2 mm shift around the rim of the detector). The station to station alignment, in terms of shifts transverse to the beam axis, must be matched within 2 mm.
5. **Flatness:** The center of a circular slice of a tube must not deviate by more than a perpendicular distance of 0.5 mm from the ideal long axis of symmetry. This is a requirement for wire stability at high voltage.
6. **Roundness:** The tube inner radius must not deviate by more than 0.5 mm towards the center of the tube from the ideal radius of the tube. This is a requirement for wire stability at high voltage.

### 7.3.5 Geometry requirements

These requirements are constrained by the size of the experimental hall.

1. **Station depth in  $z$ :** Each full detector station should not take more than 40.5 cm of space in  $z$  (the beam direction).
2. **Acceptance:** Each full detector station should cover radii between 38 cm and 240 cm.

### 7.3.6 Correction dipole requirements

1. **Installation interference:** The correction dipoles and their associated cabling should not restrict or interfere with the installation of the muon detector stations and their supporting infrastructure.

2. **Radial size:** The muon system needs to provide coverage down to 38 cm (Geometry requirement 2). The correction dipoles and their associated cabling should not restrict or interfere with this coverage.

### 7.3.7 Control and monitoring

1. **Environmental monitoring:** The muon system needs environmental monitoring (pressure and temperature). In order to be sensitive to 1/10th of the plateau region in the smallest plank (the best case), the monitoring must resolve a change equivalent to a change in HV of 10V or a change in gas gain of  $1 \times 10^4$  (nominal gain is expected to be  $1 \times 10^5$ ). This corresponds to 1/200th of an atmosphere and 1 degree C.
2. **Gas mixture monitoring:** We need to monitor the gas mixture for changes in mixture conditions equal to 0.1% (*e.g.* a change of a mixture of 85/15 Ar/CO<sub>2</sub> to 85.1/14.9).
3. **HV monitoring:** The muon system needs monitoring of the high voltage power supply voltage with a resolution of 2–3 V and current with a resolution of 0.1  $\mu$ A.
4. **Gas gain monitoring:** The muon system requires monitoring of the gas gain and particularly needs to be alert to aging issues. The gas gain monitor must have a resolution equal to roughly 0.1% of the range of the plateau region, or, repeated samples of the gain over the course of a 24 hour period must produce a measurement of the derivative in the gas gain with a resolution of about  $3 \times 10^{-5}/(\text{day})$ , roughly  $1 \times 10^4/(\text{life of the experiment})$ .
5. **Gas contaminant monitoring:** The gas mixture must be monitored for contaminants with a gas mass spectrograph.

### 7.3.8 Software requirements

The software for the muon system refers to algorithms for track finding, monitoring systems, and diagnostic tools.

1. **Software standards:** Software development will conform to the *BTeV Software Standards*
2. **Muon Identification:** Muon identification software must be written which will perform track matching from the upstream spectrometer (a combination of pixel and straw tracks) to either hits or track segments in the muon system. The matching will be performed using the expected errors from the upstream spectrometer and the muon system and a confidence level will be assessed for the agreement. Where possible, an independent measurement of muon momentum will be calculated.

3. **Muon Calibration:** Software must be written to determine the geometry of the muon system and the efficiency of individual counters. These measurements will be estimated from data and included into the muon identification software at periodic intervals concurrent with significant changes in geometry or efficiency.
4. **Front End:** The programmable components in the front end electronics must have software capable of setting and verifying thresholds, pulsing sets of channels, sparsifying and gating the signals coming from the tubes, identifying the board electronically, and communicating with the slow control system. Additional functionality will be included to fully exploit the capabilities of the hardware (*e.g.* the ability to shut off a channel if we fully develop channel fusing).
5. **Monitoring:** Software must be developed to monitor changes in muon system performance using the data and to monitor changes in the physical environment of the detector (*e.g.* temperature, high voltage, current to the plank, pressure to an octant, gas flow to an octant, status of valves in the gas system, gas gain, gas impurities, gas mixing percentage, etc.). This software will have limits where operators will receive an alert if parameters exceed limits. Implicit in this requirement is an interface to BTeV DAQ for slow controls.

### 7.3.9 ES&H requirements

The muon system will have subsystems (electrical and gas handling), which could constitute safety hazards. The electrical will have sub-systems that have low voltage and high current, as well as high voltage and low current.

1. **Electrical safety:** All electrical aspects of the muon system will conform to the Fermilab ES&H manual on electrical safety.
2. **Gas handling safety:** All aspects of the gas handling system will conform to the Fermilab ES&H manual on gas systems.

### 7.3.10 Electrical requirements

1. **Compliance with BTeV Electronics Standards:** The muon system will comply with BTeV standards and the Fermilab ES&H manual on electrical safety.

### 7.3.11 Front-end electronics requirements

1. **Noise on FE:** The digital section of the front-end cards must not impact the performance of the analog portion, consistent with the physics goals of BTeV. The low and high voltage delivery must not impact the performance, consistent with the physics goals of BTeV.

2. **Thresholds:** Thresholds must extend from no higher than 0.1 fC to 16 fC with a resolution of 0.03 fC.
3. **Channel granularity:** The maximum number of channels to be controlled by a single threshold is 8.
4. **Channel control:** A common high voltage is to be sent to each plank.
5. **Fusing:** Fusing of low voltage will be done with fuses that self-recover.

### 7.3.12 Internal Interlocks

1. **HV over-current:** Individual high voltage channels must have a programmable over-current trip.
2. **HV interlock:** The high voltage system must have an interlock that prevents delivery of high voltage in the event of a need to shut off the system quickly.
3. **Gas interlock:** The gas system must have an interlock that prevents delivery of gas, or shunts the main delivery to either a known pure gas source or nitrogen, in the event of a need to shut off the main gas system quickly.
4. **LV interlock:** The low voltage system must have an interlock that prevents delivery of low voltage voltage in the event of a need to shut off the system quickly.

## 7.4 Technical Description

As shown in Fig. 7.1, two toroids, 1 m long with 1.5 T fields, provide the bending power. These toroids are described in detail in Section 3.3.2. Additional information can also be found in Chapter 3. The muon detectors will be set up in three stations, one between the toroids and two behind the toroids. The momentum can be measured using the two, well shielded, downstream stations and the nominal beam constraint. The station between the two toroids ( $\mu 1$ ) provides a powerful confirming hit to eliminate fake tracks. The geometry was chosen after careful consideration of many factors. Magnetizing both of the 1 m iron shields significantly improves momentum resolution which helps reduce background. The amount of iron shielding is selected to be the maximum allowed while still maintaining good angular coverage and fitting inside the C0 detector hall. Extra shielding was added near the third station after early GEANT simulations found high occupancies in that station. This extra shielding consists of 10 cm of iron shielding on either side of the third station plus a 5 cm thick collar around the beam pipe centered on the third station at a radius of 30–35 cm (just inside the muon detector).

The angular acceptance of the muon detector should ideally correspond to the acceptance of the spectrometer, which is 300 mr. However, the physical constraints of the experimental hall do not permit this. The detector radius is chosen to be as large as possible, 240 cm

(nearly touching the floor of the enclosure), which corresponds to a polar angle acceptance at the last muon detector station of 200 mr. Fortunately, wider angle muons, which are outside of the acceptance of the muon detector, tend also to have lower energy and can be identified by the Ring Imaging Cherenkov detector (see Section 5.7.2.1).

There are additional constraints on the inner radius of the detector. The BTeV analysis magnet is part of the Tevatron lattice and deflects the circulating beams. This deflection is compensated by dipole magnets at each end of the C0 enclosure. Moreover, the quadrupoles that focus the beam at the IR must be as close to the IR as possible. To achieve this, it has become necessary to save longitudinal space by inserting the compensating dipoles in the muon toroid as shown in Fig. 7.1. This defines the inner radius of the muon detector to be 38 cm, or about 40 mr. The presence of the magnet coils also creates potential for particle leakage which must be carefully shielded.

### 7.4.1 Muon detectors

The basic building block in the construction of a detector station is a **plank** of thin walled (0.01") 3/8" diameter stainless steel proportional tubes as shown in Fig. 7.2. Stainless steel was chosen because of its sturdy mechanical properties, its immunity to magnetic fields, and the fact that the oxide layer on stainless steel is conductive, which significantly reduces Malter effect.

Thirty-two tubes, arranged in a double layer with an offset of half a tube are glued at each end to a brass gas manifold and supported in the middle by brass rib pieces. A brass sheet is soldered or spot welded to the outside of the brass manifold to maintain electrical continuity. This sheet is soldered to conductive copper tape wrapped around the end of each tube and to the circuit boards at each end of a plank. This design provides a sturdy, self-supporting building block which also acts as a Faraday cage to reduce external RF noise. Proportional tubes were selected because they are robust and have the necessary rate capability.

The 5.3 mm effective wire spacing of this design has an effective spatial resolution of  $5.3 \text{ mm} / \sqrt{12} = 1.5 \text{ mm}$  with no dead regions between tubes. This meets our requirements for momentum resolution, drift time, and occupancy.

To minimize occupancy at small radii and improve pattern recognition, each detector station consists of eight overlapping pie shaped "octants," shown in Fig. 7.3. There are four views ( $r$ ,  $u$ ,  $v$ , and  $r$ ) in each octant as shown in Fig. 7.3. The  $r$  (radial) view is repeated primarily to provide redundancy for the most important view in terms of momentum measurement and pattern recognition in the trigger (we require hits in 3 of 4 views to define a good muon in the trigger). It is possible though, to use the redundant  $r$  view as an aid for reconstructing track segments within a station. This allows us to make a more robust muon identification for two reasons: 1) very wide angle (characteristic of hadronic punch through) tracks which cause hits over several tubes in a plank can be mitigated with an additional view, and 2), the identification of wider angle, lower momentum, muons which fail to penetrate the entire system, can be performed with less misidentification. The  $u$  and  $v$  views are rotated  $\pm 22.5^\circ$  to measure  $\phi$  and resolve hit ambiguities, reducing the misidentification rate. The

Radial coverage	38–240 cm
Full (3-station) polar angular coverage	40–200 mrad
Partial ( $\geq 1$ -station) polar angular coverage	30–260 mrad
Toroid Z-locations (center)	870, 1010 cm
Station Z-locations (center)	942, 1082, 1197 cm
Total Length	4 m (includes toroids)
Toroid Length (each)	1 m
Toroidal Fields	1.5 T
Tube cell inner diameter	9.0 mm
Effective pitch:	5.3 mm
Spatial resolution	1.5 mm
Total channels	36,864
Momentum resolution	$\sigma_p/p = 19\% \oplus 0.6\% \times p$

Table 7.2: Parameters of the BTeV muon system.

basic installation unit of the system is an **octant** mounted on an octant plate. The octant is made of 12 planks and covers  $1/8$  of the azimuthal angle. Octants are mounted on octant plates which cover  $1/4$  of the azimuthal angle; thus two adjacent layers of octant plates (arranged in a wheel) provide full coverage for a single view.

A summary of the baseline BTeV muon system is given in Table 7.2. The total channel count comes from  $3 \text{ stations} \times 4 \text{ views/station} \times 8 \text{ octants/view} \times 12 \text{ planks/octants} \times 32 \text{ tubes/plank} = 36,864 \text{ channels}$ .

### 7.4.2 Front-end electronics

The front-end electronics will be similar to those used for the CDF central outer tracker (COT); circuit boards to deliver high voltage and a circuit board with electronics to amplify and digitize the tube signal. Both boards will be located at the end of each 32-channel plank.

We plan to use the ASDQ integrated circuit developed at the University of Pennsylvania to amplify and digitize the signals coming from the proportional tubes. This chip is used in the Run-II CDF COT for a similar purpose. The ASDQ, amplifies the first 8–10 ns of the the signal and outputs an LVDS signal. This chip, when mounted on a circuit board, has a low effective threshold of about  $\sim 2 \text{ fC}$  (confirmed by tests at Vanderbilt). The chip also features a double pulse resolution of  $\sim 20 \text{ ns}$ . The ASDQ digital signals will be sparsified, serialized, and read out on-board using the standard BTeV readout protocol. A fast copper link will transfer the data from the front-ends to a data control board (DCB). There will also be a serial link for slow control signals and a beam crossing clock sharing the same RJ-45 cable with the fast copper data link. A schematic diagram of the system is shown in Fig. 7.4

The design of the electronics emphasizes reduced noise. Less noise allows us to operate the tubes at a lower gain and gives us more headroom to increase gain if needed later. Lower gain means the tubes age more slowly. Having a broader gain control gives us more

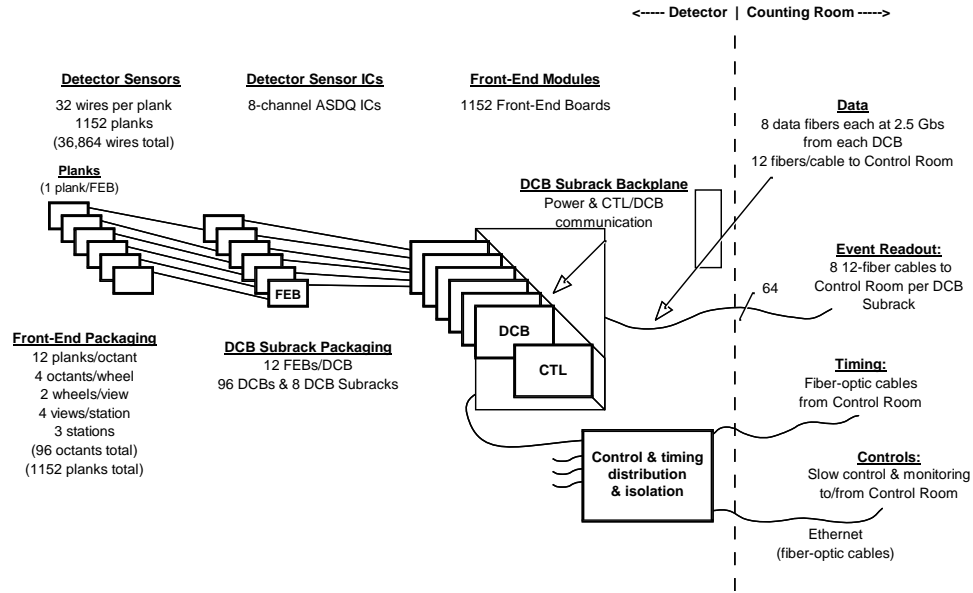


Figure 7.4: Block diagram of BTeV Muon Detector front-end electronics.

flexibility if we need to raise voltages. Since the ASDQ has a threshold control for 8 channels, we also have some flexibility within a plank for setting different gains and thresholds. This is especially true if our gas choice offers a wide plateau region for operating the plank at high efficiency (see Section 7.6.3).

Since the ASDQ chip will be common to both the muon and the straw systems, this production will be done in parallel with the straw detector. In the event that the process currently used to fabricate the ASDQ disappears, the design will be migrated to a new process. Funds for the migration, if needed, are included in the straw detector budget.

### 7.4.3 Mounting, support, and infrastructure

#### 7.4.3.1 Mounting and support

The muon detector planks will be assembled octant modules prior to installation in the collision hall. Each module will consist of planks sandwiched between two 1/8" aluminum





Figure 7.5: Two octant modules are in position to be joined together. The lower two wheels system are arranged to form a locomotive “bogie” and bear all of the weight during the installation process. The system rotates on a set of wheels placed at the circumference. After the first two modules are joined, the two-module system is rolled into a position to allow for the installation of the third module.

plates, forming a “sealed” unit which contains cabling, etc. Four octant plates will be joined to form a “wheel” as they are installed about the correction dipole. Fig. 7.5 shows a stage in the installation process where the first plate is joined to a second plate. The resultant sections will then rotate on wheels placed around the circumference to make room for a third plate.

Fig. 7.6 shows some of the construction details for the radial octant plate, while Fig. 7.7 illustrates the method for attaching two plates during installation. As shown in Fig. 7.6, in order to leave room for electronics, cabling and gas piping, each wheel will include half of a given view. Hence each 4 view muon detector station will consist of 8 mounting wheels.

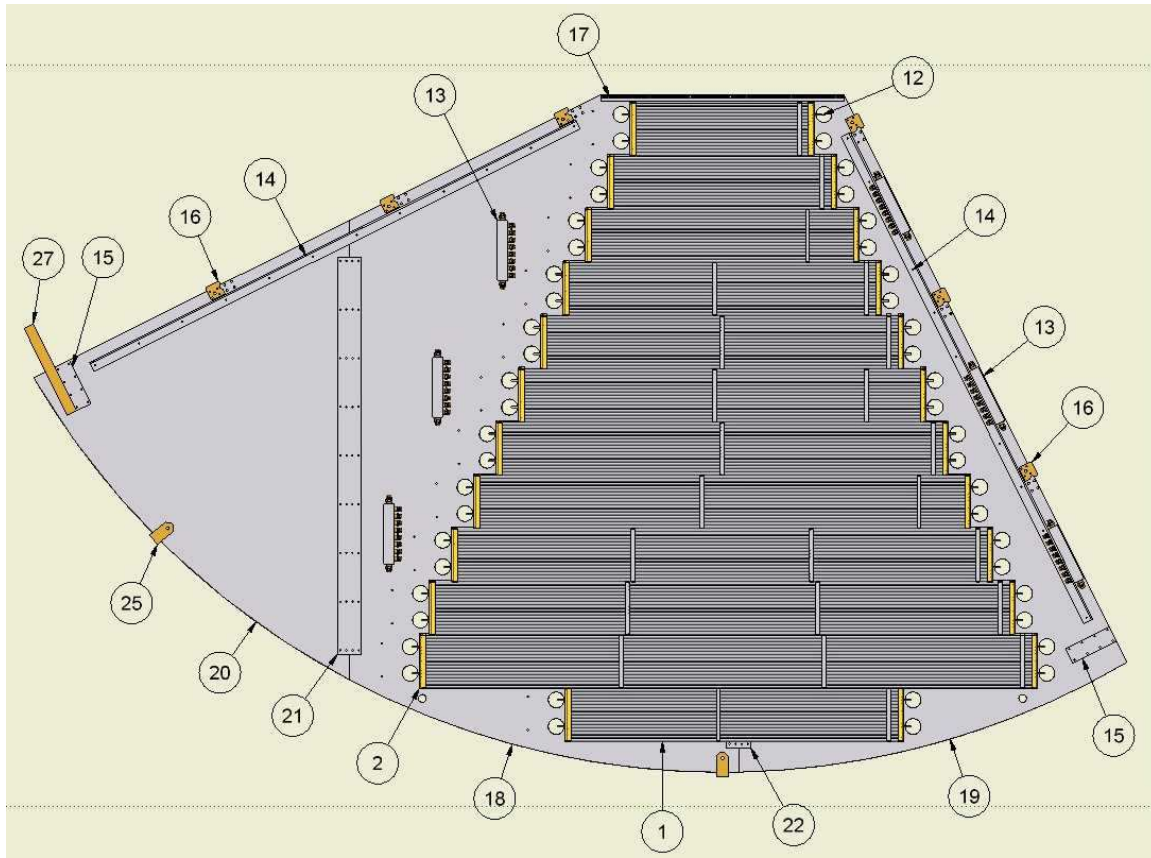


Figure 7.6: Assembly details of a radial octant plate. Each 1/4" thick radial plate is constructed out of three sections that are joined together using joint-bars (part 21 and 22). The blank area to the left of the tubes will be used for gas and electronics access. Gas will be distributed from three manifold assemblies (part 13). Stiffening-angles (part 14) are included to inhibit the bending of the octant plate during installation. The radial edges of this plate and adjacent plate are connected by knitting- brackets (part 15) and tie-bars (part 27).

#### 7.4.3.2 Gas system

We plan to use an Argon- $\text{CO}_2$  mixture, probably in the ratio 85:15. Gas studies at Vanderbilt have determined that this mixture provides a wide plateau region which makes it forgiving of variations in pressure, temperature, etc. This gas is also fast enough to ensure that ionization from adjacent beam crossings (a minimum 132 ns apart) will not be picked up with high efficiency. Finally, Ar- $\text{CO}_2$  is inorganic and does not suffer from hydrocarbon build up which is seen in high rate detectors which use organic gases, e.g. Argon-Ethane. Evidence for wire chamber aging in high-rate environments even with Ar- $\text{CO}_2$  has been found which is postulated to come from contaminants. We plan to minimize the contaminant problem in several ways. First, the entire gas system will be made of metal (copper, brass, and/or

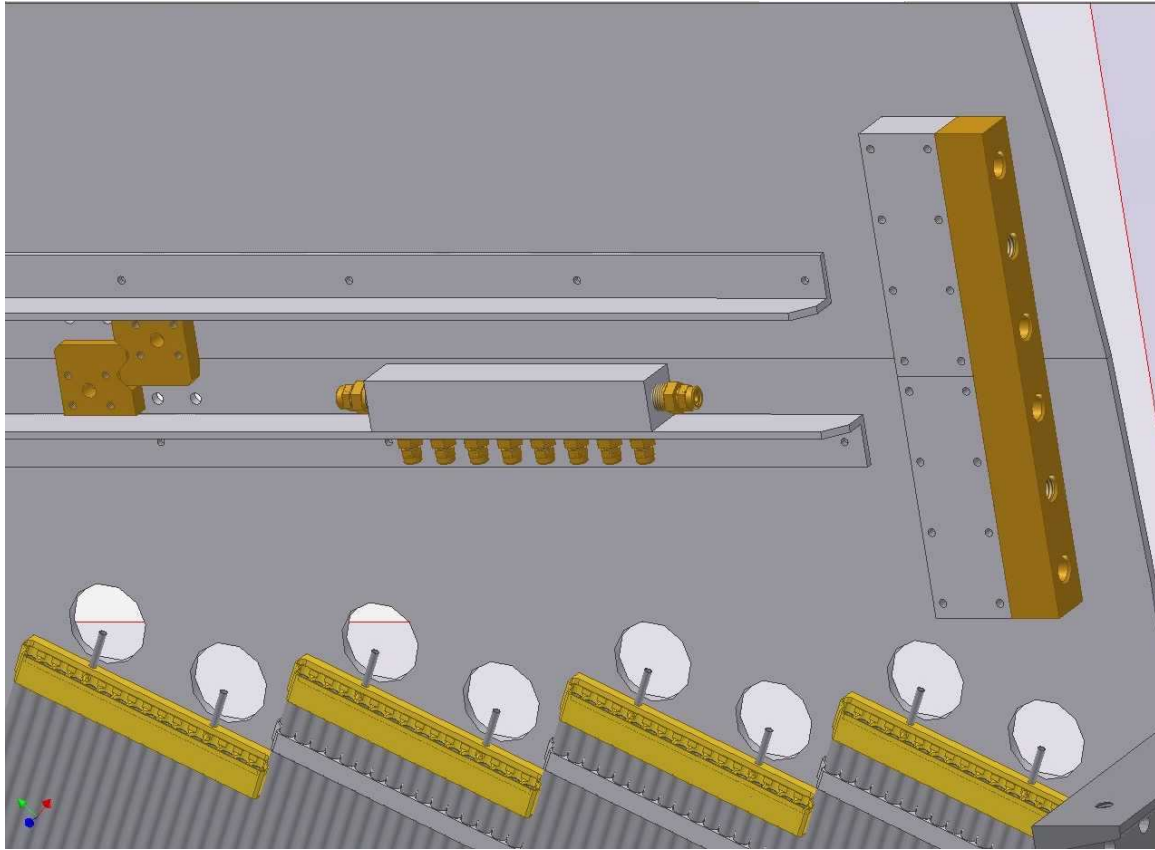


Figure 7.7: We show details of how the plates are joined together as the mounting wheel is constructed. The “knitting-brackets” impede relative radial motion between the two plates and are overlapped to impede motion transverse to the plate plane. The tie-bar prevents one plate from folding about two radial edges that join. We also show more details of the manifold assembly and stiffening-angles. The tie-bar consists of 1.25” by 1.25” square brass bar. The radial stiffening-angle also extends 1.25” from the surface of the plate. Once a wheel is assembled, it will be supported from the lift blocks (part 25) as illustrated by Fig. 7.25. We have holes in the plate near each gas connection to the plank manifold to allow us to accommodate the width of the gas fitting.

stainless steel) which is much more inert than plastic products. Second, we plan to test the delivered Argon and  $\text{CO}_2$  gas. Third, we will monitor the gas gain continuously using a gas gain monitor with an Fe-55 source as shown in Fig. 7.8. Finally, we will use a gas mass spectrograph to check the mixing and to check for impurities in the gas.

The gas system starts with pure Argon and  $\text{CO}_2$  which are mixed in a mixing system. The gas flow is split several times in several different manifolds until reaching the planks. Gas flow will be completely parallel, that is, no gas will go through more than one plank. The gas system will be designed to allow up to 5 gas volume exchanges per day in the plank

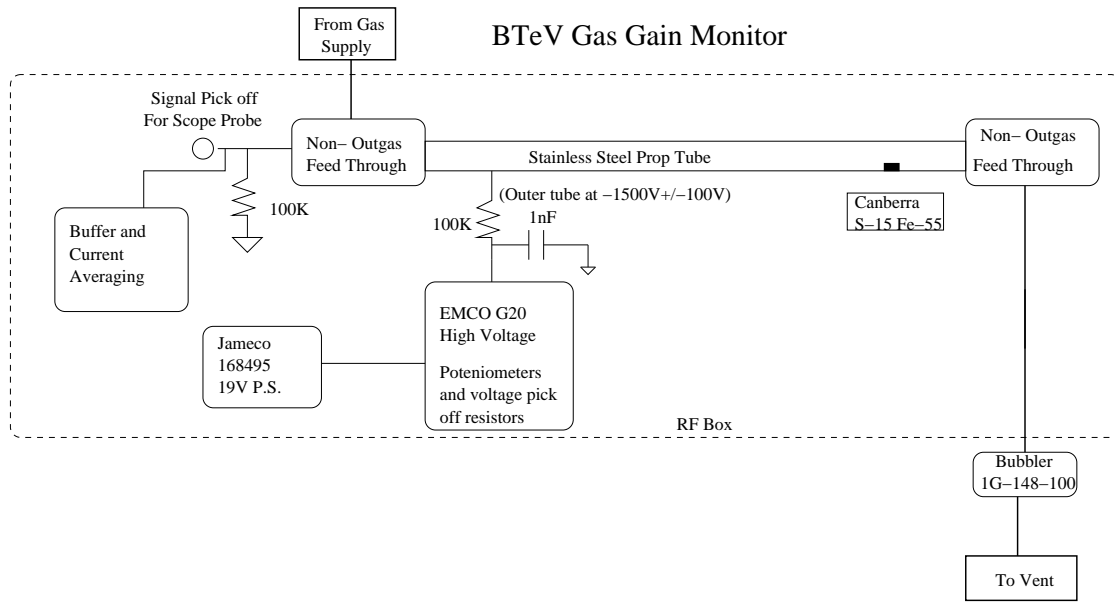


Figure 7.8: Design of gas gain monitor for the muon detector in the BTeV experiment.

closest to the beam (about 3.5 liters/min). We show the design for the gas mixing system in Fig. 7.9 and the design for the overall gas system in Fig. 7.10.

We will also utilize gas gain monitors to monitor the gas gain over time. These will be placed at the input and output ends of the gas system and will be composed of single tubes and an Fe-55 source.

#### 7.4.3.3 High and low voltage

A controllable high voltage will be delivered to each plank, and the current will be monitored on all 1,152 channels. The high voltage system will be capable of delivering sufficient current so that the highest rate tubes near the beam will not lose performance. We are currently looking at a high voltage system from CAEN which is a candidate for use by several detectors. We expect to have a maximum voltage need of 1750 V and a maximum current needed of  $2 \mu\text{A}$ . The front-end boards need power for both the ASDQ's and the FPGA/digital portion of the front end board. Our cost estimate is based on the the amount of power measured when the combined analog and digital board was being driven at its maximum expected signal rate. The final design will depend on the system chosen by BTeV to supply low voltage for several detectors.

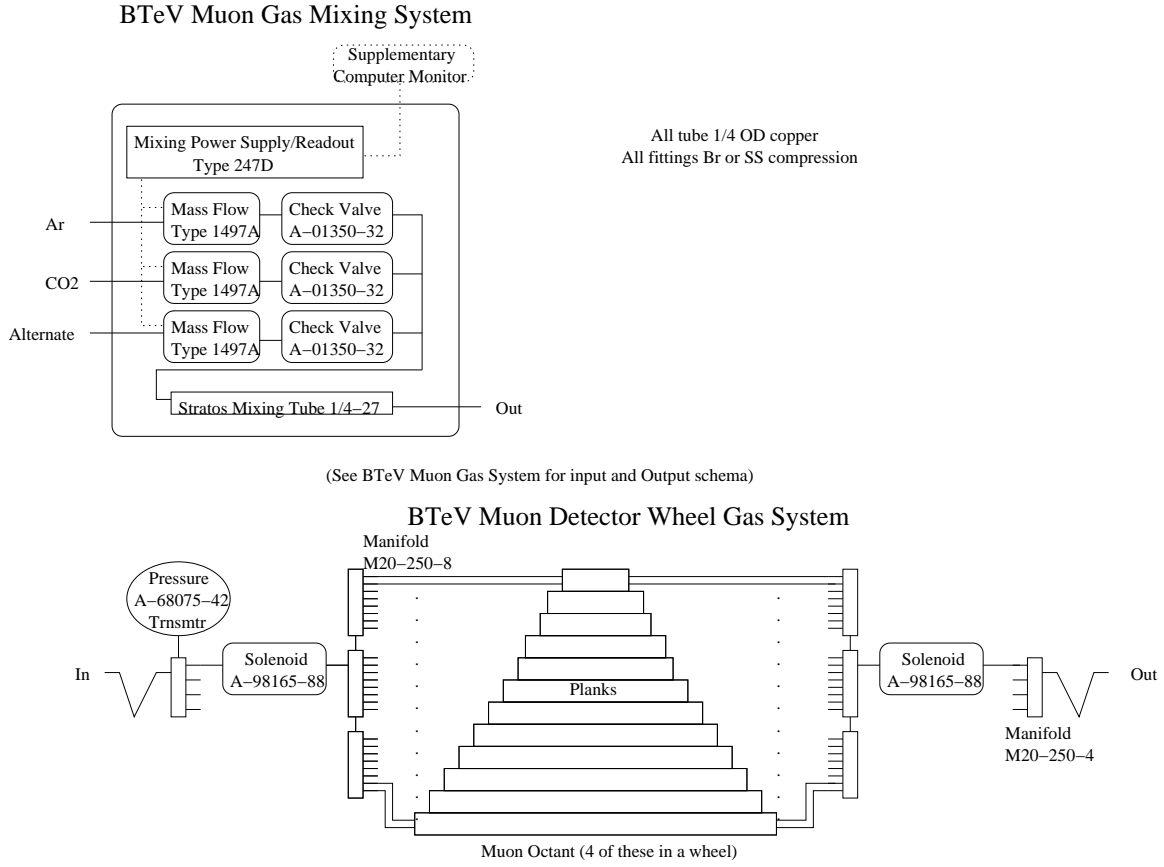


Figure 7.9: The design of the gas mixing system (left), and the delivery schema to the collection of detector planks on an octant.

## 7.5 Design trade-offs

### 7.5.1 Magnetized vs. non-magnetized toroids

The BTeV muon system has the two goals of providing clean off-line identification of muon tracks as well as providing an complementary trigger to the main BTeV detached vertex trigger. We believe that the only way to achieve adequate rejection for this complementary trigger is to select  $J/\psi \rightarrow \mu^+\mu^-$  candidates by requiring two opposite sign, moderate momentum penetrating particles. We further believe that the ability to make a redundant momentum measurement of a muon candidate in the muon system will significantly reduce misidentification of hadrons due to their in-flight decay prior to entering the muon filter.

In the early phases of the muon system design, we investigated the possibility of exploiting the magnetic dispersion of the central dipole to make a momentum measurement by extrapolating the hits in the muon system to the nominal beam collision center. We were unable to achieve a fractional momentum resolution much better than a constant  $\sigma_p/p = 200\%$

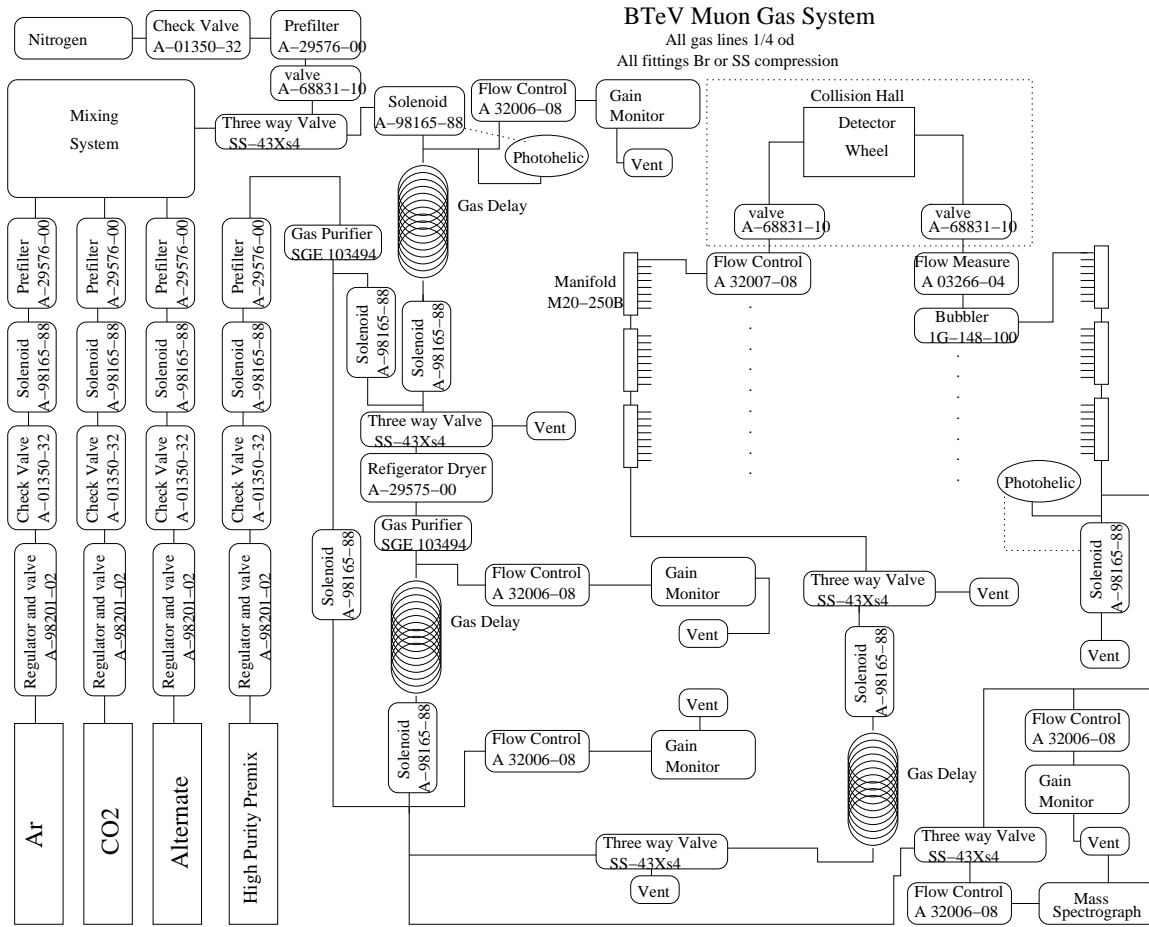


Figure 7.10: The overall design of the gas system. There are redundant layers of monitoring and delivery.

with any of the possible detector scenarios considered. About 1/3 of the momentum smearing came from the event-by-event variation of the interaction point, and 2/3 came from substantial multiple scattering in the electromagnetic calorimetry and the steel hadronic absorbers themselves. The fundamental problem was the effective dipole bend center was too far upstream of the multiple scattering sources to make a useful momentum measurement.

These considerations lead us to consider the momentum resolution achievable using a magnetized toroid. Again the momentum measurement would be derived by extrapolating the measured track trajectory in the muon system through the magnetic toroid and central dipole to a nominal beam center. We found a single 1 meter thick saturated toroid provided insufficient bending power to produce a suitable trigger. In particular, the fractional momentum resolution of such a single magnetized toroid system would vary from 25 to 40% depending on the azimuth of the muon track. Essentially, the bending power of the central dipole would “fight” the bending power of toroid because of their different field geometries.

We finally settled on the present design that has two one meter thick magnetized toroids and three measurement stations. This layout produces a fairly uniform fractional momentum resolution of better than 20% over the full momentum range relevant to  $J/\psi \rightarrow \mu^+\mu^-$  in BTeV given the intrinsic spacial resolution of our proportional tubes.

See BTeV-doc-970 [1] for an early, but more thorough, exploration of toroid and shielding possibilities.

## 7.6 Past Research and Development Work

### 7.6.1 Summer 1999 beam test

In the spring of 1999, we constructed 10 planks of varying lengths (see below). These were transported to Fermilab in June for a test beam run. A stand on which the planks could be mounted was designed and built to allow the planks to be rotated and offset. The front-end electronics were sample ASD8B cards from the University of Pennsylvania which provided amplification, shaping, and discriminating of the signal from the proportional tubes. Testing these boards revealed a high susceptibility to ambient RF noise. To reduce this noise, boxes to enclose the electronics were constructed out of circuit board and wrapped in copper tape. Interface cards to provide high voltage to the tubes and low voltage to the electronics were designed and assembled. An interface card to convert the LVDS signal, output by the ASD8B card, to ECL was also designed and built. The muon data acquisition system was written using a CAMAC interface. The TDC data from the planks and the latches from the trigger scintillators were recorded. Reconstruction software and an online event display were written in order to interpret the data. The detector setup can be seen in Fig. 7.11. As a result of our experience in this test beam, several changes were made to the original plank mechanical and electrical design.

### 7.6.2 Plank design/construction

The first round of plank prototypes (10 planks of 32 tubes) were constructed in 1999. These planks were constructed (see BTeV-doc-991 [2]) in the following way:

1. Tubes were cut to length in the machine shop from purchased stock.
2. Each tube was cleaned in an Alconox solution, rinsed, and dried with compressed air.
3. As shown in Fig. 7.12, a gold-plated tungsten wire was strung through a Delrin insert on one end of the tube, through the tube, and through another Delrin insert. The Delrin insert consists of a tubular piece of Delrin with a lip at one end to hold it at the edge of a tube. A hole drilled through the center of the Delrin contains a small brass tube (crimp pin) extending out. The brass crimp pin for this prototype contained a double funnel inside to center the wire (a function now included in the Delrin insert





Figure 7.11: The BTeV muon system setup for the 1999 test beam run. Five planks are visible in this photograph. Noise problems required shielding with aluminum foil and copper tape.

which allows us to use a stock brass tube for a crimp pin). Each Delrin insert also had three small holes for gas flow.

4. After stringing, one end of the tube was crimped. The Delrin insert was inserted into the tube. Then a resistor lead was inserted in the brass crimp pin (along with the wire) and a commercial crimp tool was used to crimp everything together.
5. After crimping one end, the other end was attached to a calibrated weight to achieve the proper tension and the other end was crimped.
6. Continuity and high voltage tests on each tube ensured the crimp held and the wire did not break.



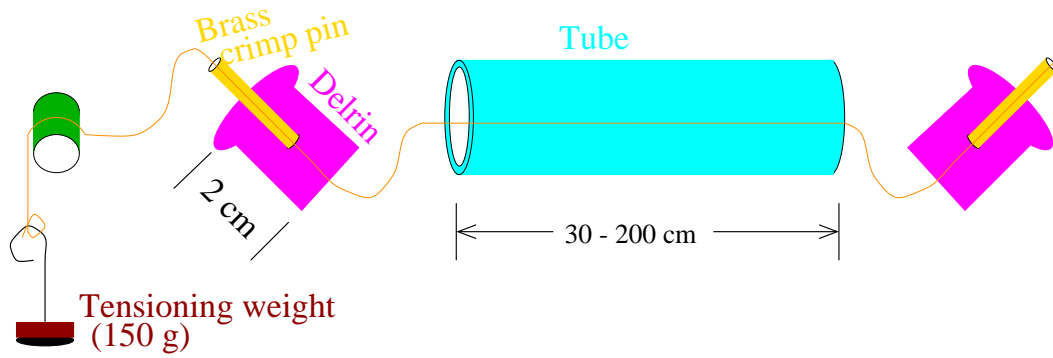


Figure 7.12: Diagram of the stringing process.

7. A plank was constructed from 32 strung tubes. The endcaps were machined from Noryl (plastic) and contained one hole for gas and 32 small holes for the end of the crimp pins (which connect to the electronics). The endcaps were glued to the end of planks.

The construction of 10 planks in the spring of 1999 provided us with valuable information. We found that  $30\text{ }\mu\text{m}$  and  $50\text{ }\mu\text{m}$  wire both work well while the  $20\text{ }\mu\text{m}$  wire was harder to string and was not needed for the muon system. We found that one crimp often did not hold the wire in place while two crimps were almost always sufficient. The crimp was also not airtight requiring glue or solder on the end of the crimp pins to ensure a good seal.

In the summer 1999 beam test, plateau curves showed that the planks were  $>95\%$  efficient at 1.8 kV for a  $30\text{ }\mu\text{m}$  wire with Ar-CO<sub>2</sub> gas. This agreed with our expectations. However, cross talk between channels was very high which resulted in many tubes in a plank firing with only one incident particle. This prevented us from measuring individual tube efficiency or position resolution.

The susceptibility to external noise and extensive cross talk led to several design changes. The ASDQ (one of the successors to the ASD8B chip used in the beam test) was selected for the real muon system. Tests have shown this chip to be more resistant to external RF noise. We also redesigned the high voltage distribution card to reduce crosstalk. Finally, the plank design was changed to use a brass manifold, instead of plastic, which was soldered to the stainless steel tubes to provide a Faraday cage. These modifications solved the cross talk and external noise problems. The changes to the design also required changes in plank construction. Since the Delrin insert might melt or slip during the soldering process, the tubes were strung after soldering the brass manifold. A new homemade crimp tool was created to work in the restricted space available. Another change was the creation of an aluminum box to contain the electronics. This box bolts to the brass manifold, providing the last part of the Faraday cage.

Prototypes of the new design were then fabricated, and problems were encountered with the stringing process: crimps with the new tool were not as reliable and the entire process took significantly more time. Therefore, we made a final change to the design. We went back to stringing the tubes individually, then gluing them into the gas manifolds instead

of soldering. To provide electrical continuity, conductive copper tape is applied around the circumference of the tube before stringing. A brass sheet is then soldered to the tubes, the gas manifold and the circuit boards at the end of a plank after the main assembly and gluing are completed.

### 7.6.3 Plank and gas tests

A prototype plank of the latest type has been made and tested. This plank as well as three of the previous iteration (brass manifold soldered to the tubes) are seen in a cosmic ray test stand in Fig. 7.13. The latest design incorporates the new plank construction, a CDF central outer tracker front-end card with ASDQ chips, and a redesigned high-voltage distribution card. Results from the cosmic ray test stand indicate a tube efficiency greater than 99%. The noise level is very near the theoretical minimum (the 2 fC of the ASDQ chip).

A variety of Argon- $\text{CO}_2$  gas mixtures were tested in the cosmic ray test setup. The gas gain results for several mixtures of Ar- $\text{CO}_2$  are plotted versus voltage in Fig. 7.14. These gains were obtained using an Fe-55 source. Also shown in Fig. 7.14 are plateau curves for an Ar- $\text{CO}_2$  mixture of 85:15; the current choice for the muon system. Fig. 7.15 shows the spread in first arrival times of hits in a plank with an Ar- $\text{CO}_2$  mixture of 85:15. The spread is found to be about 100 ns, fast enough to run with a minimum possible Tevatron bunch crossing time of 132 ns, and even better suited to a longer Tevatron clock due to the after pulsing effects (about 15% of tracks produce an extra pulse beyond 100 ns, 2% beyond 200 ns, etc.) present in Ar- $\text{CO}_2$ .

### 7.6.4 Construction database

We have developed a database system to collect and track information during detector construction and commissioning. As each detector element is constructed or tested, the relevant information will be entered into the database for later retrieval and correlation studies. A single database will be used by all institutions working on the BTeV muon system. Each proportional tube, electronics board, and larger items will have a bar code attached for easy tracking. Also, all raw materials used in the construction of the detector will be tracked from source to final location.

### 7.6.5 Wire tension measurement

To ensure that each tube is strung with a wire of the correct tension, the tension of each wire is measured by placing the plank in a magnetic field, driving the wire with a sinusoidal current, and measuring the induced EMF to find the resonant frequency. From this value the tension is computed. We have developed a test stand which automatically measures the tensions in a plank full of tubes and stores the resulting information in the construction tracking database.

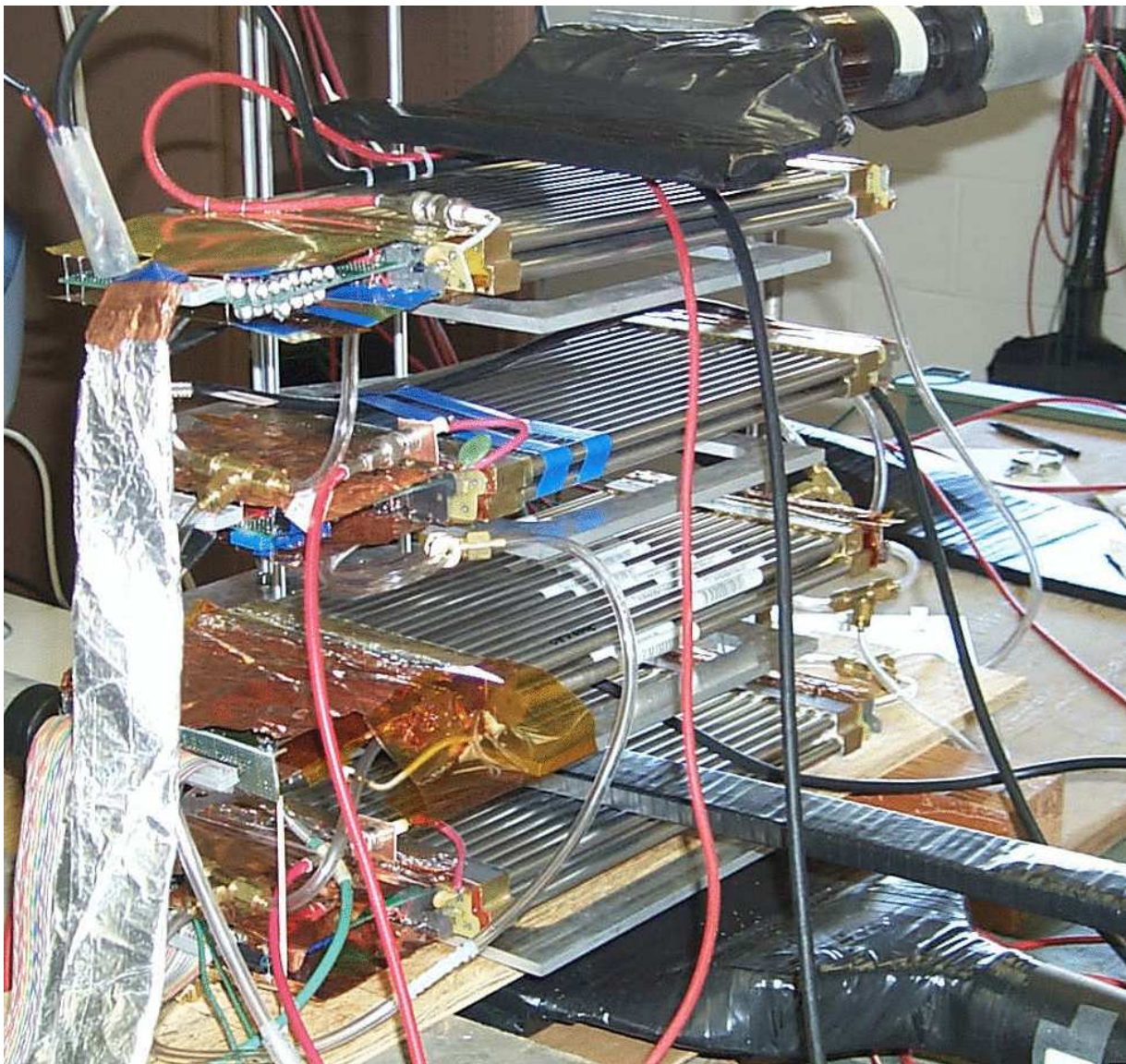


Figure 7.13: Photograph of the muon system cosmic ray test stand with four planks and several scintillators.

### 7.6.6 Detector construction and support

In the process of developing installation and support plans for the muon system we developed a 1/5 scale model of the muon system shown in Fig. 7.16. This model also includes the muon detector environment such as walls and toroids. In our initial plan, the muon planks would be mounted on quad plates which would then be hoisted into position using a series of overhead winch manipulations. Based on our experiences with this model, we concluded that installation as well as disassembly for repair would take a prohibitively long time since

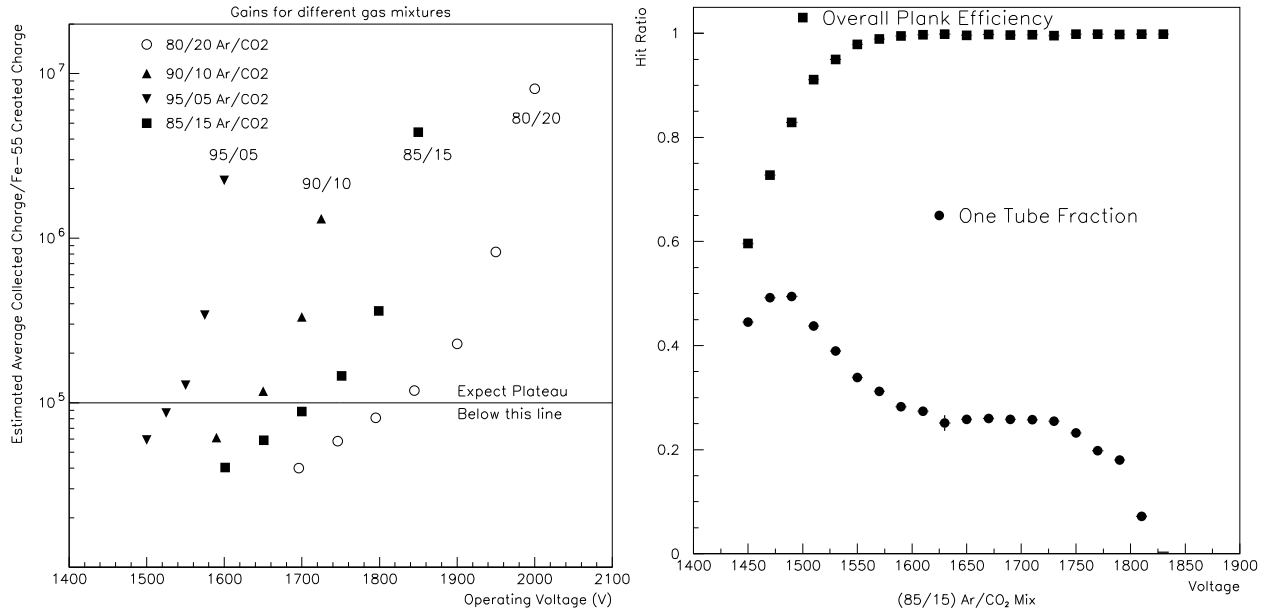


Figure 7.14: Left: measured gain of various mixtures of Ar/CO<sub>2</sub> versus voltage. Right: plateau curves for 85:15 mixture of Ar–CO<sub>2</sub>; the top curve shows plank efficiency versus voltage and the bottom curve shows the ratio of single hits to all hits. A broad plateau region is observed in the region of 1600 V to 1750 V.

many separate hoisting manipulations were required. For this reason, we developed the new plan described in Section 7.4.3.

The octant mounting scheme has been redesigned to provide greater stability and ease of assembly. Two thinner sheets of aluminum are used rather than one sheet for mounting and stiffening bars are included; both add strength and rigidity to the octant module. Further, the cable and gas connections have been simplified to allow fast connect/disconnect in the case of a dipole replacement. The new design allows us to construct just one “flavor” of electronics as well. This means the the orientation of readout and termination are constant with respect to a plank, and less circuit board types need to be produced. A view of the proposed new octant design is shown in Figure 7.17.

A full-sized mockup of a single wheel (there are four wheels per station) has been created and assembled by University of Illinois personell. The first installation test was done with a wheel where extra weight to simulate the planks was *not* present in the wheel. Assembling the entire wheel required less than four hours of labor. The completed structure is shown in Figure 7.18. This configuration weighs about 60% of the final (with planks) configuration, so the additional weight is not considered to be a problem. Another test with a fully weighted wheel will be performed soon.

A survey of the flatness of the wheel, as installed, was performed [3]. Improvements on the flatness are expected with improved stiffener bars and rigidity supplied by the installed planks.

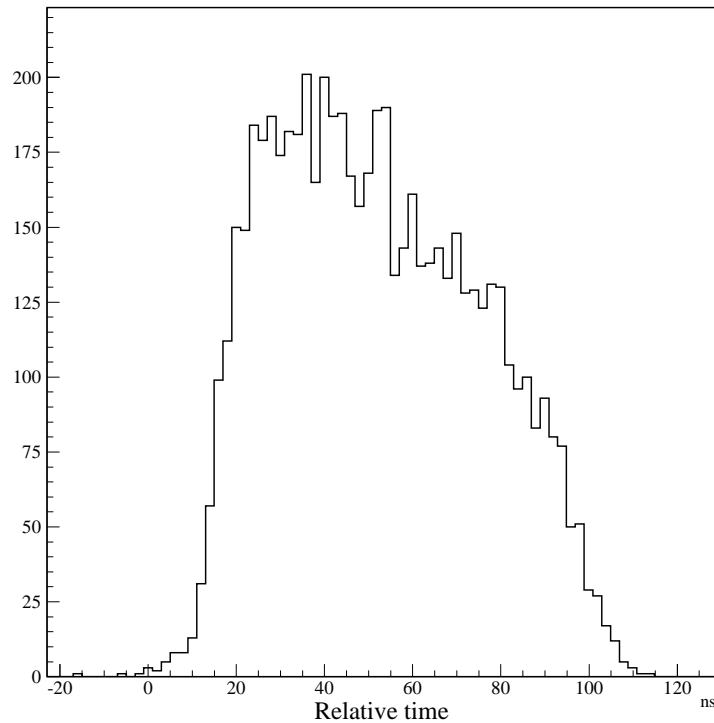


Figure 7.15: Arrival times of the *first* hits in a plank of proportional tubes (relative to an independent trigger) in a cosmic ray test stand. The spread is less than the anticipated 132 ns (fastest) bunch crossing time of the Tevatron, and robust for a gas with some after pulsing, like Ar-CO<sub>2</sub>, for a longer Tevatron clock.

### 7.6.7 Front-end electronics

Since we are using the muon system in the trigger, and we want to separate beam crossings, we chose our electronics to react to the leading edge of the signal from the proportional tube. We have chosen to use the ASDQ chip to accomplish the fast analog to digital conversion of the proportional tube signal. This chip or its variants are a popular choice for tracking, and our group has a long experience with using this chip family successfully. The straw detector is using the chip as well and BTeV is committed to transferring the chip to a new process if needed, though at present (Spring 2004) Maxim does not plan to obsolete the process for the ASDQ in the foreseeable future. There has been a conversion of the process used for the ASDQ, Cpi, from 4 in. to 6 in. wafers, but Maxim has waived the expense for conversion of the ASDQ.

Each plank is a self contained data acquisition and control unit. This means that the front end board on the plank has extensive digital functionality. It also means that there is a potential to induce significant noise into the analog portion of the board. In our determination of the gas mixture to use, we used a board that was originally designed for the CDF Central Outer Tracker (COT). This board contained no digital functionality other than discriminator output of the ASDQ. We were able to operate the COT card with our prototype



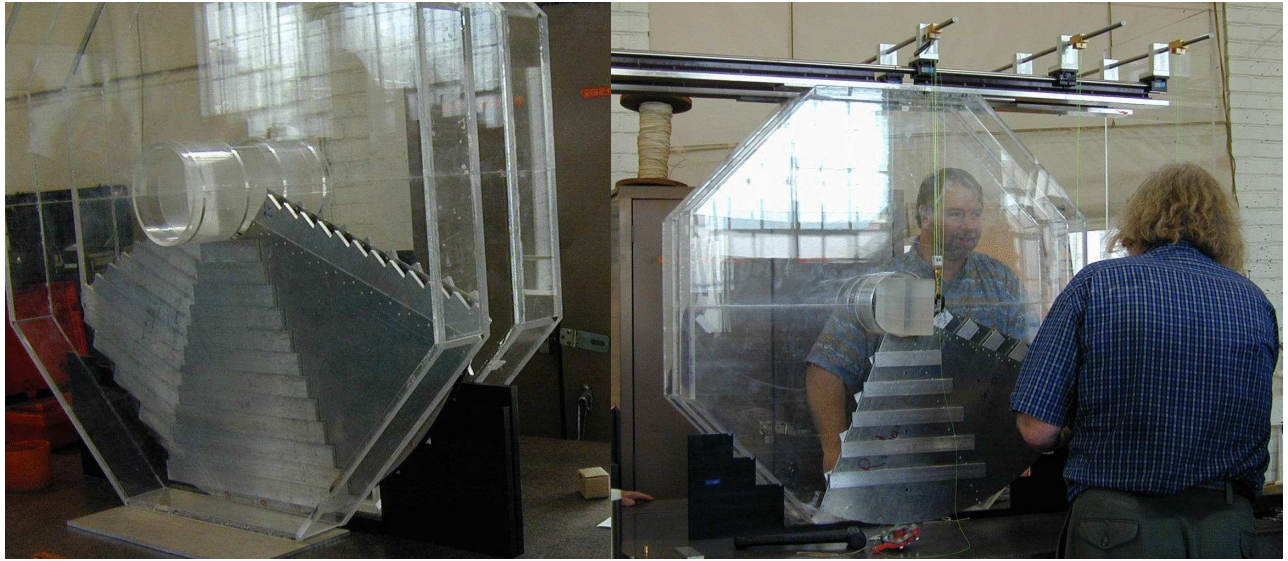


Figure 7.16: Photographs of the 1/5-scale model of the original mounting scheme. Left: two quads, back to back, between the Plexiglas toroids. Right: view showing the overhead support and installation system.

plank at an efficiency exceeding 99% with a signal threshold that was slightly better than the specification for the “average” ASDQ chip. These tests are detailed in the gas section. Melding the ASDQ COT card successfully with extensive digital circuitry at the location of the detector was our primary concern in our prototyping efforts.

In Fig. 7.20 we show the board diagram for the noise and functionality tests performed at Fermilab in the spring and summer of 2002. In the tests it was important to determine that the new card performed as well as the COT card while delivering on the promise of digital functionality. In tests without the muon detector attached, a threshold of 2 fC was attained with less than 1 Hz of noise. This is similar to the performance of our plank prototype with the COT card.

The tests performed were rather extreme. Digital traces were placed on the board and connected to unused I/O pins of the FPGA. These lines were exercised while we looked at the output of the ASDQ. When we attached a muon plank to the prototype front end board (see Fig. 7.21) we had to increase the threshold from 2 fC to 2.5 fC to maintain 1 Hz/channel noise at 100% (pulser) efficiency. Subsequently, we discovered that the threshold could be lowered by removing a kludge that was made to the threshold circuitry. We also connected a scintillation counter trigger in coincidence and demonstrated that the board could be triggered (see Fig. 7.22). A side benefit of this test was the determination that the leading edge of the signal coming from the ASDQ can be localized to within 5 ns of the trigger signal. This makes it possible to add tube correlations in addition to selecting an acceptance window to the FPGA programming.

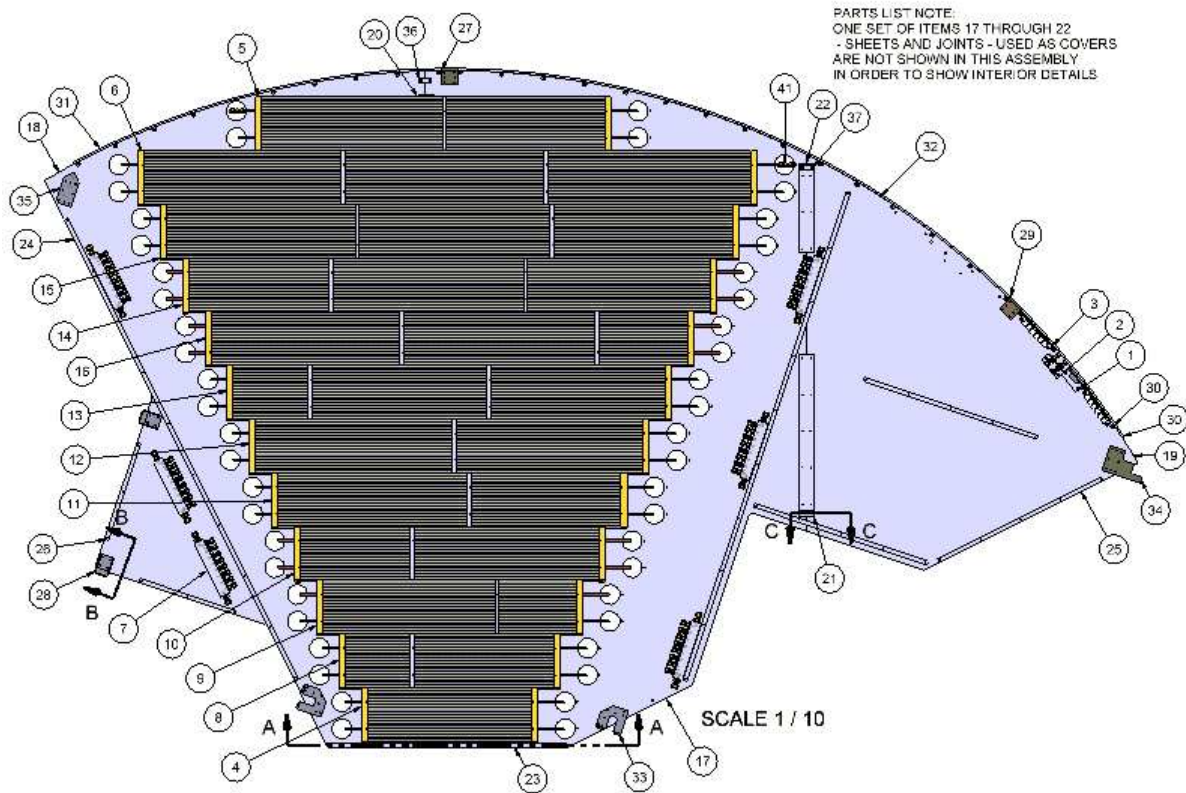


Figure 7.17: A cutaway view of the new octant design. Note the additional locking and guiding features located at 33, for instance, in the figure. Also note the clustering of services such as gas, HV, LV etc. at the upper right hand side.

The conclusion from the testing of the prototype with digital readout is that this approach works well.

## 7.7 Planned Research and Development Work

We will continue gas gain and plank efficiency measurements in our cosmic ray test stand. Refinements of the plank construction will also be investigated in hopes of finding a method which reduces the construction time while maintaining the needed features.

### 7.7.1 MTEST beam test

We plan to construct 3–5 more planks to test during the beam test in the summer-winter of 2004. This test run will allow us to perform many of the studies which we were unable to make in 1999 due to noise problems. These studies include measuring speeds and responses



Figure 7.18: A full sized mockup of a muon detector mounting wheel. Built and installed at the University of Illinois.



## Muon Detector Data Flow and Control

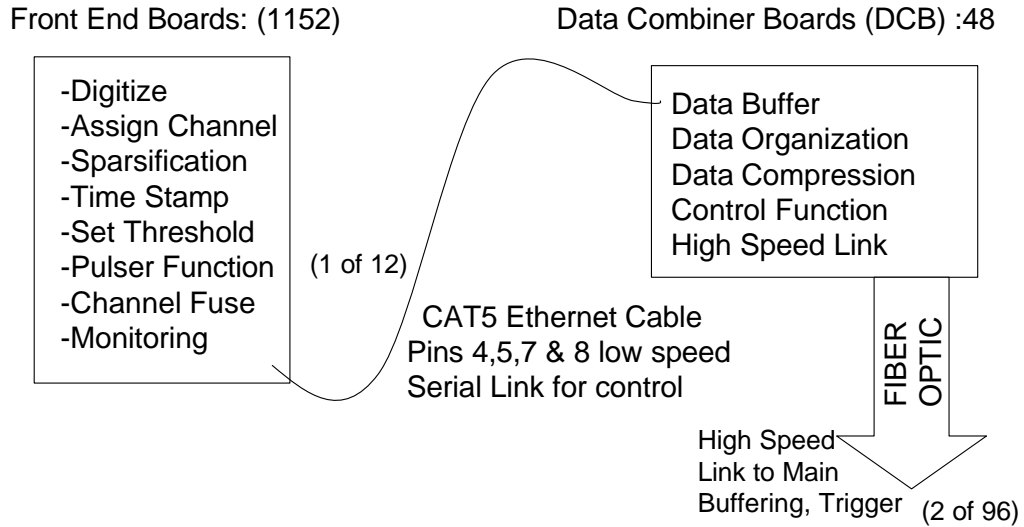


Figure 7.19: Diagram outlining the functions of the Front-End board and the data combiner board. The connection between the boards is done via commercially available CAT-5 cable. We intend to use the “dark wire” in this standard as a low speed serial link. Sparsified data with a time stamp will be sent via the high speed link, while control and monitoring functions will be done via the slow link.

of various gasses, measuring high rate effects, and measuring individual tube efficiency and resolution. We expect the results of these tests to validate our design changes. We have already installed a high precision silicon tracker to help facilitate our (and other groups) beam tests.

### 7.7.2 High dose test

We plan to perform a high dose test of our detector to check for problems with the materials we are using in the construction of our detector. We need to perform this test as soon as possible, in case design changes are needed.

We would like to put a plank somewhere in the Tevatron or Booster where it will receive a high dose of particles from beam backgrounds. Many materials have problems with outgassing after such exposures, and the only way to be absolutely sure that our materials will not have problems is to check them. We would also run gas through the plank (with electronics) at a rate commensurate with our plans for actual running conditions, and monitor the plank. We may also connect high voltage and if so we will need to monitor current draws, etc.

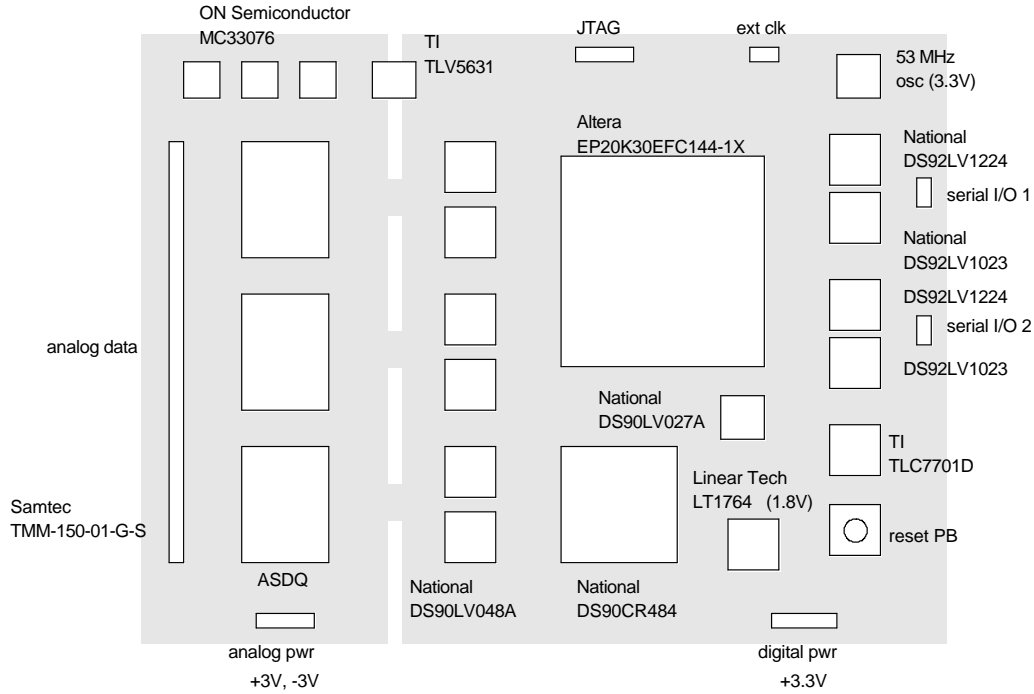


Figure 7.20: Circuit Board diagram for the prototype electronics of the muon detector. The board is actually overloaded to perform noise and transmitter studies. Notice that this board is designed to operate with LVTTTL logic, while the actual production board will make extensive use of LVDS logic. LVDS is the natural output of the ASDQ chip and is an inherently low noise logic standard.

### 7.7.3 Prototype electronics and plank interface

Later in the design process, we will make a pre-production prototype containing the actual electronic components we will use in the production. We feel it is premature at this stage to finalize the design of the digital portion of the board. Commercial chips come and go with remarkable volatility, and we want to be able to take advantage of the best choices when we are prepared to build the production electronics.

We will also study providing channel by channel fusing for the high voltage delivery. This project is currently in the conceptual stage. A possible conceptual design is shown in Fig. 7.23.

We have been investigating different materials for the electrical connection between the tubes and the readout electronics. In preliminary studies, we have had a great success using conductive epoxy Tra Duct 2902 as a replacement for soldering the tubes to the gas manifolds. This epoxy is known to be chamber friendly and is being used by the straws and many LHC experiments. We are also trying to replace the conducting sheet that connects

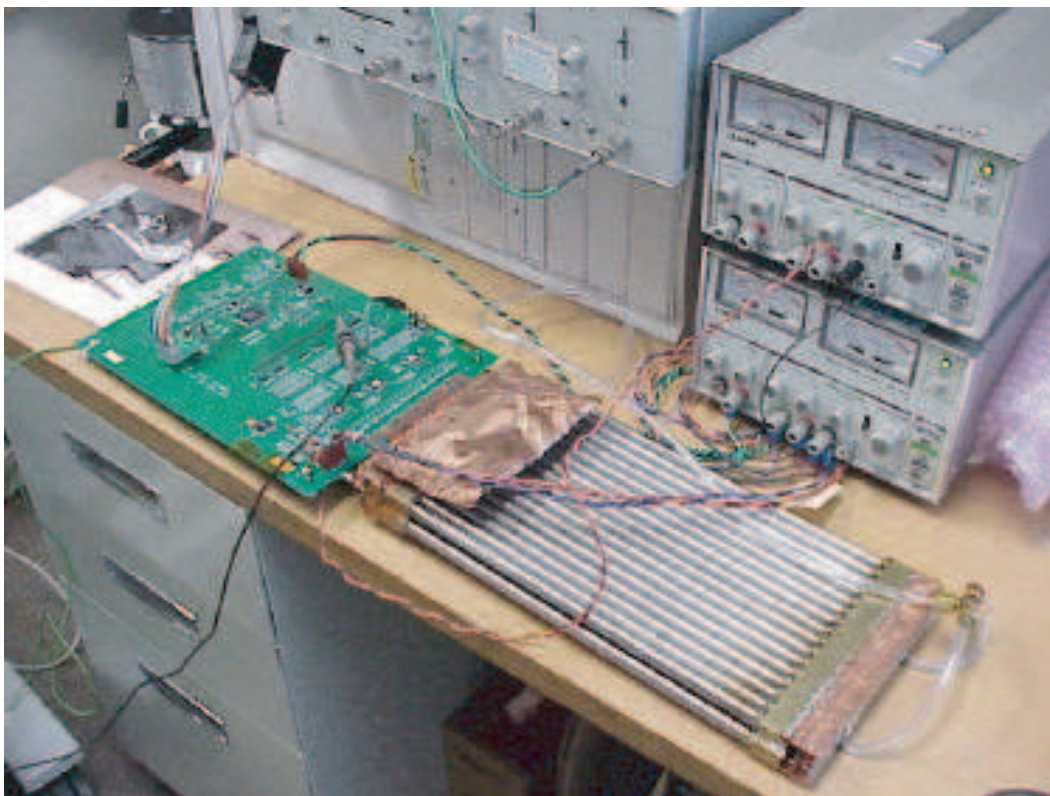


Figure 7.21: Front End prototype hooked up to a prototype plank. Notice especially the unsophisticated nature of the power delivery, the digital I/O, and the lack of an RF enclosure for the board. We find that the robust nature of the design is present in systems of several planks as well. We are hoping that this will offer us us some latitude in making final design choices that can both ease construction and lower cost without compromising performance.

the gas manifold and the readout electronics with a conductive rubber gasket. This gasket material has been employed successfully in the CDF experiment for many years and would facilitate a very easy connection. This is important as it allows us some more flexibility in how we schedule the delivery of components. I.e. a completed plank need not be wedded to its final electronics until just prior to being installed in an octant.

#### 7.7.4 Mechanical refinements and tests

We plan on testing several design changes which address difficulties in the current design. Illinois has redesigned the gas manifold to allow a plank to be restrung if needed. This will not be a simple procedure, but it will at least be possible. Also included in the redesign of the gas manifold are provisions for easier machining of the gas inlet, more brass for a

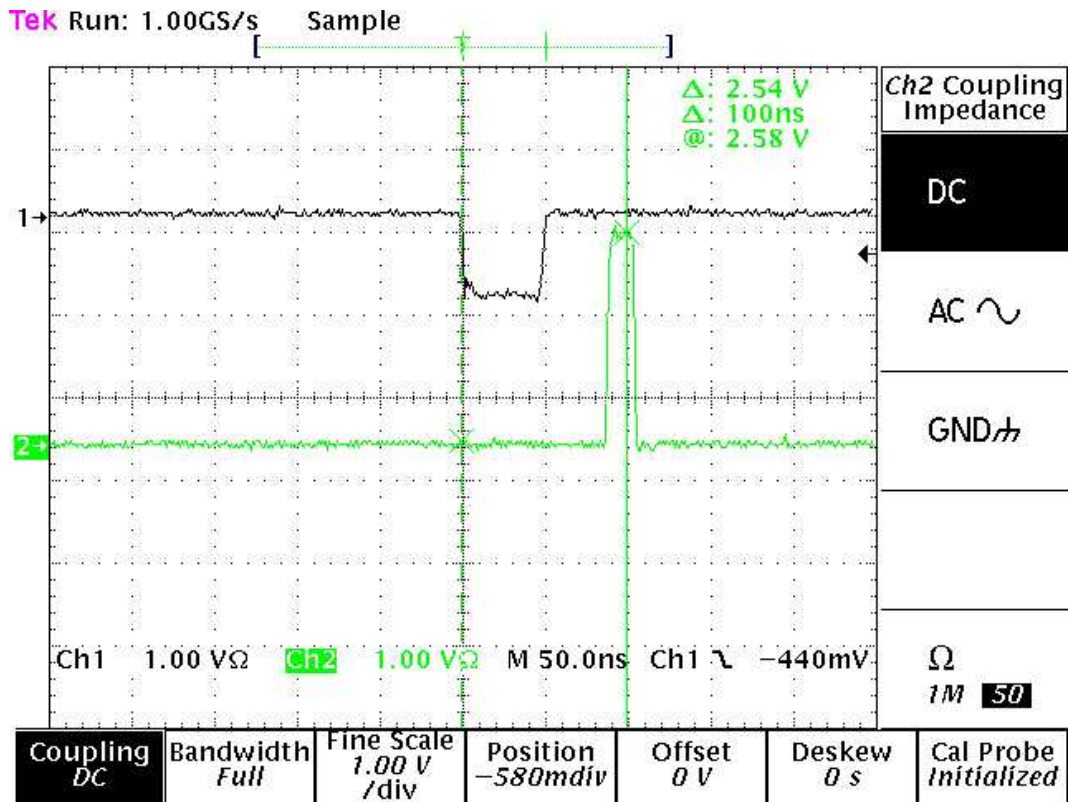


Figure 7.22: Output of the “or” of the connected plank channels (bottom trace 2) of the front end board prototype in response to a cosmic ray trigger(top trace 1).

connection to a conductive gasket, and extra brass to allow for epoxy potting and greater mechanical strength.

The central rib design has been simplified and moved to aluminum.

We are testing the calculations related to wire stability with a test jig. This will allow us to firm up our flatness requirement over the face of an octant. Figure 7.24 is a picture of the setup.

### 7.7.5 Octant test stand

One important aspect of our quality and assurance plan is a test stand capable of fully testing all aspects of an octant. This includes checks of the gas, high voltage, and low voltage systems, as well as a check of the readout of all detector channels and their electronics. We want to design, build, test, and iterate a prototype test stand. Based on this experience we will finalize the design of the octant test stand.

We will purchase readout electronics, high voltage and low voltage supplies, and gas system components. For the readout, we will design and build a relatively simple board that

## High Voltage Fuse Conceptual Design

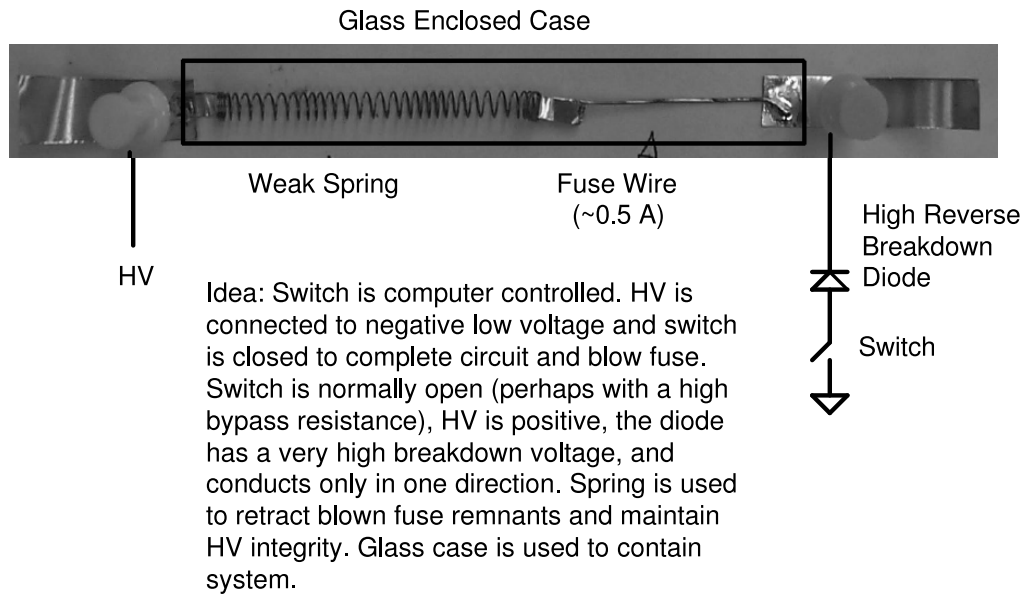


Figure 7.23: Conceptual design for High Voltage fuse. The spring overcomes the tendency for fuse remnants to cause high voltage sparks.



Figure 7.24: Test rig for looking at wire stability at high voltage for one of our long (6 ft.) planks.

consists of 8 fiber receivers and 8 data buffers. This card will be read out by a DSP card that plugs into the PCI bus on a PC. This card has been designed by colleagues at Vanderbilt who will build one for us and let us use their software.

We plan to assemble the prototype test stand prior to building the pre-production octants. We will test, debug and improve our design during the 4–5 month period in which these octants come together. Planks will be fabricated at each university site (Illinois, Puerto Rico–Mayaguez, and Vanderbilt), shipped to the pre-production assembly site at Illinois, and gradually assembled into the pre-production octants. Whether these octants will form mounting wheels (we will have enough for two) or a quadrant ( $1/4$  of the azimuthal angle in each station with some redundancy) of the full detector for combined tracking tests or some combination of the two is still to be determined.

### **7.7.6 Plank construction jig**

We will be designing an adjustable jig which will be used to maintain precise tube lengths and properly orient the gas manifolds with respect to the tubes and mounting plates during the assembly process. Such a jig is required to efficiently assemble the large number of tubes of many different lengths with adequate precision to allow us to mount the array in the confined space available.

### **7.7.7 Prototype gas system**

During the running of BTeV, we plan to carefully monitor our gas mixture. Given our high rate environment, aging of our system is a significant concern. We need to monitor our gas supply carefully to verify that it does not contain dangerous levels of contaminants (hydrocarbons, water, etc.). We will therefore continually monitor the gas gain using a small test chamber and Fe-55 source, and will use a gas mass spectrograph to check the mixture ratio and to check for impurities. In order to gain experience with this hardware, and develop our methods and procedures, we plan to procure the necessary components and test them thoroughly. One of our priorities will be to test polypropylene tubing. According to outgas studies, this is a good material for chamber use, and the use of a flexible tubing in the hook-up of the planks in the octants is highly desirable.

### **7.7.8 C0 background studies**

We would like to build a system of detectors to install in the C0 hall, and use them to measure background rates. While the beam conditions will not be identical to those during BTeV running, our measurements can be compared to calculations and used as a check of those calculations.

For these studies, we plan to reuse the muon scintillator counters from the fixed-target experiment FOCUS. These counters were built and operated by the University of Illinois and University of Puerto Rico groups that are working on the BTeV muon system.

The muon scintillation counters have been taken to the University of Illinois, repaired and roughly gain balanced using a radioactive source. Roughly 15% of the counters required repairs. A frame has been designed to hold these counters in an array that resembles the BTeV muon detector design. We believe we will have enough counters to either cover the full azimuth, or to cover half of the azimuth with two layers to suppress firings due to tube noise. We may be able to switch between these two configurations rapidly if the need arises.

### 7.7.9 Simulation and reconstruction work

A significant effort has already been expended on creating an accurate muon simulation in the BTeVGeant framework, including the complicated magnetic field resulting from having a dipole magnet inside a toroidal magnet. We plan to further verify these simulations by comparing with those obtained from inclusive simulations like MARS which include non-interaction region phenomena like beam scraping.

The BTeVGeant simulation was used to develop and evaluate the current dimuon trigger. Progress will continue on developing the dimuon trigger algorithm and hardware implementation. We will also investigate the effects of more noise, reduced efficiency, increased luminosity, geometry misalignments, etc.

We plan to work on developing full muon reconstruction code in order to be able to fully evaluate our misidentification rate and provide a better baseline for determining muon trigger efficiency. We also would like to investigate hybrid trigger schemes which utilize information from the muon system and vertex trigger to, for instance, trigger on beauty semileptonic decays more effectively than with the vertex trigger alone. These triggers would be implemented in the global level one trigger.

## 7.8 Production Plan

This section describes the plans for production, production testing, and production quality assurance of the BTeV muon system. The various components that need to be produced are (1) the sensor planes, which includes front-end electronics and cabling, and (2) support systems such as gas, low-voltage, and high-voltage. By far the largest task is the construction of the sensor planes, which will be built in modules at university sites (Illinois, Puerto Rico–Mayaguez, and Vanderbilt). These modules will then be delivered to Fermilab for installation. Our delivery, installation, integration, and shake-down plan (including the construction and installation of the mechanical support for the sensor planes) are described in the next section.

**Octants** mounted on octant plates are the basic installation unit of the muon system. An octant covers  $1/8$  of the azimuthal angle in one view, so there are 8 octants per view and 32 octants per station. Four octant plates are assembled into a wheel; two wheels make up a view.

Octant plates will be assembled at Illinois and Vanderbilt and shipped to Fermilab for installation there. A fully assembled octant plate will have all front-end electronics installed,

as well as gas connections, low and high voltage cables, slow-control cables, and signal cables that are “interior” to the octant. When an octant is delivered to the C0 hall, it will only be necessary to attach it to the muon system mounting structure and make electronic, electrical, and gas connections to external devices (such as the experimental DAQ and to muon system low voltage supplies). The octant will have been fully tested prior to installation: all readout, electrical, and supply connections will have been verified at the octant assembly site prior to shipping.

For a one-arm muon system, there will be 3 detector stations, with 4 views per station, 8 octants per view, and 12 planks per octant. This results in 1,152 planks or 36,864 tubes (electronics channels). Planks range in length from 2 to 6 feet. We will build eight complete octants (96 planks, 3,072 tubes) during the pre-production stage (which we will use to shake down and evaluate our production lines and methods). During production we will make two additional views worth of planks to use as spares. These additional planks must be made at the same time to minimize the cost of the necessary parts and labor.

## **7.8.1 Construction overview**

Muon octants will be fabricated at university sites and delivered pre-tested to Fermilab. Installation at Fermilab will involve attaching each octant to the support structure and connecting it to electrical, electronics, and gas. There are three main tasks in the construction of an octant: (1) plank fabrication, (2) front-end electronics fabrication, and (3) assembly of planks into octants.

### **7.8.1.1 Pre-production**

In order to shake down and evaluate our production lines and methods, we will make eight pre-production octants. These octants will be fully instrumented so that we can fully debug and evaluate our testing and quality assurance program. This means that they will have a full complement of front-end electronics, gas supply lines, low and high voltage cables, slow-control cables, and readout cables. All of this “internal” cabling, as well as each of the proportional tube counters, will be tested and certified during the production process. Each of the plank production lines will fabricate planks during this pre-production stage, the electronics production process will be implemented, and the octants will be assembled at one or both of the octant assembly sites. Once the fabrication and testing of these octants is complete, we will evaluate all aspects of the process and make adjustments as necessary, and then begin the full production process of the full system.

### **7.8.1.2 Quantities of materials needed**

The quantities of parts, planks, octants, etc., that must be acquired or fabricated are driven by the numbers listed in Table 7.3. For example, the total number of planks that will be installed in the base system can be determined by multiplying the planks/octant (12), octants/wheel (4), wheels/station (8), stations/arm (3), and arms/spectrometer (1), which



Item	Value	Item	Value
Planks/octant (1 view)	12	Pre-production octants	8
Octants/wheel	4	Spare octants	16
Wheels/view	2	Fraction of problem planks	0.1
Views/station	4	Fraction of problem manifolds	0.1
Stations/arm	3	Fraction of problem support ribs	0.1
Arms (in the BTeV detector)	1	Fraction of problem Delrin inserts	0.1
Tubes/plank	32	Fraction of problem misc. parts	0.1
Manifolds/plank	2	Fraction of re-strung tubes	0.25
Support ribs/plank	2	Wire waste/tube strung (ft.)	2.5
Gas connections/manifold	2	Tube safety factor	2
Delrin inserts/prop. tube	2		
Average tube length (ft.)	4.1		
Longest tube (ft.)	6.5		

Table 7.3: Numbers and assumptions for the muon system. These determine the quantities of parts, planks, and octants that need to be fabricated. The meaning or derivation of these numbers is explained in the text.

gives 1,152. Multiplying this by tubes/plank (32) gives the number of proportional tube channels in the base system (36,864).

Manifolds, support ribs, gas connections, and Delrin inserts are all parts used to construct planks. The numbers given for these items in Table 7.3 are the number that will be in the base system. For example, there will be 2 Delrin inserts per proportional tube, or a total of 73,728 inserts.

The average tube length and longest tube are used in calculating the amount of tubing required. The remaining numbers in the table are important for calculating the total amount of materials (such as tubing) and parts that must be acquired/fabricated when accounting for spares, waste, mistakes, and so on. For example, the *fraction of problem planks* is our assumption of the number of finished planks that will be found to be bad by our quality assurance program (QAP). Once a plank is finished, it cannot be restrung or “rescued.” If a plank is found to be bad, a new one must be made. So, if we need 100 planks, this fraction (0.1) predicts that we will have to make 110. Similarly, the *fraction of re-strung tubes* is an estimate of the number of tubes that have to be restrung because a crimp doesn’t hold, the tension is inadequate (too low), or the tube doesn’t hold high voltage. The *wire waste per tube strung* is the amount of extra wire required when stringing a tube (1) to make sure the wire in the tube is clean and has no kinks, and (2) to connect to the tensioning part of the stringing apparatus. The *tube safety factor* is added because we don’t know what lengths of planks will be bad and have to be re-made. We will buy the stainless steel tubes pre-cut to length, and will buy extra of each length to make sure we have enough of each of the required lengths. The “2” here does not mean we will buy twice as many tubes as needed, it

	Pre-Production				Production					Sum
Item	Base	Bad Plnk	Re-string	Total	Installed	Spares	Bad Plnk	Re-string	Total	Total
Planks	96	10	0	106	1152	192	135	0	1479	1585
Tubes	3072	320	0	3392	36864	6144	4320	0	47328	50720
Octants	8	0	0	8	96	16	0	0	112	120
Gas manifolds	212	22	0	234	2535	423	297	0	3255	3489
Support Ribs	212	22	0	234	2535	423	297	0	3255	3489
Delrin End Plugs	6759	704	1866	9329	81101	13517	9504	26031	130153	139482
SS Tubing (feet)	12595	2080	0	14675	151142	25190	35424	0	211757	226432
Sense Wire (feet)	20275	2880	5789	28944	243302	40550	28512	78091	390456	419400
Crimp tubes	6759	704	1866	9329	81101	13517	9504	26031	130153	139482
Crimp wires	6759	704	1866	9329	81101	13517	9504	26031	130153	139482
Brass tabs	6759	704	1866	9329	81101	13517	9504	26031	130153	139482
Hose clamps	423	44	0	467	5069	845	594	0	6508	6975
Gas connect. tubes	423	44	0	467	5069	845	594	0	6508	6975

Table 7.4: Production quantities determined using the numbers and assumptions listed in Table 7.3.

means we will buy twice as many tubes as necessary to build all the bad planks, a 10% effect. These fractions and estimates are based on our experience stringing about 25 prototypes.

### 7.8.1.3 Pre-production and production quantities

Using the numbers in Table 7.3, we can calculate the number of parts, planks, and octants that must be acquired or fabricated. The resulting numbers are shown in Table 7.4. The calculations are based on two premises. First of all, it will be very difficult and expensive to get the assembly lines going to make planks, and to crank up production of the parts (manifolds, support ribs, Delrin inserts). Therefore, we must make all required quantities during production, and will not plan on going back and making more later. This means that all parts and materials, such as the stainless steel tubes for our proportional tubes, will be purchased during the production phase; it will not help to buy more later. Having to buy all necessary materials in advance complicates calculations of the required quantities. An

example is the Delrin end plugs. We must have enough extra to account for re-stringing (the plugs usually can't be saved), enough to re-make planks that are found to be bad after they are finished, and for plugs that are found to be defective after they are made. The second premise is that if a bad plank is found after it is completed (one of the wires breaks, or has insufficient tension), it will not be possible to save any of the parts used to make it. A new equivalent plank will have to be made with all new parts. Fortunately, because of the tests we will perform on the tubes after they are strung and before they are assembled into a plank, we do not believe this will happen very often.

The derivation of some of the entries in Table 7.4 is trivial. For example, the number of *installed* planks in the production section is simply the number of planks needed for a working detector, as calculated in section 4.2 above. The number of *bad planks* is just the number we need to build (from the *installed* and *spares* columns) times the *fraction of problem planks* from Table 7.3. Others are less obvious. For example, the number of *installed* Delrin end plugs in the production section is the number needed for the detector plus the number we assume will be defective (see *fraction of problem Delrin inserts* in Table 7.3).

## 7.8.2 Plank fabrication

Plank fabrication involves several steps: acquire parts and materials, fabricate parts that need to be machined, string individual proportional tubes, test them, assemble the tubes into planks and test the planks, attach electronics to the planks, and test the planks in a cosmic ray test stand. Three plank fabrication lines will be established at Illinois, Puerto Rico, and Vanderbilt.

### 7.8.2.1 Parts of a plank

There are 11 different parts or materials needed to make a plank, not including the electronics. Each proportional tube will be made from a thin-walled (0.01 inch thick) **stainless steel tube** (3/8 inch in diameter) with a 30 micron gold plated tungsten **sense wire**. The sense wire is tensioned to 75% of its yield point, or 150 grams. A **Delrin insert** goes in each end of the tube to electrically isolate the wire from the tube and center the wire in the tube. It also has three gas holes. A **brass crimp tube** is inserted in each end plug, the sense wire exits the tube at each end through the plug and this tube. A thicker **crimp wire** is inserted into the crimp tube after the wire is threaded through, this helps the crimp hold the sense wire in place. Completed tubes are assembled into planks, which are held together at the ends by brass **gas manifolds** (see Fig. 1). For longer planks, the tubes will also be supported along their length by brass or aluminum **support ribs**, which will maintain the spacing of the tubes. The stainless steel tubes are glued into the manifolds at each end, the glue provides structural support and a gas seal. A brass sheet is soldered or spot welded to the outside of the brass manifold to maintain electrical continuity and RF integrity. This sheet is soldered to conductive copper tape wrapped around the end of each tube and to the circuit boards at each end of a plank. The open end of the gas manifold is sealed by a **circuit board** with sockets on the inside that accept the brass crimp pins, these sockets

will provide the connection to the front-end electronics. Two stainless steel **gas tubes** will be glued into holes in each manifold, these will be connected to the gas supply lines with **hose clamps**.

### 7.8.2.2 Acquisition of materials and supplies

The materials needed to build the muon system planks should all be readily available stock items with the exception of the thin walled stainless steel tubes and the sense wire. These will require some lead time in purchasing (*i.e.* roughly 3 months before delivery of the first stainless tubes). The brass (including the crimp tubes) and Delrin required are standard stock items. Once delivery starts, all parts could be in hand in a matter of months. We may decide to stretch acquisition out for budgetary reasons, however.

### 7.8.3 Fabrication of manifolds, support ribs, and Delrin inserts

A major portion of the work required to build the planks needed for BTeV is fabricating the gas manifolds, support ribs, and Delrin inserts (which includes inserting the brass crimp pin). These three parts require substantial machining. The Vanderbilt Science Machine Shop will do the machining of the first two parts. The Vanderbilt machine shop has the computer controlled milling systems needed to make these parts in bulk already, and can make these parts substantially cheaper than a commercial shop. Fabrication of the Delrin inserts may be done by a commercial machine shop, or may be done in the Vanderbilt shop. For this part, commercial shops may be able to compete on price.

The manifolds and support ribs will require roughly two years to make. This is also roughly how long it will take to string and assemble all the planks, so the two will proceed in tandem. It will therefore be very important that the shop work be kept on schedule, so as not to delay the manpower intensive plank stringing operations.

#### 7.8.3.1 Tube stringing and plank assembly

Plank stringing and assembly is the most labor intensive part of the muon system construction project. We have built roughly 25 prototype planks. Based on this experience, we have produced Table 7.5, which breaks plank assembly into sub-tasks and estimates the time and personnel required to perform each.

The times in Table 7.5 are under “optimal” conditions, in which we have the parts required and the operation is running smoothly. In estimating our total required labor, we increase the total time per plank by 15% to account for inefficiencies. We also increase the time required to make the first few planks because we assume it will take some time to “ramp up” to smooth operation of the assembly lines. We assumed it would take twice as much time for each production line to make their first 3–4 planks. The total times for the pre-production and production runs are summarized in Table 7.6. These numbers can be divided by 3 to get the times for each institution.

<b>Task (times are in hours)</b>	<b>Time</b>	<b>UG</b>	<b>Grad</b>	<b>PD</b>	<b>Tech</b>	<b>Facul.</b>
Project management/supervision	0.50					0.5
Wash and prep tubes	0.50	0.40	0.10			
Wash and prep machined parts	0.50	0.40	0.10			
Wash and prep other parts	0.20	0.20				
QAP: Inspect parts after prep	0.10			0.10		
Spot-weld brass tab to tubes, add bar code	1.00		1.00			
QAP: Inspect spot welds	0.10			0.10		
String tubes, includes restringing	6.00	2.00	3.00		1.00	
QAP: Visual inspect strung tubes	0.10			0.10		
QAP: Individual tube tension measurement	1.00		1.00			
QAP: HV test in air (meas. current at 1.5 kV)	0.50	0.50				
QAP: Inspect tension/HV results	0.10			0.10		
Glue plank together	3.20		1.90	0.30	1.00	
Solder circuit board end cap to manifolds	1.00		0.70	0.10	0.20	
Glue gas connections tubes in	0.50	0.50				
Attach electronics	1.00		0.70	0.10	0.20	
QAP: Gas leak test	0.50		0.50			
QAP: Plank tension measurement	1.00		1.00			
QAP: Visual inspection	0.10			0.10		
QAP: Cosmic ray test stand, analyze data	2.00		1.00	1.00		
<b>TOTALS</b>	<b>19.90</b>	<b>4.00</b>	<b>11.00</b>	<b>2.00</b>	<b>2.40</b>	<b>0.5</b>

Table 7.5: Plank assembly sub-tasks and the labor and personnel required for each. These times are for the fabrication of one plank. UG stands for undergraduate student, PD means post-doc.

<b>Task (times are in days)</b>	<b>Time</b>	<b>UG</b>	<b>Grad</b>	<b>PD</b>	<b>Tech</b>	<b>Facul.</b>
Pre-prod times incl. inefficiency	337.55	67.85	186.59	33.93	40.71	8.48
Prod. times incl. inefficiency	4256.61	855.60	2352.90	427.80	513.36	106.95

Table 7.6: Labor required to make all pre-production and production planks.

Individual tubes will be strung in a stringing jig. This is a two person operation. After stringing and testing, the gas manifolds that go on each end of a plank are assembled with 32 tubes, and this assembly is then glued together. Interface cards, which are circuit boards that hold the offset capacitors and provide the final gas seal, are soldered onto the open end of each gas manifold. This operation also solders the brass tabs from the tubes to the manifolds and provides electrical continuity for noise suppression. The circuit boards also connect to the individual sense wires and provide the signal path to the front-end electronics.

Once the circuit boards are in place, the front-end electronics are attached, and the plank is ready for the cosmic ray test stand and, if it passes our QAP, is ready to be assembled into octants.

Each site will produce one plank per day on average. This includes all testing and assembly.

### **7.8.3.2 Plank Quality Assurance Program (QAP)**

Tests and measurements are performed at all stages of plank production as a part of our quality assurance program.

After each proportional tube is strung, it is tested for continuity and to see if it has slipped out of the crimp at either end (and is shorted to the tube walls). The wire is re-strung if a problem is detected. Then the tube is tested to verify that it will hold high voltage (1600 Volts) in air, and the wire tension is determined by finding the resonant frequency of the wire in a uniform magnetic field when a variable frequency AC current is applied to the wire. If any tubes are out of tolerance or fail outright, they will be re-strung.

Once the tubes are glued together into planks and the interface cards are soldered into place, we will retest the tension of each wire and do a leak test on the plank. If the plank passes these tests, the plank will be installed in a cosmic ray test stand and we will do plateau curves and measure efficiencies and noise rates for each tube. An inventory control system based on bar codes will be used at all points during the construction. Information such as test results, parts used, and the personnel performing the work will all be recorded in a database associated with the bar code that will be attached to each tube and to each plank. A bar code reader will be used to scan in the bar code on each plank or tube. Additional information will be entered via easy to use computer interfaces which will be tailored for each step in the process. Each front-end electronics card will also have a bar code label. Information on which electronics card is associated with which plank, and which tubes are associated with which plank, will be logged and modified as changes are made.

### **7.8.4 Electronics QAP**

It is essential to identify electronics problems as early as possible. All fabricated ASDQ chips are tested before they are used in the circuit board assembly. The tests are well understood and were used by the University of Pennsylvania during the ASDQ vetting process for the CDF production. The expected yield and additional costs for testing are included in our cost estimate. All fabricated circuit boards must pass an electrical test at the fabricator's

location. All stuffed circuit boards will be programmed at the end of the assembly process by the assembler and a power-up go or no-go will be indicated. This allows us to identify production problems early. Once assembled boards arrive at Vanderbilt, they will be placed in a fixture that mimics the electrical environment we expect during data taking. Any errors will be noted, and no boards that are less than 99% efficient will be allowed to be placed on a plank. The cards that interface the ASDQ-FPGA boards to the detector will be continuity and high-pot tested at 2000 V before being mated with the planks and the ASDQ-FPGA boards.

### **7.8.5 Octant assembly and QAP**

The detector modules (octants) will be assembled from the planks at both Illinois and Vanderbilt. Puerto Rico may participate at this stage if it can be shown that shipping the octants from there is not prohibitively expensive. The planks for each module will be held together by attaching them to pre-drilled and slotted 1/4" aluminum sheets called octant plates.

The internal signal, gas, and HV connections will be established as the octant is assembled. These connections will be verified in an octant test stand which will provide gas, control signals, and low and high voltages to all planks in the octant. We will verify that each channel (proportional tube) is operating as expected and that it can be read out. Once complete, each octant will be packed and readied for transport to Fermilab. A portion of the octant plate which is not used for mounting planks can be removed to facilitate shipping if convenient (see Fig. 7.6).

## **7.9 Installation, Integration and Testing Plans (at C0)**

This section describes the installation, integration and testing plans for the BTeV muon system. As described above, the octants shipped to Fermilab will already have undergone a rigorous testing and quality assurance program at the production sites. They will be ready for installation and, unless they are damaged in shipment, ready to go.

### **7.9.1 Transportation of muon detector octants to C0**

The octants will be delivered to C0 as they are fabricated at the production sites. They will be stored at C0 or some other appropriate place, and installed during periods in which we have extended access to the hall.

#### **7.9.1.1 Equipment required**

The octants which will be shipped to Fermilab will be too heavy to carry reliably without assistance. A roller cart will be required to move them. The required carts will be built in the Illinois machine shop and shipped to Fermilab and the other octant production site at

Vanderbilt University. The octants will be shipped to Fermilab; we are still working out how this will be done. We will either rent trucks and move them ourselves, or ship them with a commercial carrier.

#### **7.9.1.2 Special handling**

The proportional tubes that make up the muon system will be made from stainless steel tubes strung with 30 micron gold-plated tungsten wire. The wires will be held in place with by crimped brass tubes at each end. The planks themselves will be extremely sturdy and strong, and the electronics and other connections internal to the octant will be very robust. The concern with the detectors is that some of the crimps holding the wire in place will fail or that wires will break, especially during shipping. This will be our major concern in determining how we will move the octants to Fermilab.

### **7.9.2 Installation of muon system elements at C0**

The muon octants are designed so that they can be inserted from the wide aisle side of the detector hall. One dynamically creates a mounting “wheel.” The first octant plate is inserted from the side and then rolled to the bottom position on a series of rollers that contact the octant plate circumference. The next octant plate is then attached to the previous plate using specially designed knitter brackets. One then rolls the two octant partial wheel into a position that allows the attachment of the third plate. Once all 4 plates of a wheel are assembled, the wheel is lifted off of the floor and mounted from beams attached to the toroid, as illustrated in Fig. 7.25 and the floor wheels (bogies) are removed and used for the installation of the next wheel. In all, 8 wheels are used for each station.

The process can be reversed for repairs. In the worse case, the replacement or repairs of a single plank will require de-cabling its wheel and sequential dismounting and rotation of the wheel until the affected octant is in a convenient position for repairs.

#### **7.9.2.1 Installation steps**

**Testing of octants on arrival:** When the octants arrive at C0 from the production sites, we will retest them with the same test system used at the production sites: testing gas flow, current draw, readout of all channels, etc. Any problems will be fixed.

**Installation of octant support structure:** The octants will then form “mounting wheels” during installation. These mounting wheels will be supported from the sides and top of the toroid and filter using a set of specially designed hangers which attach to fixtures on the wheel assembly.

**Installation of relay racks, gas system, and other support infrastructure:** We assume that the installation of relay racks and other support infrastructure (such as the gas system) will occur as early as possible. Low voltage and high voltage supplies, as well as



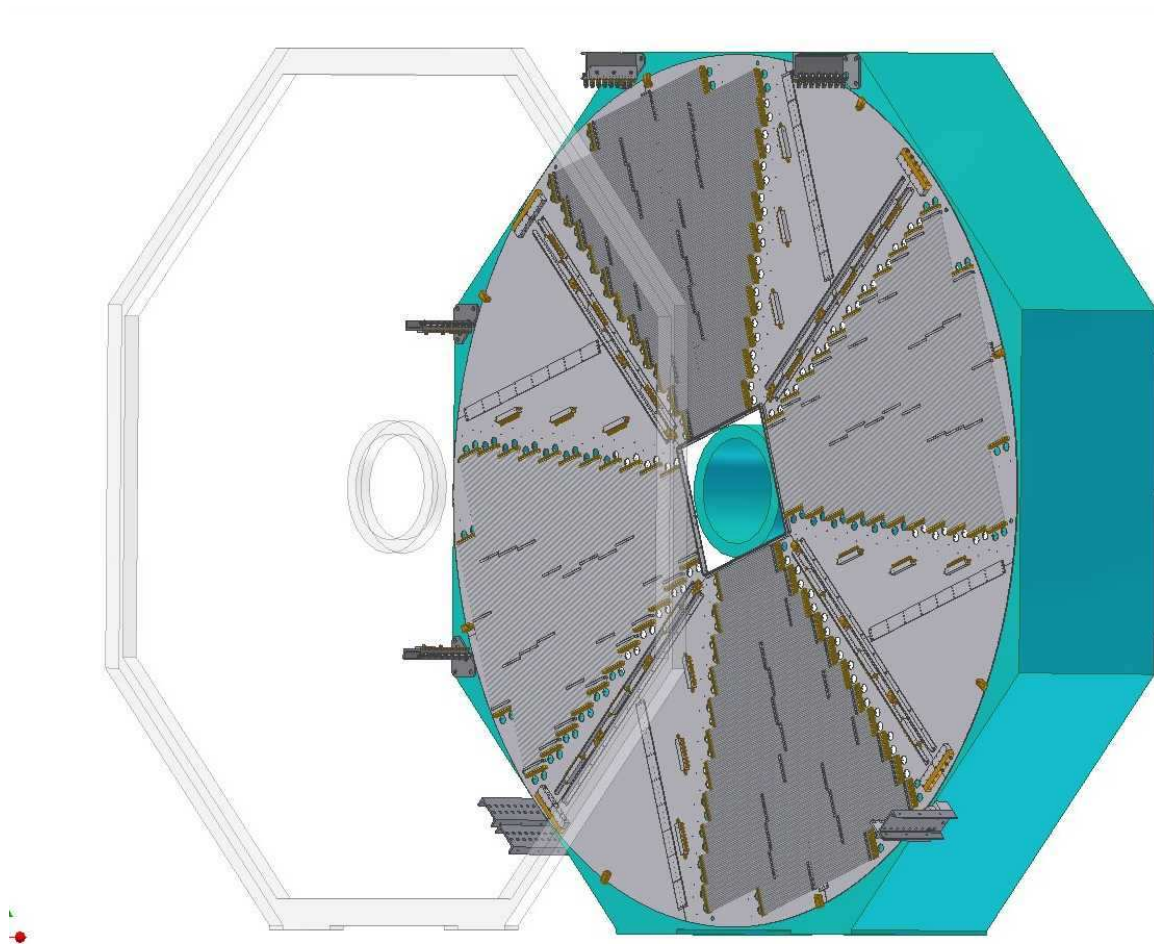


Figure 7.25: The mounting wheel will be supported from beams attached to the toroid. The upper two beams will support the  $\approx 1500$  lb weight of each wheel, the additional beams will prevent the wheel from swaying.

data acquisition hardware, can be installed as needed (*i.e.* as new octants requiring them are installed, if possible).

**Suspension of octants:** The mounting wheel will be supported from beams attached between the toroids. The upper two beams will support the  $\approx 1500$  lb weight of each wheel as shown in Fig. 7.26. Additional beams will prevent the wheel from swaying. In principle, the muon system can roll with the toroid if one needs to move the toroids to service accelerator magnets.

We plan to install over a long period of time, as octants become available, and during extended shutdowns.

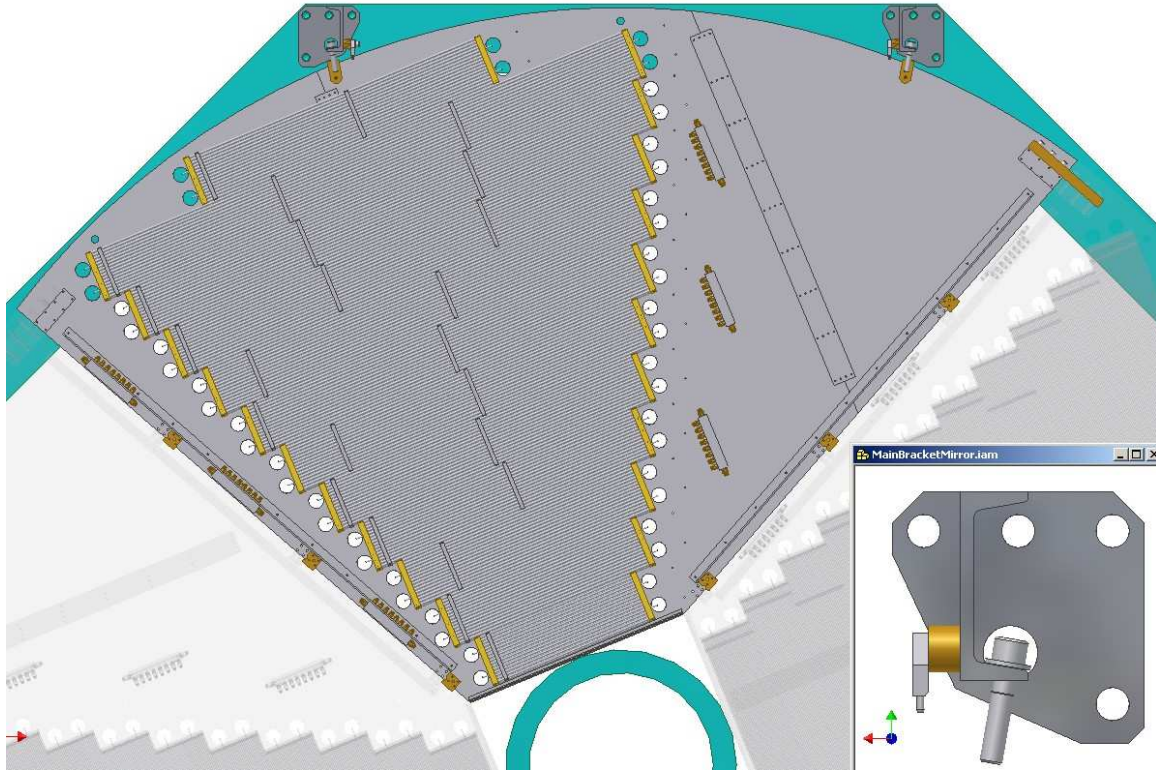


Figure 7.26: Details of the hanging brackets used to support the octant plate wheel assemblies.

**Low and high voltage, DAQ hardware installation:** These items will hopefully be available as needed, *i.e.* as new octants are installed. We will install them at the same time as their corresponding octants, or ahead of time if they are available.

**Connection of electrical, gas, and electronics:** Once all the octants in a wheel are installed we make all gas, electrical, data acquisition, and slow control connections. We will then proceed to test these connections as described below.

#### 7.9.2.2 Equipment required

For installation, special rigging will need to be assembled; again this will be provided by Illinois. This is envisioned as a special installation stand that will allow manipulation of each octant as it is being positioned into its mounting wheel.

### 7.9.2.3 Personnel required

The octants will be installed by members of the muon group. However, the support structure (beams) for the views will need to be installed by Fermilab personnel (welders, riggers, ...). In addition, DAQ personnel may be needed to help with connection of the octants to the DAQ.

### 7.9.2.4 Time required

We estimate that it will take up to 12 hours to install each wheel of 4 octants, which translates to 4 days per station or 12 days for the full detector. This does not include connections, which we estimate will take an equal amount of time. We believe the time to install octants will decrease as we get better at it. Note that in real time this will take roughly two years, as we plan to install octants as they become available and as opportunities exist to gain access to the experimental hall for extended periods. The first octants should start arriving at C0 in late 2006. The final octants should be ready by the summer of 2008.

## 7.9.3 Testing of muon system elements at C0

### 7.9.3.1 Stand-alone subsystem testing

**Mechanical:** As each octant is installed, the gas system will be tested for leaks and proper flow.

**Electrical/electronics:** As each octant is installed and connected, we will (carefully) bring them up to voltage and verify that they are drawing the expected current. We will check a channel or two in each plank with a scope to verify that they seem to be behaving as expected (expected noise level, signals look OK, etc.). We will then readout each channel and verify that each is connected to the DAQ and functioning as expected.

**Software:** When a view is installed, we should be able to look for cosmic rays, and to look at beam background when the accelerator is on. As we add views to each station, we can start to do more sophisticated tests and can start to debug our readout software, reconstruction software, and the muon trigger. We may determine the installation order to make best use of these kinds of tests.

**Personnel required:** Muon group (and muon trigger group) personnel can perform all stand alone testing, although some interaction with the DAQ and trigger groups will be important.

**Time required:** This activity will go on over an extended period of time (two years), as described above. This will give us plenty of time to debug our software and to perform multiple tests; we should not have a problem keeping up.

### 7.9.3.2 Combined systems testing

**Electrical/electronics/readout/software:** We hope to be using the DAQ early on, even in our “stand alone” tests. We also hope to use these tests to debug the muon trigger. So, the above “stand alone” tests will also be integration tests with the DAQ and trigger, two important elements that we connect with. We also will want to investigate higher level triggering, which will require information from the tracking systems. Once the tracking systems become available, we will start these tests.

**Personnel required:** Muon group (and muon trigger group) personnel will participate. Some interaction with the DAQ, trigger, and tracking groups will be required.

**Time required:** This activity will go on over an extended period of time (two years), as described above. This will give us plenty of time to debug our software and to perform multiple tests; we should not have a problem keeping up.

### 7.9.3.3 Completion of commissioning

The muon detector will be considered fully commissioned when the entire system is under voltage, gas is flowing, and near-horizontal hits from cosmic rays or beam backgrounds are able to be read out through the DAQ.

## 7.10 Performance

Extensive simulations of this detector as well as previous iterations have been performed. These simulations use BTeVGeant which is based on GEANT3. These simulations have been used to help determine the best geometry, shielding scenarios, etc. The simulations have also been used to develop and validate the dimuon trigger.

The BTeVGeant simulations include a full tracing of particles produced by signal and minimum bias interactions at the nominal luminosity of  $2 \times 10^{32} \text{cm}^{-2} \text{s}^{-1}$ . This tracing includes decays, hadronic and electromagnetic interactions, multiple Coulomb scattering, etc. The full BTeV detector geometry is used including beam pipes and support structures, as well as detector elements. The magnetic field in the muon region includes the effect of the muon toroids and the compensating dipole and is calculated with the POISSON program. The muon proportional tube response to charged particles is to fire if a particle passes within 85% of the inner radius of a tube.

### 7.10.1 Occupancies

At our nominal luminosity of  $2 \times 10^{32} \text{cm}^{-2} \text{s}^{-1}$  and a minimum bunch spacing of 132 ns, we expect 2 minimum bias interactions/crossing which are simulated using a Poisson distribution with mean of two. Table 7.7 and Fig. 7.27 summarize the detector occupancies obtained from

	Station 1	Station 2	Station 3	Total
Average number of hits per crossing	42	8	9	54
Average occupancy	0.34%	0.06%	0.07%	0.15%
Maximum channel occupancy	2.5%	0.24%	0.52%	
Maximum plank occupancy	1.6%	0.17%	0.31%	

Table 7.7: Muon detector occupancies obtained from BTeVGeant simulations with an average of 2 minimum bias interactions per crossing and a crossing rate of 7.6 MHz (132 ns bunch spacing). These numbers should be multiplied by 3 for 396 ns bunch spacing. Average occupancy is the occupancy of the detector in a single crossing. Maximum channel occupancy is the maximum hit rate for the innermost channel. Maximum plank occupancy is the average per channel hit rate of the innermost plank.

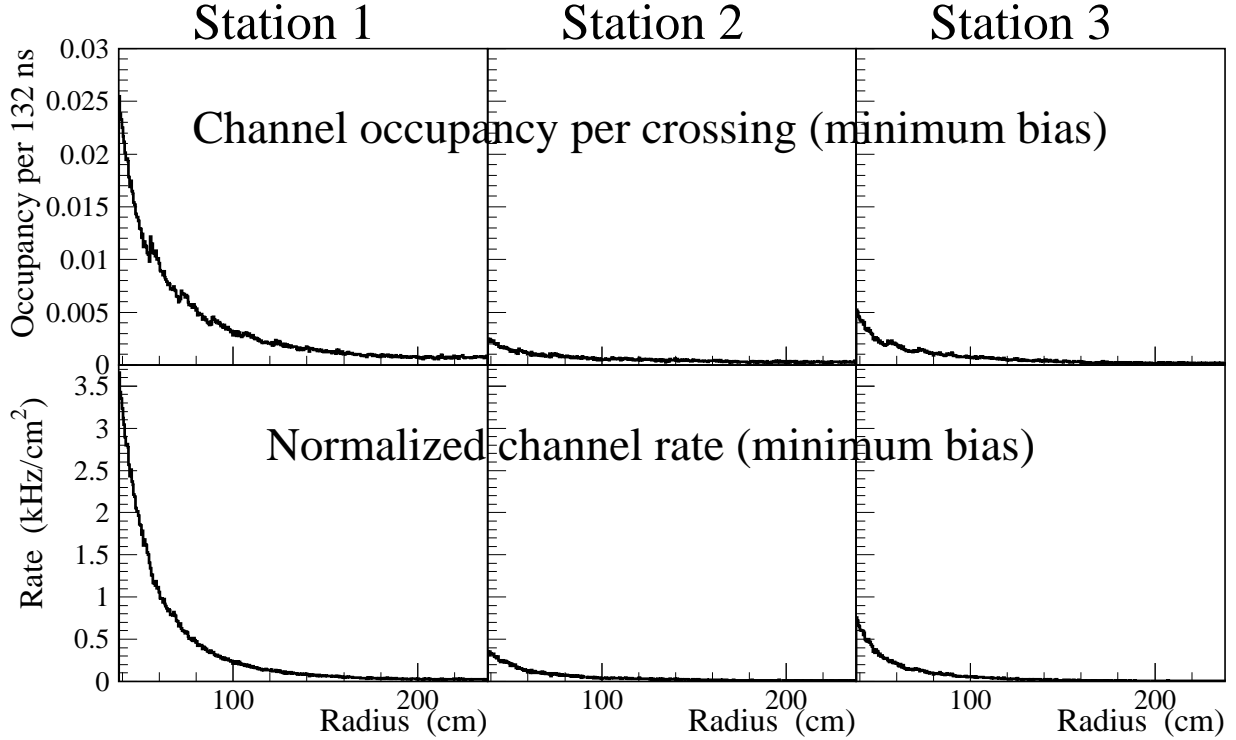


Figure 7.27: Radial distributions of tube occupancies (top) and normalized rate (bottom). These results are from the first radial view in each station, averaged over the eight octants.

BTeVGeant under this scenario. These occupancies should be multiplied by 3 for operation at 396 ns between crossing and an average of 6 interactions/crossing. Even at 396 ns, these occupancies and rates are fairly low by modern detector standards.

### 7.10.2 Dimuon trigger

The muon trigger is described in more detail in Chapter ???. However, a major goal of the muon detector is to be able to generate a stand alone dimuon trigger and therefore the design and performance of the muon detector and trigger are closely related. The University of Illinois has designed a simple trigger which can be easily implemented using Field Programmable Gate Arrays (FPGA) and Digital Signal Processors (DSP). The trigger development started by noticing that good muons are well described by the equation  $R2 = a + bR1 + cR0$  where  $a$ ,  $b$ , and  $c$  are constants and  $R2$ ,  $R1$ ,  $R0$  are the numbers of the tubes hit by a good muon. This equation describes a plane in the 3-dimensional space defined by  $R0$ ,  $R1$ , and  $R2$ . Four of these equations are generated (one for each view). In each view a muon candidate is found when three hits match the equation (within a user definable error). If three out of four views find a muon candidate (of the same sign) then a good muon is found. In this algorithm, each octant is treated independently. The dimuon trigger is satisfied if two good muons of opposite sign and from different octants are found. Two muons which travel through the same octant or a muon which crosses octants will be lost by the trigger.

The University of Illinois group used the results of BTeVGeant simulations to tune this trigger and determine efficiency for signal and rejection of background. The signal mode is  $B^0 \rightarrow J/\psi K_S^0$  where  $J/\psi \rightarrow \mu^+ \mu^-$ . The background is minimum bias. The signal and background events are generated assuming 2 interactions/crossing. The trigger algorithm described above can obtain an efficiency of 80% with a rejection rate of 500:1 which is well above our design goals of 50% efficiency with a rejection rate of 300:1. Here, efficiency is relative to all events where both muons pass through all three muon chambers and the rejection rate is the inverse of the minimum bias efficiency. More severe running conditions such as 3–4 interactions/crossing and tube efficiencies as low as 95% still give a broad range of options for greater than 50% efficiency with a rejection rate better than 500:1. Details of these studies and their relevance to running with a bunch spacing of 396 ns can be found in Section ??.

## 7.11 Test Results

In the summer of 1999 we conducted our first test beam run using our first prototype of the detector and electronics. The tubes were quite efficient but susceptible to external RF noise and cross talk. This led us to redesign the high-voltage distribution card, construct the manifolds out of brass (conductor) instead of Noryl (insulator), and electrically connect the manifold to the tubes providing a Faraday cage. Also, a newer version of the amplifier/shaper/discriminator (ASD) chip is now being used. After several iterations we now have a design, described above, which we have proven can be built and provides the necessary capability. It has been tested in a cosmic ray test stand at Vanderbilt. We find tube efficiencies above 99% with a gas of 85:15 Ar-CO<sub>2</sub>. The noise level is consistent with the inherent noise of the ASD chip and the cross talk is negligible. We plan to test these proto-

types in a test beam during the fall of 2003 to verify the cosmic ray results and determine any rate limitations of the detector.

# Bibliography

- [1] J. Wiss, BTeV-doc-970, <http://www-btev.fnal.gov/cgi-bin/DocDB/ShowDocument?docid=970>
- [2] P. Sheldon and K. Stenson, BTeV-doc-991, <http://www-btev.fnal.gov/cgi-bin/public/DocDB/RetrieveFile?docid=991>)
- [3] J. Wiss, BTeV-doc-3405, <http://www-btev.fnal.gov/cgi-bin/DocDB/RetrieveFile?docid=3405>)



# Chapter 8

## Forward Straw Detector

### 8.1 Introduction

This Chapter describes the Straw Detector which together with the Forward Silicon Tracker forms the the forward charged particle tracking system. The major functions of the forward tracking system are to provide high precision momentum measurements for tracks found in the pixel system, to reconstruct and measure all parameters for tracks which do not pass through the vertex detector (such as  $K_s$  and  $\Lambda^0$  daughter tracks), and to project tracks into the RICH counters, EM calorimeters, and Muon detectors.

### 8.2 Requirements

The requirements of the Straw Detector are:

- Provide tracking coverage in each arm of the BTeV detector from the outer edge of the Forward Silicon Tracker out to 300 mrad.
- Provide robust pattern recognition for charged particles in conjunction with the pixel detector.
- Achieve a momentum resolution of  $\sim 1\%$  for 100 GeV tracks. This can be achieved with a single straw position resolution of  $200\mu\text{m}$ .
- Material budget as low as possible ( $\sim 1\% X_0/\text{station}$ ) to minimize multiple scattering, energy loss, secondary interactions, and photon conversions.
- Drift time less than 132 nsec. Although the Tevatron will probably operate with a time of 396 nsec between bunch crossings we allow for the possibility of running with 132 nsec between bunch crossings.
- Be able to operate at a luminosity of  $2 \times 10^{32} \text{ cm}^{-2} \text{ s}^{-1}$  for 10 years.
- Be mechanically robust and modular so it can be installed around the beam pipe.

## 8.3 Baseline Design

The baseline forward tracking system consists of 7 stations, placed transversely to the beam at various distances from the interaction point. Three stations are placed in the dipole magnet, three stations in the field-free region just upstream of the RICH, and one station just downstream of the RICH. The entire system extends over a distance of  $\sim 7$  m and provides  $\theta$ -angle coverage from  $\sim \pm 10$  mrad up to  $\pm 300$  mrad.

The design of the forward tracking system has been driven by the high density of tracks produced in the forward direction, especially with multiple interactions per crossing. Most of the solid angle is instrumented using straw tube drift chambers. Straws have been chosen because they can be used to make large chambers with small cell size, and because they can be built to surround the beam pipe without requiring a heavy frame near the beam. The track density very close to the beam requires detectors with even higher granularity; we have chosen to instrument the central section of each station with silicon microstrip detectors.

The forward straw tube tracker consists of stations that provide 3 coordinate measurements,  $X$ ,  $U$  and  $V$ , where the two stereo views,  $U$  and  $V$ , are at  $\pm 11.3^\circ$  around the  $Y$  bend coordinate. With three layers per view, this configuration provides excellent resolution in the bend plane while maintaining a robust ability to reject ghost combinations of hits. It has sufficient redundancy to achieve a high detection efficiency and to resolve the left/right ambiguity a very large fraction of the time.

The unit of construction is the 'module' consisting of forty-eight straws of 4 mm diameter, arranged in three rows of 16. The modules are then assembled in a frame to form a 'half-view' (Fig. 8.1). Three sides of the frame are made of aluminum extrusions. On the fourth side, which is in the active area of the detector, the tension is supported by a low mass carbon fiber strut. In the region around the beam-pipe, straws are terminated at a carbon fiber gas manifold. In order to keep the straws at a constant humidity we plan to flow dry nitrogen in a volume surrounding the straws.

All the sense wires for the straws that do not terminate at the central gas manifold are divided electrically using a small glass capillary bead following the technique used for the ATLAS TRT [1]. This cuts the occupancy rates in half. In addition, within a 26 cm square region around the beam-pipe, all sense wires will use 2 capillary beads to deaden the central section of the wire. This region is covered by the Silicon Strip Tracker.

Table 8.1 lists all the geometric parameters and the main characteristics of the Straw Detector.

## 8.4 Detector Components

### 8.4.1 Module Description

Straws are assembled in groups called modules. A module consists of 48 straws of 4 mm diameter containing wire centering devices and mounted to two end plates. Straws and endplates are aligned to each other during module assembly. The end plates have alignment

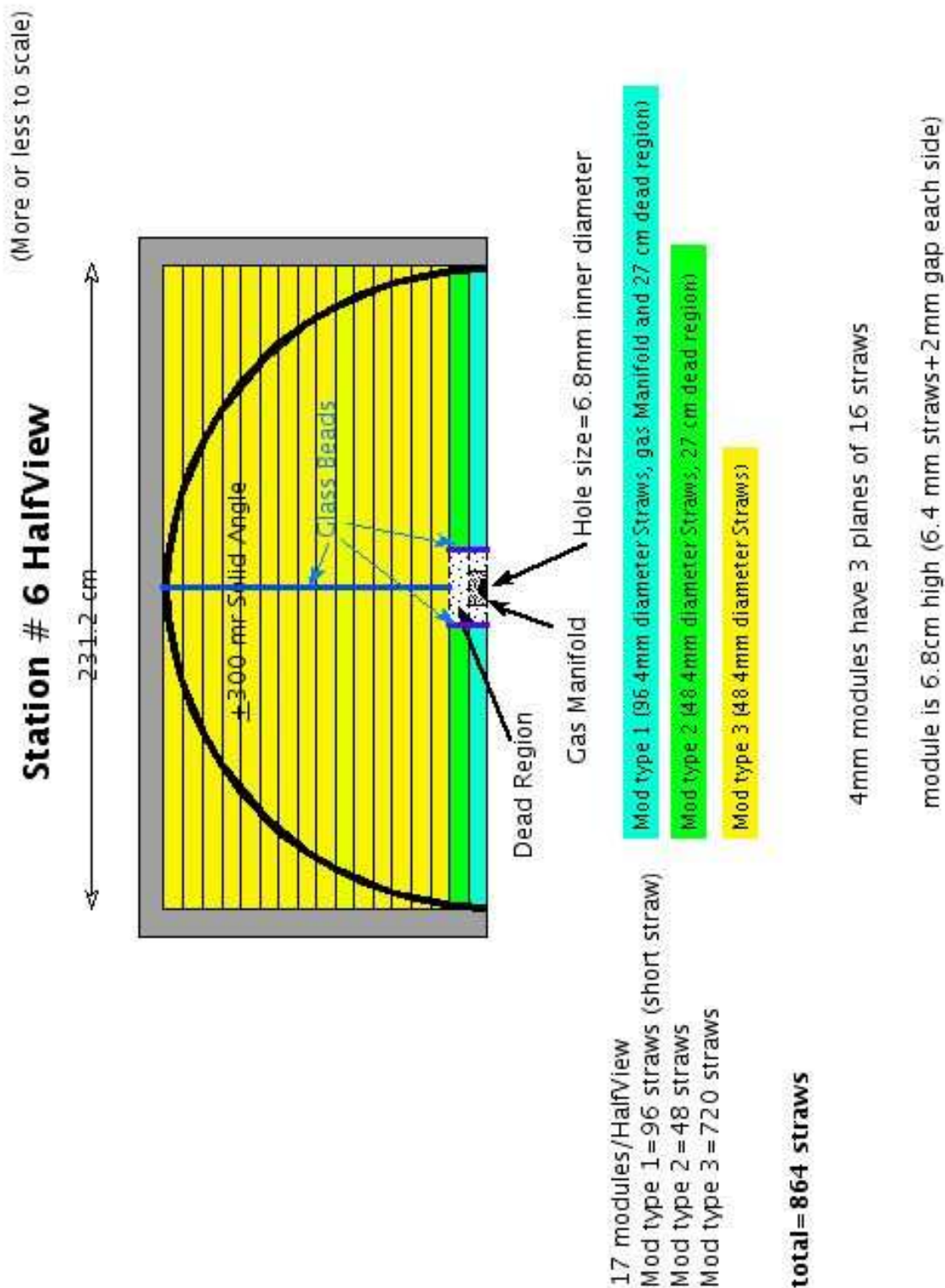


Figure 8.1: Straw Detector Half-View

Table 8.1: Properties of the baseline forward Straw Detector

Property	Value
Straw size	4 mm diameter
Central hole	26 cm $\times$ 26 cm
Total Stations	7
Z positions (cm)	96, 138, 196, 288, 332, 382, 725
Active Half size (cm)	28.0, 42.0, 63.0, 91.0, 105.0, 119.0, 189.0
Views per station	3 (X,U,V)
Layers per view	3
Total number of straws	26208
Total station thickness	0.9% $X_0$
Total channels	52416
Readout	ASDQ + TDC , sparsified

holes that allow modules to be aligned properly when mounted to the frame of the Half-view assembly. Fig 8.2 shows a module on the module assembly fixture.

The components of a module are the straws, twistors (wire centering device), end plugs and end plates. Straws are electrically and structurally connected to the end plates with electrically conductive epoxy and structural epoxy.

Straws are assembled into modules primarily for production benefits. However, the use of modules also provides an option for replacing damaged straws prior to the installation of the half-view frame. The primary production benefit of modules comes from the ability to make the structural, electrical and alignment connection to a significant number of straws with each bonding operation. Epoxy bonds can be made simultaneously without concern for excess epoxy affecting the close packing of adjacent straws. The use of modules also allows the operation of bonding to straws to be decoupled from the assembly and wiring of half-view frames.

The straws and end plates are aligned to each other with a module assembly fixture and that alignment is fixed by the electrically conductive epoxy that attaches the straws to the end plate. The end plugs aid the structural connection and gas seal of the straws to the end plates but they do not set the alignment.

The straw module closest to the beamline is physically two modules attached to a carbon fiber manifold which surrounds the beampipe (see section 8.4.4.5).

## 8.4.2 Module Components

### 8.4.2.1 Straws

The basic detecting element is the straw – a tube made by winding two strips of thin film ( $\sim 1$  cm wide) around a mandrel. The final choice of material will be made when we have finished testing both mechanical properties and radiation aging.



Figure 8.2: Straw Module

The original prototype straw tube was developed by the University of Indiana, based on the design of the Atlas straws. An aluminum conduction layer is placed between two Kapton films, the inner one next to the gas volume being a carbon loaded, low resistivity film (Kapton XC) to form a protective barrier. We measured the surface resistivity of the aluminum coated, carbon loaded Kapton film of this prototype to be  $0.5\Omega/\text{square}$ .

The other options for straw material are copper coated kapton and copper coated mylar.

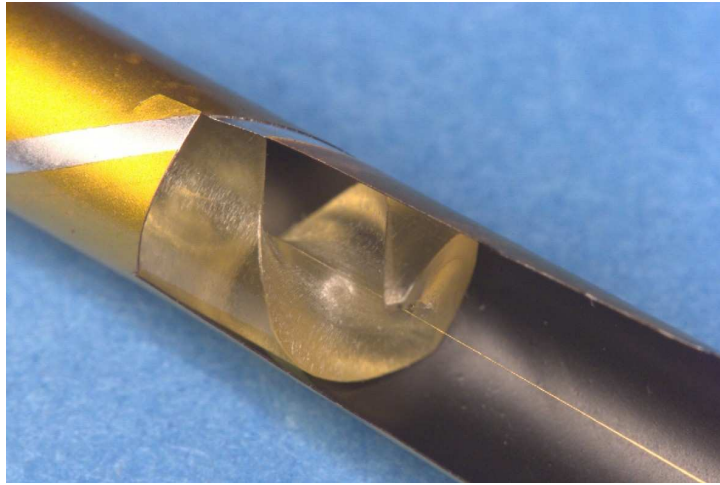


Figure 8.3: Straw cut away to show twister and anode wire

#### 8.4.2.2 Signal Wire, Wire supports – twisters

The sense wire for the straw cells is 25 micron diameter gold plated tungsten held under 50 grams of tension. In addition, the sense wires will be divided electrically using a small glass capillary bead [1]. This cuts the occupancy rates in half.

The wire-centering device is called a twister (see Fig 8.3). Twistlers were proposed for the SSC SDC Tracker detector and have been used in the construction of the ATLAS TRT detector. The twister is machined from Ultem®1000 plastic. The helix of the twister centers the wire in the straw but allows free flow of gas past the twister. The outside diameter of the twister is nominally 25  $\mu\text{m}$  smaller than the inside diameter of the straw. The twister is held in place by a low melting point thermoplastic adhesive that has been applied to the outside of the twister prior to insertion in the straw. After the twister has been inserted and positioned, the adhesive is re-softened by blowing hot air over the outside of the straw.

Ultem (polyetherimide) was selected for the twister material based on testing and evaluations made for the ATLAS TRT detector. Ultem has almost the same radiation hardness as polyimide and PEEK materials but has better adhesion properties.

Twister dimensions will be inspected by sampling from batches and measuring the position of a wire strung through the twister. Figure 8.4 shows the fixture used for inspecting prototype twistlers. It was learned during the prototype phase that small burrs on the ends of the twister could lead to wire alignment problems. Prototype twistlers have been obtained from two vendors that meet specifications.

Twistlers are located at the ends of the straws. They are also located at intermediate positions so that that any unsupported length of anode wire is no greater than 80 cm.

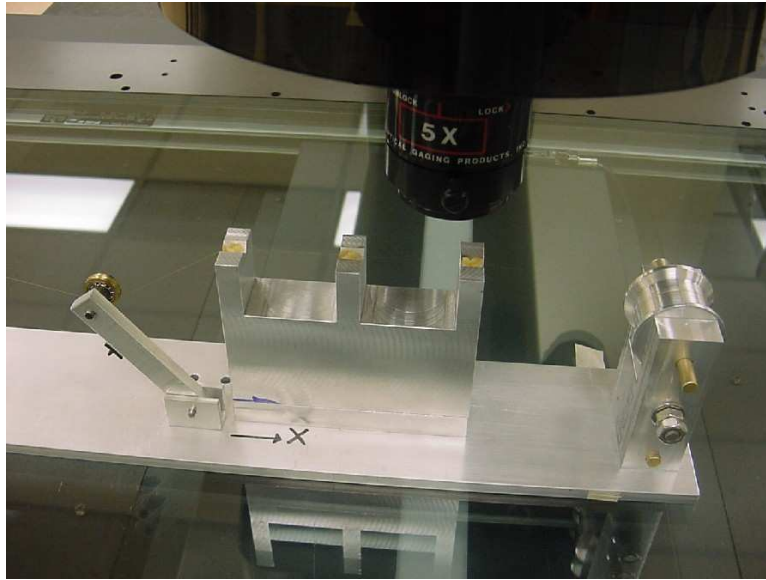


Figure 8.4: Twister Inspection fixture

#### 8.4.2.3 End Plugs

End plugs are fabricated from the same Ultem®1000 plastic as the twister. The end plug is stepped in diameter to allow for the close packed connection of the straws and module end plate (see Fig 8.5). The anode wire passes freely through the end plug with the alignment of the wire being controlled by the adjacent twister. The end plug serves the following functions. It provides the structural connection of the straws to the module end plate. It acts as an insulator between the anode wire and the grounded end plate. It presents a restriction in gas flow to provide for balanced flow among all straws in a module. The ends of the end plugs are tapered to assist passage of the anode wire and lead wire as it is blown through the straw during wire stringing.

The prototype end plugs have been machined. The lower tolerance of the end plug may permit the production parts to be fabricated by injection molding. Ultem is an injection moldable thermoplastic. Molding issues such as mold part lines and mold release agents will need to be investigated before a decision about molding of the end plugs can be made.

#### 8.4.2.4 Module End Plate

The module end plates are made from aluminum alloy. The material was selected for machining properties and weight. In prototypes, no problems have been encountered in maintaining electrical contact with the aluminum end plate. The left and right end plates of a module are mirror images of one another. The end plate has four tapped holes and two precision holes that are used to mount and align the module to the half-view frame. The front face of the end plate has a recessed pocket where the tips of the end plugs extend.



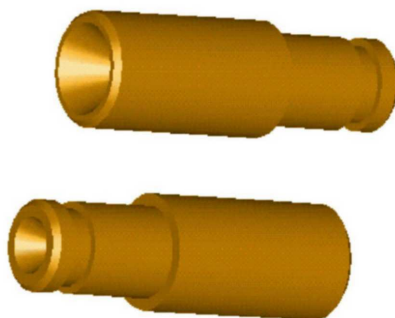


Figure 8.5: Endplugs

The module end plates for stations 1 and 2 are different from all other end plates (see Fig 8.6). Because of space constraints within the vertex magnet, the ends of the half-view frames of the U and V views must be  $11.3^\circ$  from perpendicular with the axis of the straws. To accommodate this angle, the module end plate design is modified. The holes for the end plugs are at an angle of  $11.3^\circ$  from perpendicular and the back face of the end plate is shingled. The shingled face provides a surface that is perpendicular to the end of the straw and the shoulder of the end plug.

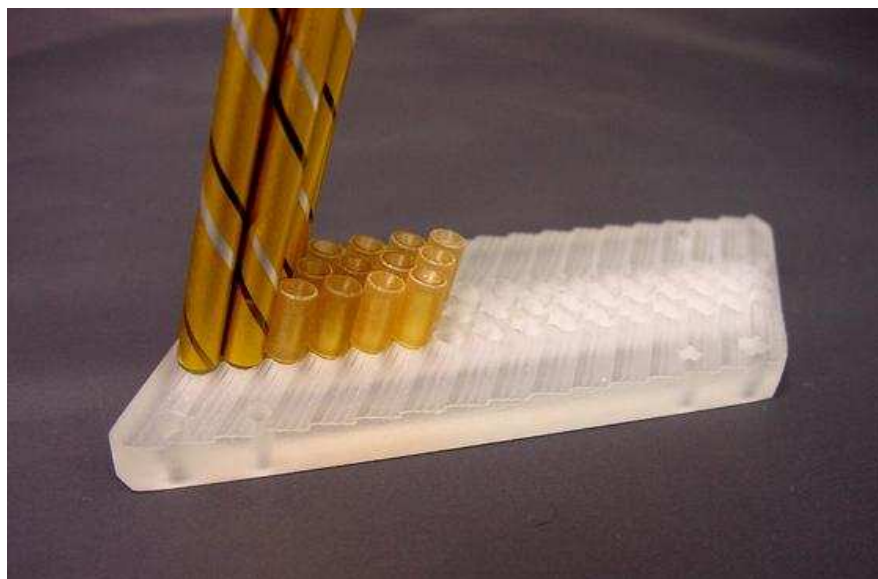


Figure 8.6: Endplate for stations 1 and 2



### 8.4.3 Half-view frame description

The half-view frame is the structure that holds and aligns the modules for one view of a station. The half-view frame designs for stations 3,4,5 and 6 are very similar and scale in height and width for the coverage of the station. The half-view frame designs for stations 1 and 2 are similar to 3-6 except that the long and short sides attach at  $11.3^\circ$  from perpendicular. Station 7 has a different design based on super-modules (see section 8.4.6).

The straw modules are attached to the short sides of the half-view frame. The short sides are made from aluminum extrusions. They contain the front-end readout electronics. They also contain internal channels for cooling the electronics and maintaining the frame at a constant temperature to achieve the required dimensional stability. The chamber gas is distributed to the straw modules through passages in the frame. Fig. 8.7 shows a detail of the modules installed in a half-view frame.

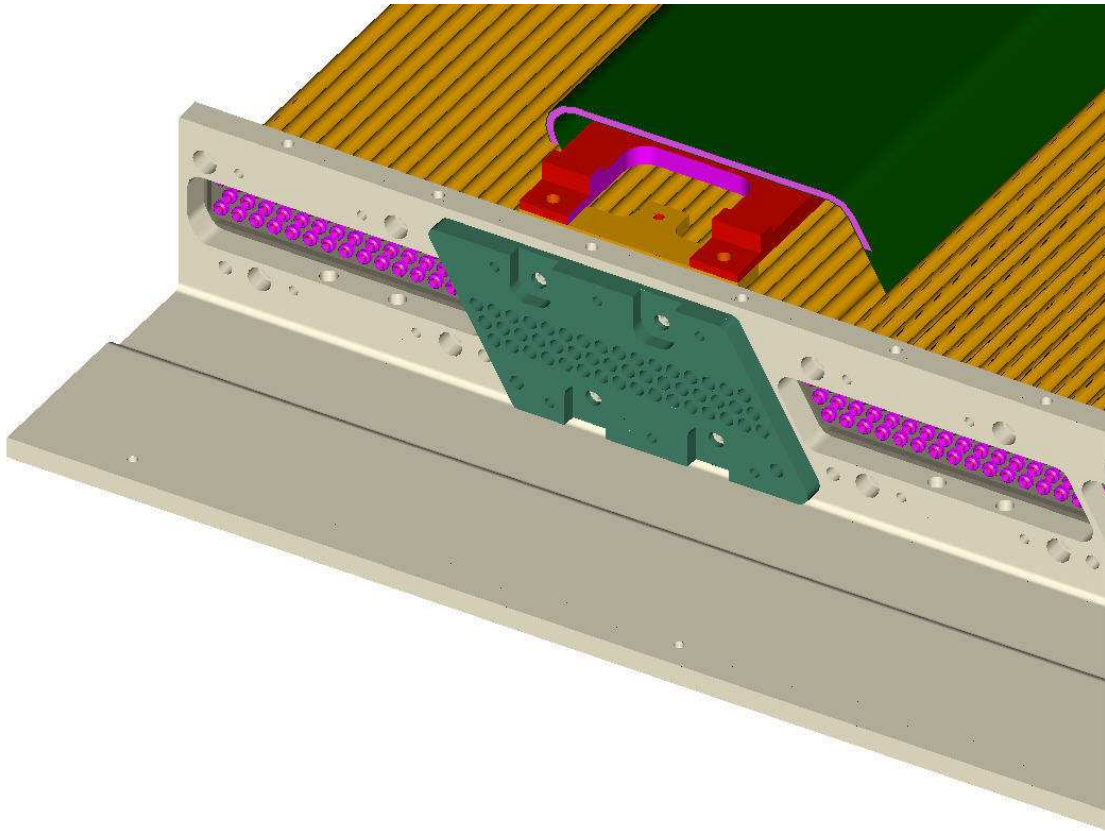


Figure 8.7: Detail of modules installed in half-view frame

The half-view frame holds the tension in the straws. The long sides of the frame act as columns to react the tension load of the straws. The side closest to the particle beam is made from carbon fiber reinforced plastic (CFRP) in order to minimize material. The side away

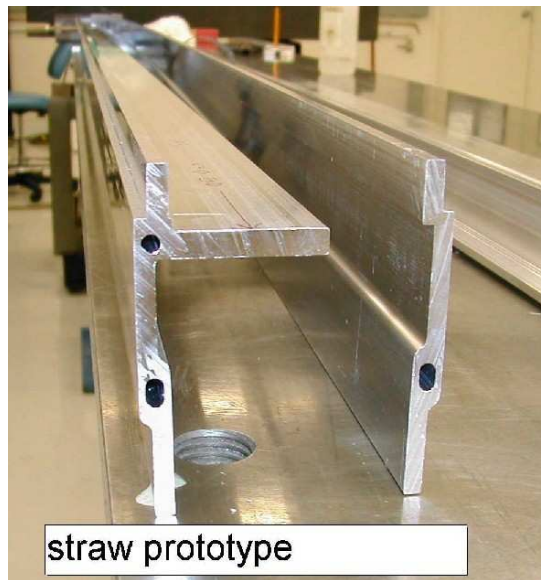


Figure 8.8: Extrusions for half-view frame

from the beam is made from aluminum. The frame also supports wires that are attached to the straws at intermediate locations along the length of the straws. These wires maintain the lateral alignment of the straws.

#### 8.4.4 Half-view frame components

##### 8.4.4.1 End Extrusions

The short sides of the half-view frame are made from aluminum extrusions. Aluminum extrusions were chosen because it is an economical method for producing the structural shape that fits the space constraints. The use of an extrusion also allow the cooling and gas to be supplied with passages incorporated into the structural shape (see Fig 8.8).

Prototype extrusions were obtained to verify that the required structural shape could be manufactured with internal passages. The prototype extrusions were also used to verify that the straightness and twist tolerances required for the half-view frames could be achieved. Inspections of sample extrusions confirm that the critical faces of the extrusion can be produced flat without requiring any additional fabrication operations. Not all extrusions are flat along the entire length but all have flat sections that can be used for the smaller stations. We expect that production extrusions will require inspection and sorting to select the appropriate section for the size of the half-view frame (see Fig 8.9).

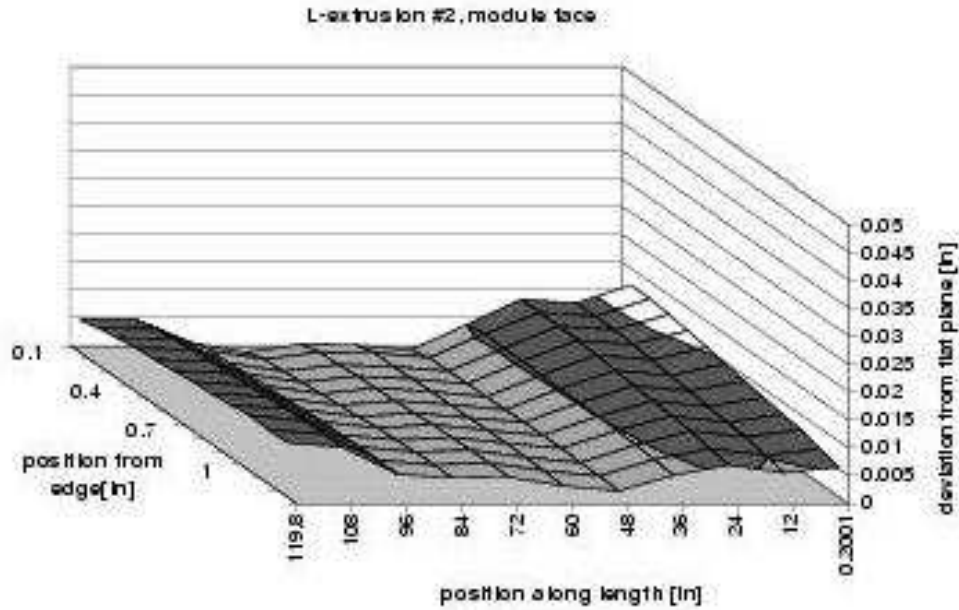


Figure 8.9: Flatness measurements of extrusions

#### 8.4.4.2 Extrusion Machining

The ends of the half-view frame are made from segments of the extrusions that have been machined with the features for mounting the straw modules (see Fig 8.10). The features are a repeating pattern for each module. The features include a parallelogram shaped cutout for accessing the ends of the straws, pinholes for aligning the module, mounting holes for the module end-plate and wire tension plate (anode plate). In addition cross-drilled holes connect the gas supply passage of the extrusion with each module. Module-to-module spacing is controlled by the alignment pinholes of the machined extrusion and corresponding holes in the module end-plates.

#### 8.4.4.3 Half-View Frame Deflection

The most significant load on the half-view frames is a result of the tension of the straws and anode wires. The tension load from each module is approximately 12 kg and that leads to a distributed load on the end extrusions of approximately 1.8 kg/cm. The deflections of the station 3 and station 6 half-view frames have been analyzed by finite element methods (see Fig 8.11).

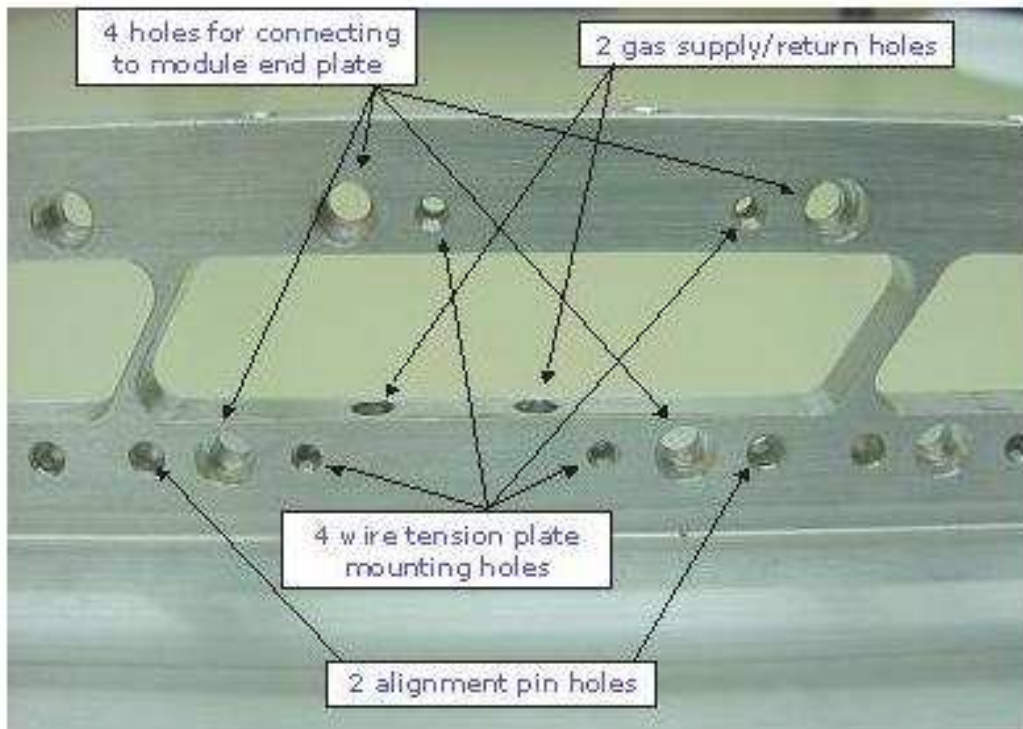


Figure 8.10: Extrusion showing machined holes

The deflection at the middle of the chamber for station 6 was determined to be 0.5 mm. Straws tensioned to 200 g will stretch approximately 3.1 mm. Without compensation the tension in the straws in the middle of the half-view would be approximately 32% less than the tension in the straws near the ends. Thus some compensation method such as shims will likely be used to assure a more balanced tension among all the straws in a half-view. The anode wire for station 6 stretches approximately 5.8 mm and thus the wires near the middle would lose approximately 17% of their tension with the deflection of the extrusion. It has not been determined whether any compensation to maintain uniform wire tension is required.

#### 8.4.4.4 Half-View Frame Strut

The load from the straw and wire tension on the extrusion is reacted by two struts that hold the extrusions apart. The design of the inner strut must be optimized so that it can reliably carry the compressive load with minimum material. The critical buckling load must have a sufficient safety factor to assure that any small imperfections in the shape or material of the strut do not lead to elastic buckling. Initially a strut design was investigated that would allow a standard module to be assembled after the strut was connected to the half-view

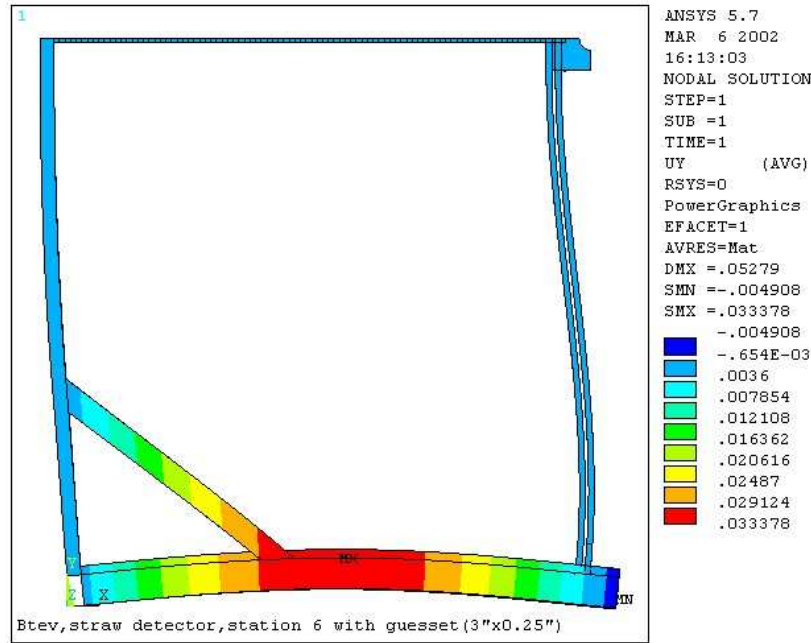


Figure 8.11: Finite element analysis of deflection of straw half-view frame

frame. This assembly goal required a C-shaped strut that allowed a module to slide through the open side of the C. However, an open section like a C-shape is not torsionally stiff and is not able to react the tension of the straws without excessive twisting. Two alternate design options are being developed. The first option involves a closed section in the shape of a parallelogram so that one straw module can fit inside. The strut shape would allow a standard module to be slid inside before assembling the strut and module into the half-view frame. The second option is structurally more efficient but requires a special straw module that is assembled as part of the strut when the strut is constructed. This second option is similar to the module for the silicon support described in section 8.4.5.

Two prototype struts of the first option type were tested until failure under compressive loads. The prototypes are considerably shorter than the full length required and therefore test the section design with regard to local strength. The first prototype had a length of 10.5" and failed at 610 lbs. The second prototype with a slightly modified design was 14" long and failed at 916 lbs. The expected load at station 6 is 224 lbs. A cross section of the second prototype is shown in Fig. 8.12. More details can be found in a BTeV internal document[2].

#### 8.4.4.5 Center Manifold

To provide clearance for the beam pipe the inner-most module of each half-view frame is interrupted near the beam pipe. One side of the half-length module connects to the center



Figure 8.12: Cross section of prototype carbon fiber strut

manifold, which is attached to the middle of the half-view frame strut. The center manifold serves two functions. First it provides the tension connection between the two half-length manifolds to carry the load of the straws and anode wires from one half-length module to the other half-length module. Second, it provides the flow path for chamber gas from one half-length module to the other. The center manifold is shown in Fig. 8.13.



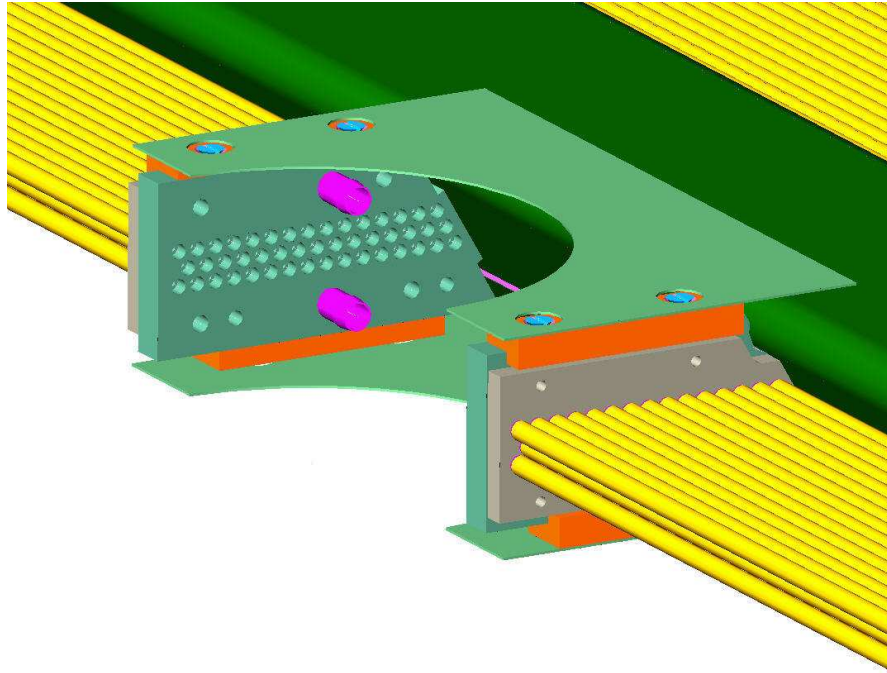


Figure 8.13: Carbon Fiber Center Manifold

### 8.4.5 Special Module for Forward Silicon support

A special module (MOX) that replaces the 2 modules that surround the beam-pipe in the X-view has been designed by INFN Frascati to support the forward silicon planes at each station. It is shown in Fig. 8.14. The straws in this module are embedded in rohacell so they are kept straight without needing to be under tension. The rohacell is surrounded by a carbon fiber shell. A carbon fiber disk to support the forward silicon is attached to the module shell.

Fig. 8.15 shows a detail of this module around the beam-pipe. The straw tubes are glued to the end plate as done for the other modules. However the glue must meet less stringent requirements than the glue used on other modules, since in this part of the detector neither electrical conduction (wire is deadened few centimeters from the endplate on the beam side to limit rate) nor mechanical tension on the straws is required. The main function of this glue is therefore that of sealing, and a wide variety of options are available.

Since no tension is applied to the straws of the M0X, this end plate can be made of very light material such as polyimide, etc.

Wires are pinned to the anode pinning plate. In Fig. 8.15 the anode pinning plate is cut out so that it is possible to see the straw endplate described above. The anode pinning plate is designed to withstand the tension of 98 wires at 50g per wire. This plate has to be gas tight. The gas flowing from the upper half of the M0X is collected in the gap between the two plates described above, will flow to the lower gas gap through low-Z tubing, and then to the lower half of M0X.

The total material in the assembly is expected to be approximately 0.7% of a radiation length. Initial studies of the deformation of the module under the weight of the silicon strip assembly indicate that this is acceptable. A more detailed finite element analysis will be done soon.

Deformations of the special module will be monitored in real-time by use of Fiber Bragg Grating(FBG) sensors[3]. FBG sensors will be embedded in the carbon fiber structure and will provide monitoring of straws and silicon detector positions[4]. The FBG sensors will also be adopted for accurate monitoring of the Pixel detector supporting structure and will thus provide a highly reliable monitoring technique for the overall geometry of the forward tracking detectors.

### 8.4.6 Station 7

Station 7 of the Straw Detector will be constructed in super-modules to enable it to be installed around the beam-pipe in the restricted space between the RICH and the ECAL. Each view is composed of 8 super-modules assembled together by a light-weight channel type outer frame. Each super-module is approximately 400 cm x 5 cm x 43 cm, with an aluminum extrusion at each end for mounting 6 modules. The super-module shell frame is a bridge that connects the two aluminum extrusions and is made of CFRP with a thickness of 0.5 mm. Each super-module weighs about 10 lbs. and can be handled individually for installation.



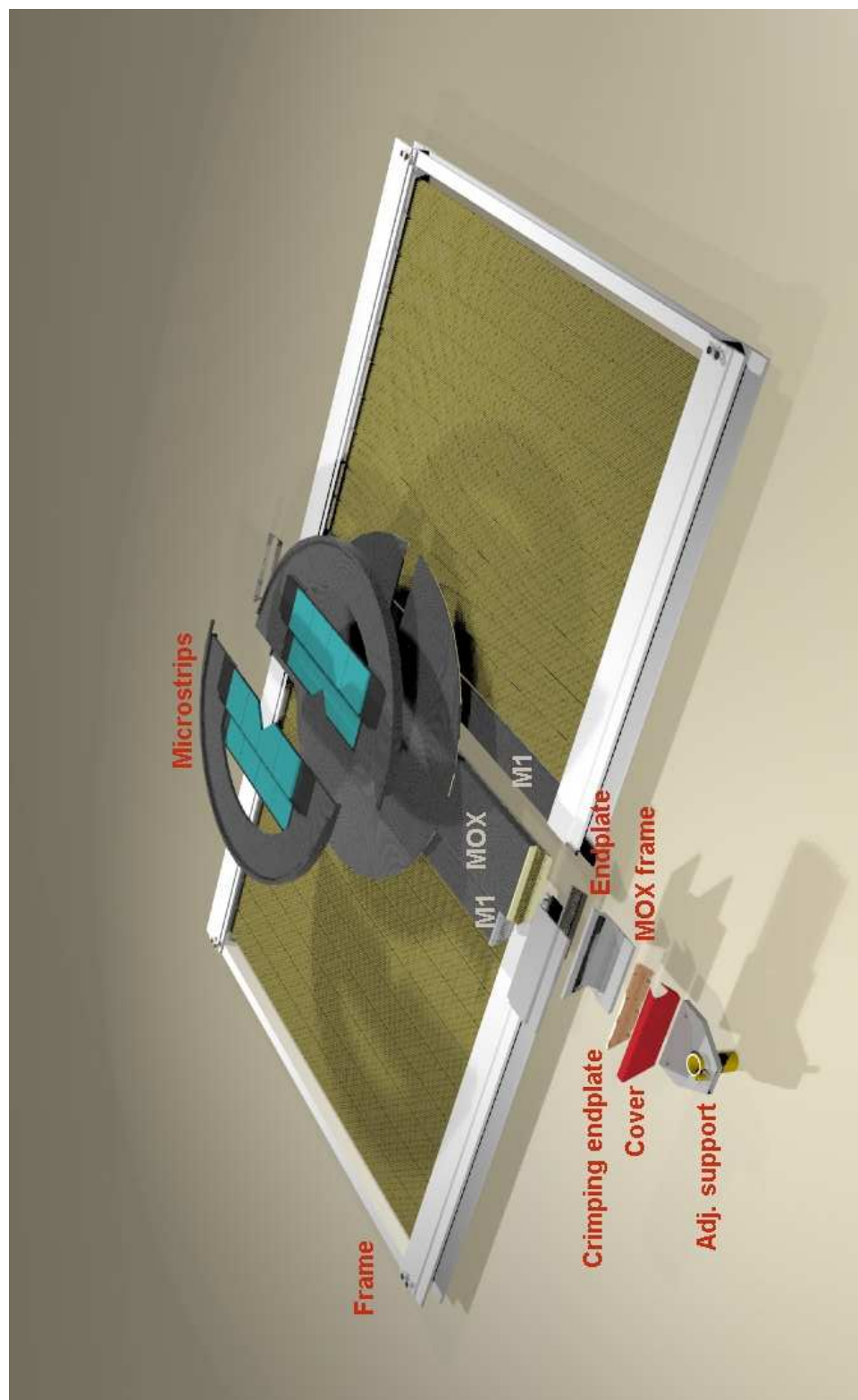


Figure 8.14: Special module to support forward silicon



Figure 8.15: Detail of the MOX around the beam-pipe

In addition to connecting the two aluminum extrusions, the super-module must support a force of about 12 Kg/module due to the tension in the straws and wires.

Four fiber sheets form a hollow tube type frame, as shown in Fig 8.16. The two faces of the major plane of the frame have 10 holes 28 cm in diameter to provide access to the straws and to reduce the weight of the frame.

To understand the mechanical behavior of the super-module frame, the engineering group developed finite element models to simulate the behavior of the frame under various working conditions. It was found that the maximum deflection in the major plane of the frame is about 0.0076 mm and the maximum deflection in the perpendicular direction is 0.0069 mm. Using the Linear Buckling method it was found that the super-module will not fail until the axial load increases from 12 Kg/module to 86 Kg/module.

#### 8.4.7 Beam-Line Supports

The straw half-views for stations 1-6 will be assembled into full stations as described in section 8.8.3. Stations 1-3 will be mounted directly to the dipole magnet at four corners with a kinematic support system. Station 4 will be attached to the magnet flux plate. Fig 8.17 shows the support mechanism for Station 3.

For Station 7 each view will be mounted independently. The supports will be cantilevered off the toroid magnets, see Fig 8.18.

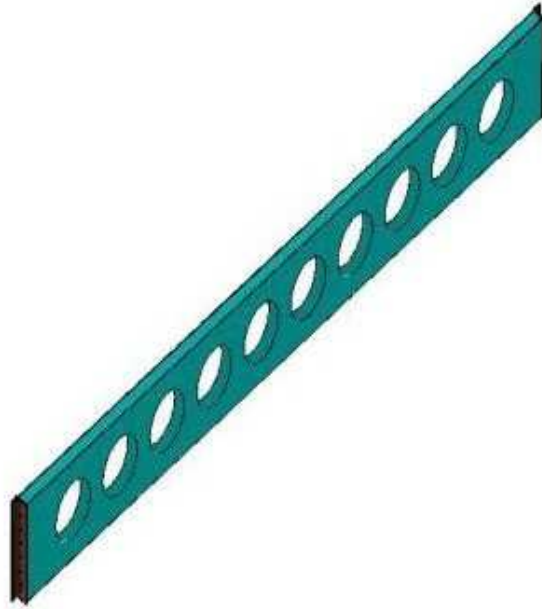


Figure 8.16: Station 7 super-module

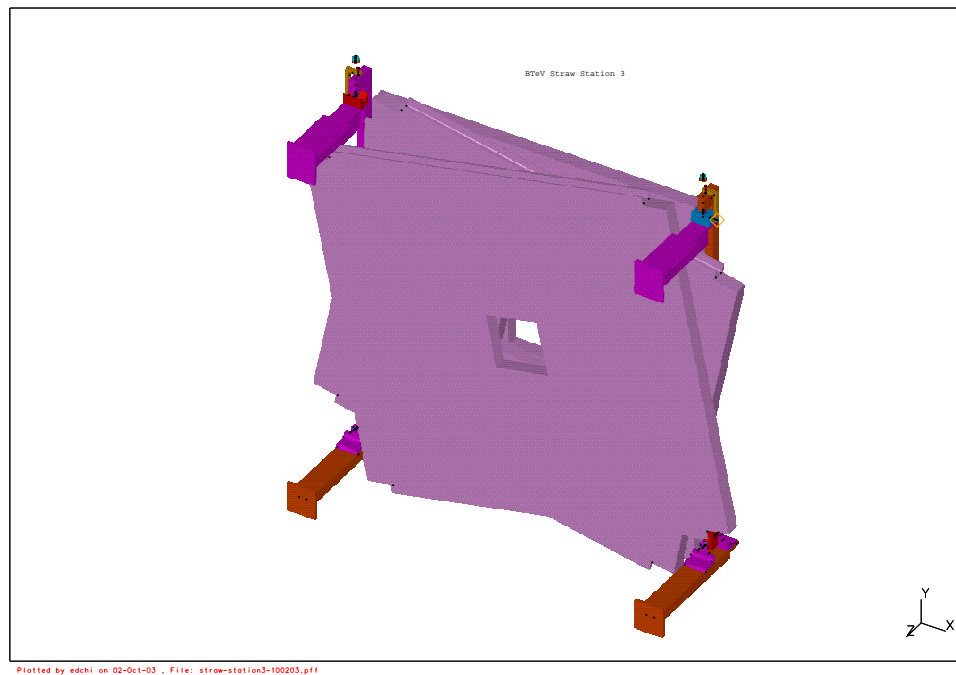


Figure 8.17: Station 3 support structure

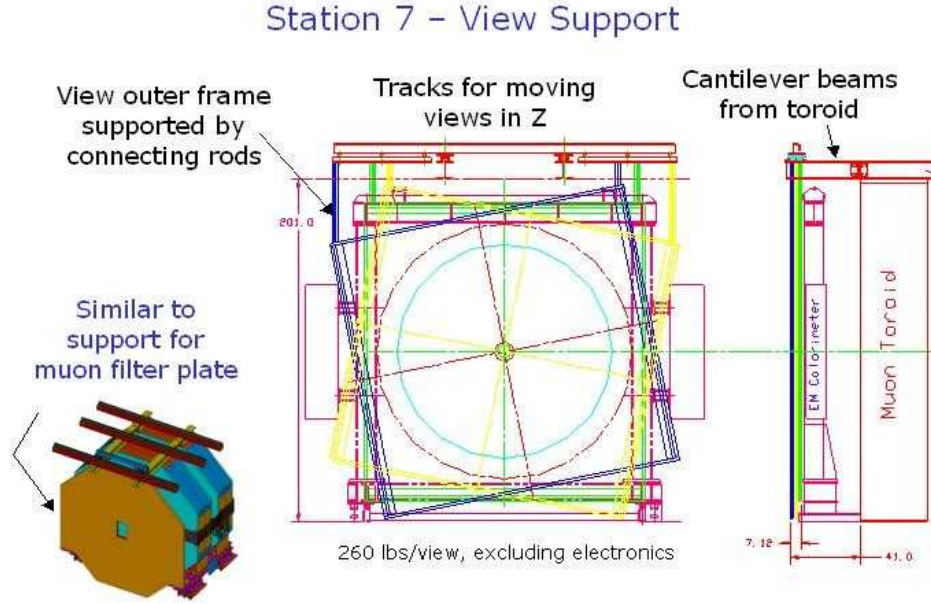


Figure 8.18: Station 7 support structure

Table 8.2: Material budget of Straw Chamber

Material	Fraction of $X_0$ /station
Straw walls (kapton + Aluminum)	0.50%
Wires	0.13%
Gas	0.02%
Twisters	0.04%
Carbon Fiber struts	0.09%
Mylar windows	0.15%
Total	0.93%

#### 8.4.8 Material Budget

The total amount of material per station is about 0.9% of a radiation length averaged over the active region outside the central gas manifold and inside the frame. The largest fraction comes from the kapton. Details are shown in Table 8.2. The material in the center gas manifold region is the manifold itself plus tension plates to hold the wires. The average material in this region is about 3%  $X_0$ .

## 8.5 Calibration, Monitoring and Control Systems

### 8.5.1 Straw Gas System

For BTeV straw cells we plan to determine the gas mixture which optimizes drift time resolution, efficiency, and stability of operation.

Closely associated with the choice of gas mixture will be the determination of optimal gas gain at which to operate the detector. Higher values of gas gain are known to introduce space-charge effects which can lead to significant non-linearities in the straw response. The probability that self-limiting streamer discharges occur rises quickly with gas gain. This in turn leads to an overloading of the front-end electronics and introduces deadtime in the amplifier/shaper/discriminator circuitry. The baseline choice of gas is an 80:20 mixture of Argon-CO<sub>2</sub>. The drift speed is adequate, being about 50  $\mu\text{m}/\text{ns}$  giving a maximum drift time of about 40 ns for a 4 mm diameter straw. An advantage of Argon-CO<sub>2</sub> is that it does not have deposits due to polymerization which occurs with hydrocarbon gases in a high rate environment. Aging in Argon-CO<sub>2</sub> is thought to be mostly due to contamination of the gas. To minimize this we will use stainless steel tubing and test all gas before it is used in the straw chambers. It is particularly important to remove all trace of sulfur compounds if we use copper cathodes. We plan to continuously monitor the gas gain, drift speed and gas composition.

The design of the BTeV straw chambers from a gas perspective has been evaluated, and a system to supply these chambers has been designed. The flow distribution was studied with a three-dimensional ANSYS diffusion finite element model. The detailed results are given in a BTeV internal document[5]. Within a module of 48 straws, the flow distribution varies about 15% which is adequate. The flow between modules will be balanced by placing a restriction at the inlet of each straw module, which can be accomplished by reducing the diameter of the two flow paths feeding each module, or placing a sintered metal orifice in the flow path. The gas flow distribution to an 8-module half-view is shown in Fig 8.19. The gas supply system is based upon the E815 Argon-Ethane flammable gas mixing system. In order to maintain the straws at a stable humidity, each straw half-view will have mylar windows within which we will flow dry nitrogen.

#### 8.5.1.1 Gas Monitoring

We intend to monitor the straw chamber fill gas for gas gain determination, pollutant level and drift velocity determination.

Accurate knowledge of the gas gain is necessary to set a working voltage for the straw anodes that optimizes overall straw performance (i.e., optimizes detection efficiency and minimizes likelihood of after pulsing and streamer generation). We intend to measure the gas gain of the straw fill gas by irradiating a small number of 4 mm diameter straws with an  $^{55}\text{Fe}$  source and then pulse height analyzing the resulting straw output signal to monitor the peak position corresponding to an energy deposition of 5.9 keV. Depending on the magnitude of the gas gain variations, the high voltage applied to the straw anodes can then be altered in

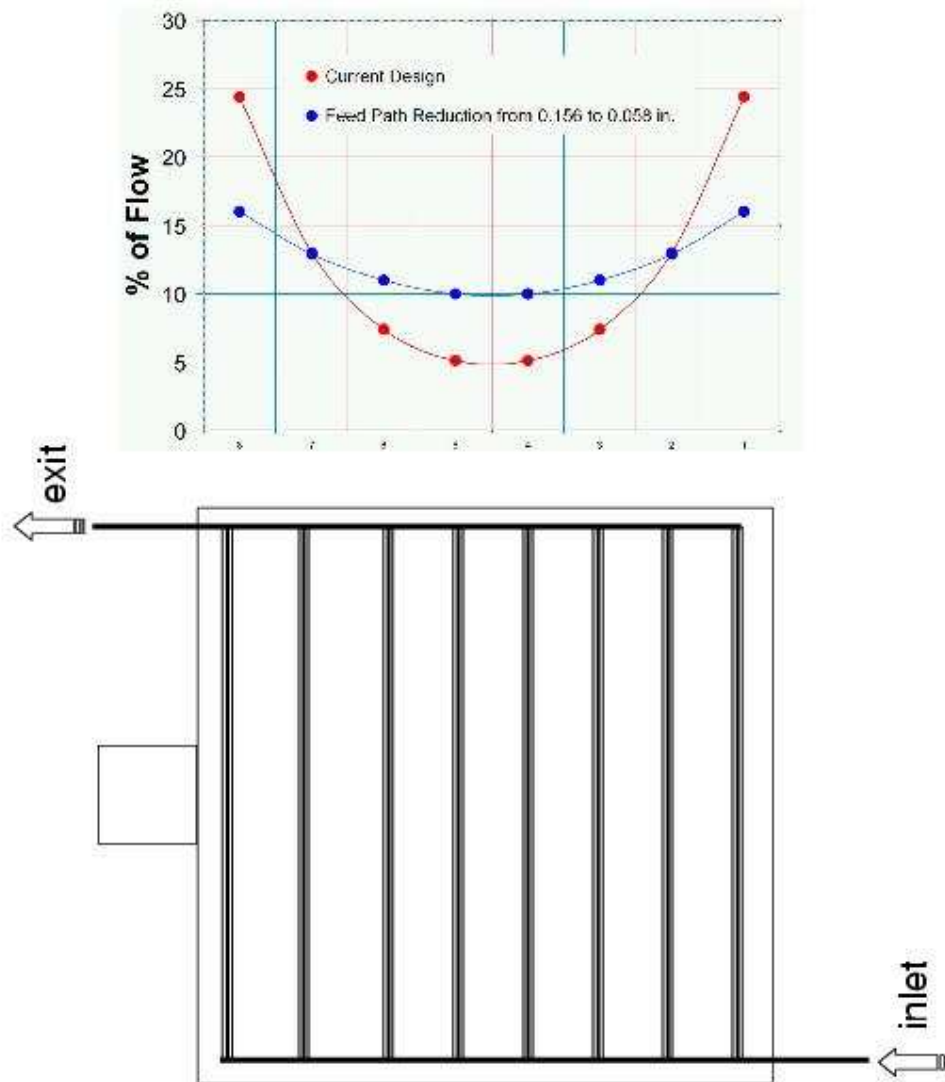


Figure 8.19: Gas Flow

a sensible fashion. The monitoring straw tubes will be built from hardware used to construct the actual tracking chamber and the readout electronics will be non-exotic.

The pollutant level of the straw chamber fill gas will be measured by feeding the exhaust gas from the straw stations into a mass spectrometer/gas chromatograph. (The fill gas will also be qualified before it is admitted to the chambers.) This diagnostic information will be coupled with the drift velocity monitoring measurement to help maximize tracker performance and to help diagnose problems like low or time-dependent detection efficiency. Precise details of the system are not yet fixed since the requisite pollutant sensitivity and the full spectrum of likely pollutants depend on key details like the choice of fill gas, still undecided at this point.

Prototype work has started on developing a special monitoring chamber that would measure the drift velocity of the straw fill gas. Accurate knowledge of the electronic drift speed is required for optimal straw tracking resolution. Light from a N<sub>2</sub> laser is directed into a special box-shaped chamber that would measure the electron drift speed in a uniform electric field. The laser permits the straightforward generation of a strobe to mark the start of the electrons' drift and the chamber would be filled with the exhaust gas from the straw stations, ensuring the test chamber uses the same gas as the actual tracking chambers. Preliminary estimates show that a fractional accuracy of 1% in the electron drift speed is practicable, consistent with our requirements. The exact number of test chambers to be used is not yet fixed.

## 8.5.2 Water Cooling System

The Straw Detector frames are cooled by flowing water through the aluminum extrusions. Each U-shaped extrusion has 2 cooling channels.

The cooling system will have two 50 gpm water pumps outside the collision hall. Normally one pump will be running and the other will serve as a backup. Above the pumps will be a water expansion tank to supply a positive pressure to the pumps and to vent air from the system. The cooling system will be a closed loop with no copper or copper alloy materials to avoid galvanic corrosion in the aluminum extrusions. The return flow will pass through a heat exchanger in which chilled water will flow to keep the straw cooling water at the desired temperature. The straw chambers will operate at the ambient temperature of the collision hall.

In the collision hall there will be one main supply and one main return water header on each side of the detector. The cooling channels in the aluminum extrusions will connect to these headers. Each half station will have a manual valve to balance the flow between stations.

The heat load, flow rates and temperature differences are shown in Table 8.3.

Table 8.3: Heat Load and Flow rates in Straw Detector Cooling System

Station	Power/station (W)	Flow rate/station for 0.3C temp rise (L/min)	Pressure drop in cooling channel (Bars)	Temp difference Extrusion-water (C)
1	184	9.7	0.005	0.57
2	276	13.7	0.013	0.45
3	415	21.6	0.042	0.35
4	599	30.6	0.108	0.27
5	691	35.1	0.156	0.24
6	783	39.6	0.217	0.22

### 8.5.3 Environmental Control and Monitoring

In order to keep the straws straight it is necessary to keep them from sagging due to changes in temperature and humidity. Relative humidity will be kept close to 0% by flowing dry nitrogen in a closed volume around each half-view. We require that the temperature in the C0 hall to be stable to  $\pm 1^\circ\text{C}$ , though there may be several degrees temperature difference between the top and bottom of the hall. The frames of the straw half-views will have the temperature controlled by flowing chilled water through them.

Each half-view will have a temperature and humidity sensor and the high voltage will be turned off if either is out a pre-determined acceptable range. Sensirion manufactures a compact, inexpensive line of chips (SHTxx) that would satisfy our requirements for temperature and humidity sensors.

## 8.6 Performance

### 8.6.1 Resolution

The momentum resolution as a function of track momentum is shown in Fig 8.20. We expect to have a single straw position resolution of  $150\mu\text{m}$ . We have constructed a two module prototype detector which is currently in the test beam. Fig. 8.21 shows a test beam particle passing through the straw prototype and wire chambers upstream and downstream. First results from the test beam data are described in Section 8.9.7.

### 8.6.2 Occupancy and Tracking efficiency

If BTeV runs with a 396 nsec bunch spacing, the occupancies in the the Straw detector will be about three times higher than was expected at the time of the BTeV proposal. This leads us to consider whether it would be advantageous to increase the size of the forward silicon strip planes ie. increase the size of the “dead” region of the straw detector. There will be a



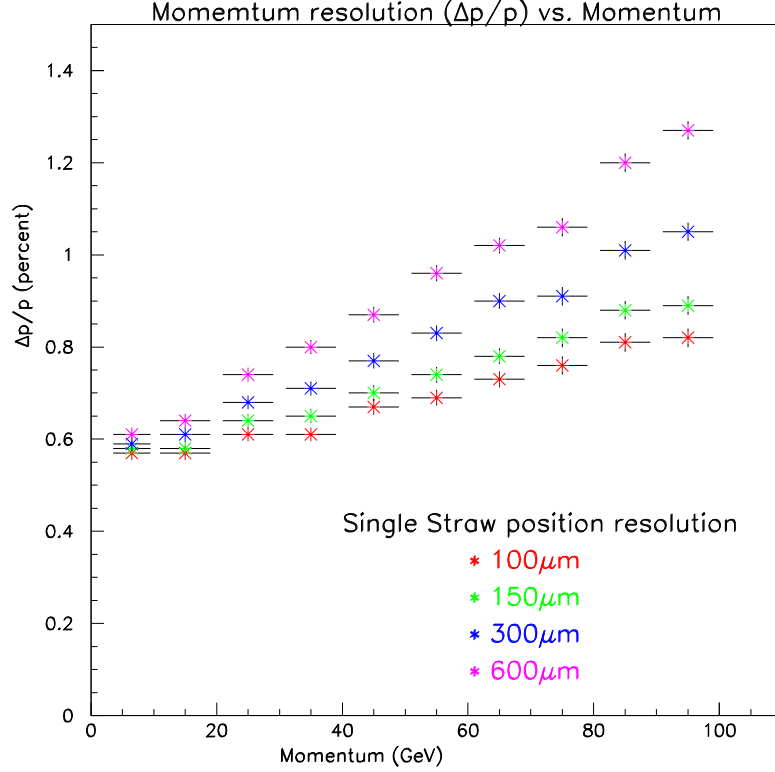


Figure 8.20: Momentum resolution as a function of track momentum, for tracks that pass through at least 6 forward tracking stations

compromise between the reduced occupancy and the increased material which leads to more multiple scattering.

The baseline design has silicon planes 27cm x 27cm. We have studied occupancies and tracking efficiencies comparing this baseline size with an alternative design having silicon planes 40cm x 40cm.

Figure 8.22 shows the occupancy of the Straw detector at Station 6 for a B interaction accompanied by a varying number of minimum bias interactions for the two different size silicon planes. The occupancy in the center of the detector drops by about 25% with the larger silicon planes.

The tracking efficiency was studied for two cases; firstly for tracks that have hits in at least 4 pixel stations so that a seed track can be found in the pixel region and projected downstream to the forward tracking stations, and secondly for tracks such as those from the decay of  $K_s$ s or  $\Lambda^0$ s that do not have enough pixel hits to seed the track in the pixel region. The efficiency for pixel seeded tracks with momentum greater than 3 GeV and with hits in

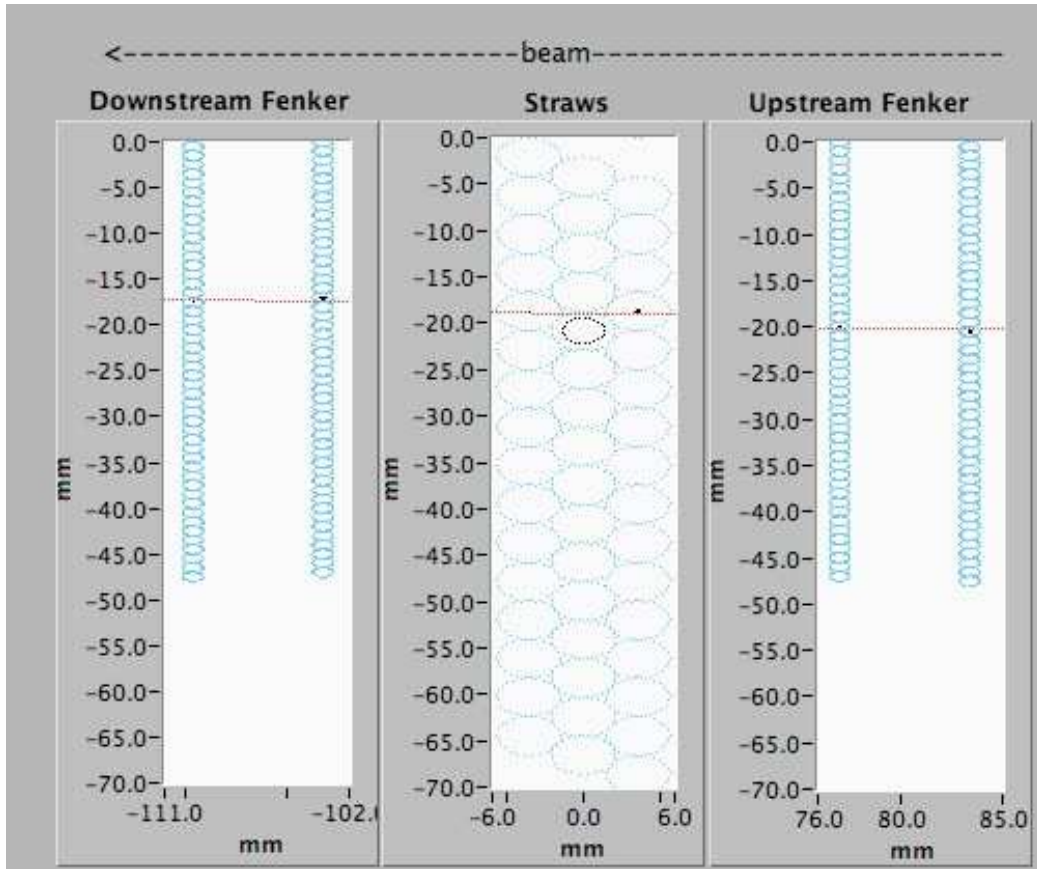


Figure 8.21: Track from test beam passing through straw prototype detector and wire chambers

at least four downstream stations drops from 98% at 2 interactions/crossing to 95% at 9 interactions/crossing but there is no improvement with larger silicon planes.

For tracks without pixel hits we also see no improvement in efficiency with larger silicon planes, but there is a reduction in the number of ghost tracks. We believe that increasing the size of the silicon planes does not give enough improvement in performance to justify the increase in cost.

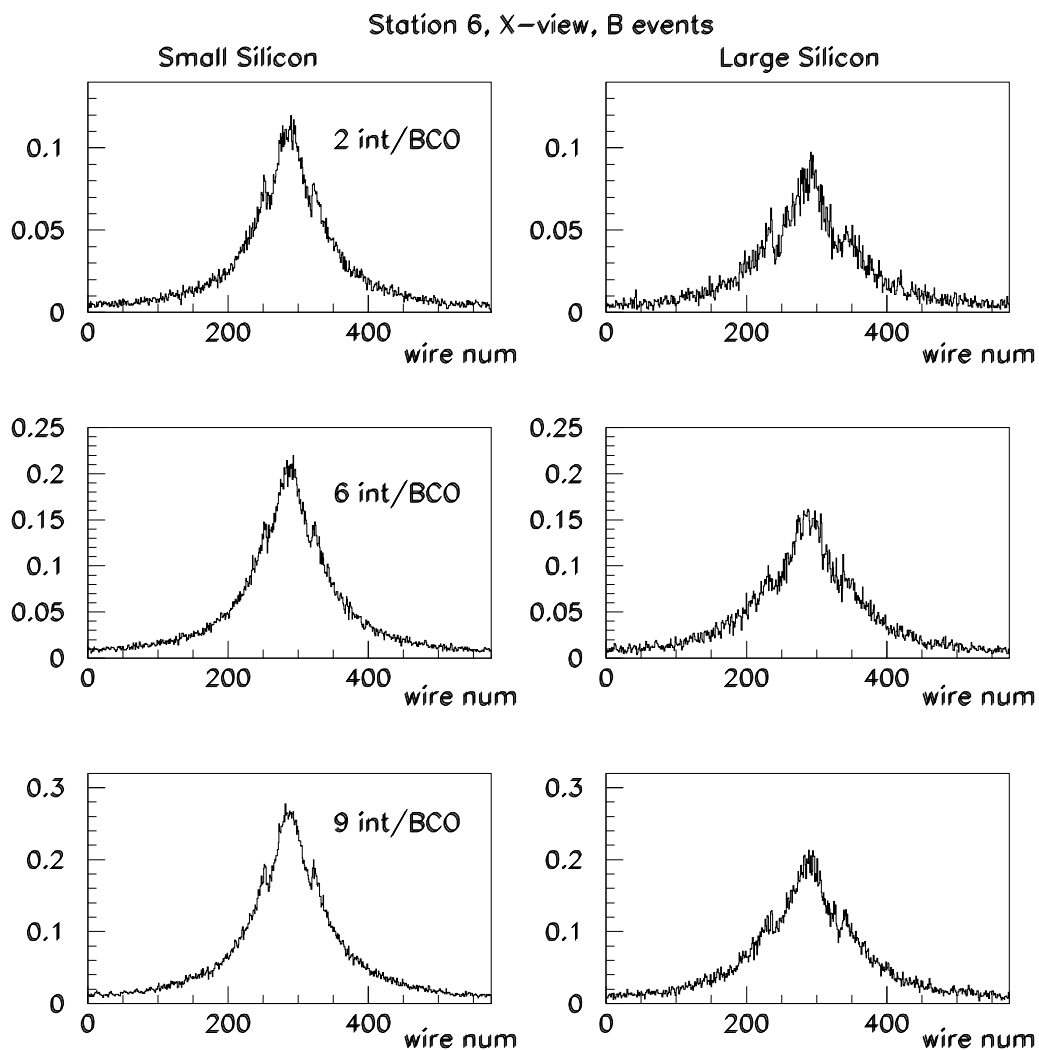


Figure 8.22: Occupancy of Straw Station 6, X-view for a B interaction plus 2,6 or 9 minimum bias interactions. Left side: Dead area 27x27 cm; Right side: dead area 40x40 cm

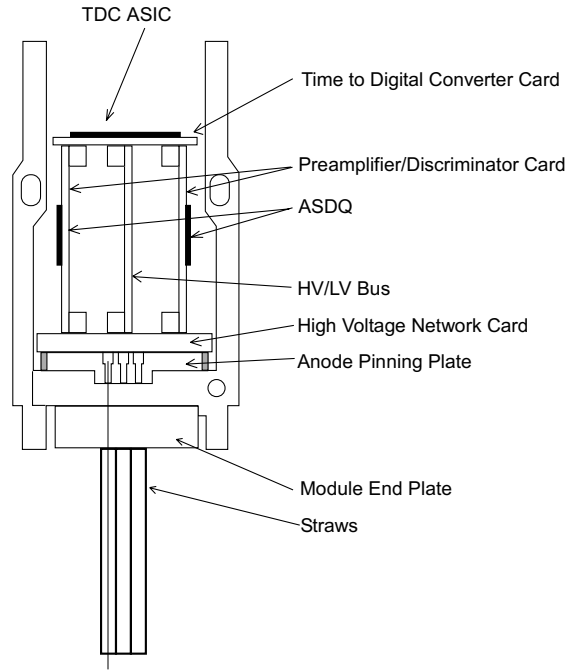


Figure 8.23: Schematic view of Electronics Packaging inside Straw Frame. The ASDQ's are located on the side nearest the channel to facilitate cooling (liquid cooling channels are located in the channel sides).

## 8.7 Front-End Electronics

### 8.7.1 Introduction

The Straw Front-End Electronics is composed of 6 blocks. They are the Anode Pinning Plate, the High Voltage Network Card, the High Voltage/Low Voltage Bus, the Preamplifier/Discriminator Card, the Time to Digital Converter Card, and the daughter card of the Data Combiner Board. The following description is based upon the modularity of the straw detector, with a single module containing 48 straws. Each straw will be electrically divided by an insulating-glass bead. With this setup, we read out both sides of a straw. Fig 8.23 shows a conceptual view on how the electronics are architecturally arranged in the channel of a straw frame.

### 8.7.2 Anode Pinning Plate (APP)

The APP (Fig 8.24) is used to keep the  $25\ \mu\text{m}$  diameter, gold-plated tungsten anode wire at a nominal tension of 50 grams. It is the same shape as the module end-plate, made of Noryl plastic, with brass eyelets inserted into the 48 holes. During the wire stringing process, the anode wire is threaded through the eyelets, and captured by a tapered brass pin, which

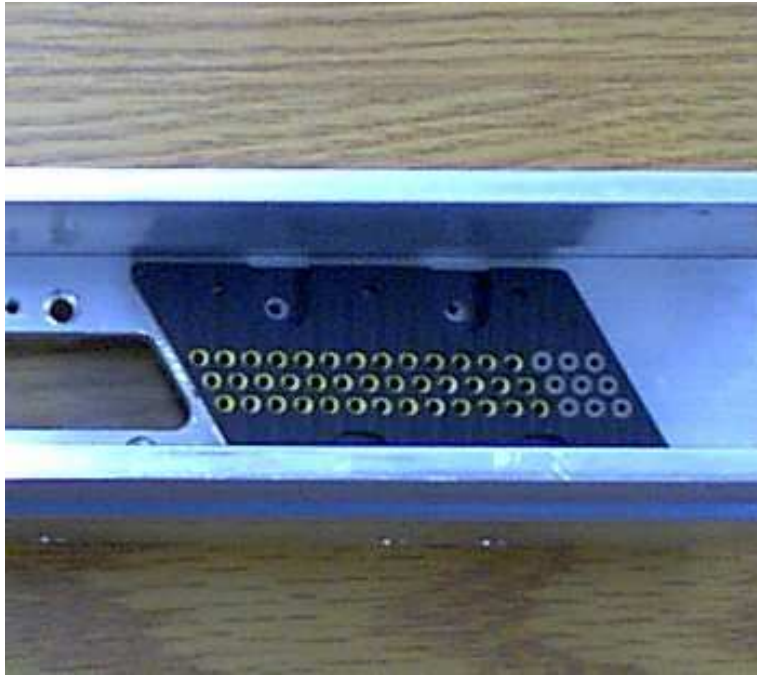


Figure 8.24: Anode Pinning Block shown in Straw Frame. The brass eyelets can be seen in the majority of the holes, while the conductive elastomer (gray color) can be seen in the right three rows.

just fits into the inner diameter of the brass eyelet. We have been monitoring the holding capability of this system for over a year with no apparent problem in its ability to hold the wire tension.

The depth of the holes in the APP insures that the heads of the brass pins are significantly lower than the APP top surface. In order to make electrical contact to the anode wire, conductive elastomer inserts (cylindrical in shape with a coaxial hole to clear the head of the brass pin) are inserted over the brass pin and into the APP hole. Electrical contact is made between the upper face of the brass eyelet and the lower face of the conductive elastomer. The conductive elastomer is a snug fit into the hole. The height of the conductive elastomer is just short of reaching the top of the hole. Contact with this surface is made by conducting pads on the High Voltage Network Card.

### 8.7.3 High Voltage Network Card (HVNC)

The High Voltage Network Card is the means to deliver the high voltage to the anode, and to bring the straw signal to the Preamplifier/Discriminator Card. The Straw Detector is operated with a positive high voltage on the anode and the straw cathode at ground. This is done for two reasons: firstly for safety as the cathodes at negative high voltage might pose a safety hazard during construction and testing, and secondly because we want the capability

to disconnect the high voltage from a single straw in case of breakdown. Since the straw cathodes are closely packed, this might be quite difficult to achieve. With the high voltage on the anode, it can be simply disconnected from the HV by cutting a trace on the HVNC.

Due to the close packing of the straws, the desire to disable a single wire, and the close proximity of high voltage traces to signal traces, the printed circuit board layout demands a multi-layer board. The side of the HVNC closest to the APP has 48 pads which protrude enough to make contact with the 48 conductive elastomers of the APP. Each of the protruding pads has a via to the inner board layer. In this layer the traces are routed to the top of the HVNC in a manner to enable the layout of the pads for the load resistors, blocking capacitors, and connectors which carry the straw signals to two 24-channel Preamp/Discriminator boards.

Under normal running operations, the case of a broken anode wire would be handled by turning off the HV to the entire 48 channel module. At a later date, when access time to the detector permits, the trace to the load resistors of the broken channel would be cut to disable the wire. Under extraordinary conditions, an attempt to fix a straw channel might be attempted, but most likely only if the particular straw detector has been removed from the experimental hall.

#### **8.7.4 High Voltage/Low Voltage Bus (HVLVB)**

The HVLVB is a single printed circuit board that we will use to bus the high and low voltages to all the modules in a straw half-view frame. The HVLVB connects the high voltage through pins to the HVNC, and low voltage to the TDCC card. Our base plans use a single high voltage channel per straw module. If a wire breaks in a single module, the HV will be turned off for the entire module. It might be more effective to arrange the HV so that a single channel supplies the HV for a single plane in 3 adjacent modules. In that way, a single broken wire will not completely disable the tracking over an entire 3-plane module of straws. The final arrangement of the HV bus will be decided after further study of other possible failure modes of the straw system. However either arrangement should be easily handled in the HVLVB. Both sides of the Straw Chamber will have a HVLVB. At this time we intend that the HV in any one straw will originate from a single HV channel supply. This is to insure that the central anode insulating glass bead will not have to hold off a possible large HV difference caused by turn-on or turn-off lag in the power supplies.

#### **8.7.5 Preamplifier/Discriminator Card (PDC)**

We are currently planning to use the ASDQ preamplifier/discriminator chip in our PDC card. The ASDQ was developed at the University of Pennsylvania for the CDF Detector at Fermilab[6]. While we do not plan to use the "Q" feature of the ASDQ (a charge measurement) for the straw detector, nevertheless the chip itself adequately meets our requirements of low threshold and robustness. Each PDC will hold three 8-channel ASDQ's, so that each straw module will require two PDC's per side, for a total of four PDC's per straw module.

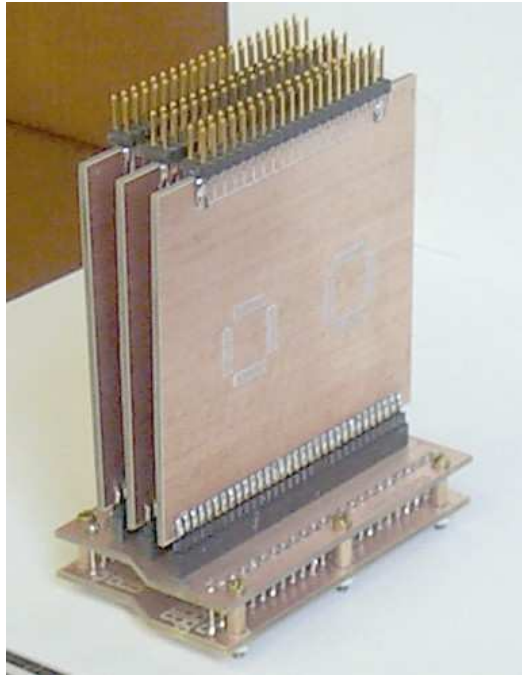


Figure 8.25: Prototype of Preamplifier/Discriminator Card and High Voltage Network Card (H.Powell and W. Stephens, UVA). This shows a prototype version of the 16 channel PDC(2 ASDQ chips/PDC) mounted on a prototype HVNC.

The two PDC's plug into the HVNC with the ASDQ inputs being coupled to the low voltage side of the blocking capacitor. The differential outputs of the ASDQ are sent to the output connector on the PDC. As currently planned, the two PDC's are plugged into the HVNC at a 90 degree angle, similar to that for a prototype 16 channel PDC as shown in Fig 8.25. The Time-to-Digital Converter card straddles the output connectors of the two PDCs. While we are constructing the detector, the Time-to-Digital Converter card will be replaced by a simple connector card so that we will have access to the discriminator outputs for testing and QC. All control and power of the PDC will be supplied from the TDCC card connector.

### 8.7.6 Time to Digital Converter Card (TDCC)

The TDCC card is the control card for the entire module front-end electronics. It receives the clock and control signals from the Data Acquisition System, supplies thresholds for the ASDQ's on the PDC, and performs a time analysis on the ASDQ Discriminator outputs. It is responsible for sending data on every beam crossing, and also controls the calibration of the ASDQ's and the Time to Digital Converter. A strong motivation of the Straw Electronics System design is to minimize the cable plant. The Straw Detectors are large flat detectors. They are relatively thin in order to minimize the longitudinal footprint of the BTeV Detector. This makes it difficult to mechanically support a large number of cables. These cables include

signal, control, high voltage and low voltage cables. The high voltage and low voltage will be distributed internally by a bus to the local module. Due to constraints of available space and conflicts with other detectors, the cabling is planned to run inside of the electronics channel in the straw frame and exit at the outer edge. The design for the TDCC and its component ASIC chips is specifically driven to minimize the number of input control and output data cables. We expect to use two input twisted pair lines and two output twisted pairs line per module side.

### 8.7.7 TDC ASIC

We are undertaking the development of a 48 channel ASIC which will supply the functionality of a Time to Digital Converter to measure the drift time of the tracks in the straws, and at the same time will also give us the interface into the BTeV DAQ system. These two functions will be discussed separately as the "TDC" and the "I/O Interface". There will be one TDC ASIC per TDC card.

#### 8.7.7.1 TDC Requirements

- Time resolution/range: The charged particle tracking requirement for the straw detector is to measure a track position with an rms precision of  $200\text{ }\mu\text{m}$  per straw. For the typical gases and applied high voltage that we plan to use, the electron drift velocity is about  $50\text{ }\mu\text{m/ns}$ . Therefore the  $200\text{ }\mu\text{m}$  precision equates to a timing spread of 4ns rms. For other reasons (which will be discussed in the "I/O Interface section"), we have decided that the time resolution of the TDC is adequately handled by a bit size of 1.65 ns. This bit size itself has a nominal rms spread of 0.5ns. This adds only a negligible amount to the uncertainty of our time measurement. The standard straw size for the BTeV Straw detector is 4mm diameter, so the maximum drift time for an electron is  $\sim 40\text{ ns}$ . The entire drift time is covered by a 5 bit TDC ( 50ns). We are considering a fine/coarse TDC setting which would allow us to double the TDC range, simply to ease the initial setup of the system during the commissioning phase of the experiment. This can be accomplished by either halving the clock speed or alternatively simply doubling the total number of bits by delaying the reception of the timeout pulse.
- Single hit Capability: The straw detector is operated under conditions where the time between beam crossings is longer than the maximum drift times of a track within the straw. Any single track may give an analog signal into the discriminator ranging from 20 ns (track impact parameter near straw edge) up to a signal which is as long as the entire drift time (the case where a track has zero impact parameter to the anode wire, and clusters drift in over the entire radius of the straw). There is no intrinsic way to separate out two tracks from the case of multiple electron clusters from a single track. This means that multi-hit capability is unnecessary. Because a single track will give rise to multiple hits, and since we are only interested in the earliest hit, the TDC will be operated in "start" mode. Only the earliest hit will be recorded by the TDC.



- **Readout Capability:** The TDC is designed to handle beam crossings which occur at a 7.5MHz rate (132ns crossing time). The BTeV DAQ requires that each detector report its data from every crossing into a data buffer. In order to handle this requirement, the TDC will need to sparsify its data, reporting only the channels which have been hit during the particular crossing. In order to achieve this, and to relax the instantaneous bandwidth requirements for the data output link, we plan to include a local FIFO which will average over statistical fluctuations in the data rate. The size of this FIFO is related to the excess bandwidth that our output links will have, and at this time is still under study. Under normal circumstances, the FIFO size will be large enough so that there will be a negligible probability that it will overflow on a 2~3 hr time scale. However occasionally we expect abnormal conditions to arise (e.g. particle spray due to a beam instability, or electronics oscillating). This could cause the FIFO to overflow. In order to handle these cases, we plan to flag and truncate new events when the FIFO reaches 80% of its capacity. When the FIFO depth lowers itself to the 50% occupancy level, new events will again be let into the FIFO input. In this way we should receive a selection of the offending events in order to plan an online fix to the problem (if its origin is due to the detector). Obviously there must be a monitor process running at the upper levels of the online software which is looking for these error occurrences. As mentioned above, our design was for a 132ns crossing time. However it now may be more likely that the crossings will be kept at the 396 ns level (36x36), but with an increase of events per crossing. As far as the electronics are concerned, 396 ns crossing is less difficult than the 132 ns case (a case of fratricide in our single hit TDC as occupancy rates increase), so we anticipate no difficulties with the TDC readout.

## 8.7.8 I/O Interface

### 8.7.8.1 I/O Introduction

The I/O interface is based upon a 7.5 MHz clock (132 ns), which is referenced to the Tevatron 53 MHz RF clock. The Tevatron RF structure has 1113 53 MHz rf buckets, which fill the circumference of the ring. The number 1113 can be factorized into 3, 7, and 53, which represent the RF symmetry of the Tevatron. The 7.5 MHz clock is just the symmetry given by 7 bunch spacing. There are 159 (3\*53) of these ticks around the Tevatron. Beam can in principle be placed in any of the 1113 rf buckets, but typically is placed into the buckets given by the symmetry of the Tevatron and its injector (FNAL Main Injector). Typically 3-fold symmetry is used in the bunch loading scheme, so that the original BTeV running condition includes 3 trains of 36 bunches. Within a given train, the bunches are separated by 132ns. Since the future running may contain a different number of bunches: 3 x12—the current 396 ns spacing, or possibly 3 x 24 (264 ns spacing), it was decided to keep the original 7.5MHz clock requirement, because it could handle any of these beam scenarios. Gaps between trains (i.e. the incomplete filling of every possible "tick") is driven by the need to account for the rise and fall time of the Tevatron Injection Kicker Pulsed Magnets. The control of the TDCC is done on the reception of a command every 132ns. These commands may run from "Start

TDC (and readout when finished)", to "Load ASDQ DAC Threshold buffer with new value", to "Read ASDQ DAC threshold buffer value", to simply "No Operation". In addition to the command itself, the reception allows the ASIC to resynchronize itself to the clock. This clock is used internally (at multiplied frequencies) for the TDC clock (1.56 ns is derived from the 12<sup>th</sup> harmonic of the accelerator RF clock) and the Data output clock. If possible it will be used as the crossing timing clock, with the idea again to minimize the number of cables in the electronics. The command structure is still in its conceptual stages, but it will allow us to use (in principle at least) everyone of the 159 "ticks" as an operation. Operations which require data readout (such as "real" data, TDC calibration data and internal register readback) will, of course, be controlled from the application environment to be consistent with the output bandwidth of the datalinks and the BTeV DAQ. Separation of the data into the proper streams will be done in the Data Combiner Board (DCB). The following is a brief (and tentative) version of the expected commands.

- NOP: No operation this tick. Primarily use to keep clock synchronization
- Start TDC: The TDCs are strobed with a start pulse. When timeout occurs, data are placed in the TDC FIFO buffer and readout occurs as soon as possible.
- Start TDC Calibration: The ASDQ's are strobed with a calibration pulse whose amplitude and relative timing are given by respective registers. The TDC is also started. When timeout occurs, the data are placed on the TDC FIFO buffer and readout occurs as soon as possible.
- Load ASDQ Threshold Buffer: A new value is loaded into the ASDQ threshold register, which then strobes a DAC to supply the ASDQ with an analog threshold voltage.
- Load TDC Offset Value: A new value is loaded into the TDC Offset register. This time represents the relative offset to the actual bunch crossing from the decoded "Start TDC" timing. Used with the TDC Timeout Value to put a window around the valid TDC Data region.
- Load TDC Timeout Value: A new value is loaded into the TDC Timeout register. The time at which the TDC stops. Any TDC channel which has not registered a hit by this time is considered "empty" when the data is sparsified.
- Load Calibration Pulse Amplitude: A new value is loaded into the Calibration Pulse Amplitude register. This amplitude will be used to keep track of the ASDQ channel response.
- Load Calibration Pulse Delay: A new value is loaded into the Calibration Pulse Delay register. This will be used to track the TDC time calibration (although it isn't completely independent of the TDC timing).

In addition to all the load commands, there will also be a corresponding "Read" command, which will place the current value of the particular register into the TDC FIFO, with the "tick" tagging given by the reception "tick" of the "Read" command. Readout of the TDC FIFO will be asynchronous and "on demand" simply by there being data in the FIFO.

It appears at this time that the data output bandwidth can be successfully handled by two 636 MHz serial links ( $636\text{ MHz}=12*53\text{MHz}$ ) per module. The clock will be recovered by standard techniques at the Data Combiner Board (DCB) receiver. There will be a readout every 132ns, whether there is data or not, simply to keep the clock synchronized. The sync readouts will be as minimal a length as possible, consistent with their function. As has been described, both crossing TDC data and readback register values and calibration data are in a single data stream. The separation of the streams will be done in the DCB, where the data "ticks" are known. "Real" data will be routed to the correct buffers by the DCB. It will be the responsibility of calibration/monitor software routines to give the DCB the correct routing for these data.

### 8.7.8.2 Overview of I/O Implementation

We present here a design for a system of moving data from the front-end electronics to the Data Combiner Board (DCB) and a mechanism for sending timing and control data to the Front End Module (FEM).

The design of the baseline system has been shaped by the following considerations:

- Radiation environment. Since radiation exposure for these electronics is anticipated to be on the order of 20 kilorad per year, all of the front-end electronics need to be designed to be radiation tolerant. For this reason, no commercial chips are used on the front-end.

Although commercial rad-hard FPGAs are available, they have proven to be too expensive for our application. Fiber optic components are not used for the front-end electronics due to their susceptibility to radiation-induced scintillation.

- Electromagnetic compatibility. Crosstalk between signal lines can cause data errors either on the Data Combiner end (where event data is received) or near the front-end electronics (where control/timing data is received). It is critical that we avoid the introduction of noise in the detector system. For these reasons all front-end electronics need to be designed so as to avoid transmitting or receiving EM energy.
- Limited physical space. The physical design of the detector sub-systems is controlled by consideration of physics goals. Little room is available for front-end electronics and/or cables and connectors.
- Cable length. The location of the Data Combiner racks relative to the detector front-end electronics is not entirely settled. It is anticipated, however, that the cables for the front-end data transport will be between 10 and 20 meters in length.

- Limiting the cable infrastructure. There are several reasons for reducing the cable infrastructure as much as is practical. As mentioned above, physical space for cables is at a premium. Also, the mass of the cables is going to affect the design of the mechanical supporting structures for the detector. Another reason for limiting the size of the cable infrastructure has to do with the way that the BTEV detector is assembled within the collision hall. Most of the detector subsystems have to be installed sequentially. Limiting the number and volume of the cables will improve the efficiency with which we are able to assemble the detector in the collision hall during the available time windows, and to access the detectors for repair.

The trend in industry has been to utilize high-speed point-to-point serial lines, differentially driven, to efficiently move data. More recently, cable equalization chips have become commercially available which compensate for the frequency dependent characteristics of twisted pair (copper) cables.

The use of cable equalization has made it possible to move data faster and over longer distances using copper wire than was previously the case. An example is a system shown in one application note demonstrating the recovery of 3.2 Gbps serial data at the end of 100 ft, 75 $\Omega$ , coax cable; with only 0.16 unit interval of deterministic jitter.

The baseline design takes advantage of these trends by using four point-to-point serial links, each implemented with a differentially driven twisted pair, to service each Front End Module.

The first differential pair (the "T/C link") sends beam crossing time and control data from the Data Combiner board to the Front End Module. Two differential pairs send event data in the other direction, from the FEM to the DCB. The last differential pair sends a 132ns clock (called the "Refclk") from the DCB to the FEM.

The following observations apply to the Event Data links, T/C link and Refclk links:

- Shielded, twisted pair, category 6 cable (or equivalent), with foil shields for each individual pair and an electrically isolated overall shield for the cable, are used to limit EM emissions and receptivity.
- Each differential pair is terminated at the receiver end with the characteristic impedance of the cable.
- Receiver-end cable equalization and transmitter-end pre-compensation are used for the event data channel and timing/control channel, respectively.
- CML ("current mode logic") is used for signaling in both directions.
- All data is encoded in the 8B10B format.
- A Running Disparity Counter maintains DC balance (where the same number of 0's and 1's are sent on each twisted pair) by selecting the disparity of each data word transmitted.

### 8.7.8.3 Reference Clock

The Reference clock (or "Refclk") is the only high precision timing signal provided to the FEM by the DCB. This clock is derived from the Accelerator RF system, has a period of 132ns and performs three functions. The first is to provide the FEM with a precise reference for the beam- crossing clock. The rising edge of the Refclk, as received at the FEM, occurs at the beam crossing time. Not every 132 nsec interval will have beam. Intervals with beam will have a bit set in the T/C data word, see section 8.7.8.4 below.

The second function of the Refclk is to allow the DCB and the FEM to each generate a local T/C link bit clock. The DCB uses a PLL to generate a local T/C link bit clock (20x the frequency of the Refclk) and uses this clock to send T/C link data in synchronization with the Refclk. Separately, the FEM uses a Delay Locked Loop to multiply the Refclk by 20 to generate its own T/C link bit.

The third function of the Refclk is to allow the FEM to drive the Event data link. The FEM uses the Refclk to generate the Event Data state clock (84 times the frequency of the Refclk). The Event Data state machine uses this clock to transfer data from the output buffer to the output shift register and for shifting the data out one bit at a time.

REFCLK and REFCLK\* are sourced by the DCB and differentially driven using CML signaling. A CML- compatible commercial pre-emphasis chip is used to compensate for the frequency dependent characteristic of the cable.

### 8.7.8.4 Timing and Control (T/C) Interface

The T/C link sends beam crossing time and control data from the DCB to the FEM. A 20-bit T/C data word is sent every 132ns and the data is encoded in 8B10B format. The FEM takes the 132ns Refclk and uses a Delay Locked Loop to multiply it by 20 for use as a local T/C link bit clock to recapture the T/C link data.

Each T/C data word (16 bits after 8B10B decoding) is used to attribute certain markers to beam crossing intervals, and to implement a simple protocol for writing to and reading from the CSR registers within the FEM.

TCDAT and TCDAT\* are sourced by the DCB and differentially driven using CML signaling. A CML- compatible commercial pre-emphasis chip is used to compensate for the frequency dependent characteristic of the cable.

#### *T/C Data Format*

Each Timing/Control word is transmitted in the form of 20 bits. The FEM uses an 8B10B decoder to detect the (10-bit) word boundaries and translates the 10-bit data back to 8-bit data using a lookup table. After 8B10B decoding, each Timing/Control word consists of 16 bits (2 contiguous 8-bit bytes).

The format for each word is shown below. Because the 16-bit T/C data is received as 2 contiguous bytes, the "high word" bit is used to mark which one is the MSB byte and which is the LSB byte. Data is always sent in big-endian format, where the MSB (with the 'High Word' bit set) comes before the LSB (where the 'High Word' bit is cleared).

<hr/> MSB byte:	
7	'High Word' <= '1'
6	'BC' marker
5	'A' marker
4	not used
3:1	Function code: '0XX' no operation '100' write address '101' read address '110' write data '111' read data
0	Address/Data Bit 7
<hr/> LSB byte:	
7	'High Word' <= '0'
6:0	Address/Data Bits 6:0

The 'BC' marker indicates that a 132ns interval (a 'tick') is occupied and that a collision may occur during this crossing. The 'BC' marker is '0' for all ticks within the Abort gap; the 'BC' marker is also '0' for 2 of every 3 ticks (not including the Abort gaps), when the accelerator is operation in 396ns mode.

The FEM will initiate the acquisition of physics data during each crossing that is designated with the BC marker, unless this operation is disabled by writing to one of the CSR registers in this module. It is therefore equivalent to a 'START\_TDC' operation, for example.

The 'A' marker designates that a 132ns interval is 'Bunch 0' and the Tick counter (which increments on every rising edge of Refclk) should be reset to 0.

### *T/C Data Timing*

Because T/C data is sent as a serial stream, T/C data that is received by the FEM during the interval starting at T+0ns is not fully received (and captured) until time T+132ns. The FEM holds each T/C word for another 132ns (until T+264ns), so that the on-board logic has a generous setup time before the markers are acted upon, on the rising edge of Refclk.

### *T/C CSR Register Access*

Besides marking which 132ns intervals are designated as occupied and which one is Bunch0, the Timing/Control word also has the ability to command the FEM to either read a single CSR register (the data is tagged by the Register ID and added to the Output FIFO), or to write a 8 bit value to a designated CSR register.

- Write Address: In order to write to the address register, the function code is set to '100' and the Register ID (0...255) is written to the Address/Data field.

- Read Address: In order to read back the value of the address register, the function code is set to '101'. The value of the Address/Data field is ignored.
- Write CSR: Writing to one of the 256 available CSR registers is done by setting the function code to '110' and putting the data (value = 0...255) in the Address/Data field. The Write operation always assumes that a Register ID has already been written to the Address register.
- Read CSR: Reading a CSR register is done by setting the function code to '111'. The Address/Data field is ignored.

#### 8.7.8.5 Event Data Interface

All event register data is written to an Output FIFO. A finite state machine on the FEM monitors the state of the Output FIFO and transfers data to the Event Data link whenever the FIFO is non-empty. The FSM transfers data from the Output FIFO at 63.6 Mbyte/s

This data is then encoded into 8B10B format using a lookup table, loaded into a shift register and clocked out at  $12 \times 53\text{Mbps} \Rightarrow 636\text{ Mbps}$ , and differentially driven on the (EVDAT, EVDAT\*) signal pair.

EVDAT and EVDAT\* are sourced by the FEM and differentially driven using CML signaling. A CML-compatible commercial cable-equalizer chip on the DCB (on the receiver end of EVDAT/EVDAT\*) is used to compensate for the frequency dependent characteristic of the cable.

##### *Event Data Format*

The Event Data link is used to transfer the following from the FEM to the DCB:

- Physics data. Data resulting from the conversion from a physics detector system.
- Calibration data. Data resulting from artificial stimulation of the detector elements or front end electronics.
- Register data. Data resulting from a Read Address or Read CSR operation.
- Test pattern data. Data resulting from a special test pattern mode, for testing the operation of the T/C link or Event Data link.

The format of the data written to the Output FIFO will depend upon the specific system, however it must be structured in a way that allows the DCB to distinguish between these different data types and to associate data from the same event into some type of record. In most cases it will be necessary for the structure of the data to accommodate a variable record length.

#### 8.7.8.6 8B/10B Encoding and the Disparity Counter

8B10B is the name of a data coding system where 8-bit data is translated via a lookup table into 10-bit code. This translated data has the property that the maximum run length of identical bits is 5, aiding in the recovery of the bit clock on the receiving end.

A second property of this coding system is the existence of a unique 'Sync' pattern that can be used to resynchronize the framing clock of the receiver with the transmitter. The Event Data state machine inserts 'Sync' words into the data stream whenever the Output FIFO is empty.

Each valid 8B10B character has a disparity of 0, +2 or -2. For every non-zero code, there exists an alternative code with the opposite disparity.

In order to maintain DC balance, the Event Data interface (on the FEM) and the T/C interface (on the DC) use a running disparity counter (RDC) to determine whether to use the positive disparity or negative disparity code for each data word.

#### 8.7.8.7 Cabling

##### *Cable Packaging Requirements*

The proposed mapping of differential pairs to cables is based upon the following considerations:

- Some detector sub-systems (specifically the Straw detector) require 2 Event Data links per electronic package to accommodate the anticipated rate of event data, plus a nominal safety factor.
- The Refclk and T/C links are intended to support multiple receivers, so long as the following are true:
  - These signals are routed in daisy-chain fashion, where they visit one receiver then the second, where the transmission line is terminated.
  - The path length between the two receivers is no more than 1 cm.
  - The two receivers can distinguish between the registers on each by using different register addresses (where appropriate).
  - Standard rules for routing high speed differential signals are followed, including the following:
    - \* Use of a ground plane
    - \* Keeping the signals in differential pair the same length.
    - \* Stub avoidance
    - \* Via minimization
    - \* These signals should always maintain the same reference plane (the power or ground plane closest to the signal).



- Mixing near-end (transmitter) signals and far-end (receiver) signals on the same connector may cause crosstalk between the two, due to the fact that the near-end signal is going to be strong in amplitude and the far-end signal is going to be attenuated by the length of the cable.

### *Cable Packaging Design*

The proposed cable definition uses two 2-pair cables, with 4-contact IEEE 1394 type connectors on each end:

Cable 1:	
Pin 1	Event Data(0)
Pin 2	Event Data_(0)
Pin 3	Event Data(1)
Pin 4	Event Data_(1)
Cable 2:	
Pin 1	RefClk
Pin 2	RefClk_
Pin 3	TCDat
Pin 4	TCDat_

Still under consideration is an alternative cable packaging plan consisting of the use of 4-pair, ISO category-6 shielded cables and category-6 RJ-45 connectors.

#### **8.7.8.8 Customized Interface Circuit (ASIC)**

Commercially available chips are used wherever possible within this design. On the other hand, an application specific custom IC is necessary to act as an interface on the FEM end. It is hoped that the uncommitted detector subsystems will be able to use the TDC ASIC planned for the straw detector system, taking advantage of the low incremental cost of producing additional chips.

#### **8.7.9 Data Combiner Board (DCB) - Straw Daughter Card**

As described above, the TDC ASIC has a built in command functionality, but no pre-knowledge of the beam time structure. That knowledge is based in a lookup table in a daughter card of the DCB, which has been specialized to the needs of the Straw Front end. This daughter card has a 159 element lookup table, one for each 132ns "tick". Each element has been loaded with one of the possible commands. This daughter card also contains the circuitry to run our input and output serial links.

### 8.7.10 Straw High Voltage System

The straw tube anodes will be biased by dedicated high voltage (HV) power supplies controlled and monitored by conventional slow control techniques. Each HV power supply channel will bias a set of 96 straw channels by applying voltage to the anode wires at both ends of a set of 48 straws. Thus a minimum of 558 HV power supply channels will be required. Each HV channel will be capable of applying bias voltages up to +2200 V, and be able to source up to  $200\ \mu\text{A}$  of current, consistent with our Monte Carlo estimates of maximum occupancy levels and incorporating a substantial safety factor.

The HV power supply modules will be placed in relay racks and located in a low radiation area of the C0 interaction hall. Connection to the forward tracker will be through intervening multi-conductor cables and patch panels. HV will be distributed within a straw frame to individual straw channels via a high voltage bus built from double-sided printed circuit boards. Connection is made between the bus traces and HV voltage cards that connect directly to the straw anodes. Electrical tests have verified that the trace topology on the bus resists arcing well beyond any anticipated working high voltage. The final vendor for the HV system is not yet decided. Monitoring and control software will be developed after the final vendor is selected.

### 8.7.11 Straw Low Voltage System

The straw tube front end electronics will be powered by dedicated low voltage (LV) power supplies controlled and monitored by conventional slow control techniques. The LV supplies will power both the front end amplifier/discriminator card and the TDC card, and will need to provide  $\pm 3\ \text{V}$ . The precise current required is not yet known since the TDC cards are not yet designed. Similar to the HV power system, the LV power supply modules will be placed in relay racks and located in a low radiation area of the C0 interaction hall. Connection to the forward tracker will be through intervening multi-conductor cables and patch panels.

LV will be distributed within a straw frame to front end electronics cards via a bus built from printed circuit boards (PCBs). Prototype bus design has begun. Connection will be made between the bus traces and either the TDC card or the amplifier/discriminator card, whichever is more practicable. (Power would then be delivered to the other card via connectors joining the two.) The final vendor for the LV system is not yet decided. Monitoring and control software will be developed after the final vendor is selected.

## 8.8 Installation, Integration and Testing Plans

### 8.8.1 Summary of Testing Prior to Moving to C0

The Straw Detector will be assembled in half-views, including front-end boards and signal cables, and fully tested before moving to C0. Each wire will be tension tested and checked to see that it holds high voltage as it is strung, and then again when the half-view assembly is complete. Cabling and gas and cooling water lines will be attached and leak tested. The wire positions will be surveyed with respect to external fiducials on the half-view frames. Each half-view has an environmental sensor to monitor temperature and humidity; the readout from this will be tested. The functionality of the front-end electronics will be tested with pulses injected at the pre-amplifier inputs. The threshold voltages and other programmable registers will be set and read back. The full data readout chain will be tested with a radioactive source and/or cosmic rays.

### 8.8.2 Transportation of Straw Detector Equipment to C0

All straw detector equipment will be staged at Fermilab Lab 3 prior to moving to C0. Detectors will be moved as full stations for stations 1-6 and as super-modules for station 7. Equipment will be moved from Lab 3 to C0 by Fermilab Material Distribution Department trucks and drivers. The stations will be packaged for transportation on the tooling used for installation at C0. For transportation, frames will have casters attached to facilitate movement. Super-modules will be crated in either wooden boxes or on 'Unistrut' type frames. The straw half-views will be transported in half-view transportation frames. The transportation frames will have outriggers for stabilization and will accommodate casters for local movement.

Relay racks will be transported with standard tie-down precautions. The half-views may also be connected to a dry gas purge source during transportation. A transportation procedure will be prepared for the transportation operation.

All relay racks can be loaded and transported in one-half day. The smaller straw stations ( can be loaded and transported in less than one-half day. The larger straw stations may require one or two full days for loading and transportation.

### 8.8.3 Installation of Straw Detector at C0

At C0 stations 1-6 will then be split into 2 half-stations – each with an X,U and V half-view attached to a back plate (see Fig. 8.26).

The half-station assemblies will be transported into the collision hall and moved into position with a dedicated cart. The cart will have provisions for safely positioning the assembly onto a rail system for docking. Stations 1-6 will first be mounted around the beam-pipe at the mouth of the SM3 magnet. Before sliding them along the beam-line into their docking positions, utility connections will be attached and tested.

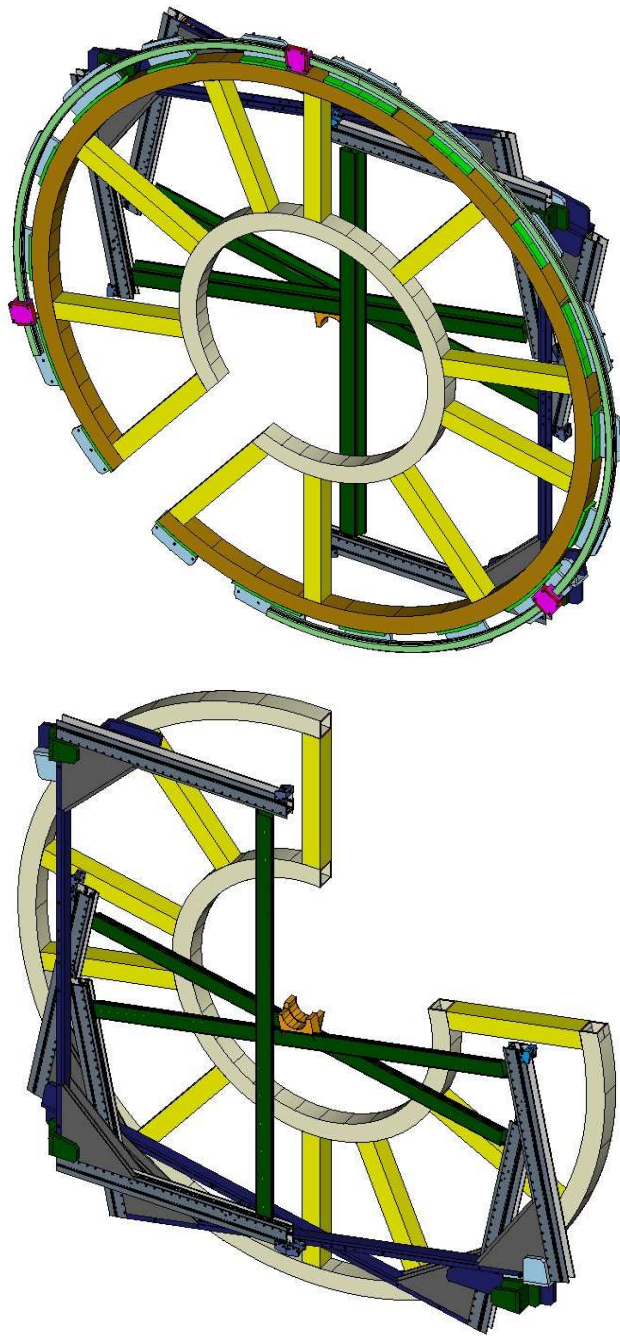


Figure 8.26: Straw Station assembly – 2 half-stations with back plates

Power supply cables and signal cables will be attached, then the fully assembled station will be slid into the proper z position with a set of longitudinal rails. Once at the proper z position the station will be lowered a few centimeters and attached to more stable support brackets. At this point the X-module for the silicon support can be slid into position in the gap in the X-view.

The straw stations must be installed in the following order: 1,2,3,6,5,4. Station 7 will be treated separately as it is in a very confined space between the RICH and the ECAL. The positions of the straw stations will be surveyed using external fiducials on the half-view frames.

### 8.8.4 Testing at C0

After installation the following tests will be done:

- Leak test gas and cooling water systems.
- Test temperature and humidity monitoring and check that power supplies are shut off in the event of a cooling failure, or if humidity is too high.
- Test gas monitoring systems (gas gain, drift velocity, contaminant level), check functionality and integrate into slow control system and database.
- Check that all modules hold HV.
- Threshold voltages and other programmable registers will be set and read back
- Test Front-end electronics with pulses injected at pre-amp inputs
- Test readout into Data Combiner boards

## 8.9 R&D , Open Design Issues

### 8.9.1 Prototype Detector

We have constructed a 2 module prototype detector for test beam studies and to explore construction issues (see Fig 8.27). The construction of a module proceeds as follows: the straws are cut to the correct length and twisters are glued in; the three layers of straws are set up on a corrugated base to form a close-packed array; the end-plugs are inserted into the module end-plates and silver epoxy is injected into the region around the end-plugs; the endplates are attached to the straws; finally the outside of the endplates is potted with structural epoxy.

We have adapted the wire stringing fixture from the one used by Atlas. The 25  $\mu\text{m}$  gold-plated tungsten anode wires are inserted into the straws by blowing a lead through, tying the anode wire to the lead wire and pulling the lead wire back. A weight is hung from the wire to

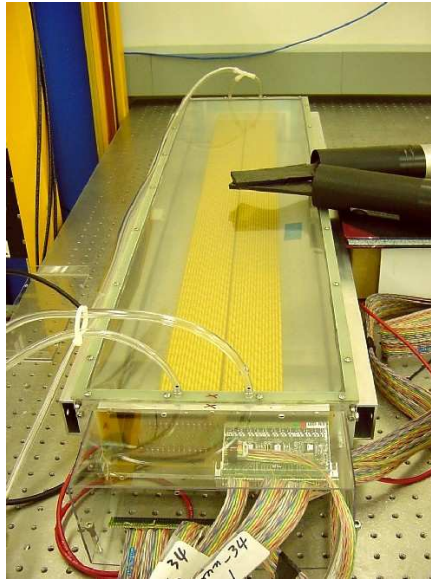


Figure 8.27: Straw prototype chamber

apply the correct tension. During production it will be necessary to have an efficient method of checking the tension of each wire as it is strung. We have set up an acoustic excitation method for measuring the tension – a loudspeaker is used to induce a mechanical resonance in the wire. A potential of 80V is put on the wire so the capacitance variation induces a signal. We use a LabView data acquisition system that generated a variable frequency to drive the loudspeaker and plots the response as a function of frequency. The resonance is easily observed.

The prototype is read out using COT cards (from the CDF Central Outer Tracker). Each COT card has three 8-channel ASDQ chips. The output of the COT cards is converted from LVDS to ECL via a translator board so we can use existing LeCroy TDCs.

We have done efficiency tests with cosmic rays and get a 95% efficiency for both Argon/CO<sub>2</sub> and Argon/Ethane. This is as expected given the thickness of the kapton walls and some gaps due to out-of-roundness of the straws.

### 8.9.2 Straw Material

The first order of straws made with Kapton XC as described in section 8.4.2.1 above, were manufactured by Stone Industrial, Maryland. We found two major problems with these straws. They are not perfectly round making close packing difficult, and about 20% of the straws leak due to lack of glue between the 2 layers. We have since obtained a shipment of straws from Lamina Dielectrics, England, and are currently doing extensive quality control checks.

We have discovered that kapton loses tension when exposed to various gases, in particular it is very sensitive to even low levels of ethanol[7].

One of the gases considered for use is a 50:50 mixture of Argon-ethane; however this requires a small fraction of alcohol to be added to prevent aging. We will need to use a gas mixture without ethanol or a different straw material – eg. copper coated kapton or copper coated mylar. Mylar has a lower coefficient of hygroscopic expansion and lower gas permeability for all gases where data exists so may be a preferable material. It is not as radiation hard as kapton but that should not be a problem with the radiation levels expected at the straw chambers.

The specifications from Dupont claim that the gas permeability of mylar is significantly reduced (up to factor of 100) by a metalization layer, this probably applies to kapton as well. We have recently received a shipment of copper coated mylar straws. Unfortunately they appear to have a large number of surface defects of unknown origin. This is under investigation. We plan to order some copper coated kapton straws in the near future. The CKM experiment has done a number of studies of this type of straw and has had no problems.

Another problem with the Kapton XC straws is that we see a significant amount of dark current after exposure to radiation when using an Argon/Ethane/ethanol gas mixture (see section 8.9.4).

### 8.9.3 Gas Studies

Since the use of an Argon-ethane gas mixture in the kapton straws is problematic (see section 8.9.2), and since additives such as  $\text{CF}_4$  are not desirable because of their corrosive effect on the glass capillaries, we have studied various mixtures of Argon- $\text{CO}_2$  as a possible gas for the BTeV straw detectors. Another advantage of Argon- $\text{CO}_2$  is that it is not susceptible to the polymerization which occurs when hydrocarbon gases are used in a high rate environment. The various features that have been investigated include:

- gain
- efficiency
- operating voltage
- drift time
- spatial resolutions
- after pulse frequency
- streamer frequency

We have investigated these performance parameters with a range of Argon/ $\text{CO}_2$  mixtures. We have compared the measurements with Garfield[8] simulations, and have also used Garfield calculations to determine expected behavior of the various mixtures for all parameters except the after pulses and streamers.

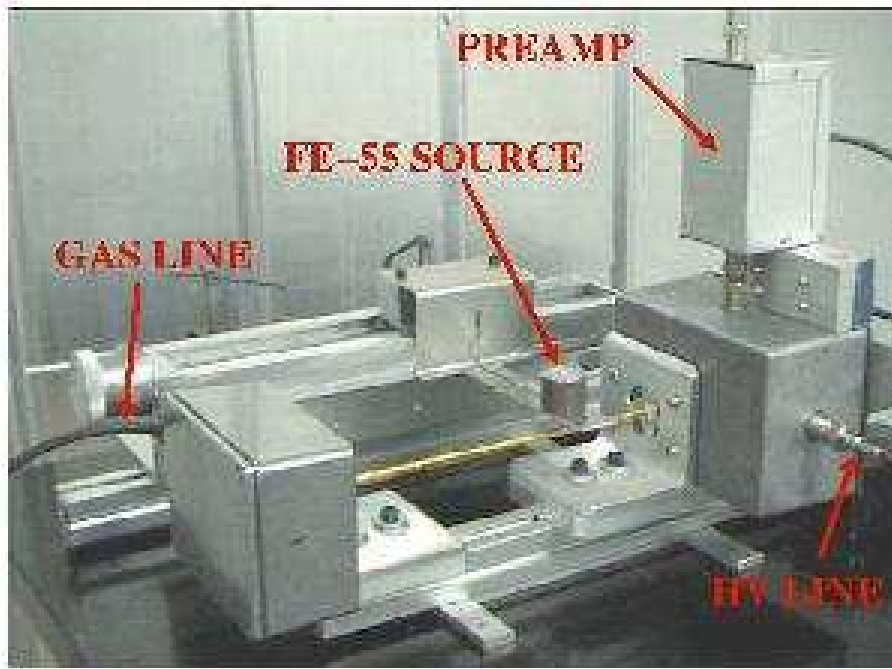


Figure 8.28: The short single straw prototype and  $^{55}\text{Fe}$  source configuration for the Ar/CO<sub>2</sub> tests

### 8.9.3.1 Gain

An  $^{55}\text{Fe}$  photon source (5.9 keV energy) was used to determine gain of the various gas mixtures. The  $^{55}\text{Fe}$  photon interactions in the Argon produce an average of 210 e<sup>-</sup> in a very localized region (100-200  $\mu\text{m}$ ) so the intrinsic gain of a particular gas mixture at a given voltage can be determined by measurement of the integrated charge of the straw signals. The gas mixtures have been tested with the short single straw prototype arrangement shown in Fig 8.28. The straw is 4 mm in diameter with a length of 220 mm. The anode wire is 25.4  $\mu\text{m}$  gold-plated tungsten.

Measurements of efficiency plateau, gas gain, drift time, pulse shape and other parameters have been performed to provide a baseline for other mixtures and to determine the reliability of the Garfield simulations. Once the Garfield simulation was verified, it was used to predict the efficiencies and spatial resolutions of the straw detector.

Initially, we purged the straw with Argon-CO<sub>2</sub> 80/20 at a high rate (14 cc/min) and then studied the dark current as a function of voltage. We found that the straw drew 0.1-2 na current between 800 and 1500V (the voltage range determined to be appropriate for this mixture).

After purging, the straw detector was exposed to the  $^{55}\text{Fe}$  source. The pulse shapes due to the  $^{55}\text{Fe}$  photon interactions were investigated and compared to Garfield simulations. Shown in Fig 8.29 is the average of 250 pulses at 1300V from the straw before the preampli-



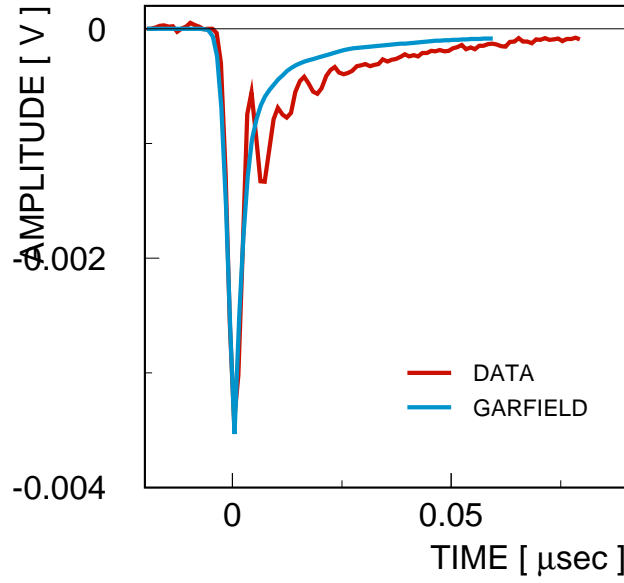


Figure 8.29: Comparison of pulse shapes from data and Garfield simulation

fier. For comparison, we show the average of 33 pulses simulated in Garfield. There is good agreement generally. The post-amplifier pulses were also compared with a Garfield simulation that included a simulation of the amplifier and were found to be in good agreement. From these studies we determined that integrating over a 300ns gate applied to the pulse obtained directly from the straw would capture 55% of the charge generated by the photon interactions.

The pulse height spectrum resulting from integrating over 300ns is shown in Fig 8.30. Both the K shell escape peak and the full peak are quite visible. The measured ratio of energies of the two peaks is 2.20, in good agreement with the expected 2.19. The measured escape fraction of interactions is 14.6% also in good agreement with the expected escape fraction of 15%.

To determine the intrinsic gain of the 80/20 gas mixture, a 300 ns integration of pulses directly from the straw using the integration function of a fast scope was performed. On average, after subtraction of pedestal and allowing for the 55% collection efficiency of a 300ns gate, the 5.9 keV  $^{55}\text{Fe}$  photons produced an average charge of 4 pC at 1450V. Using 210 e<sup>-</sup> as the average charge deposited by the average of the escape and full peaks in this spectrum, the intrinsic gain was determined to be  $1.2 \times 10^5$  at 1450V. Using this technique, the two points labeled as "scope" in the gain vs. voltage shown in Fig 8.31 were obtained. We also measured the integrated charge post preamplifier vs. gain to obtain the variation with voltage over a wider range of voltage. We have used a FOCUS/BNL831 amplifier whose gain has been measured. We also incorporated a simulation of the amplifier in the Garfield simulations. However, since the preamplifier pulse shaping loses a large and unknown fraction of the charge, the scope measurements were used for absolute normalization of the post

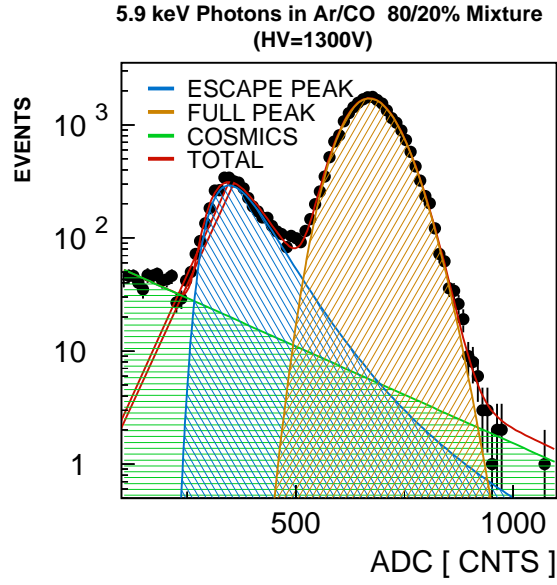


Figure 8.30: Pulse height distribution from Ar/CO<sub>2</sub> 80/20 mixture from 5.9 KeV photons from a <sup>55</sup>Fe source. The dots are the measurements and the red line is the fit of two skewed Gaussian distributions on top of an exponential background due to cosmic rays.

preamplifier measurements. The Garfield simulation of the gain vs. voltage curve is in good agreement with the post preamplifier ADC measurements except at the highest voltages which show some sign of saturation. The lowest voltage achievable was determined by the noise level from the straw which is equivalent to 27 fC deposited at the wire. This noise prevented us from operating at much below 1100V for this particular mixture.

### 8.9.3.2 Operating Voltage

The plateau curve shown in Fig 8.32 was obtained for the Ar/CO<sub>2</sub> 80/20 mixture using an <sup>55</sup>Fe source and setting the threshold of the discriminator just above the noise level. As can be seen, the plateau is more than ample for operation using 80/20 Ar/CO<sub>2</sub> as the gas for the straw detector.

### 8.9.3.3 Drift Velocity

The drift time for the Ar/CO<sub>2</sub> 80/20 mixture was measured using collimated <sup>106</sup>Ru  $\beta$  source with a 3.5 MeV end point which illuminated the entire straw diameter. The TDC spectrum shown in Fig 8.33 was accumulated using a scintillator signal as start and the straw signal as a stop. Full width at 20% of height is 33ns and base to base is less than 50 ns, so an Ar/CO<sub>2</sub> 80/20 is certainly more than adequate for a 396 ns or 132 ns bunch crossing frequency for 4 mm straws.

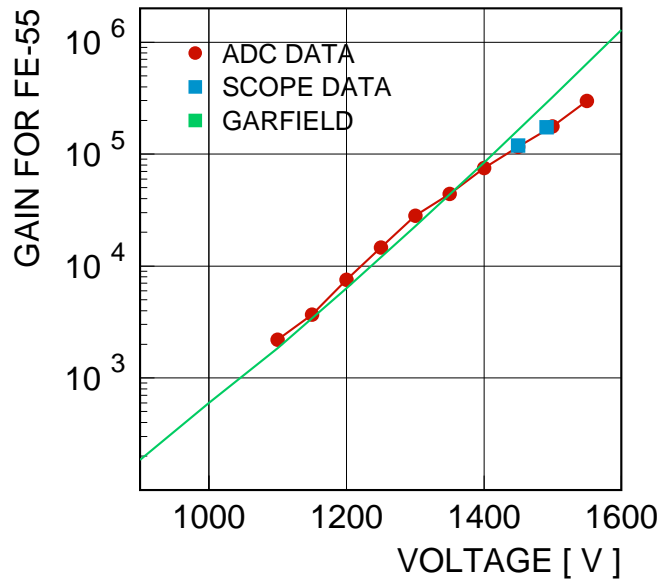


Figure 8.31: Gain vs. Voltage for Ar/CO<sub>2</sub> 80/20 mixture. The solid line is the expected dependence of the gain on voltage from a Garfield simulation. The squares are actual measurements before the preamplifier, obtained using the integrating feature of the scope. The circles are post-amplifier measurements, obtained using an ADC, which have been absolutely normalized using the scope data.

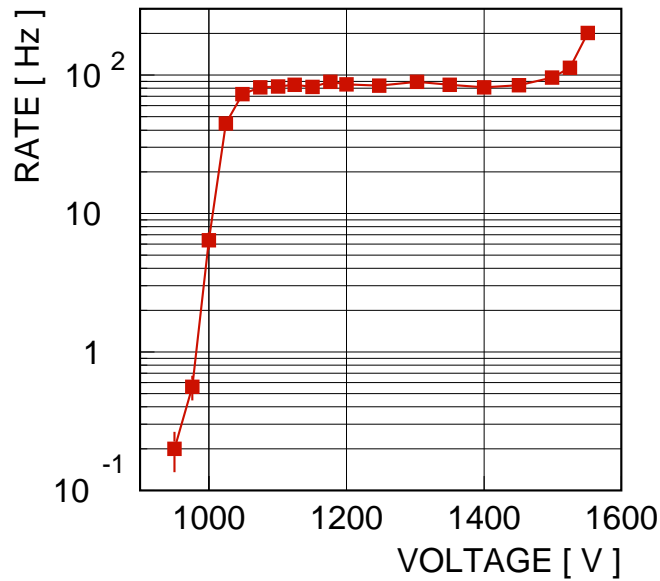


Figure 8.32: Plateau obtained for Ar/CO<sub>2</sub> 80/20

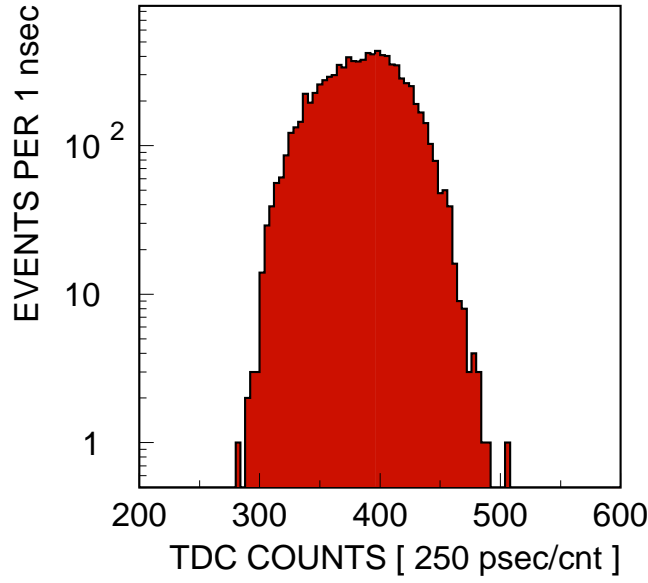


Figure 8.33: TDC distribution for 80/20 Ar/CO<sub>2</sub>

#### 8.9.3.4 Straw Efficiency

The efficiency for minimum ionizing particles passing through the straw at different distances from the anode wire can be predicted as a function of applied voltage using Garfield. The Garfield threshold is varied until the threshold behavior of the plateau curve of Fig 8.32 is matched by the Garfield simulation. To obtain a good fit to the data, the pulse shape post preamp had to be simulated well since the discriminator threshold is applied after the preamp. Once this was accomplished, curves of efficiency vs. distance of the minimum ionizing track from the anode wire (as shown in Fig 8.34) were obtained for the 80/20 mixture. As can be seen, to have acceptable efficiencies over the majority of the straw diameter, the straw must be operated at a voltage  $> 1350$  V.

#### 8.9.3.5 Spatial Resolution

Using the Garfield simulations of efficiency we can also predict the intrinsic resolution of a gas mixture at a given voltage by studying the correlation of time versus distance. The simulations predict the range of distances from the anode wire corresponding to what is observed, i.e. the time of arrival of the electrons at the anode wire. A plot of resolutions obtained from a the fit of the distributions of distances corresponding to given times is shown in Fig 8.35 for several voltages. Once again, in order to obtain "intrinsic" resolutions (ones which do not include any uncertainties due to the experimental algorithms used to translate times to distances) better than  $100 \mu\text{m}$ , the operating voltages for the 80/20 mixture must be set above 1350V.

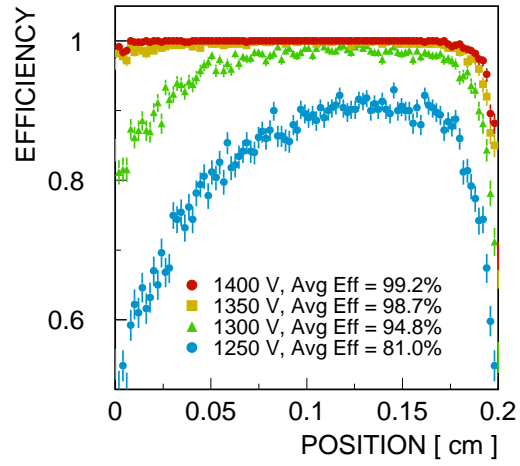


Figure 8.34: Garfield calculations of efficiencies for minimum ionizing particles vs. distance from the anode wires for an 80/20 Ar/CO<sub>2</sub> mixture at various voltages.

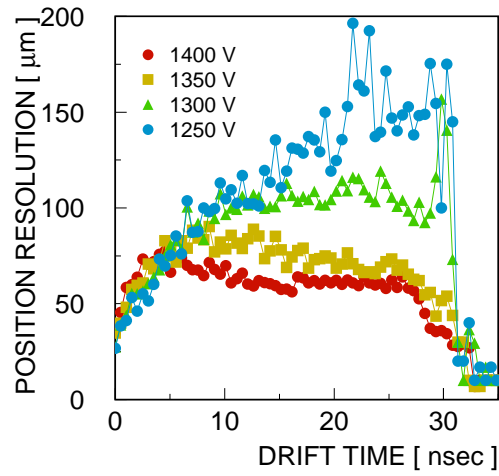


Figure 8.35: Garfield calculations of "intrinsic position resolution vs. drift distance at a variety of voltages

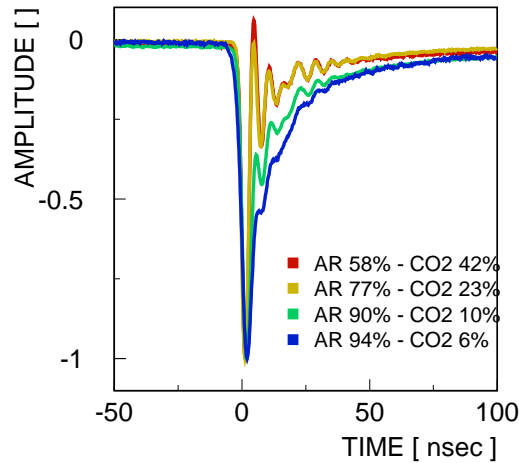


Figure 8.36: Variation of observed pulse shape with percentage CO<sub>2</sub>

#### 8.9.3.6 Streamers and After-pulsing

Without a quenching component, a gas such as Ar/CO<sub>2</sub> is more prone to large Geiger type pulses (streamers) or after-pulsing due to interaction of secondary photons in the walls of the straw. We have started studying the prevalence and voltage onset of these phenomena.

#### 8.9.3.7 Other Ar/CO<sub>2</sub> Mixtures

Varying the percentage of CO<sub>2</sub> changes the performance of the straw dramatically in some case. In Fig 8.36, the behavior of the pulse shape is shown as observed for several gas mixtures. As the percentage of CO<sub>2</sub> is decreased, the pulse broadens in time, an undesirable effect. Fig 8.37 shows gain vs. voltage curves for the various Ar/CO<sub>2</sub> gas mixtures.

Taking the ratio of observed gain divided by the exponential fit of the gain vs. voltage variations for the various mixtures, we obtain the curves shown in Fig 8.38. We observe the onset of saturation effects around  $2 \times 10^4$  gain for all Ar/CO<sub>2</sub> mixtures but is less pronounced in the mixtures with lower CO<sub>2</sub> percentages. In addition, the dramatic increase in pulse height that signals the beginning of the streamer mode occurs earlier and in the mixtures with higher CO<sub>2</sub> content.

In Fig 8.39 is shown the drift time distributions obtained using the <sup>106</sup>Ru beta source for a number of gas mixtures. As can be seen, the time distribution broadens with decreasing CO<sub>2</sub> percentage, also an undesirable effect.

The increase of drift time with decreasing CO<sub>2</sub> content is shown in Fig 8.40 compared to the expected changes of drift time with CO<sub>2</sub> percentage obtained from Garfield simulations. As can be seen, the agreement is excellent.

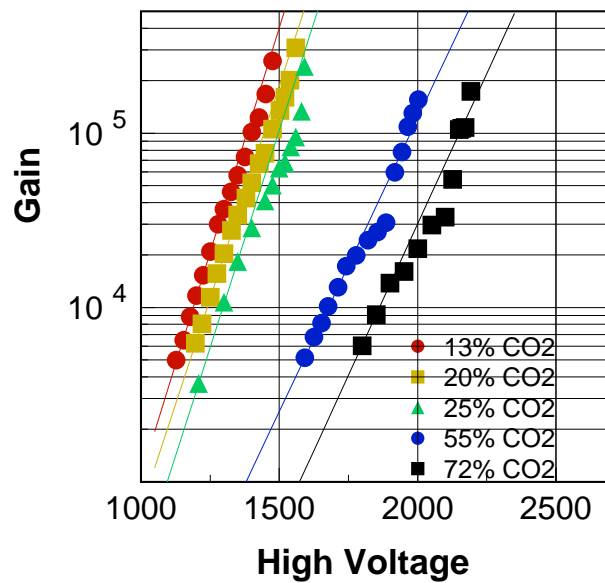


Figure 8.37: Gain as a function of HV for several Ar/CO<sub>2</sub> mixtures

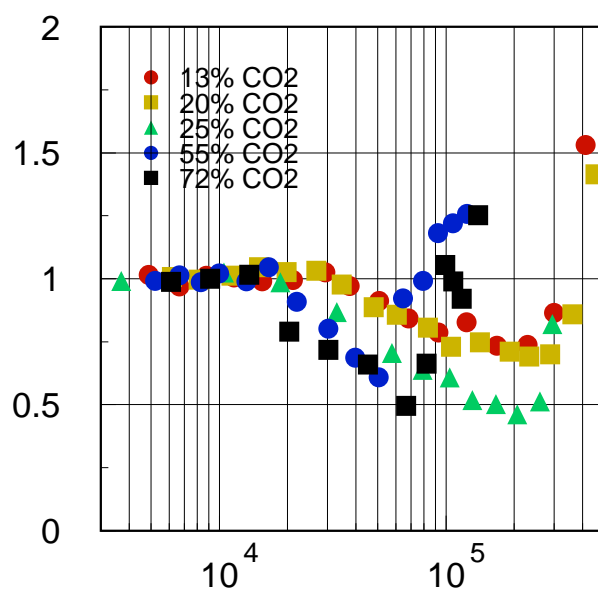


Figure 8.38: Ratio of measured gains to Garfield predictions for various Ar/CO<sub>2</sub> mixtures.

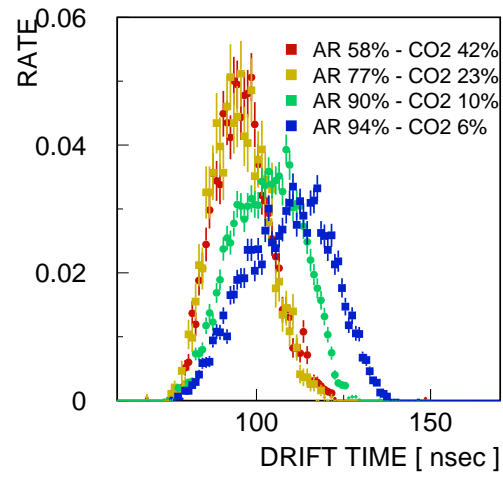


Figure 8.39: Time distribution for various Ar/CO<sub>2</sub> mixtures

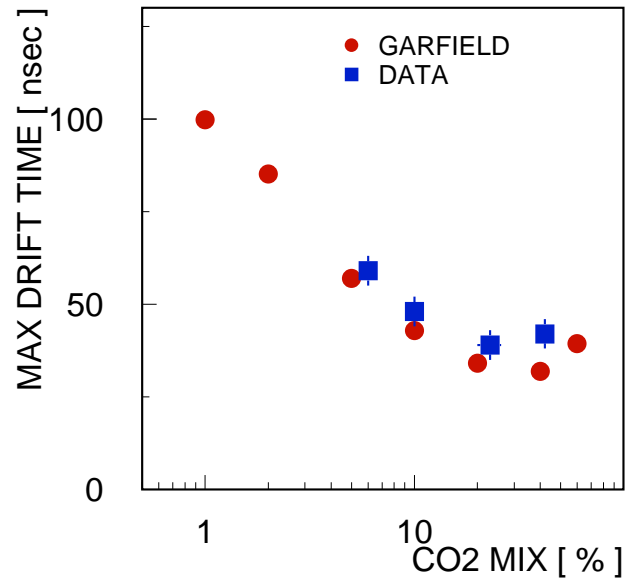


Figure 8.40: Variation of drift time with CO<sub>2</sub> percentage. The squares are measurements. The circles are Garfield calculations



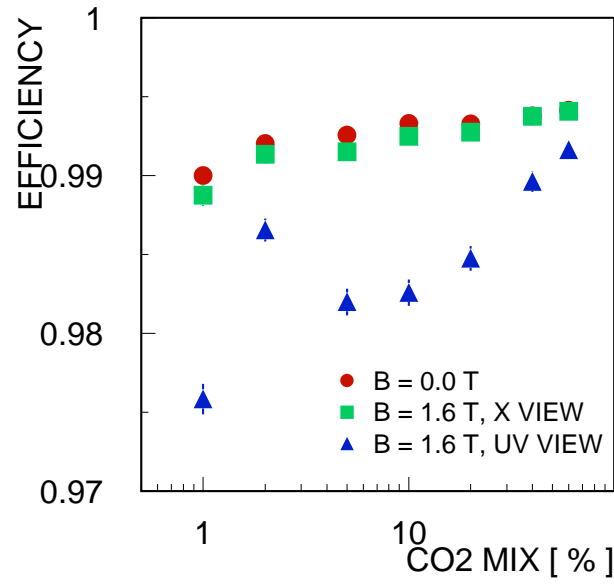


Figure 8.41: Garfield predictions of efficiency vs CO<sub>2</sub> percentage for no magnetic field and for 1.6T axial (UV) and transverse (X) fields

Finally, Garfield predictions of the variation of efficiency with percentage CO<sub>2</sub> is shown in Fig 8.41 at zero field (all calculations are made at an effective gain of  $10^5$  for the given gas mixture). Included are predictions for 1.6T axial and transverse fields. A small amount of efficiency is lost in the axial field configuration but the overall performance is still expected to be acceptable.

The general conclusions from the simulations is that the correct percentage of Ar/CO<sub>2</sub> should be greater than 10% for fast drift times but less than 30% to keep operating voltages as low as possible.

## 8.9.4 Aging studies

### 8.9.4.1 Introduction

We have done extensive aging studies for the straws for a number of candidate gas mixtures, including argon/ethane (50/50) and argon/ethane (50/50) with 0.5% ethanol, at different dose rates. We have done preliminary studies with argon/CO<sub>2</sub>. The gain of the chamber is monitored by a Fe-55 source. The loss of gain is parameterized as the percentage gain loss per Coulomb of charge deposited on unit length of the wire. We analyze the wire and the cathode by Scanning Electron Microscopy (SEM) and Energy Dispersive Spectra (EDS) after each exposure to look for damage and deposits.

### 8.9.4.2 Description of the tests

We have constructed several short (40-60 cm) straw chambers for the aging tests. The straws are of standard design (Kapton XC). Each single straw is tensioned to 250 g between two gas boxes which are fixed on a rail. The anode is 25  $\mu$ m diameter gold-plated tungsten wire, strung to 50 g tension. The gas mixture is prepared from argon (99.95% pure) and ethane (99.0% pure in liquid form) bottles by electronic mass flow-controllers. The ratio of argon to ethane was fixed to 50/50 to take advantage of a large body of experience with this gas mixture in the literature [9]. The gas flow-rate is typically 8-10 cc/min. Taking the volume of the gas boxes into account, this corresponds to about 10-50 volume changes per day. This gas flow-rate, while high compared to what is expected for the actual experiment, removes uncertainties about the aging results. The high voltage for the chamber is supplied by a stand-alone HV power supply whose current is monitored to detect the presence of dark current.

### 8.9.4.3 Gain measurements

The straw chambers were exposed to a radioactive source to accelerate the aging. The source is a 100 mCi <sup>90</sup>Sr  $\beta$  emitter which has a half-life of 28.5 y. The end-point energy of the electrons is 0.546 MeV. The electrons are collimated to about 0.5 cm in width. The width of the irradiated area of the straw is increased by the scattering of the low energy electrons in air. The width of the irradiated area of the straw is determined independently by a Geiger Counter and from the measured width of the gain profile. In most cases, we observed widths ranging from 0.5 to 1.0 cm. The peak dose on the wire is computed based on the total charge from the HV power supply assuming a Gaussian irradiation profile. The gain of the chamber in the irradiated region is measured by a Fe-55 source periodically. The 5.9 keV photons from Fe-55 source convert to about 230 ionization electrons in the chamber. The signal from the chamber is integrated by an oscilloscope or an ADC. The absolute gain is determined by integrating the Fe55 signal without amplification for 200-300 ns.

Table 8.4: Summary of aging results for argon/ethane (50/50) gas mixture

Dose rate (C/day)	Total dose (C)	Peak dose (C/cm)	Loss of gain (%/C/cm)	Other observations
0.01	0.1	0.05	< 5	No detectable loss of gain
0.02	1.2	0.5	50	No dark current
0.4	0.7	0.7	20	Total loss of gain after 2 days Gain recovered to 80% of initial value after 2 weeks

#### 8.9.4.4 Results with argon/ethane

We have done several aging tests with the argon/ethane (50/50) mixture at different dose rates. The results are summarized in Table 8.4. We started with a low dose rate of about 0.01 C/cm/day up to about 0.1 C. The loss of gain was not noticeable. The test was repeated with a dose rate of 0.02 C/day for about 60 days. The loss of gain was significant when the dose reached 2 C/cm. The loss of gain is attributed to deposits on the anode wire, confirmed by SEM and EDS studies which showed extensive deposits on the wire (see Fig. 8.43. It is noteworthy that there was no visible damage to the cathode. We also did not observe dark currents in this gas. We have also investigated the case when the dose rate is very high, about 0.4 C/day. The chamber completely lost its gain after 2 days of irradiation. After purging the chamber with the same gas mixture for about 2 weeks, the chamber recovered 80% of the gain, having a permanent loss of about 20%.

#### 8.9.4.5 Results with argon/ethane with 0.5% ethanol

It has been reported in the literature that additives such as water and ethanol can slow down the aging of wire chambers. We have therefore conducted an aging study with the argon/ethane (50/50) mixture laced with 0.5% ethanol. The ethanol (90% pure) was kept at -1 degree C by a chiller. The percentage of ethanol in the mixture, based on calculated saturated vapor pressure of ethanol at -1 degree C, is 1.5%. We diluted the gas by a factor of 3 to reduce the ethanol content to 0.5%. The choice of 0.5% was based on some prior experience with this gas mixture. The straw was aged in the same way as in the case without ethanol. A preliminary aging test was done for 10 days at a dose rate of about 0.1 C/day. The accumulated peak dose was about 0.5 C/cm. We did not observe any loss of gain at this dose. We then irradiated a different region of the same chamber for 20 days at the same dose rate. At the end of the aging process, the gain profile showed an average gain loss of about 8%/C/cm, significantly lower than the case without ethanol. We, however, observed appreciable dark currents after a dose of about 0.7 C. The current is source induced; the dark current dropped to zero when we removed the source, but the dark current was re-ignited when the source was reintroduced. The results are summarized in Table 8.5.

Table 8.5: Summary of aging results for argon/ethane (50/50) with 0.5% ethanol

Dose rate (C/day)	Total dose (C)	Peak dose (C/cm)	Loss of gain (%/C/cm)	Other observations
0.1	1.0	0.5	< 5	Substantial dark current was observed after 0.7 C total dose
0.1	4.3	1.7	8	

#### 8.9.4.6 Results with argon/carbon dioxide (80/20)

As described in section 8.9.2, other concerns of the straw materials have prompted us to consider using an argon/CO<sub>2</sub> gas mixture for the straw chambers. Gas mixtures without hydrocarbons are known to be more resilient to aging under harsh radiation environment. On the other hand, it has been reported in the literature that anode aging in argon/CO<sub>2</sub> mix is very sensitive to silicon impurities[10]-[12]. We have constructed a somewhat longer (80 cm) prototype straw chamber to study the aging in an argon/CO<sub>2</sub> mixture. We started with an argon/CO<sub>2</sub> ratio of 80/20. The experimental setup and aging conditions are similar to previous tests. We have done three aging tests at different dose rates using separate regions of the same chamber. The first test was done at a rather high dose rate of about 0.1 C/day. We observed a significant loss of gain, of the order of 50%, after a dose of 2 C/cm. The second test was done at about the same dose rate and the loss of gain in the second test  $\sim 40\%$  at 2 C/cm was consistent with the observation of the first test. We continued the second test to 4 C/cm, and observed 60% gain loss. The third test was done at a dose rate of 0.07 C/day. We did not observe significant loss of gain until the dose reached 0.6 C/cm, at which point the percentage loss of gain is about 8%. The results are summarized in Table 3. We will continue the third test until we reach a dose of 1 C/cm. We plan to do SEM and EDS scans of the three irradiated regions after the third test. In all the aging tests done with argon/CO<sub>2</sub>, we did not observe any significant ( $< 50$  nA) dark current. The results are summarized in Table 8.6.

Table 8.6: Summary of aging results for argon/CO<sub>2</sub> (80/20) gas mixture

Dose rate (C/day)	Total dose (C)	Peak dose (C/cm)	Loss of gain (%/C/cm)	Other observations
0.1	2.0	2.0	47	No dark current observed
0.1	4.0	4.0	60	No dark current observed
0.07	0.6	0.6	8	Test in progress, no dark current observed

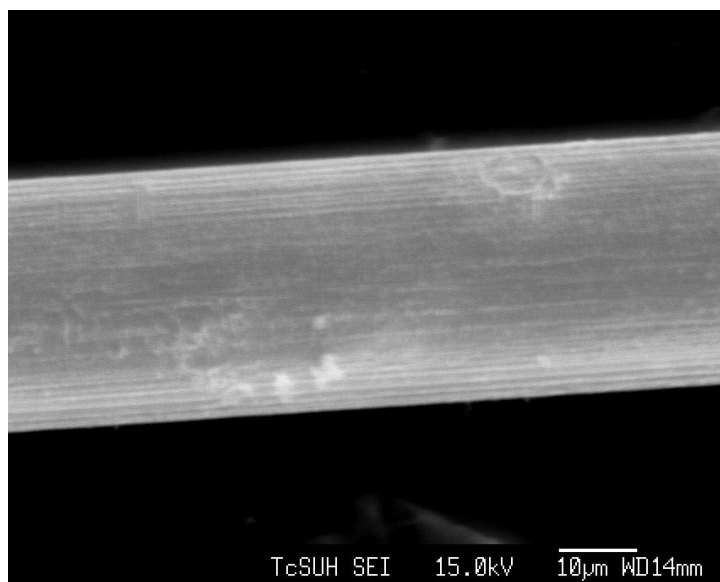


Figure 8.42: SEM picture of a wire far away from the irradiated region. Some imperfections of the wire (streaks and dimples) are visible.

#### 8.9.4.7 SEM/EDS scans

We analyzed the aged wires by Scanning Electron Microscopy (SEM) and Energy Dispersive Spectra (EDS). In a typical run, a 15 keV electron beam impinges on the sample while the emitted X-rays from the sample are analyzed. The SEM image of a good wire is shown in Fig. 8.42 where the streaks of the drawn wire are visible. One can also see some other forms of imperfections on the wire, such as a "dimple" in Fig. 8.42. Fig. 8.43 shows a wire that was exposed to about 1 C/cm of radiation in argon/ethane; the deposits are very visible. The corresponding EDS spectrum provides an elemental analysis of the deposits. Most of the deposits have high carbon content, even though other elements were also seen.

#### 8.9.4.8 Conclusions

We have studied the aging properties of straws in argon/ethane (50/50) mixture with and without ethanol and argon/CO<sub>2</sub> (80/20). Argon/ethane alone shows significant aging at the level of 1 C/cm, the expected total dose in 10 years of running in the worst region. The addition of 0.5% of ethanol to the mixture improves the aging performance of the chamber. The loss of gain is below 10% after a dose of 1 C/cm, but the chamber shows significant dark current after about 0.7 C. Argon/CO<sub>2</sub> looks very promising both in retaining gain and not showing dark current at the dose level of 1 C/cm. We will continue the study to optimize its aging performance.

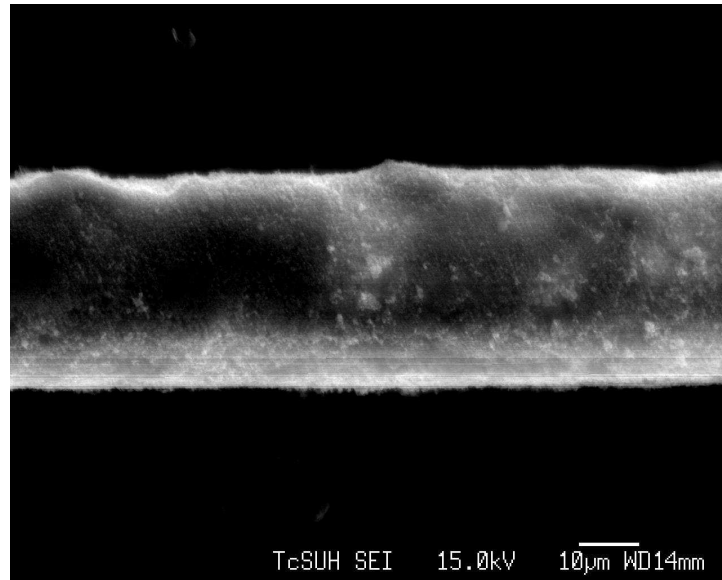


Figure 8.43: SEM picture of an aged wire. The dose of this region is about 1 C/cm.

### 8.9.5 Capillary Fusing

Because of hit occupancy of individual straws, the anode wires of each straw will be divided into two parts using a glass bead "capillary" as the joint between the two segments of the wire. The technique has been used in Atlas Transition Radiation Tracker.

The adoption of glass capillaries as the joints for the segments immediately restricts the use of certain minority components of the gas mixtures such as  $\text{CF}_4$  which was found by Atlas to have a corrosive effect on the glass beads.

The process by which the capillary is inserted and fused to the two wire segments is schematically shown in Figure 8.44.

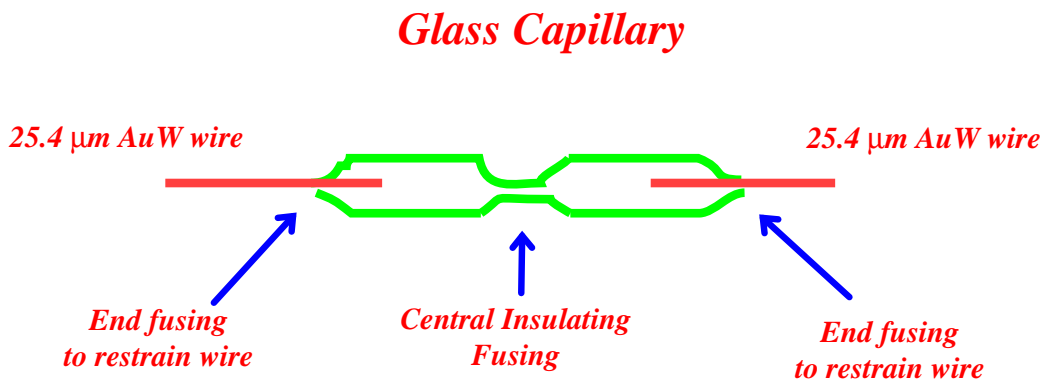


Figure 8.44: Capillary Fusing Technique

As shown in Figure 8.44 there are three fuse points required to join anode wire segments together within the straw. The central fusing is done to insure that the wire segments are electrically insulated from each other. The two end fuses are, obviously, done to provide the mechanical connection between the two segments of the wire.

Based on an estimate of approximately 26K anode wires, this procedure requires some 78K fusing operations. Thus, attention to ease and efficiency of the technique is important. The capillaries themselves are prepared by cutting a glass tube into 6 mm segments with a diamond saw to insure smooth ends. Once the capillaries are prepared and ready for fusing, the fusing operation is done in two steps using two different fusing devices. The central fusing is performed on one device and the resulting capillaries are inspected under a binocular microscope to insure that the capillary is closed. This operation will proceed in parallel to the second end fusing operation insuring a supply of centrally fused and inspected capillaries will always be available to for the second stage end fusing operation.

In the end fusing operation, the anode wire is spooled out to a predetermined length and cut. The ends of the 25  $\mu\text{m}$  gold-plated tungsten wire are inserted by hand using a microscope for positioning into the ends of the centrally fused capillary. The ends are then fused to complete the process. The anode wire together with its capillary is then spooled up to be later unspooled when the wire threading into the various straws is performed. The results of both fusing processes will be recorded by digital camera and a record will be kept on disk for inspection by a supervisor at the end of each shift.

Shown in Fig 8.45 is an overall picture of the prototype fusing mechanism that has been developed at the University of Virginia to accomplish this task. The propane flame used to melt the glass is visible as well as the tongue and groove arrangement for placement of the capillary.

Fig 8.46 shows a view through a binocular microscope of the capillary as it is placed in the holding groove. The configuration of the groove and tongue/slot. is the configuration for central fusing. The extension of this prototype to the configuration for the end fusing is simply a double propane flame and two tongue/slot arrangements for either end of the capillary.

Fig 8.47 shows the capillary being transported through the propane flame by an automated system consisting of a motor/screw-jack arrangement. The height of the capillary above the flame, the temperature of the flame ( 1100°C), and the speed of the transport through the flame were all carefully adjusted.

In addition, the capillary must be restrained since the velocity of the propane gas in the flame is enough to distort the capillaries. All of these parameters have been studied and determined with our prototype and capillaries have been successfully fused. Fig 8.48 shows a successfully center fused capillary.

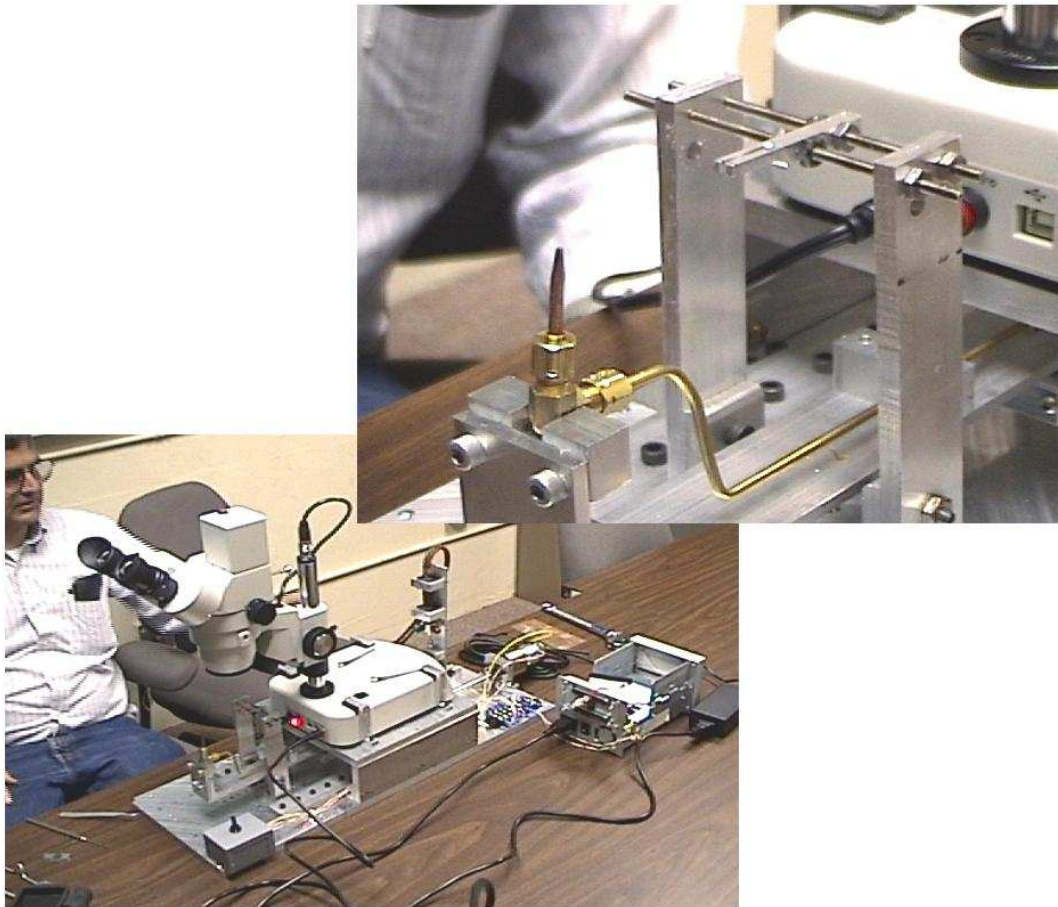


Figure 8.45: The UVa Prototype Capillary Fuser



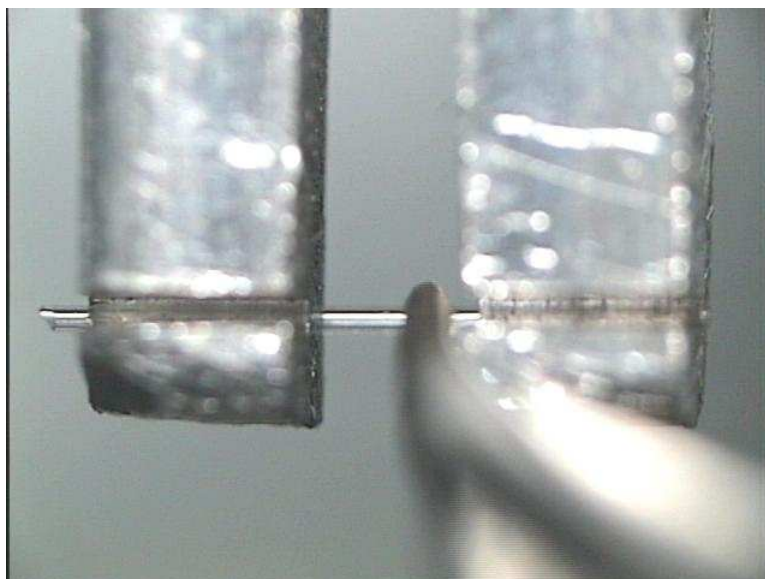


Figure 8.46: Tongue/Groove for seating capillary

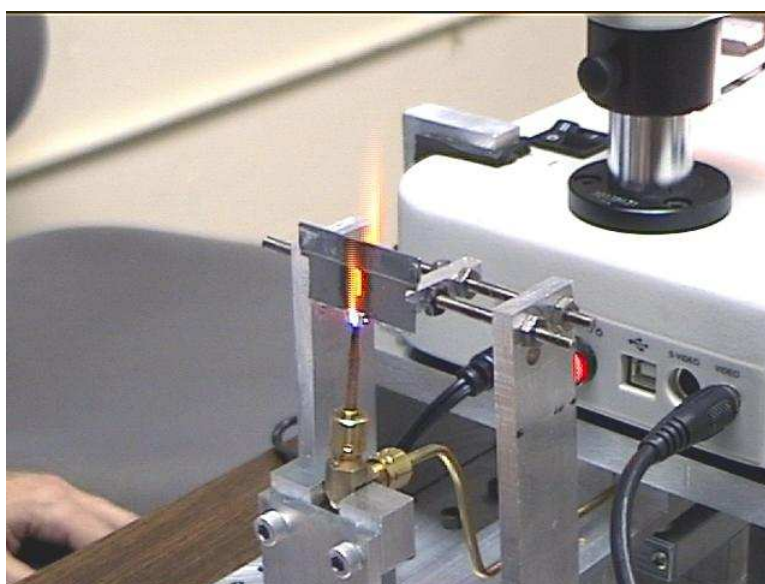


Figure 8.47: The restrained capillary is transported through the 1100°C propane flame

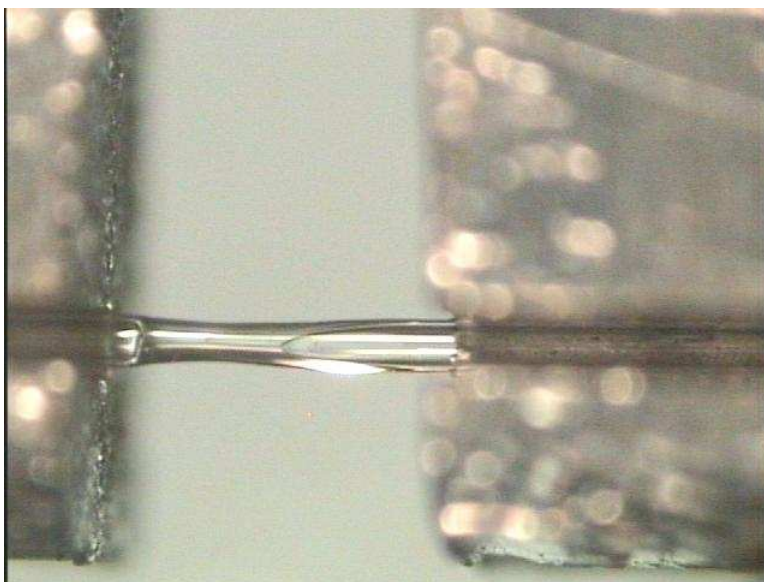


Figure 8.48: A centrally fused capillary

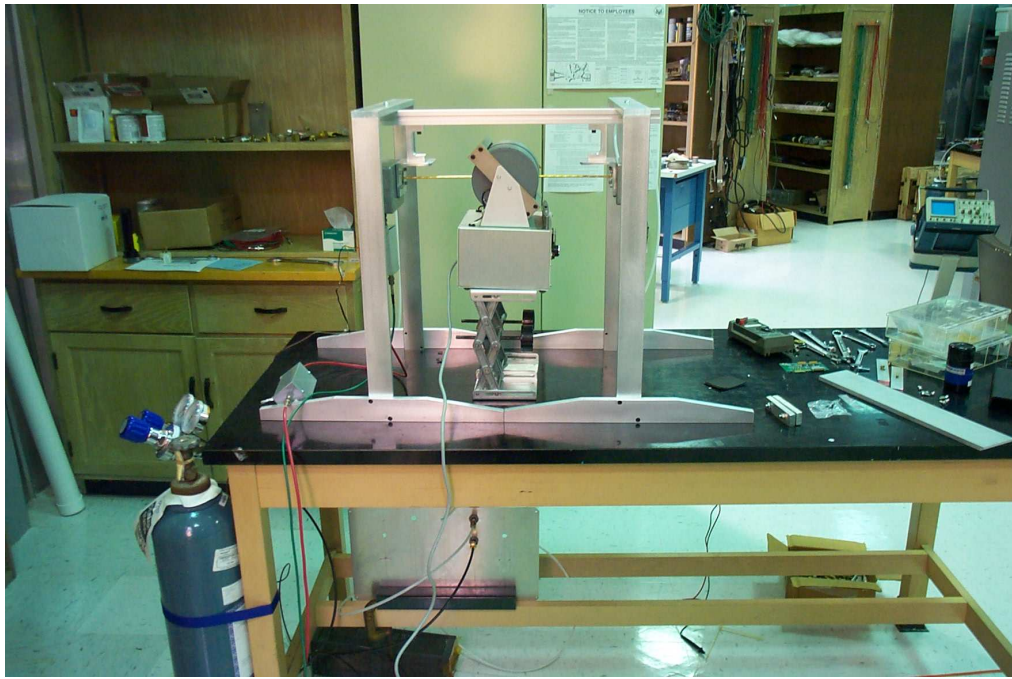


Figure 8.49: Electromagnet/Single Straw Prototype Test Setup

### 8.9.6 Magnetic Field Effects

Some of the straw chambers will operate within a magnetic field of 1.6T (oriented in the horizontal direction). Thus a 1.6T field will be imposed transversely on the vertical straw chamber views of Stations 1 and 2 (and with a lesser field on Station 3). The two  $11^\circ$  views will have an almost axial field imposed on them.

Therefore, studies of the effects of the transverse and axial fields have been started to see if there is any loss of amplitude or distortion of the time distributions due to these fields.

While a full 1.6T field could not be obtained, we have done studies of transverse field effects studies using an electromagnet that produced a 0.75T field transverse to a single 4mm diameter straw prototype. We show the arrangement of the single straw prototype and electromagnet in Fig 8.49.

We oriented the straw so that the field was transverse to the straw and irradiated the straw with a Fe55 photon source. The preliminary data on amplitude effects that has been obtained with a 0.75T transverse field on and field off is shown in Fig 8.50 . The gas mixture used was Ar/CO<sub>2</sub> 80/20 with the voltage set to 1400V. This was the gas mixture and voltage used for all magnetic field tests. As can be seen (and as was expected), no obvious effect of a transverse field was seen.

Because of the geometry of the single straw prototype and the electromagnet pole tips, it was difficult to obtain the axial field configuration. In order to get a substantial axial field, we have used permanent magnets rather than continue with the electromagnet. A permanent

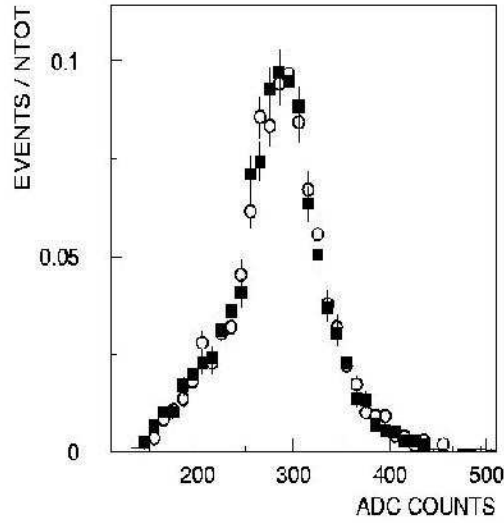


Figure 8.50: Transverse field effect study: Amplitude of signals with transverse magnetic field 0.75T on (circles) and off (squares). Argon-CO<sub>2</sub> 80/20 mixture operated at 1400V

magnet array made of segments of Neodymium 35, an alloy of neodymium iron and boron (NdFeB) which has a very high permanent field (residual induction = 1.23T) and good resistance to demagnetization was used. With the arrangement of segments of Neodymium 35 shown in Fig 8.51 , an axial field of 0.52 T was attained as shown in Fig 8.52. This setup will be installed in the test beam.

### 8.9.7 Beam Test Results

In April–May 2004, collaborators from Fermilab, SMU, UH and UVa took data with 96-straw prototype at Fermilab Beam Test Facility. This section describes first results from the test beam run while the data is still being analyzed.

The experimental setup used during this test is shown in Figure 8.53. Protons from Fermilab Main Injector with energy of 120 GeV cross three layers of straws in the 96-straw prototype. The detailed description of the straw prototype is in Section 8.9.1. Proportional wire chambers (PWC), one on each side of the straw prototype, provide measurements of beam position in vertical direction with  $\pm 250\mu\text{m}$  uncertainty. Each PWC has two Y planes with 1 mm cell size shifted by half of a cell width. Signals from straws and PWCs go to LeCroy TDCs. A coincidence of two scintillator counters (SCINT#1 and SCINT#2) provide trigger for DAQ and common STOP signal for TDC measurements.

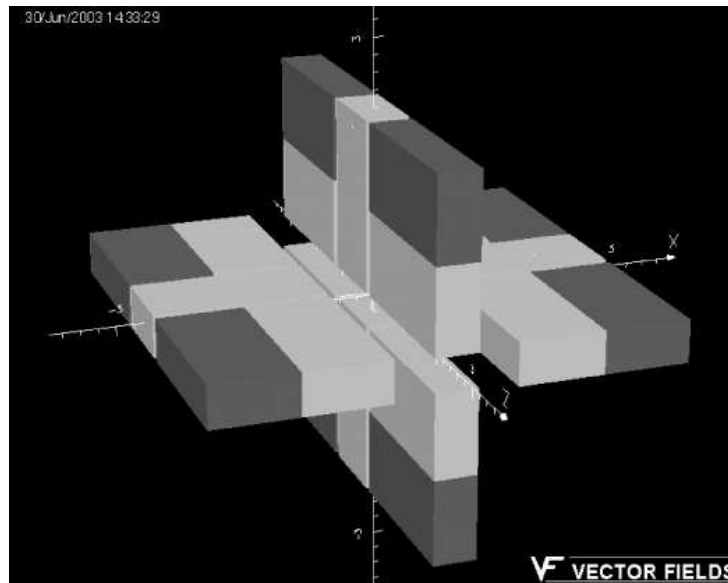


Figure 8.51: Configuration of Neodymium 35 segments to achieve a 0.52T axial field. The light gray segments are the Neodymium 35 pieces and the dark gray are Fe in the arrangement. The axial field is oriented along the z axis.

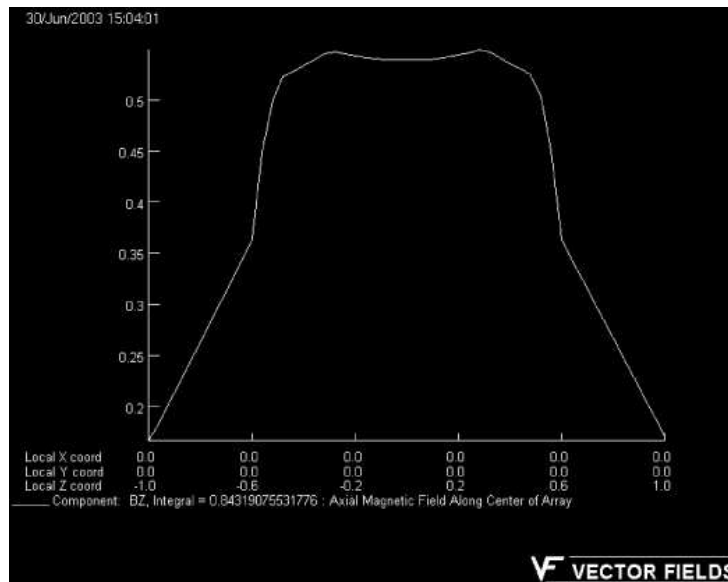


Figure 8.52: Field along the z axis of the Neodymium 35 configuration of Fig. II.4. The units of the vertical axis are Tesla and the horizontal axis are in inches.

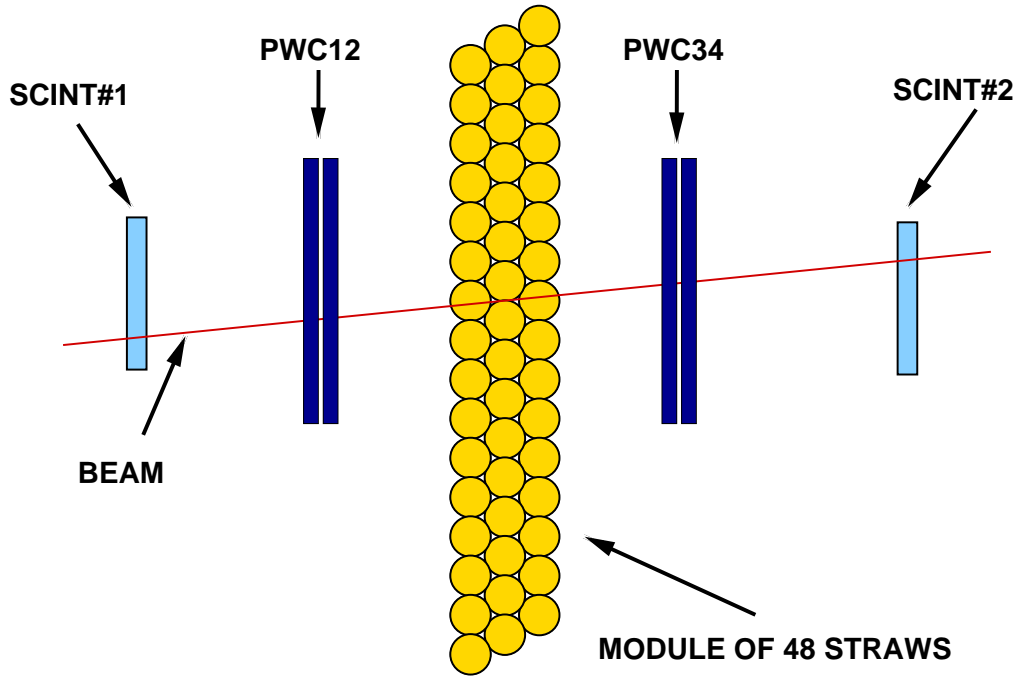


Figure 8.53: Experimental setup used during the Beam Test

The proton beam was wide enough to illuminate several straws. The measured beam size is  $\text{FWHM}=26$  mm. Protons were almost horizontal with very small variations in slope. The measured average track slope is  $-12.0$  mrad. The measured standard deviation of slope fluctuations is  $1.5$  mrad.

The efficiency and position resolution of the straw detector was determined for several Ar-CO<sub>2</sub> gas mixtures. Typically, the performance of a straw depends on a combination of gas multiplication and discriminator threshold: the higher gas gain the better efficiency and resolution of the detector; the higher discriminator threshold the poorer efficiency and the resolution. A combination of gas gain and discriminator threshold can be described by a single parameter, the *effective threshold*, defined as the number of electrons arriving to anode wire simultaneously that will have 50% probability to produce a pulse above the threshold. For example, a 5.9 keV X-ray produces about 210 electrons in Ar-CO<sub>2</sub> 80/20 mixture. These electrons drift towards the anode and arrive at the anode wire almost simultaneously. It was measured that pulses from 5.9 keV X-ray source have a 50% probability of being above a 500 mV ASDQ discriminator threshold at HV=1140 V which corresponds to gas gain of about  $1.52\text{E}+2$ . Therefore, the *effective threshold* for these conditions is  $210e$ . If HV is increased to obtain gas gain of  $1.0\text{E}+5$  without changing the discriminator threshold, the *effective threshold* is reduced to  $3.2e$ .

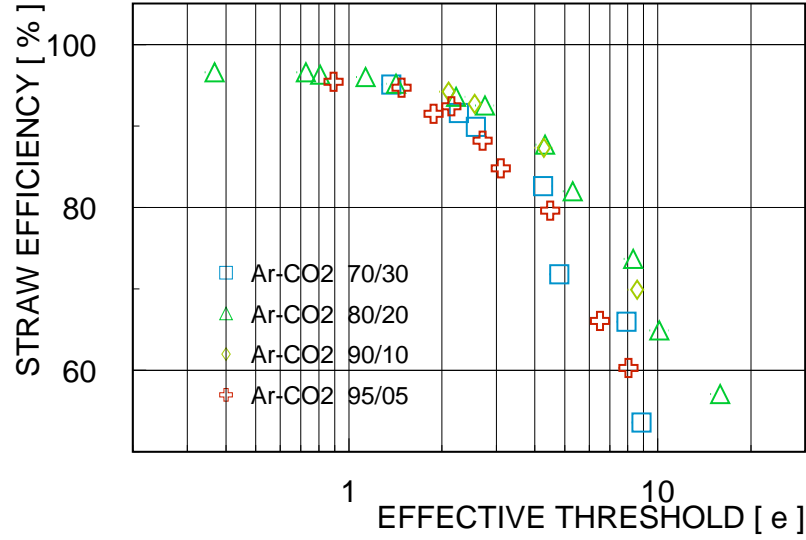


Figure 8.54: Average efficiency of a single straw layer vs “effective threshold” value for several Ar-CO<sub>2</sub> gas mixtures

#### 8.9.7.1 Average Efficiency

The average efficiency of a single layer of straws in the prototype detector was measured for various Ar-CO<sub>2</sub> gas mixtures. The efficiency was calculated as a ratio of the number of single track events with in-time TDC hit in the straw layer over the total number of single track events. A TDC hit was in-time if measured drift time was between -5 ns and +65 ns. This time window is wide enough to accommodate entire range of drift times for all studied gas mixtures. The contribution of accidental hit activity to the layer efficiency was estimated and was found to be negligible. The results are shown in Figure 8.54

Although there is a visible difference in straw efficiency for different gas mixtures at higher values of effective threshold, all mixtures provide an efficiency of 96.5% at the threshold of 1e and below. This measurement includes the inefficiency of a straw layer due to dead spaces between the straws.

#### 8.9.7.2 Position Resolution

To measure position resolution of the straw detector, we use single track events with in-time hits in all three layers of straws, see Figure 8.55. For a straight track, drift distances in each straw have a simple relationship:

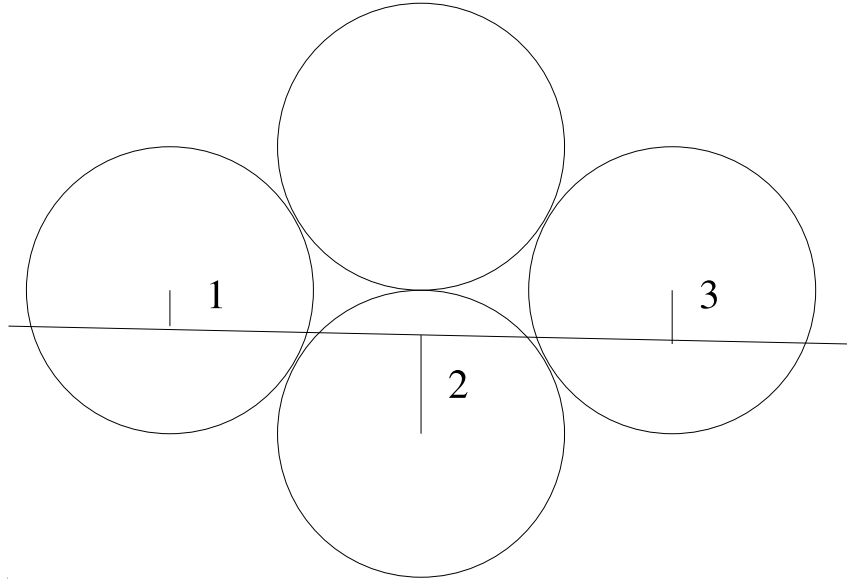


Figure 8.55: A single track event with in-time hits in all three layers of straws

$$\frac{d_1 + d_3}{2} + d_2 = d_{max} = 2mm \quad (8.1)$$

Figure 8.56 shows the correlations between measured TDC values in three layers of straws for single track events. The drift time is T0-TDC with T0=175 ns. Drift distance can be calculated with X(T) functions extracted from data.

The standard deviation of a distribution of measured  $d_{max}$  values is proportional to average position resolution of the straw detector. The coefficient of proportionality is  $\sqrt{1.5}$ .

Figure 8.57 shows the results for measured average position resolution of a straw as a function of effective threshold for several Ar-CO<sub>2</sub> gas mixtures. The CO<sub>2</sub> concentration of 10%-20% provides better position resolution. With this straw prototype we achieved the average position resolution of 160  $\mu m$  at effective threshold of 1e and below. The measured values for position resolution includes such effects as differences in performance of individual straws due to anode wire offsets, non-roundness of straws and straw-to-straw variations in discriminator threshold values.

### 8.9.7.3 Effects of Nitrogen Contamination

BTeV straw detectors will be submerged in dry nitrogen buffer volume to protect straws from humidity variations in atmosphere. We studied effects of possible active gas contamination by nitrogen due to straw leaks. We compare the performance of straw detectors with Ar-CO<sub>2</sub> 80/20 and Ar-CO<sub>2</sub>-N<sub>2</sub> 79.5/19.5/1.0 gas mixtures. The results are shown in Figure 8.58. The presence of 1% of nitrogen in Ar-CO<sub>2</sub> 80/20 mixture reduces gas gain by about 20% and



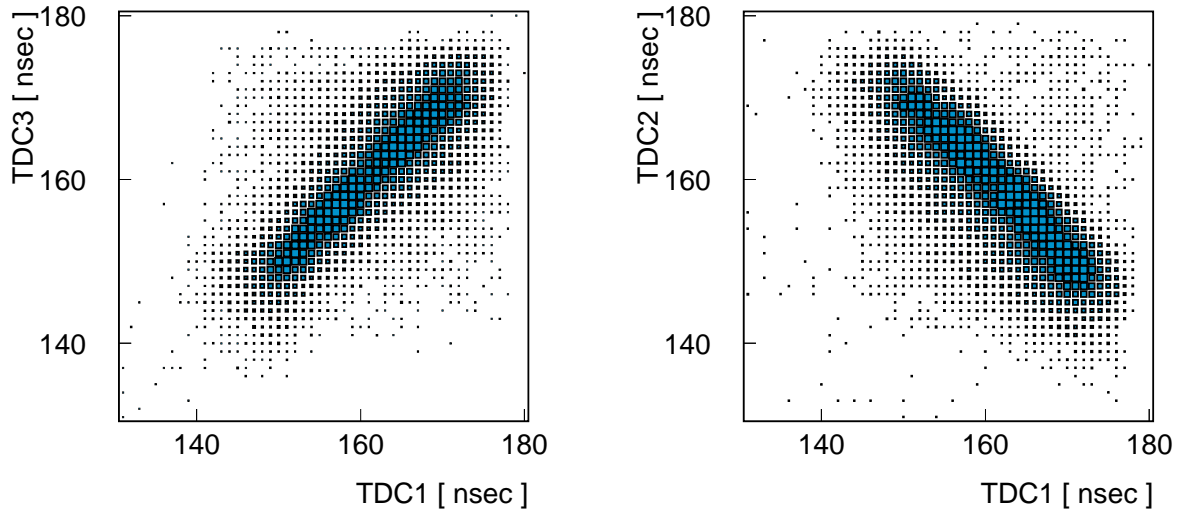


Figure 8.56: Scattered plot of measured TDC values for straws 1 vs 3 and 1 vs 2 (see Figure 8.55) Measurements are taken in Ar-CO<sub>2</sub> 80/20 gas mixtures at HV=1450 V

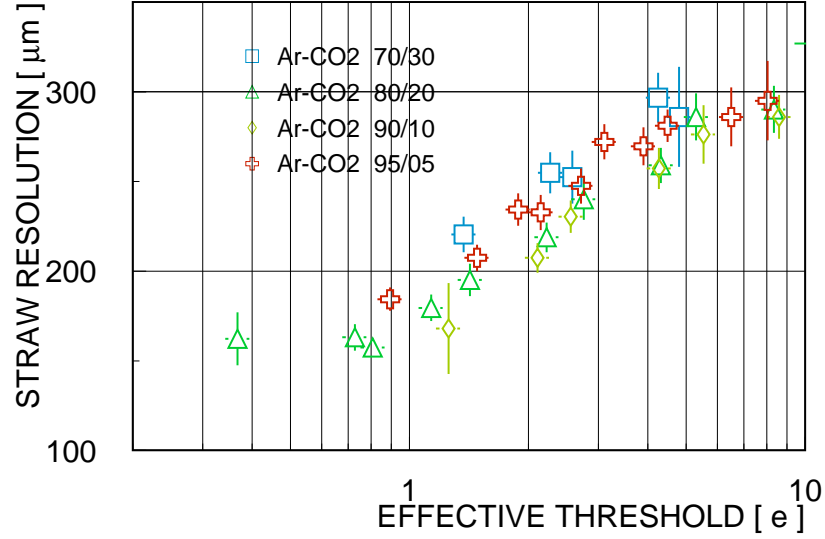


Figure 8.57: Measured average position resolution of a straw vs “effective threshold” for several Ar-CO<sub>2</sub> gas mixtures

therefore increases the effective threshold by the same amount. Once the high voltage is adjusted to compensate this gain loss, there is no visible degradation straw efficiency and position resolution as a function of effective threshold.

#### **8.9.7.4 Conclusions**

While the test beam data is still being analyzed, first results show that we have achieved average efficiency of a single straw layer of 96.5% and average position resolution of a straw of 160  $\mu\text{m}$ . The  $\text{CO}_2$  concentration of 10%-20% is found to be optimal. The measured efficiency includes dead regions between the straws. The measured position resolution includes possible effects from non-roundness of the straws, wire offsets and straw-to-straw variations in discriminator thresholds. As it was mentioned in Section 8.9.2, this prototype was constructed with straws that have large deviations from round shape. The possible consequences are degradation in efficiency due to increase in dead space between the straws and degradation in average position resolution due to straw-to-straw variations in non-round shape. We expect to build straw chambers with straws of much higher quality which will result in better efficiency and resolution.

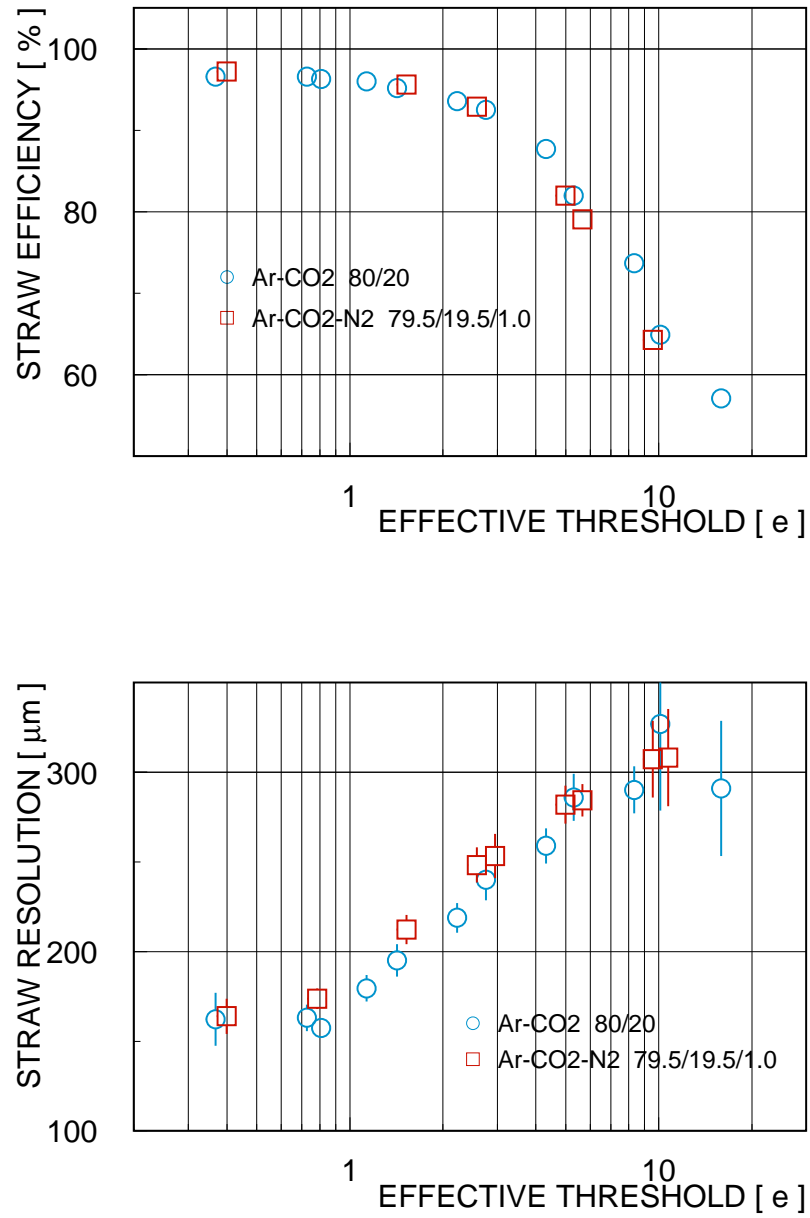


Figure 8.58: Effects of presence of 1% of nitrogen in Ar-CO<sub>2</sub> 80/20 gas mixture on average efficiency of a single straw layer (top plot) and on average position resolution of a straw (bottom plot) as a function of “effective threshold”

## **8.10 Production, Production Testing, and Quality Assurance Plan**

The production of the Straw Detector is broken into major production sites. These sites include the Straw Preparation Site, the Anode Preparation Site, the Module Assembly sites, the Half-View Assembly sites, the Half-View Survey Site, the Electronics Sites, and the Monitor Site. Other work includes miscellaneous systems, fixturing and tooling, and Test Beam Studies. It should be noted that the assigned "Responsible Institutions" are not finalized.

### **8.10.1 Straw Preparation Site**

Responsible Institutions: University of Houston

The Straw Preparation site is responsible for receiving the straws, and wire centering devices from the manufacturers, quality control, and producing a straw of the correct length for a given station. The quality control on a straw will include a test for leak tightness, cathode continuity, and straightness, before any preparation work is done. Some small fraction of the straws will be placed under environmental tests to insure that our mechanical model of the straw remains true. The quality control on a wire centering device will be done through sampling methods. The parameters of interest are the depth of the centering groove, and a surface quality check. A "finished" straw will have the wire centering devices inserted to the prescribed depth for a given module and station number. The Straw Production versus Station number will be monitored via a database so that the Straw production will keep the supply of straws to the Module Assembly Site sufficient so that an orderly schedule of Half-Views Assemblies can continue.

### **8.10.2 Anode Preparation Site**

Responsible Institution: University of Virginia, Southern Methodist University

The Anode Preparation Sites are responsible for receiving the anode wire and glass capillary tubes from the manufacturers, quality control, and production of completed anode wires of the correct length for a given station. The quality control will include testing the anode wire for diameter, smoothness, tensile strength, and conductivity. These tests will be done using sampling methods. A "finished" anode will be composed of insulated segments of wire fused together by a glass capillary. Depending upon the particular module number in a station, there may be either two or three wire segments per anode. The Anode Production versus Station and module number will be monitored via a database so that the anode production will keep an orderly supply of anodes flowing to the Half-View Sites.

### **8.10.3 Module Assembly Sites, including MOX-Silicon Support**

Responsible Institutions: University of Virginia, Fermilab, Frascati

The module assembly site receives the straws from the Straw Preparation site, the straw end-plugs and module endplates from the manufacturers. Quality control is done on the end-plugs (by sampling) and on the module endplates by explicit measurements. A "finished" module will be composed of 48 straws, with glued end-plugs, and glued to two module endplates. The gluing will be done with silver epoxy which provides the electrical connection from the module end-plate to the straw cathode. Quality control on a module will include a leak test and cathode continuity to the end-plate. Since the straw material is sensitive to environmental conditions, it is important that a strict control be made on the relative humidity and temperature of the assembly room at the time the module is glued. This information will be recorded into the production database along with the module ID.

The special X modules(MOX) for supporting the silicon strip stations will be constructed at Frascati.

#### **8.10.4 Half-View Assembly Sites**

Responsible Institutions: University of Virginia, Fermilab

The Half-View Assembly Site receives the modules from the Module Assembly Sites, the anodes from the Anode Preparation Site, the Half- View Frames, the High Voltage Network (HVN) card from the manufacturer, the anode pinning block from the manufacturer, and other various and sundry items necessary for the Half-View Production. If not already done, the HVN card will be burned in for high voltage, otherwise high voltage testing will be done on a sampled set of cards. The Half-View Frames will be quality controlled by direct measurements of the frames. A Half-View will be constructed by inserting the appropriate modules, along with the anode pinning block into the Half-View frame. At this point, the frame can be tensioned, leak tested, and repaired if needed. Then the anodes will be strung. The tension in the anode will be measured online and stored in a database. If the tension is outside limits, the anode can be redone. When a module (or a group of modules) in a Half-View has been strung, it can then be tested for proper operation by flowing a non-flammable chamber gas. In order to do this, the HVN card and a Front End Electronics Board (containing a preamp and a discriminator) must be attached to the frame at the module site. By using a radioactive source, we can count pulses to check that the operation is within specifications. This will be recorded into a database. If the module is outside specifications, repair can then be done. A "finished" Half-View will then be put into storage, with a supply of dry nitrogen gas attached to the input gas supply.

#### **8.10.5 Electronics Sites**

Responsible Institution: Fermilab, University of Virginia, Southern Methodist University, University of Houston

The Electronics Sites are responsible for production and testing of the Front End Electronics Boards: the High Voltage Network (HVN) card, the High/Low Voltage Bus (H/LVB), the Preamp-Discriminator Board (PDB), the Time to Digital Converter (TDC) board. The

HVN card receives positive high voltage from HV power supplies, and buffers it through a load resistor to all straws in a given module. The HVN card also provides high voltage blocking capacitors to the PDB such that the preamp inputs can operate at a virtual ground. The HVN cards will need to be "burned in" in order to insure that they can hold off the high voltage. The H/LVB distributes the high and low voltages inside the frame. The PDB will contain the preamplifier/ discriminator. The TDC board contains not only the TDC function, but also miscellaneous control and communication circuitry to the Data Combiner Boards (DCB). These functions may be implemented in custom circuitry. Quality control on each element will be made before installation in the Half-View Detector. The entire front end system will undergo complete testing at the Survey Site.

### **8.10.6 Survey Site**

Responsible Institution: Fermilab

The Survey Site receives the finished Half-Views from the Half-View Assembly Site. Its function is to measure the location of the anode wires at a point close to the wire centering devices inside the straws with respect to a known set of fiducials on the Half-View Frame. If this wire location is known at each wire centering device site, then the wire position along the straw is simply a straight line between adjacent wire centering devices. This data will be recorded and stored in a database, which will eventually be part of the Straw Detector geometry. The entire front end electronics system will also undergo complete testing at the Survey Site.

### **8.10.7 Gas and Environmental Monitoring Site**

Responsible Institution: Southern Methodist University

The Straw Detector measures position in the straw by determining the time between the interaction and the time the drifting electrons arrive at the anode wire. This drift time can be sensitive to the molecular density of the gas inside the straw. This density depends upon the temperature and atmospheric pressure. The monitoring of the drift speed will take place in several monitors. One monitor will measure the barometric pressure and temperature in the C0 Pit. Another monitor will actually measure the drift speeds in the chamber gas. Another concern with the Straw Detector is the aging which may occur in the high occupancy straws near the beam pipe. We will have gas monitor detectors in which the aging is accelerated by external radioactive sources. We will measure the gain (which is sensitive to aging effects) in these detectors both before the gas enters and after the chamber gas exits the Straw Detector. Any aging seen in these detectors will pre-alert us to problems before they actually occur in the Straw Detector. The straw material is very sensitive to both temperature and humidity. Since the straws are held in place by externally tensioning the straws on the Half-View Frame, it is necessary to keep the Straw Detector within temperature and humidity limits. It will be necessary to monitor these quantities both globally in C0 as well as internally in each sealed Half-View. In case the humidity or temperature climbs outside of tolerances,

the Straw High Voltage must be turned off in order to prevent damage. This Environmental monitor will be responsible for these actions.

### **8.10.8 Other Systems**

Responsible Institution-Fermilab, Frascati, University of Houston, University of Virginia, Southern Methodist University

These systems include the gas system for the straws, the cooling system for the frames and electronics, high and low voltage power supplies and supporting cabling. The quality control on these systems will be done as they are designed and built, or when they are received.

### **8.10.9 Various tooling and fixtures**

Responsible Institutions- Fermilab, Frascati, University of Houston, University of Virginia, Southern Methodist University

All the previous sites will depend upon an infrastructure of tooling and fixtures, including the mechanical design and assembly of the half-view frames. This equipment will be prototyped and designed prior to the start of production. To a great extent, we will rely on previous designs from the Atlas Straw Collaboration, adapted to our particular needs. At this time it appears that the tooling will be constructed at the site where it is expected to be used.

### **8.10.10 Test Beam Studies**

Responsible Institutions- Fermilab, Frascati, University of Houston, University of Virginia, Southern Methodist University

Various beam tests will be done using both prototypes and actual production Half-Views. All the Straw Collaboration members will participate in the Test Beam setups, runs, and analysis.

# Bibliography

- [1] ATLAS Inner Detector Technical Design Report, CERN/LHCC/97-16,17.
- [2] D. Olis, “Load Test of Short Prototype Struts for the BTeV Straw Frame ”, BTeV Doc 2475
- [3] M. Caponero et al., “Use of Fiber Bragg Grating Sensors for detector position monitoring”, BTeV Doc 1297.
- [4] M. Caponero et al., “Composite Materials for FBG”, BTeV Doc 1064
- [5] T. Tope, “BTeV Straw Gas System ”, BTeV Doc 259
- [6] F.M. Newcomer, R. Van Berg, J. Van der Spiegel and H.H. Williams, Nucl. Instrum. Meth. A 283 (1989) 806.
- [7] Results of tension tests for various gases are described in BTeV internal documents:  
P. Kasper, “Straw Tension for different gas mixtures”, BTeV Doc 1686,  
B. Nitti, “Axial Stretch, Temperature, and Humidity Effects on Straw Sag”, BTeV Doc 2610,  
F. di Falco, “Study of tensile response of kapton and mylar strips to Ar and CO2 mixtures”, BTeV Doc 2361
- [8] R. Veenhof, “Garfield Version 7.02” CERN-CNL-2000-001, Vol XXXV, issue no 1, <http://garfield.web.cern.ch/garfield>
- [9] “Aging in large cdf tracking chambers ”, M. Binkley *et al.*, FERMILAB-CONF-02-041-E, Mar 2002, and references therein. To be published in Proceedings of International Workshop on Aging Phenomena in Gaseous Detectors, Hamburg, Germany, 2-5 Oct 2001.
- [10] “Aging studies of cms muon chamber prototypes ”, T. Ferguson et al., Nucl.Instrum.Meth. **A 488**,240-257,2002;
- [11] “Aging studies for the Atlas transition radiation tracker (TRT)”, T. Akesson *et al.*, Oct 2001, to be published in Proceedings of International Workshop on Aging Phenomena in Gaseous Detectors, Hamburg, Germany, 2-5 Oct 2001;



- [12] “Aging properties of straw proportional tubes with A XE-CO-2-CF-4 gas mixture ”,  
M. Capeans *et al.*, Nucl.Instrum.Meth.**A337**, 122-126,1993;

# Chapter 9

## Forward Silicon Tracker

### 9.1 Introduction

The ability of BTeV to study beauty and charm decays to unprecedented precision is critically linked to the performance of its tracking system. The BTeV tracking system is based on the pixel detectors, which identify the tracks and determine their momentum in the vicinity of the interaction region, and on seven stations of straw and silicon strip planes, which cover an acceptance of about  $300\text{ mrad}$  in the forward region. Silicon strip planes are placed in the innermost region, around the beam pipe, where the particle flux is very high, and cover the acceptance from the beam pipe to the inner edge of the Forward Straw system, which starts at  $13\text{ cm}$ .

Our design consists of stations with three planes of  $320\text{ }\mu\text{m}$  thick single-sided silicon strip detectors with  $100\text{ }\mu\text{m}$  pitch. The silicon sensors, which have an area of about  $7.9 \times 7.9\text{ cm}^2$ , are arranged in ladders of 4 daisy-chained sensors each, in such a way that four adjacent ladders form a plane as illustrated in Fig. 9.1.

The ladders are mounted on a low-mass carbon fiber support which is designed to ensure a proper relative alignment among all the elements of a single plane and also among different planes within the same station.

The carbon fiber supports (see Fig. 9.18) can be stacked and properly rotated to provide three views in each station,  $X$ ,  $U$  and  $V$ . The two stereo views,  $U$  and  $V$ , are at  $\pm 11.3^\circ$  around the  $Y$  bend coordinate. Each plane contains 6144 read out channels; the entire system of 7 stations has 129,024 channels in total (1 arm).

The Si-sensors are the standard  $p$ -on- $n$  type and are produced with the same technology developed by the CMS collaboration for their IB2 detectors. They have an outer  $p^+$  guard ring structure suitable for break-down voltages of 700-1000V and an inner ring used to bias the implant through arrays of poly-Silicon resistors.

The front-end electronics is distributed along the two opposite edges of each plane and is cooled by a fluid circulating in a duct embedded in the support structure around the periphery of the plane. The preamplifier chips are AC coupled to the strips by means of

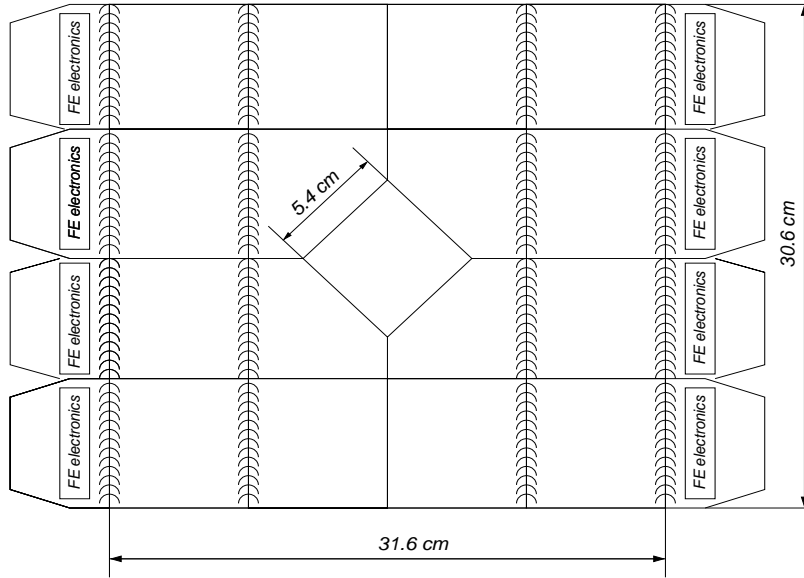


Figure 9.1: Sketch of a Forward Silicon Tracker plane. It consists of four ladders, each with four daisy-chained Si-sensors. The two pairs of sensors on each ladder are read out separately by the front-end electronic chips placed at the two ends of the same ladder. There is some overlap between adjacent ladders to ensure good efficiency over the entire plane.

capacitors directly integrated on the sensors. Each channel is read out in binary mode providing a  $\sigma = 100 \mu\text{m}/\sqrt{12} = 29 \mu\text{m}$  resolution, adequate for our physics goals.

The hybrid circuits, which hold the read out chips at each end of the ladders, are connected to the periphery of the forward acceptance cone by means of a very light Kapton flex cable, which carries all the necessary power supplies, control and data signals. A complete description of all the required items is detailed in section 9.5, (Hybrids and Flex cables).

Table 9.1 lists all the geometric parameters and the main characteristics of the Forward Silicon Tracker system. This configuration has sufficient segmentation to handle the high hit multiplicities that are expected when  $b\bar{b}$  events are produced. Indeed, the peak occupancy value in the Forward Silicon Tracker as predicted by BTeV GEANT is only about 2.4%, for a  $b\bar{b}$  event produced at the design luminosity of  $2 \times 10^{32} \text{ cm}^{-2} \text{ s}^{-1}$ , accompanied by an average of six minimum bias events at 396 ns bunch spacing.

We do not foresee any major problems in building these detectors since we can profit from the enormous experience accumulated in this field in the last few years.

## 9.2 Forward Silicon Tracker general requirements

The Forward Silicon Tracker has to fulfill the following general requirements, which are dictated by the physics goals of BTeV.

Property	Value
Silicon Sensors	$\sim 7.9 \times 7.9 \text{ cm}^2$ , <i>p-on-n</i> type
Pitch	$100 \text{ }\mu\text{m}$
Thickness	$320 \text{ }\mu\text{m}$
Sensor configuration	4 ladders with 4 sensors each
Coverage	$30.6 \times 31.6 \text{ cm}^2$
Central Hole	$5.4 \times 5.4 \text{ cm}^2$ ( $7.9 \times 7.9 \text{ cm}^2$ for last station)
Total Stations	7
Z Positions	85.5, 127.5, 185.5, 277.5, 321.5, 371.5, 714.5
Views per Station	3 (X,U,V)
Channels per view	6, 144
Total Channels	129, 024
Read out	Sparsified Binary

Table 9.1: Properties of the Forward Silicon Tracker.

### 9.2.1 Resolution and mass

The granularity of each micro-strip plane is one of the defining characteristics of the system. The granularity has been chosen to keep the occupancy per strip at the level of a few percent when a  $b\bar{b}$  event is produced at  $2 \times 10^{32} \text{ cm}^{-2} \text{ s}^{-1}$  luminosity. At the chosen value of  $100 \text{ }\mu\text{m}$  pitch, a strip binary read-out is enough to ensure an adequate position resolution for high momentum measurement. Particular care should be devoted to reduce the amount of material in the micro-strip planes.

- **Granularity:** the strips must have a pitch of  $100 \text{ }\mu\text{m}$  and a length equal to one half the length of the ladder.
- **Position Resolution:** the spatial resolution of each micro-strip plane must be of the order of  $30 \text{ }\mu\text{m}$ , corresponding to that achievable by reading out the micro-strips in binary mode
- **Material Budget:** each station should have no more than 1.5 % of a radiation length (averaged over a  $30 \text{ cm}$  radius circle around the beam pipe), including all support structure material.

### 9.2.2 Read Out

BTeV is designed to operate at a luminosity of  $2 \times 10^{32} \text{ cm}^{-2} \text{ s}^{-1}$  with beam-crossing intervals or 132 ns or 396 ns. In the latter case, an average of 6 interactions per beam crossing are expected. No Level 1 Trigger is available to read out micro-strip data. All hit data must be read out in a zero suppressed format, and spurious hit data must be minimized. The Forward Silicon Tracker must have high enough bandwidth so that all data from every beam

crossing can be read out and temporarily stored for high-level trigger decision and eventually data acquisition.

The specifications for the read out chip are given in Sec. 9.4. The general specifications for the full read out system are:

- **Noise:** the noise rate of the system must be less than  $10^{-3}$  per strip.
- **Efficiency:** at design luminosity, each micro-strip plane must have a hit efficiency of 95 % during its entire operational lifetime. This includes losses due to dead strips, noisy strips whose output is suppressed, and any loss of data by read out electronics, or read out dead time.
- **Read out bandwidth:** the Forward Silicon Tracker read out should be very fast and data-driven. This means that all hit strip data have to be read out and be available to the trigger processor every bunch crossing.

### 9.2.3 Radiation hardness

The anticipated radiation field at the Forward Silicon Tracker has been estimated with BTeV GEANT and MARS calculations. The hottest regions will be those nearest the beam on each detector element. Radiation hardness requirements are driven by the most exposed plane near the interaction region. Here, the integrated number of minimum ionizing charged particles per ten years of running at a luminosity of  $2 \times 10^{32} \text{ cm}^{-2} \text{ s}^{-1}$  has a peak value of  $\sim 2 \times 10^{14} \text{ cm}^{-2}$  on the inner detector edge around the beam pipe and falls off to a value of  $\sim 10^{13} \text{ cm}^{-2}$  on the detector periphery, where read out electronics are located. The detector components must continue operating in this environment, with acceptable levels of signal-to-noise, operating voltages, efficiency, and spatial resolution.

- **Radiation Tolerance:** All the components of the Forward Silicon Tracker, including read out chips, sensors and glues must remain operational up to 10 years of BTeV running at the nominal luminosity.

### 9.2.4 Dimensions

The Forward Silicon Tracker detector dimensions are chosen to cover all the inner zone of the forward acceptance, where the particle flux is too high to be handled by straws. The inner hole on the planes is determined by the radius of the beam pipe, which is constant for all stations except the last one.

- **Size of micro-strip planes:** the dimensions of the active area of the micro-strip planes must be  $27 \times 27 \text{ cm}^2$  at least.
- **Size of the inner hole:** the size of the inner hole in the micro-strip planes should be  $5.4 \times 5.4 \text{ cm}^2$  for the first 6 stations and  $7.9 \times 7.9 \text{ cm}^2$  for the last one.

## 9.2.5 Electrical & Magnetic Interference

The Forward Silicon Tracker must be designed to withstand the magnetic forces that occur on materials inside the vertex magnet and in its extensive fringe field region. In addition, it must be able to withstand the transient-induced eddy current forces that occur on any electrically conducting material when the vertex magnet is ramped to maximum current, or, more importantly, when it trips off.

- **Immunity from dipole magnet:** The whole Forward Silicon Tracker and its read out electronics must not be affected by the presence of the 1.6 T magnetic field or by tripping of the magnet.

## 9.3 Sensors

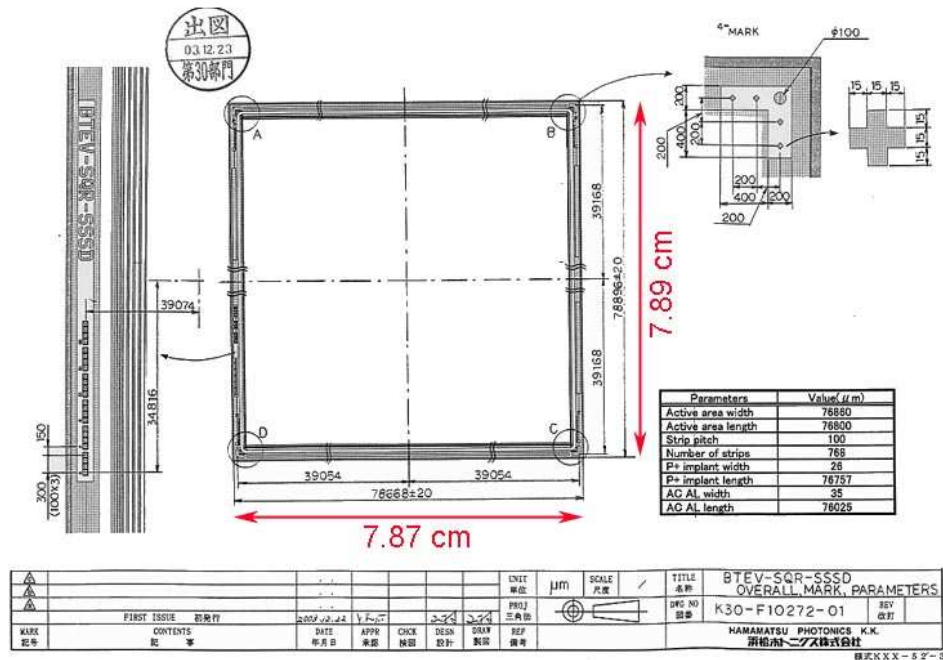


Figure 9.2: Details of the silicon strip sensors. Shown are the alignment markers placed along the sensor borders.

The sensors we plan to use have a 100  $\mu m$  pitch and 320  $\mu m$  thickness. Referring to Fig. 9.1, the shape of the employed sensors is square,  $\sim 7.9 \times 7.9 \text{ cm}^2$ , with the exception of the four sensors surrounding the hole for the beam pipe. In this case two kinds of sensors with a corner cut-out at  $45^\circ$  are adopted, one the mirror image of the other.

The most important parameter that has to be taken into account in order to define the type and the technology of the BTeV sensors is the radiation environment where they are



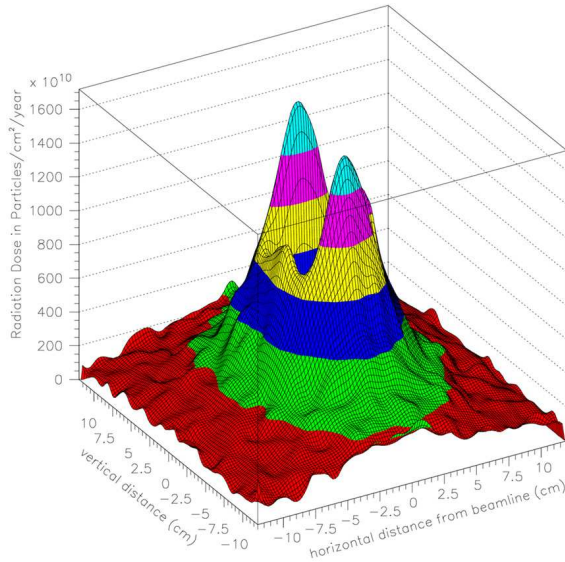


Figure 9.4: Radiation dose as a function of position in Forward Silicon Tracker Station # 1. The horizontal magnetic field concentrates more particles above and below the square central beam hole than on either side.

still remains lower than 400 V. This fluence corresponds to about twice the expected dose for 10 years of BTeV operation (we used the conversion factors quoted in [5]). By lowering the bulk resistivity at  $1\text{--}3\text{ K}\Omega\text{ cm}$ , one can even improve the radiation hardness by shifting toward higher values the fluence at which the *type-inversion* takes place. The second critical parameter that was measured as a function of the irradiation dose is the breakdown voltage. With a proper choice of technology [6] the breakdown voltage still remains higher than 500 V after the same dose of  $\sim 2 \times 10^{14}/\text{cm}^2$  1 MeV neutrons. For these sensors, a particular ratio between strip width and pitch,  $w/p = 0.25$ , was chosen as a compromise between a low total strip capacitance and a stable detector operation at high voltage. Each strip had a metal overhang in order to enhance the breakdown performance. It was determined that for the  $\langle 100 \rangle$  crystal orientation the inter-strip capacitance does not depend on the irradiation dose.

On the basis of the previous arguments, the Si-sensors we intend to use in BTeV are of the standard *p-on-n* type and are produced with the same technology developed by the CMS collaboration for their IB2 detectors. They have an outer  $p^+$  guard ring structure suitable for break-down voltages of 700-1000V and an inner ring used to bias the implant through arrays of poly-Silicon resistors. These sensors can be provided by several vendors, such as Hamamatsu, ST or SINTEF. We bought a dozen of these sensors from CMS (CMS IB2 sensors,  $61 \times 116\text{ mm}^2$  active area,  $120\text{ }\mu\text{m}$  pitch,  $320\text{ }\mu\text{m}$  thickness,  $30\text{ }\mu\text{m}$  implant width,  $\langle 100 \rangle$  crystal type) to certify their performance and their radiation tolerance at the doses expected in BTeV. Our preliminary results from the irradiation tests we performed in the



summer 2004 at the University of Indiana Cyclotron Facility demonstrate that this type of sensors can be safely used in BTeV without any important degradation of their performance for at least ten years.

After an absorbed dose of 5 MRad (equivalent to the maximum dose expected in a small annular region surrounding the beam-pipe after ten years of operation in BTeV), the loss of signal is limited to only a few percent, provided the bias voltage is raised to 350 V. The reverse current can be heavily reduced in the range of a few tens of microAmperes, with enormous benefits in terms of noise, if the sensors are run at a temperature around  $-10^{\circ}\text{C}$ . For additional details of our measurements on irradiated sensors we invite the reader to refer to the specific R&D section at the end of this chapter.

The general layout of the sensors we intend to use in BTeV is given in Fig. 9.2 and the details of the strips and the guard-ring in Fig. 9.3.

## 9.4 Electronic read out

The front-end processing of the signals from the Forward Silicon Tracker will be performed by custom-designed ICs mounted on hybrid circuits that distribute power and signals, and thermally interface the ICs to the cooling system. The ICs consist of 128 channels, each connected to a detector strip. The signals from the strips, after amplification and shaping, are compared to a preset threshold. To achieve the required position resolution, the channels have to provide only a binary information (hit / no hit), generating a logic 1 at the output if a signal exceeding the threshold is detected. An additional 3 bit analog information will be provided by a Flash ADC for calibration and monitoring purposes. The dimensions of the read out IC are expected to be about  $7.5 \times 4.5 \text{ mm}^2$ , while the power dissipation will be about 4 mW/channel. For each channel with a signal above threshold the strip number, the chip identification number, and the related bunch crossing number will be read out and transmitted to a Power/Data Splitter Board and afterwards to the Data Combiner Board. The read out chips use the same programming and data output interface as the pixel read out ICs, so the same DAQ system can be used. The data output from the Forward Silicon Tracker will be sparsified, i.e. will consist only of those channels generating a hit above a suitably chosen threshold.

### 9.4.1 Read out chip

#### Requirements

The micro-strip electronics must ensure that the detector system operates with adequate efficiency, but also must be robust and easy to test, and must facilitate testing and monitoring of the micro-strip sensors. AC coupling is assumed between the strips and the read out electronics.

- **Binary read out:** The micro-strip read out should be binary with a threshold of about 0.2 MIP.

- **Dynamic Range:** The dynamic range of the front-end chip should cover up to 2 MIP's.
- **Peaking Time:** The peaking time of the front-end signal at the shaper output should ensure that the comparator output be latched in the correct bunch crossing (at 132 *ns* or 396 *ns* bunch crossing period).
- **Noise:** The equivalent r.m.s. noise of the front-end electronics has to be  $\sim 1000 e^-$  at  $C_D=20 pF$  and should not increase significantly after irradiation.
- **Threshold and Dispersion:** Each microstrip channel will be read out by comparing its signal to a settable threshold around 0.2 MIP. This analog threshold shall be adjustable via digital control for each channel. Typical settings shall be from 2000 to 5000 equivalent electrons at the input. Threshold dispersion must be low enough that the noise figure of the analog section of the front-end,  $\sim 1000$  electrons, would not be significantly degraded. Typically, this should be 400 electrons at most and should be stable during its entire operational lifetime.
- **Comparator Time Resolution:** The comparator must be fast enough to guarantee that the output can be latched in the correct bunch crossing (at 132 *ns* or 396 *ns* bunch crossing period)
- **Time Stamp:** Each Forward Silicon Tracker hit must be given a correct timestamp which identifies the beam crossing number.
- **Masking, Kill and Inject:** Each Forward Silicon Tracker channel must be testable by charge injection to the front-end amplifier. By digital control, it shall be possible to turn off any micro-strip element from the read out chain.
- **Cross-talk:** Must be less than 2%
- **Power Consumption:** The power consumption of each read out channel must be less than 4 *mW*
- **Control of Analog Circuitry on Power-Up:** Upon power-up, the read out chip shall be operational at default settings.
- **Memory of Downloaded Control of Analog Circuitry:** Changes to default settings shall be downloadable via the read out chip control circuitry, and stored by the read out chip until a new power-up cycle or additional change to default settings.
- **Read-back of Downloadable Information:** All the data that can be downloaded also shall be readable. This includes data that has been modified from the default values and the default values as applied on each chip when not modified.
- **Data Sparsification:** The data output from the Forward Silicon Tracker shall only consist of those channels that are above the settable threshold.

- **Micro-Strip output data content:** The Forward Silicon Tracker hit data must include the beam crossing number, chip identification number, and the micro-strip hits for that beam crossing.
- **Efficiency:** At design luminosity, the Forward Silicon Tracker read out must have a hit efficiency of at least 99% during its entire operational lifetime. This includes any loss of data by read out electronics or read out dead time.
- **Read out bandwidth:** The Forward Silicon Tracker read out should be very fast and data-driven. This means that (on average) all hit strip data have to be read out and be available to the trigger processor every bunch crossing.
- **Radiation Tolerance:** All the components of the Forward Silicon Tracker read out system must remain operational up to 10 years of BTeV running at the nominal luminosity.

## Implementation

The Fermilab Silicon Strip read out (FSSR) chip is a mixed-signal circuit occupying an area of about  $7.5 \times 4.5 \text{ mm}^2$ . It can be described as including four logic sections, as shown in Fig. 9.5. They are the core, the programmable registers and digital-to-analog converters, the programming interface and the data output interface. The architecture of the digital back-end is called pseudo-Pixel. It is based on the BTeV pixel read out chip, FPIX2. The I/O protocols for the two chips are identical. The 128 strips serviced by one chip are subdivided into 16 sets of 8 strips. Each set is made to behave like a single column in the FPIX2 architecture. While FPIX2 is a  $22 \times 128$  array of pixels, FSSR will look like a  $16 \times 8$  FPIX2. The same programming and data interface used in FPIX2 is used again in FSSR. This implies that there will be a 24 bit data word output by the FSSR. 3 bits will be used for the analog information provided by the Flash ADC, 4 bits will be necessary to encode the strip number, 5 bits will be used to encode the set number, 8 bits will be used for the BCO number and 1 bit will be used as the sync bit. This leaves 2 extra bits. The chosen architecture is called pseudo-Pixel. It is essentially identical to the architecture of the pixel read out chip FPIX. The 128 strips serviced by one chip are sub-divided into 16 sets of 8 strips. Each set is made to behave like a single column in the FPIX architecture. While FPIX is a  $22 \times 128$  array of pixels, FSSR will look like a  $16 \times 8$  FPIX. The same programming interface and data interface implemented in FPIX is used again in the FSSR. This implies that there will be a 24 bit data word output by the FSSR. Four bits will be necessary to encode the strip number; 5 bits will be used to encode the set number; 8 bits will be used for the BCO number and 1 bit will be used for the sync bit. This leaves 6 extra bits.

The FSSR core consists of 128 analog read out channels, logically subdivided in 16 sets of 8 channels each, the end-of-set logic (16 blocks, one for each set of front-end channels) and the core logic, which controls the data flow from the core to the data output interface. The programming interface accepts commands and data from a serial input bus and, in response to a command, provides data on a serial output bus. The programmable registers

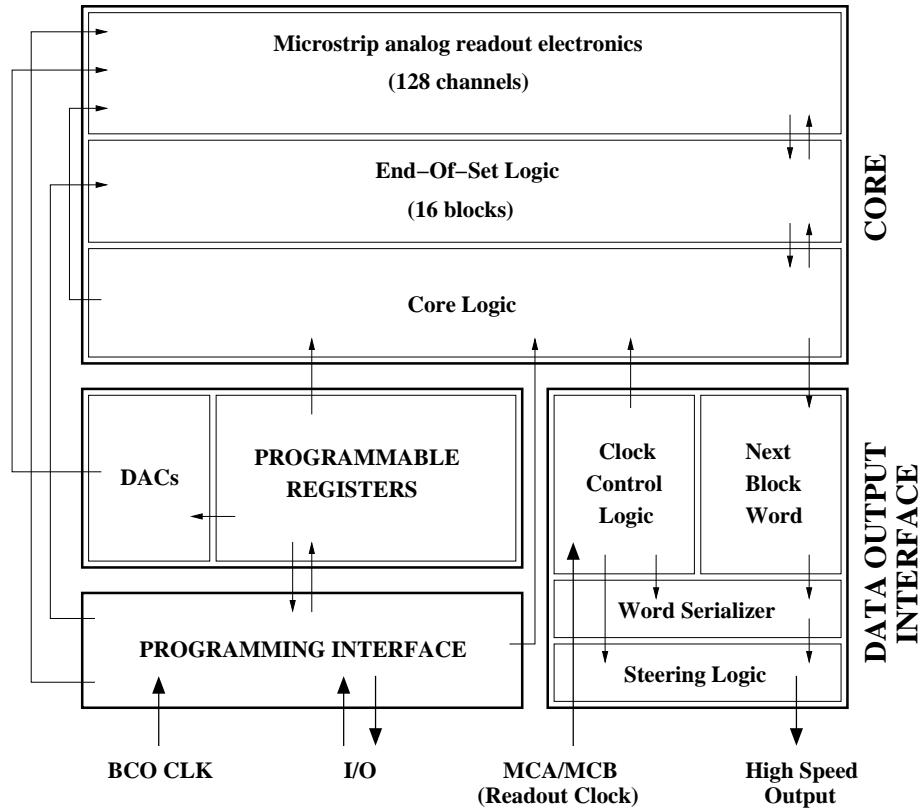


Figure 9.5: FSSR chip block diagram. Arrows represent control and data flow.

are used to store input values for DACs that provide currents and voltages required by the core, for instance the threshold levels for the discriminator in the analog channel. They also have additional functions, such as controlling data output speed and selecting the pattern for charge injection tests. The data output interface accepts data from the core, serializes the data and transmits them off-chip, using a point-to-point protocol. All I/O (except the test signal injection) is differential and is fed by means of Low Voltage Differential Signaling (LVDS). Analog bias is fed to the analog channel blocks, with the exception of the discriminator.

The analog section of the FSSR Core consists of 128 channels, each including a charge preamplifier, an integrator, a shaper and a discriminator. A symmetric baseline restorer is included to achieve baseline shift suppression. The block diagram of the analog channel is shown in Fig. 9.6.

The Core communicates with the other FSSR logical blocks through the Core Logic. The 128 front-end channels are subdivided in 16 sets of eight channels each. Each of the 16 blocks composing the End-Of-Set Logic deals with one of the eight channel sets. Operation of the FSSR Core is similar to the FPIX Core and is schematically represented in Fig. 9.7. The ChipHit and ChipHasData lines shown in the picture are two diagnostic signals. In

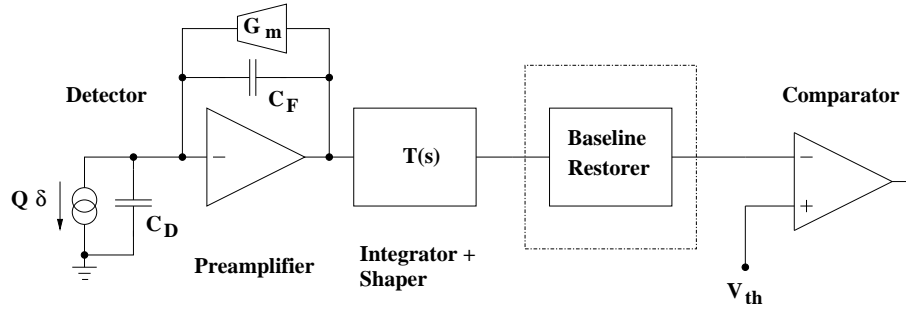


Figure 9.6: FSSR analog channel block diagram.  $G_m$  is the preamplifier transconductor,  $C_F$  is the preamplifier feedback capacitance,  $C_D$  is the detector simulating capacitor and  $V_{th}$  is the discriminator threshold voltage. For the sake of simplicity, integrator and shaper are represented by a single block, whose transfer function is  $T(s)$ .

particular, ChipHit goes high whenever a discriminator fires while ChipHasData goes high every time the core has data to output.

The Programming Interface is the same as in FPIX. It provides a means for the user to control the operation of the FSSR chip, and to load and read back the contents of any of the Programmable Registers.

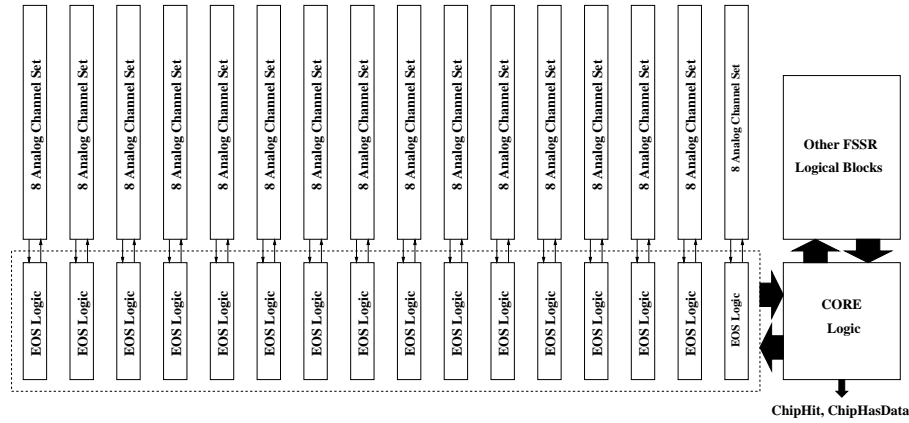


Figure 9.7: Block diagram of the FSSR Core.

## R&D

The R&D to support the development of the FSSR chip begun in 2002. The chosen technology for integration is a deep submicron CMOS process, which can be made highly radiation resistant with some proper layout prescriptions such as enclosed NMOS transistors and guard rings. The chip is fabricated in the TSMC (Taiwan) process with  $0.25 \mu m$  minimum feature

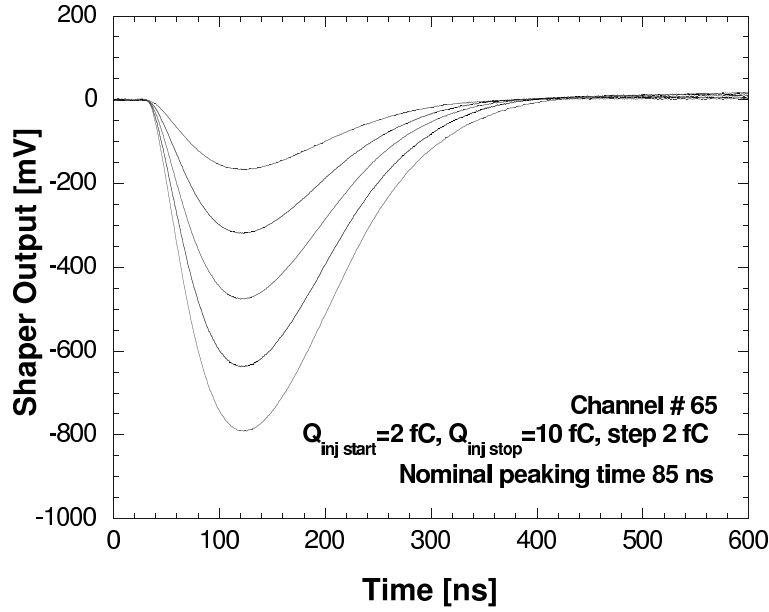


Figure 9.8: Waveforms at the output of the shaper in the FSSR prototype at a peaking time setting  $t_P=85$  ns.

size, which has been successfully used for the implementation of the FPIX pixel read out chip. This allows us to use FPIX as a prototype for the FSSR back-end, reducing the number of needed prototypes and the overall cost.

The read out architecture[11], with the 128 front-end channels subdivided into 16 sets of eight channels each, was tested with realistic data created by Monte Carlo analysis of the interaction region, running with a back-end clock equal to 4 times the BCO clock frequency. Verilog simulations indicate the chip will be able to operate with the required 99% efficiency. The analog section of the chip [9] [10] was optimized from the standpoint of noise, comparator threshold dispersion and sensitivity to variations of process parameters. It is possible to select the peaking time of the signal at the shaper output (60 ns, 85 ns, 125 ns) by changing the value of capacitors in the integrator and in the shaper. In this way the noise performances of the chip can be optimised according to the signal occupancy, preserving the required efficiency. The first FSSR prototype was submitted in July 2003. This prototype has the same structure as the final chip. It consists of 114 analog channels connected to a full back-end section. The prototype was successfully tested. Both the analog front-end and the digital back-end were found to function properly. Fig. 9.8 and Fig. 9.9 show the measured signal waveforms at the shaper output and the Equivalent Noise Charge ENC as a function of the detector capacitance CD. These data are in very good agreement with simulations, and noise performance is within the specifications. ENC values for channels with different input device differ by 10-15 %. Presently (September 2004) work is under way to perform tests with strip detectors. Table 9.2 shows the main measured parameters of the analog section. Given

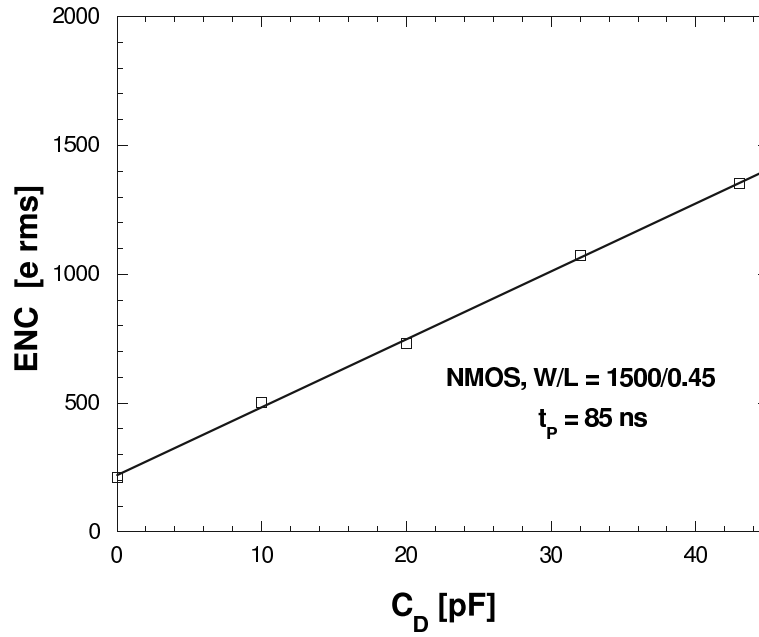


Figure 9.9: Equivalent Noise Charge ENC as a function of the detector capacitance  $C_D$  at a peaking time setting  $t_P=85$  ns in the FSSR prototype. The preamplifier input device is an NMOS with  $W/L=1500/0.45$ .

the successful results of the first prototype, the submission of a full-scale, 128-channels chip prototype is foreseen in late 2004. This version will have the full functionality of the final production chip. With respect to the first prototype, the preamplifier gain will be increased to reduce threshold dispersion. The 3 bit Flash ADC will be also added to get the analog information necessary for calibration and monitoring of the system.

Power dissipation	$P=3$ mW			
Preamplifier input device	NMOS, $W/L = 1500/0.45$			
Charge sensitivity	$G_Q=75$ mV/fC			
Comparator rms threshold dispersion	Without baseline restorer: $\sigma Q_{th}= 800$ e rms With baseline restorer: $\sigma Q_{th}= 450$ e rms			
Signal peaking time at the shaper output		$t_P=60$ ns	$t_P=85$ ns	$t_P=125$ ns
Equivalent Noise Charge at $C_D=20$ pF	W. basel. res.	900 $e^-$ rms	750 $e^-$ rms	600 $e^-$ rms
	W.o. basel. res.	1100 $e^-$ rms	870 $e^-$ rms	750 $e^-$ rms

Table 9.2: Measured parameters of the analog section of the prototype FSSR chip.

## 9.5 Hybrids and Flex cables

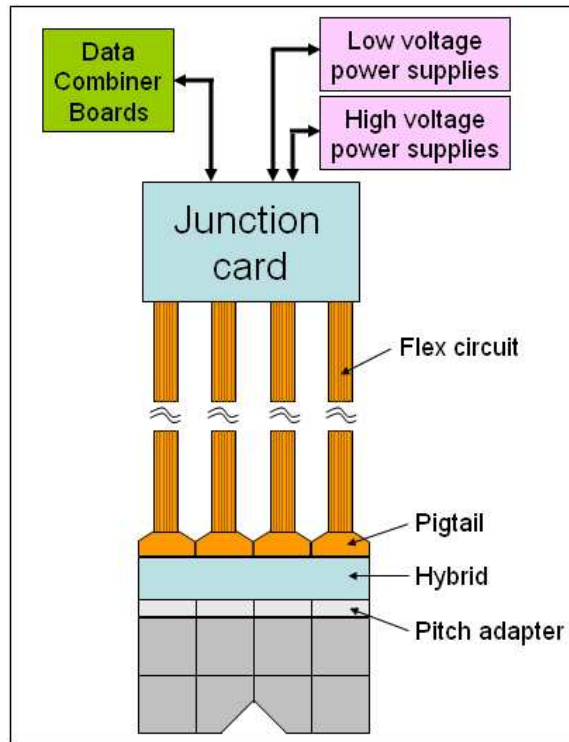


Figure 9.10: Organization and cabling of the Forward Silicon Tracker electronics: the Junction Card, located outside the acceptance region, repeats the signals between the read out chips and the Data Combiner Board and distributes the power to the chips and the sensors. The electrical connection between the Junction Card and the detectors is provided by very low-mass flex cables.

Fig. 9.10 provides a sketch of the organization and cabling of the electronics of the Forward Silicon Tracker. The Data Combiner Boards are the interfaces to the BTeV DAQ. The Junction Card, located outside the acceptance region, repeats the signals between the read out chips and the Data Combiner Board and distributes the power to the chips and the sensors. Silicon sensors are connected to the read out chips on the hybrids via pitch-adaptor circuits, whose function is to provide a correct matching between the different granularity of the wire bonding pads of the hybrid and the micro-strip; hybrids, in turn, are connected to the Junction Card through very low-mass flex cables, whose first short portion, the *pigtail*, can be detached thanks to miniaturized connectors; and, finally, the Junction Card is connected to the power supplies and to the Data Combiner Board by means of regular cables. The actual modularity of the electronics is that indicated in the sketch: one Data Combiner Board serves one Junction Card, which, in turn, serves four hybrids, i.e. four half-ladders. The hybrid substrate is composed of Beryllium Oxide, a very reliable technology which was



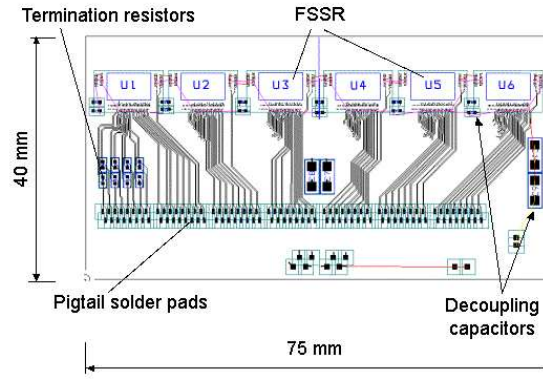


Figure 9.11: Layout of the hybrid circuit lodging six FSSR read-out chips.

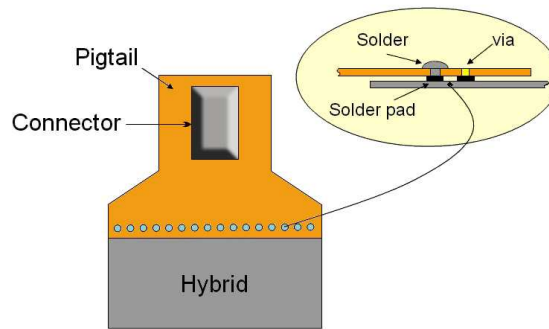


Figure 9.12: Schematics of the *pig-tail* which connects the hybrid circuit to the flex cable.

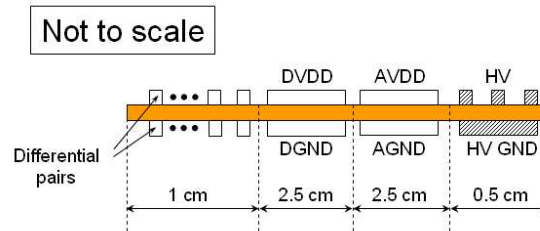


Figure 9.13: Cross section of the flex cable. Signal differential pairs, digital (DVDD) and analog (AVDD) low-voltage power supply as well as high-voltage power supply (HV) are shown. The mean radiation length of these cables is about 0.2 %.

successfully employed for the proposed RUN IIb upgrade of the CDF Silicon tracker. Details

of the hybrid circuit, the pig-tail flex cable and the flex cable are given in Fig. 9.11, Fig. 9.12 and Fig. 9.13, respectively.

In the present prototype version of the hybrid, see Fig. 9.11, we connected to the flex-cable all the serial data outputs and controls of the read out chips. These sum up to 56 differential signals or 112 lines. In the final layout, both for the hybrids as well as for the flex-cables, we will use only the lines required by our expected data-rate.

## 9.6 Mechanical support and cooling system

### 9.6.1 Requirements

The mechanical structure of the Forward Silicon Tracker system and the embedded cooling system have to fulfill the following requirements.

#### 9.6.1.1 Mechanical Support System

Each micro-strip detector plane must be divided in two halves to allow for assembly around the beam pipe. Since each half could be pre-assembled with extreme accuracy in a properly equipped lab and even the relative alignment between the two halves of a plane could be guaranteed by an adequate mechanical design, particular attention should be devoted to define requirements for the final assembly procedure in the experimental hall. Proper alignment marks should be provided both on the mechanical structure of the system and on some fixed reference of the hall. Proper survey instrumentation should be available for the final assembly. Once the detector stations are positioned with a precision of  $250\ \mu m$ , fine alignment can be established offline by a conventional track-residuals minimization procedure. The main requirement is to ensure sufficient stability of the system to maintain the alignment. Alignment monitors should be included in the design to maintain online control of the most critical points of the structure and eventually to set alarms.

- **Low Mass:** the Forward Silicon Tracker mechanical support structure should have low enough mass to meet the previous general requirements.
- **Division in halves:** the mechanical structure of each plane should be divided in two halves to allow for the final assembly around the beam pipe and to permit maintenance without breaking vacuum.
- **Alignment Marks:** The Forward Silicon Tracker must provide suitable alignment marks for surveying during each phase of the assembly.
- **Alignment on the halves:** The alignment accuracy between components and relative to the reference marks on each half of a plane should be better than  $10\ \mu m$ .

- **Alignment of the two halves:** The alignment accuracy between the two halves of the same plane should be better than  $30\ \mu m$  and should be guaranteed by a proper mechanical design.
- **Alignment of different planes:** The relative alignment accuracy among different planes within the same station should be better than  $50\ \mu m$ .
- **Alignment of different stations:** The alignment accuracy of different stations should be  $250\ \mu m$  with respect to the external reference marks.
- **Operating Temperature:** The design must take into account that the operating temperature of the detector will be around  $\sim -10\ ^\circ C$  and  $-5\ ^\circ C$ . Thermal stress must be considered so that the mechanical stability of the system will not be affected.
- **Alignment Stability:** The alignment stability should be in the range of a few tens of micron in the real experimental conditions.
- **Alignment Monitor:** The alignment of the system must be monitored during the operation by means of a suitable device which allows for a better than  $20\ \mu m$  precision.

#### 9.6.1.2 Cooling System

The amount of heat dissipated by the read out electronics is expected to be  $12\ W$  per half plane and is concentrated on the hybrid circuits where the chips are located. The Forward Silicon Tracker is expected to operate at a temperature around  $-10\ ^\circ C$ . The effects of radiation damage are minimized by maintaining these temperatures even when the devices are not in use. Thus, a cooling system must be designed to operate within this temperature range. Since the heat load is concentrated in a few spots of the system it is practically impossible to achieve a good uniformity of the temperature across the whole detector. Nevertheless a suitable cooling system should be designed to maintain a sufficient temperature uniformity in the whole structure and even on the sensors to avoid any appreciable degradation of the detector performance. The temperature must be controlled and reproducible. Since the operation is well below the temperatures at which the devices will be assembled, the coefficients of thermal expansion must be considered in the mechanical designs.

- **Thermal Uniformity:** the maximum temperature excursion in all the system but the front-end chips, once equilibrium is reached, shall not exceed  $\pm 5\ ^\circ C$  on any plane.
- **Thermal Stability:** the temperature stability in all the parts of the system must be better than  $\pm 2\ ^\circ C$  during its operational lifetime .
- **Temperature Reproducibility:** the average temperature of the system shall be reproducible (under active control) to  $\pm 1\ ^\circ C$ .
- **Temperature Read-back:** The temperature of each ladder hybrid shall be readable to a precision of  $\pm 0.5\ ^\circ C$ .

## 9.6.2 Implementation

The support structure we are designing in collaboration with a specialized Italian company consists of several practically identical elements, which must be combined together to assemble a station. The basic element of the system is a *ladder*, depicted in Fig. 9.14, consisting of

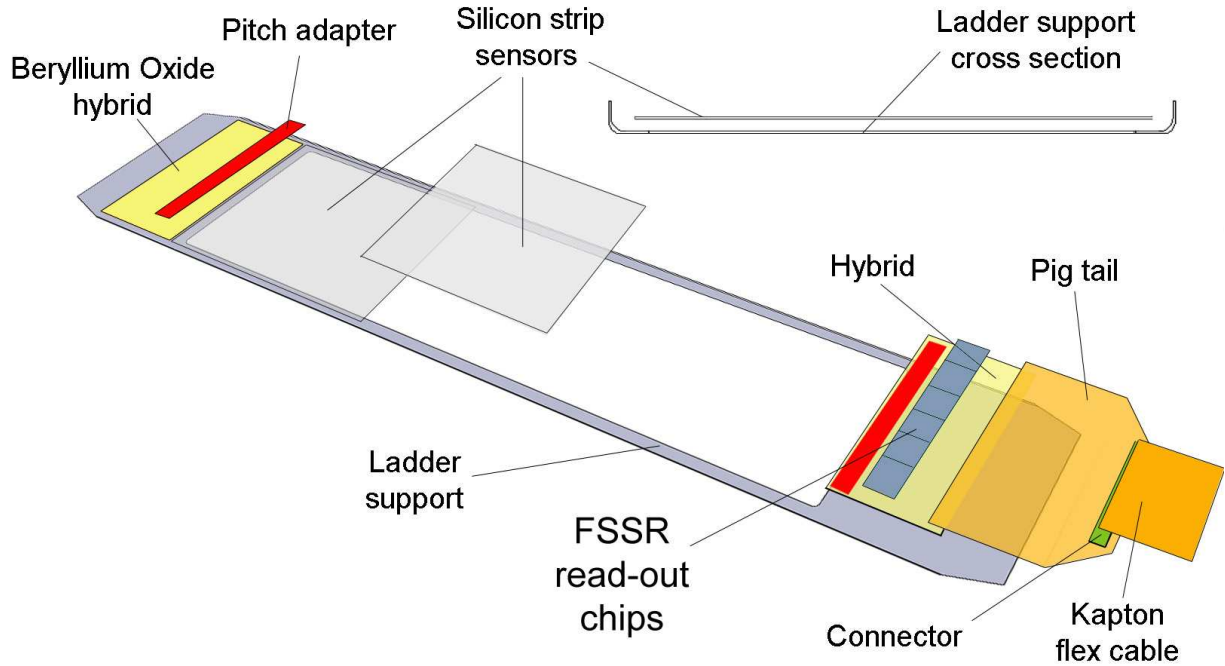


Figure 9.14: Sketch of a ladder support and the relative placing of silicon strip sensors, hybrid circuit, pig-tail fan-out and kapton flex cable.

a thin carbon fiber support and capable of holding four silicon strip sensors and the read-out hybrid circuit at the two opposite ends. The element of the structure, which serves as support for a half plane, is sketched in Fig. 9.15. It consists of a very light composite structure made of a sandwich of two thin carbon fiber layers with Rohacell inside. The two ladders of the half plane are attached on the opposite sides of this structure, one on front plane, the other on the back plane. A cooling duct is located inside the structure and reaches the regions where the hybrid circuits are located and the heat load is concentrated. The total material on each plane, including the support, the ladders with sensors, hybrids and pitch adapter is about 0.4 % of a radiation length (averaged over a 30 cm radius circle around the beam pipe), thus meeting our requirements.

The structure is designed in such a way that two half-planes can be coupled together to form a plane and three planes can be stacked to form a station. The relative positioning of the six elements comprising the station is guaranteed by suitable pins, to provide a relative

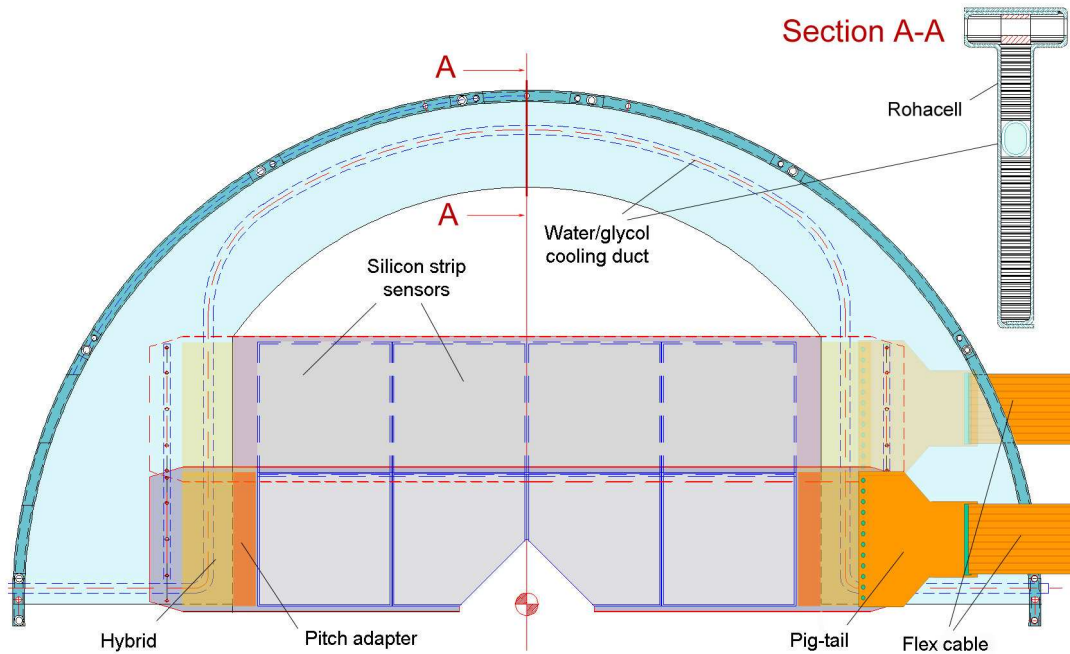


Figure 9.15: Sketch of the mechanical support of a Forward Silicon Tracker half-plane. It consists of a very light composite structure made of a sandwich of two thin carbon fiber layers with Rohacell inside. The two ladders of the half plane are attached on the opposite sides of this structure, one on the front plane, the other on the back plane. A cooling duct runs through the structure and reaches the regions where the hybrid circuits are located and the heat load is concentrated.

alignment of the two halves of a plane to within  $10\ \mu\text{m}$  and that of different planes to within  $20\ \mu\text{m}$ .

By covering the bottom and the top of the stack with a very light material, having some additional care for the interface with the beam pipe (see Fig. 9.19), we naturally define a station enclosure, in which we can improve the temperature uniformity. Indeed, once the stack is immersed in a dry-air atmosphere, the gas exchange with the outside will be drastically reduced and even the dry gas filling the enclosure will be efficiently cooled by the inner walls of the carbon fiber structure, which are in close contact with the embedded cooling ducts.

The support structure described above, constitutes what we call the “*micro-strip inner support*” since an additional structure, “*the outer support*”, is required to hold the stations in their final position around the beam pipe. For this additional support we developed a solution designed to reduce as much as possible the amount of material in the acceptance. Since the straw tubes in this region are interrupted because of the presence of the beam-

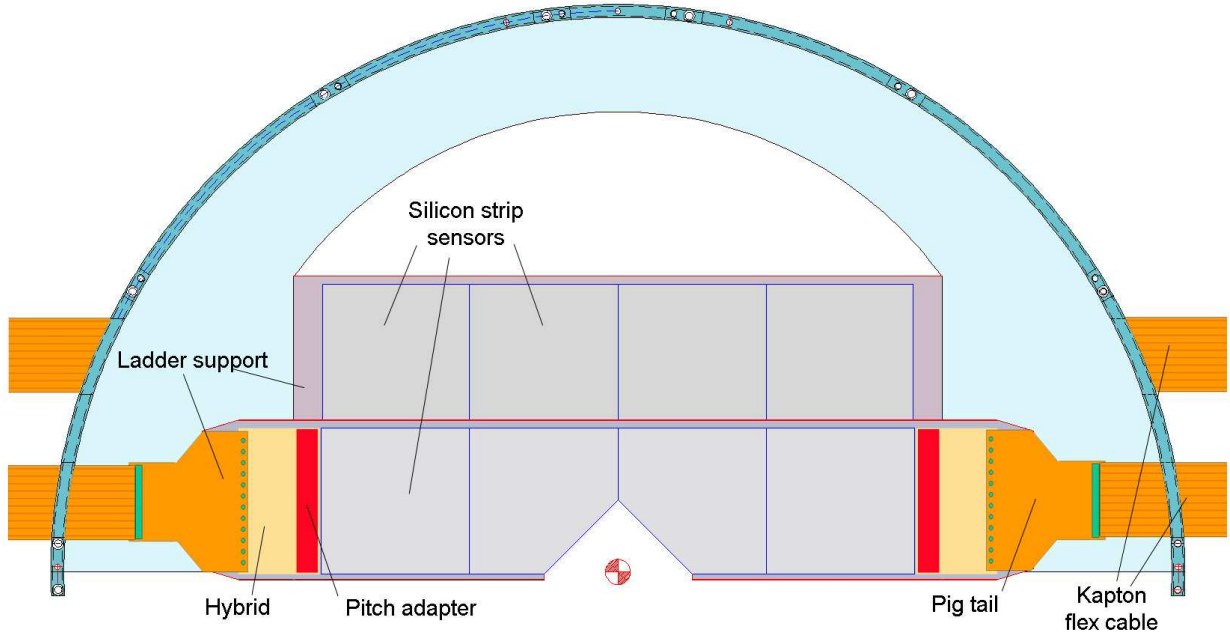


Figure 9.16: Sketch of the Forward Silicon Tracker support showing the organization of flex-cables, which cross the structure through dedicated slots.

pipe and thus require a support which can take their tension, we designed a structure which serves as support both for the straw tubes and the Forward Silicon Tracker station. This additional support is directly integrated in the straw structure as shown in Fig. 9.17. The straws of the two central modules (Module-0 straws) of the X-view are assembled inside a carbon-fiber Rohacell composite strut, which provides them with the adequate tension and has a central disk to support the Forward Silicon Tracker station. This solution avoids any duplication of unnecessary material in the experiment acceptance cone. The central disk and the underlying strut have a radial slot to allow for assembly around the beam pipe. The Forward Silicon Tracker inner supports are assembled directly on the disk as illustrated in Fig. 9.18. On the same figure we also show how this structure couples with the nearby standard straw chambers. The disk also serves as the bottom cover of the station enclosure once complemented with a proper insert to fill the slot.

At this point, the only missing pieces of the mosaic are the station top-cover and the interface with the beam pipe. In Fig. 9.19 we give a possible solution: once a tube of very light material, such as Rohacell, is fit into the hole of the outer support disk, then a cover with the same shape of the previous disk, but much lighter, can be put on the top of the structure to obtain an ideal enclosure to run the Forward Silicon Tracker. Clearly, this

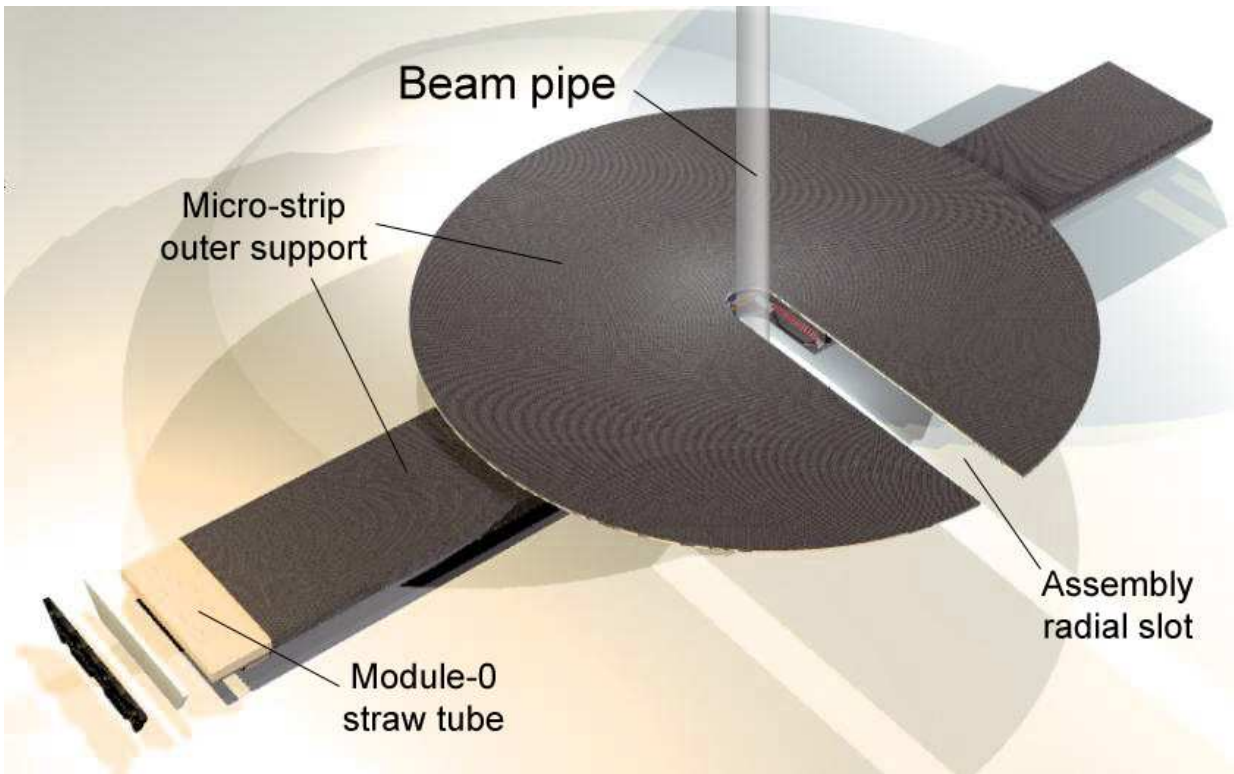


Figure 9.17: The Forward Silicon Tracker outer support structure. It is directly integrated in the nearby X-view straw structure and provides support for the Forward Silicon Tracker stations and the straws themselves. The central disk and the underlying strut have a radial slot to allow for assembly around the beam pipe.

structure should be immersed into a dry-gas atmosphere at room temperature, which must be purged with high enough flow to avoid condensation on the external walls of the inner support and to prevent from cooling the nearby regions.

### 9.6.3 Fiber grating positioning monitor

A series of Fiber Bragg Gratings (FBGs) will provide real time strain monitoring of the Forward Silicon Tracker support. As already described in the pixel detector chapter, FBG sensors are optical strain gages placed inside the optical fiber core and consequently will not add any additional mass to the one of the fiber. The fiber diameter is about 200 microns including the acrylate coating. It is possible to multiplex several of them in the same fiber.

In Fig. 9.20 we have considered a number of sensors per fiber that varies from a minimum of three to a maximum of six. The sensors are capable of measuring strain along the fiber direction. Using this information it is possible to reconstruct the elastic displacement of the structure. The FBG colored in blue in the picture are mainly devoted to determine the bending of the support along the X-Y plane while the green ones are devoted to determine



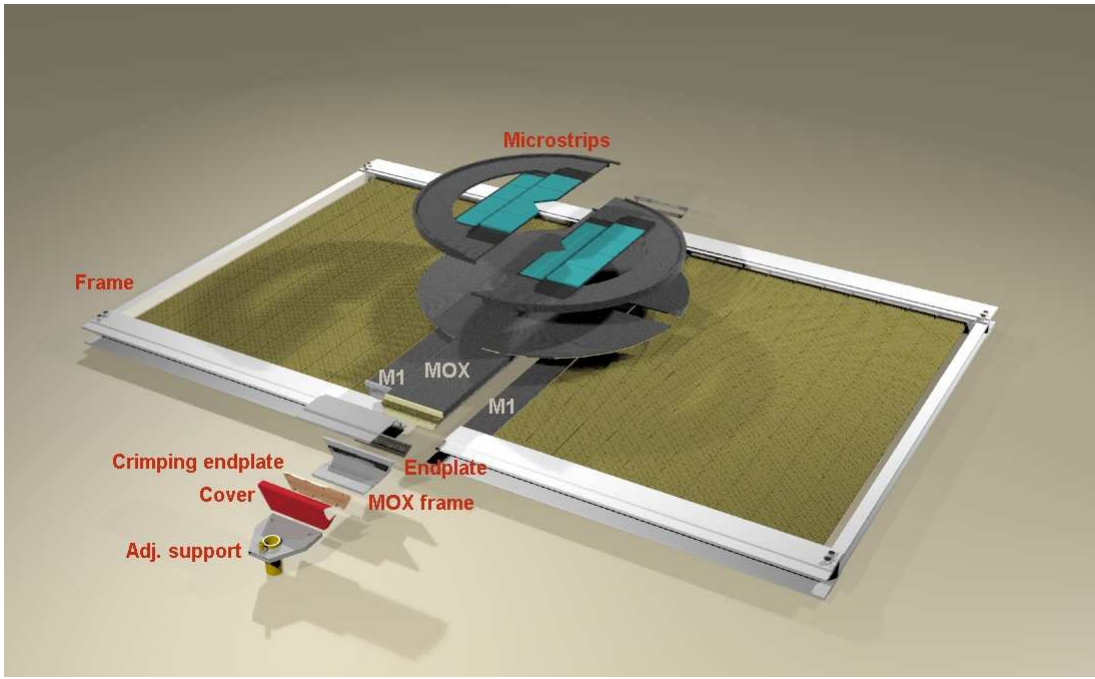


Figure 9.18: Assembly of the Forward Silicon Tracker planes on the outer support structure. The expanded view shows the regular straw tubes in the proximity of the central gap, the Forward Silicon Tracker outer support, which contains the straws to fill the gap, and the two halves of the first Forward Silicon Tracker plane to be assembled on the central disk.

the bending of the support along the Y-Z plane. There are also four more sensors, shown in red in the picture, that measure the strain in the orthogonal direction with respect to the others (in order to avoid confusion only two sensors have been drawn). These will contribute to the reconstruction of torsional deformations. Finally the sensors in pink are required to monitor the deformation of the plate. As can be seen, the sensors are positioned in such a way to be able to separate bending from pure traction. In fact all sensors are organized in couples. For instance, for each blue sensor on the left, you will have another blue sensor on the right, that allows the separation of pure traction in the Y direction from the bending in the X-Y plane. Analogous considerations can be performed for the other sensors. The blue sensor on the upper left is in the same fiber as the green ones so that this fiber will contain 5 sensors. The other three blue sensors are in an independent fiber. The four red sensors are in another independent fiber. Finally in a fourth fiber six more sensors are considered for monitoring the plate deformations. So with this configuration we have 12 sensors for monitoring deformed shapes of the vertical support and 6 sensors for the plate. The total number of sensors required is  $18 \times 6$  stations = 108 sensors. Actually at the present stage of study this number of sensors seems underestimated if a high resolution deformation monitoring is required; for this reason the requested number of sensors is 168 typically organized in strings of four sensors per fiber.



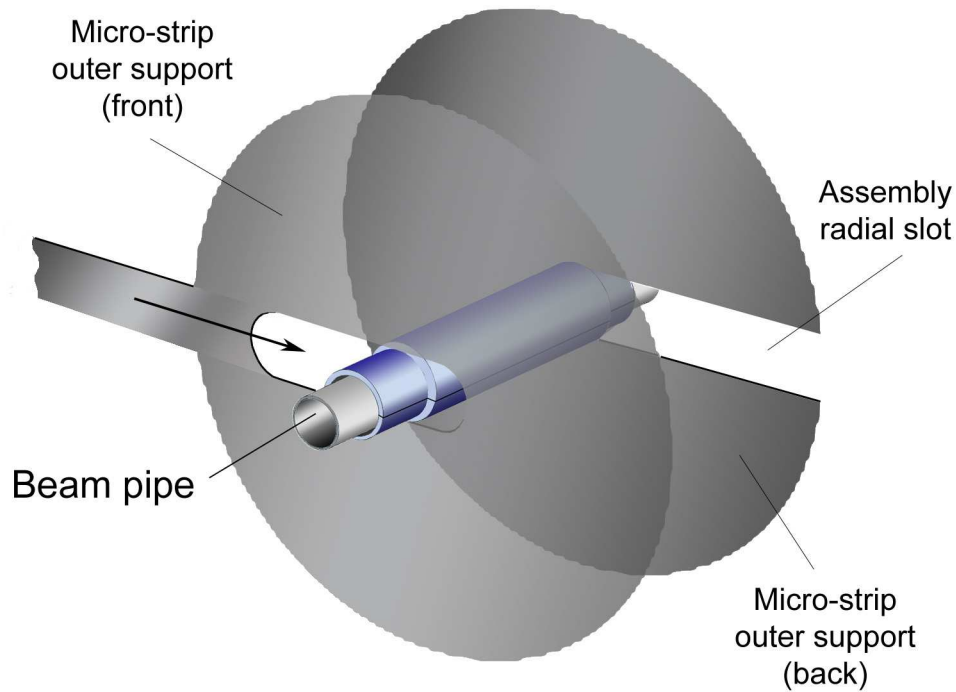


Figure 9.19: Sketch of the beam-pipe interface for Forward Silicon Tracker stations. A tube of very light material, such as Rohacell, is fit into the hole of the outer support disk; a cover with the same shape of the previous disk, but much lighter, is then put on the top of the station structure to create the Forward Silicon Tracker station enclosure.

#### 9.6.4 Cooling system

The cooling system for the Forward Silicon Tracker employs a water-glycol liquid mixture flowing in a closed loop circuit at  $-20^{\circ}\text{C}$  and sub-atmospheric pressure. It is designed to absorb the heat generated by the read out electronics. In addition, another system is required to ensure a dry-gas environment to run the Forward Silicon Tracker and to prevent them from cooling the regions around the station enclosures. In designing and costing these systems we heavily used the analogous project developed for D0 RUN IIb upgrade.

The total power dissipated by our electronics will be 500-600 W; including the heat coming from external sources, such as power dumped into the coolant by the circulation pump, the warm dry-gas flowing outside the station enclosures and the losses along the lines, the total power to absorb should not exceed 1 KW.

The coolant distribution system consists of a closed-loop line which starts from an open reservoir, crosses in parallel all the support elements of the stations, enters the chiller/pump unit and finally goes back to the initial reservoir. The pressure in the loop is set by the open reservoir: it starts from 1 Atm and progressively drops until it reaches the minimum value

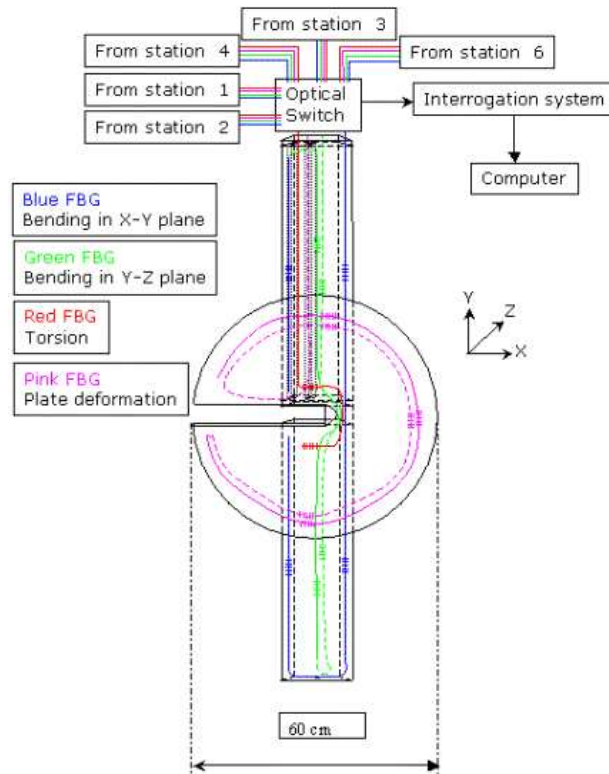


Figure 9.20: Sketch of the FBG positioning monitor system

at the input of the chiller pump. The coolant reaches all the station locations through a vacuum-jacketed supply pipe; it is distributed through manifolds to each duct embedded in the station structure and it is recollected on a vacuum-jacketed return pipe. An air-separator tank is inserted on the line just before the chiller. The system is provided with a backup chiller unit and a backup vacuum pump for the air separator.

The dry-gas distribution system employs dry-air at room temperature to purge all the sections of the acceptance cone along the beam axis where the stations are located. These sections can be easily delimited by very light Mylar foils placed on both sides of the external frame carrying the Junction Cards, to which the flex cables are connected. The dry-air enters the sections from the sides and leaves from a narrow annular opening around the beam-pipe. Given the substantial lack of any sealing, significant flows of dry-air will be required to guarantee an adequate purge of the sections.

## 9.7 R & D

### 9.7.1 Sensors characterization and irradiation tests

We bought three sensors from CMS (CMS IB2 sensors,  $61 \times 116 \text{ mm}^2$  active area,  $120 \mu\text{m}$  pitch,  $320 \mu\text{m}$  thickness,  $30 \mu\text{m}$  implant width,  $< 100 >$  crystal type) and have recently purchased another sample of ten to study their characteristics and performance. In particular we are interested in understanding the behavior of these sensors when only a small region of them is just going through the *type-inversion* process.

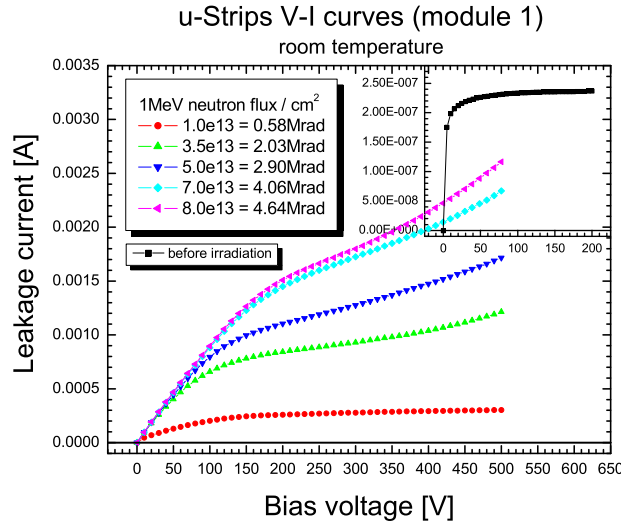


Figure 9.21: V-I curves for different values of the irradiation dose. The histogram in the inset shows the same characteristics curve before the irradiation.

This represents a kind of steady situation for the sensors during their operation in BTeV. Indeed, the *type-inversion* will be initially located on the inner edge of the sensors and then, will slowly move toward the opposite edge. Operating the sensor in this situation is particularly critical since strips will cross regions characterized by a continuous change of the doping, from a *n* type bulk, essentially equal to that of non irradiated sensors, to a *p* type bulk, passing through a condition where the bulk has no effective doping. The depletion voltage will consequently vary over a wide spectrum of values, reaching a minimum where the *type-inversion* is taking place.

During the summer of 2003 we irradiated two CMS sensors at the Indiana University cyclotron up to a dose of about 5 Mrad. This dose corresponds to what we expect to accumulate in BTeV in 10 years of operation. The sensors were exposed to a 200 MeV proton beam having roughly a gaussian profile with a  $\sigma \sim 1 \text{ cm}$ . The beam was centered

on the middle point of one edge of the sensors to reproduce the conditions of the irradiation they will receive in BTeV.

In Fig. 9.21 we show the  $V$ - $I$  curves at different doses for sensor 1. The inset shows the behavior before the irradiation. The measurements were taken at  $26^\circ\text{C}$  (room temperature). Fig. 9.22 compares the  $V$ - $I$  characteristics just after the irradiation with that measured the following day, once the sensor was cooled down to  $-17^\circ\text{C}$  the leakage current became more than two orders of magnitude lower. In Fig. 9.23 we quote the measured leakage current

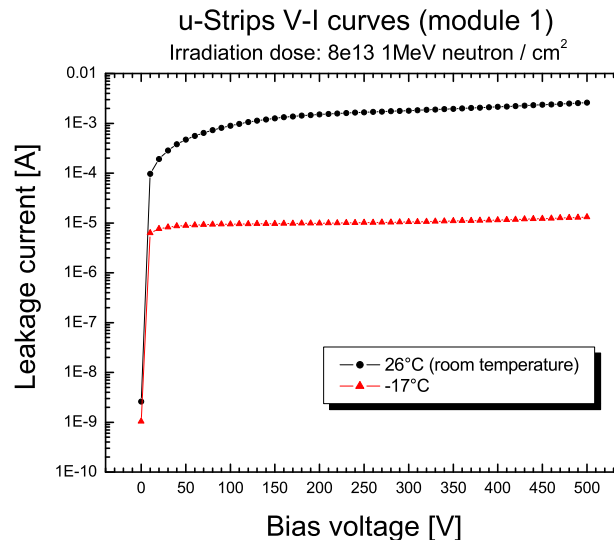


Figure 9.22: The  $V$ - $I$  characteristics of the irradiated detector at two temperatures. The black curve at room temperature,  $+26^\circ\text{C}$ , just minutes after the irradiation, the red line the next day, after cooling the detector down to  $-17^\circ\text{C}$ .

as a function of the absorbed dose at a fixed bias voltage,  $V_B = 400\text{ V}$ , and compare measurements with what we should expect from the theory. The agreement is very good at high temperature; at  $-17^\circ\text{C}$  the measured values are a little lower than expectations probably because the actual temperature of the sensors in the refrigerator was lower than that reported by a thermometer which was placed above them but not in direct contact.

Two different setups have been used to fully characterize the sensors before the irradiation tests:

- *A laser test-bench*: an  $XY$  micrometric table with a collimated laser source mounted on the  $Z$  axis (Nd:YAG laser,  $\lambda = 1064\text{ nm}$ ,  $\sim 2\text{ mm}$  absorption length in Silicon). Measurements are carried out with a PC-based commercial data acquisition system, VA-DAQ, manufactured by Integrated Detector & Electronics (IdeAs), Fig. 9.24.

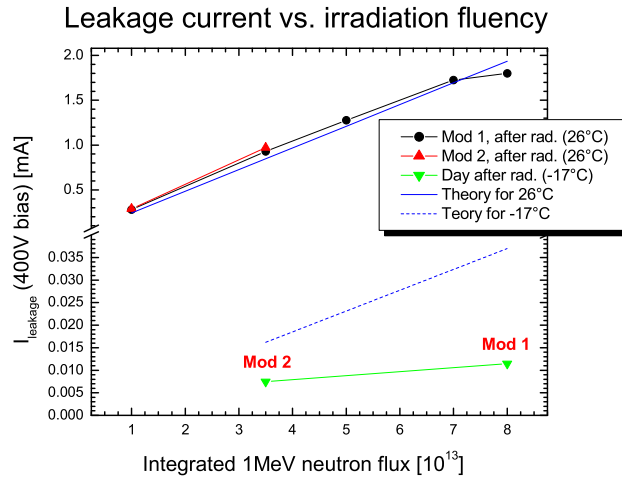


Figure 9.23: Leakage current as a function of the absorbed dose at a fixed bias voltage of 400V and for two different temperatures. Theoretical expectations are superimposed as indicated in the figure.

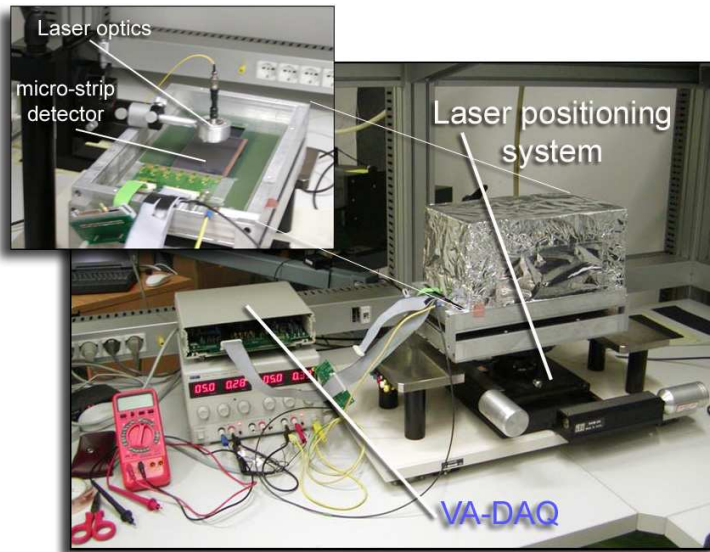


Figure 9.24: The laser test-bench, used to characterize the detectors, as described in the text.

- *A cosmic ray telescope*: a telescope of 6 micro-strip stations, each featuring two 384 channel detectors for  $X$  and  $Y$  measurements. Measurements are carried out using a

custom DAQ (borrowed from the AGILE space-borne experiment). The DAQ is based on a VME system and uses the TAA1 chips, also manufactured by IdeAs, Fig. 9.25.

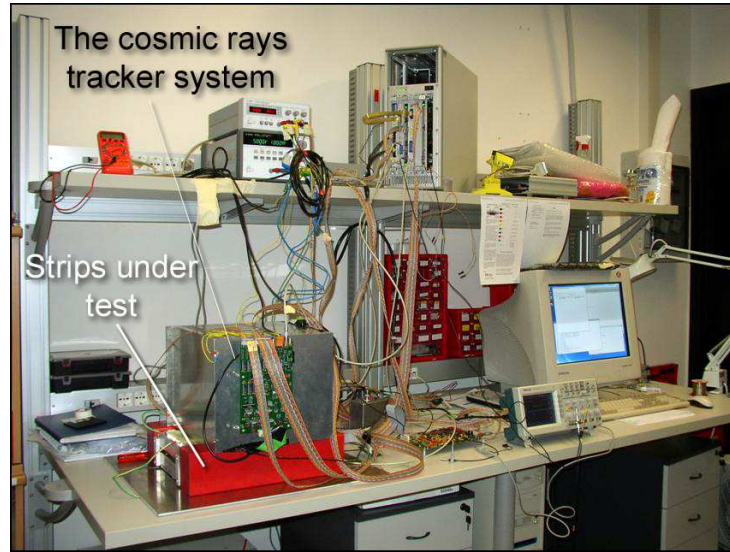


Figure 9.25: The cosmic rays tracker system, used to characterize the detectors, as described in the text.

The read out chips used were the VA/TA chips manufactured by IdeAs.

We will comment on some of the measurements we performed. In Fig. 9.26 we show the result of scanning a sensor with the laser source. The total collected charge by the illuminated strips is reported as a function of the position on the sensor. The gain of all channels was equalized by measuring the MIP peak of cosmic rays with the second setup. The projection of the previous plot along the strips is given in Fig. 9.27. On this particular sensor, we observe a drop of about 5% in the collected charge from the end of the strip nearest the read out chip to the opposite end.

A final step in the characterization of the detectors has been the analysis of data taken using the irradiated detector (5 MRad ). A setup very similar to the non-irradiated one was used, but the whole system was placed in a thermally controlled environment to keep the temperature constantly down to  $-13^{\circ}\text{C}$  and thus, to slow down the reverse annealing effect. (See Fig. 9.28) We first accumulated a set of measurements on a non-irradiated detector, in order to set a reference, and then repeated that same set on the irradiated one. The various positions of the laser spot are presented in Fig. 9.29, corresponding to a scan of the sensor along a central strip, whose end point was centered in the highest irradiation area of the incoming beam. The voltage bias was 160V for the non-irradiated detector, above the full depletion, and 350V for the irradiated one. The results are shown in Fig. 9.30a; the upper (blue) points, corresponding to the non-irradiated detector, feature a drop in charge collection of about 7% moving away from the read out chip. The lower (red) points,



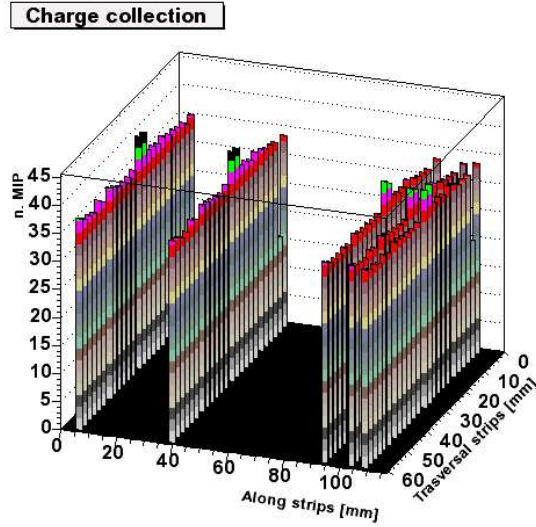


Figure 9.26: Scan of a CMS sensor with the laser source before the irradiation. The total collected charge by the illuminated strips is reported as a function of the position of the laser on the sensor.

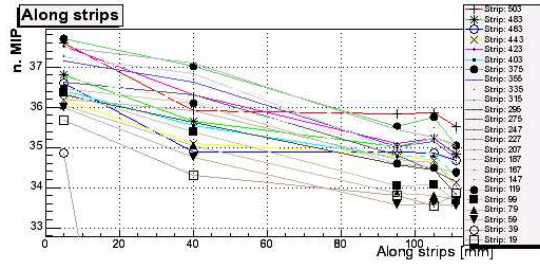


Figure 9.27: Total charge collected as a function of position of the laser source along the strips.

corresponding to measurements on the irradiated detector, show an additional drop in charge collection of about 5%, entirely due to irradiation damage.

In Fig. 9.30b, we show the collected charge as a function of the bias-voltage for each position on the irradiated sensor. These results are very preliminary since we still need to check for systematic effects, but they are certain enough to demonstrate that these sensors can be safely employed in BTeV for at least ten years, without any important degradation of performance. The measured loss in charge collection is limited to a few percent even operating them at a bias-voltage value of 350 V which is well below the breakdown region.

In conclusion, these measurements confirm the excellent performance of the CMS sensors and make us confident that they represent an excellent choice for BTeV.



Figure 9.28: The setup used to measure irradiation effects. *a)* The irradiation target of the Indiana University Cyclotron Facility. *b)* The aluminum cage lodging the irradiated sensor. *c)* The hut containing the measurement setup: visible is the laser and the alignment camera. *d)* The coolant refrigerator, used to maintain the detector at a constant  $-13^{\circ}\text{C}$ . *e)* The rack with the laser control system.

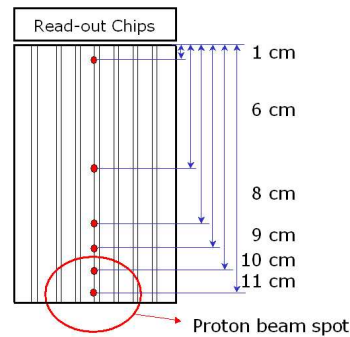


Figure 9.29: Laser spot positions for several charge collection measurement along a strip in the central region. The end point was centered in the highest irradiation area of the incoming beam.



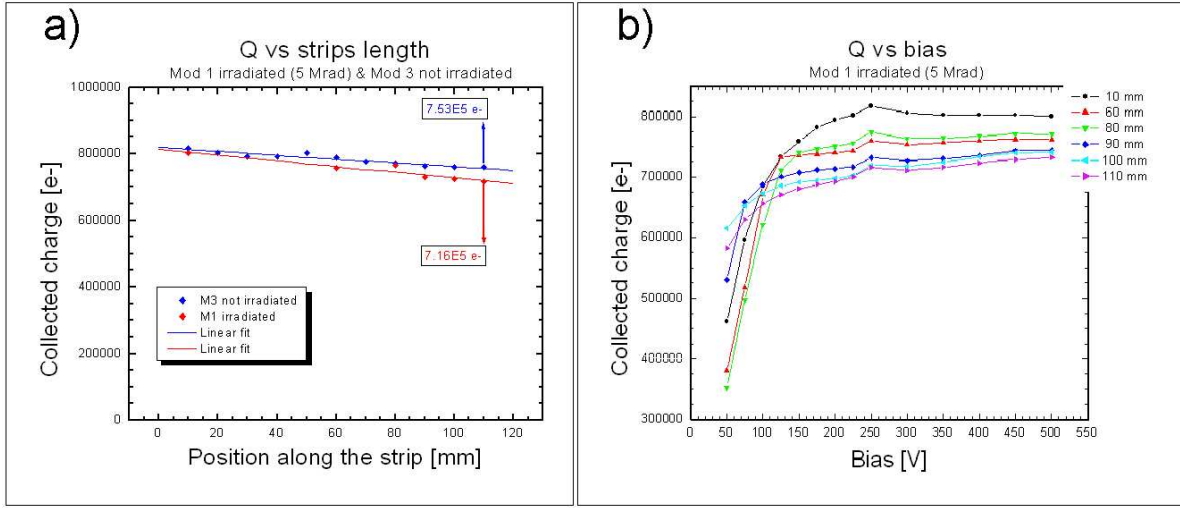


Figure 9.30: Charge collection along the strip. In fig. *a*, showing the collected charge vs. position along strip, the upper (blue) points are relative to the non-irradiated detector, lower (red) points to the 5 MRad irradiated one. Fig. *b* shows collected charge vs. bias voltage for different positions along the strip.

## 9.8 DAQ system for tests and production

### 9.8.1 Introduction

This section describes the DAQ system we developed for tests and diagnostics during the R&D and the production phases of the Forward Silicon Tracker. The same DAQ system will also be used by other BTeV groups for test beam activities. During the design and implementation process of the DAQ, several modern computing techniques have been tested and employed; we will certainly make fruitful use of the expertise acquired at this stage for the design of many aspects of the final DAQ system.

This rather sophisticated read-out system has been successfully used to make extensive laboratory tests with the pixel detector and is installed and operational at the test beam (we remind readers that the digital read-out chip is the same for both pixels and silicon strips).

### 9.8.2 Description

The DAQ design is based on the PCI bus protocol, a widespread standard in the computing industry, which offers several benefits, one being its relatively low cost and another the large amount of available core software to develop custom applications. The digital part of the Forward Silicon Tracker front-end is designed to be practically the same as that of the pixel detector, thereby allowing for a common read-out scheme for these two detectors.

In their final configurations, both the pixel and the silicon strip detectors will be read out in a sparsified mode, with no external trigger to drive the incoming data flux. Any system devised to read the data from of these detectors must be able to cope with two different clocks, the one used by the read-out chips and the one used by the read-out processes on the host computer (usually the CPU clock). The different pace of these clocks, along with possible rate fluctuations due to varying beam intensities, can create bottlenecks in the transition of data from the detectors to the final mass storage on the host computer. This problem has been the central focus of our design of the DAQ, in order to allow the system to operate in an efficient and lossless way under a sustained high data rate.

In our design each detector is connected to a PMC (Programmable Mezzanine Card) [7] featuring a suitably micro-programmed FPGA (Xilinx Virtex II) in charge of taking care of formatting and time-stamping the data produced by the detector. The PMC is then connected to a PTA (PCI Test Adapter) board [8] featuring an Altera FPGA (for data-flow and initialization control) along with two 1 Mb memories. Several PTA boards are lodged together on a PCI bus extender and finally connected to a host DAQ PC (Fig. 9.31 shows a schematic representation of the data flow).

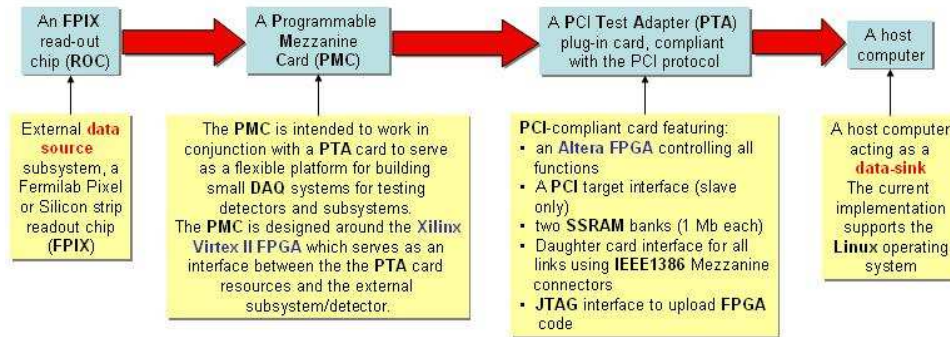


Figure 9.31: Schematic representation of the data flow from the detectors to the mass-storage, through the PMC mezzanine and the PCI cards.

Each time a strip generates data above threshold, the address, along with time-stamp information (and pulse height in the case of pixels), suitably formatted, are sent to a PTA board to be stored in one of its two local memories. The FPGA's are programmed to handle the swapping between these two local memories and the synchronization with the external read-out process (running on the host DAQ PC) to smoothly handle a sustained data rate, adequate to the test beam requirements.

The principle of operation of this read-out scheme is the following (Fig. 9.32):

- Data are received from a detector by the corresponding PMC card and fed into one of the two internal memories of its sibling PTA board.

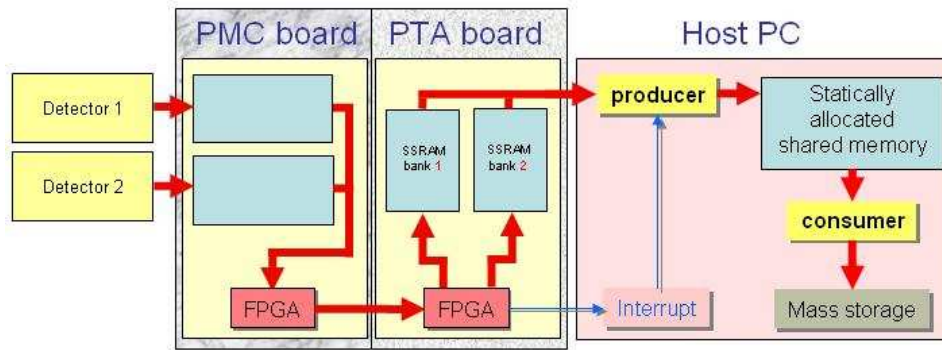


Figure 9.32: Schematic representation of the main components of the read-out chain. Producer and consumer, described in text, are the processes responsible, respectively, for reading out the FPIX chip into the shared memory and from there to the host computer.

- As soon as any memory in the system is full, all PTA boards are synchronously commanded to swap the data-flow to their memories: those used so far are frozen and immediately made available for read-out by the host computer, while the others are used to continue reading events from the detectors without any data loss. The memories on the PTA boards, therefore, act as a first level compensation buffer to account for rate fluctuations (Fig. 9.32).
- Events are then fed, by a producer process, to the host computer on a statically allocated shared memory, implemented as circular buffer (this is accomplished by a specialized process). This shared memory, usually much larger than the memory banks on the PTA boards, by a factor 50 at least, acts as a second level compensation buffer. While the PTA memories compensate rate fluctuation for an individual detector, the global shared memory does the job for all the detectors together.
- Data are then continuously flushed from this memory to mass storage by a *consumer* process, which builds events on the fly and makes them persistent.

A crucial aspect of this design is to keep the event-builder algorithm as simple and efficient as possible. An event, defined as *the set of all hits marked by the same time-stamp*, is in general spread out over several PTA boards which can in principle receive data at different rates. In absence of a specifically defined strategy to synchronize the flushing of these memories, this sparse read-out makes the event builder extremely cumbersome and inefficient, since hits of an event will be located at progressively more distant locations in the shared memory. The event builder sorting algorithm will then need to explore larger and larger sections of the memory in order to assemble all the hits of an event. Moreover, should the distance between the locations of all hits of an event become larger than the available

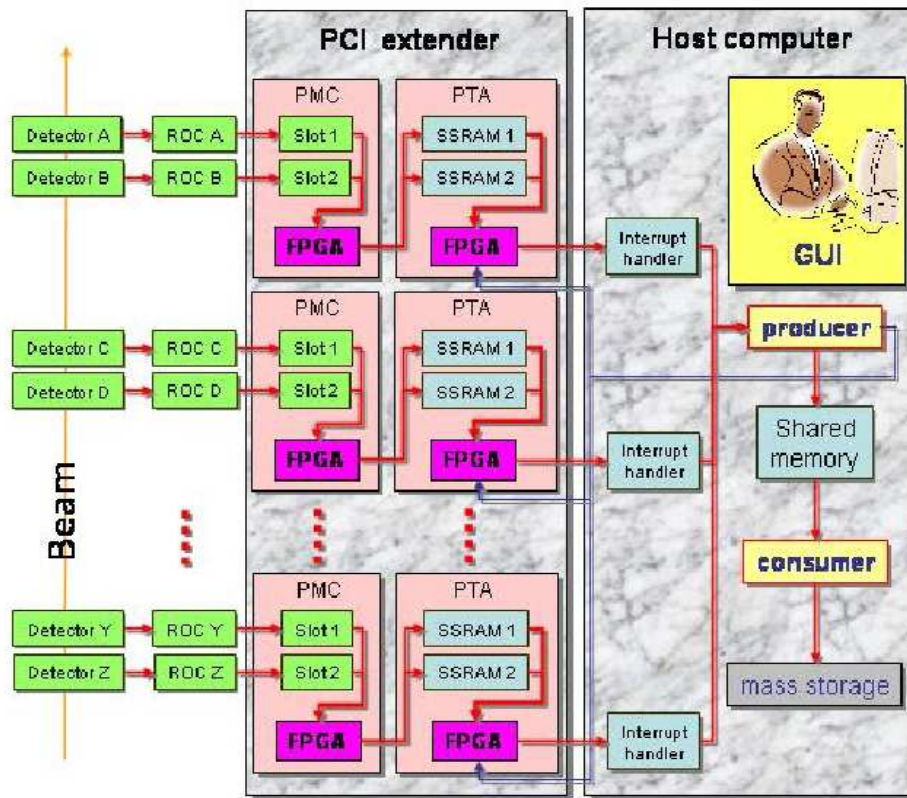


Figure 9.33: Schematic representation of a complete test-beam setup.

shared memory we could start losing events, since the pointer in the circular buffer will be reset and old locations will be overwritten.

We have therefore designed the mechanism of memory-swap synchronization to restrict the components of an event to be contained in a limited amount of memory, taking advantage of our ability to program the FPGA to generate interrupt signals. Interrupts are used to alert the read-out process that a memory on one of the PTA cards is full, in order to force a swap of all the memories in the other cooperating PTA boards (Fig. 9.33)

This is an event-driven scheme: data are collected as soon as they are produced by a detector, and no burden is placed on the DAQ software to generate signals to start and synchronize a read-out chain. This is important, since it allows testing the full functionality of the detector in an environment similar to the one envisaged for the final data taking, where no trigger is used to read out events.

Several components of this read-out have already been implemented on a Linux platform:

- The PTA board and the microprogramming of the FPGA to send and generate control

signals and interrupts. This stage required acquiring considerable expertise in using the Quartus software, used to generate code for the Altera FPGA.

- An abstract interface to the underlying PCI driver; we started using a commercially, license-bound PCI driver by Jungo, and later developed our own version. The abstract interface allows the DAQ code to be formally and factually independent of the particular choice of driver, enhancing its widespread portability.
- The interrupt-handler processes, in charge of starting the read-out of a PCI memory, synchronizing the memory-swap and the read-out of all other boards and transferring data to the external shared memory.
- The read-out process, owner of the shared memory and responsible for synchronizing with the consumer process to event-build the outgoing data and flush to a storage media. The event builder also has been implemented as a virtual class, in order to allow for different read-out schema at run-time and thus for different kinds of detectors to be read-out, greatly enhancing the potential use of this read-out DAQ.
- A package for message transmission among cooperating processes (based on the native Linux IPC system V protocol)
- A complete graphical user interface to allow users to drive the read-out process, both in a test-bench environment and in a more complex test-beam environment.
- A set of diagnostic and monitoring tools: these gather data from the DAQ by sockets on the network, where the read-out processes make information available for remote processes to use. This allows people to monitor all aspects of the test-beam progress from remote institutions in a very efficient way, without placing any computation burden on the CPU which is driving the read-out.

## 9.9 Forward Silicon Tracker Production Plan

### 9.9.1 Introduction

This document describes how we think to organize the production of all the Forward Silicon Tracker once the final design is defined and proven to satisfy all the requirements by means of tests of suitable prototypes, and before the installation at C0. It is worth noting that the Forward Silicon Tracker System consists of 7 stations, each of them having three micro-strip planes, the first measuring the X-coordinate, the second the U-coordinate and the third the V-coordinate, U and V being at  $\pm 11.30$  around the Y bend coordinate. Each plane covers an area of  $30.6 \times 31.6 \text{ cm}^2$ , has a  $100 \mu\text{m}$  strip pitch and is  $320 \mu\text{m}$  thick. The basic building block of the Forward Silicon Tracker detectors is the ladder, an array of four Silicon sensors with the read-out electronics on hybrid circuits at the two opposite ends and its own support structure. Forward Silicon Tracker planes are formed by properly combining four ladders

on very light and high precision carbon-fiber frames. Stations are obtained by stacking and rotating three identical planes. It is important to recall that the plane structure is divisible in two halves to allow for the final assembly around the beam pipe

### **9.9.2 Logical Organization of the Production**

The Production will start once the plane and station prototypes are tested and approved. We expect this to happen in fiscal year 2007.

The main deliverables of the Forward Silicon Tracker production are:

- The Half-Planes, which will be mounted around the beam pipe during the installation at C0;
- The External Support Mechanics, which will hold the stations in the right position along the beam pipe;
- The Cooling System, which will feed the cooling ducts embedded in the plane supports;
- The External Cables, which will carry signals, controls and power supplies in the region outside the acceptance cone of the apparatus;
- The Low & High Voltage Power Supplies;
- The Junction Card;
- The Data Combiner Boards.

All these deliverables are produced in a completely independent and parallel way. In the following sections we describe the organization of the production of each deliverable. A database will keep track of all the production steps of the deliverables. It will contain all the test records and shipping logs and will be accessible on the web. Its structure will be defined on the basis of the experience gained building the prototypes.

### **9.9.3 Half-Plane Production**

The Half-Plane Production consists of the production of the ladders and the plane supports, which can proceed in parallel, followed by the assembly of the ladders on the supports. Several tests during the production process require test stands equipped with DAQ to read out the FE chips. These tests are required to check the full functionality of the bare FE-chips, the Hybrids and the ladders before and after the assembly on the supports.

### 9.9.3.1 Ladder Production

The main components of a ladder are

- **Sensors**
- **Read out Chips**
- **Hybrids**
- **Flex Cables**
- **Mechanical Structure**

They will be provided by external companies and sent to SiDet for acceptance tests. Once accepted, the parts will be used to assemble the ladders.

- **Sensors**

Responsible Institutes: **Colorado U., INFN-Milano**

The main checks we plan to execute on sensors are to monitor their production process and to certify the radiation tolerance. They will be performed on 5-10% only of the total wafers. They include measurements of the test structures inserted on each wafer and a complete characterization of a sensor on the same wafer, strip by strip, before and after a high irradiation dose with protons. We think that once these checks have been performed, we can safely rely on the measurement data provided by the vendor for the remaining detectors. In any case, all sensors will be I-V and C-V characterized to be accepted. A probe station and a clean room will be required for these measurements. The test and shipment records of all the wafers will be stored in the database.

- **Read out Chips**

Responsible Institutes: **Fermilab, INFN Milano, INFN Pavia**

The read out chips will be delivered to us on 8 inch wafers. All the wafers will be probed at Fermilab, Milano and Pavia before further processing. One or more wafers will be diced so that we can carry out characterization tests to check on functionalities and performance. A probe station and a test stand with DAQ are necessary for these tests. The known good dies on each wafer will be marked. The test records and shipment records of all the wafers will be stored in the database.

- **Hybrids**

Responsible Institute: **Fermilab, Colorado U., INFN-Milano, INFN Pavia**

Hybrid Production requires the preliminary production of the Forward Silicon Tracker read out chips, which will then be assembled on the hybrid boards together with all the other required electronics, such as by-pass capacitors and temperature monitors.

The read out ICs will be selected by us before being sent to the vendor for the hybrid production. Once delivered at SiDet, Hybrids will be tested for acceptance. For these tests we plan to develop a test stand, which automatically checks the functionality and performance of all the channels. The test records, shipment records and reference to the used read out chips of all the hybrids will be stored in the database. We will later fix the tolerance in terms of percentage of channels not properly working on a single Hybrid. It will largely depend on the quality of the sensors, meaning that the higher the sensor quality, the lower the tolerance on Hybrids.

- **Flex Cables**

Responsible Institute: **Fermilab, INFN-Milano**

Flex Cables will be supplied by a vendor with the required connectors mounted on both ends and with certified characteristics in terms of impedance between lines and resistance. We plan to execute some checks of the characteristics on 10% only of cables for each delivery. The test records and shipment records of all the flex cables will be stored in the database.

- **Mechanical Structure**

Responsible Institutes: **Colorado U., INFN Milano**

The mechanical structure of the ladders will be provided by the same company producing all the carbon-fiber supports of the Forward Silicon Tracker, with a certified degree of planarity to avoid any torsion effect during the ladder assembly. We do not plan to execute any particular check on these structures, but an accurate visual inspection and a planarity check on a granite table.

- **Ladder Assembly**

Responsible Institutes: **Colorado U., Fermilab, INFN Milano**

Once a sufficient number of components are received and accepted, the ladder assembly process can begin. We plan to assemble 50% of the ladders at SiDet and have the other 50% assembled by an Italian specialized company. How to tune the minimal amount of parts necessary to start an assembly run will be decided later on, when enough experience has been gained in this job. The assembly will require the development of special mounting jigs to ensure the alignment of strips within few microns and the use of special bonding tools to wire-bond sensors and FE chips. Assembled ladders will be extensively tested both in pulse mode and with laser at SiDet using a test stand with DAQ to read out all the channels. We will define a ladder acceptance procedure, which will also specify the maximum tolerable amount of broken channels per ladder. The test records of all the ladders and reference to the used hybrids, flex cables and sensors will be stored in the database.



### 9.9.3.2 Plane Support Production

Responsible Institutes: **Colorado U., INFN Milano**

Plane Supports will be provided by the same company producing all the carbon-fiber supports of the Forward Silicon Tracker, with the required certified accuracy. They will be tested at SiDet by measuring the relative accuracy when two halves are joined together to form a plane support and when three plane supports are stacked to form a station. These tests will be performed by measuring the relative positions of the reference marks present on each half of the plane supports by means of a high precision *coordinate measuring machine* (CMM). Plane Supports will be tested also to check the cooling duct embedded in the structure. It has to be leak checked and pressure tested. The test records and shipment records of all the plane supports will be stored in the database.

### 9.9.3.3 Half-Plane Assembly

Responsible Institutes: **Colorado U., Fermilab, INFN Milano**

When two ladders and one half-plane structure are tested and declared accepted, a Half-Plane can be assembled. The alignment of the ladders will be checked at SiDet on a high precision *coordinate measuring machine* (CMM). Once two half-planes are assembled, they will be joined together to form a complete detector plane and will be tested, using a test stand equipped with a DAQ, in pulse mode and with laser in the final plane configuration with the proper cooling system. Temperature in the most critical spots will be monitored to check the efficiency of the cooling system. Structure deformations will be monitored as well on a *CMM* table. The test records of all the half-planes and reference to the used ladders and plane supports will be stored in the database.

### 9.9.3.4 Test Stands

Responsible Institutes: **Fermilab, INFN-Milano, INFN-Pavia**

To carry out full electronic test of the read out chips, the hybrids and the ladders, test stands will be set up at INFN Milano, INFN Pavia and SiDet. It is assumed that the test stands will be common to all sites, sharing the same hardware and software platform. The test stands will use the DAQ developed by FNAL and Milano for the pixel test beam.

## 9.9.4 External Support Mechanics

Responsible Institute: **Colorado U., INFN-LNF, INFN-Milano**

The External Support for Forward Silicon Stations provides a twofold function. On one side, it holds the station in the proper position around the beam-pipe; on the other side, it incorporates and supports the straws of the module 0 of the nearby straws plane. Straws are indeed embedded in the central bar of this support structure within a Rohacel foam. The External Supports for Forward Silicon Stations will be provided and certified by the same company producing all the other supports for the Forward Silicon Tracker system. They will

then be filled with straws at Frascati, fully tested and then sent to FNAL. Once delivered at SiDet, they will be measured on a CMM table to check for the accuracy of the main support points. The test records and shipment records of all the external supports will be stored in the database.

### 9.9.5 Cooling System

Responsible Institutes: **Colorado U., INFN-Milano, INFN-Pavia**

The cooling system, excluding the ducts embedded into the support structures, consists of the chilling fluid unit, the coolant circulation and distribution system, the station enclosures and all the instruments and probes to monitor temperature and coolant flows. The station enclosures provide the proper dry-gas atmosphere around the detectors in each station. The chilling fluid units produce the fluid to cool the electronics and the gas flowing in the enclosures. The system will be assembled by the Pavia and Colorado U. groups at FNAL. During production, all the parts of the cooling system will be tested before the final assembly and the test records will be stored in the data-base. The prototype cooling system developed during the R&D phase will be used to test the ladders and the planes during their production at SiDet.

### 9.9.6 External Cables

Responsible Institute: **Colorado U., Fermilab**

The external cables for the micro-strip system includes LV, HV and data cables. The Fermilab group will be responsible for the procurement and testing of all the external cables with relative connectors, but the Low Voltage cables, which will be procured and tested by Colorado U.

### 9.9.7 Low & High Voltage Power Supplies

Responsible Institute: **Colorado U.**

Both low and high voltage power supplies have to be floating and well isolated from ground. We assume we will buy commercially available Power Supply Systems.

### 9.9.8 Junction Cards

Responsible Institute: **Fermilab**

The Junction Card repeats the signals between the read out chips and the Data Combiner Board and distributes the power to the chips and the sensors. These boards will be developed, tested and produced by the Fermilab CD electrical engineering department.

### 9.9.9 Data Combiner Boards

Responsible Institute: **Fermilab**

The Forward Silicon Tracker Data Combiner Boards will be used to assemble the data from the ladders and sort them according to time-stamps. They are exactly the same as the pixel DCBs. One data combiner board will be needed per half-station. Procurement, assembly and testing of these boards will be done by the Fermilab group for all the BTeV detectors.

## **9.10 Installation, Integration and Testing Plans (at C0) for the Forward Silicon Tracker**

### **9.10.1 Introduction**

This is a general description of the Installation, Integration and Testing Plans for the Forward Silicon Tracker. As explained in the Production Document, once micro-strip half planes are assembled and checked at SiDet, they are ready for the final installation at C0. It is worth noting that micro-strip half planes are already internally aligned to ensure a sufficient relative precision when combined to form a plane and even a station. This means that the most crucial operation during the installation is to position the first plane, on the basis of which the station is built. Micro-strip installation should be coordinated with that of straw tubes since micro-strips can be installed only once the straws of the same station are already installed. The installation of the full Forward Silicon Tracker system consists of seven almost identical procedures of single station installation. We estimate that each installation will take about three days, including a full check of all the station functionality and performance. In the present staged scenario, we plan to install stations 1, 2, 5 and 6 in the 2009 shutdown and the remaining stations 3, 4 and seven in the next year shutdown. The Forward Silicon Tracker installation, just described, requires the preliminary installation of all the external electronics, the cables and cooling lines.

### **9.10.2 Preliminary installation of the Forward Silicon Tracker services**

The preliminary installation of the micro-strip services consists of the installation and debugging of all the external electronics, such as DCBs and PSs, in the proper racks, the dressing of the cables between the racks and the outer frame of each station, and the dressing of the cooling lines, both for fluid and for dry-air, between the access points provided in the experimental hall and the outer frame of each station. It is mandatory that this work be done well before the time slots allocated for micro-strip installation.

#### **9.10.2.1 Personnel and Time Required**

DCBs and PSs will be set up, run and debugged by the micro-strip group personnel. We assume that a crew of two technicians can pull all the cables for one station in one day under

the supervision of one physicist. There are 24 200' long HV cables, 6 10 m long LV cables and 12 10m long data cables for each station. At the same time, a crew of two technicians should be able to prepare the distribution and return lines for the liquid coolant and the dry-air distribution line in 5 days. Debugging and repairing of cables and cooling lines would require other two days of a specialized technician. All the operation should not take more than 10 working days. We certainly need the assistance of a surveying crew to define the positions for cable and line dressing for two days.

In total we need:

- FNAL Survey Crew: 2 days
- FNAL Tech: 2 days/station (7 stations = 14 days)
- FNAL Tech: 10 days
- FNAL Senior Tech: 2 days
- Milano Physicist: 10 days
- Milano EE: 10 days
- CU Physicist: 10 days
- CU ME: 10 days

### **9.10.3 Summary of Testing Prior to Moving to C0**

All the possible tests and adjustments will be done at SiDet before transportation to C0. Half planes are completely checked for functionality and performance using the final DAQ, if ready, or the PCI based version developed for the pixel test beam. Even the mechanical structure of the stations have been designed to minimize the alignment operations during the final installation. Half planes can be simply combined to form a plane and planes can be stacked to form a station in such a way that the relative internal alignment within the required precision is guaranteed. Only checks with optical instruments are necessary to verify that nothing unexpected happened.

### **9.10.4 Transportation of Level 2 Subproject Elements to C0**

#### **9.10.4.1 Equipment Required**

Special boxes with shock absorbers will be prepared for half plane transportation to C0. A minivan will be enough for this transportation.

#### **9.10.4.2 Special Handling**

Particular attention should be paid during the transportation to avoid shocks that could destroy the internal alignment. The material is extremely fragile.

#### **9.10.4.3 Personnel and Time Required**

If possible, our micro-strip group will personally take care of the transportation to C0. We foresee 7 transportations to C0, one for each station installation. We do not intend to move any component from SiDet if not necessary. Each transportation will not require more than half an hour.

### **9.10.5 Installation of Level 2 Subproject Elements at C0**

#### **9.10.5.1 Installation Steps**

The installation sequence for a single station consists of the following steps:

- Installation of the station support and all the connections to power supplies, cooling system, and DAQ and control.
- Installation of the first plane.
- Installation of the second plane.
- Installation of the third plane.
- Installation of the station enclosure.

#### **9.10.5.2 Equipment Required**

High accuracy surveying equipment is required to measure the position of the fiducials on the station support and on the half plane structures, and to align them with respect to the external fiducials.

#### **9.10.5.3 Special Handling Issues**

All the components of the system are extremely fragile and should be assembled in a pretty clean environment.

#### **9.10.5.4 Potential Impact on Other Level 2 Subproject Element**

The Forward Silicon Tracker installation is strictly correlated with that of the straw tubes. We plan to install micro-strips only once the straw tubes of the same station are already installed. Presumably both micro-strips and straws will share the same external mechanical structure, which can slide into the final position on high precision rails.

#### 9.10.5.5 Personnel and Time Required

The micro-strip group will take care of the major steps of the installation process. We certainly need the assistance of a surveying crew during all the installation to measure the position of the fiducials and a senior technician to provide and check the connections to the cooling system ducts, both for coolant and dry-air. We estimate that one day is enough to physically install one station and to carry out the obvious checks for continuity of the connections.

In total we need:

- FNAL Survey Crew: 1 day/station (7 stations = 7 days)
- FNAL Senior Tech: 1 day/station (7 stations = 7 days)
- Milano Physicist: 1 day/station (7 stations = 7 days)
- Milano EE: 1 day/station (7 stations = 7 days)
- CU Physicist: 1 day/station (7 stations = 7 days)
- CU ME: 1 day/station (7 stations = 7 days)

#### 9.10.6 Testing at C0

During the station assembly we plan to execute only some tests to check for the continuity of all the connections; cooling lines, in particular, have to be leak checked and pressure tested. Once the station is completely installed and sealed inside its enclosure, it can be turned on and run. Cooling circuit parameters, such as flows and temperatures, will be continuously monitored while the system is approaching its stationary regime. An extensive check of all the functionality and performance of the station detectors will be carried out by electrically pulsing the FE chips and reading it out through the final DAQ system. Particular care will be devoted to establish a clean grounding of the system. Once the station is fully checked, it will be ready for the final positioning. The station will be smoothly rolled into the final position together with the straw chambers. A final survey of all the fiducials on the station support will be done before to declare the station "*installed and operational*".

##### 9.10.6.1 Stand-Alone Subsystem Testing

The station will be tested as a stand-alone subsystem by electrically pulsing the FE chips. The major requirements to carry out this test are described in the following subsections.

- **Mechanical:**

The cooling system needed for micro-strip stations, including the dry-air purge system, should have been installed, debugged and tested well before the installation of the first station. Analogously, piping from the chiller units to the station positions in the

experimental hall should have been installed and leak and pressure checked. Obviously, the mechanical structure to roll both the micro-strip and straw stations into the final position, should be ready and calibrated.

- **Electrical/Electronics:**

All the cables for data and power supply should have been already installed and should reach the proper station locations and be ready for the connection. The final quiet AC mains should be installed and tested. The power supply systems should be operational both for high and low voltages. The Data Combiner Boards should be installed and fully checked for read out. The final bunch crossing clock should be available, or at least a fake one should be generated. All the alarms and monitors should be in place and operational (readable).

- **Software:**

The final DAQ should be ready and operational, or at least a part of that, which would allow us to read out the system through our Data Combiner Boards. It should accept and process in *OR* mode a variety of calibration triggers synchronized with the main bunch crossing frequency. Event builders should be ready for each subsystem. We will take care of all the specific software development to test and calibrate our system.

- **Personnel and Time Required:**

The micro-strip group will take care of the major steps of these stand-alone tests. For the first day we need the assistance of an expert of the cooling system to set up and run the system and another expert to check the functionality of the monitor/control system. At the end of these tests, we need a survey crew to certify the final positioning, when the station is rolled into the final position. We plan to execute all these tests on each stations in about two/three days.

In total we need:

- FNAL Survey Crew: 1 day/station (7 stations = 7 days)
- FNAL ME: 1 day/station (7 stations = 7 days)
- FNAL SE: 1 day/station (7 stations = 7 days)
- Milano Physicist: 2 days/station (7 stations = 14 days)
- Milano PostDoc: 2 days/station (7 stations = 14 days)
- Pavia EE: 2 days/station (7 stations = 14 days)
- CU Physicist: 2 days/station (7 stations = 14 days)
- CU ME: 2 days/station (7 stations = 14 days)
- CU PostDoc: 2 days/station (7 stations = 14 days)

#### **9.10.6.2 Multiple Subsystem Testing**

As described above, our *stand alone* tests will also be integration tests with the DAQ and other systems, such as the trigger and the monitor/control system. We will continue to refine this kind of tests and to debug the system up to the end of the shutdown periods available for installation.

#### **9.10.6.3 Software**

We plan to refine and update our software as required by the debugging process.

#### **9.10.6.4 Mechanical**

We plan to carefully watch the cooling system performance and possibly refine its tuning during all the available shutdown period.

#### **9.10.6.5 Personnel and Time Required**

Certainly the micro-strip group and the availability of the DAQ and cooling plant experts. The duration of these multiple subsystem tests will be roughly 10 weeks, 2 weeks in the first shutdown and 8 in the second shutdown once the foreseen micro-strip installations are completed.

In total we need:

- FNAL ME: 20 days
- FNAL SE: 20 days
- Milano Physicist: 50 days
- Milano PostDoc: 50 days
- Pavia EE: 50 days
- CU Physicist: 50 days
- CU PostDoc: 50 days



# Bibliography

- [1] G. Tonelli, *et al.*, “The R&D program for silicon detectors in CMS”; Nucl. Instrum. Meth. A 435 (1999) 109.
- [2] Nucl. Instr. and Meth. A 466 (2001) 308-326
- [3] “The Silicon Sensors for the Compact Muon Solenoid Tracker - Design and Qualification Procedure” CMS Note 2003/015
- [4] CERN Tracker TDR, CERN/LHCC 98-6 CMS TDR 5 (1998)
- [5] “Notes on the Fluency Normalization Based on the NIEL Scaling Hypothesis” ROSE/TN/2000-02
- [6] “Investigation of Design Parameters and Choice of Substrate Resistivity and Crystal Orientation for the CMS Silicon micro-strip Detector” CMS Note 2000/011
- [7] “Programmable Mezzanine Card” Pixel Detector Project Document ESE-PIX-20001101
- [8] “PCI Test Adapter Card” Pixel Detector Project Document [http://www-ese.fnal.gov/ESEPROJ/BTeV/TestStands/PCI\\_Test\\_Adapter.pdf](http://www-ese.fnal.gov/ESEPROJ/BTeV/TestStands/PCI_Test_Adapter.pdf)
- [9] Valerio Re, **et. al.**, “Status of the Design of the Analog Channel for the Strip Detector read out (Dec. 2002)”, BTeV-doc-1553-v2.
- [10] Valerio Re, **et. al.**, “Status of the Design of the Analog Channel for the Strip Detector read out (Feb. 2003)”, BTeV-doc-1554-v2.
- [11] J. Hoff, **et. al.**, “FSSR Status Report: Completion of the Functional Design Phase”, BTeV-doc-1718-v4.
- [12] J. Hoff, **et. al.**, “Read out Architectures for the BTeV Strip Detector”, BTeV-doc-1551-v1.
- [13] L. Ratti, **et. al.**, “The Fermilab Silicon Strip Readout Test Chip”, BTeV-doc-2866-v1.

# Chapter 10

## Front End Electronics

### 10.1 Introduction

The data acquisition systems of high rate HEP experiments typically rely on a “Level-1” trigger to reject most data before it is read out of the front-end electronics. In these experiments, data from a small fraction of the detector are read out quickly and input to the trigger system. After a relatively short and fixed length of time (typically less than a few microseconds), a trigger decision is made. During this time, data are stored in the front-end electronics or on passive elements such as delay cables. Only after a Level-1 accept occurs is most of the data read out of the front-end electronics.

By contrast, the BTeV Level-1 trigger system will take a relatively long time to make its decisions. Moreover, the time required by the Level-1 trigger will vary significantly from crossing to crossing; most crossings will be processed by the trigger system in hundreds of microseconds, but some may take orders of magnitude longer. This long, and variable, trigger latency makes it impractical to store data in the BTeV front-end electronics. Instead, all data from the entire BTeV detector, for every beam crossing, will be digitized, zero suppressed, and read out into buffer memory.

The front-end electronics associated with the different elements of the BTeV spectrometer share an architecture (see Figure 10.1). Data are digitized and zero-suppressed in electronics mounted on the detector and/or in electronics located in racks very close to the detector. Data from a number of front-end elements are collected by modules called Data Combiner Boards (DCB’s) that are also located in the collision hall. The DCB’s transmit the data over optical fiber links to the counting house. Some of the data streams are input directly into Level-1 Buffers; other data streams undergo another step of reformatting before being input to the Level-1 Buffers. Two types of custom serial links are used to transport data from on-detector or near-detector electronics and the DCB’s. One type of link is used by the pixel and silicon strip detectors. The other type of link is used by the remaining subsystems.

The Data Combiner Boards are located in 6U Eurocard subracks. A “Clock Distributor” module, also located in the collision hall, distributes a 7.6 MHz (1/132 ns) clock over equal time copper links to the DCB’s. In normal operation, this clock is derived from the

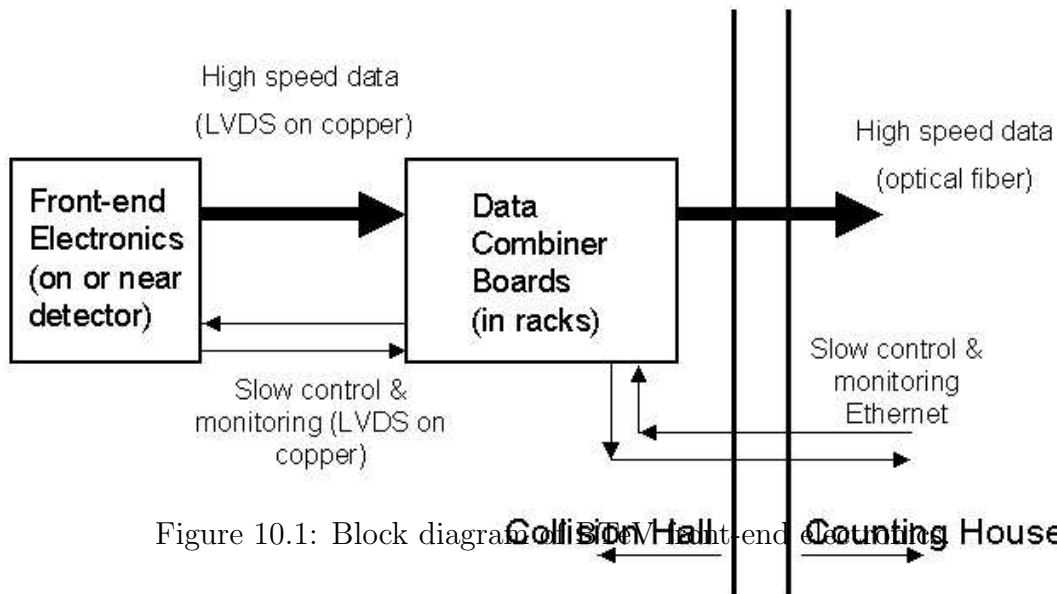


Figure 10.1: Block diagram of the Pixel Detector system.

Accelerator clock. Equal time point-to-point links between the Clock Distributor and the DCB's are also used for a “synchronize” signal that is used to synchronize various commands given to the DCB's. The Clock Distributor and the DCB's use Ethernet for slow control and monitoring communications.

## 10.2 Pixel Detector

### 10.2.1 Overview

The basic building block of the pixel detector is the module. A module consists of a silicon sensor bump bonded, depending on its size, to 4, 5, 6, or 8 FPIX2 readout chips. The chips are mounted on a High Density Interconnect (HDI) flexible printed circuit, and wire bonded to it. FPIX2 readout chips communicate with pixel DCB's using Low Voltage Differential Signaling (LVDS) over copper serial links. All of the FPIX2 chips attached to an HDI share one slow control and monitoring link, as well as common digital and analog supply voltages and grounds. Hit data is output from the FPIX2 chips on 140 Mbps point-to-point links. Chips nearest the beam are configured to use six data output links. Those further away from the beam are configured to use 4, 2, or 1 data output link.

Signals are carried on lightweight flexible cables between the HDI's and printed circuit boards on the sides of the pixel vacuum box. These printed circuit “feed through” boards carry the signals across the vacuum seal. Signals are carried between the feed through boards and the DCB's on conventional high-density cables (~10 m long). The DCB's are located in racks mounted on the outside of the return yoke of the BTeV dipole magnet. Two DCB's are used for each half-station.

## 10.2.2 Component Quantities and Locations

Table 10.1 summarizes the number of sensor modules, readout chips, DCB's, DCB subracks, and data links used in the pixel detector. Each of the sixty half-stations in the pixel detector contains one "x" half-plane and one "y" half-plane. "X" half-planes have the pixels oriented so that a precision position measurement is made in the x (non-bend) direction; "y" half-planes have the pixels oriented to make precision y measurements. A block diagram of the system is given in Figure 10.2.

	Number per "x" half-plane	Number per "y" half-plane	Number in complete detector
4-chip sensor modules	2	0	120
5-chip sensor modules	0	9	540
6-chip sensor modules	0	7	420
8-chip sensor modules	5	0	300
FPIX2 IC's	48	87	8100
DCB's	see text	see text	120
DCB subracks	NA	NA	10
140 Mbps data links to DCB's	108	149	15420
2.5 Gbps data links from DCB's	NA	NA	960

Table 10.1: Component Count

## 10.2.3 Data Structure

Each pixel hit output from an FPIX2 chip consists of 23 bits of data: an 8-bit beam crossing number, a 7-bit row number, a 5-bit column number, and a 3-bit pulse height. One additional bit is used to mark word boundaries, so 24 bits are transmitted per pixel hit. The DCB's add a 7-bit chip ID number to each hit and extend the beam crossing number to 11 bits before sending the data on commercial optical fiber links upstairs to the counting house. The data output by the FPIX2 chips is not strictly time-ordered. Time order is restored, the crossing number is further extended, and pixel data is reformatted into 16-bit words by Pixel Preprocessor boards located in the counting house. The reformatted data is stored in Level-1 Buffers and input to the Pixel Trigger Processor.

## 10.2.4 Occupancy and Data Rate Estimate

Detailed simulations have been run to verify that the FPIX2 readout chips will have adequate output bandwidth, even at luminosities much higher than the BTeV design luminosity of  $2 \times 10^{32} \text{ cm}^{-2} \text{ sec}^{-1}$ . These simulations used events generated by PYTHIA and BTeV GEANT. They included charge sharing in the pixel sensors due to geometry (track angle with respect to the detector) and charge carrier diffusion. They also included photon conversions and

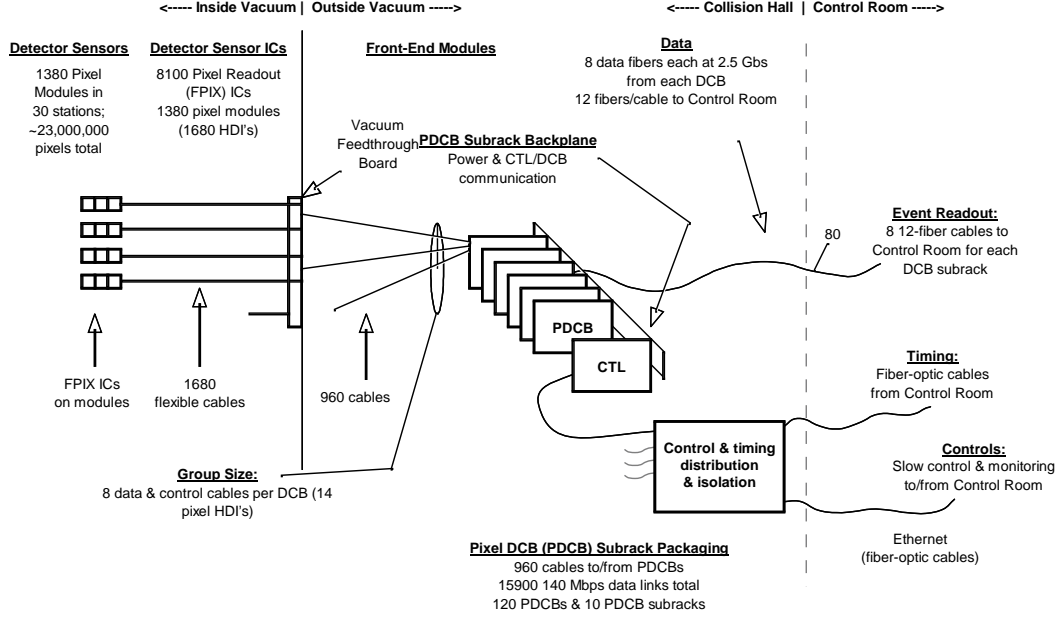


Figure 10.2: Block diagram of BTeV Pixel Detector front-end electronics.

interactions in material. Low energy delta rays (below the threshold used in GEANT) were not included in the simulations, but our 1999 test beam data indicate that this is a small effect.

The simulations show that, on average, each interaction generates just under 0.6 pixel hits in the 128 row by 22 column region of the central station closest to the beam that is covered by a single FPIX2 readout chip. The same simulations show that the occupancy falls off like  $r^{-1.6}$ . The average occupancy is approximately 0.1 pixel hits per interaction per FPIX2 readout chip.

Regardless of the operating mode of the Tevatron, the BTeV design luminosity of  $2 \times 10^{32} \text{ cm}^{-2} \text{ sec}^{-1}$  corresponds to a peak interaction rate of approximately 15.2 MHz. Therefore, the data rate into the pixel DCB's is estimated to be:

$$0.1 \left( \frac{\text{hits/interaction}}{FPIX2} \right) \times 8100 (FPIX2's) \times 24 \left( \frac{\text{bits}}{\text{hit}} \right) \times 15.2 \times 10^6 \left( \frac{\text{interactions}}{\text{sec}} \right) = 0.3 Tbps. \quad (10.1)$$

This is to be compared with the aggregate output bandwidth of the FPIX2 readout chips of more than 2 Tbps. At design luminosity, the data rate into each DCB is approximately 2.5 Gbps. The data rate from the DCB's to the pixel preprocessors is  $\sim 40\%$  higher, since 10 bits are added to each 23 bit data word. Data will be transmitted on commercial optical fiber links from the DCB's to the pixel preprocessors. The final choice of link has not yet

been made, but one possibility is that the 12 DCB's in a subrack may share eight 12-channel Molex parallel optical links with a bandwidth in excess of 2.5 Gbps per optical fiber. Each DCB would transmit data on 8 fibers with an aggregate bandwidth in excess of 20 Gbps.

### 10.2.5 Initialization, Control, and Monitoring

Slow control and monitoring of the FPIX2 pixel readout chips is accomplished through the FPIX2 programming interface, which operates independently of the data output interface. All FPIX2's on a single HDI share a synchronous serial programming link. The BCO clock is used to clock this link. Individual FPIX2 chips are identified by a 5-bit chip id, which is set by internal wire bonds. Commands to write to registers can be sent from the DCB to individual chips or broadcast to all the chips that share a programming link. Read commands must be sent to a single chip.

At the beginning of data taking, a variety of internal FPIX2 registers must be set. These include registers that control the operation of each chip as a whole, such as the discrimination thresholds and internal bias voltages and currents, and two registers that control individual pixel cells (pixel kill and test charge inject). All registers can be reset to default settings with a single command.

All control registers (except kill and inject) can be read non-destructively. During data taking, registers are periodically read back and their contents checked. If a bit error is detected (the Single Event Upset rate has been measured to be very low, but is non-zero), the register is reset. Most errors can be corrected without halting data acquisition.

Pulser calibration data will be taken during beam gaps and other times when no collisions are occurring. These data will be used to verify operational parameters such as discrimination levels and lists of dead and hot pixels.

## 10.3 RICH Detector

### 10.3.1 Overview

The RICH detector includes two different subsystems: the gas RICH, which has two viable solutions for the photon detector system, either hybrid photon detectors (HPD's) or multi-anode photomultiplier tubes (MAPMT's), and the liquid radiator RICH, which uses 3" photomultiplier tubes as photon detectors. These subsystems have very different analog signal properties, but their readout has the same conceptual design. Photodetector elements are connected to the readout electronics hosted in the front end hybrids (FE-HYB) described in more detail in the RICH detector section of the TDR. Several hybrids are connected with a front end multiplexer board (FE-MUX) that provides the interface between these front end hybrids and the associated data combiner board (DCB).

The HPD readout system consists of 153,872 readout channels grouped into 944 front end hybrids: each hybrid processes the signals from the 163 HPD pixels. More details on the technology used to implement the front end hybrids and the custom made ASICs

(VA\_BTTeV) is available in the RICH TDR section. The grouping of front end hybrids into FE-MUX boards parallels the mechanical grouping of HPD's. Signals from up to 6 HPD hybrids are combined in a single multiplexer board that provides local buffering of the HPD hits, time stamps and bidirectional data transfer between the DCB's and the FE-HYB's. The design of the FE-MUX boards is such that they can be used with the cables and DCB design adopted for other BTeV subdetectors. The alternative approach, based on MAPMT's, includes a similar number of readout channels (144,256). Each MAPMT includes 16 pixels. 8 MAPMT share the same front end hybrid, similar in conceptual design to the HPD front end hybrid. Also in this case front end multiplexer boards provide the interface between the RICH front end hybrids and the DCB's. Finally, the liquid radiator system includes 5048 PMT's. We plan to read them out with the same front end ASIC's developed for the MAPMT's.

### 10.3.2 Component Quantities

Table 10.2 summarizes the number of front end hybrids, multiplexer boards, DCB's, and serial link data cables used in the RICH readout system. A block diagram of the system is given in Figure 10.3.

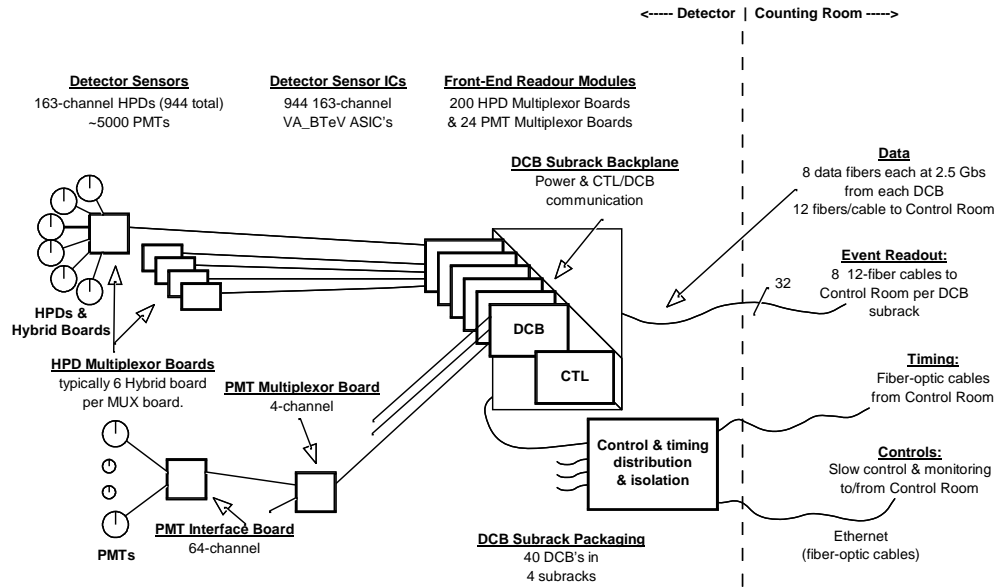


Figure 10.3: Block diagram of BTeV RICH Detector front-end electronics (shows the HPD option for the gas RICH).

Gas RICH	FE hybrids	FE MUX	Data link cables	DCB's
HPD Option	944	200	517	30
MAPMT Option	1196	332	682	36
Liquid RICH	FE hybrids	FE MUX	Data link cables	DCB's
PMT	80	24	58	4

Table 10.2: FE Modules, DCB's, and I/O cables required for the RICH detector subsystems (assuming a 16-bit data word is used).

### 10.3.3 Data structure

The output data from each front end hybrid is a bit stream containing one bit of information for every detection element for a given beam crossing. The conceptual design will be discussed with reference to the HPD system. In this case, each front end hybrid generates a 163-bit data word for each crossing. In order to use standard 50 pin connectors and cables and minimize interconnection cost, this information is shipped in 5 bursts, using a 151 MHz clock, phase locked with the BCO clock, that is provided by the DCB's to the FE-MUX boards.

The multiplexer board receives this information and generates the output data to be shipped to the DCB's. A FPGA in the front end multiplexer board takes the information from the 6 front end hybrids and stores the hit channel addresses in a FIFO memory. For each bunch crossing, the first step is to save in the FIFO the event data block (sparsified addresses). The format for the data block has not yet been finalized. If the data is stored in 18-bit words, then the only header information required is a BCO time stamp. If 16-bit words are used, header records will also be required to indicate which section of the detector the following data belongs to. In either case, the header records are followed by a list of addresses identifying the channels recording a hit during the specified BCO.

Data transfer from the FIFO to the DCB uses a 500 Mbps serial data output link also used by many of the other BTeV detector components. A slow control and timing link is included in the same cable bundle. The number of data links that are needed for each front end multiplexer board is strongly affected by the location of the photosensitive detector. The occupancy is quite different at the various HPD locations, as discussed in more detail below. The number of DCB's and data links required is also slightly dependent on the data format chosen. Our present design incorporates a variable number of serial lines depending upon the location of the front end multiplexer board. This system is suitable for any beam configuration envisaged so far, including effects of electronics noise and 20% excess capacity to account for unforeseen effects. The DCB's collect information from several FE-MUX boards and send the information, suitably grouped and formatted, to the data acquisition buffers.



### 10.3.4 Occupancy and Data Rate Studies

An extensive discussion of the occupancy studies that we performed, both in the case of 132 ns and 396 ns beam crossing period and with different assumptions for the number of interactions, has already been presented in the RICH detector description. Here we summarize the work done to determine that the readout architecture is suitable even for the hottest region in the gas RICH detector. To this purpose we have combined our physics simulation with a model of the readout system.

We have used BTeV Geant to simulate elastic and inelastic collisions. For the 132 ns scenario, we have generated events with a number of interaction per crossing following a Poisson distribution with mean 2. For the 396 ns scenario we have followed a similar approach, with a mean value of 6 interaction per crossing. We have added to the physics hits an extra 1% of noise hits. For each event, data blocks are stored in a local FIFO and then shipped to the DCB's with multiple serial lines as described before.

At 2 interactions per crossing and 132 ns crossing period, the hottest group of HPD's registers an average of 66.2 hits per crossing, of which 57 are induced by Cherenkov photons and 9.2 are noise hits. Assuming 16-bit words, this corresponds to an average data rate from the hottest multiplexer card of 8 Gbps. This multiplexer will be serviced by 20 output links with an aggregate bandwidth of 10 Gbps. If the Tevatron operates with 396 ns between crossings, then the hottest group of HPD's will register three times as many Cherenkov photons (171) but essentially the same number of noise hits (8). Thus, a readout solution which works for 132 ns operation will be more than adequate for 396 ns operation.

These simulations show that the overwhelming majority of the data produced by the RICH is produced by the HPD's. With 132 ns between crossings, and an average of two interactions per crossing, the total number of HPD hits due to light produced by tracks is 1040 per crossing. The estimated electronic noise (1% of all channels) adds another 1528 hits, so the total number of hits per crossing is 2568. Assuming a 16-bit word data format, and ignoring the small contribution to the total amount of data due to header words, the aggregate data rate is estimated to be:

$$\frac{2568hits}{132ns} \times \frac{16bits}{hit} = 0.31Tbps. \quad (10.2)$$

With 396 ns between crossings and an average of six interactions per crossing, the number of hits produced by tracks triples, but the number of noise hits remains constant, so the total number of hits per crossing is only 4943. This implies a slightly lower total data rate of:

$$\frac{4943hits}{396ns} \times \frac{16bits}{hit} = 0.20Tbps. \quad (10.3)$$

### 10.3.5 Initialization, Control and Monitoring

Prior to data taking, an initialization sequence needs to be run to set the operation mode of the front end ASICs (e.g. calibration or normal run), the list of channels that are enabled

and fine-tune the threshold of individual channels. Moreover there are some analog voltages that need to be set. The initialization sequence requires a clock and a serial line that shifts the information in the relevant registers. Commands to write the registers will be sent from the DCB's. A serial read-back of the initialization sequence can be performed for monitoring purposes.

During data taking several parameters will be monitored. In particular, the temperature on all the front end hybrids and key voltages and currents will be monitored through the slow control system. Additional quantities monitored include the expansion volume, the gas and liquid recirculation system and the cooling system. The RICH slow control will be implemented in the framework of the BTeV control and monitoring system.

Periodic calibrations will be performed during times when no collisions are occurring using a pulser to inject a controlled amount of charge on a calibration capacitor located on the front end board. In addition LEDs interspersed in the detector volume allow calibration of the overall photodetector system.

## 10.4 Electromagnetic Calorimeter

### 10.4.1 Overview

The Electromagnetic Calorimeter is comprised of approximately 10,100 lead tungstate crystals. The crystals are  $28\text{mm} \times 28\text{mm} \times 220\text{mm}$  and are arranged in a fashion that results in a circular array with a radius of 1.6 meters. Bonded to the back of each crystal is a photomultiplier tube that detects the light generated in the crystal and converts the light to an electrical signal.

Power is provided to the photomultiplier tubes by high-voltage power supplies located outside of the collision hall. Connections between the PMTs and the power supply cables are accomplished with circuitry on PMT bases. Multiple voltages are used for each PMT and groups of approximately 100 PMTs are ganged together, sharing common power supply channels.

Analog signals from the photomultiplier tubes are sent via copper cable to custom electronics located in 20 electronics subracks positioned in racks near the calorimeter. Each Analog-to-Digital Converter (ADC) Card has 32 channels of electronics. This set of electronics digitizes the analog signals from the PMTs and performs zero suppression on the data. The analog-to-digital conversion is accomplished with a full-custom application-specific integrated circuit (ASIC) that is a new version in a series known as the QIE (charge Integrating and Encoding) chip developed at Fermilab. There are 16 ADC Cards per subrack. Power distribution and board-to-board communication within the subrack is accomplished with a custom backplane. The design and construction of these racks, or the cable connection methodology between the racks and the detector, allows the calorimeter to move 16 inches in the z-direction.

Data generated by the ADC Cards is sent to Data Combiner Boards which concentrate and pass the data on to the remaining portions of the data acquisition system. The Data

Combiner Board also provides synchronization signals to the ADC Card and provides a path for signals implementing slow control and monitoring functions. Data is sent from the ADC cards to the DCB's using the same 500 Mbps serial links used in a number of other BTeV subsystems. A 32-channel ADC card can be configured to use as many as 16 500 Mbps links or as few as one link. 16 links provides enough bandwidth so that no zero suppression is required, even with a time between crossings of 132 ns. ADC cards servicing crystals very close to the beam will be configured with 16 data output links. Those servicing crystals further from the beam will be configured to use fewer links. Most of the ADC cards will require only one 500 Mbps output link.

The Data Combiner Boards used for EMCal readout will be very similar, if not identical, to those used by many of the other BTeV detector subsystems. Each DCB will accept inputs from up to 48 500 Mbps data links on 24 separate cables. The number of EMCal DCB's will be determined by cabling and packaging convenience and by the number of data link cables required. Our present design calls for 24 DCB's.

#### 10.4.2 Component Quantities and Locations

PMT's	10100
32 channel Transition Cards	316
32 channel ADC Cards	316
QIE9 ASIC's	10100
ADC Subracks	20
DCB's	24
DCB Subracks	2

Table 10.3: Component Count

A block diagram of the Electromagnetic Calorimeter front end electronics is given in Figure 10.4. Table 10.3 summarizes the number of components used in this system.

#### 10.4.3 Data Structure

The data word generated by a QIE9 will include an 8-bit mantissa, a 3-bit range (exponent), and a 2-bit capacitor id. This output will be compared with a digital threshold on the ADC card. Only channels that are above a programmable threshold will be read out. For each crossing, the ADC card will create a header word containing a beam crossing number (time stamp) and possibly a count of the number of values being read out. Hit data will consist of a channel number and a 13-bit QIE value. If 16-bit data words are used, then 2 words of data will be required for each hit.



Calibration of the QIE chips and associated electronics will be accomplished (during periods when no collisions can occur) with a DC current source that delivers a known amount of charge to the QIE inputs.

## 10.5 Muon Detector

### 10.5.1 Overview

The basic building block in the construction of a detector station is a “plank” of 3/8” diameter stainless steel proportional tubes. There are 32 tubes in each plank, arranged in two rows of 16 offset by half a tube diameter. These are held together with aluminum ribs and by the brass gas manifolds which are glued to the end of each plank. Each plank is a sturdy, self-supporting building block which acts as an excellent Faraday cage. All the tubes in the plank are terminated on one end and read out on the other. There are a total of 1152 planks in the muon detector. The data from each plank is sparsified at the detector by an FPGA (or equivalent) and sent to DCB’s using LVDS over copper serial links. Each serial link consists of a single cable with an RJ45 connector, capable of supporting 2 additional links, one of which will be used for slow control. These links are identical to those which will be used to carry data to the DCB’s for the Forward Straw detector, the Electromagnetic Calorimeter, and the RICH detector.

To minimize occupancy at small radii, planks of increasing length are arranged into pie shaped octants. To minimize pattern recognition confusion, three arrangements of planks ( $r$ ,  $u$ , or  $v$ ) are used. The  $r$  views are radial. The  $u$  and  $v$  views are rotated  $\pm 22.5$  degrees with respect to the radial views and measure the azimuthal angle,  $\phi$ . A collection of 8 octants of like arrangement is called a view, and a collection of 4 views is called a station. In order to provide redundancy in the most important view in terms of pattern recognition for the trigger and momentum measurement, the  $r$  view is repeated in each station. The whole muon detector is three stations located at the end of the BTeV experiment, interspersed between and after magnetized iron toroids and shielding. A block diagram of the front end electronics is shown in Fig. 10.5.

### 10.5.2 Component Quantities and Locations

ASDQ chips will perform the analog to digital conversion of the proportional tube signals. For our purposes, each ASDQ chip consists of 8 channels of amplifier, shaper and discriminator with a common threshold. In Table 10.4, we summarize the number of planks, ASDQ readout chips, FPGA’s, DCB’s, DCB subracks, and data links used in the muon detector.

### 10.5.3 Data Structure

The data from the muon front end system will have 2 formats depending on the number of hits in the plank. A data header consists of a 12 bit plank ID consisting of 4 bits(plank)

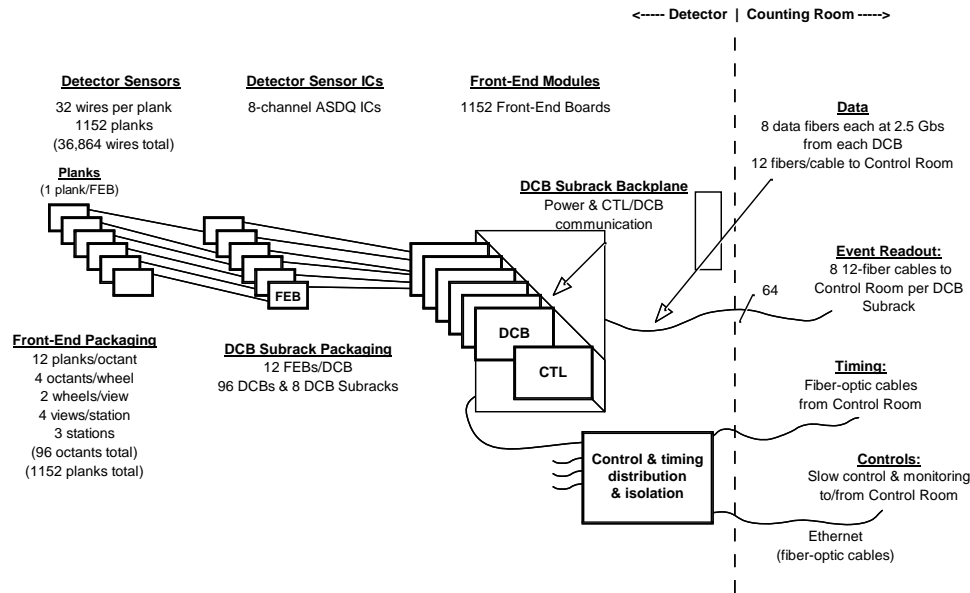


Figure 10.5: Block diagram of BTeV Muon Detector front-end electronics.

	Number per “plank”	Number per “octant”	Number per detector
Tubes	32	384	36,864
ASDQ	4	48	4608
FPGA	1	12	1152
DCB’s	1/12	1	96
DCB subracks	1/192	1/16	6
500 Mbps data links to DCB’s	1	12	1152

Table 10.4: Component Count

+3 bits(octant) +2 bits(view)+2 bits (station), an 8 bit beam crossing number, a 1 bit data type and either a 3 bit word count followed by up to 5, 5 bit words, or a 32 bit hitmap. Since the data coming from the muon system is easily time ordered, the DCB’s can optimize sparsification over the entire octant before sending the data to the Level-1 Buffers and the muon trigger.

	Station 1	Station 2	Station 3	Total
Average number of hits per crossing	42	8	9	54
Average occupancy	0.34%	0.06%	0.07%	0.15%
Maximum channel occupancy	2.5%	0.24%	0.52%	
Maximum plank occupancy	1.6%	0.17%	0.31%	

Table 10.5: Muon detector occupancies obtained from BTeVGeant simulations with an average of 2 minimum bias interactions per crossing and a crossing rate of 7.6 MHz (132 ns bunch spacing). Average occupancy is the occupancy of the detector in a single crossing. Maximum channel occupancy is the maximum hit rate for the innermost channel. Maximum plank occupancy is the average per channel hit rate of the innermost plank.

### 10.5.4 Occupancy and Data Rate Estimate

At a nominal luminosity of  $2 \times 10^{32} \text{cm}^{-2} \text{s}^{-1}$  and a bunch spacing of 132 ns, we expect 2 minimum bias interactions/crossing which are simulated using a Poisson distribution with mean of two. In Table 10.5 we summarize the detector occupancies obtained from BTeVGeant under this scenario. These occupancies and rates are fairly low by modern detector standards, and will remain low even if the interactions/crossing is increased.

Our estimate for the highest data average data rate coming from a single plank is estimated to be:

$$0.016(\text{Average Occupancy}) \times 32(\text{chnls}) \times 28(\text{bits}) \times 15.2 \times 10^6 \left( \frac{\text{interactions}}{\text{sec}} \right) = 0.22 \text{ Gbps}$$

Our estimate for the highest average data rate into into a single muon DCB, under the assumption that each hit is unique in a plank, is expected to be:

$$0.0034(\text{Average Occupancy}) \times 384(\text{channels}) \times 28(\text{bits}) \times 15.2 \times 10^6 \left( \frac{\text{interactions}}{\text{sec}} \right) = 0.56 \text{ Gbps}$$

Our estimate for the highest average data rate coming from the muon system, under the assumption that each hit is unique in a plank, is expected to be:

$$54(\text{Average total hits}) \times 28(\text{bits}) \times 15.2 \times 10^6 \left( \frac{\text{interactions}}{\text{sec}} \right) = 23 \text{ Gbps}$$

These estimates do not take into account noise in the detector. From our prototype tests, the noise/plank is small, on the order of 10 hz/tube. This adds an additional:

$$1152(\text{channels}) \times 28(\text{bits}) \times 10/\text{sec} = 0.32 \text{ Mbps}$$

to the data rate coming from the detector.

### 10.5.5 Installation, Control and Monitoring

Slow control, monitoring and data output from the muon front end boards is accomplished through the FPGA on the card. Slow serial links will be used for monitoring and control, and fast links will be used for the data output.

The data output will be gated at a nominal width of 120 ns. In preliminary tests it was determined that the arrival time of a data pulse could be localized to within 5 ns inside this gate, adding the possibility that a TDC function could be included in the FPGA programming. In order to form an output data word identifier, we assign an ID for each plank. Each front end card has a 16 bit chip ID which is linked to the bar code placed on the card during construction. All the test data from the ASDQ's on the card, the card itself, the plank, and the individual tubes in a plank will be linked in a database and tracked during construction. Placement of a plank in an octant will also be stored during construction and checked against the internal ID during the octant test. The location will then be used to assign the correct 12 bit sequence, stored in non-volatile memory, for the data word attached to the hits during readout. (The 16 bit card ID can be used as well, and the 12 bit data word ID can be assigned in the DCB in the event of a malfunction.)

A programmable default configuration will be set for the card which can be invoked with a reset to the card. The configuration of the card will be periodically checked via the slow control and a reset issued if needed. In addition to the monitoring, the setting of the threshold DAC's and various other control lines to the ASDQ, the slow control is used to invoke a test pulse common to each ASDQ and synchronized to the beam crossing clock. The beam crossing clock is delivered to the front end via the other serial line reserved for slow data.

## 10.6 Forward Straw Detector

### 10.6.1 Overview

The basic building block of the forward straw detector is the straw module. A straw module consists of 48 straws. Straw modules are combined to make up a view, and 3 views (wires vertical and tilted at plus and minus 30 degrees from vertical) make up a station. Seven stations are spread out longitudinally along the beam from station 1 (nearest the interaction point) to station 7 (furthest).

High voltage distribution, hit detection and time-to-digital conversion are performed by an "electronics package." The sense wires in high occupancy straw modules have a glass bead in the middle, effectively dividing the wire in two. These straw modules are serviced by two electronics packages; lower occupancy modules are serviced by one.

ASDQ ASIC's amplify and discriminate the straw anode wire signals. A Fermilab-designed 24-channel TDC ASIC measures the drift times. Each electronics package communicates with the Data Combiner Board (DCB) using 4 differentially driven, twisted pair (copper) serial links, two used for communications from the DCB's and two used for data



from the electronics package. A 132-ns Reference Clock is used to generate all precision clocks used within the electronics package, such as the beam crossing clock. A 151.1 Mbps “Timing and Control” link defines beam crossing markers and initiates CSR read/write functions. Two “event data” links, operating at 636 Mbps (with 8b/10b encoding and a bandwidth of 509 Mbps) move data from the electronics package to the Data Combiner Board. One data link is devoted to each of the two TDC ASIC’s in the electronics package.

Commercially available receiver-equalization chips are used to compensate for the frequency dependent characteristic of the copper cables and restore the eye diagram of data on the event data links. Commercially available driver-end pre-emphasis chips are used to partially correct the same frequency dependent characteristic for the Reference Clock and Timing/Control links. Note that these components are located away from the straw modules, on the DCB.

## 10.6.2 Component Quantities and Locations

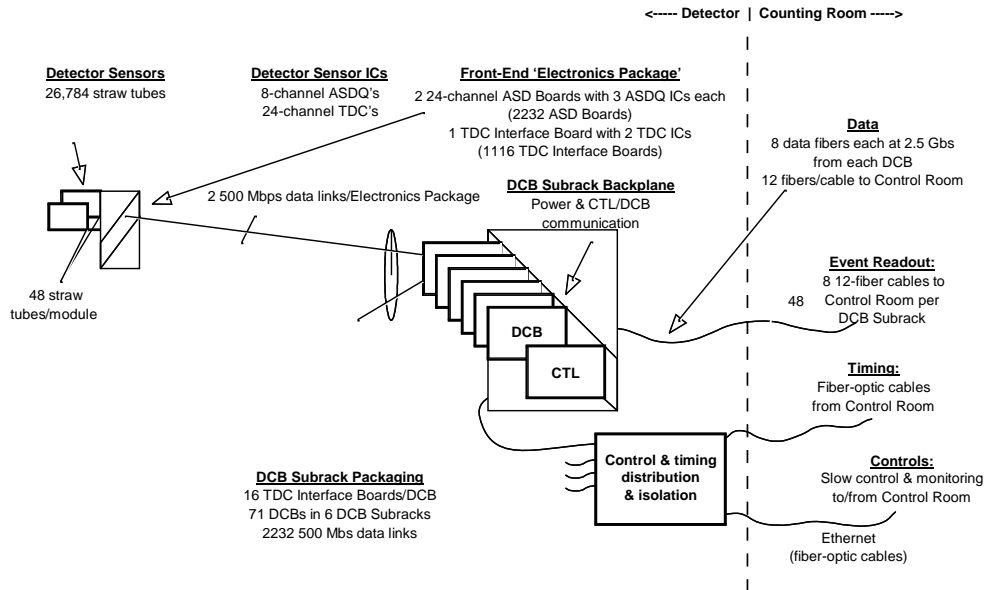


Figure 10.6: Block diagram of BTeV Forward Straw Detector front end electronics.

Table 10.6 summarizes the number of straw modules, electronics packages, ASDQ's, TDC's, and DCB's used in the Forward Straw Detector. A block diagram of the system is given in Figure 10.6.

Station (3 views)	Modules	Straws	Electronics Packages	TDC Cards	TDC Chips	ASDQ Cards	ASDQ Chips	DCB's
1	24	1152	48	48	96	96	288	3
2	36	1728	72	72	144	144	432	5
3	54	2592	108	108	216	216	648	7
4	78	3744	156	156	312	312	936	10
5	90	4320	180	180	360	360	1080	11
6	102	4896	204	204	408	408	1224	13
7	174	8352	348	348	696	696	2088	22
Total	558	26784	1116	1116	2232	2232	6696	71

Table 10.6: Component Count

### 10.6.3 Data Structure

The format of the data word generated by the TDC ASIC has not yet been specified. Each TDC ASIC will generate a “header” word every 132 ns which will ensure that data is assigned to the correct crossing number. In the data rate estimates given below, we assume that this header word is 16-bits long. Drift times will be encoded using 5-7 bits. Another 5 bits are required to specify which of 24 wires is hit. If each hit is packed into a 16 bit word, a few more bits may be used in the wire number to minimize the amount of data reformatting which must be done in the DCB's.

### 10.6.4 Occupancy and Data Rate Estimate

Simulations have been done on the expected occupancy of all modules in the detector. The required output bandwidth (assuming 16-bit data words) for the worst-case module in each station, and for the station as a whole, is shown in Table 10.7. The occupancies listed were calculated assuming a luminosity of  $2 \times 10^{32} \text{ cm}^{-2} \text{ sec}^{-1}$  and a time between crossings of 132 ns. If the time between crossings is 396 ns, the worst case occupancies will be slightly less than three times higher. The data rate out of the front end electronics will be essentially unchanged.

The aggregate data rate output from the straw system DCB's to the Level-1 buffers can be estimated as follows. The average number of hits per crossing, given two interactions per crossing, is approximately 1050. The data stream will contain many fewer header records than the data stream input to the DCB's, since packets will be sent only for crossings containing hit data, and many front end data streams will be merged. Ignoring header records (and using one 16-bit word per hit) the data rate out of the straw system DCB's is estimated to be:

$$\frac{1050 \text{ hits}}{132 \text{ ns}} \times \frac{16 \text{ bits}}{\text{hit}} = 127 \text{ Gbps.} \quad (10.5)$$

Station	Maximum Occupancy	Maximum Bit Rate	Bit Rate for Station
1	4.1%	240 Mbps	21.2 Gbps
2	4.9%	264 Mbps	30.2 Gbps
3	5.8%	290 Mbps	42.0 Gbps
4	6.2%	302 Mbps	54.7 Gbps
5	6.6%	313 Mbps	62.3 Gbps
6	6.6%	313 Mbps	68.7 Gbps
7	8.0%	354 Mbps	119.5 Gbps
Total			400 Gbps

Table 10.7: Worst case occupancy and data rates

### 10.6.5 Initialization, Control, and Monitoring

The TDC ASIC's will include digital to analog converters. Some of these DAC's will be used to provide discriminator threshold voltages for the ASDQ chips. The threshold values will be reloaded at the beginning of each store. Two test modes are envisioned for the data link between the TDC's and the DCB's; a loopback test in which data is sent from the DCB's to the TDC's and back to the DCB's, and a simpler test in which the TDC's generate a fixed pattern which can be verified by the DCB's. The TDC's will also include a self-test feature in which pulses will be input to each channel at known times. Monitoring of configuration data, and link and TDC tests will occur between stores and perhaps in the beam abort gaps.

## 10.7 Forward Silicon Detector

### 10.7.1 Overview

The Forward Silicon Detector includes seven identical stations, each with three planes, all of identical construction. Each plane comprises four ladders, and each ladder in turn is made up of four sensors. Strips on the sensors closer to the center of the ladder are wire bonded to the outside sensors and connected to FSSR readout chips located at both ends of the ladders. The FSSR readout chips share an architecture with the FPIX2 pixel readout chips. The FSSR's communicate with DCB's using LVDS over copper serial links. All of the FSSR chips on one end of a ladder share one slow control and monitoring link, as well as common digital and analog voltage and ground. Hit data is output from the FSSR chips on 140 Mbps point-to-point links. Chips on ladders close to the beam are configured to use four data output links. Those on ladders further from the beam are configured to use two data output links.

Signals are carried on lightweight flexible cables between the ends of the ladders and “splitter boards” located outside the active area of the straw chambers. Signals are carried between the splitter boards and the DCB’s on conventional high-density cables ( $\sim 5$  m long). The DCB’s are located in racks mounted as close as practical to the silicon strip stations. Each DCB is connected to 12 half ladders, so there are two DCB’s per station.

### 10.7.2 Component Quantities and Locations

Table 10.8 summarizes the number of ladders, sensor wafers, readout chips, DCB’s, DCB subracks, and data links used in the forward silicon detector.

	Number per plane	Number in complete detector
4-sensor ladders	4	84
sensor wafers	16	336
FSSR IC’s	48	1008
DCB’s	see text	14
DCB subracks	see text	2
140 Mbps data links to DCB’s	144	3024
2.5 Gbps data links from DCB’s	NA	168

Table 10.8: Component Count. Each of the seven FSIL stations contains three planes. Each ladder has 700 strips read out per end and is instrumented with six FSSR readout chips on each end.

### 10.7.3 Data Structure

The silicon strip hit format is exactly the same as the pixel hit format. This choice of format was made to simplify the design of the FSSR readout chip, even though at least 7 of the 23 bits are not needed to encode silicon strip data. Like the pixel DCB’s the silicon DCB’s add a 7 bit chip number to each data word. Also, the data from the FSSR’s, like data from the FPIX2’s, is not strictly time-ordered. As in the pixel system, time order will be restored by the modules in the control room that receive the silicon data. It is not yet determined whether or not the silicon DCB’s need to extend the beam crossing number before transmitting data to the counting room, or whether or not the silicon DCB’s will reformat the data received from the FSSR’s to eliminate unused bits.

### 10.7.4 Occupancy and Data Rate Estimate

In minimum bias interactions generated by Pythia and simulated by BTeV GEANT, an average of 97 hits are generated in the Forward Silicon Detector per interaction. Assuming



## 10.8 Data Rate Summary

The data rate into the DCB's and the number of DCB's used for each of the detector subsystems is summarized in Table 10.9.

Detector Subsystem	Data Rate into DCB's	Number of DCB's
Pixel Detector	300 Gbps	120
RICH Detector	200-310 Gbps	40
EM Calorimeter	240 Gbps	24
Muon Detector	23 Gbps	96
Forward Straw Detector	400 Gbps	71
Forward Silicon Detector	47 Gbps	14
Total	1.2-1.3 Tbps	364

Table 10.9: Data Rate into the Data Combiner Boards